Ondes 'electromagn'etiques TBF observ'ees par DEMETER

Frantisek Nemec

ÉCOLE DOCTORALE SCIENCES ET TECHNOLOGIE
LPC2E/CNRS Orléans / Université Charles à Prague

THÈSE EN COTUTELLE INTERNATIONALE présentée par :

František NĚMEC

soutenue le : 3 Septembre 2009

pour obtenir le grade de :
Docteur de l'université d'Orléans
et de l'université Charles à Prague

Discipline : physique des plasmas

Ondes électromagnétiques TBF observées par DEMETER

THÈSE dirigée par :

M. Michel PARROT	CNRS Orléans
M. Ondřej SANTOLÍK	Université Charles à Prague

RAPPORTEURS :

M. Vladimír FIALA	Institut de Physique de l'atmosphère
M. Jacques ZLOTNICKI	Observatoire Physique du Globe, Clermont-Ferrand

JURY :

Mme Věra HRACHOVÁ	Université Charles à Prague
M. Vladimír FIALA	Institut de Physique de l'atmosphère
M. Ondřej SANTOLÍK	Université Charles à Prague
M. Thierry DUDOK DE WIT	Université d'Orléans
M. Michel PARROT	CNRS Orléans
M. Jacques ZLOTNICKI	Observatoire Physique du Globe, Clermont-Ferrand

Remerciements

De nombreuses personnes ont contribué à l'accomplissement de ce travail de thèse par leur aide, leur soutien, leurs idées et leurs conseils. Je tiens ici à les remercier très sincèrement.

En premier lieu je voudrais remercier mes deux directeurs de thèse : Michel Parrot et Ondřej Santolík. M. Parrot a dirigé mes recherches pendant mes séjours au Laboratoire de Physique et Chimie de l'Environnement et de l'Espace (LPC2E) à Orléans. Il est le responsable scientifique du satellite DEMETER et aussi l'investigateur principal des capteurs magnétiques. Il a partagé avec moi ses connaissances profondes en traitement du signal et en analyse des données. Je le remercie également pour son effort consacré à l'amélioration du manuscrit. O. Santolík a pris la responsabilité de superviser mon travail à l'Université Charles à Prague. Je le remercie pour les conseils et les discussions scientifiques très formatrices. Je voudrais aussi le remercier de m'avoir initié à la physique des plasma spatiaux. Il m'a encouragé à démarrer une thèse de doctorat en collaboration avec le LPC2E et il m'a incité à participer à de nombreux congrès, conférences et ateliers internationaux. Ses idées originales se cachent derrière les résultats présentés dans cette thèse.

Je tiens à remercier les membres du jury d'avoir accepté de consacrer du temps à l'évaluation de ce travail. Je remercie en particulier les rapporteurs V. Fiala et J. Zlotnicki pour leurs nombreuses suggestions qui ont contribué à l'amélioration de ce manuscrit.

Le travail présenté est basé sur l'utilisation extensive des données du satellite DEMETER, je tiens également à remercier les chercheurs et les techniciens qui ont contribué à la réussite de cette mission. Je remercie en particulier J. J. Berthelier qui est l'investigateur principal des capteurs électriques. Enfin, je remercie J. Y. Brochot pour son aide sur l'analyse et la distribution des données.

Finalement, je remercie toute l'équipe du LPC2E pour l'ambiance chaleureuse et stimulante dont j'ai bénéficié pendant mes séjours. Je remercie également mes collègues de l'Université Charles à Prague et de l'IAP à Prague pour leur soutien.

Table des matières

Table des figures

Liste des tableaux

Liste des acronymes

BANT Boîtier d'Acquisition de Numérisation et de Traitement

CNES Centre National d'Etudes Spatiales

CNRS Centre National de la Recherche Scientifique

DEMETER Detection of Electro-Magnetic Emissions Transmitted from Earthquake Regions

EBF Extrême Basse Fréquence (15 Hz – 1 kHz)

EM Électro-Magnétique

HF Haute Fréquence (10 kHz – 3.175 MHz)

IAP Instrument Analyseur de Plasma

ICE Instrument Capteur Électrique

IDP Instrument Détecteur de Particules

IMSC Instrument Magnétomètre Search-Coil

ISL Instrument Sonde de Langmuir

LPC2E Laboratoire de Physique et Chimie de l'Environnement et de l'Espace

LT Temps Local (Local Time)

MLT Temps Local Magnétique (Magnetic Local Time)

MLR Magnetospheric Line Radiation

PLHR Power Line Harmonic Radiation

TBF Très Basse Fréquence (15 Hz – 17.4 kHz)

UBF Ultra Basse Fréquence (0 – 15 Hz)

UT Temps Universel (Universal Time)

Résumé

Les résultats expérimentaux basés sur les donnés du satellite DEMETER (orbite circulaire, altitude $\approx$ 700 km) sont présentés dans cette thèse. En particulier, nous nous sommes concentrés sur l'analyse des ondes électromagnétiques dans la bande de fréquence TBF (jusqu'à 20 kHz). Deux phénomènes différents ont été traités :

1. les effets liés á l'activité sismique
2. un type particulier d'ondes électromagnétiques – les émissions ayant des structures fréquentielles linéaires

Le Chapitre 1 présente un bref résumé de ces effets. Un historique des connaissances que l'on avait sur ces sujets est présenté avec des citations appropriées. Le Chapitre 2 contient la description du satellite DEMETER, en se concentrant sur les instruments et les paramètres particuliers que nous avons utilisés.

Puis, il y a deux chapitres dans lesquels nous décrivons les résultats obtenus, un chapitre pour chacun des deux sujets principaux. Étant donné que nous avons déjà publié la majorité des résultats dans des journaux scientifiques, ces chapitres ne sont pas très longs et utilisent beaucoup des citations. Tous les papiers cités sont disponibles en Annexe E.

Finalement, le Chapitre 5 présente une liste des résultats principaux, montrant les progrès scientifiques que nous avons fait concernant la compréhension des phénomènes analysés.

Chapitre 1

Connaissances sur les phénomènes sélectionnés

1.1 Effets liés à l'activité sismique

1.1.1 Préface

Les perturbations électromagnétiques probablement connectées à l'activité sismique sont connues depuis relativement longtemps (*Milne*, 1890). Mais jusqu'au début des années 80, on n'a pas prêté beaucoup d'attention à ces effets, parce que les mesures n'étaient pas assez claires ni suffisamment décrites. Les deux papiers publiés en 1982 (*Gokhberg et al.*, 1982; *Warwick et al.*, 1982) changèrent cet état d'esprit, et déclenchèrent de très nombreuses études sur, non seulement ces effets électromagnétiques, mais aussi sur les phénomènes qui peuvent leurs être associés (variations de paramètres atmosphériques et ionosphériques). L'étude de ces effets est spécialement importante pour leur application car les travaux publiés montrent qu'ils ont lieu quelques jours/heures avant le choc principal. Il y a donc une possibilité d'application pour la prédiction des tremblements de terre à court-terme.

L'étude des effets liés à l'activité sismique est un problème difficile – l'intensité supposée des signaux correspondants est très faible et leur existence même est mise en doute par une partie de la communauté scientifique. Le problème le plus important est l'impossibilité de la répétition des mesures et donc la possibilité que les effets observés pendant (ou peu avant) les tremblements de terre ont une origine différente, non lié à l'activité sismique. L'approche la plus convaincante pour vérifier l'existence de ces effets est probablement l'étude statistique en utilisant un grand nombre de tremblements de terre. Malheureusement, jusqu'à maintenant toutes les tentatives de faire cette étude comportaient un nombre d'événements insuffisant. L'écart type des anomalies attribuées aux tremblements de terre était ainsi trop grand, comparable ou plus grand que l'amplitude reportée des anomalies.

Dans ce chapitre nous allons décrire les mesures effectuées par des satellites dans l'ionosphère et magnétosphère en relation avec l'activité sismique. L'avantage principale

des satellites en comparaison avec des expériences au sol est qu'en utilisant un seul satellite on peut couvrir la plupart des zones sismiques, arrivant ainsi à obtenir un grand nombre de tremblements de terre, ce qui est indispensable pour une étude statistique. Une simulation simple peut montrer que, pendant deux ans, un satellite polaire peut approcher plus de 400 tremblements de terre de magnitude plus grande que 5 et à une distance entre la projection du satellite au sol et l'épicentre du tremblement de terre inférieure à 5 degrés en latitude et longitude.

1.1.2 Limitations principales de cette synthèse

Nous ne nous sommes pas intéressés aux effets après les tremblements de terre (*Calais and Minster*, 1995; *Artru et al.*, 2005), parce qu'ils ne peuvent pas être utilisés pour la prédiction.

Étant donné que les résultats présentés dans cette thèse sont expérimentaux, avec l'idée principale de vérifier statistiquement l'existence des effets ionosphèriques liés à l'activité sismique, nous ne nous sommes pas particulièrement intéressés aux mécanismes possibles de génération de ces effets. Quelques mécanismes capables de les expliquer ont été proposés, mais ils manquent une validation expérimentale directe. Ces mécanismes sont basés sur des idées diverses : la génération directe des émissions électromagnétiques dans la lithosphère (*Molchanov et al.*, 1995; *Molchanov and Hayakawa*, 1998; *Frid et al.*, 2003), la propagation des ondes acoustiques de gravité de l'épicentre jusqu'à l'ionosphère (*Mareev et al.*, 2002), l'influence du champ électrique unidirectionnel sur l'ionosphère (*Sorokin et al.*, 2001; *Grimalsky et al.*, 2003) ou l'émanation des gaz radioactifs (*Pulinets*, 2004). Une description détaillée de ces mécanismes est donnée par exemple dans les monographies (*Hayakawa and Fujinawa*, 1994; *Hayakawa*, 1999; *Hayakawa and Molchanov*, 2002), les livres (*Gokhberg et al.*, 1995; *Pulinets and Boyarchuk*, 2004), les éditions spéciales (*Parrot and Johnston*, 1989, 1993; *Hayakawa and Ogawa*, 1992; *Hayakawa*, 1996, 2002, 2004) et les références contenues dans ces ouvrages.

Nous étudierons seulement les observations des ondes électromagnétiques effectuées par le satellite DEMETER, parce que nous nous limitons exclusivement à l'étude de ce type de phénomène. Les autres phénomènes qu'il serait possible d'étudier avec un satellite sont par exemple les variations de la densité ou de la température du plasma ou des changements dans la population des particules énergétiques – mais on ne va pas les discuter dans cette thèse.

1.1.3 Synthèse sur les connaissances actuelles

Les données mesurées par beaucoup de satellites ont été utilisées pour analyser les effets électromagnétiques liés à l'activité sismique, mais hormis le satellite DEMETER (voir le Chapitre 2) ce n'était pas l'objectif principal de ces missions.

Gokhberg et al. (1983) ont présenté des perturbations dans l'ionosphère au-dessus de la région épicentrale de tremblements de terre imminents. En utilisant le satellite OGO-6,

ils ont montré que le bruit intégré dans la gamme de fréquence 100 - 500 Hz augmente quand le satellite est près du tremblement de terre (M_s 5.4, distance $<$ 480 km, 14 heures avant le choc principal). En étudiant plusieurs observations faites par le satellite Intercosmos-19, *Larkina et al.* (1983) ont conclus qu'il y a une augmentation de l'intensité des émissions dans la gamme EBF/TBF entre une dizaine de minutes et plusieurs heures avant et après des tremblements de terre. La région affectée s'étend en longitude et l'effet est plus marqué aux environs de 15 kHz (la fréquence maximale de l'analyse). Quand le satellite est proche du tremblement de terre, l'effet est aussi observé aux fréquences plus basses. Les émissions sont surtout électrostatiques. *Larkina et al.* (1989) ont présenté une étude de quelques orbites proche d'un tremblement de terre de magnitude 5.9. Ils ont montré que les émissions anormales aux fréquences 0.1 – 16 kHz se sont prolongées entre $\pm 60°$ en longitude géographique et $\pm 2°$ en latitude géographique autour de l'épicentre.

Parrot and Lefeuvre (1985) ont publié une étude statistique en utilisant des données du satellite géostationnaire GEOS-2. Dans le cas d'un satellite géostationnaire les ondes doivent se propager à une distance plus grande, mais l'avantage principale est qu'on peut étudier les effets en fonction du temps, comme on reste toujours à la même distance de l'épicentre. Deux ensembles de données ont été utilisés : 1) les données électriques et magnétiques mesurées pendant le temps des tremblements de terre de magnitude supérieure à 4.7 et avec la longitude de l'épicentre prés du satellite 2) les données aléatoires. En utilisant un critère basé sur l'intensité relative des ondes dans la gamme de fréquence 0.3 - 10 kHz, ils ont obtenu une corrélation positive de 44%. La même analyse pour les données aléatoires a donné une corrélation de 41%, ce qui est très similaire. Quand la distance en longitude avec les épicentres a été réduite, la corrélation a augmentée à 51%, pour les épicentres au-dessus du continent à 54%. Aucune caractéristique spécifique ne fut trouvée par *Matthews and Lebreton* (1985) en utilisant l'inspection visuelle et les données du même satellite GEOS-2 dans la gamme de fréquence 0.3 - 11 Hz. Cependant, ils n'utilisèrent que trois mois des données et tous les tremblements de terre inclus avaient des magnitudes inférieures à 5.

Parrot and Mogilevsky (1989) et *Parrot* (1990) ont analysé les données du satellite AUREOL-3 (apogée 2000 km, perigée 400 km) et ils ont montré que l'intensité des ondes électromagnétiques aux fréquences plus basses que 800 Hz augmente près de l'épicentre des tremblements de terre. Cependant, ces études sont seulement des études de cas – la corrélation trouvée ne doit pas alors nécessairement résultée d'un lien causatif. En utilisant le même satellite AUREOL-3, *Gal'perin et al.* (1992) ont fait des observations simultanées d'ondes EBF et d'augmentation de la précipitation des électrons de haute énergie quand le satellite passait au même L que l'épicentre (L est le paramètre de McIlwain – la distance en rayons de la Terre ou une ligne de force particulière du champ magnétique terrestre croise l'équateur magnétique).

Serebryakova et al. (1992) utilisèrent les données du satellite COSMOS-1809 (orbite presque circulaire, altitude 970 km) dans la gamme de fréquence 140 Hz - 15 kHz pour montrer qu'il y a des émissions intenses aux fréquences plus basses que 450 Hz quand le satellite est au même L que le tremblement de terre et quand la distance longitudinale est

moins que 10°.

Aucune signature des effets liés aux tremblements de terre n'a été trouvée dans les données mesurées par le satellite DE-2 (apogée 1300 km, perigée 300 km) par *Henderson et al.* (1993). Ils ont comparé 63 "orbites sismiques" près des tremblements de terre (la projection du satellite au sol croise la latitude géographique du tremblement de terre à moins de ±20° en longitude géographique) avec 61 "orbites de contrôle" (aucun tremblement de terre près de la projection du satellite au sol, mais ayant les mêmes latitudes, longitudes, temps locaux et activité magnétique que les orbites sismiques). L'analyse statistique a montré qu'il y avait une émission dans les données électriques avec une amplitude plus grande que 10 μV/m dans au moins 1 de 20 bandes de fréquence entre 4 Hz et 512 kHz sur 40/63 orbites sismiques. Une émission d'une telle intensité fut observée aussi sur 38/61 orbites de contrôle. Il n'y avait alors aucune différence significative entre les deux. Les auteurs ont conclu que les effets liés à l'activité sismique peuvent exister, mais qu'il est très difficile les trouver, et que plus de données sont nécessaires.

Molchanov et al. (1993) ont utilisé les données du satellite Intercosmos-24 (apogée 2500 km, perigée 500 km) pour analyser 28 événements avec les caractéristiques suivantes : $M > 5.2$, latitude invariante des données (latitude géomagnétique ou une ligne de force particulière du champ magnétique terrestre touche la surface de la Terre) Lat.Inv. $< 45°$, différence entre la latitude invariante des données et la latitude invariante de l'épicentre ΔLat.Inv $< 10°$, la différence temporelle entre les données et le tremblement de terre $|\Delta t| < 48$ h. Ils ont inspecté visuellement les données dans les gammes EBF et TBF. Des sursauts d'émissions ont été observé entre $-10°$ et $+10°$ de la latitude géomagnétique pour 15 événements. Ils ont conclus que les émissions sont observées dans deux gammes de fréquence, UBF-EBF (< 1000 Hz) et TBF (10-15 kHz) et que la probabilité d'occurrence est maximale 6-24 heures avant le choc principal. Ils ont aussi rapporté que les émissions peuvent être présentes loin de l'épicentre, mais aux mêmes valeurs de L.

Les mesures par le satellite AUREOL-3 près de 325 tremblements de terre de $M > 5.0$ ont été analysées par *Parrot* (1994b). Les données sont traitées seulement quand leur séparation temporelle du choc principal est inférieure à 24 heures et quand la latitude invariante est inférieure à 45°. L'amplitude moyenne de l'intensité des ondes est représentée en fonction de la distance à l'épicentre (en latitude et en longitude). Les résultats indiquent que les ondes électromagnétiques liées à l'activité sismique sont limitées en longitude, mais sont dispersées en latitude.

Une comparaison des divers papiers décrits au-dessus a été présentée par *Parrot* (1994c). Il a noté que les résultats obtenus sont significativement différents et qu'on ne peut pas faire une conclusion claire concernant l'existence de ces effets. En plus, dans la plupart de cas le nombre des événements considérés est trop petit pour une étude statistiquement significative et les méthodes utilisées ne sont pas souvent optimales.

Rodger et al. (1996) ont analysé les données du satellite ISIS-2 (orbite presque circulaire, altitude environ 1400 km) dans un intervalle temporel de ±48 h près de 37 événements de magnitude $M > 5.0$. Les tremblements de terre ont été choisis au-dessus des continents quand le satellite passe à la latitude invariante de l'épicentre où prés de la région conjuguée.

Aucune différence significative ne fut trouvée entre les orbites sismiques (152) et les orbites de contrôle (143) en utilisant une inspection visuelle.

Plus récemment, *Molchanov et al.* (2006) ont analysé les signaux des émetteurs TBF détectés par le satellite DEMETER. Ils ont montré qu'il y a une diminution de l'intensité des signaux liée à l'occurrence de tremblements de terre importants. Les dimensions de la région affectée sont assez grandes (1000 - 5000 km). Les auteurs ont proposé aussi un modèle basé sur les ondes acoustiques de gravité et la turbulence ionosphèrique.

Finalement, il y a les articles *Němec et al.* (2008b, 2009b) inclus dans cette thèse dont les résultats principaux sont décrits dans le Chapitre 3.

1.2 Émissions avec des structures fréquentielles linéaires

1.2.1 Préface

Certaines émissions électromagnétiques observées dans la magnétosphère sont parfois – quand elles sont représentées sous forme de spectrogramme fréquence-temps – composées de quelques "lignes" intenses (il y a une dépendance linéaire de la fréquence en fonction du temps). Ces lignes sont souvent presque horizontales (leur fréquence ne change pratiquement pas) et leur intervalle en fréquence est quasi constant. Ces émissions s'appellent habituellement "Magnetospheric Line Radiation" (MLR)[1]. On les a observées avec des instruments placés au sol (*Helliwell et al.*, 1975; *Park and Helliwell*, 1978; *Matthews and Yearby*, 1981; *Park and Helliwell*, 1981, 1983; *Yearby et al.*, 1983; *Rodger et al.*, 1999a, 2000a,b; *Manninen*, 2005) ainsi qu'avec des satellites de faible altitude (*Bell et al.*, 1982; *Koons et al.*, 1978; *Tomizawa and Yoshino*, 1985; *Parrot*, 1994a; *Rodger et al.*, 1995; *Parrot et al.*, 2005, 2006a, 2007; *Parrot and Němec*, 2009). L'évidence de leur propagation dans la magnétosphère a été établie, mais les observations directes par des satellites sont plutôt rares et l'origine de ces événements n'est pas bien compris.

Dans certains cas, la séparation en fréquence des lignes qui forment les événements est égale à 50 Hz ou 60 Hz (ou 100 Hz ou 120 Hz), correspondant ainsi à la fréquence principale des systèmes électriques sur la surface de la Terre. On croit que ce type d'émissions est causé par le rayonnement électromagnétique de ces systèmes (lignes électriques, usines, etc.) et les émissions s'appellent habituellement "Power Line Harmonic Radiation" (PLHR)[2]. Certains auteurs (*Rodger et al.*, 1995; *Parrot et al.*, 2005) ont aussi utilisé le nom "Tram Lines" (TL) pour éviter de postuler sur l'origine de ces émissions.

L'étude de ces émissions est importante pour deux raisons principales : 1) Elles représentent un phénomène intéressant dont l'origine n'est pas bien comprise et qui est au moins partiellement liée à l'activité humaine. 2) Il est probable que près de l'équateur magnétique ces ondes électromagnétiques agissent sur les particules contenues dans les cein-

[1]Nous utilisons l'abréviation "MLR" dans toute cette thèse.
[2]Nous utilisons l'abréviation "PLHR" dans toute cette thèse

tures de radiation, en influant sur leur distribution et en contribuant à leur précipitation.

1.2.2 Récapitulation sur les connaissances actuelles

Rodger et al. (1995) ont analysé des observations de MLR avec les satellites ISIS 1 et ISIS 2. Ils ont vérifié les fréquences des "lignes" et aussi l'intervalle de fréquence entre ces lignes, mais ils n'ont trouvé aucune corrélation avec les multiples du 50 ou 60 Hz. Néanmoins, ils ont rapporté l'existence d'événements de type "tram lines", qui sont caractérisés par des lignes très étroites et une fréquence constante. Ces événements semblent se trouver près des harmoniques du 50 ou 60 Hz. La même conclusion a été obtenue avec les mesures au sol effectuées à Halley dans l'Antarctique (*Rodger et al.*, 1999a, 2000a,b).

L'existence "d'effet du dimanche" a été rapportée par *Park and Miller* (1979) – la fréquence de l'occurrence des événements PLHR a été significativement moindre les dimanches par comparaison avec les autres jours de la semaine. En plus, l'intensité des ondes électromagnétiques entre 2 et 4 kHz a été plus faible les dimanches. Les auteurs ont proposé que les deux effets sont dus à la moindre consommation d'électricité pendant les week-ends et que les événements PLHR peuvent être assez importants. *Parrot* (1991) et *Molchanov et al.* (1991) ont attribué l'effet non seulement à la moindre consommation d'électricité pendant les week-ends, mais aussi à une répartition différente du courant dans les systèmes électriques.

Dans une récapitulation des observations de PLHR et MLR par des satellites aussi bien que par des instruments au sol *Bullough* (1995) a discuté la possibilité que les MLR aient comme origine les PLHR. Cette idée a été examinée plus en détail par *Nunn et al.* (1999) en utilisant des simulations numériques.

Parrot (1994a) a décrit 5 observations d'événements MLR par le satellite AUREOL 3. Dans tous les cas la séparation des lignes en fréquence était de 50 Hz ($\pm 1\%$). Les lignes n'ont pas été observées aux multiples exactes du 50 Hz, mais leurs fréquences changeaient avec le temps (1 - 8 Hz/s). Les événements ont été observés pendant une faible activité magnétique et surtout pendant la nuit.

Quatre événements de type "tram lines" observées par le satellite DEMETER ont été rapportés par *Parrot et al.* (2005). La séparation des lignes en fréquence est près de 50 Hz ou de 50/3 Hz (la fréquence du courant utilisée pour certains chemins de fer). La fréquence des lignes était presque constante et elles ont été observées pendant une activité magnétique moyenne. Les auteurs ont aussi utilisé l'analyse de la propagation des ondes pour montrer que les événements viennent de la région au-dessous du satellite. L'augmentation de l'intensité près de l'équateur géomagnétique est l'indication des interactions ondes-particules.

Parrot et al. (2006a) ont présenté une étude sur les émissions électromagnétiques harmoniques dans la bande EBF observées par le satellite DEMETER pendant des périodes où l'activité géomagnétique est forte. Ils ont proposé que les ondes sont générées dans la région de l'équateur géomagnétique aux harmoniques de la fréquence cyclotronique des protons. Après la génération les ondes peuvent se propager dans la magnétosphère et –

finalement – suivre un gradient de la densité jusqu'à l'ionosphère. Ces émissions peuvent participer à la précipitation des électrons énergiques.

Une étude d'un événement MLR à grande échelle a été présentée par *Parrot et al.* (2007). Les mesures simultanées par le satellite DEMETER et des instruments au sol montrent la grand étendue spatiale et temporelle de l'événement (7,400,000 km^2, 2 heures). Les auteurs ont aussi proposé que l'événement MLR est dû à l'événement PLHR qui se propage dans l'ionosphère et la magnétosphère et qui est affecté par des interactions ondes-particules non-linéaires dans le région de l'équateur géomagnétique.

Finalement, il y a les articles *Němec et al.* (2006b, 2007b,c, 2008c, 2009a,c) inclus dans cette thèse dont les résultats principaux sont décrits dans le Chapitre 4.

Chapitre 2

Satellite DEMETER

2.1 Objectif de la mission

Dans cette thèse nous utilisons les données du satellite DEMETER (Detection of Electro-Magnetic Emissions Transmitted from Earthquake Regions). C'est un micro-satellite (130 kg) français développé par le CNES (Centre National d'Études Spatiales) en coopération avec LPC2E/CNRS (Laboratoire de Physique et Chimie de l'Environnement et de l'Espace / Centre National de la Recherche Scientifique) à Orléans. Il a été lancé le 29 juin 2004. La durée planifiée de la mission était originalement de 2 ans, mais compte tenu du bon fonctionnement du satellite et des observations nouvelles, la durée a été prolongée. A ce jour (Mai 2009) le satellite est toujours en activité. L'altitude de l'orbite était originalement 710 km, mais elle fut diminuée à environ 660 km en Décembre 2005. L'inclination de l'orbite est 98° et le satellite fait à peu prés 14 orbites par jour. DEMETER est un satellite quasi synchronisé avec le Soleil ; il est toujours situé dans le jour à 10 :30 LT ou la nuit à 22 :30 LT.

Le premier objectif du satellite DEMETER est une étude des effets ionosphériques liés aux tremblements de terre et des phénomènes qui les accompagnent. Parmi les autres objectifs de la mission il y a l'analyse des effets ionosphériques induits par l'activité humaine et l'acquisition des informations sur l'environnement électromagnétique de la Terre. Un objectif ultime de ce satellite est d'aider à comprendre les mécanismes de génération de tous ces phénomènes.

Il y a deux modes d'opération principales du satellite DEMETER. Pendant le premier, qui s'appelle "Survey", des données sont rassemblées au-dessus de toute la surface de la Terre, sauf les régions avec une latitude géomagnétique plus grande que 65 degrés. Pendant ce mode les données sont pré-analysées à bord du satellite pour réduire la quantité des données à 25 ko/s. Dans le deuxième mode, qui s'appelle "Burst", des données plus détaillées sont rassemblées. La quantité totale des données dans ce mode est 1.7 Mo/s. Le mode "Burst" est normalement actif au-dessus des régions sismiques (voir la Figure 2.1), mais on peut le changer si nécessaire. Les données sont déposées dans la mémoire du satellite, d'ou elles sont transmises deux fois par jour à la station de réception à Toulouse. Le

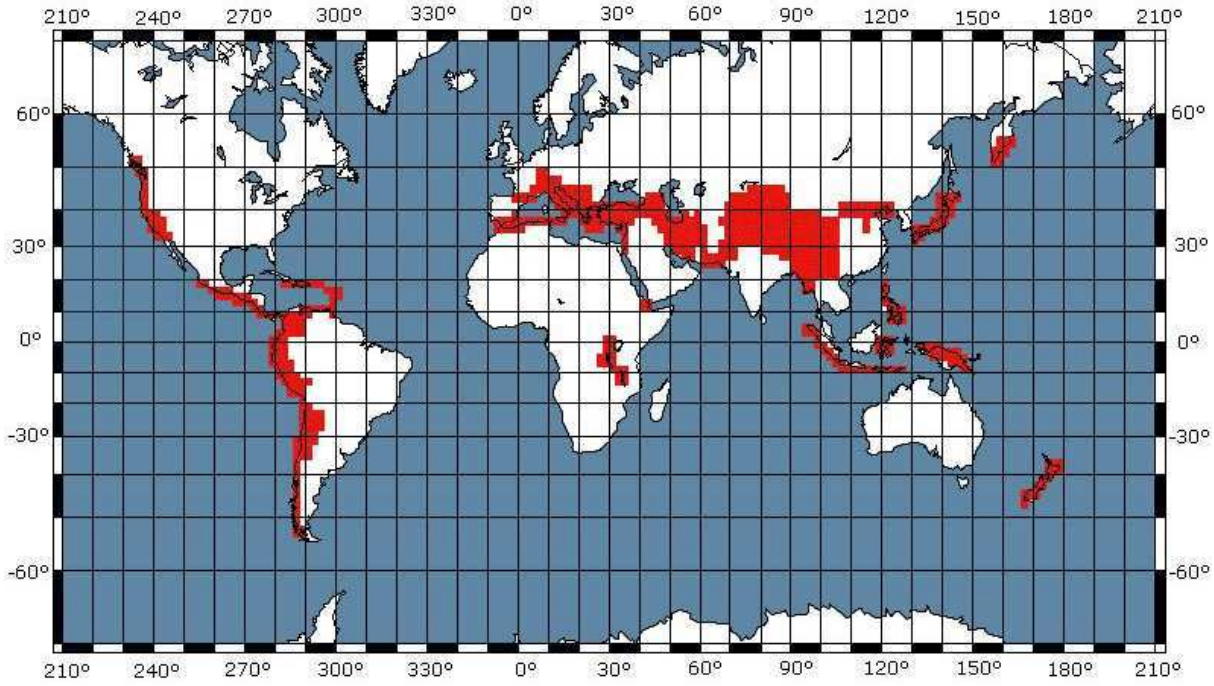

FIG. 2.1 – Carte du monde avec les régions sismiques indiquées. Le satellite implicitement travaille en mode "Burst" au-dessus de ces régions.

centre de mission où les données sont déposées et pré-analysées est situé au LPC2E/CNRS à Orléans.

2.2 Expériences à bord

Les instruments à bord du satellite permettent les mesures des six composantes électromagnétiques dans une large bande de fréquences. Par ailleurs, on peut déterminer un grand nombre de paramètres du plasma : la composition des ions, la température et la densité des électrons et des ions et le flux des électrons énergiques. Il y a cinq instruments à bord, tous connectés au Boîtier d'Acquisition de Numérisation et de Traitement (BANT) :

- ICE (Instrument Capteur Électrique) – quatre sondes électriques pour la mesure dans la gamme de fréquence jusqu'à 3,5 MHz
- IMSC (Instrument Magnétomètre Search Coil) – trois sondes magnétiques pour la mesure dans la gamme de fréquence de quelques Hz jusqu'à 18 kHz
- IAP (Instrument Analyseur de Plasma) – analyseur des ions
- IDP (Instrument Détecteur de Particules) – détecteur des particules énergétiques
- ISL (Instrument Sonde de Langmuir) – sonde de Langmuir

Nous allons décrire plus en détail les deux premiers instruments destinés à la mesure des champs électromagnétiques (*Berthelier et al.*, 2006; *Parrot et al.*, 2006b) que nous

utilisons dans la thèse.

2.2.1 Instrument ICE

L'instrument ICE se compose de quatre sondes, un pré-amplificateur et l'électronique associée au module BANT. En mesurant la différence des potentiels électriques entre les deux sondes, on peut déterminer la composante électrique dans la direction définie par eux. En utilisant les paires de sondes différentes, on peut ainsi déterminer toutes les trois composantes du champ électrique. L'électronique se compose de la partie analogue avec des filtres et des amplificateurs et la partie digitale pour la numérisation de la forme d'onde et l'obtention des spectres de puissance.

Il y a quatre bandes de fréquences différentes :
– UBF (Ultra Basse Fréquence) – jusqu'à 15 Hz
– EBF (Extrême Basse Fréquence) – entre 15 Hz et 1 kHz
– TBF (Très Basse Fréquence) – entre 15 Hz et 17.4 kHz
– HF (Haute Fréquence) – entre 10 kHz et 3.175 MHz

En fonction de la bande de fréquence et du mode du satellite les données sont enregistrées comme des formes d'ondes (burst) ou des spectres de puissance (burst + survey).

Bande UBF

Indépendamment du mode du satellite les signaux de toutes les quatre sondes sont filtrées, amplifiées, numérisées et enregistrées. Nous n'employons pas cette bande de fréquence dans la thèse.

Bande EBF

En mode "Burst", les trois composantes du champ électrique sont mesurées. Dans cette bande les trois composantes du champ magnétique sont aussi mesurées, ce qui permet l'analyse détaillée de la propagation des ondes électromagnétiques.

Bande TBF

Une seule composante du champ électrique est mesurée. En mode "Survey" seulement un spectre de puissance est obtenu. En fonction du mode d'instrument il y a trois types possibles des spectres, décrits dans le Tableau 2.1. En mode "Burst" on obtient aussi la forme d'onde.

Bande HF

Une seule composante du champ électrique est mesurée. Nous n'employons pas cette bande de fréquence dans la thèse.

Type du spectre	N_f	Δf	Δt	t_{ave}	f_{ave}
Type 0	1024	19.531 Hz	2.048 s	40	1
Type 1	1024	19.531 Hz	0.512 s	10	1
Type 2	256	78.125 Hz	2.048 s	40	4

TAB. 2.1 – Types possibles des spectres de l'instrument ICE en mode "Survey", la bande TBF (type du spectre, nombre de fréquences, résolution en fréquence, résolution en temps, nombre de spectres ramenés à une moyenne et nombre des fréquences ramenées à une moyenne).

2.2.2 Instrument IMSC

L'instrument IMSC se compose de trois capteurs magnétiques du type "search-coil". Les modes de fonctionnement sont semblables à l'instrument ICE. La seule différence est que cette fois il n'y a que deux bandes de fréquence : EBF et TBF.

2.3 Niveaux de l'analyse de données

Les données sont analysées suivant trois niveaux principaux. Le "Niveau 0" correspond directement aux données mesurées, avant le calibrage. Le "Niveau 1" concernent les données déjà calibrées et transformées en unité physique. Finalement, le "Niveau 2" correspond aux figures générées avec ces données. À part ces trois niveaux, il y a aussi le "Niveau 3", correspondant aux programmes qui sont exécutés directement au centre de la mission à Orléans.

2.4 Données utilisées

Nous avons utilisé les mesures électriques aussi bien que les mesures magnétiques. Pour les études systématiques (l'analyse des effets liés á l'activité sismique en Chapitre 3, l'analyse systématique des événements MLR en Section 4.3) nous avons utilisâmes le mode "Survey" et la bande TBF, parce qu'il est actif au dessus de toute la surface de la Terre. Quand la résolution en fréquence n'était pas suffisante, nous avons utilisé le mode "Burst" (l'analyse des événements PLHR et MLR, voir Section 4.2 et Section 4.3, respectivement). Finalement, pour l'analyse des événements aux fréquences plus basses nous Avons utilisé la bande EBF, parce que dans cette bande la mesure des six composants du champ électromagnétique permet de faire l'analyse détaillée de la propagation des ondes électromagnétiques (des émissions électromagnétiques harmoniques dans la bande EBF, voir Section 4.4).

Chapitre 3

Effets liés à l'activité sismique

3.1 Préface

Nous nous sommes concentrés sur l'analyse systématique des effets électromagnétiques liés aux tremblements de terre. L'avantage principal d'utiliser les données provenant d'un satellite est qu'il peut survoler un grand nombre de tremblements de terre. Mais d'un autre côté, il y a des émissions électromagnétiques non-liées à l'activité sismique assez importantes aux altitudes de DEMETER. Du fait que l'intensité de ces émissions fluctue beaucoup, ils peuvent facilement cacher des effets potentiels liés à l'activité sismique. La question essentielle à laquelle nous voulons répondre est donc : "Est-ce qu'il y a une corrélation entre l'activité sismique et l'intensité des ondes électromagnétiques dans l'ionosphère ?". Pour être capable de découvrir des effets liés aux tremblements de terre qui sont (s'ils existent) probablement très faibles, nous avons développé une analyse des données en plusieurs étapes (*Němec et al.*, 2008b, 2009b).

Dans la première étape nous avons construit une base de données des émissions électromagnétiques. Elle contient la distribution normale de l'intensité des émissions obtenue en utilisant toutes les données mesurées. Les données dans cette base sont organisées en fonction des paramètres suivants :

- fréquence (16 intervalles de 117 Hz chacun)
- latitude géomagnétique (36 intervalles de 10 degrés chacun)
- longitude géomagnétique (66 intervalles de 2 degrés chacun)
- heure locale magnétique (2 cas : le jour et la nuit)
- Kp index (3 cas : Kp 0–1o, Kp 1+ – 2+, Kp 3+ et plus)
- saison de l'année (2 cas : octobre–avril, mai-septembre)

Chaque cellule de cette base (décrite par une combinaison des paramètres ci-dessus) contient un histogramme des intensités mesurées. L'annexe A contient un exemple de la représentation graphique de cette base sous forme des cartes d'émissions électromagnétiques (la valeur médiane de l'intensité en fonction de la latitude et la longitude géomagnétiques).

Dans une deuxième étape, l'intensité des émissions électromagnétiques mesurées à

proximité des tremblements de terre est évaluée en utilisant la base obtenue dans la première étape. L'idée essentielle étant d'éliminer les fluctuations de l'intensité non-liées aux tremblements de terre, nous n'avons pas utilisé pendant cette analyse l'intensité E_i mesurée des ondes électromagnétiques, mais la valeur de la probabilité cumulative F_i définie par :

$$F_i = \int_{-\infty}^{E_i} f(E)\, dE \tag{3.1}$$

où $f(E)$ est la fonction de la densité de probabilité obtenue pour la même fréquence, la même position du satellite et pendant des conditions magnétosphériques semblables. Ainsi, on obtient une probabilité d'existence des ondes électromagnétiques ayant une intensité inférieure ou égale à l'intensité mesurée. Finalement, les valeurs F_i à proximité des tremblements de terre sont évaluées pour déterminer si elles sont différentes de la normale. Nous avons développé deux méthodes possibles de cette évaluation. Leurs caractéristiques et les résultats principaux sont décrits dans les Chapitres 3.2 et 3.3.

3.2 Analyse en utilisant la méthode des époques superposées (d'après *Němec et al.* (2008b))

Cette méthode est basée sur l'utilisation des époques superposées. On construit la matrice en organisant les valeurs F_i en fonction des paramètres suivants :

- fréquence (16 intervalles comme dans la première étape)
- temps avant / après le tremblement de terre (48 intervalles de temps, résolution 4 heures, 5 jours avant le choc principal jusqu'à 3 jours après)
- distance entre la projection du satellite au sol et l'épicentre du tremblement de terre (10 intervalles, résolution $1° \approx 110$ km)

S'il y a plus d'un tremblement de terre à proximité des données actuelles au maximum 10 degrés de séparation spatiale entre la projection du satellite au sol et l'épicentre, un choc principal moins de 5 jours après et 3 jours avant), les données ne sont pas incluses dans l'analyse. Cette condition revient à ne traiter que les tremblements de terre "isolés" dans l'espace et dans le temps.

Pour chaque cellule b de la matrice (définie par les 3 paramètres au-dessus) on peut définir "l'intensité probabiliste" I_b :

$$I_b = \frac{\sum_{i=1}^{M_b} F_i}{M_b} - 0.5 \tag{3.2}$$

où M_b est le nombre des valeurs de la probabilité cumulative F_i collectées dans la cellule b. Si les intensités observées étaient significativement plus faibles ou plus fortes que normalement, les valeurs correspondantes de la probabilité cumulative seraient significativement différentes de 0.5 et la valeur résultante de l'intensité probabiliste serait significativement différent de 0. On peut éliminer ainsi l'influence de la distribution d'intensité des ondes naturelles sur la statistique. Néanmoins, il y a toujours un problème qui doit être considéré : quelle valeur correspond au mot "significativement" ? Pour répondre à cette question nous utilisons les caractéristiques élémentaires de l'intensité probabiliste.

Les valeurs F_i de la probabilité cumulative calculées en utilisant toutes les données sont distribuées uniformément entre 0 et 1. C'est une conséquence directe de leur définition (*Press et al.*, 1992). En les moyennant dans des cellules en fonction de la position et du temps, on totalise beaucoup de ces valeurs. D'après le théorème de la limite centrale et en supposant que le nombre des valeurs M_b est assez grand, les valeurs I_b ont ainsi une distribution normale avec la valeur moyenne 0 et un écart type σ_b. Si toutes les valeurs F_i étaient indépendantes, on pourrait calculer σ_b comme :

$$\sigma_b = \frac{1}{\sqrt{12 M_b}} \tag{3.3}$$

Le problème est que toutes les valeurs F_i ne sont pas indépendantes. Le calcul de σ_b est ainsi un peu plus difficile et il est décrit en détail dans *Němec et al.* (2008b).

En sachant l'écart type σ_b de l'intensité probabiliste I_b dans la cellule b, on peut définir l'intensité probabiliste normalisée Υ_b :

$$\Upsilon_b = \frac{I_b}{\sigma_b} \tag{3.4}$$

L'avantage de ce concept est que nous connaissons exactement la distribution de Υ_b sauf l'influence des tremblements de terre : la valeur moyenne est égale à 0 et l'écart type est égal à 1.

Les travaux précédents ayant montré que la profondeur de l'épicentre peut être importante pour les effets liés aux tremblements de terre (*Rodger et al.*, 1999b). Suivant ces travaux, nous avons divisé les tremblements de terre en deux groupes : les tremblements de terre peu profonds (profondeur moins de ou égale à 40 km) et les tremblements de terre profonds (profondeur plus de 40 km). En plus, les données mesurées pendant le jour et pendant la nuit ont été traitées séparément, parce que les conditions dans l'ionosphère sont complètement différentes. Finalement, toutes les 4 combinaisons possibles de peu profonds/profonds tremblements de terre et jour/nuit ont été examinées pour chercher la présence d'effets liés à l'activité sismique. Toutes les données électriques et magnétiques dans la bande TBF mesurées par DEMETER jusqu'à février, 2007 ont été incluses dans l'analyse, ce qui correspond à $\approx$ 11500 heures de mesures pendant $\approx$ 20000 demi-orbites. Selon le catalogue des tremblements de terre fournis par l'USGS (http://neic.usgs.gov/neis/epic/epic_global.html), $\approx$ 9000 tremblements de terre de magnitude supérieure ou égale à 4.8 se sont produits dans tout le monde. Nous avons inclus tous ces tremblements de terre dans l'analyse.

La Figure 3.1 représente l'intensité probabiliste normalisée obtenue pour les données électriques mesurées pendant la nuit près de tremblements de terre peu profonds (distance entre la projection du satellite au sol et l'épicentre d'un tremblement de terre inférieure à 330 km). Les résultats sont présentés en fonction de la fréquence et du temps relatif au choc principal. On peut voir que peu (0 - 4 heures) avant le choc principal il y a une diminution de l'intensité des ondes dans une gamme de fréquence 1-2 kHz. La variation correspond à environ 3 écart type pour les tremblements de terre de magnitude supérieure à 4.8 (à gauche) et à environ 4 écart type pour les tremblements de terre de magnitude supérieure à 5.0 (à droite). Une diminution de l'intensité des ondes a été observée aussi dans les données magnétiques, mais elle est plus faible, probablement à cause de la sensibilité moindre de l'instrument magnétique. Aucun effet n'a été observé pendant le jour. Aucun effet n'a été observé pour les tremblements de terre profonds.

La Figure 3.2 montre que les dimensions spatiales de la région affectée sont environ de 350 km, correspondant ainsi à peu près aux dimensions de la zone de préparation estimée par la formule de *Dobrovolsky et al.* (1979) : 140 km pour des tremblements de terre de magnitude 5.0 et 380 km pour des tremblements de terre de magnitude 6.0.

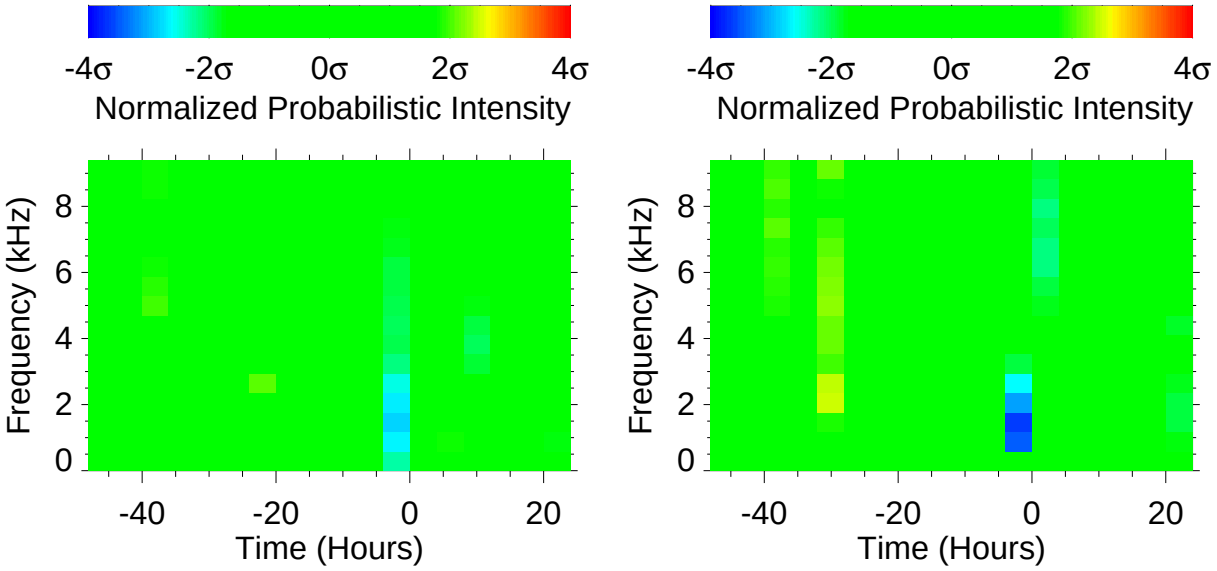

FIG. 3.1 – (à gauche) Spectrogramme fréquence-temps de l'intensité probabiliste normalisée obtenu en utilisant les données électriques mesurées pendant la nuit à des distances entre la projection du satellite au sol et l'épicentre d'un tremblement de terre inférieures à 330 km. Seuls les tremblements de terre de magnitude supérieure ou égale à 4.8 et de profondeur inférieure ou égale à 40 km ont été traités. Les données mesurées pour toutes les valeurs de l'index Kp et toutes les saisons de l'année sont incluses. (à droite) Les même résultats, mais cette fois obtenus pour les tremblements de terre de magnitude supérieure ou égale à 5.0. (d'après *Němec et al.* (2008b))

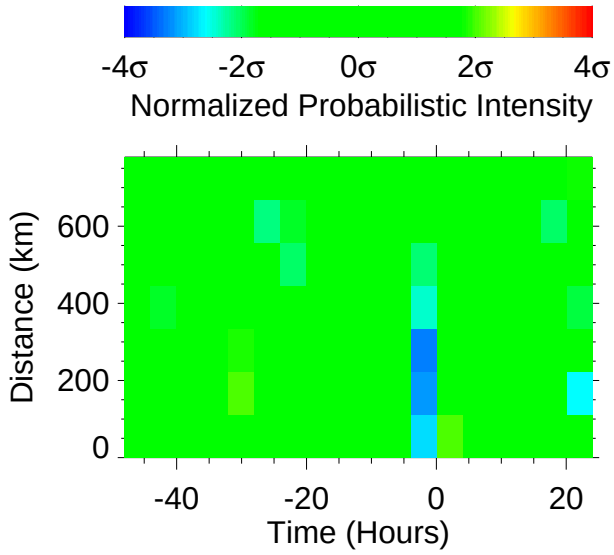

FIG. 3.2 – L'intensité probabiliste normalisée (voir le texte) obtenue en utilisant les données électriques mesurées pendant la nuit en fonction de la distance à l'épicentre et du temps relatif au choc principal. Seuls les tremblements de terre de magnitude supérieure à 5.0 et de profondeur inférieure à 40 km ont été traités. La bande de fréquence 1055-2383 Hz a été utilisée. (d'après *Němec et al.* (2008b))

3.3 Analyse en utilisant le test Mann-Whitney (d'après *Němec et al.* (2009b))

En utilisant les résultats de *Němec et al.* (2008b) nous analysons seulement les données mesurées pendant la nuit dans la gamme de fréquence 1.6 - 1.8 kHz et dans l'intervalle du temps 0-4 heures avant le choc principal. Ceux sont exactement les paramètres pour lesquels la diminution d'intensité des ondes a été observée. Nous choisissons le point

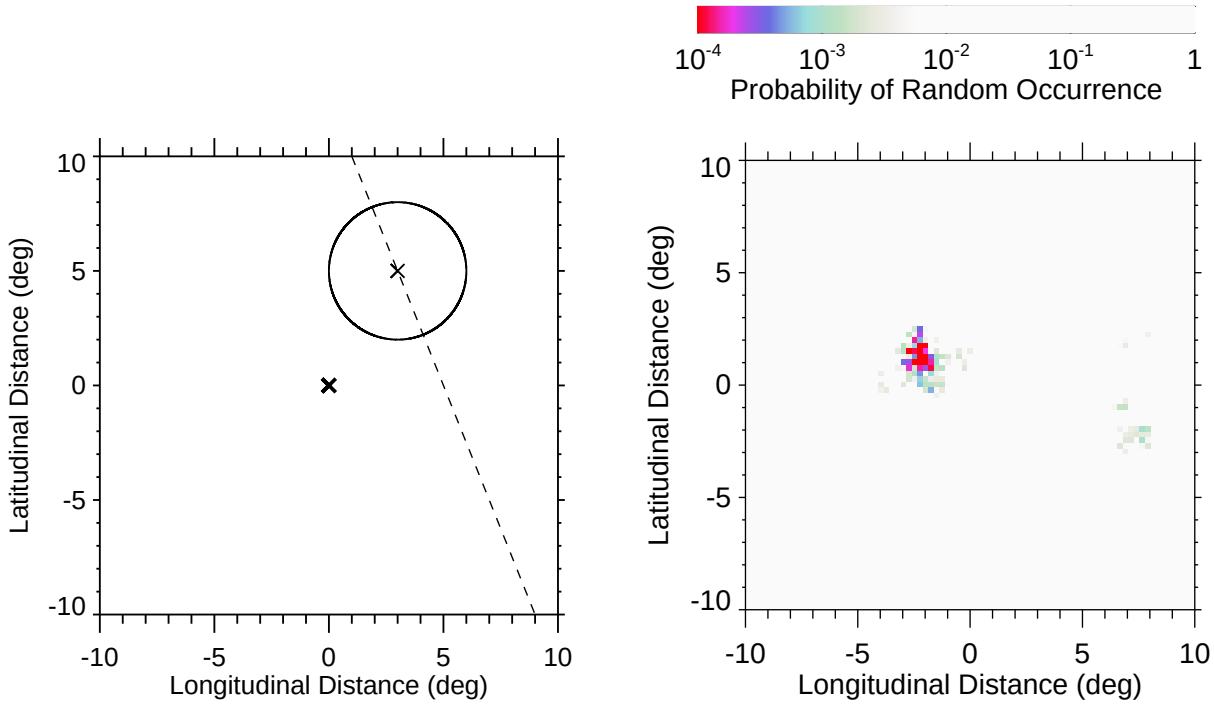

FIG. 3.3 – (á gauche) Schéma de la géométrie utilisée pour le calcul latitude-longitude. (à droite) Probabilité que ce rapport des diminutions et augmentations de l'intensité des ondes soit par hasard. Les tremblements de terre de magnitude supérieure ou égale à 5.0 et de profondeur inférieure ou égale à 40 km ont été traités. (d'après *Němec et al.* (2009b))

P près de l'épicentre des tremblements de terre. Pour chaque demi-orbite du satellite près de ce point (distance entre la projection du satellite au sol et le point inférieure à 3 degrés) nous vérifions si les valeurs de la probabilité cumulative près du point P sont inférieures ou supérieures aux valeurs normales. Pour le décider, nous utilisons le test Mann-Whitney. C'est un test statistique non-paramétrique qui permet – au niveau de la signification demandée – de décider si les deux populations X et Y ont la même valeur moyenne ou non (*Sheskin*, 2000). Comme population X nous prenons les valeurs de la probabilité cumulative près du point P et comme population Y nous prenons les valeurs de la probabilité cumulative sur le reste de demi-orbite (voir la Figure 3.3, le panneau à gauche). La raison de ce traitement est que les mesures pendant chaque demi-orbite du satellite durent

seulement environ 35 minutes – c'est une période relativement courte par comparaison avec l'échelle temporelle des changements majeurs de l'intensité des ondes dans l'ionosphère. Les valeurs mesurées pendant la même demi-orbite sont ainsi dépendantes et il est raisonnable de prendre les valeurs de la probabilité cumulative obtenues loin de l'épicentre pendant la même demi-orbite comme valeurs de référence.

Finalement, on évalue l'importance statistique des résultats obtenus. Pour chaque événement (pour chaque demi-orbite que est suffisamment près du point P) et pour le niveau de signification prédéfini il y a les trois possibilités suivantes :

1. Les valeurs de la probabilité cumulative près du point P sont inférieures à celles dans le reste de la demi-orbite.
2. Les valeurs de la probabilité cumulative près du point P sont supérieures à celles dans le reste de la demi-orbite.
3. Les valeurs de la probabilité cumulative sont presque les mêmes près du point P et dans le reste de la demi-orbite : on ne peut pas décider qu'elles sont inférieures/supérieures avec le niveau de signification prédéfini.

Les événements pour lesquels on ne peut pas décider au niveau de la signification prédéfini ne sont plus considéres. Nous calculons le nombre des événements pour lesquels les valeurs de la probabilité cumulative près du point P sont inférieures au reste de la demi-orbite (N_d) et, de la même manière, nous calculons le nombre des événements pour lesquels les valeurs de la probabilité cumulative près du point P sont supérieures au reste de la demi-orbite (N_i). En utilisant directement les deux valeurs N_d et N_i on peut calculer la probabilité de leur présence accidentelle. S'il n'y avait aucun effet lié à l'activité sismique, la probabilité p_i de l'augmentation de l'intensité près du point P serait égale à la probabilité p_d de la diminution de l'intensité près du point P et les valeurs N_i et N_d seraient ainsi approximativement les mêmes. Si les valeurs N_i et N_d sont très différentes, l'intensité des ondes électromagnétiques est différente près du point P en comparaison avec le reste des orbites, indiquant ainsi l'existence des effets liés à l'activité sismique. L'évaluation de la probabilité de la présence accidentelle est très facile. Car $p_i = p_d$ pour le cas hors effets sismiques, et nous devons simplement traiter la distribution binomiale.

Toutes les données électriques de nuit dans la bande TBF mesurées par DEMETER jusqu'à mars, 2008 ont été incluses dans l'analyse, ce qui correspond à $\approx$ 9000 heures de mesures pendant $\approx$ 15500 demi-orbites. Selon le catalogue des tremblements de terre fournis par l'USGS, $\approx$ 9500 tremblements de terre de magnitude supérieure ou égale à 4.8 et de profondeur inférieure à 40 km se sont produits dans tout le monde. Nous avons inclus tous ces tremblements de terre dans l'analyse. Parmi ces tremblements de terre, il y a plus de 5500 tremblements de terre de magnitude supérieure ou égale à 5.0.

Le panneau à droite de la Figure 3.3 montre les résultats obtenus en fonction de la position du point P relativement aux épicentres des tremblements de terre. Seuls les tremblements de terre importants ($M \geq 5.0$) et peu profonds (profondeur < 40 km) ont été traités. L'échelle représente la probabilité de présence des valeurs N_i et N_d par hasard. On peut voir que le seul effet exceptionnel est localisé près de l'épicentre des tremblements de terre, déplacé d'environ 2° à l'ouest et aussi un peu au nord. Il représente une diminution de

l'intensité des ondes (on ne peut pas décider du niveau, parce que l'on considère seulement la probabilité de présence des valeurs N_i et N_d par hasard, et non l'amplitude). Un niveau de signification de 0.01 a été utilisé, ce qui donne environ 50 événements dans chaque celulle de la figure.

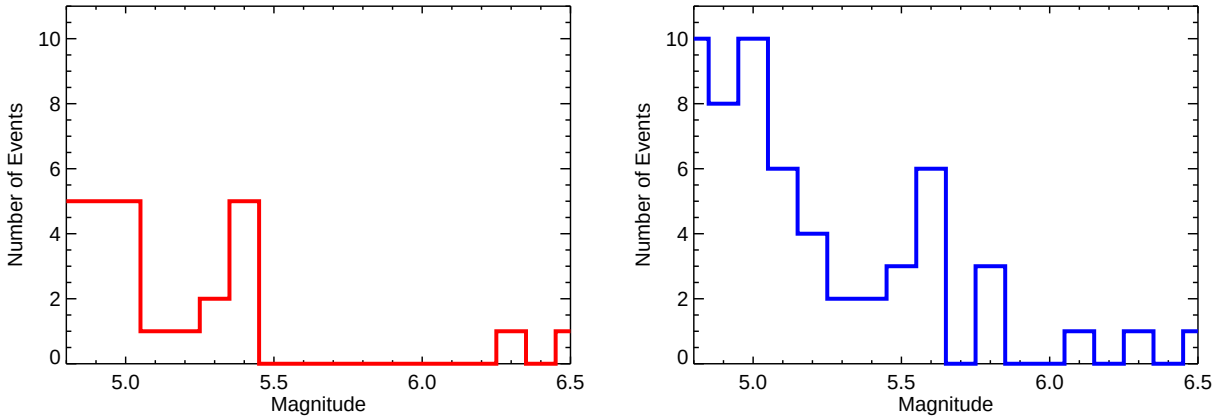

FIG. 3.4 – (à gauche) Nombre des événements avec une augmentation de l'intensité des ondes prés de l'épicentre des tremblements de terre (N_i) en fonction de la magnitude des tremblements de terre. (à droite) Nombre des événements avec une diminution de l'intensité des ondes prés de l'épicentre des tremblements de terre (N_d) en fonction de la magnitude des tremblements de terre. (d'après *Němec et al.* (2009b))

De plus, nous avons vérifié la dépendance de cet effet aux paramètres suivants : le magnitude du tremblement de terre, la profondeur du tremblement de terre et la hauteur absolue de la surface solide au-dessus de l'hypocentre (si le tremblement de terre est au-dessous d'un océan ou au-dessous du continent). Le niveau de signification pour le test Mann-Whitney utilisé a toujours été 0.01.

La Figure 3.4 montre les résultats obtenus pour la dépendance avec la magnitude des tremblements de terre. Le panneau à gauche représente la valeur N_i en fonction de la magnitude des tremblements de terre, le panneau à droite représente la même dépendance obtenue pour la valeur N_d. Tous les tremblements de terre peu profonds (profondeur < 40 km) ont été inclus. On peut voir que pour des magnitudes suffisamment grandes ($M \geq 5.5$) il y a presque toujours une diminution de l'intensité des ondes près des tremblements de terre (15 événements sur 17).

La Figure 3.5 est similaire à la Figure 3.4, mais cette fois elle concerne l'effet de la profondeur. Tous les importants ($M \geq 5.0$) tremblements de terre ont été inclus. On peut voir que pour les tremblements de terre peu profonds (profondeur < 20 km), la diminution d'intensité des ondes près de ces tremblements de terre est plus fréquente.

La Figure 3.6 représente une combinaison des dépendances de la Figure 3.4 et de la Figure 3.5. Elle montre le nombre relatif de la diminution d'intensité des ondes ($N_d/(N_d + N_i)$) en fonction de la magnitude et de la profondeur. Un nombre relatif de la diminution

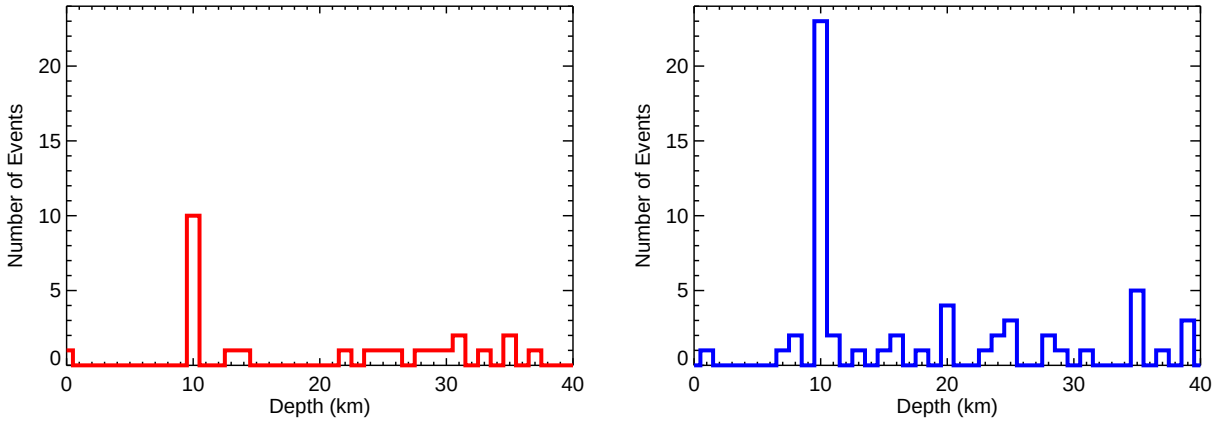

FIG. 3.5 – Comme la Figure 3.4, mais en fonction de la profondeur des tremblements de terre. (d'après *Němec et al.* (2009b))

d'intensité égal à 0.5 signifie que $N_d = N_i$ prés des tremblements de terre, et il n'y a pas de changement d'intensité des ondes spécifiques. Un nombre relatif de la diminution d'intensité égal à 1 signifie que pour tous les événements les valeurs de la probabilité cumulative sont significativement plus petits prés des tremblements de terre que dans le reste des demi-orbites (ou il n'a pas été possible de décider en utilisant le test Mann-Whitney et le niveau de signification choisi). Il y a environ 10 événements dans chaque celulle. On peut voir que le nombre relatif de la diminution d'intensité est près de 0.5 pour les tremblements de terre profonds et faibles ($d \geq 26$, $M < 5.0$ – à gauche, dessus), montrant ainsi aucun changement spécifique de l'intensité. Pour les tremblements de terre peu profonds et assez grands ($d \leq 25$, $M > 5.4$ – à droite, dessous), le nombre relatif de la diminution d'intensité est égal à 1.

La Figure 3.7 est similaire aux Figures 3.4 et 3.5, mais cette fois les résultats ont été obtenus pour la dépendance avec la hauteur absolue de la surface solide au-dessus des hypocentres des tremblements de terre (magnitude ≥ 5.0). Le nombre de tremblements de terre au-dessous des océans est plus grand que le nombre des tremblements de terre au-dessous du continent, mais on n'observe aucun effet de diminution d'intensité avec l'altitude : le ratio N_d/N_i est à peu près le même pour toutes les altitudes. Cette information pourrait aider à comprendre les mécanismes responsables de cet effet : certains mécanismes proposés (*Parrot*, 1995) peuvent exister pour des tremblements de terre au-dessous des océans aussi bien que pour des tremblements de terre au-dessous du continent (par exemple l'émanation des gaz radioactifs), mais d'autres peuvent exister seulement pour des tremblements de terre au-dessous du continent.

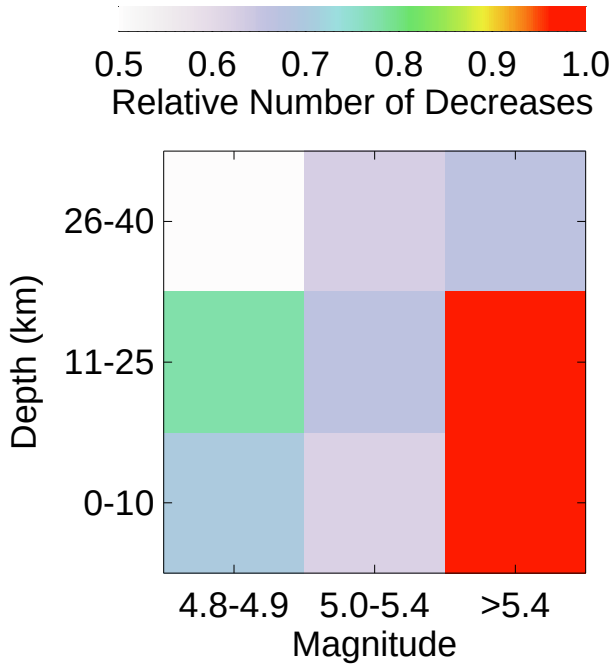

FIG. 3.6 – Nombre de diminutions de l'intensité des ondes prés des tremblements de terre en fonction de leur profondeur et leur magnitude. (d'après *Němec et al.* (2009b))

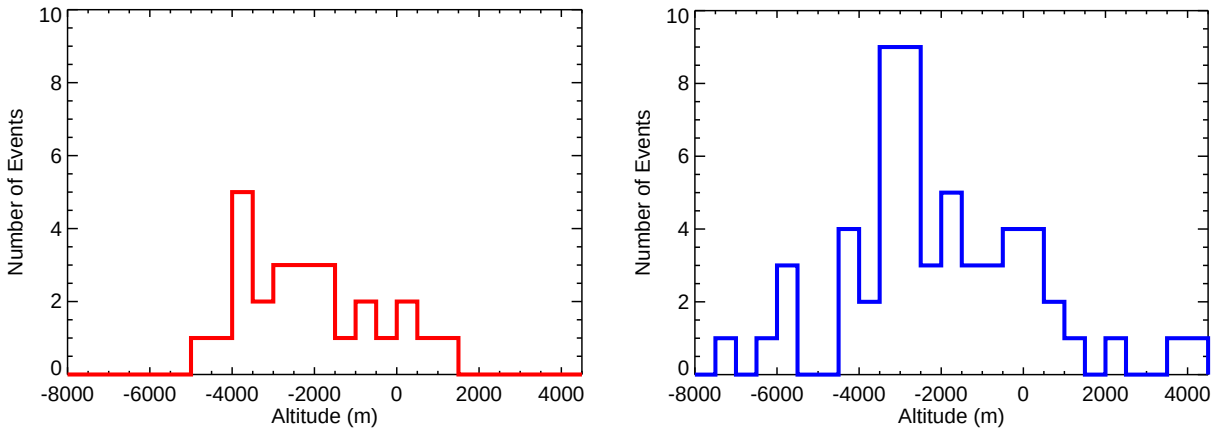

FIG. 3.7 – Comme la Figure 3.4, mais en fonction de l'altitude de la surface au-dessus de l'épicentre des tremblements de terre. (d'après *Němec et al.* (2009b))

3.4 Synthèse

En résumé, nous avons montré les points suivants :

1. Il y a une corrélation entre l'intensité des ondes électromagnétiques TBF dans l'ionosphère et l'activité sismique.
2. L'effet est observé seulement pendant la nuit. Il n'y a aucun effet similaire pendant le jour.
3. L'intensité des ondes électromagnétiques dans une gamme de fréquence $1 - 2$ kHz est plus faible que normalement peu ($0 - 4$ heures) avant le choc principal. Les dimensions spatiales de la région affectée sont de quelques centaines de kilomètres.
4. L'effet est plus fort pour les tremblements de terre de forte magnitude.
5. L'effet est plus fort pour les tremblements de terre moins profonds. Aucun effet a été observé pour les tremblements de terre très profonds (une profondeur > 40 km).
6. L'effet est observé pour les tremblements de terre sous la mer aussi bien que pour les tremblements de terre sur les continents.
7. L'effet semble déplacé d'environ 2° à l'Ouest des épicentres des tremblements de terre.

Chapitre 4

Émissions avec des structures linéaires

4.1 Préface (d'après *Němec et al.* (2007b))

Nous nous sommes intéressés à l'étude systématique des événements ayant des structures fréquentielles linéaires (voir le Chapitre 1.2). En utilisant une identification automatique de ces événements (*Němec et al.*, 2006b) ainsi qu'une identification visuelle nous avons obtenu – à notre connaissance – le plus grand ensemble d'événements observées par des satellites jusqu'ici. Nous avons trouvé qu'il y a trois types différents d'événements : PLHR, MLR et émissions électromagnétiques harmoniques dans la bande EBF. Dans cette section nous allons présenter la classification de ces événements. Les trois sections qui suivent présentent les résultats les plus importants que nous avons obtenus pour chaque type d'émissions. Une description plus détaillée de ces résultats peut être trouvée dans les papiers appropriés attachés en annexe.

Les émissions du type PLHR sont des événements avec une structure ayant des lignes dont la séparation en fréquence est 50/100 Hz ou 60/120 Hz. La Figure 4.1 représente un exemple de ce type d'émissions. Les données ont été mesurées en Février 1, 2006 après 19:06:32 UT quand le satellite se trouvait au-dessus des États-Unis. Trois lignes aux fréquences 2100 Hz, 2160 Hz et 2220 Hz sont clairement visibles – la séparation des lignes en fréquence est ainsi 60 Hz. D'autres exemples d'émissions PLHR sont présentés dans l'Annexe B.

Les émissions dont la séparation en fréquence entre les lignes individuelles est ni 50/100 Hz ni 60/120 Hz peuvent être des événements MLR ou des émissions électromagnétiques harmoniques dans la bande EBF. La classification entre les deux n'est pas toujours claire. La différence principale est que les événements MLR sont observés à des fréquences plus hautes et à des latitudes plus grandes. La Figure 4.2 représente un exemple de ces émissions de type MLR. Les données ont été mesurées le Janvier 19, 2007 après 06:26:02 UT. On peut voir beaucoup des lignes presque horizontales dans la gamme de fréquence entre 2 et 4 kHz. Un exemple d'émission électromagnétique harmonique dans la bande EBF est présenté dans la Figure 4.3. Les données ont été mesurées le Novembre 10,

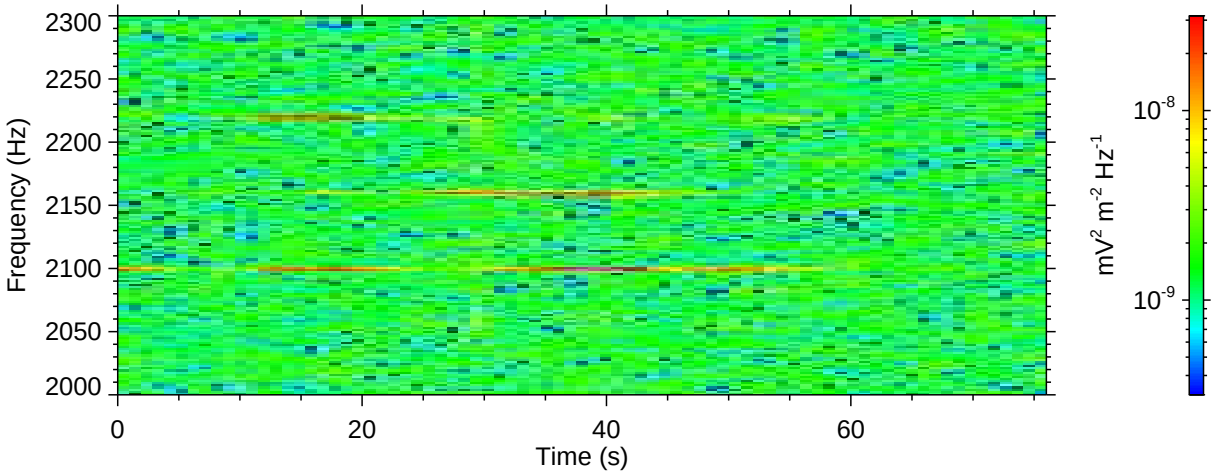

FIG. 4.1 – Spectrogramme fréquence-temps des fluctuations du champ électrique correspondant à un événement PLHR. Les données ont été mesurées le Février 1, 2006 après 19:06:32 UT quand le satellite se trouvait au-dessus des États-Unis. Des lignes sont visibles aux fréquences 2100 Hz, 2160 Hz et 2220 Hz, et la séparation en fréquence de ces lignes est ainsi 60 Hz. (d'après *Němec et al.* (2007c))

2004 après 00:50:30 UT. La diminution d'intensité des ondes à des fréquences inférieures à 450 Hz est causée par la coupure près de la fréquence locale cyclotronique des protons (*Santolík et al.*, 2006). D'autres exemples d'émissions MLR et d'émissions électromagnétiques harmoniques dans la bande EBF sont présentés dans les Annexes C et D.

Les Figures 4.4 et 4.5 montrent les différences principales entre les événements PLHR (49 événements inclus) et les autres événements (la mélange de MLR et des émissions électromagnétiques harmoniques dans la bande EBF, 23 événements en total). L'activé géomagnétique (exprimée en utilisant la valeur de l'index Kp) pendant l'observation des événements est vérifiée dans la Figure 4.4. On peut voir que les événements PLHR sont observées pendant tous les niveaux de l'activité géomagnétique, il n'y a aucune différence entre la distribution des valeurs Kp pendant l'occurrence des événements PLHR et la distribution des valeurs Kp normale. D'un autre côté, les événements MLR / les émissions électromagnétiques harmoniques dans la bande EBF sont plus observées pendant une activité géomagnétique soutenue.

Le panneau à gauche de la Figure 4.5 montre les fréquences centrales des émissions PLHR en les comparant avec les émissions ayant une structure fréquencielle linéaire. On peut voir que les événements PLHR sont plus souvent observées dans la gamme de fréquence 2-3 kHz. Le panneau à droite de la Figure 4.5 représente l'intensité maximale des événements, montrant que l'intensité des événements du type PLHR est assez faible en comparaison de celles des événements MLR / émissions électromagnétiques harmoniques dans la bande EBF (on peut aussi bien le voir dans les exemples des Figures 4.1, 4.2 et 4.3).

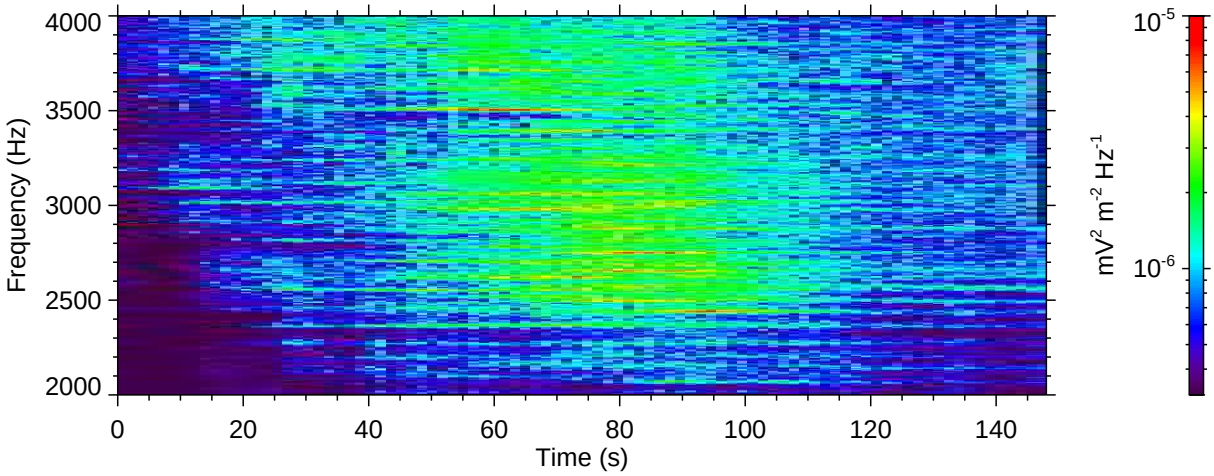

FIG. 4.2 – Spectrogramme fréquence-temps des fluctuations du champ électrique correspondant à un événement MLR. Les données ont été mesurées le Janvier 19, 2007 après 06:26:02 UT.

La Figure 4.6 montre bien la différence entre des événements MLR et des émissions électromagnétiques harmoniques dans la bande EBF. Les fréquences centrales des événements en fonction de la latitude géomagnétique forment deux groupes distincts. La première classe comprend des événements aux fréquences inférieures à environ 1 kHz localisées près de l'équateur magnétique ($\lambda_m < 15°$) – ces événements sont les émissions électromagnétiques harmoniques dans la bande EBF. La deuxième classe comprend des événements aux fréquences plus hautes localisées aux latitudes plus grandes ($\lambda_m > 40°$) – ces événements sont les émissions du type MLR.

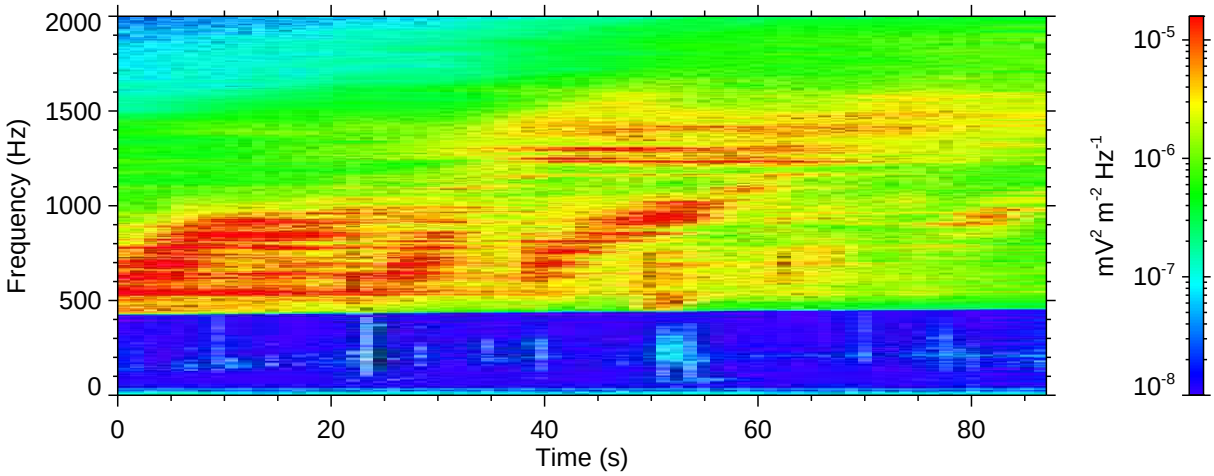

FIG. 4.3 – Spectrogramme fréquence-temps des fluctuations du champ électrique correspondant à des émissions électromagnétiques harmoniques dans la bande EBF. Les données ont été mesurées le Novembre 10, 2004 après 00:50:30 UT.

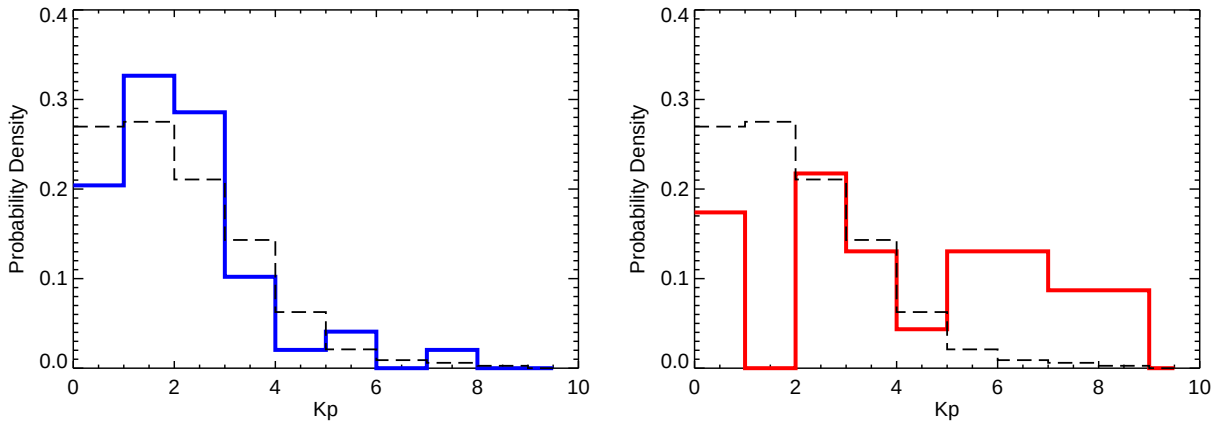

FIG. 4.4 – Histogrammes des indices Kp pendant l'observation des événements PLHR (à gauche, ligne en plein) et pendant l'observation des événements MLR / des émissions électromagnétiques harmoniques dans la bande EBF (à droite, ligne pleine). L'histogramme de tous les indices Kp pendant la période analysée est tracé dans les deux panneaux avec une ligne en tireté. (d'après *Němec et al.* (2007b))

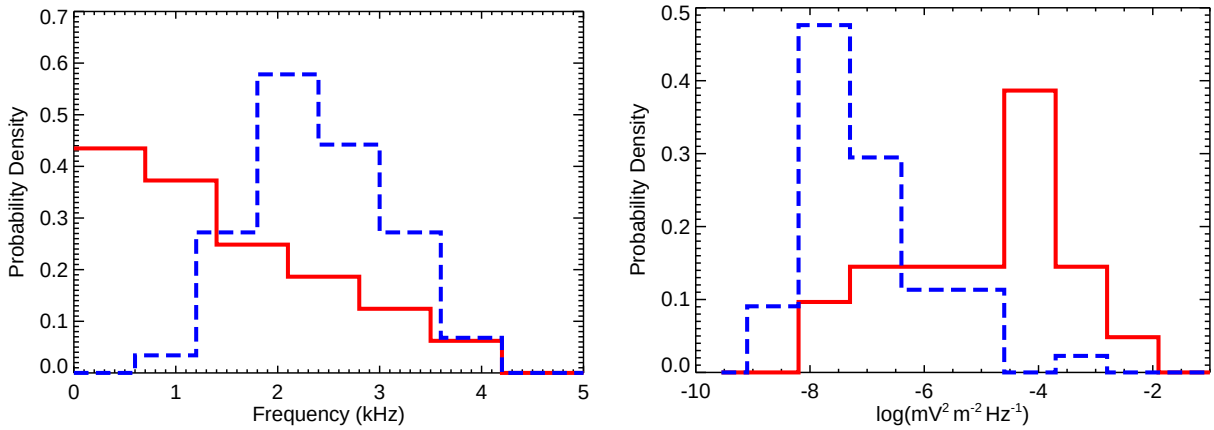

FIG. 4.5 – (à gauche) Histogrammes des fréquences centrales des événements PLHR (ligne en tireté) et des événements MLR / des émissions électromagnétiques harmoniques dans la bande EBF (ligne pleine). (à droite) Histogrammes des intensités maximales des événements PLHR (ligne en tireté) et des événements MLR / des émissions électromagnétiques harmoniques dans la bande EBF (ligne pleine). (d'après *Němec et al.* (2007b))

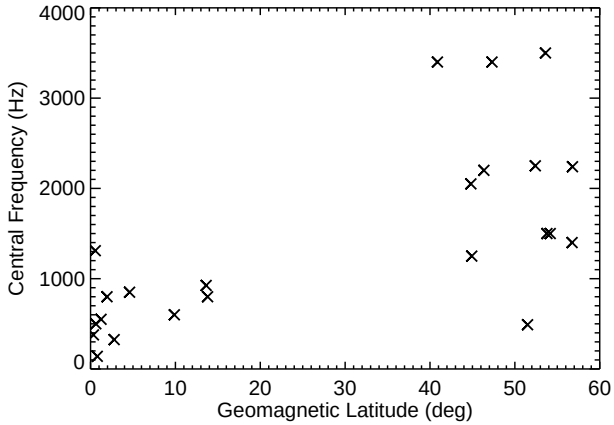

FIG. 4.6 – Fréquences centrales des événements MLR / des émissions électromagnétiques harmoniques dans la bande EBF en fonction de la latitude géomagnétique. (d'après *Němec et al.* (2007b))

4.2 Résultats obtenus pour PLHR (d'après *Němec et al.* (2006b, 2007c, 2008c))

Tous les événements PLHR analysés ont été mesurés en mode Burst et trouvés par une procédure automatique pour leur identification (*Němec et al.*, 2006b). Dans la Figure 4.7 nous présentons encore un exemple de ce type d'émissions. Les données ont été mesurées le Mars 25, 2006 après 19 :13 :32 UT quand le satellite était au-dessus de la Finlande. Le premièr panneau représente le spectrogramme fréquence-temps des fluctuations du champ électrique. Le deuxième panneau représente le spectre de puissance des 18 premières secondes de données. L'intensité des émissions est clairement plus forte pour les fréquences 1650 Hz, 1750 Hz, 1850 Hz, 1950 Hz, 2050 Hz et 2150 Hz. Une faible augmentation de l'intensité des ondes est aussi visible aux fréquences 2250 Hz, 2350 Hz et 2450 Hz. La séparation en fréquence entre les lignes individuelles est 100 Hz, ce qui correspond bien à la fréquence principale des systèmes électriques en Finlande (50 Hz).

Les locations des émissions PLHR avec une séparation en fréquence entre les lignes individuelles de 50/100 Hz sont indiquées sur la Figure 4.8 (17 événements). Les locations des émissions PLHR avec une séparation en fréquence entre les lignes individuelles de 60/120 Hz sont indiquées sur la Figure 4.9 (32 événements). Les lignes du champ magnétique et les empreintes des points des observations au sol sont indiquées par des lignes et des petits points, respectivement. Aussi, les régions avec le mode Burst toujours actif sont tracées en gris. A partir de ces figures, on peut bien voir que les locations des événements correspondent bien aux fréquences principales des systèmes électriques au-dessous du point d'observation ou au point conjugué : les événements avec une séparation des lignes individuelles en fréquence de 50/100 Hz sont observés presque toujours au-dessus de l'Europe et les événements avec une séparation en fréquence de 60/120 Hz au-dessus des États-Unis, du Brésil et du Japon.

Les Figures 4.10 et 4.11 montrent les résultats de l'étude de l'intensité des lignes individuelles que forment les événements PLHR. Sur le panneau à gauche de la Figure 4.10 on voit que l'intensité des lignes individuelles observées pendant le jour est plus faible que l'intensité des lignes individuelles observées pendant la nuit. Pour expliquer cette différence nous avons fait le calcul numérique "full-wave" de l'efficacité de couplage des ondes à la surface de la Terre jusqu'à l'altitude du satellite DEMETER. Les résultats obtenus sont tracés dans la Figure 4.11 pour la fréquence des ondes 2.5 kHz et pour deux régions différentes (la Finlande et le Japon). On peut voir, qu'il y a une différence énorme entre la couplage pendant le jour et pendant la nuit (la couplage est environ 5 fois plus facile pendant la nuit). En plus, le couplage est plus facile dans la région de la Finlande que dans la région du Japon – ceci à cause de la latitude géomagnétique différente (57.5° pour la Finlande, 23° pour le Japon). L'efficacité du couplage est meilleure aux latitudes géomagnétiques plus grandes à cause de l'inclination magnétique plus près de 90° et aussi à cause du champ magnétique plus intense. Finalement, quand on utilise cette efficacité de couplage numériquement calculée pour estimer l'intensité des événements au sol, on obtient les résultats tracés sur le panneau à droite de la Figure 4.10. On peut voir

que l'intensité rayonnée au sol est bien plus grande pendant le jour que pendant la nuit. Cela correspond bien à plus de lignes individuelles observées pendant le jour, quand la consommation d'électricité est plus grande.

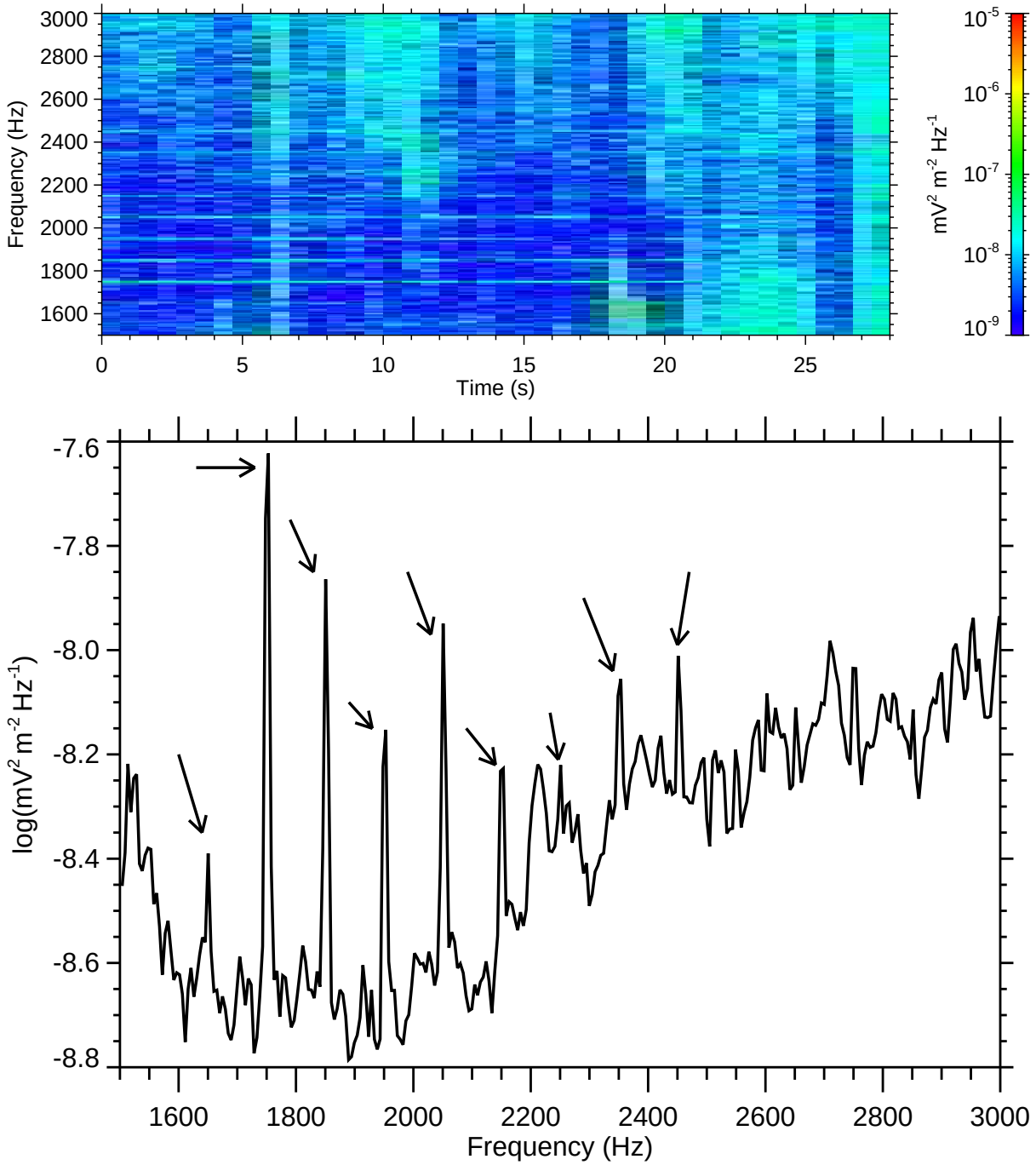

FIG. 4.7 – (dessus) Spectrogramme fréquence-temps des fluctuations du champ électrique correspondant à un des événements ayant une séparation en fréquence entre les lignes individuels de 50/100 Hz. Les données ont été mesurées le Mars 25, 2006 après 19:13:32 UT quand le satellite était au-dessus de la Finlande. (en bas) Spectre de puissance des 18 premières secondes de données. Les pics les plus importantes sont marqués par des flèches. (d'après *Němec et al.* (2007b))

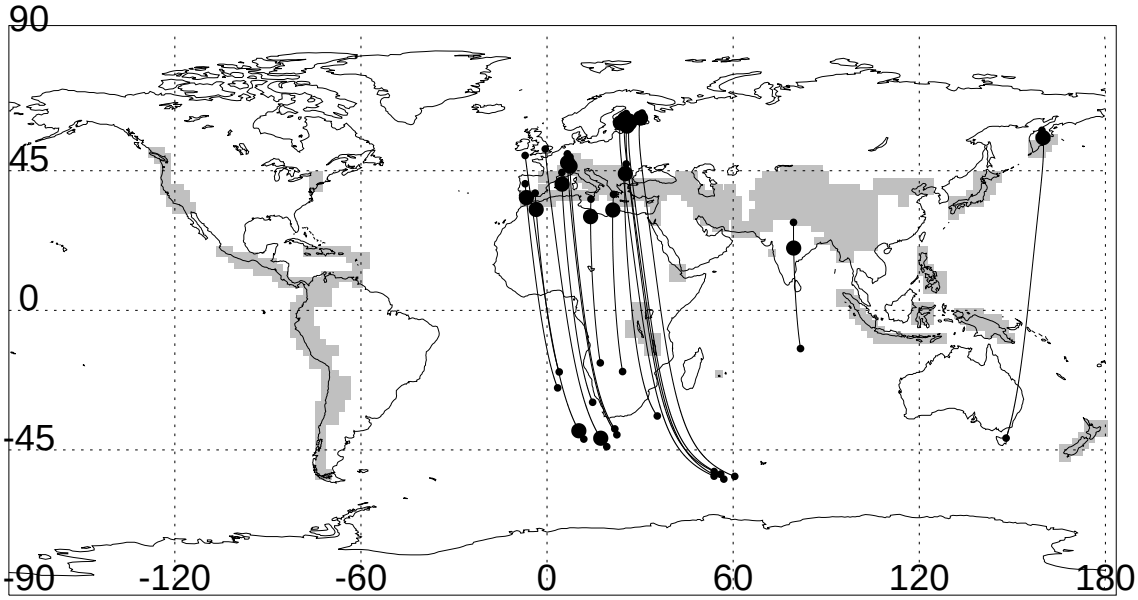

FIG. 4.8 – arte des locations géographiques des événements PLHR avec une séparation en fréquence des lignes individuelles de 50/100 Hz (grands points). Les lignes du champ magnétique et les empreintes des points d'observations au sol sont représentées par les lignes et les petits points, respectivement. Les régions avec le mode Burst toujours actif sont tracées en gris. (d'après *Němec et al.* (2007c))

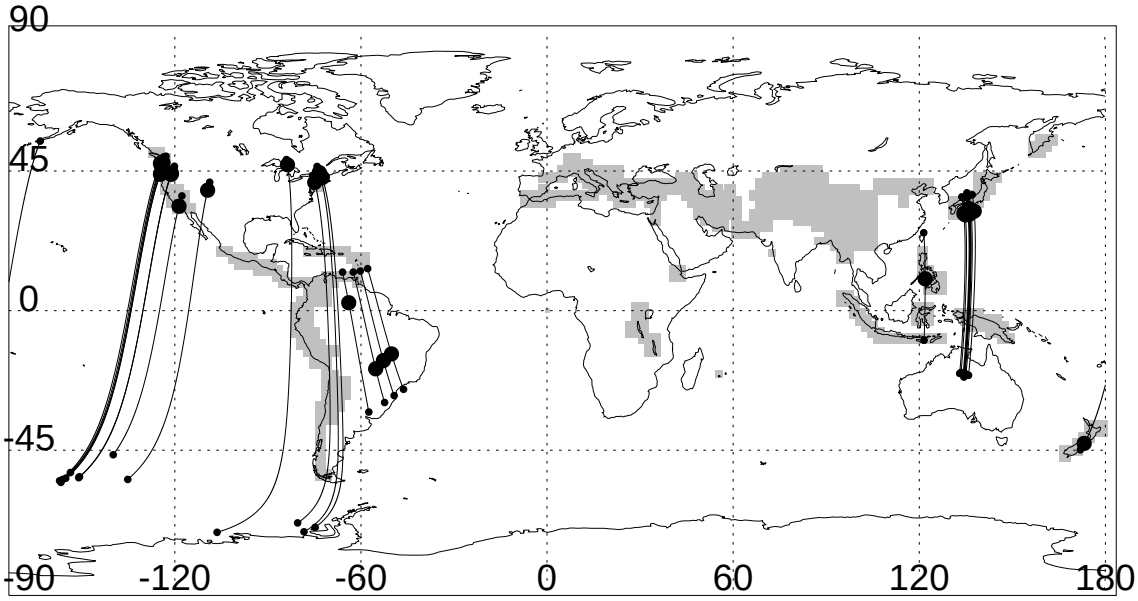

FIG. 4.9 – Identique à la Figure 4.8, mais pour les événements PLHR avec une séparation en fréquence des lignes individuelles de 60/120 Hz. (d'après *Němec et al.* (2007c))

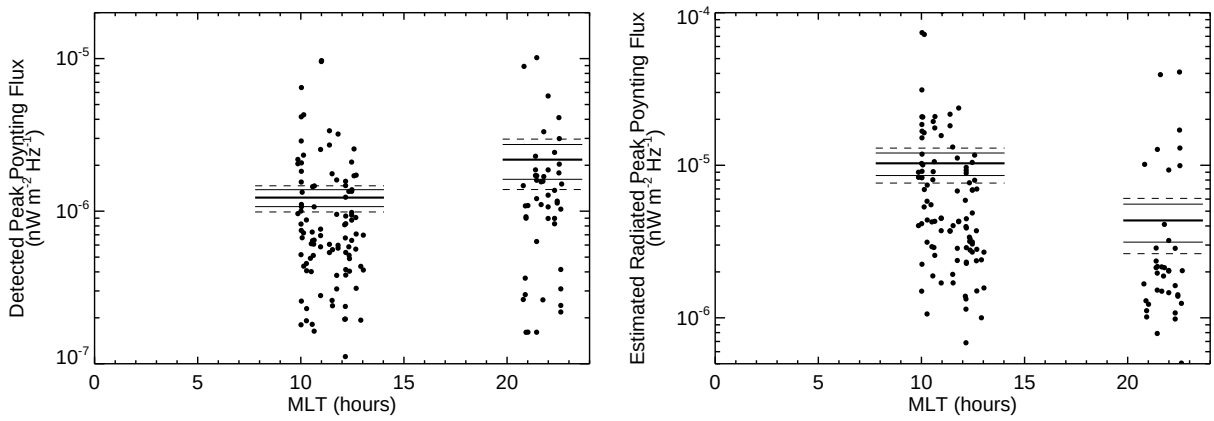

FIG. 4.10 – (à gauche) Densité spectrale du flux du vecteur de Poynting maximale correspondant aux lignes individuelles des événements PLHR en fonction du temps local magnétique. Les valeurs moyennes pour le jour/ la nuit et les écarts type correspondants sont tracés avec des traits horizontaux. (à droite) Densité spectrale du flux du vecteur de Poynting estimée pour les lignes individuelles des événements PLHR au sol en fonction du temps local magnétique. Les valeurs moyennes pour le jour / la nuit et les écarts type correspondants sont tracés avec des traits horizontaux. (d'après *Němec et al.* (2008c))

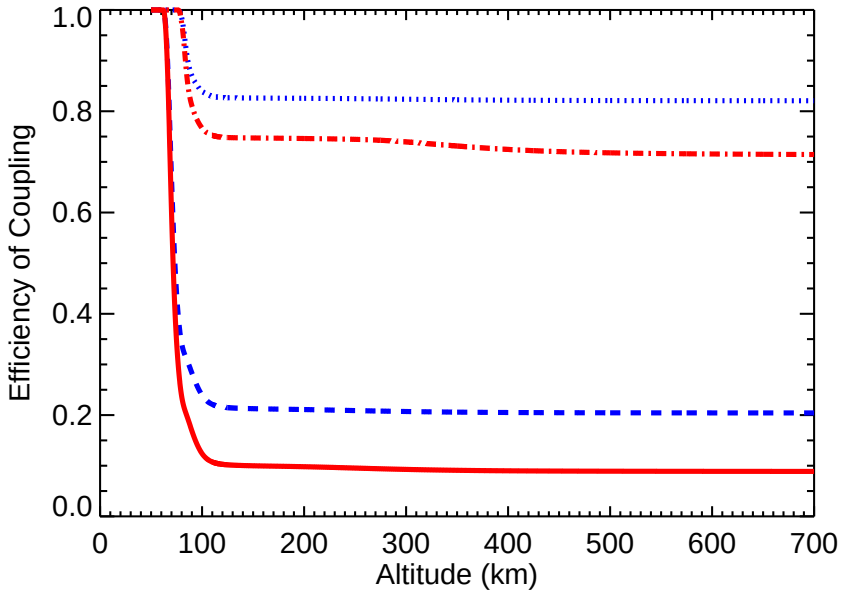

FIG. 4.11 – Efficacité de couplage de l'onde à la fréquence 2.5 kHz en fonction de l'altitude pour la nuit et la région de la Finlande (ligne en pointillé), la nuit et la région du Japon (ligne en tireté-pointillé), le jour et la région de la Finlande (ligne en tireté) et le jour et la région du Japon (ligne pleine). (d'après *Němec et al.* (2008c))

4.3 Résultats obtenus pour les MLR (d'après *Němec et al.* (2009a))

Nous avons analysé 657 événements du type MLR trouvés manuellement dans 3 ans de données Survey (*Němec et al.*, 2009a). Ces événements ont été trouvés dans 549 demi-orbites sur 26036 vérifiées (on peut avoir deux événements MLR sur une même demi-orbite, mais localisés aux points conjugués). Quand on vérifie le temps local magnétique pendant l'observation des événements, on trouve que 390 événements ont été détectées pendant le jour et 267 pendant la nuit. Cette différence est statistiquement significative (*Němec et al.*, 2009a).

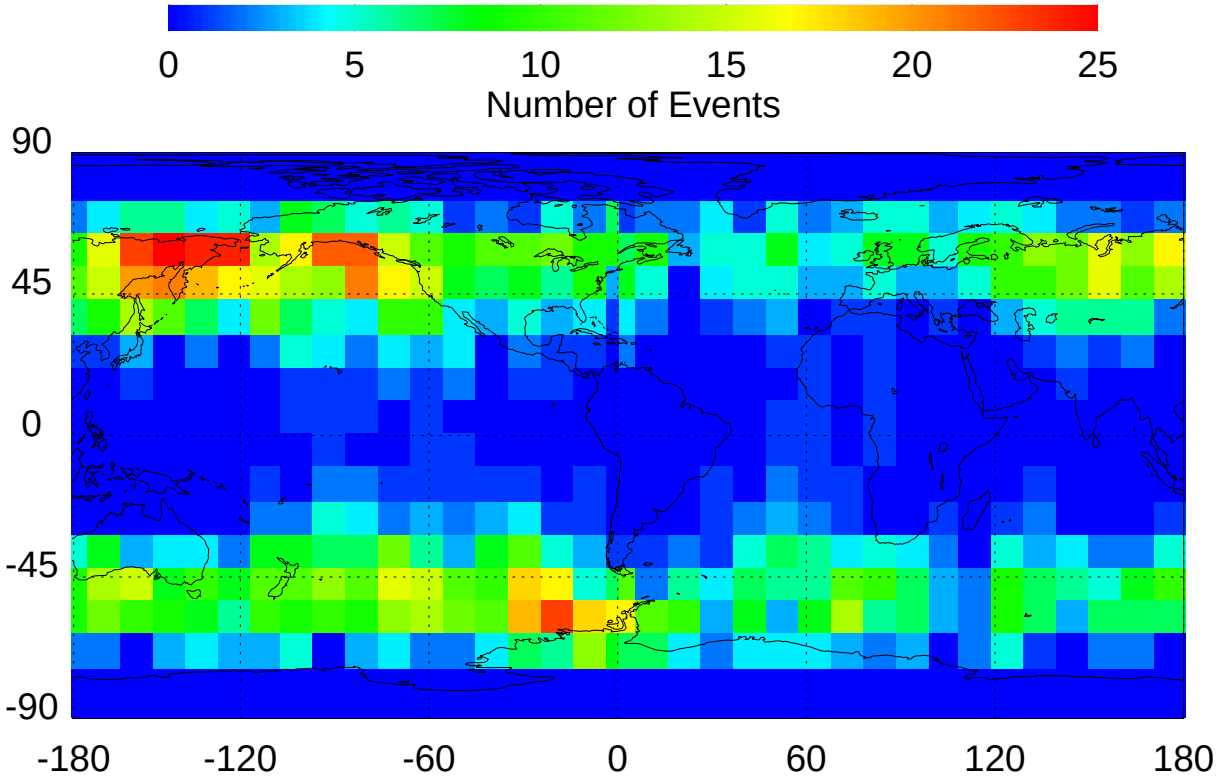

FIG. 4.12 – Carte d'occurrence des événements MLR en coordonnées géomagnétiques. Le nombre des événements dans une case latitude-longitude est marqué par la couleur. (d'après *Němec et al.* (2009a))

La Figure 4.12 représente la carte des positions de ces événements en coordonnées géomagnétiques. On peut voir que la plupart des événements est localisée aux latitudes géomagnétiques hautes (il n'y a aucun événement observés aux latitudes géomagnétiques supérieures à 65° à cause de la limitation du satellite DEMETER – voir le Chapitre 2). L'effet intéressant est qu'il y a moins d'événements au-dessus de l'Océan Atlantique. Ceci est probablement lié à l'anomalie de l'Atlantique-Sud (*Němec et al.*, 2009a).

La Figure 4.13 présente les valeurs de L centrales des événements MLR en fonction de la position de la plasmapause (*Moldwin et al.*, 2002). Elle montre que la majorité des événements est observée dans la plasmasphère (la partie à droite en bas). Quelques événements semblent être observés hors de la plasmasphère, mais on peut l'expliquer plus probablement par des imprécisions dans le modèle (*Němec et al.*, 2009a).

Les Figures 4.14 et 4.15 montrent les résultats de la méthode des époques superposées que nous avons utilisée pour vérifier si l'occurrence des événements MLR est connecté à l'activité géomagnétique. La Figure 4.14 a été obtenue pour l'index de l'activité géomagnetique Kp, la Figure 4.15 a été obtenue pour l'index de l'activité géomagnétique Dst. Le panneaux à gauche montrent la valeur moyenne de l'index approprié en fonction du temps relatif aux MLR, aussi bien que l'écart type. Les panneaux à droite montrent la valeur médiane en fonction du temps relatif aux MLR. On peut voir que les événements sont observés pendant (ou juste après) une activité géomagnétique non nulle. L'effet est statistiquement bien significatif, mais l'amplitude de l'augmentation est assez faible en comparaison avec les fluctuations normales des indices Kp et Dst (*Němec et al.*, 2009a).

Les derniers résultats que nous présentons dans cette section concernent une événement très intéressant dans laquelle une émission PLHR et une émission MLR sont observées pendant la même demi-orbite. Se pose alors la question naturelle : est-ce que cela représente un cas où les MLR sont induites par les PLHR ? La Figure 4.16 représente le spectrogramme de tout la demi-orbite. L'événement PLHR est observé environ entre 08 :01 :30 UT et 08 :04 :30 UT dans la gamme de fréquence 2800-3600 kHz. L'événement MLR se trouve dans la région conjugué, il est observé approximativement entre 08 :31 :00 UT et 08 :36 :00 UT dans la gamme de fréquence 3200-4000 kHz. Il est bien plus intense que l'événement PLHR, correspondant ainsi aux résultats décrits dans la Section 4.1.

Le panneau à gauche de la Figure 4.17 représente le spectrogramme fréquence-temps détaillé de l'événement PLHR. On peut clairement voir les lignes horizontales que forment l'événement. En plus, le mode Burst était actif, permettant ainsi de construire le spectre de puissance détaillé. Celui-ci est représenté dans le panneau à droite de la Figure 4.17. On peut identifier les fréquences avec l'intensité maximale : 2950 Hz, 3000 Hz, 3050 Hz, 3150 Hz, 3250 Hz, 3350 Hz, 3450 Hz, 3550 Hz et 3650 Hz, correspondant à la fréquence principale du système électrique 50 Hz (l'événement a été observé au-dessus de la Russie. Le spectrogramme fréquence-temps détaillé de l'événement MLR est représenté dans la Figure 4.18.

L'idée que les MLR sont générés par les PLHR est assez vielle (*Bullough*, 1995; *Nunn et al.*, 1999), mais elle a toujours manqué de validation expérimentale – ce qui fait que l'observation décrite au dessus a autant d'importance. Les événements sont localisés dans des régions conjuguées et l'événement PLHR a été observé le premièr. Cette observation ne représente pas un preuve définitive que les MLR sont générés par les PLHR, mais elle montre que – au moins pour ce cas – les deux sont probablement connectés. En plus, on comprend assez bien l'origine des événements PLHR (*Němec et al.*, 2006b, 2007c, 2008c) ; il est alors naturelle de supposer que les MLR sont affectés par les PLHR et non vice versa.

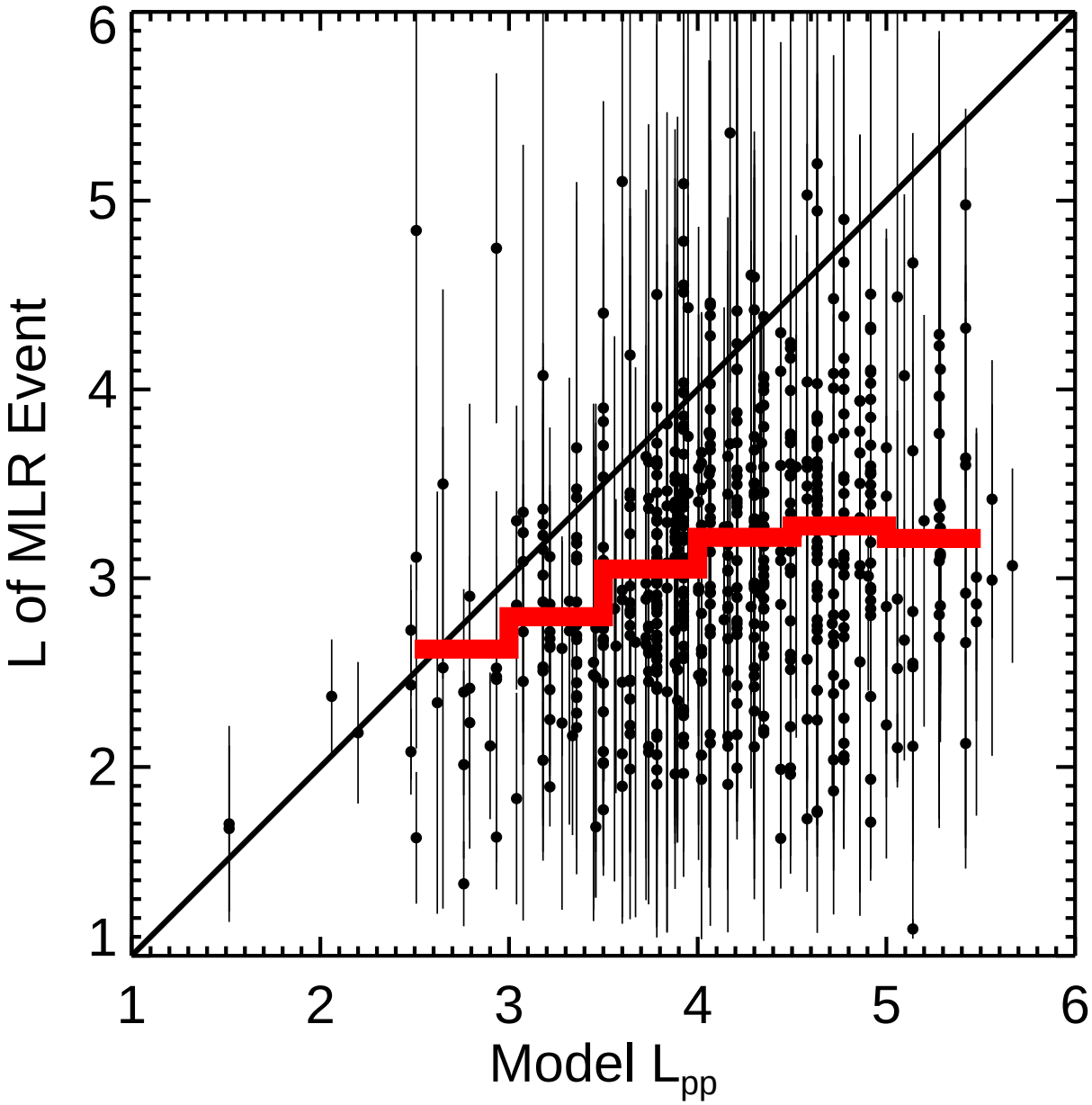

FIG. 4.13 – (points) Valeurs de L centrales des événements MLR en fonction de la position de la plasmapause (obtenue par un modèle). (ligne rouge) Valeurs moyennes des valeurs de L centrales des événements MLR. (lignes verticales) Dimensions des événements MLR. (d'après *Němec et al.* (2009a))

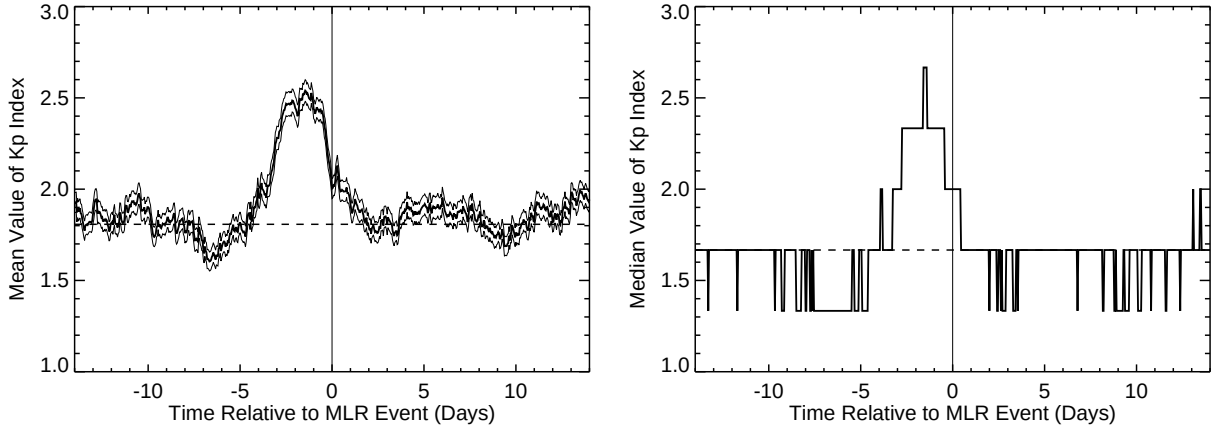

FIG. 4.14 – (à gauche) Trait fort : La valeur moyenne d'index Kp en fonction du temps relatif au temps d'observation des événements MLR. Trait fin : L'écart type de la valeur moyenne. (à droite) La valeur médiane de l'index Kp en fonction du temps relatif au temps des événements MLR. (d'après *Němec et al.* (2009a))

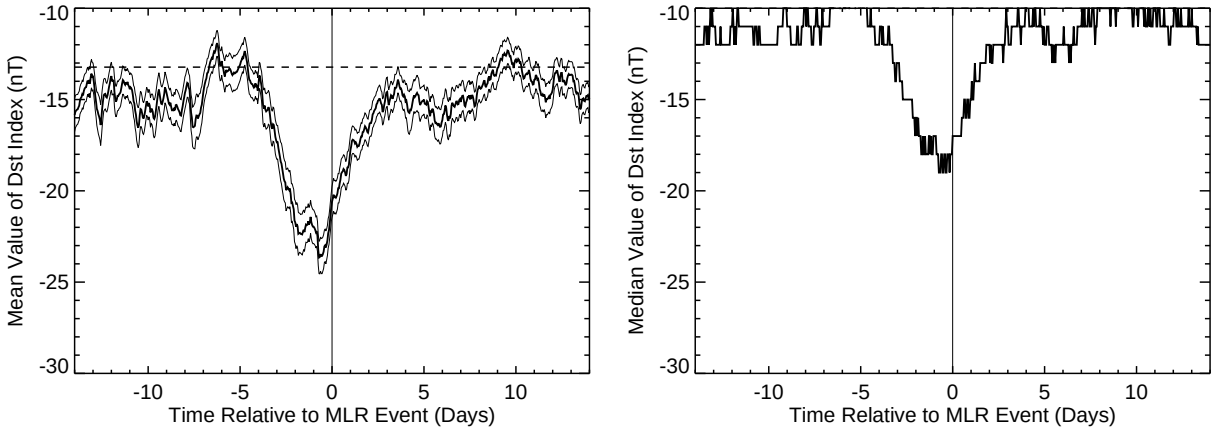

FIG. 4.15 – (à gauche) Trait fort : La valeur moyenne de l'index Dst en fonction du temps relatif au temps d'observation des événements MLR. Trait fin : L'écart type de la valeur moyenne. (à droite) La valeur médiane de l'index Dst en fonction du temps relatif au temps des événements MLR. (d'après *Němec et al.* (2009a))

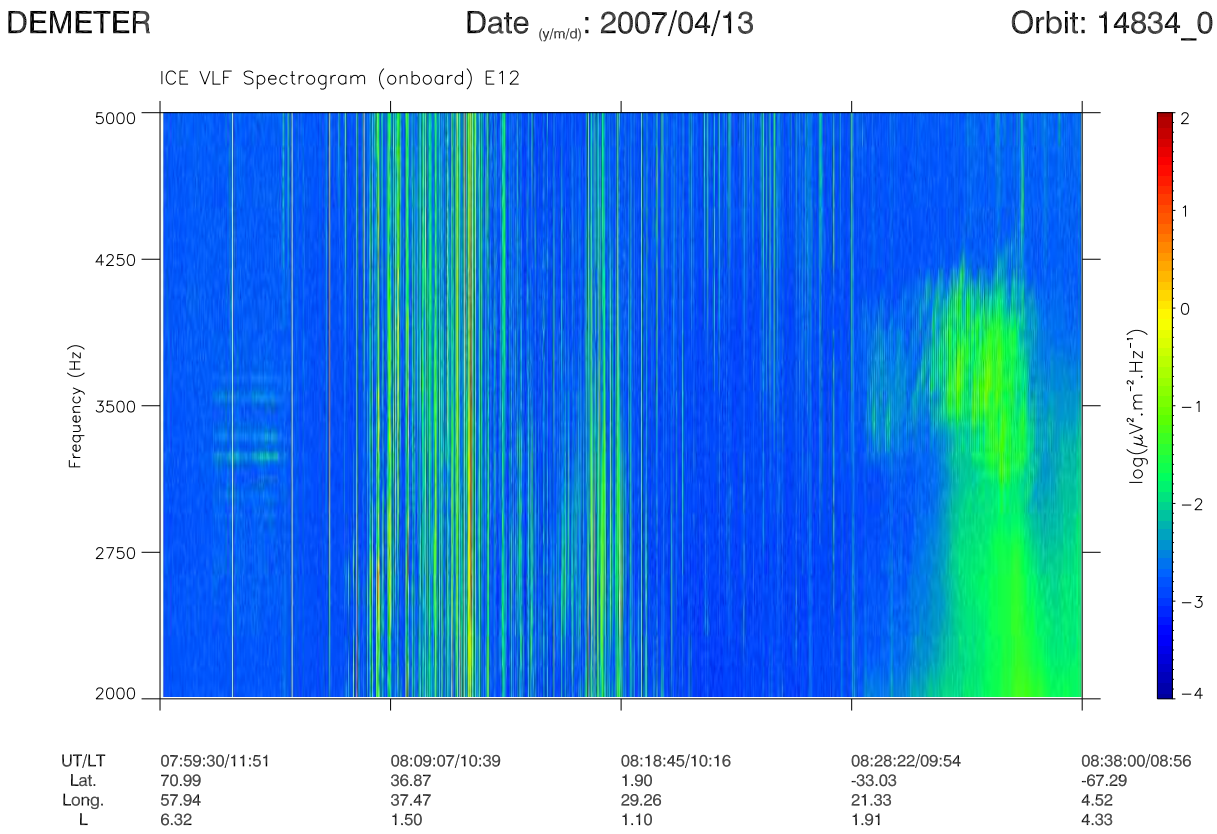

FIG. 4.16 – Spectrogramme fréquence-temps de l'orbite contenant un événement PLHR et un événement MLR dans une région conjuguée. (d'après *Němec et al.* (2009a))

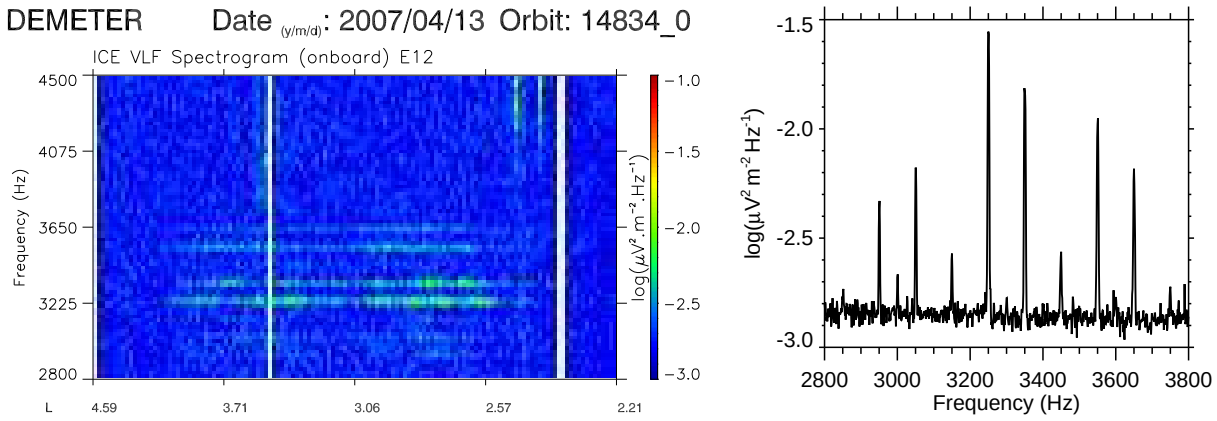

FIG. 4.17 – (à gauche) Spectrogramme fréquence-temps détaillé correspondant à l'événement PLHR de la Figure 4. (à droite) Le spectre de puissance correspondant à l'événement PLHR de la Figure 4.16. (d'après *Němec et al.* (2009a))

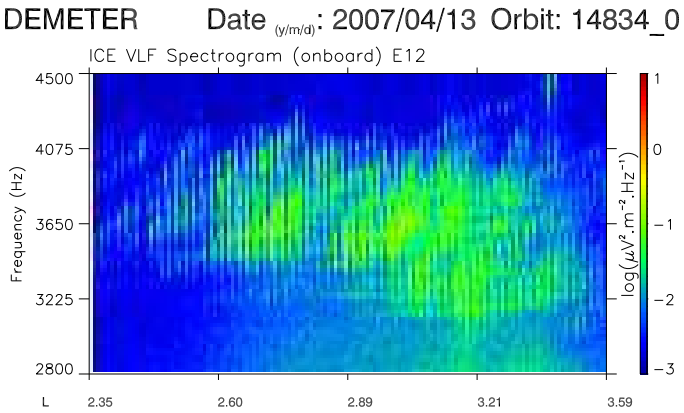

FIG. 4.18 – Spectrogramme fréquence-temps détaillé correspondant à l'événement MLR de la Figure 4.16. (d'après *Němec et al.* (2009a))

4.4 Résultats obtenus pour les émissions électromagnétiques harmoniques dans la bande EBF (d'après *Němec et al.* (2009c))

Nous avons analysé 24 événements d'émissions électromagnétiques harmoniques dans la bande EBF mesurées pendant le mode Burst. Dans ce cas, les formes d'onde des 3 magnétiques et des 3 composants électriques sont mesurées, ce qui nous permet de faire l'analyse détaillée de la propagation des ondes.

La Figure 4.19 présente un exemple de l'analyse détaillée de la propagation des ondes (*Santolík et al.*, 2006) mesurées le Mai 2006, entre 08:16:40 UT et 08:17:55 UT. Les panneaux individuels tracent les spectrogrammes fréquence-temps de : la densité spectrale des fluctuations du champ électrique, la densité spectrale des fluctuations du champ magnétique, l'ellipticité des fluctuations du champ magnétique E_B, l'ellipticité des fluctuations du champ électrique E_E, l'angle polaire du vecteur d'onde θ_k, l'angle azimutal du vecteur d'onde ϕ_k, l'angle polaire du vecteur de Poynting θ_p, l'angle azimutal du vecteur de Poynting ϕ_p et la composant du vecteur de Poynting parallèle au champ magnétique terrestre normalisée par l'écart type. Nous avons choisi la valeur de l'intensité minimale pour tracer seulement les données correspondant à l'événement.

Les valeurs de l'ellipticité des fluctuations du champ magnétique E_B et de l'ellipticité des fluctuations du champ électrique E_E varient entre -1 et 1. Les valeurs négatives correspondent à l'onde polarisée à gauche, les valeurs positives correspondent à l'onde polarisée à droite. La valeur absolue de l'ellipticité est égale au rapport entre l'axe de la polarisation mineure et l'axe de la polarisation majeure : la valeur 0 correspond à la polarisation linéaire, la valeur 1 correspond à la polarisation circulaire. Dans le troisième panneau de la Figure 4.19 on peut voir que la polarisation des fluctuations du champ magnétique est presque linéaire. La polarisation des fluctuations du champ électrique est polarisée à droite et elliptique. Les quatre panneaux suivants représentent les directions du vecteur d'onde et du vecteur de Poynting. On peut voir que les deux angles polaires θ_k et θ_p sont proche de 90 degrés, correspondant ainsi à une propagation perpendiculaire au champ magnétique terrestre. Les angles azimutaux ϕ_k et ϕ_p sont proche de ± 180 degrés, correspondant à une propagation vers la Terre. Toutes ces caractéristiques sont en accord avec la propagation en mode sifflement perpendiculairement au champ magnétique terrestre, avec des fluctuations du champ magnétique orientées parallèlement au champ magnétique terrestre et des fluctuations du champ électrique polarisées elliptiquement dans le plan perpendiculaire au champ magnétique terrestre.

Un résultat très important est présenté dans le dernier panneau de la Figure 4.19 : la composante du vecteur de Poynting parallèle au champ magnétique terrestre est orientée dans la direction opposé au champ magnétique terrestre au Sud de l'équateur magnétique et elle est orientée dans la direction du champ magnétique terrestre au Nord de l'équateur magnétique. Il y a ainsi un changement de l'orientation de la composante parallèle du flux du vecteur de Poynting près de l'équateur magnétique.

Les Figures 4.20, 4.21 et 4.22 représentent les résultats obtenus pour les 24 événements analysés en fonction de la latitude géomagnétique. Pour chaque événement et pour chaque intervalle de temps (1.64 s, voir *Němec et al.* (2009c) pour plus de détails), nous avons calculé la valeur moyenne du paramètre de la propagation choisie. Puis, chacune de ces valeurs moyennes a été représentée par un point dans la figure propre.

La Figure 4.20 représente la direction du vecteur d'onde en fonction de la latitude géomagnétique. Le panneau à droite montre que l'angle azimutal du vecteur d'onde (ϕ_k) est presque toujours près de ± 180 degrés, correspondant à une propagation vers la Terre. Le panneau à gauche montre que la composante du vecteur d'onde parallèle au champ magnétique terrestre est orientée dans la direction opposée au champ magnétique au Sud de l'équateur magnétique ($\theta_k > 90°$) et elle orientée dans la direction du champ magnétique terrestre au Nord de l'équateur magnétique ($\theta_k < 90°$). Elle est ainsi incliné "hors de l'équateur magnétique". A proximité de l'équateur magnétique il y a un changement de l'orientation de la composante parallèle du flux du vecteur de Poynting et ce vecteur de Poynting est orienté presque perpendiculairement au champ magnétique terrestre.

En plus, la dépendance de l'angle polaire correspondant au vecteur d'onde (θ_k) avec la latitude géomagnétique λ_m est presque linéaire (un coefficient de corrélation de 0.76). Nous pouvons ainsi développer un modèle simple en utilisant la théorie du plasma froid et réaliser le fit linéaire suivant :

$$\theta_k = 90 - 1.62\lambda_m \tag{4.1}$$

où θ_k et λ_m sont en degrés. Ce fit linéaire est tracé suivant une ligne épaisse dans le panneau à gauche de la Figure 4.20.

La Figure 4.21 représente la direction du vecteur de Poynting en fonction de la latitude géomagnétique. On peut voir que le vecteur de Poynting est aussi systématiquement orienté vers la Terre et qu'il y a une divergence positive de l'énergie près de l'équateur géomagnétique. En utilisant un fit linéaire 4.1 et la théorie du plasma froid nous avons calculé la dépendance théorique $\theta_p(\lambda_m)$, qui est tracé avec une ligne épaisse dans le panneau à gauche. Les paramètres suivants ont été utilisés :

- la fréquence d'onde 500 Hz, qui est la valeur typique des émissions électromagnétiques harmoniques dans la bande EBF (*Němec et al.*, 2009c)
- le champ magnétique a été calculé en utilisant l'approximation du dipole
- la densité totale des particules 30000 cm^{-3}, avec 78% d'ions oxygène, 20% d'ions hydrogène et 2% d'ions hélium. Ces valeurs sont assez typiques aux altitudes du satellite DEMETER *Santolík et al.* (2006)

On peut voir que la ligne théorique correspond bien à la dépendance observée, montrant qu'ils sont consistant avec la théorie du plasma froid et la propagation dans le mode sifflement.

Les panneaux à gauche et à droite de la Figure 4.22 représentent l'ellipticité des fluctuations magnétiques en fonction de la latitude géomagnétique et l'ellipticité des fluctuations électriques en fonction de la latitude géomagnétique, respectivement. Les lignes épaisses représentent encore la dépendance théorique en utilisant les paramètres mentionnés au-dessus. On peut voir que la polarisation des fluctuations magnétiques est presque linéaire

près de l'équateur magnétique et elle devient presque circulaire, polarisé à droite, aux latitudes géomagnétiques plus grandes. Les fluctuations électriques sont elliptiques, polarisées à droite (voir la discussion plus détaillée dans *Němec et al.* (2009c)).

Ces caractéristiques de la propagation, aussi bien que l'occurrence des émissions près de l'équateur géomagnétique, donnent l'idée que les émissions électromagnétiques harmoniques dans la bande EBF peuvent être liées aux émissions du type "equatorial noise" observées à des plus grandes distances de la Terre (par exemple par les satellites Cluster, voir *Santolík et al.* (2004); *Němec et al.* (2005, 2006a)). Ces émissions recueillies par DEMETER ont probablement la même origine et elles sont alors observés après propagation depuis des altitudes élevées. Mais il peut aussi s'agir des mêmes émissions, mais générées à des altitudes différentes proches de celles de DEMETER.

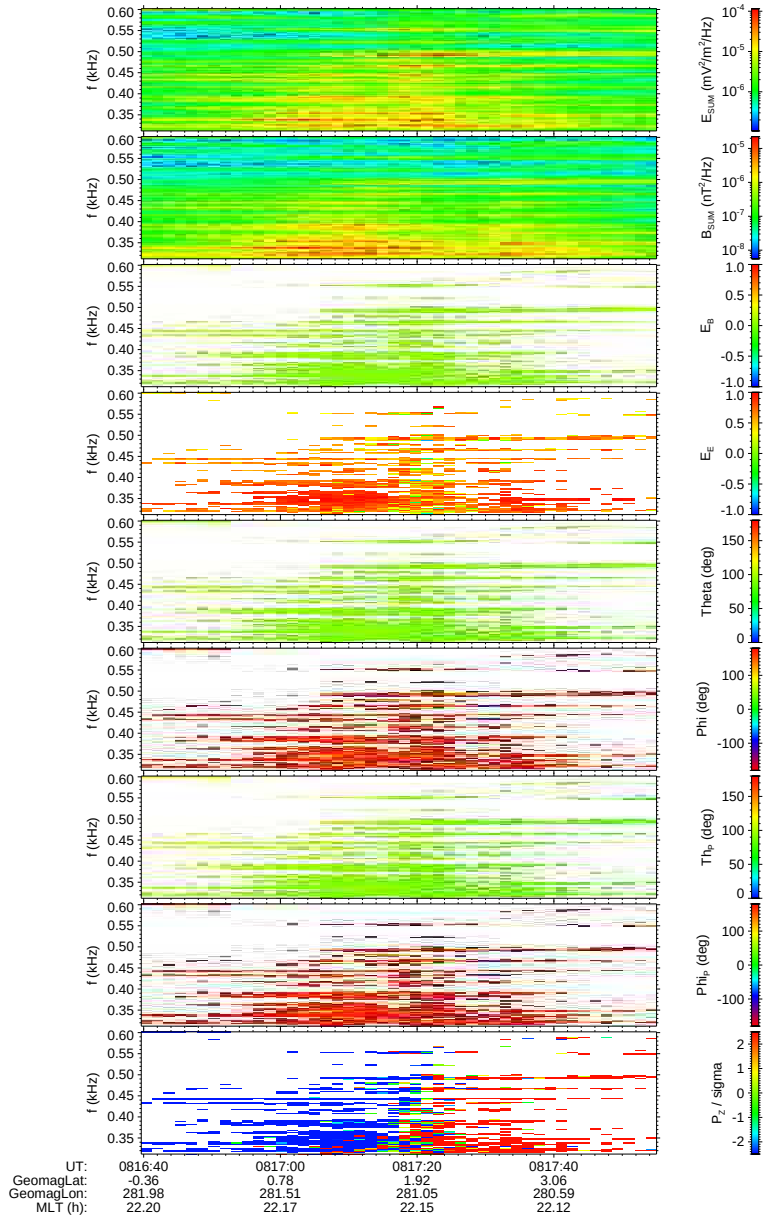

FIG. 4.19 – Analyse détaillée des ondes mesurées le Mai 16, 2005, entre 08:16:40 UT et 08:17:55 UT. Les panneaux représentent les spectrogrammes fréquence-temps de (de haut en bas) : la densité spectrale des fluctuations du champ électrique, la densité spectrale des fluctuations du champ magnétique, l'ellipticité des fluctuations du champ magnétique, l'ellipticité des fluctuations du champ électrique, l'angle polaire du vecteur d'onde, l'angle azimutal du vecteur d'onde, l'angle polaire du vecteur de Poynting, l'angle azimutal du vecteur de Poynting et la composante du vecteur de Poynting parallèle au champ magnétique normalisée par l'écart type. (d'après *Němec et al.* (2009c))

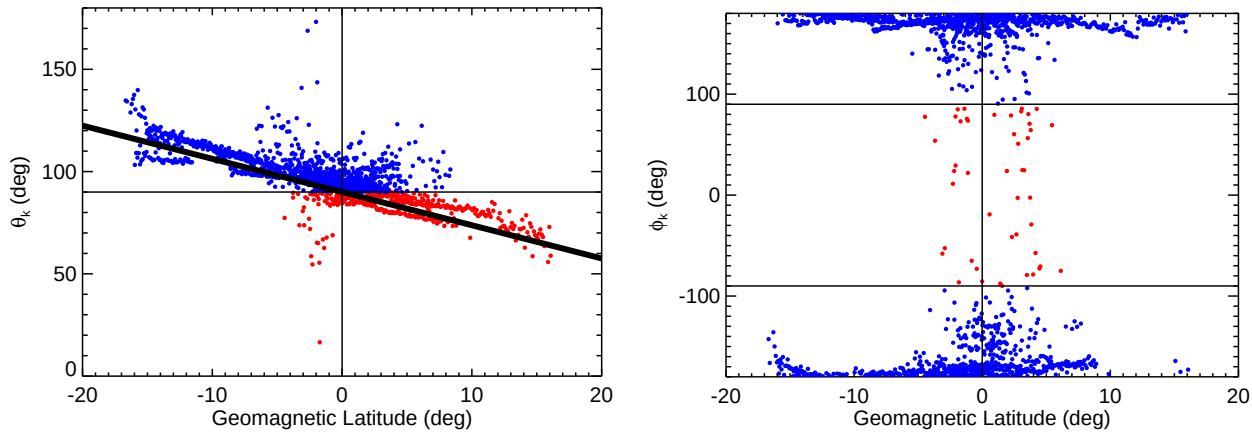

FIG. 4.20 – (à gauche) Angle polaire de la direction du vecteur d'onde en fonction de la latitude géomagnétique. La ligne épaisse représente un fit linéaire. (à droite) Angle azimutal de la direction du vecteur d'onde en fonction de la latitude géomagnétique. (d'après *Němec et al.* (2009c))

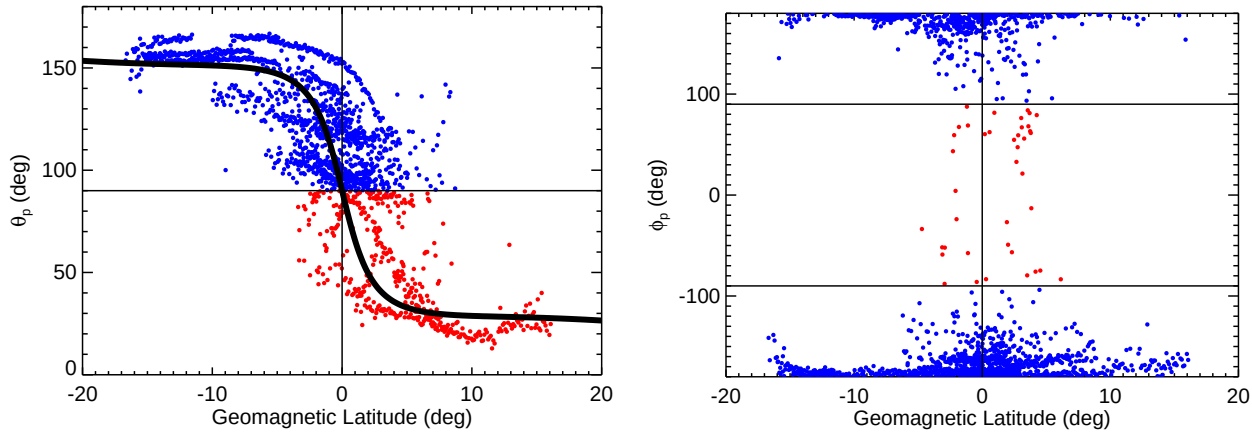

FIG. 4.21 – (à gauche) Angle polaire de la direction du vecteur de Poynting en fonction de la latitude géomagnétique. La ligne épaisse représente le résultat d'un modèle en utilisant la théorie du plasma froid (voir le texte). (à droite) Angle azimutal de la direction du vecteur de Poynting en fonction de la latitude géomagnétique. (d'après *Němec et al.* (2009c))

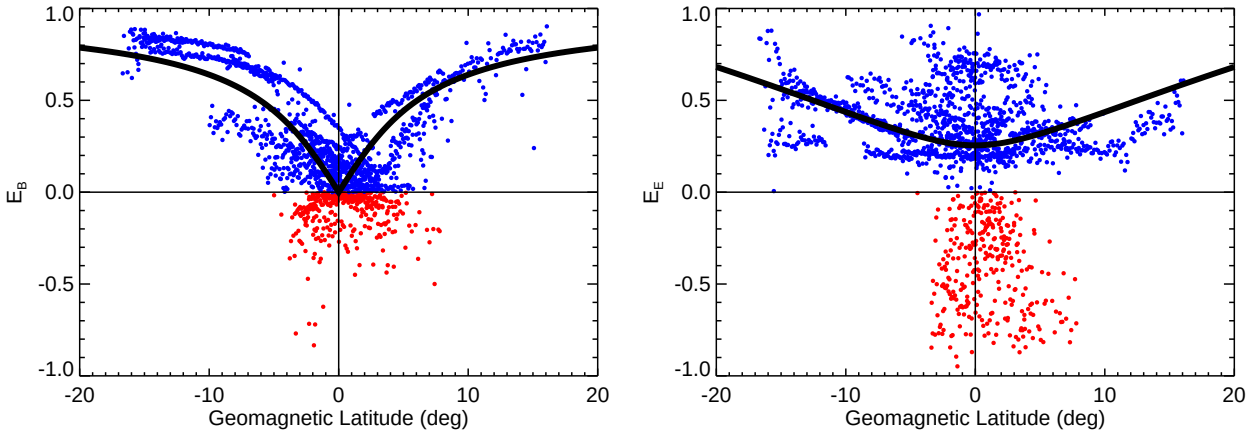

FIG. 4.22 – (à gauche) Ellipticité des fluctuations du champ magnétique en fonction de la latitude géomagnétique. (à droite) Ellipticité des fluctuations du champ électrique en fonction de la latitude géomagnétique. La ligne épaisse réprésente le résultat d'un modèle en utilisant la théorie du plasma froid. (d'après *Němec et al.* (2009c))

4.5 Synthèse

Nous avons mis en évidence les points suivants :

– PLHR (rayonnement harmonique des lignes électriques) :

1. La séparation en fréquence des lignes qui forment ces événements correspond bien à la fréquence du système électrique au-dessous du point d'observation (ou au point conjugué).
2. L'intensité des événements observés pendant le jour est plus faible que l'intensité des événements observés pendant la nuit. On peut l'expliquer en montrant l'efficacité du couplage des ondes électromagnétiques dans l'ionosphère.

– MLR (lignes magnétosphèriques) :

1. Il y a moins d'événements au-dessus de l'Océan Atlantique (à l'Est de l'anomalie de l'Atlantique-Sud).
2. Les événements sont observés (presque) uniquement dans la plasmasphère.
3. Les événements sont observés après une augmentation de l'activité géomagnétique. Cela montre que ces ondes sont générées par une mécanisme d'interaction onde-particule.

– Émissions électromagnétiques harmoniques en bande EBF :

1. Les ondes proviennent de distances plus grandes que la Terre.
2. La région de génération des ondes est localisée dans le plan de l'équateur magnétique.
3. Il est possible que ces émissions aient pour origine les émissions de "bruit équatorial" observées à plus grande distance de la Terre – ou qu'elles soient aussi un bruit équatorial généré par le même mécanisme mais plus près de la Terre.

Chapitre 5

Conclusions générales

Dans cette thèse nous avons présenté les résultats obtenus en utilisant les données électromagnétiques mesurées par le satellite DEMETER. La plupart des résultats ont déjà été publiés dans des journaux scientifiques ; ces papiers se trouvent en annexe.

Il y a beaucoup d'ondes électromagnétiques dans l'environnement ionisé autour de la Terre. Leur analyse est très importante parce que dans le plasma presque non-collisionnel ces ondes sont le seul moyen du transport de l'énergie. Dans cette thèse nous nous sommes concentrés sur deux types des ondes assez spécifiques : les ondes liées à l'activité sismique et les émissions avec des structures fréquentielles linéaires. Les deux correspondent bien aux objectifs scientifiques de la mission DEMETER. L'étude des effets en liaison avec l'activité sismique est très significative : ils sont rapportés quelques jours/heures avant le choc principal et il y a donc une possibilité d'application pour la prédiction des tremblements de terre à court-terme. Les émissions avec des structures fréquentielles sont très intéressantes, parce qu'elles sont probablement lié à l'activité humaine (au moins dans certains cas) bien que leur origine est toujours mal comprise.

Nous avons fait l'étude statistique des effets électromagnétiques liés à l'activité sismique. Deux méthodes différentes ont été utilisées : la méthode des époques superposées et la méthode qui utilise le test Mann-Whitney. Dans les deux cas, des cartes globales d'émissions électromagnétiques furent utilisées pour éliminer l'influence de la variabilité naturelle. Les résultats obtenus montrent que :

1. Il y a une corrélation entre l'intensité des ondes électromagnétiques TBF dans l'ionosphère et l'activité sismique.
2. L'effet est observé seulement pendant la nuit. Il n'y a aucun effet similaire pendant le jour.
3. L'intensité des ondes électromagnétiques dans une gamme de fréquence $1 - 2$ kHz est plus faible que normalement peu ($0 - 4$ heures) avant le choc principal. Les dimensions spatiales de la région affectée sont de quelques centaines de kilomètres.
4. L'effet est plus fort pour les tremblements de terre de forte magnitude.
5. L'effet est plus fort pour les tremblements de terre moins profonds. Aucun effet a été observé pour les tremblements de terre très profonds (une profondeur > 40 km).

6. L'effet est observé pour les tremblements de terre sous la mer aussi bien que pour les tremblements de terre sur les continents.
7. L'effet semble déplacé d'environ 2° à l'Ouest des épicentres des tremblements de terre.

Néanmoins, il est nécessaire de comprendre que cette corrélation a été trouvée seulement en utilisant un grand nombre de données et que la situation pour un seul tremblement de terre peut être assez différente. Nous espérons que les résultats de cette analyse aideront à comprendre les différents effets qui accompagnent les tremblements de terre.

Il faut maintenant regarder au cas par cas les différents séismes qui ont statistiquement contribué à la diminution du champ électrique qui a été observé pour voir s'ils ont des caractéristiques communes. Les autres paramètres mesurés par DEMETER comme les densités et températures ionique et électronique doivent être aussi prises en compte. Une piste peu venir de la fréquence à laquelle cette diminution du champ électrique a été observée. La fréquence de 1700 Hz correspond en effet à une fréquence de coupure des ondes dans le guide Terre-ionosphère la nuit. Cette fréquence de coupure affecte les ondes qui se réfléchissent au bas de la couche E c'est-a-dire vers 90 km d'altitude. Cela voudrait dire que les séismes peuvent modifier l'ionosphère à cette altitude et qu'il faudrait plutôt rechercher des perturbations de densité à cet endroit.

Nous avons fait l'étude systématique des événements électromagnétiques ayant une structure fréquencielle linéaire. Nous avons montré qu'il y a trois types différents d'émissions : PLHR, MLR et EM harmoniques dans la bande EBF. Plus, nous avons étudié chaque type séparément. Les plus importants résultats que nous avons obtenus sont :

- PLHR (rayonnement harmonique des lignes électriques) :
  1. La séparation en fréquence des lignes qui forment ces événements correspond bien à la fréquence du système électrique au-dessous du point d'observation (ou au point conjugué).
  2. L'intensité des événements observés pendant le jour est plus faible que l'intensité des événements observés pendant la nuit. On peut l'expliquer en utilisant l'efficacité du couplage des ondes électromagnétiques dans l'ionosphère.
- MLR (lignes magnétosphèriques) :
  1. Il y a moins d'événements au-dessus de l'Océan Atlantique (à l'Est de l'anomalie de l'Atlantique-Sud).
  2. Les événements sont observés (presque) uniquement dans la plasmasphère.
  3. Les événements sont observés après une augmentation de l'activité géomagnétique.
- Émissions électromagnétiques harmoniques en bande EBF :
  1. Les ondes proviennent de distances plus grandes que la Terre.
  2. La région de génération des ondes est localisée dans le plan de l'équateur magnétique.
  3. Il est possible que ces émissions aient pour origine les émissions de "bruit équatorial" observées à plus grande distance de la Terre – ou qu'elles soient

aussi un bruit équatorial généré par le même mécanisme mais plus près de la Terre.

Les résultats que nous avons obtenus sont très intéressants parce qu'ils ont permis une meilleure compréhension des effets étudiés. Cependant, il reste beaucoup de travail pour le futur. Le satellite DEMETER est toujours en activité et le nombre des données augmente chaque jour, ce qui est particulièrement important pour la statistique des effets électromagnétiques liés à l'activité sismique. Par ailleurs, bien que nous comprenons l'origine de certains événements électromagnétiques ayant une structure fréquencielle linéaire, l'origine des autres est toujours un mystère.

L'enjeu est de savoir si les émissions d'origine humaine aux harmoniques du 50 ou du 60 Hz interagissent avec les particules énergétiques contenues dans les ceintures de radiation et perturbent ainsi l'équilibre de l'environnement terrestre. Pour le moment on ne voit ces ondes à l'altitude des satellites que de manière épisodique probablement parce que leurs amplitudes sont trop faibles (et en dessous du niveau de sensibilité des capteurs). Mais on peut observer leurs effets quand elles déclenchent des émissions de plus forte intensité.

Bibliographie

Artru, J., V. Ducic, H. Kanamori, P. Lognonné, and M. Murakami (2005), Ionospheric detection of gravity waves induced by tsunamis, *Geophys. J. Int.*, *160*, 840–848.

Bell, T. F., J. P. Luette, and U. S. Inan (1982), ISEE 1 observations of VLF line radiation in the Earth's magnetosphere, *J. Geophys. Res.*, *87*(A5), 3530–3536.

Berthelier, J. J., et al. (2006), ICE, the electric field experiment on DEMETER, *Planet. Space Sci.*, *54*(5), 456–471.

Bullough, K. (1995), *Handbook of Atmospheric Electrodynamics*, vol. 2, chap. Power Line Harmonic Radiation : Sources and Environmental Effects, pp. 291–332, CRC Press, Boca Ralton, Fla.

Calais, E., and B. Minster (1995), GPS detection of ionospheric perturbations following the January 17, 1994, Northridge earthquake, *Geophys. Res. Lett.*, *22*, 1045–1048.

Dobrovolsky, I. R., S. I. Zubkov, and V. I. Myachkin (1979), Estimation of the size of earthquake preparation zones, *Pageoph.*, *117*, 1025–1044.

Frid, V., A. Rabinovitch, and D. Bahat (2003), Fracture induced electromagnetic radiation, *J. Phys. D : Appl. Phys.*, *36*, 1620–1628.

Gal'perin, Y. I., V. A. Gladyshev, N. V. Dzhordzhio, V. I. Larkina, and M. M. Mogilevskii (1992), Precipitation of high-energy captured particles in the magnetosphere above the epicenter of an incipient earthquake, *Cosmic Research*, *30*, 89–106.

Gokhberg, M. B., V. A. Morgunov, T. Yoshino, and I. Tomizawa (1982), Experimental measurement of electromagnetic emissions possibly related to earthquakes in japan, *J. Geophys. Res.*, *87*, 7824.

Gokhberg, M. B., V. A. Pilipenko, and O. A. Pokhotelov (1983), Satellite observation of the electromagnetic radiation above the epicentral region of an incipient earthquake, *Dokl. Acad. Sci. USSR Earth Sci. Ser., Engl. Transl.*, *268*(1), 5–7.

Gokhberg, M. B., V. A. Morgounov, and O. A. Pokhotelov (1995), *Earthquake Prediction : Seismo-Electromagnetic Phenomena*, Gordon and Breach Science Publishers.

Grimalsky, V. V., M. Hayakawa, V. N. Ivchenko, Y. G. Rapoport, and V. I. Zadorozhnii (2003), Penetration of an electrostatic field from the litosphere into the ionosphere and its effect on the D-region before earthquakes, *J. Atm. Solar-Terr. Phys.*, *65*, 391–407.

Hayakawa, M. (1996), Special issue : Seismo-electromagnetic phenomena, *JAE*, *116*(3).

Hayakawa, M. (1999), *Atmospheric and Ionospheric Electromagnetic Phenomena Associated with Earthquakes*, TERRAPUB, Tokyo.

Hayakawa, M. (2002), Special issue : Seismo-electromagnetics, *JAE*, *22*(3).

Hayakawa, M. (2004), Special issue : Seismo-electromagnetics and related phenomena, *PCE*, *29*(4–9).

Hayakawa, M., and Y. Fujinawa (1994), *Electromagnetic Phenomena Related to Earthquake Prediction*, TERRAPUB, Tokyo.

Hayakawa, M., and O. Molchanov (2002), *Seismo-Electromagnetics : Ltosphere-Atmosphere-Ionosphere Coupling*, TERRAPUB, Tokyo.

Hayakawa, M., and T. Ogawa (1992), Special issue : Atmospheric electricity phenomena associated with earthquakes and volcanic eruptions, *Research Letters on Atmospheric Electricity*, *112*(3).

Helliwell, R. A., J. P. Katsufrakis, T. F. Bell, and R. Raghuram (1975), VLF line radiation in the earth's magnetosphere and its association with power system radiation, *J. Geophys. Res.*, *80*, 4249–4258.

Henderson, T. R., V. S. Sonwalkar, R. A. Helliwell, U. S. Inan, and A. C. Fraser-Smith (1993), A search for ELF/VLF emissions induced by earthquakes as observed in the ionosphere by the DE-2 satellite, *JGR*, *98*(9503–9514).

Koons, H. C., M. H. Dazey, and B. C. Edgar (1978), Satellite observation of discrete VLF line radiation within transmitter-induced amplification bands, *J. Geophys. Res.*, *83*(A8), 3887–3889.

Larkina, V. I., A. V. Nalivayko, N. I. Gershenzon, M. B. Gokhberg, V. A. Liperovskiy, and S. L. Shalimov (1983), Observations of VLF emissions related with seismic activity, on the Intercosmos-19 satellite, *Geomagnetism and Aeronomy*, *23*, 684–687.

Larkina, V. I., V. V. Migulin, O. A. Molchanov, I. P. Kharkov, A. S. Inchin, and V. B. Schvetcova (1989), Some statistical results on very low frequency radiowave emissions in the upper ionosphere over earthquake zones, *Physics of the Earth and Planetary Interiors*, *57*, 100–109.

Manninen, J. (2005), *Some Aspects of ELF-VLF Emissions in Geophysical Research*, chap. Power Line Harmonic Radiation, Magnetospheric Line Radiation, pp. 53–110, 98, Sodankylä Geophysical Observatory Publications, Sodankylä, Finland.

Mareev, E. A., D. I. Iudin, and O. A. Molchanov (2002), *Seismo-Electromagnetics : Litosphere–Atmosphere–Ionosphere Coupling*, chap. Mosaic Source of Internal Gravity Waves Associated with Seismic Activity, pp. 335–342, TERRAPUB, Tokyo.

Masson, A., et al. (2009), Advances in plasmaspheric wave research with CLUSTER and IMAGE observations, *Space Sci. Rev.*, doi :10.1007/s11214-009-9508-7.

Matthews, J. P., and J. P. Lebreton (1985), A search for seismic related wave activity in the micropulsation and ULF frequency ranges using GEOS-2 data, *Ann. Geophysicae*, *3*, 739–754.

Matthews, J. P., and K. Yearby (1981), Magnetospheric VLF line radiation observed at Halley, Antarctica, *Planet. Space Sci.*, *29*, 97–106.

Milne, J. (1890), Earthquakes in connection with electric and magnetic phenomena, *Trans. Seismol. Soc. Jpn.*, *5*, 135.

Molchanov, O. A., and M. Hayakawa (1998), On the generation mechanism of ULF seismogenic electromagnetic emissions, *Physics of the Earth and Planetary Interiors*, *105*, 201–210.

Molchanov, O. A., M. Parrot, M. M. Mogilevsky, and F. Lefeuvre (1991), A theory of PLHR emissions to explain the weekly variation of ELF data observed by a low-altitude satellite, *Ann. Geophysicae*, *9*, 669–680.

Molchanov, O. A., O. A. Mazhaeva, A. N. Goliavin, and M. Hayakawa (1993), Observation by the Intercosmos-24 satellite of ELF-VLF electromagnetic emissions associated with earthquakes, *Ann. Geophysicae*, *11*, 431–440.

Molchanov, O. A., M. Hayakawa, and V. A. Rafalsky (1995), Penetration characteristics of electromagnetic emissions from an underground seismic source into the atmosphere, ionosphere, and magnetosphere, *J. Geophys. Res.*, *100*(A2), 1691–1712.

Molchanov, O. A., et al. (2006), Global diagnostics of the ionospheric perturbations related to the seismic activity using the VLF radio signals collected on the DEMETER satellite, *Natural Hazards and Earth System Sciences*, *6*, 745–753.

Moldwin, M. O., L. Downward, H. K. Rassoul, R. Amin, and R. R. Anderson (2002), A new model of the location of the plasmapause : CRRES results, *J. Geophys. Res.*, *107*(A11), doi :10.1029/2001JA009211.

Nunn, D., J. Manninen, T. Turunen, V. Trakhtengerts, and N. Erokhin (1999), On the nonlinear triggering of VLF emissions by power line harmonic radiation, *Ann. Geophysicae*, *17*, 79–94.

Němec, F., O. Santolík, K. Gereová, E. Macúšová, Y. de Conchy, and N. Cornilleau-Wehrlin (2005), Initial results of a survey of equatorial noise emissions observed by the Cluster spacecraft, *Planet. Space Sci.*, *53*, 291–298.

Němec, F., O. Santolík, K. Gereová, E. Macúšová, Y. de Conchy, M. Maksimovic, and N. Cornilleau-Wehrlin (2006a), Equatorial noise : Statistical study of its localization and the derived number density, *Adv. Space Res.*, *37*(3), 610–616.

Němec, F., O. Santolík, M. Parrot, and J. J. Berthelier (2006b), Power line harmonic radiation (PLHR) observed by the DEMETER spacecraft, *J. Geophys. Res.*, *111*(A04308), doi :10.1029/2005JA011480.

Němec, F., M. Parrot, O. Santolík, and J. J. Berthelier (2007a), On the origin of magnetospheric line radiation, *WDS Proceedings of Contributed Papers : Part II – Physics of Plasmas and Ionized Media, Matfyzpress, Prague*, pp. 64–70.

Němec, F., O. Santolík, M. Parrot, and J. J. Berthelier (2007b), Comparison of magnetospheric line radiation and power line harmonic radiation : A systematic survey using the DEMETER spacecraft, *J. Geophys. Res.*, *112*(A04301), doi :10.1029/2006JA012134.

Němec, F., O. Santolík, M. Parrot, and J. J. Berthelier (2007c), Power line harmonic radiation : A systematic study using demeter spacecraft, *Adv. Space Res.*, *40*, 398–403.

Němec, F., O. Santolík, and M. Parrot (2008a), Possible seismic influence on VLF wave intensity : Observations by a low-altitude satellite, *WDS Proceedings of Contributed Papers : Part II – Physics of Plasmas and Ionized Media, Matfyzpress, Prague*, pp. 168–171.

Němec, F., O. Santolík, M. Parrot, and J. J. Berthelier (2008b), Spacecraft observations of electromagnetic perturbations connected with seismic activity, *Geophys. Res. Lett.*, *35*(L05109), doi :10.1029/2007GL032517.

Němec, F., O. Santolík, M. Parrot, and J. Bortnik (2008c), Power line harmonic radiation observed by satellite : Properties and propagation through the ionosphere, *J. Geophys. Res.*, *113*(A08317), doi :10.1029/2008JA013184.

Němec, F., M. Parrot, O. Santolík, C. J. Rodger, M. J. Rycroft, M. Hayosh, D. Shklyar, and A. Demekhov (2009a), Survey of magnetospheric line radiation events observed by the DEMETER spacecraft, *J. Geophys. Res.*, *114*(A05203), doi :10.1029/2008JA014016.

Němec, F., O. Santolík, and M. Parrot (2009b), Decrease of intensity of ELF/VLF waves observed in the upper ionosphere close to earthquakes : a statistical study, *J. Geophys. Res.*, *114*(A04303), doi :10.1029/2008JA013972.

Němec, F., O. Santolík, and M. Parrot (2009c), Electromagnetic harmonic ELF emissions close to the geomagnetic equator observed by a low-altitude satellite, *J. Geophys. Res.*, *prepared*.

Park, C. G., and R. A. Helliwell (1978), Magnetospheric effects of power line radiation, *Science*, *200*, 727–730.

Park, C. G., and R. A. Helliwell (1981), Power line radiation in the magnetosphere, *Adv. Space Res.*, *1*, 423–437.

Park, C. G., and R. A. Helliwell (1983), Ground observations of power line radiation coupled to the ionosphere and magnetosphere, *Space Sci. Rev.*, *35*, 131–137.

Park, C. G., and T. R. Miller (1979), Sunday decreases in magnetospheric VLF wave activity, *J. Geophys. Res.*, *84*, 943–950.

Parrot, M. (1990), Electromagnetic disturbances associated with earthquakes : An analysis of ground-based and satellite data, *Journal of Scientific Exploration*, *4*(2), 203–211.

Parrot, M. (1991), Daily variations of ELF data observed by a low-altitude satellite, *Geophys. Res. Lett.*, *18*(6), 1039–1042.

Parrot, M. (1994a), Observations of power line harmonic radiation by the low-altitude AUREOL 3 satellite, *J. Geophys. Res.*, *99*(A3), 3961–3969.

Parrot, M. (1994b), Statistical study of ELF/VLF emissions recorded by a low-altitude satellite during seismic events, *J. Geophys. Res.*, *99*, 23,339–23,347.

Parrot, M. (1994c), *Electromagnetic Phenomena Related to Earthquake Prediction*, chap. Seismo-Electromagnetic Waves Detected by a Low-Altitude Satellites, pp. 361–372, TERRAPUB, Tokyo.

Parrot, M. (1995), *Handbook of Atmospheric Electrodynamics*, vol. 2, chap. Electromagnetic Noise Due to Earthquakes, pp. 95–116, CRC Press, Boca Raton, Fla.

Parrot, M., and M. Johnston (1989), Special issue : Seismoelectromagnetic effects, *Physics of the Earth and Planetary Interiors*, *57*(1–2).

Parrot, M., and M. Johnston (1993), Special issue : Seismoelectromagnetic effects, *Physics of the Earth and Planetary Interiors*, *77*.

Parrot, M., and F. Lefeuvre (1985), Correlation between GEOS VLF emissions and earthquakes, *Ann. Geophysicae*, *3*, 737–747.

Parrot, M., and M. M. Mogilevsky (1989), VLF emissions associated with earthquakes and observed in the ionosphere and the magnetosphere, *Physics of the Earth and Planetary Interiors*, *57*, 86–99.

Parrot, M., and F. Němec (2009), MLR events and associated triggered emissions observed by DEMETER, *Adv. Space Res.*, *44*, 979–986, doi :10.1016/j.asr.2009.07.001.

Parrot, M., F. Němec, O. Santolík, and J. J. Berthelier (2005), ELF magnetospheric lines observed by DEMETER, *Ann. Geophysicae*, *23*, 3301–3311.

Parrot, M., A. Buzzi, O. Santolík, J. J. Berthelier, J. A. Sauvaud, and J. P. Lebreton (2006a), New observations of electromagnetic harmonic ELF emissions in the ionosphere by the DEMETER satellite during large magnetic storms, *J. Geophys. Res.*, *111*, doi : 10.1029/2005JA011583.

Parrot, M., J. Manninen, O. Santolík, F. Němec, T. Turunen, T. Raita, and E. Macúšová (2007), Simultaneous observation on board a satellite and on the ground of large-scale magnetospheric line radiation, *Geophys. Res. Lett.*, *34*(L19102), doi : 10.1029/2007GL030630.

Parrot, M., et al. (2006b), The magnetic field experiment IMSC and its data processing onboard DEMETER : Scientific objectives, description and first results, *Planet. Space Sci.*, *54*, 441–455.

Press, W. H., S. A. Teukolsky, W. T. Vetterling, and B. P. Flannery (1992), *Numerical Recipes in C : The Art of Scientific Computing*, chap. Random Numbers, pp. 274–328, Cambridge University Press.

Pulinets, S. (2004), Ionospheric precursors of earthquakes : Recent advances in theory and practical applications, *TAO*, *15*(3), 445–467.

Pulinets, S. A., and K. A. Boyarchuk (2004), *Ionospheric Precursors of Earthquakes*, Springer, Hedelberg, New York.

Rodger, C. J., N. R. Thomson, and R. L. Dowden (1995), VLF line radiation observed by satellite, *J. Geophys. Res.*, *100*(A4), 5681–5689.

Rodger, C. J., N. R. Thomson, and R. L. Dowden (1996), A search for ELF/VLF activity associated with earthquakes using ISIS satellite data, *J. Geophys. Res.*, *101*(A6), 13,369–13,378.

Rodger, C. J., M. A. Clilverd, K. H. Yearby, and A. J. Smith (1999a), Magnetospheric line radiation observations at Halley, Antarctica, *J. Geophys. Res.*, *104*(A8), 17,441–17,447.

Rodger, C. J., R. L. Dowden, and N. R. Thomson (1999b), *Observations of Electromagnetic Activity Associated with Earthquakes by Low-Altitude Satellites*, chap. Atmospheric and Ionospheric Electromagnetic Phenomena Associated with Earthquakes, pp. 697–710, Terra Scientific Publishing, Tokyo.

Rodger, C. J., M. A. Clilverd, K. Yearby, and A. J. Smith (2000a), Is magnetospheric line radiation man-made ?, *J. Geophys. Res.*, *105*, 15,981–15,990.

Rodger, C. J., M. A. Clilverd, K. H. Yearby, and A. J. Smith (2000b), Temporal properties of magnetospheric line radiation, *J. Geophys. Res.*, *105*(A1), 329–336.

Santolík, O., F. Němec, K. Gereová, E. Macúšová, Y. de Conchy, and N. Cornilleau-Wehrlin (2004), Systematic analysis of equatorial noise below the lower hybrid frequency, *Ann. Geophysicae*, *22*, 2587–2595.

Santolík, O., F. Němec, M. Parrot, D. Lagoutte, L. Madrias, and J. J. Berthelier (2006), Analysis methods for multi-component wave measurements on board the DEMETER spacecraft, *Planet. Space Sci.*, *54*, 512–527.

Serebryakova, O. N., S. V. Bilichenko, V. M. Chmyrev, M. Parrot, J. L. Rauch, F. Lefeuvre, and O. A. Pokhotelov (1992), Electromagnetic ELF radiation from earthquake regions as observed by low-altitude satellites, *Geophys. Res. Lett.*, *19*(2), 91–94.

Sheskin, D. J. (2000), *Handbook of Parametric and Nonparametric Statistical Procedures*, 2nd ed., Chapman & Hall, CRC, Boca Raton, USA.

Sorokin, V. M., V. M. Chmyrev, and A. K. Yaschenko (2001), Electrodynamic model of the lower atmosphere and the ionosphere coupling, *J. Atm. Solar-Terr. Phys.*, *63*, 1681–1691.

Tomizawa, I., and T. Yoshino (1985), Power line radiation observed by the satellite, *J. Geomag. Geoelectr.*, *37*, 309–327.

Warwick, J. W., C. Stoker, and T. R. Meyer (1982), Radio emission associated with rock fracture : possible application to the great chilean earthquake of may 22, 1960, *J. Geophys. Res.*, *87*, 2851.

Yearby, K. H., A. J. Smith, and K. Bullough (1983), Power line harmonic radiation in Newfoundland, *J. Atm. and Terr. Phys*, *45*, 409–419.

Annexe A

Cartes des émissions électromagnétiques

Dans cette annexe nous présentons les cartes des émissions électromagnétiques obtenues pendant des conditions ionosphèriques différentes (MLT, Kp, saison de l'année). Toutes les cartes ont été obtenues pour la bande de fréquence 1055-2383 Hz – la bande dans laquelle on observe l'effet en corrélation avec l'activité sismique (voir le Chapitre 3.2 et le Chapitre 3.3). Elles illustrent donc la représentation graphique de la base de données que nous avons utilisée (voir le Chapitre 3.1).

Dans ces cartes on peut observer le mélange de deux effets principaux :

- L'influence des conditions magnétosphèriques. En particulier il y a une augmentation de l'intensité pendant le jour pour des valeurs plus grandes de Kp.
- L'influence des orages terrestres. En particulier il y a une augmentation de l'intensité pendant la nuit (quand le couplage des ondes est plus facile, voir la Figure 4.11). Les orages sont plus fréquents pendant l'été local et au-dessus des continents, ce qui explique la différence entre la Figure A.3 et la Figure A.4 : pendant l'été, les orages se produisent plus souvent au-dessus des États-Unis, de l'Europe et de l'Asie ; pendant l'hiver, les orages se produisent plus souvent au-dessus de l'Afrique du Sud et de l'Australie.

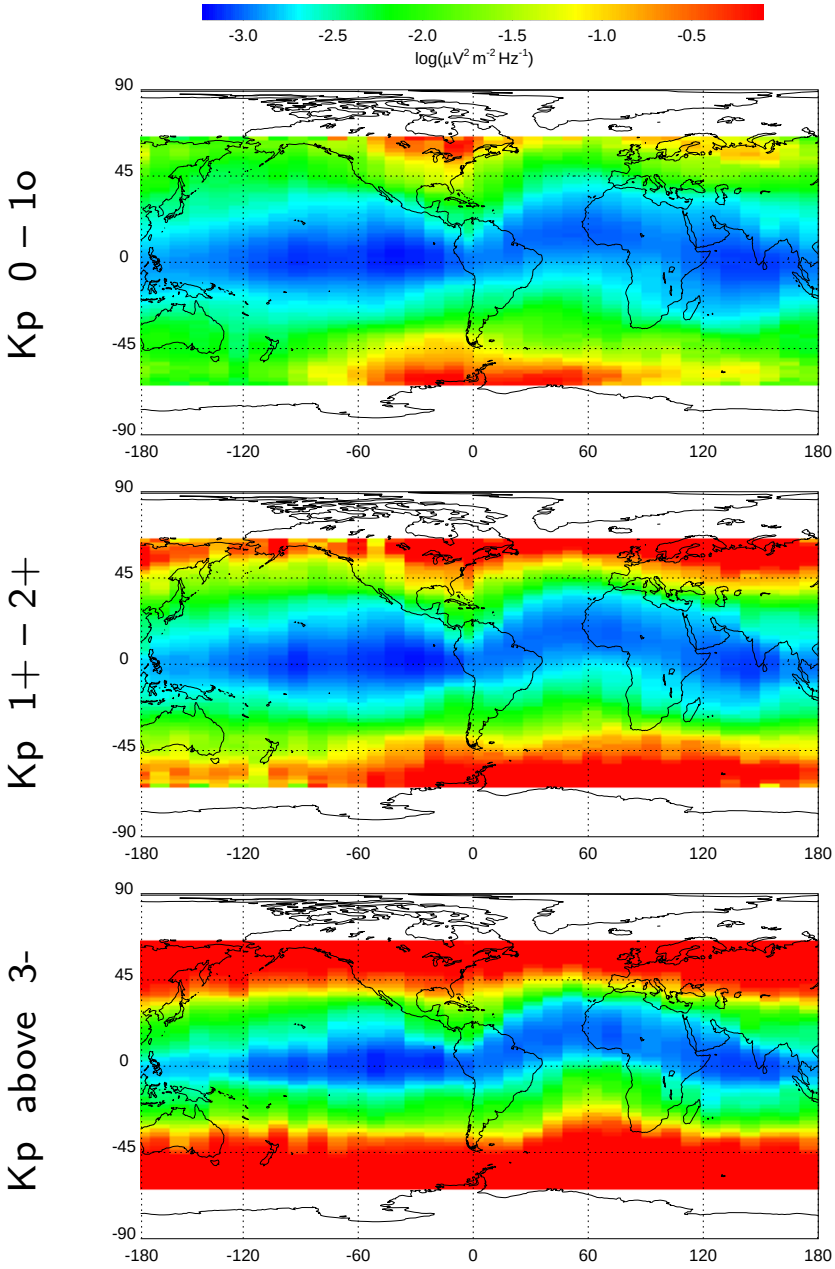

FIG. A.1 – La valeur médiane de l'intensité des fluctuations du champ électrique dans la bande de fréquence 1055-2383 Hz en fonction de la latitude et la longitude géomagnétiques. Les résultats sont tracés pour trois intervalles différents d'index Kp. Toutes les données mesurées pendant le jour et l'été (Mai-Septembre) ont été incluses.

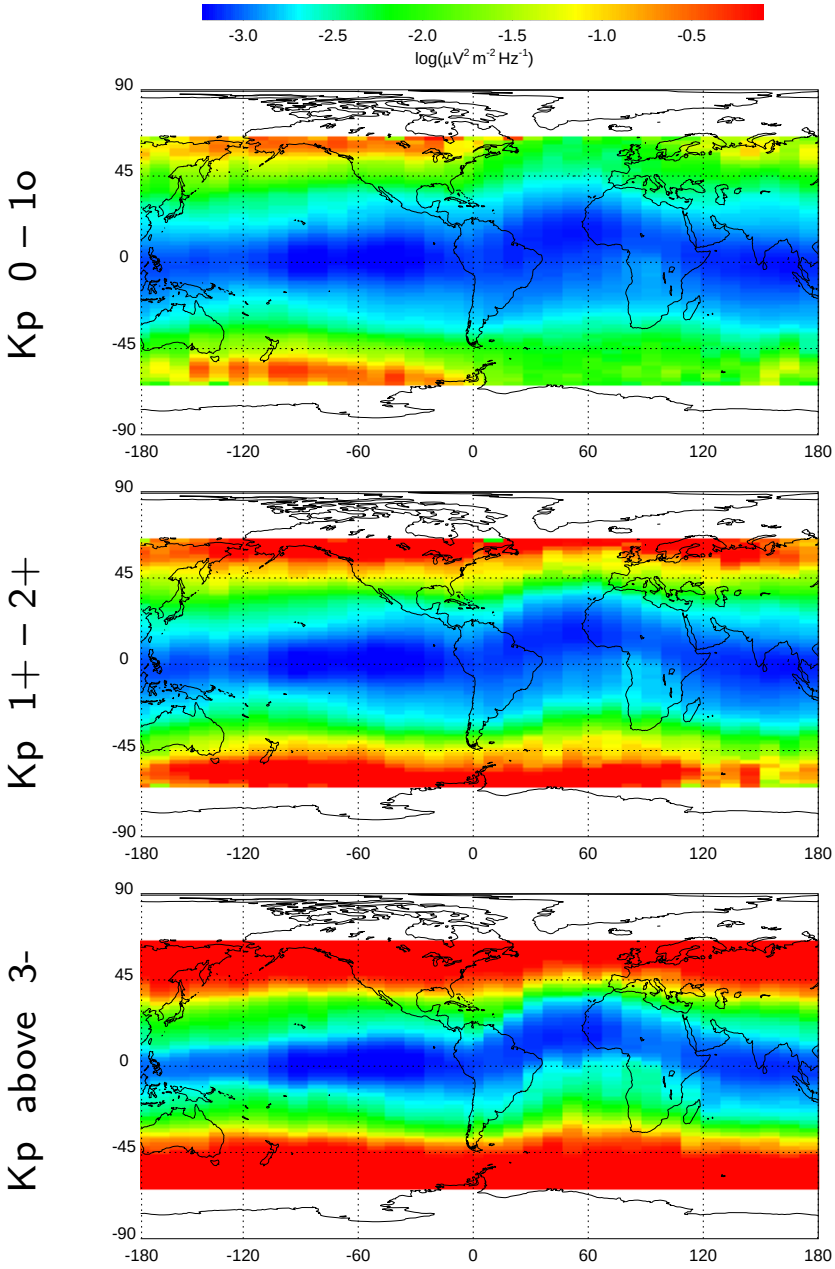

FIG. A.2 – La valeur médiane de l'intensité des fluctuations du champ électrique dans la bande de fréquence 1055-2383 Hz en fonction de la latitude et la longitude géomagnétiques. Les résultats sont tracés pour trois intervalles différents d'index Kp. Toutes les données mesurées pendant le jour et l'hiver (Octobre-Avril) ont été incluses.

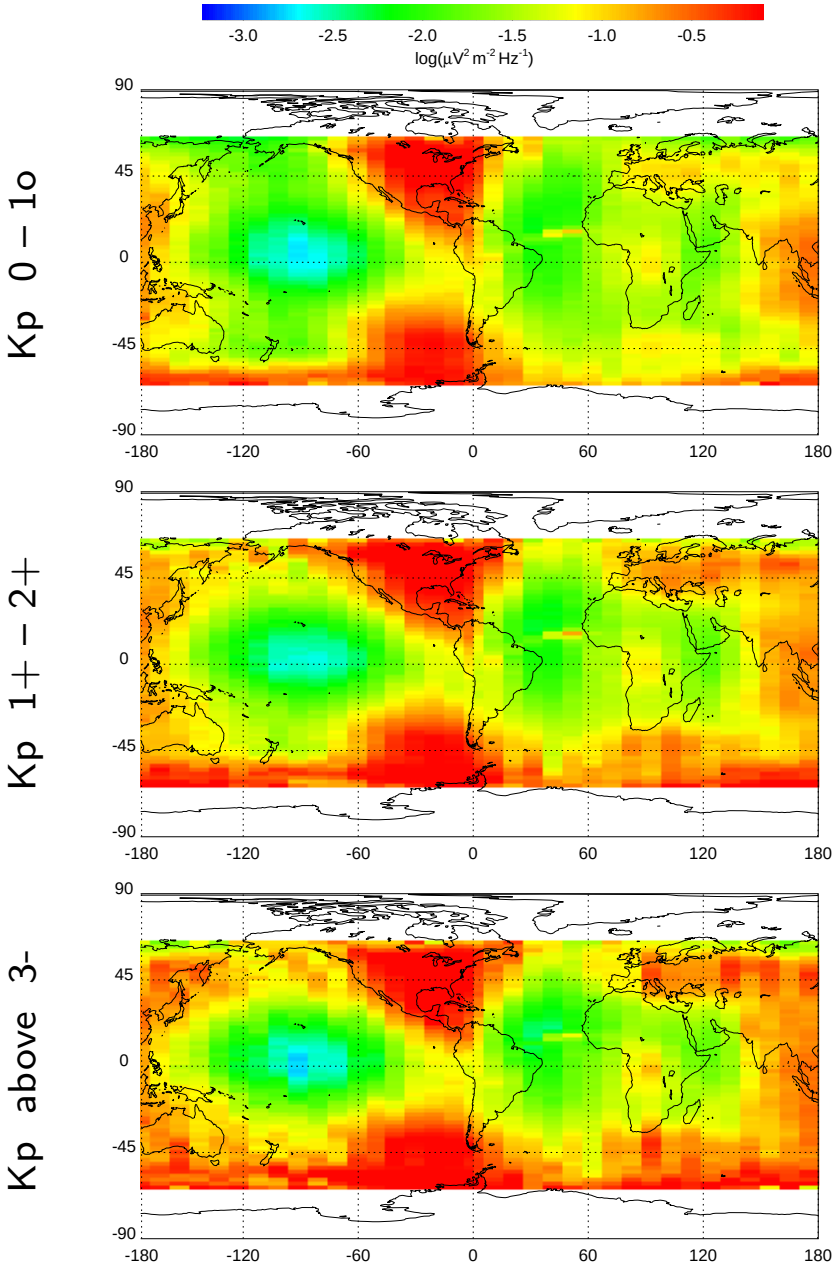

FIG. A.3 – La valeur médiane de l'intensité des fluctuations du champ électrique dans la bande de fréquence 1055-2383 Hz en fonction de la latitude et la longitude géomagnétiques. Les résultats sont tracés pour trois intervalles différents d'index Kp. Toutes les données mesurées pendant la nuit et l'été (Mai-Septembre) ont été incluses.

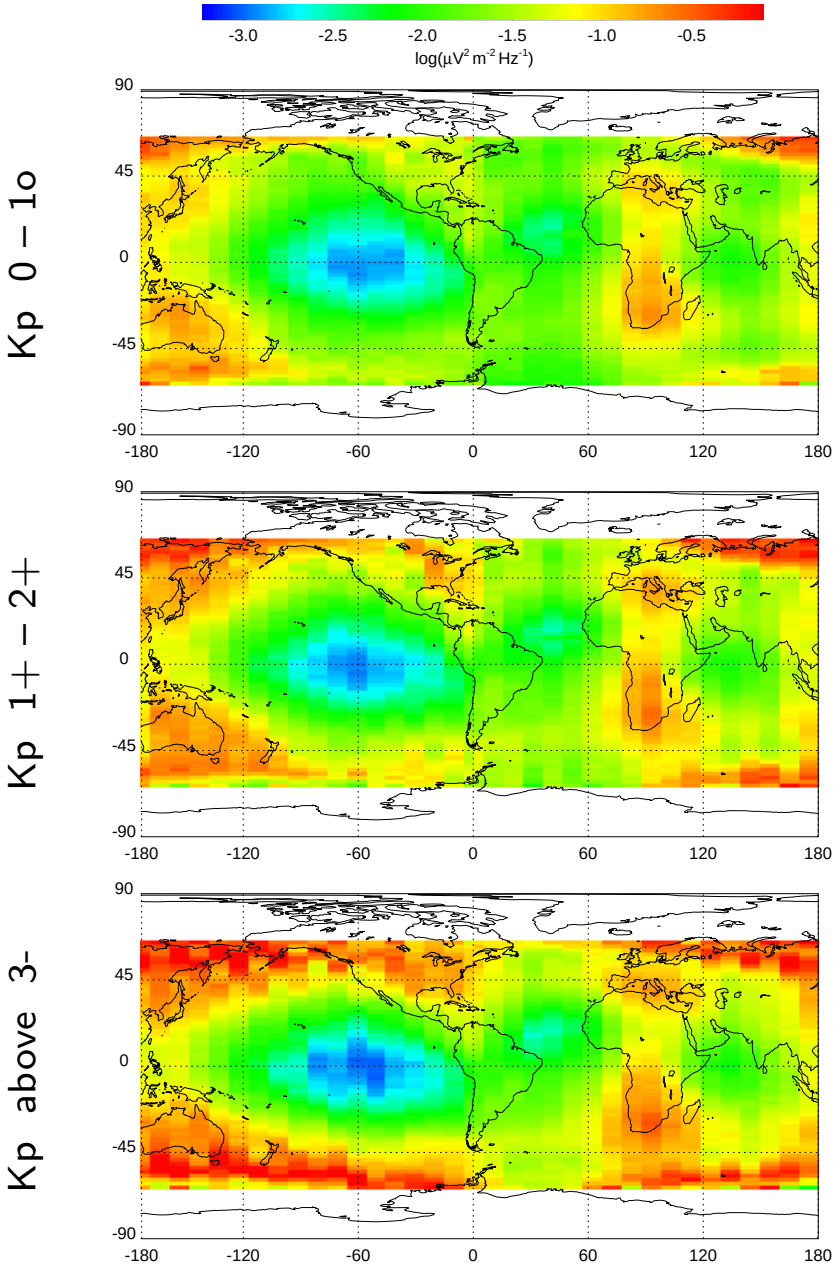

FIG. A.4 – La valeur médiane de l'intensité des fluctuations du champ électrique dans la bande de fréquence 1055-2383 Hz en fonction de la latitude et la longitude géomagnétiques. Les résultats sont tracés pour trois intervalles différents d'index Kp. Toutes les données mesurées pendant la nuit et l'hiver (Octobre-Avril) ont été incluses.

Annexe B

Autres exemples d'émissions PLHR

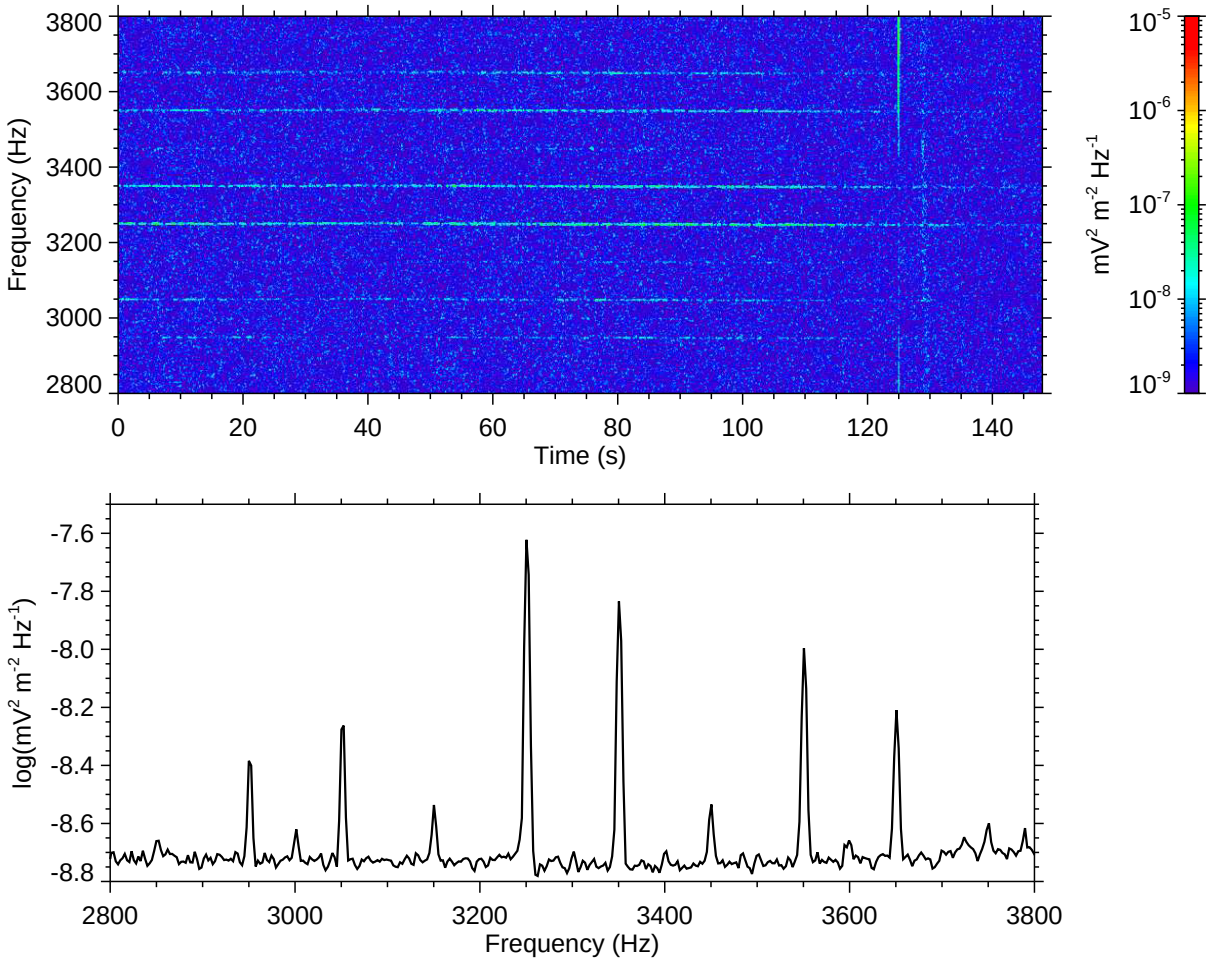

FIG. B.1 – (dessus) Spectrogramme fréquence-temps des fluctuations du champ électrique correspondant à un événement PLHR ayant une séparation en fréquence entre les lignes individuelles de 50/100 Hz. Les données ont été mesurées le 13 Avril 2007 après 08:02:33 UT quand le satellite était près de la Finlande. (en bas) Spectre de puissance. Les pics sont visibles aux fréquences 2950 Hz, (3000 Hz), 3050 Hz, 3150 Hz, 3250 Hz, 3350 Hz, 3450 Hz, 3550 Hz, (3600 Hz), 3650 Hz.

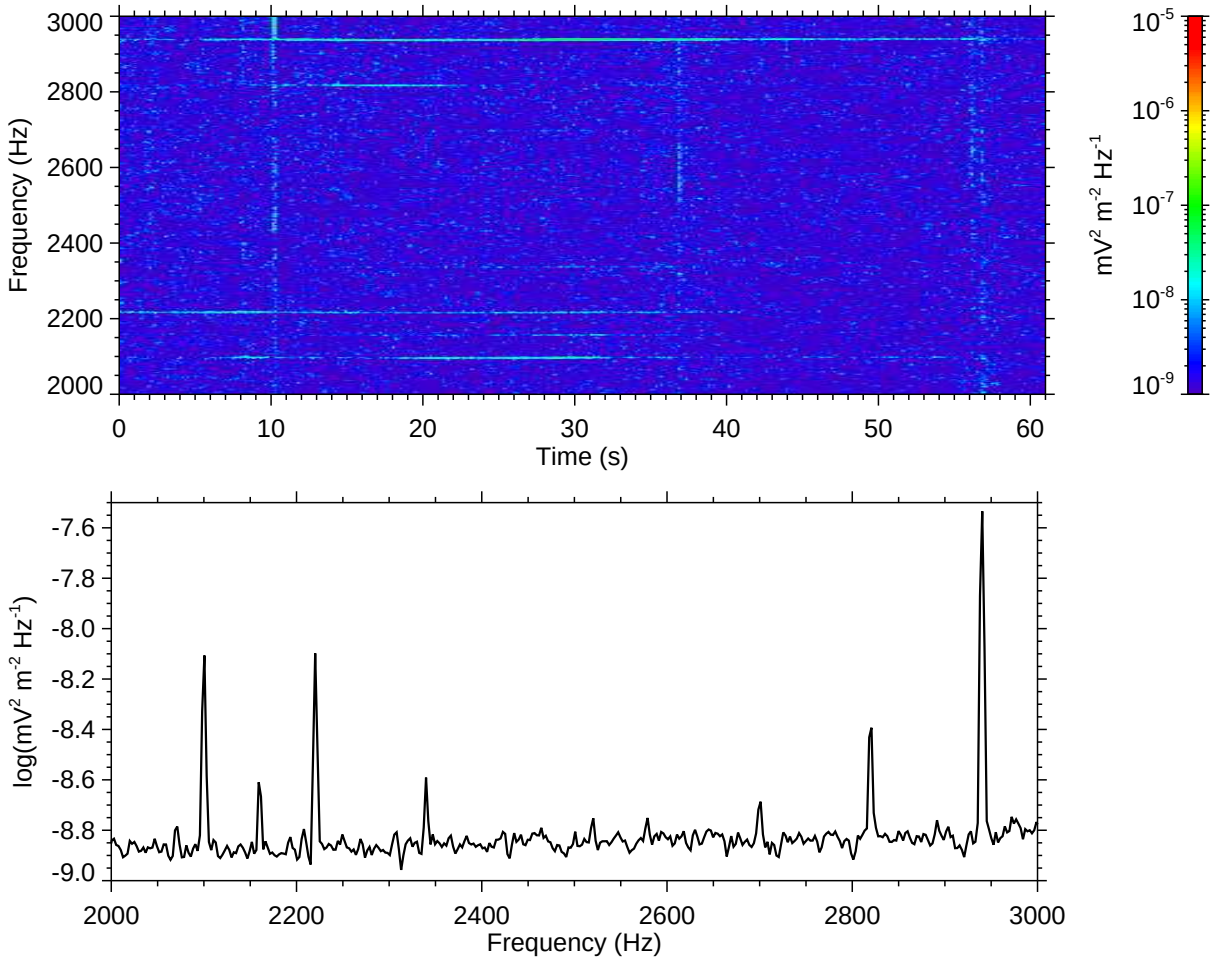

FIG. B.2 – (dessus) Spectrogramme fréquence-temps des fluctuations du champ électrique correspondant à un événement PLHR ayant une séparation en fréquence entre les lignes individuelles de 60/120 Hz. Les données ont été mesurées le 11 Février 2007 après 01:32:00 UT quand le satellite était au-dessus du Japon. (en bas) Spectre de puissance. Les pics sont visibles aux fréquences 2100 Hz, 2160 Hz, 2220 Hz, 2340 Hz, (2700 Hz), 2820 Hz, 2940 Hz.

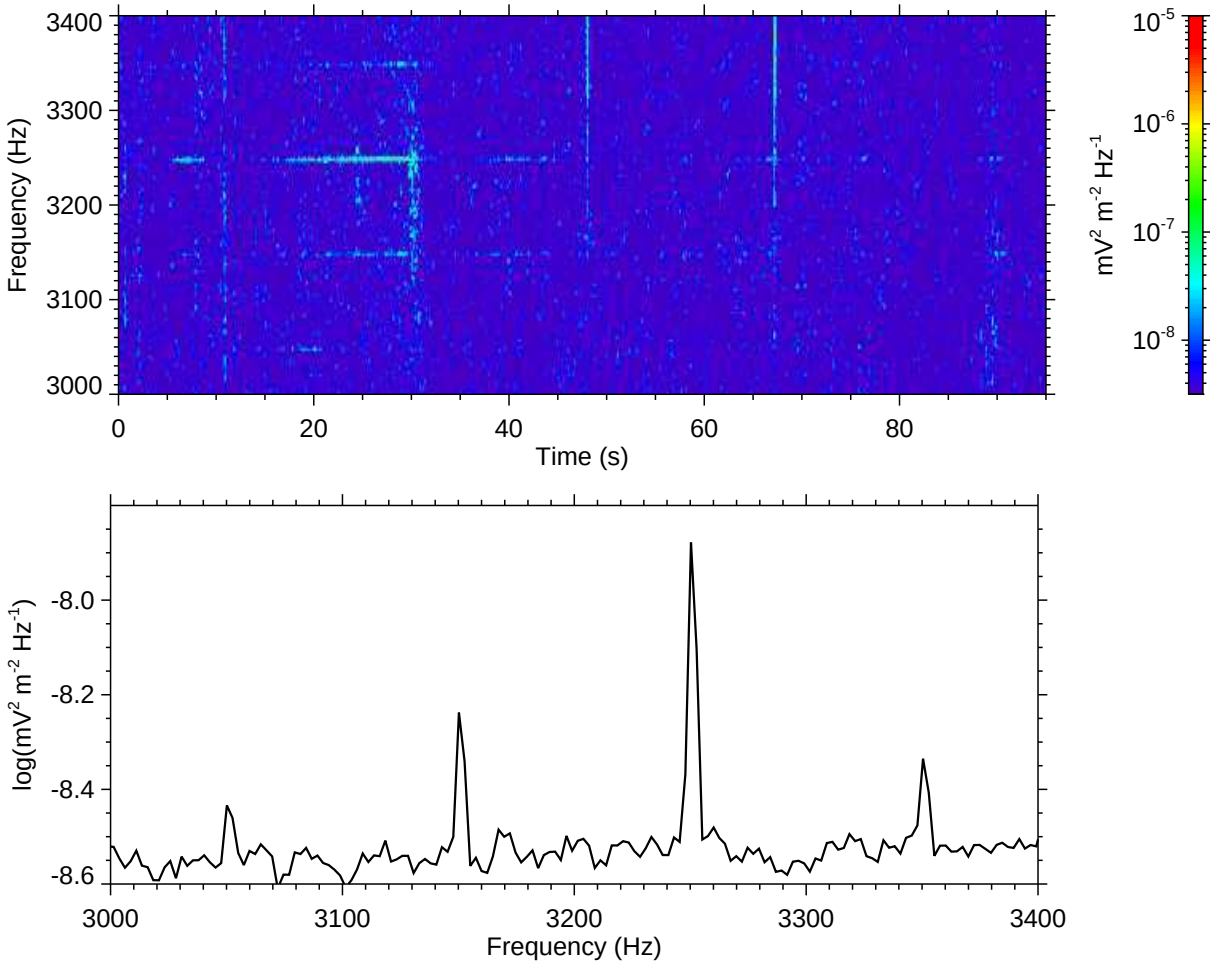

FIG. B.3 – (dessus) Spectrogramme fréquence-temps des fluctuations du champ électrique correspondant à l'événement PLHR ayant une séparation en fréquence entre les lignes individuels 50/100 Hz. Les données ont été mesurées le Décembre 23, 2007 après 10:20:29 UT quand le satellite était au-dessus de la France. (en bas) Spectre de puissance. Les pics sont visibles aux fréquences (3050 Hz), 3150 Hz, 3250 Hz, 3350 Hz.

Annexe C

Autres exemples d'émissions MLR

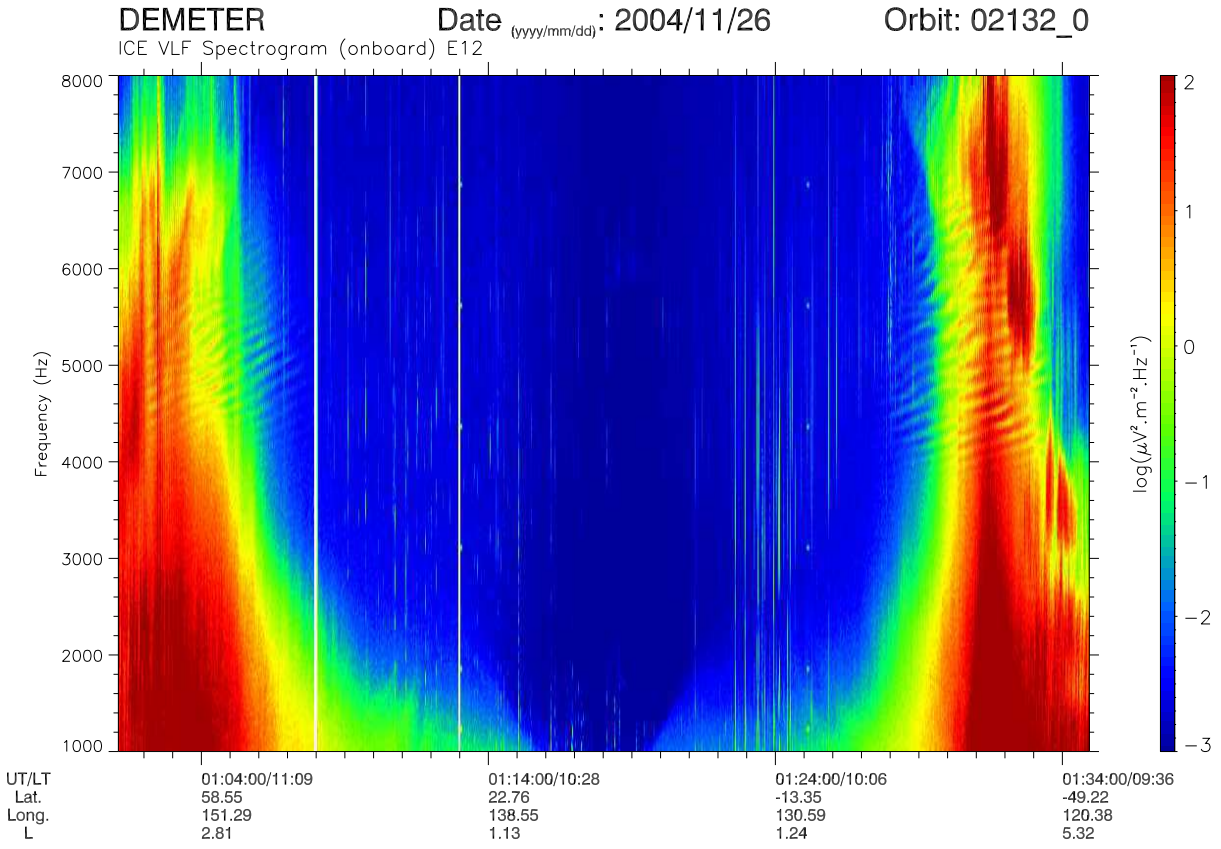

FIG. C.1 – Spectrogramme fréquence-temps de l'orbite contenant deux événements MLR dans des régions conjuguées.

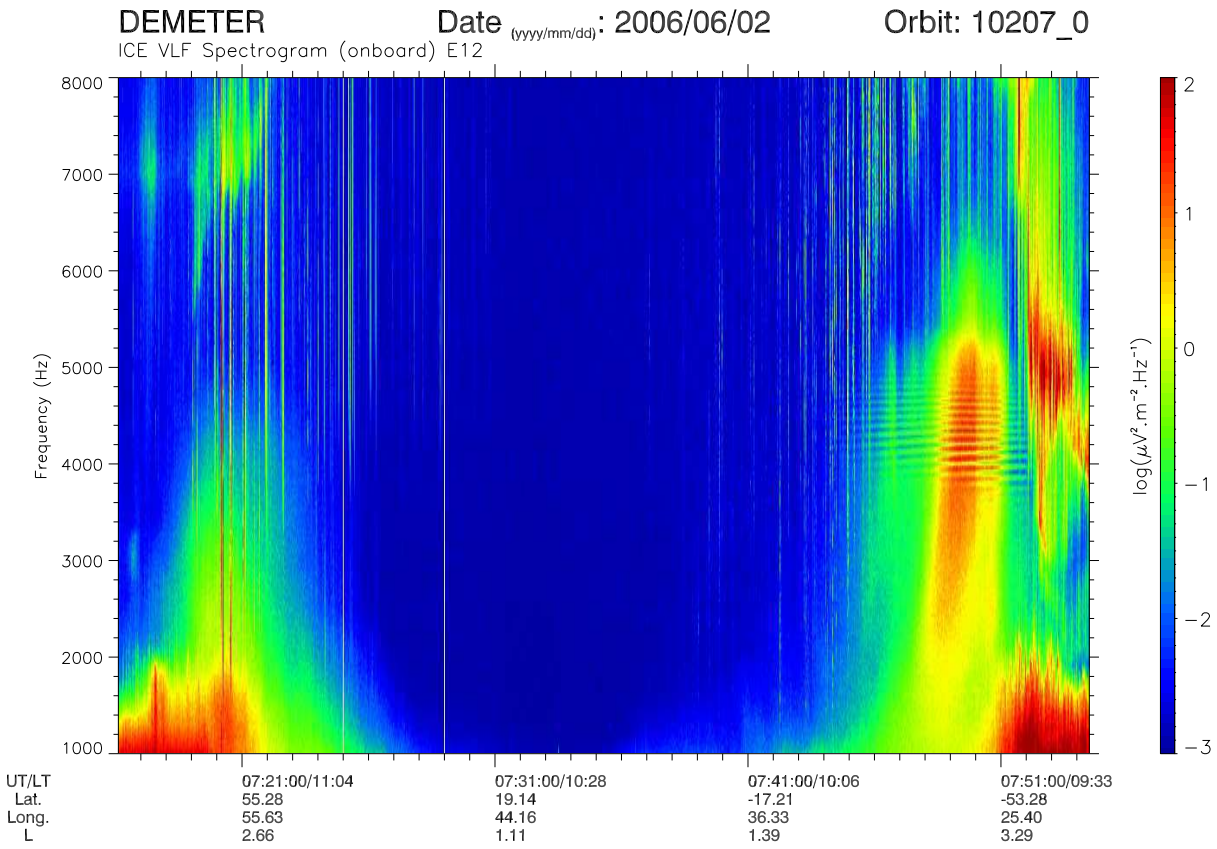

FIG. C.2 – Spectrogramme fréquence-temps de l'orbite contenant un événement MLR.

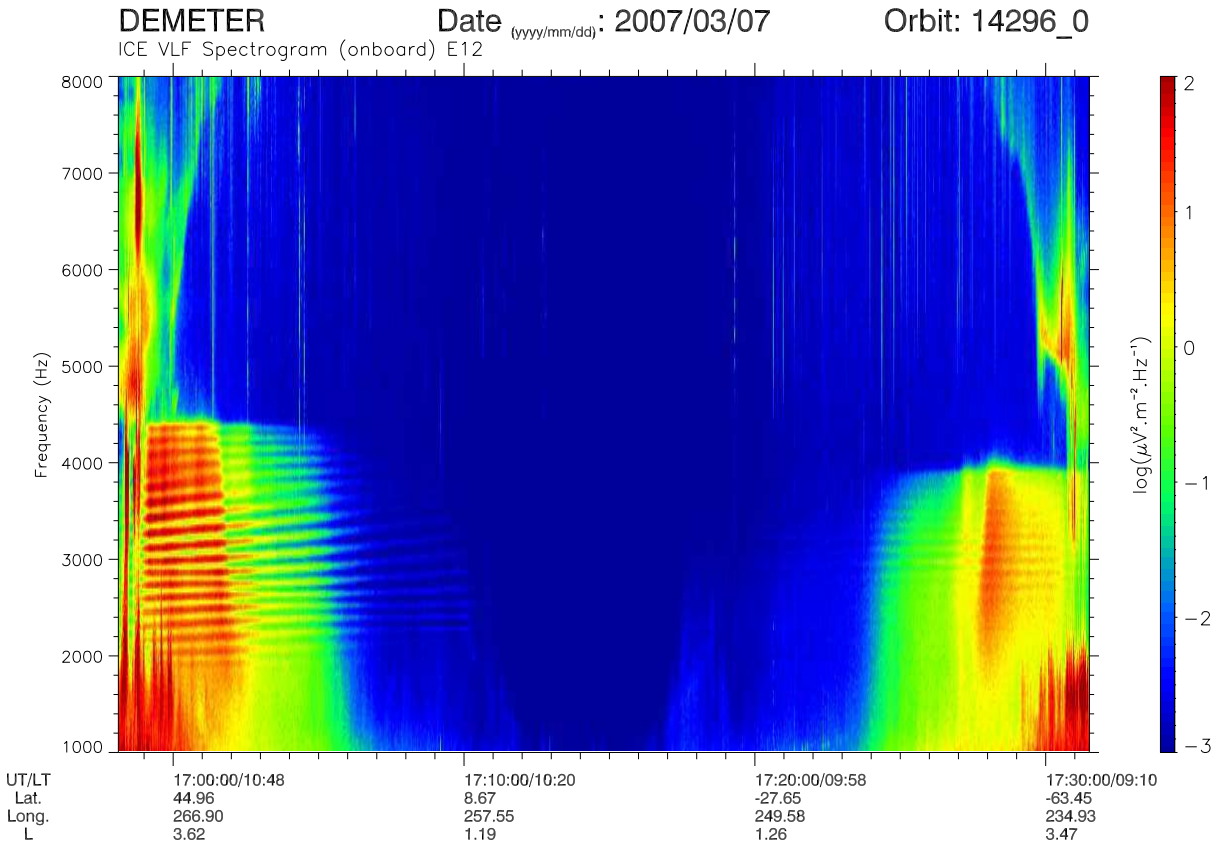

FIG. C.3 – Spectrogramme fréquence-temps de l'orbite contenant deux événements MLR dans des régions conjuguées.

Annexe D

Autres exemples d'émissions électromagnétiques harmoniques dans la bande EBF

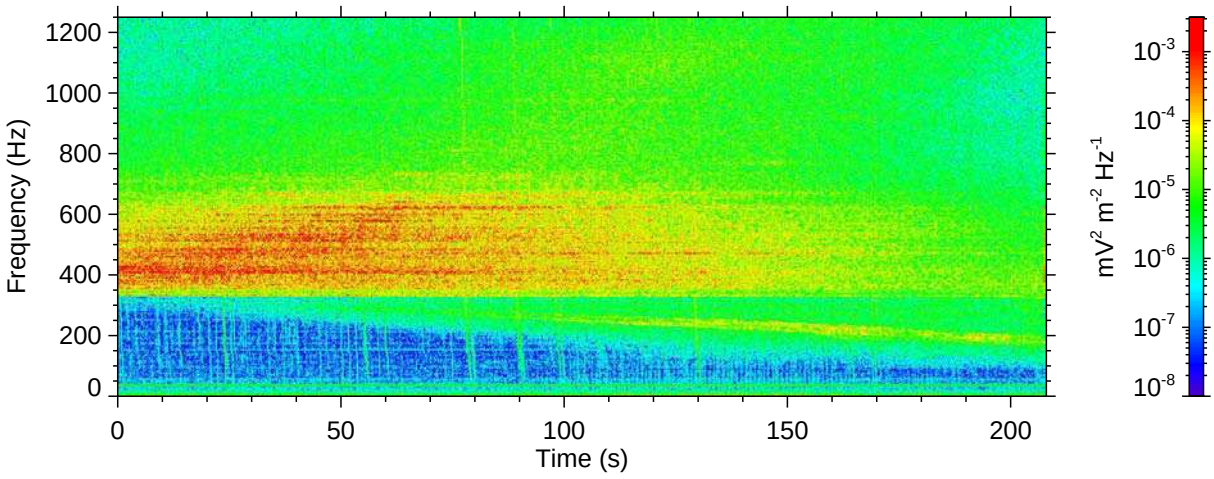

FIG. D.1 – Spectrogramme fréquence-temps des fluctuations du champ électrique correspondant à des émissions électromagnétiques harmoniques dans la bande EBF. Les données ont été mesurées le 9 Novembre 2004 après 08:19:02 UT.

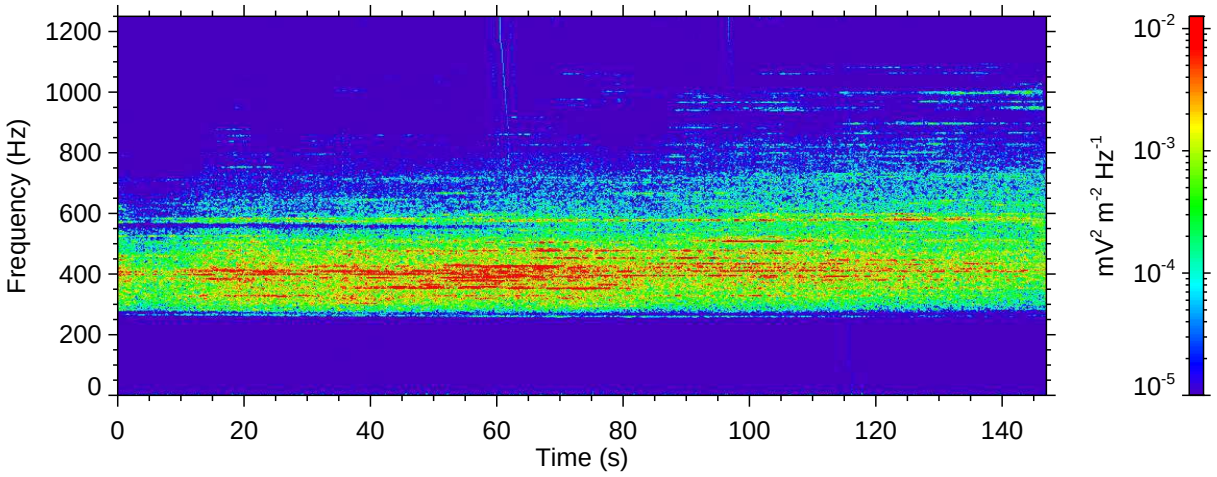

FIG. D.2 – Spectrogramme fréquence-temps des fluctuations du champ électrique correspondant à des émissions électromagnétiques harmoniques dans la bande EBF. Les données ont été mesurées le 9 Novembre 2004 après 14:59:02 UT.

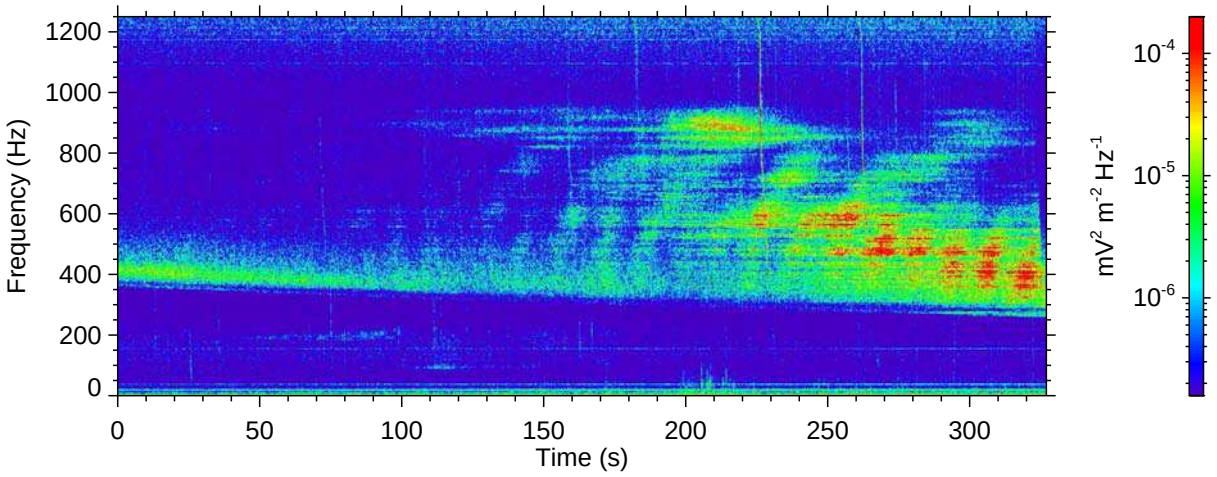

FIG. D.3 – Spectrogramme fréquence-temps des fluctuations du champ électrique correspondant à des émissions électromagnétiques harmoniques dans la bande EBF. Les données ont été mesurées le 16 Mai 2005 après 15:39:31 UT.

Annexe E

Liste des publications

Dans cette annexe il y a toutes les publications dans les journaux scientifiques dont je suis l'auteur ou le co-auteur : *Santolík et al.* (2004), *Němec et al.* (2005), *Parrot et al.* (2005), *Němec et al.* (2006a), *Němec et al.* (2006b), *Santolík et al.* (2006), *Němec et al.* (2007b), *Němec et al.* (2007c), *Parrot et al.* (2007), *Němec et al.* (2007a), *Němec et al.* (2008b), *Němec et al.* (2008c), *Němec et al.* (2008a), *Němec et al.* (2009b), *Němec et al.* (2009a), *Masson et al.* (2009), *Parrot and Němec* (2009).

Annales Geophysicae (2004) 22: 2587–2595
SRef-ID: 1432-0576/ag/2004-22-2587

Annales Geophysicae

Systematic analysis of equatorial noise below the lower hybrid frequency

O. Santolík[1], **F. Němec**[1], **K. Gereová**[1], **E. Macúšová**[1], **Y. de Conchy**[2], **and N. Cornilleau-Wehrlin**[3]

[1]Faculty of Mathematics and Physics, Charles University, V Holešovičkách 2, Prague, CZ-18000, Czech Republic
[2]LESIA/Observatoire de Paris-Meudon, F-92195, Meudon Cedex, France
[3]CETP/IPSL, 10/12 Avenue de L'Europe, Vélizy, F-78140, France

Received: 5 August 2003 – Revised: 24 November 2003 – Accepted: 11 December 2003 – Published: 14 July 2004

Part of Special Issue "Spatio-temporal analysis and multipoint measurements in space"

Abstract. We report results of a systematic analysis of a large number of observations of equatorial noise between the local proton cyclotron frequency and the local lower hybrid frequency. The analysis is based on the data collected by the STAFF-SA instruments on board the four Cluster spacecraft. The data set covers their first two years of measurement in the equatorial magnetosphere at radial distances between 3.9 and 5 Earth radii. Inspection of 781 perigee passages shows that the occurrence rate of equatorial noise is approximately 60%. We identify equatorial noise by selecting data with nearly linearly polarized magnetic field fluctuations. These waves are found within 10° of the geomagnetic equator, consistent with the published past observations. Our results show that equatorial noise has the most intense magnetic field fluctuations among all the natural emissions in the given interval of frequencies and latitudes. Electric field fluctuations of equatorial noise are also more intense compared to the average of all detected waves. Equatorial noise thus can play a non-negligible role in the dynamics of the internal magnetosphere.

Key words. Magnetospheric physics (waves in plasma) – Space plasma physics (waves and instabilities) – Radio science (magnetospheric physics)

1 Introduction

Equatorial noise is an intense natural emission of electromagnetic plasma waves observed within a few Earth radii (R_E) of geocentric radial distance, and always recorded very close to the geomagnetic equator. Its frequency interval ranges from a few Hertz to several hundreds of Hertz. These waves were first observed by Russell et al. (1970) in the outer plasmasphere at frequencies between twice the local proton cyclotron frequency (f_{H^+}) and half the lower hybrid frequency (f_{lh}). The observations were made within 2° from the equator, and the magnetic field fluctuations carried by those waves were found to be very close to the direction parallel to the static terrestrial magnetic field ($\boldsymbol{B}$). This observed polarization corresponds well to the theoretical properties of the whistler-mode waves below f_{lh} (e.g. Stix, 1992), assuming that the wave vectors are very close to perpendicular to $\boldsymbol{B}$.

Later observations (Gurnett, 1976; Perraut et al., 1982; Laakso et al., 1990; Kasahara et al., 1994; André et al., 2002) revealed that the equatorial noise occurs at radial distances between 2 and 7 R_E, and at latitudes within 10° from the magnetic equator, and that its lowest frequency could go down to the fundamental f_{H^+}. Detailed time-frequency spectrograms (Gurnett, 1976) also showed that, what appears as a noise band in the low resolution data, is in fact a superposition of many spectral lines with different frequency spacings. The term "equatorial noise" is, however, still used even for these discrete wave phenomena, to indicate the connection to the original observations of Russell et al. (1970). The generation mechanism of these waves is most probably connected to the ion-cyclotron harmonic interaction (Gurnett, 1976), with energetic protons having ring-like distribution functions at a pitch angle of 90° (Perraut et al., 1982). After being generated at the ion Bernstein wave-mode branches, the waves subsequently propagate in the electromagnetic whistler mode (also known as the extraordinary or fast magnetosonic mode). Equatorial noise thus can be observed far away from its generation region.

Multipoint observations of equatorial noise by the four Cluster spacecraft have been presented by Cornilleau-Wehrlin et al. (2003) and Santolík et al. (2002). They addressed the location of noise with respect to the equatorial plane and the spatio-temporal structure of its frequency spectra. Santolík et al. (2002) found these waves within 2° of the magnetic equator, and Cornilleau-Wehrlin et al. (2003), in another case, at about 3° of the model equator, with an extension of 0.15 R_E in the direction perpendicular to the ecliptics. Since a common feature of the equatorial noise is the presence of harmonic lines whose spacings do not match the local

Correspondence to: O. Santolík
(ondrej.santolik@mff.cuni.cz)

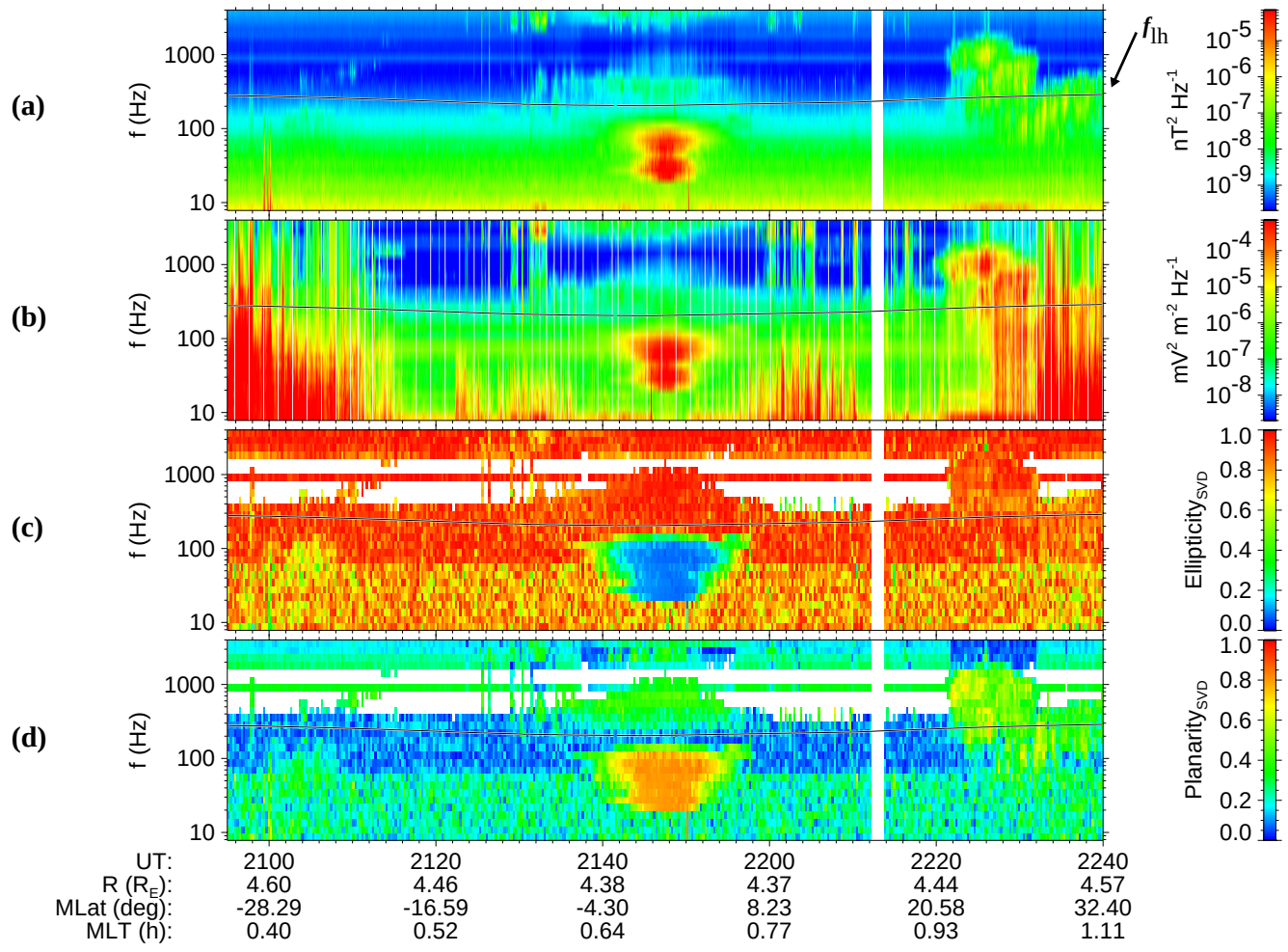

Fig. 1. Example of data collected by Cluster 4 on 17 February 2002. From the top: **(a)** sum of the power-spectral densities of the three magnetic components, **(b)** sum of the power-spectral densities of the two electric components ; **(c)** ellipticity and **(d)** planarity are determined using the singular value decomposition of the magnetic spectral matrix. Universal time (UT) and position of the spacecraft are given on the bottom of the figure using the radial distance (R) in the Earth radii (R_E), magnetic dipole latitude (MLat) in degrees, and magnetic local time (MLT) in hours. Maximum possible value of the local lower hybrid frequency (f_{lh}) is plotted over the panels (a)–(d). The data in panels (c) and (d) are not shown for weak signals below 10^{-9} nT^2 Hz^{-1}.

f_{H^+}, waves have to propagate in the radial direction, in order to move through the equatorial plane to a place with a different magnetic field strength. Santolík et al. (2002) showed a case where the wave propagation directions have a radial component.

This paper is also based on the data of the Cluster project. We present the first results of our systematic analysis of a large number of observations of equatorial noise. These emissions are, together with the whistler mode chorus, among the most intense electromagnetic waves observed in the low-latitude region of the Earth's magnetosphere, and their sensitivity to the variations of the geomagnetic activity indicates their importance for the "space weather" applications, i.e. prediction of fluxes of energetic particles as a consequence of variations of the solar input (André et al., 2002). Therefore, we focus our attention on the probability densities of the wave intensity in both electric and magnetic components. We establish a selection criterion for recognizing the equatorial noise emissions, and compare the intensities of equatorial noise with those of other emissions in the same interval of frequencies and latitudes. In Sect. 2 we will present the data set and, using an example case, we will describe our analysis methods. In Sect. 3 we will show results of the systematic analysis, in Sect. 4 we will discuss these results and, finally, in Sect. 5 we will present brief conclusions.

2 Data set and analysis methods

We use the data collected by the "spatiotemporal analysis of field fluctuations" (STAFF-SA) instruments on board the four Cluster spacecraft operated by the European Space Agency (ESA). STAFF-SA was designed for onboard calculation of power-spectral densities, mutual phases, and coherence relations of three orthogonal magnetic components and

two electric components (Cornilleau-Wehrlin et al., 1997, 2003). The analysis is made in 27 frequency channels between 8 Hz and 4 kHz, and the instrument has several measurement modes. Of those, we only use the "normal mode" in the present study. This mode provides us with the full five-component analysis in the entire frequency band of the instrument. The data are analyzed on board with the time resolution of 1 s (for the power-spectral densities) or 4 s (for the phases and coherence). The results are then compressed and transmitted to the ESA receiving stations. In the subsequent preprocessing phase the received data are calibrated and organized in Hermitian spectral matrices 5×5, one matrix per frequency channel, i.e. 27 matrices every 4 s. Each spectral matrix contains the real power-spectral densities on its main diagonal and complex cross-spectral densities as its off-diagonal elements.

We have analyzed all the preprocessed data intervals where the Cluster spacecraft were close to their perigee during the first two years of operation (2001–2002). In these portions of their orbits the spacecraft scanned the low-latitude region of the Earth's magnetosphere at all magnetic local times, and at radial distances between 3.9 and 5 R_E. The preprocessed STAFF-SA data have been organized into intervals of ≈1-hour duration, and we have selected those intervals where the instrument measured within ≈30° of the geomagnetic equator. In most cases we have joint two or three adjacent ≈1-hour intervals, to obtain a better coverage of the equatorial region. We have worked with the data of each spacecraft separately, thus increasing the amount of data intervals entering in the statistics. Discussion of this approach is presented in Sect. 4. Using that procedure, we have collected the total number of 781 data intervals of ≈1–3 h, measured in the equatorial region close to the perigee of the four Cluster spacecraft. To ensure the coherence of our results and to gain experience for their reasonable interpretation, we have visually inspected all the intervals before doing the subsequent computer analysis. This inspection showed that in 671 perigee cases the data were available in a restricted interval of latitudes within 10° of the geomagnetic equator where we expect equatorial noise to appear. Of those cases, we have identified the presence of equatorial noise in 398 intervals (59%).

Figure 1 shows an example of those data intervals where the equatorial noise emissions were present. The measurements were done by Cluster 4 on 17 February 2002. The spacecraft was close to its perigee, and we show the data recorded in the low-latitude region within ±30° of magnetic equator (magnetic latitude is determined using the dipole approximation of the Earth's magnetic field). Figures 1a and 1b represent power-spectral densities of the magnetic and electric field, respectively. Equatorial noise is the intense electromagnetic emission seen on both panels close to the center of the time interval, within a few degrees from the equator. In the frequency domain it appears as two main peaks at ≈30 Hz and ≈70 Hz. The emission is confined below the upper estimate of the lower hybrid frequency ($f_{\rm lh}$), calculated as the geometric average of the proton and electron cyclotron frequencies. To plot this estimate in Fig. 1, we use the measurements of the ambient magnetic field made on board (Balogh et al., 2001). It represents the true value of $f_{\rm lh}$ only in a dense plasma, with the plasma frequency much larger than the electron cyclotron frequency, which is always the case in the plasmasphere.

Multidimensional measurements of electric and magnetic fields allow us to analyze polarization properties of equatorial noise emissions. Ellipticity L_p of polarization of the magnetic field fluctuations is shown in Fig. 1c. We use the singular value decomposition technique from Eq. (13) of Santolík et al. (2003), defining $L_p{=}w_2/w_1$, where w_1 and w_2 are the two largest singular values of the magnetic spectral matrix. In the idealized case of exactly planar polarization, the result represents the ratio of the lengths of the minor and major axes of the polarization ellipse. It varies between 0 (linear polarization) and 1 (circular polarization). The equatorial noise can be easily distinguished by its polarization close to linear, as it was first described by Russell et al. (1970). Very similar results have been obtained using classical methods based on eigenvalue analysis (e.g. Samson, 1973). The abrupt change in the L_p values at a constant frequency of 62.5 Hz outside the equatorial noise emission is an instrumental effect. It is connected to the boundary between the frequency bands of the STAFF-SA instrument, where different averaging of measured data is done during the onboard analysis.

Figure 1d represents the planarity F of the polarization of magnetic field fluctuations from Eq. (12) of Santolík et al. (2003). It is defined as $F{=}1{-}\sqrt{w_3}/\sqrt{w_1}$, where w_1 and w_3 are, respectively, the maximum and the minimum singular values of the magnetic spectral matrix. In an idealized case of random fluctuations, F reflects the ratio of the shortest and the longest axes of the 3-D polarization ellipsoid, defined by standard deviations of magnetic noise. A value close to 0 would mean that the fluctuations appear in all three axes of the ellipsoid with the same probability, whereas a value of 1 would represent a strict confinement of the fluctuations to a single 2-D plane. Note that the boundary at 62.5 Hz seen in Fig. 1d is the same instrumental effect as described in the previous paragraph. For the equatorial noise, the value of F ≈0.8 suggests that the magnetic field fluctuates very close to a single plane, with a small fraction of random 3-D fluctuations. Values of F and L_p are obviously interdependent in that sense, that a given L_p sets a lower limit of possible values of F, $1{-}\sqrt{L_p}{\le}F{\le}1$. On the other hand, a given F doesn't have any implication for possible values of L_p.

3 Systematic analysis of the entire data set

The polarization analysis shown in Fig. 1 has been done with the entire data set recorded during the perigee portions of the 781 orbits of the Cluster spacecraft. We have selected the frequency channels between 8 Hz (the lowest frequency analyzed by the STAFF-SA instrument) and 300 Hz (the upper estimate of the maximum $f_{\rm lh}$ throughout the data set). This

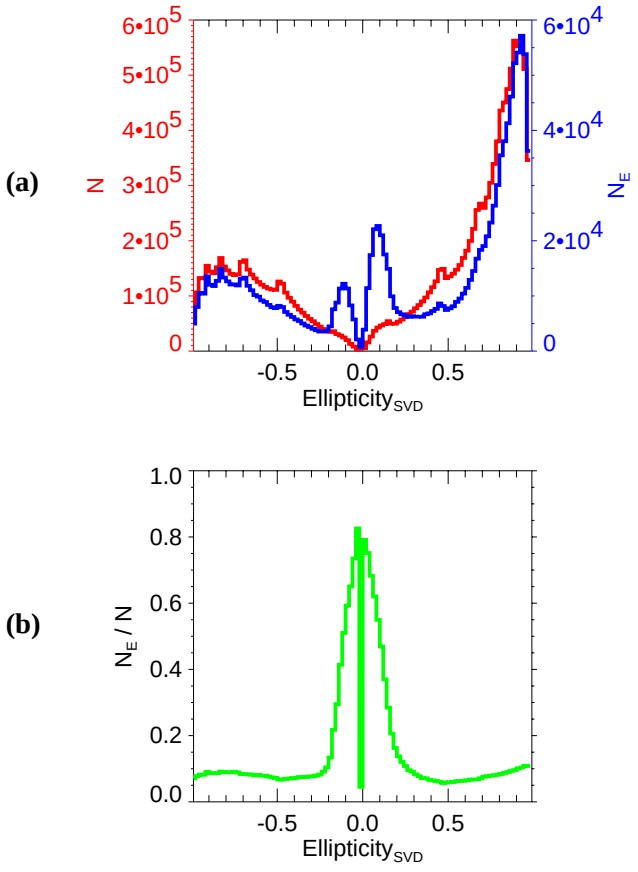

Fig. 2. Histograms of modified ellipticity $L_s L_p$ (see text) determined using the singular value decomposition of the magnetic spectral matrix. **(a)** Histogram of all 1.4×10^7 time-frequency points, plotted in red with the left-hand-side vertical scale; and of selected 1.3×10^6 intense events above 10^{-6} nT^2 Hz^{-1}, plotted in blue, with the right-hand-side vertical scale. **(b)** Normalized histogram of the elipticity of the intense events.

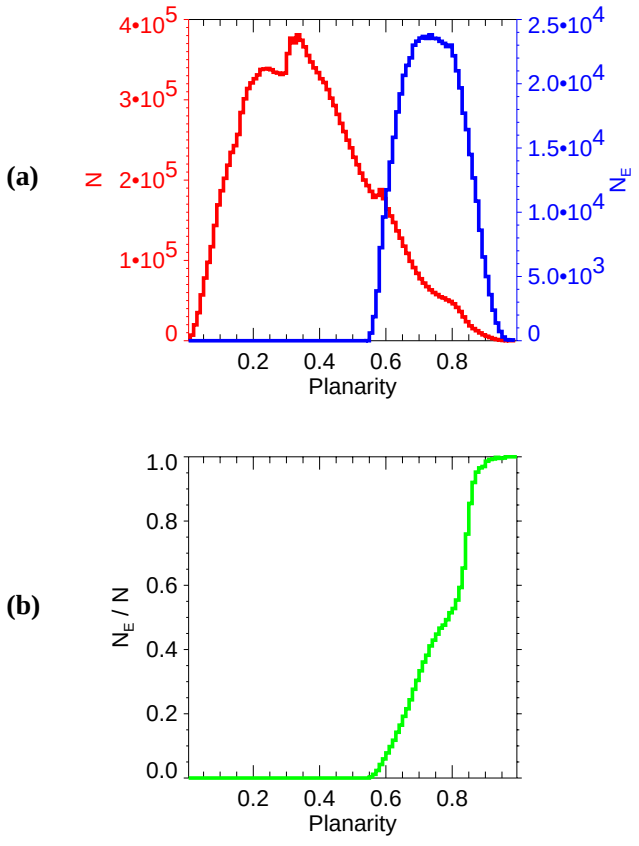

Fig. 3. Histograms of the planarity determined using the singular value decomposition of the magnetic spectral matrix. **(a)** Histogram for all 1.4×10^7 time-frequency points, plotted in red with the left-hand-side vertical scale; and for selected 5.4×10^5 nearly linearly polarized events with $L_p < 0.2$, plotted in blue, with the right-hand-side vertical scale. **(b)** A normalized histogram for the nearly linearly polarized waves.

means that we use only the 16 lowest frequency channels of the instrument. The analysis has been further limited to the data measured within $\pm30°$ of magnetic latitude from the magnetic equator. If this interval of latitudes is completely covered by the data, it would, given the orbital parameters of Cluster satellites, correspond to a time interval of approximately 1 h and 40 min, i.e. with the 4-second time resolution, to 1500 measurements. Since the selected time intervals do not always cover that total range of latitudes, the average number in our data set is ≈1100 measurements per interval. For the 781 perigee passages, we thus have the total number of $16\times1100\times781 \approx 1.4\times10^7$ time-frequency points. In these points we have analyzed measured spectral matrices which served as input data for calculations of the average power-spectral densities of the magnetic and electric fluctuations, ellipticity, and planarity (see Sect. 2).

Figure 2 shows histograms constructed from the obtained ellipticity values. The results are now slightly modified compared to the method used in Fig. 1c. The purpose is to reflect the sense of rotation of the wave magnetic field. We multiply L_p by a sign coefficient L_s, which is either -1, or $+1$ according to the sign of the phase shift between the two components of magnetic fluctuations perpendicular to $\boldsymbol{B}$. The value of -1 represents the left-hand polarized waves (the sense of the ion cyclotron motion) and the value of $+1$ represents the right-hand polarized waves, (the sense of the electron cyclotron motion). If the polarization is linear, and the corresponding phase shifts are either $0°$ or $\pm180°$, then L_p is zero and L_s may be defined as -1 or $+1$, with no effect on the resulting product $L_s L_p$. Similarly, if the polarization is close to linear, L_p is close to zero, and the influence of L_s on the result is negligible. The values $L_s L_p$ of ±1 then correspond to exactly circular polarization (right- or left-handed), absolute values less than 1 mean elliptic polarization, and the value of zero still represents strictly linearly polarized waves.

To obtain the histograms in Fig. 2, the interval $\langle -1, +1\rangle$ has been divided into 100 consecutive subintervals, and the number of cases contained in each of these subintervals has been counted. The entire data set mainly contains right-hand, nearly circularly polarized waves with some small fraction of

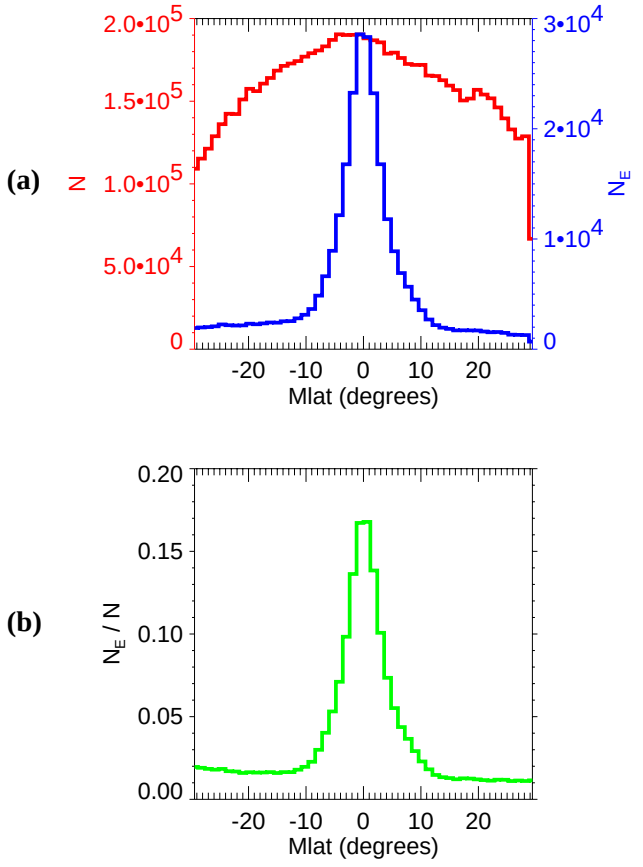

Fig. 4. The same as in Fig. 3, but for the magnetic dipole latitude.

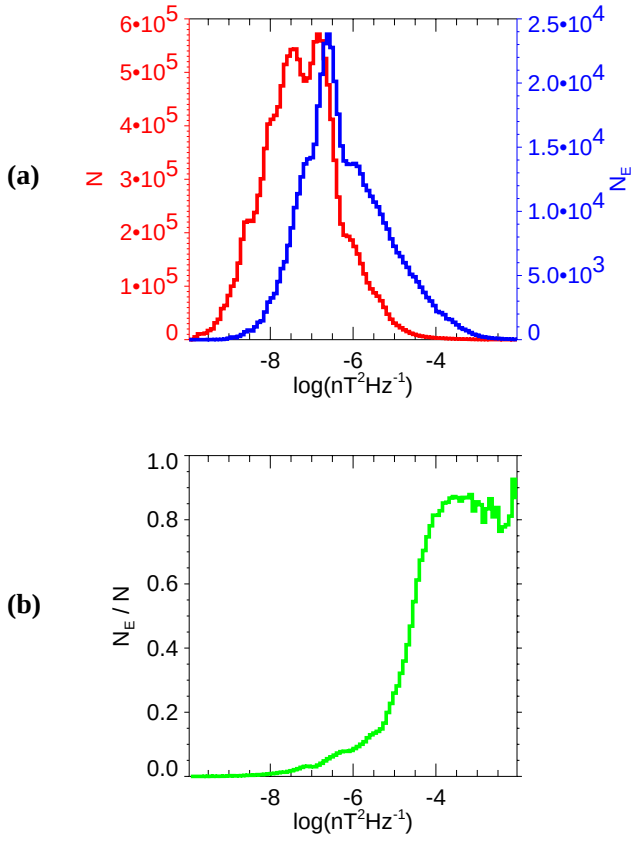

Fig. 5. The same as in Fig. 3, but for the sum of the power-spectral densities of the three components of magnetic field fluctuations.

left-hand polarized waves (red curve in Fig. 2a). Note that the onboard compression algorithm leads to phase quantization effects reflected on the histogram as a set of superposed small-amplitude peaks. If we now select just the most intense waves with the magnetic spectral densities larger than $10^{-6}\,\mathrm{nT^2\,Hz^{-1}}$, we obtain a non-negligible fraction of nearly linearly polarized waves with the absolute value of ellipticity below ≈0.2 (blue curve in Fig. 2a). The artifacts introduced by the onboard compression are removed if we calculate the relative fraction of the intense waves among all the recorded measurements. This normalized histogram of ellipticity (Fig. 2b) is obtained as the ratio of the blue and red histograms from Fig. 2a. It clearly shows that the majority of nearly linearly polarized waves is more intense than $10^{-6}\,\mathrm{nT^2\,Hz^{-1}}$, forming a distinct peak around zero ellipticity in Fig. 2b, with a maximum close to 80%. Based on our visual inspection of all the available data from the perigee passages of the Cluster satellites, we can identify those intense linearly polarized waves with the equatorial noise emissions. As we will show next, this identification proves true, considering our results on the magnetic latitudes of these waves. From Fig. 2b we can also estimate a reasonable threshold of 0.2 for the ellipticity L_p, bounding the peak of the intense linearly polarized waves. This threshold will be used in the following to identify the equatorial noise emissions.

Results for the planarity of the magnetic field polarization are shown in Fig. 3. We use the same analysis method as for the example case in Fig. 1d. The obtained values have been counted in 100 subintervals between 0 and 1 to construct the histograms in Fig. 3. The histogram for all events (red curve in Fig. 3a) shows a broad peak shifted toward lower values, with a maximum around 0.3. For the selected nearly linearly polarized waves with $L_p < 0.2$ (blue curve in Fig. 3a) the peak is clearly moved towards higher values of the planarity. Its maximum is now slightly below 0.8. As we have shown in Sect. 2, possible values of the planarity F are limited, given the ellipticity L_p. For $L_p < 0.2$ we cannot obtain F lower than ≈0.55. Normalized histogram of the planarity values for the nearly linearly polarized waves is shown in Fig. 3b. We can see that 100% of the observations of high planarity values (>0.9) correspond to the nearly linearly polarized waves. This fraction decreases toward lower planarity values down to the cutoff at $F \approx 0.55$.

Figure 4 presents the histograms of the magnetic dipole latitudes of the events. To obtain these histograms, the interval from $-30°$ to $+30°$ has been divided into 50 consecutive subintervals. The histogram for all events (red curve and left-hand scale in Fig. 4a) is not a constant function of the magnetic latitude because of the particular method we used to select the data set. Since we always selected the data intervals containing the measurements close to the magnetic

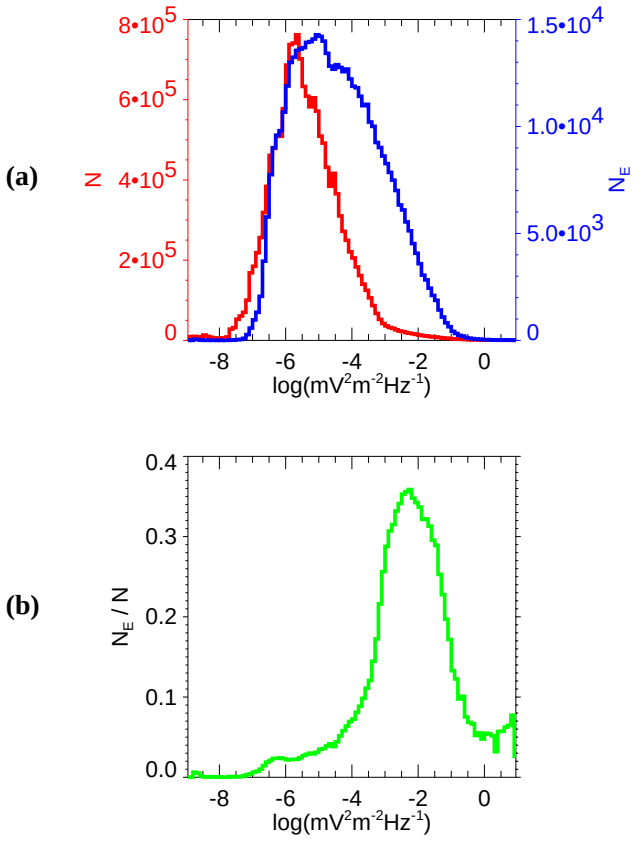

Fig. 6. The same as in Fig. 3, but for the sum of the power-spectral densities of the two measured components of electric field fluctuations.

equator, the histogram shows a broad peak centered at the zero latitude. This is therefore a purely artificial effect.

The histogram looks quite different for the waves with $L_p < 0.2$ (blue curve and right-hand scale in Fig. 4a). The maximum is again close to the equator, but the peak is now much narrower, with the majority of events confined within 10° of the magnetic equator. The ratio of the two histograms, shown in Fig. 4b, again forms a narrow peak, with approximately the same width. It moreover shows that about 17% of all events observed close to the magnetic equator is nearly linearly polarized. This fraction decreases toward higher latitudes. For latitudes to the south of $-10°$ and to the north of $+10°$, it goes down to 1–2%. This residual value will be discussed in Sect. 4. The majority of the observed nearly linearly polarized waves is, however, clearly concentrated close to the equator. This further validates this selection criterion for the equatorial noise emissions.

In the analysis presented in Fig. 2 we have used a threshold of 10^{-6} nT^2 Hz^{-1} to select intense waves. Figure 5 shows more details on the distribution of the obtained values of the magnetic power-spectral density. To construct the histograms, the interval between 10^{-10} and 10^{-2} nT^2 Hz^{-1} has been divided into 100 consecutive logarithmic subintervals. The histogram of all events (red curve and left-hand scale in Fig. 5a) peaks close to 10^{-7} nT^2 Hz^{-1}, steeply decreases just below 10^{-6} nT^2 Hz^{-1}, and forms a decreasing tail at higher intensities.

The main peak is only slightly higher for the waves with $L_p < 0.2$ (blue curve and right-hand scale in Fig. 5a), but the high-intensity tail extends to significantly higher intensities with a higher probability. The ratio of the two histograms, shown in Fig. 5b, reveals that the linearly polarized waves dominate the most intense emissions with the magnetic power-spectral density above 10^{-4} nT^2 Hz^{-1}, leaving only about 20% of those intense events to waves with a different polarization. Oppositely, a very low relative fraction of nearly linearly polarized waves is observed for less intense waves below 10^{-6} nT^2 Hz^{-1}.

Figure 6 shows histograms of the electric power-spectral density in a similar format as in Fig. 5. We use the interval of values between 10^{-9} and 10^{1} mV^2 m^{-2} Hz^{-1}, again divided into 100 consecutive logarithmic subintervals. The histogram of all events (red curve in Fig. 6a) has a peak value close to 10^{-5} mV^2 m^{-2} Hz^{-1}, about one order of magnitude lower than the histogram for the nearly linearly polarized waves (blue curve). Above 10^{-4} mV^2 m^{-2} Hz^{-1}, the probability density for the $L_p < 0.2$ subset of events is shifted by about two orders of magnitude higher. The relative fraction of the nearly linearly polarized waves (the ratio of the two histograms shown in Fig. 6b) doesn't reach such as high values as in the case of the magnetic field fluctuations. It shows a peak fraction of about 35% for relatively intense waves slightly below 10^{-2} mV^2 m^{-2} Hz^{-1}, but for higher intensities the relative fraction again decreases down to about 5%. This means that other types of polarization dominate at those extremely high intensities.

4 Discussion

The most important simplification in our analysis method is the selection criterion we use to recognize the equatorial noise emissions. To analyze large volumes of data it is inevitable to use an automatic recognition procedure, always taking the risk that some data points are either not selected when they should be, or selected by mistake. On the other hand, the advantage of this approach is that the selection is absolutely objective, based on a well-defined criterion, thus removing all possibilities for subjective case-by-case judgement which could bias the resulting statistics. In this study we have chosen to set up a relatively simple criterion based on the ellipticity of the magnetic field fluctuations, using known characteristics of the equatorial noise and the visual inspection of all the cases. To verify this approach we have checked the resulting statistics of magnetic latitude and planarity of polarization.

The only main problem of this selection criterion has been found in the analysis of magnetic latitudes (Fig. 4b). We have obtained a constant fraction of 1–2% of the nearly linearly polarized waves for magnetic latitudes below $-10°$ and above $+10°$. If we have no other explanation of these waves, it would mean that the linearly polarized equatorial noise

extends in latitude at least 30° from the magnetic equator. This would be in contradiction with the results published in the past. An alternative explanation could be that these observations correspond to linearly polarized signals that we wrongly classify as equatorial noise. We suppose the phenomenon is connected to the low-frequency magnetic noise of the instrument. We can see in Fig. 1c that the instrumental noise creates patchy appearances of nearly linear polarization well outside the compact time-frequency region of the natural equatorial noise. Since these spots of linear polarization are evenly distributed at all latitudes, the result is the observed 1–2% floor on the normalized histogram.

To test this hypothesis we have further narrowed our selection criteria to include only the most intense waves, with the magnetic spectral density larger than $10^{-6}\,\mathrm{nT^2\,Hz^{-1}}$. This condition has been combined with the threshold $L_p < 0.2$. In such a way, the influence of the weak instrumental noise has been eliminated. The resulting normalized histogram (Fig. 7) proves that the main peak close to the equator remains in place as we see it in Fig. 4b but the 1–2% floor disappears. More precisely, the main peak reaches somewhat lower values of ≈10%, and the fraction becomes negligible outside the interval of magnetic latitudes between −10° and +10°. This confirms the hypothesis that the 1–2% floor in Fig. 4b is owing to the instrumental noise.

In the present study, we have made another simplification in analyzing the data of the four Cluster spacecraft separately. The approach naturally increases the volume of data entering in the statistics by a factor of 4. However, all the spacecraft pass through the equatorial region in relatively short intervals of time, from less than one minute up to about 45 min, depending on the actual configuration of the spacecraft orbits. We can then question the hypothesis of the independence of the four data sets obtained by the different spacecraft. The geomagnetic conditions certainly are very similar for the four spacecraft during their closely separated perigee passages, but, nevertheless, the internal structure of the equatorial noise emissions can be highly variable at spatiotemporal scales comparable to the separation of the spacecraft (Santolík et al., 2002). In our data set we can find cases where the position of the peak intensity and the latitudinal extent of the equatorial noise are nearly the same on the four spacecraft, and other cases where these parameters are considerably different. Detailed analysis of these differences is beyond the scope of the present paper but for the purpose of this discussion we can conclude that the total number of independent cases can be up to 4 times lower, if we consider as independent only those passages separated by at least one full orbital period of the spacecraft (2 days and 9 h). This still does not decrease the total volume of data below any reasonable limit of statistical reliability (recall that the total number of time-frequency points is 1.4×10^7 – after using the most severe selection criteria in Fig. 7 this number still reaches a value of 2×10^5).

The analysis of the electric and magnetic power-spectral densities is the main purpose of this work. The results show that, without any doubt, the nearly linearly polarized emissions are the most intense ones in the given interval of frequencies and latitudes, as concerns the magnetic field fluctuations. Electric field fluctuations of these emissions are also more intense compared to the average of all detected waves but still their relative fraction in Fig. 6b decreases at very high intensities of more than $10^{-2}\,\mathrm{mV^2\,m^{-2}\,Hz^{-1}}$. It then appears interesting to determine what kind of waves constitutes those in approximately 95% of the intense events. Here we must take into account that the selection criterion is based on the polarization of the magnetic fluctuations and does not take into account the polarization of the wave electric field. Intense electrostatic waves thus would not be selected even if they were linearly polarized because they are not accompanied by a magnetic field signal. Thus, we interpret these intense waves as broadband electrostatic noise, often occurring at higher latitudes which are magnetically connected to the Southern and Northern auroral regions. An example can be seen in Fig. 1b where broad-band electrostatic fluctuations are mainly observed at magnetic latitudes below −25° and above +25°. Projected along the approximately dipolar magnetic field lines on the Earth's surface, these positions correspond, respectively, to auroral latitudes below −65°, and above +65°.

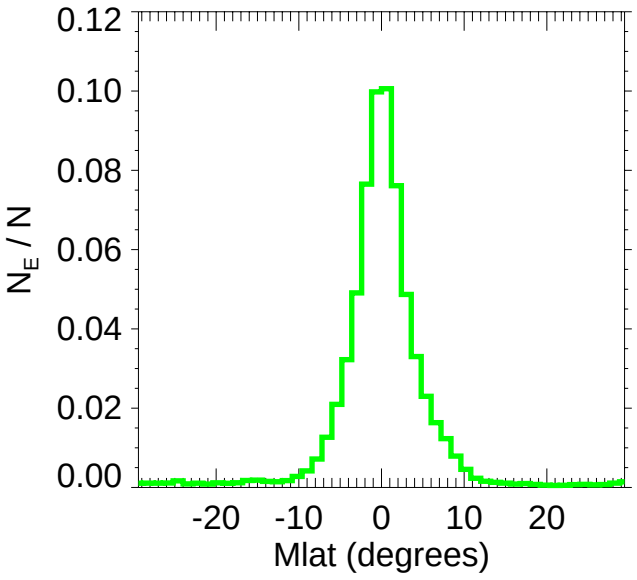

Fig. 7. The same as in Fig. 4b, but with the additional selection criterion of the magnetic spectral density larger than $10^{-6}\,\mathrm{nT^2\,Hz^{-1}}$.

The final note of this discussion concerns the significance of our results. We have proven that equatorial noise is the most intense electromagnetic emission within 30° of the geomagnetic equator, in the frequency range between f_{H^+} and f_{lh}, and in the range of radial distances between 4 and $5\,R_E$. As we have shown in Sect. 2, equatorial noise is detected in approximately 60% of all passages of the Cluster spacecraft through the equatorial region at 4–$5\,R_E$. This high occurrence rate, together with the relatively high observed intensities, indicate that the importance of equatorial noise may be not as marginal, as would suggest the low number of papers

concerning these emissions which can be found in the public literature. Our results suggest an analogy with natural emissions of whistler-mode chorus (generally observed above f_{lh}), which are also very intense, and which are believed to significantly influence the dynamics of the energetic electrons in the Earth's outer radiation belt (Meredith et al., 2003; Horne et al., 2003; Horne and Thorne, 2003). According to the most accepted generation mechanism of equatorial noise (Gurnett, 1976; Perraut et al., 1982), its amplification is fed by the free energy in the distribution functions of energetic ions, which may be significantly influenced by interactions with these waves.

Natural emissions of equatorial noise can thus play a non-negligible role in the dynamics of the internal magnetosphere. Equatorial noise can lead to modifications of the distribution functions of energetic ions, possibly causing their perpendicular heating or, on the other hand, phase-space diffusion and eventual precipitation into the Earth's atmosphere. All those arguments are, however, still rather speculative, and global effects of equatorial noise have yet to be quantitatively determined. Our results may indicate that this future research is worth being done.

5 Conclusions

We have described the first results of a systematic study of equatorial noise observed by the Cluster spacecraft between the local proton cyclotron frequency and the local lower hybrid frequency. This study has been based on the data measured by the STAFF-SA instrument during its first two years of operation. We have analyzed data collected during 781 perigee intervals of the four Cluster spacecraft at radial distances between 3.9 and 5 Earth radii, and at magnetic latitudes between $-30°$ and $+30°$. Inspection of these intervals has shown that the occurrence rate of equatorial noise is approximately 60%.

Polarization analysis of magnetic field fluctuations has allowed us to select nearly linearly polarized waves with ellipticities below 0.2. These waves have been found to have the highest planarity among all the collected wave observations. They have been mainly found within $10°$ of the geomagnetic equator. A small fraction of these waves observed at higher latitudes can be explained by the influence of instrumental noise. These results indicate, consistent with the subjective experience gained from the visual inspection of the entire data set, that the low-ellipticity criterion is able to identify equatorial noise with a reasonable success.

Equatorial noise has been shown to have the most intense magnetic field fluctuations among all the natural emissions in the given interval of frequencies and latitudes, being detected in approximately 80% of the cases where the magnetic power-spectral density exceeds $10^{-4}\,\mathrm{nT^2\,Hz^{-1}}$. Electric field fluctuations of equatorial noise are more intense compared to the average of all detected waves but their relative fraction decreases at very high intensities of more than $10^{-2}\,\mathrm{mV^2\,m^{-2}\,Hz^{-1}}$, owing to the 95% domination of the broad band electrostatic noise.

The relatively high observed intensities and high occurrence ratios of equatorial noise indicate that these natural emissions can play a role in the dynamics of energetic ions in the internal magnetosphere. More research is needed to quantify their influence.

Acknowledgements. We sincerely thank Chris Harvey of CESR Toulouse, Michel Parrot of LPCE Orleans, Milan Maksimovic of the Meudon Observatory, and other colleagues from the STAFF team for construction, calibration and operations of the instrument and for fruitful discussions of the data. We gratefully acknowledge "space weather" discussions with François Lefeuvre of LPCE Orleans, who significantly influenced the principal direction of this research. Our thanks are due to the PI of the FGM instrument (A. Balogh) for the DC magnetic field data used for reference and coordinate transformations, and to the Hungarian Cluster Data Center which provides auxiliary data. ESA and CNES are thanked for their support for the STAFF experiment. This research was supported by the Czech Grant Agency grant No. 202/03/0832.

Topical Editor T. Pulkkinen thanks a referee for his help in evaluating this paper.

References

André, R., Lefeuvre, F., Simonet, F., and Inan, U. S.: A first approach to model the low-frequency wave activity in the plasmasphere, Ann. Geophys., 20, 981–996, 2002.

Balogh, A., Carr, C. M., Acuña, M. H., et al.: The Cluster Magnetic Field Investigation: overview of in-flight performance and initial results, Ann. Geophys., 19, 1207–1217, 2001.

Cornilleau-Wehrlin, N., Chauveau, P., Louis, S., et al.: The Cluster spatio-temporal analysis of field fluctuations (STAFF) experiment, Space Sci. Rev., 79, 107–136, 1997.

Cornilleau-Wehrlin, N., Chanteur, G., Perraut, S., et al.: First results obtained by the Cluster STAFF experiment, Ann. Geophys., 21, 437–456, 2003.

Gurnett, D. A.: Plasma wave interactions with energetic ions near the magnetic equator, J. Geophys. Res., 81, 2765–2770, 1976.

Horne, R. B., Glauert, S. A., and Thorne, R. M.: Resonant diffusion of radiation belt electrons by whistler-mode chorus, Geophys. Res. Lett., 30, 9, 1493, doi:10.1029/2003GL016963, 2003.

Horne, R. B. and Thorne, R. M.: Relativistic electron acceleration and precipitation during resonant interactions with whistler-mode chorus, Geophys. Res. Lett., 30, 10, 1527, doi:10.1029/2003GL016973, 2003.

Kasahara, Y., Kenmochi, H., and Kimura, I.: Propagation characteristics of the ELF emissions observed by the satellite Akebono in the magnetic equatorial plane, Radio Sci., 29, 751–767, 1994.

Laakso, H., Junginger, H., Roux, A., Schmidt, R., and de Villedary, C.: Magnetosonic waves above f_c (H+) at geostationary orbit: GEOS 2 results, J. Geophys. Res., 95, 10 609–10 621, 1990.

Meredith, N. P., Cain, M., Horne, R. B., Thorne, R. M., Summers, D., and Anderson, R. R.: Evidence for chorus-driven electron acceleration to relativistic energies from a survey of geomagnetically disturbed periods, J. Geophys. Res., 108, A6, 1248, doi:10.1029/2002JA009764, 2003.

Perraut, S., Roux, A., Robert, P., Gendrin, R., Sauvaud, J.-A., Bosqued, J.-M., Kremser, G., and Korth, A.: A systematic study of ULF waves above F_{H^+} from GEOS 1 and 2 measurements

and their relationships with proton ring distributions, J. Geophys. Res., 87, 6219–6236, 1982.

Russell, C. T., Holzer, R. E., and Smith, E. J.: OGO 3 observations of ELF noise in the magnetosphere: 2. The nature of the equatorial noise, J. Geophys. Res., 73, 755–768, 1970.

Samson, J. C.: Descriptions of the polarization states of vector processes: Applications to ULF magnetic fileds, Geophys. J. R. Astron. Soc., 34, 403–419, 1973.

Santolík, O., Pickett, J. S., Gurnett, D. A., Maksimovic, M., and Cornilleau-Wehrlin, N.: Spatiotemporal variability and propagation of equatorial noise observed by Cluster, J. Geophys. Res., 107, A12, 1495, doi:10.1029/2001JA009159, 2002.

Santolík, O., Parrot, M., and Lefeuvre, F.: Singular value decomposition methods for wave propagation analysis, Radio. Sci., 38, 1, 1010, doi:10.1029/2000RS002523, 2003.

Stix, T. H.: Waves in Plasmas, Am. Inst. of Phys., New York, 1992.

Available online at www.sciencedirect.com
SCIENCE DIRECT®
Planetary and Space Science 53 (2005) 291–298
Planetary and Space Science
www.elsevier.com/locate/pss

Initial results of a survey of equatorial noise emissions observed by the Cluster spacecraft

F. Němec[a,*], O. Santolík[a], K. Gereová[a], E. Macúšová[a], Y. de Conchy[b], N. Cornilleau-Wehrlin[c]

[a]*Faculty of Mathematics and Physics, Charles University, V Holesovickach 2, 180 00 Prague, Czech Republic*
[b]*LESIA, Observatoire de Paris—Meudon, France*
[c]*CETP/IPSL, Velizy, France*

Accepted 12 September 2004

Abstract

Initial results of a survey of equatorial noise emissions are presented. These plasma wave emissions are observed in the inner magnetosphere close to the geomagnetic equator at frequencies below the local lower hybrid frequency. We use the data recorded by the four Cluster spacecraft during the first 24 months of measurements. The data set was processed in three steps. First, we have selected the data with a nearly linear polarization corresponding to the known properties of the equatorial noise. Second, we have found parameters of a Gaussian model of the frequency-averaged power-spectral density of the selected waves as a function of the geomagnetic latitude. Third, we have analyzed the data as a function of frequency in the latitudinal interval defined by the width of the Gaussian model. Our results show that most intensity peaks of equatorial noise occur within 2° of the magnetic equator and the full-width at half-maximum (FWHM) of these peaks is below 3° in the majority of cases. The most probable frequency of the emissions is between 4 and 5 local proton cyclotron frequencies. The probability density of occurrence of the emissions then slowly decreases toward higher frequencies. Multipoint measurements indicate that the variations of the ratios of amplitudes of the equatorial noise emissions measured on different spacecraft do not increase at spatial scales up to 0.7 Earth radii in the equatorial plane. On the other hand, the variations do increase with time delay between measurements in an interval from tenths to hundreds of minutes.

Keywords: Cluster; STAFF-SA; Equatorial noise

1. Introduction

Equatorial noise is an intense electromagnetic emission observed in the vicinity of the geomagnetic equator. It occurs at radial distances of a few Earth radii and at frequencies from a few hertz to several hundreds of hertz. The plasma waves of this type were first observed by Russell et al. (1970) within 2° from the equator at frequencies between twice the local proton cyclotron frequency (f_{H+}) and half the lower hybrid frequency (f_{lh}). These observations showed that the equatorial noise is an intense, almost linearly polarized emission. Gurnett (1976) analyzed detailed time–frequency spectrograms recorded by the Hawkeye spacecraft. The results showed that the apparent broadband, noise-like spectrum observed in low-resolution spectrograms, is in fact a system of many spectral lines with different frequency spacings. He suggested that these lines are created by ion cyclotron harmonic interaction in a region where the local cyclotron frequency matches the observed spacing. After being generated, the waves propagate in the electromagnetic whistler mode to the observation point, which can thus lie far away from

*Corresponding author.
E-mail address: frantisek.nemec@ruk.cuni.cz (F. Němec).

0032-0633/$ - see front matter © 2004 Elsevier Ltd. All rights reserved.
doi:10.1016/j.pss.2004.09.055

their region of generation. Perraut et al. (1982) proposed a wave generation model using ring-like distribution functions at a pitch angle of 90°. Successive observations (Laakso et al., 1990; Kasahara et al., 1994) revealed that the equatorial noise occurs at radial distances between 2 and $7R_E$, and at latitudes within 10° from the magnetic equator. The emissions have been detected at frequencies above the local f_{cH+}.

Multipoint observations of equatorial noise have been done by the four spacecraft of the Cluster project (Cornilleau-Wehrlin et al., 2003). Santolík et al. (2002) reported results of high-resolution measurement in the morning sector, demonstrating a narrow latitudinal extent of the emissions with a typical width of 2°, centered near the minimum-B equator. They showed that the wave vector had a radial component. Since the Poynting vector also has a radial component, the waves could propagate from a generation region where ion cyclotron frequencies matched the observed fine structure of spectral lines. Santolík et al. (2004) presented a systematic analysis of a large number of observations of equatorial noise based on the data of the STAFF-SA instruments (Spatio-temporal analysis of field fluctuations) on board the four Cluster spacecraft. The occurrence rate of equatorial noise was found to be approximately 60%. Equatorial noise was identified by selecting data with nearly linearly polarized magnetic field fluctuations. The results showed that equatorial noise had very intense magnetic field fluctuations and thus could play a non-negligible role in the dynamics of the internal magnetosphere.

This paper is also based on the data of the Cluster project. We present results of a survey of equatorial noise, using a Gaussian model of the distribution of the power-spectral density as a function of latitude. In Section 2, we will present the data set and describe our analysis methods. In Section 3, we will describe results of the systematic analysis, in Section 4, we will discuss them, and, finally, in Section 5, we will present brief conclusions.

2. Data set and processing

The data that we have used were collected during the first 24 months of operation of the STAFF-SA instruments on board the four Cluster spacecraft (Cornilleau-Wehrlin et al., 1997), which are operated at mutual separation distances of hundreds to thousands of kilometers by the European Space Agency (ESA). The instrument mode we use in the present study provides us with the five-component analysis of three magnetic and two electric components in 27 frequency channels between 8 Hz and 4 kHz. In each frequency channel, the data are analyzed on board the spacecraft, forming 5×5 Hermitian spectral matrices. These matrices are then recorded with a time resolution of 1 s for the power-spectral densities (main diagonal of the spectral matrix), and 4 s for the phases and coherence (off diagonal elements of the spectral matrix). We have analyzed all the data intervals where the Cluster spacecraft were close to the equatorial plane during their perigee passages. These intervals contain data, which are measured at radial distances between 3.9 and $5R_E$ and which cover all magnetic local times.

Figs. 1 and 2 show an example of data intervals containing equatorial noise emissions. The measurements were done by Cluster 1 and 3 on November 25, 2002. Top two panels contain spectrograms representing power-spectral densities of the magnetic and electric field fluctuations, respectively. Equatorial noise is the intense electromagnetic emission seen close to the center of the time interval, within a few degrees from the equator. The emission occurs below the upper estimate of local lower hybrid frequency plotted in spectrograms. This is calculated as the geometric average of the proton and electron cyclotron frequencies.

Middle panel contains spectrogram representing ellipticity of polarization of magnetic field fluctuations. This is determined by the singular value decomposition (SVD) method (Santolík et al., 2003) and varies between 0 (linear polarization) and 1 (circular polarization). It can be seen, that the equatorial noise can be easily distinguished by its polarization close to linear (Russell et al., 1970). The fourth panel contains spectrogram representing the planarity of magnetic field fluctuations, which is again determined by the SVD method and varies between 0 and 1 (a value of 1 would represent a strict confinement of the fluctuations to a single plane). For the equatorial noise the value of ≈ 0.8 suggests that the magnetic field fluctuates very close to a single plane, with a small fraction of random 3-D fluctuations.

Bottom panel contains spectrogram representing spectral density of the Poynting flux. These show that equatorial noise emissions bear a relatively large amount of energy compared, for instance, to the whistler-mode emissions (chorus) observed at higher frequencies.

It can be seen that the characteristics of the same equatorial noise emission observed by different Cluster spacecraft can significantly differ (e.g. in our example case the emission observed by Cluster 3 is almost 10 times more intense than the emission observed by Cluster 1—see Fig. 3 for details). This difference is caused by the time delay between the spacecraft (one spacecraft is approaching the equatorial plane earlier than the other one). More precise explanation of this phenomenon will be presented at the end of Section 3 and discussed at the end of Section 4.

In order to enable identification of equatorial noise emissions, we have processed the data in several steps. First, we have selected the data measured within ±10° of magnetic latitude from the magnetic equator and

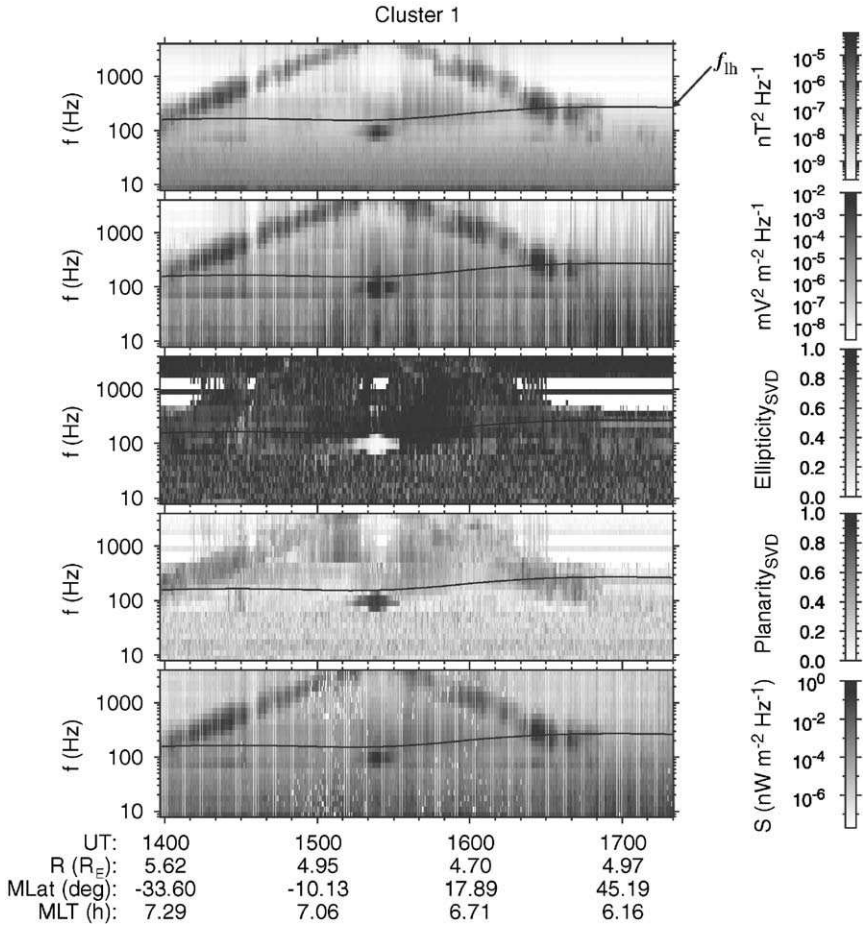

Fig. 1. Example of data collected by Cluster 1 on November 25, 2002. From the top: time–frequency power spectrograms of the magnetic and electric field fluctuations, ellipticity of polarization, planarity of polarization, and spectral density of the Poynting flux. Equatorial noise is the intense electromagnetic emission close to the center of time interval, below the local lower hybrid frequency (f_{lh}). The equatorial noise emission can be distinguished by a low ellipticity and high planarity. The ellipticity and planarity are determined using the singular value decomposition of the magnetic spectral matrix.

frequency channels between 8 and 300 Hz (the upper estimate of the maximum f_{lh} throughout the data set), which represents 16 lowest frequency channels of the instrument. Next, we have selected the data by an ellipticity threshold. As it is discussed by Santolík et al. (2004), a choice of ellipticity lower than 0.2 is a good criterion to select equatorial noise emissions. We have then calculated average power-spectral density from the selected data in the selected frequency channels, and we have found the parameters of a Gaussian model as a function of the geomagnetic latitude λ. This non-linear least-squares procedure used a model

$$A = A_0 \exp\left(-\frac{4 \ln 2(\lambda - \lambda_c)^2}{\Delta^2}\right) \quad (1)$$

of the measured frequency-averaged electric and magnetic power-spectral densities. In Eq. (1), A is a model power-spectral density of the electric or magnetic field fluctuations, A_0 is the value of the corresponding intensity peak, λ_c is the position of this peak and Δ is a full-width at half-maximum (FWHM) of the Gaussian model. Fig. 3 shows the results of this procedure for the example case presented in Figs. 1 and 2. The reason for using a Gaussian model was that it is the simplest one which describes all the properties of equatorial noise emissions that we are interested in.

The above procedure has been done with 748 data intervals obtained during the first 24 months of the operation of the STAFF-SA instruments onboard all the four Cluster spacecraft. For each of these cases, we have visually compared the results of the Gaussian model with the corresponding original data. We have then decided whether the data contain an equatorial noise emission and whether this emission is well described by the model (whether the fit was successful). This decision was made visually from case to case. There were two possible options expressing the correctness of

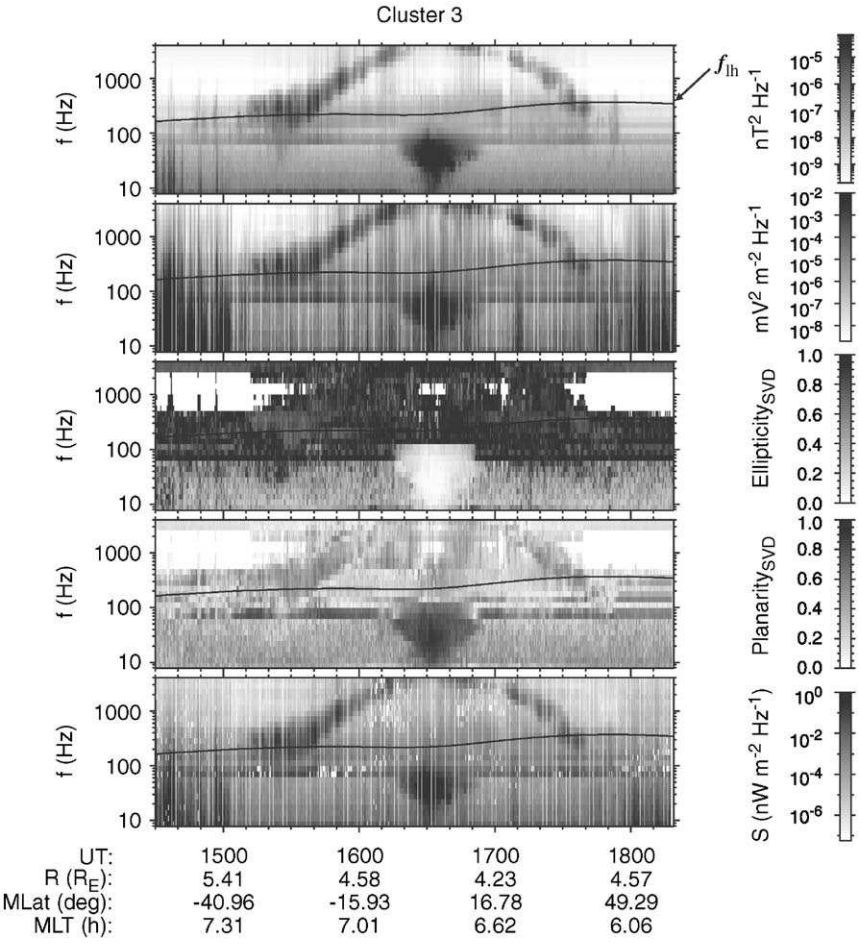

Fig. 2. The same as in Fig. 1 but for the Cluster 3 data.

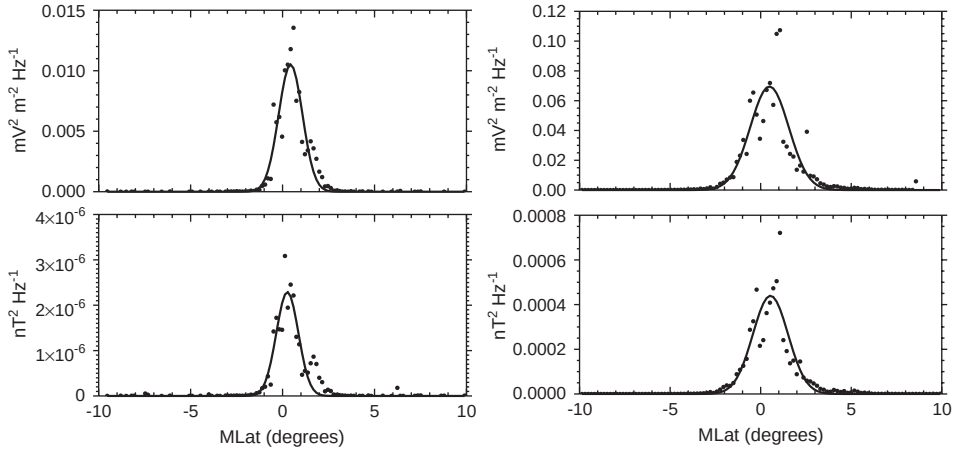

Fig. 3. Non-linear least-squares fit of a Gaussian function on the electric (top) and magnetic (bottom) field power-spectral densities between 8 and 300 Hz from Figs. 1 and 2 for Cluster 1 (left) and Cluster 3 (right). The experimental frequency-averaged power-spectral densities of selected data are represented by points, model results are plotted by lines.

the fit: successful fit and bad data. Fig. 3 shows an example of data classified as a successful fit, Fig. 4 shows an example of data classified as bad data.

We have thus obtained 401 successful cases for the power-spectral density of the electric field fluctuations, and 362 cases for the power-spectral density of the magnetic field fluctuations.

For further analysis we used results of this Gaussian model, working again with the original frequency-dependent data. We selected the cases where the fit

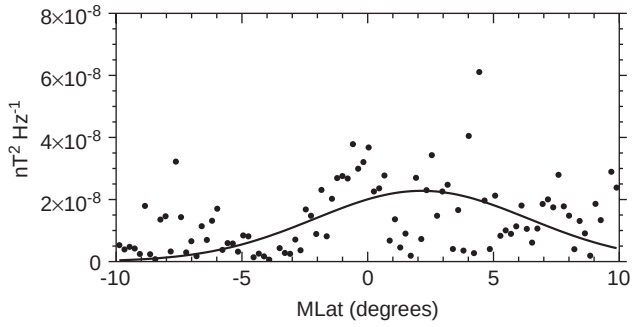

Fig. 4. An example of fit classified as Bad data (there is no equatorial emission present).

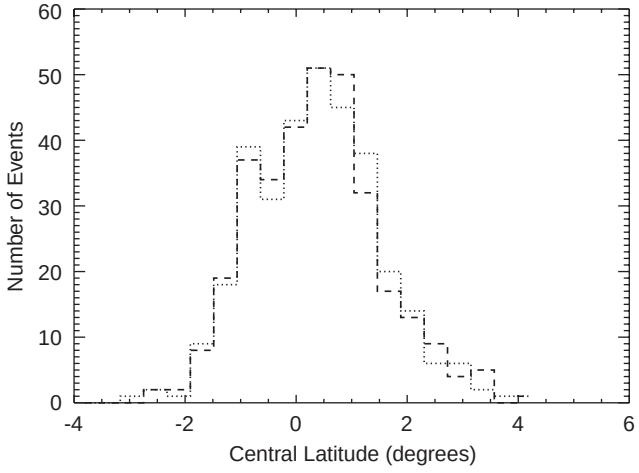

Fig. 5. Histogram of central latitudes of the peak of electric (dashed) and magnetic (dotted) power-spectral densities.

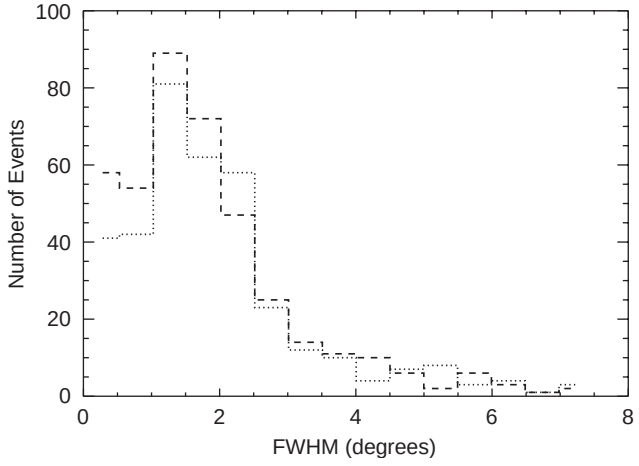

Fig. 6. Histogram of the FWHM of the Gaussian model of electric (dashed) and magnetic (dotted) power-spectral densities.

was successful for both the electric and magnetic power-spectral densities, obtaining 339 intervals. For each of these cases, we have calculated a time-averaged spectral matrix over the time interval where the spacecraft was situated inside the latitudinal interval from $\lambda_c - \Delta$ to $\lambda_c + \Delta$. The averaging was done for each of the 16 lowest frequency channels separately.

3. Results of a systematic study

Figs. 5 and 6 show resulting model parameters for the 401 successful cases for the modeled power-spectral density of the electric field fluctuations, and 362 cases for the power-spectral density of the magnetic field fluctuations. Fig. 5 presents a histogram of central latitudes (λ_c in Eq. (1)) of the peak of electric and magnetic power-spectral densities. Most central latitudes occur within 2° from the geomagnetic equator. Fig. 6 presents the histogram of the FWHM (Δ in Eq. (1)) of the Gaussian model of electric and magnetic power-spectral densities. It is below 3° in the majority of cases. Results for both electric and magnetic field fluctuations are very similar in Figs. 5 and 6.

Fig. 7 shows the probability density of frequencies of equatorial noise emissions normalized to the local proton cyclotron frequency (f_{cH+}). It was obtained from the analysis of the 16 × 339 time-averaged spectral matrices mentioned above. For each of the matrices, we know the frequency, the ellipticity of polarization of the magnetic field component of the emission, and the average intensity of the local magnetic field (from which we determine f_{cH+}). To determine whether the equatorial noise occurs in a given frequency channel or not, we have used the same ellipticity threshold as in the first step of our data processing method. We have again assumed, that if the value of ellipticity calculated from the averaged spectral matrix is lower than 0.2 (polarization close to linear), observed emission is of the equatorial noise type. Fig. 7 shows that the most probable frequency of emissions is between 4 and $5f_{cH+}$ and the probability density slowly decreases towards the higher frequencies. Note that the width of the peak is probably affected by the approximately 30% relative widths of the frequency channels of the STAFF-SA instrument (Cornilleau-Wehrlin et al., 1997). This finite width necessarily leads to broadening of peaks and smoothing of gradients in the resulting spectrum.

Fig. 8 represents the comparison of the same equatorial noise emissions observed by different Cluster spacecraft, which follow almost the same orbits. We have made all 6 possible combinations of the four spacecraft for the perigee passages where successful fits from all the spacecraft were simultaneously available, obtaining the total number of 324 combinations in 54 passages. These combinations correspond to points plotted in Fig. 8. Each of the points represents the ratio of the two amplitudes A_0 of the Gaussian model (1) for

the power-spectral density of the electric field fluctuations, calculated from the data of two different spacecraft. When we plot all of them in one figure we can see that the amplitude variations increase with time difference between the spacecraft (this means the difference between times when the peak of amplitude was observed). This is illustrated by our example Figs. 1 and 2, where observations from Cluster 1 and 3 significantly differ. The reason is that during that orbit Cluster 3 reaches approximately the same point as Cluster 1 with more than 1 h delay. The amplitude variations do not show any clear trend while increasing the separation of the spacecraft in the equatorial plane.

4. Discussion

The most important simplifications in our analysis method occur during the data processing. In order to identify the equatorial noise emissions in such a large amount of data, it is necessary to define some universal identification criteria. There is always a risk, that some points, which should be selected as an equatorial noise, will not be selected and, on the other hand, that the points which should not be selected will be. We have tried to overcome this problem by combining an automatic pre-selection procedure with a visual case-by-case identification. The automatic procedure was used to select only the nearly linearly polarized waves which criterion is well justified by the known properties of the equatorial noise emissions (e.g., Russell et al., 1970). The subsequent visual recognition always contains some degree of subjective judgement but we have not found a reliable automatic procedure which would easily replace this step. A completely automatic equatorial noise recognition would probably require a much more refined model of the intensity distributions which is out of the scope of the present paper. We believe that the subjective element does not bias the statistical results we have presented.

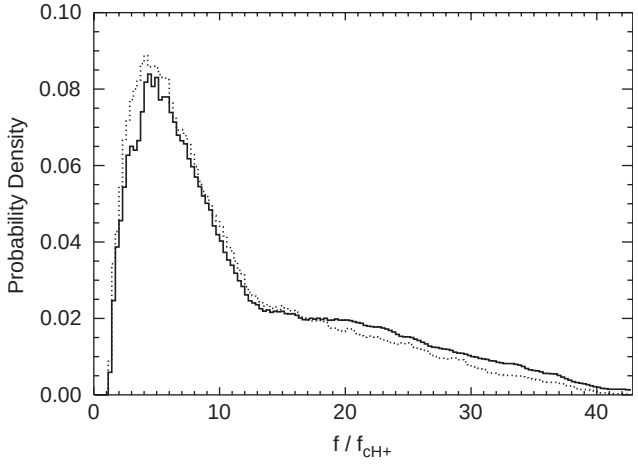

Fig. 7. Probability density of frequencies of equatorial noise. There is a maximum at frequencies between 4 and 5 proton cyclotron frequencies (f_{cH+}). The ellipticity threshold was used for the solid curve and both ellipticity and intensity thresholds were used for the dotted curve (values of the thresholds are defined in the text).

Another problem is that our Gaussian model (as well as any other model) is only an approximation which simplifies the real situation. We can see in Fig. 3 that the experimental points are rather scattered around the model curve, indicating deviations from the model. In some other cases we can note systematic enhancements of the power-spectral density in the "wings" of the model Gaussian function, making the real peak slightly wider compared to the model. This problem could be resolved by making a more complex model with additional degrees of freedom allowing such deviations from a simple Gaussian function. In this work, we have chosen to keep the model as simple as possible. The resulting parameters then have to be interpreted as global characteristics.

The peaks of the Gaussian model are distributed within 2° of the dipole magnetic equator. Contrary to what could be expected, histogram of central latitudes of the peak of electric and magnetic power-spectral densities (Fig. 5) is not exactly symmetric around the

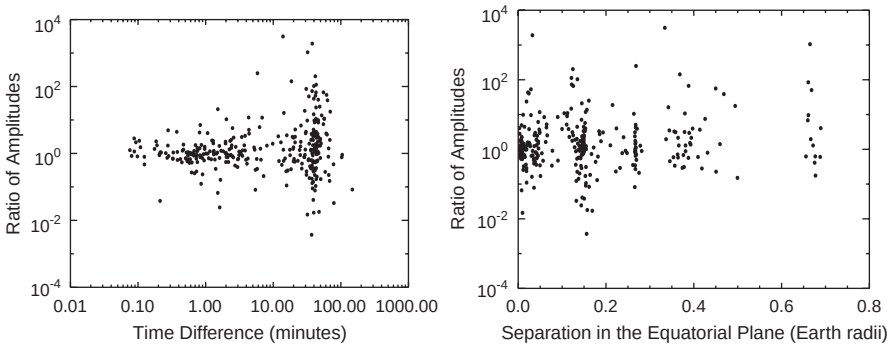

Fig. 8. Comparison of the same equatorial noise emissions observed by different Cluster spacecraft. We obtain six points for each observation (all combinations of 4 spacecraft).

zero geomagnetic latitude. We can see that the maximum number of events is slightly moved towards the positive latitudes. This is most probably caused by the definition of magnetic latitude we have used. We use the magnetic latitude related to the ideal dipole model of the geomagnetic field. The equator in this model is defined by a plane perpendicular to the dipole axis. The true geomagnetic equator is, however, defined by a point where the magnetic field is minimum along a particular field line (min-B equator). If we use a more realistic model of the magnetic field (e.g., Tsyganenko, 1989) we obtain a typical difference of the order of one degree compared to the position of the dipole equator (see the calculations of Santolík et al., 2002). These differences approximately correspond to the width of the peak in Fig. 5. The observed systematic shift towards the positive latitudes is a fraction of the total width and therefore is probably not significant. If we used a better model compared to the dipole approximation of the magnetic equator, we expect that the peaks would be more confined in the equatorial plane. Detailed analysis of this effect is under way and will be published later.

Spatio-temporal analysis based on multi-point measurements and drawn in Fig. 8 hides one basic problem, the problem of a scale. Although multi-point measurements indicate that the amplitude of emissions varies with time rather than with the position in the equatorial plane, the problem is that we do not have any clear connection between scales we compare. Our results have been obtained for separations below 0.7 Earth radii in the equatorial plane, and for time delays between tenths and hundreds of minutes. Extension of these intervals will require further measurements. Our present results could be explained by a source illuminating an area with a linear dimension of at least 0.7 Earth radii in the equatorial plane. Substantial time variations of such a source would occur at scales longer than a few minutes.

5. Conclusions

We have presented initial results of a survey study of equatorial noise emissions observed by Cluster spacecraft between the local proton cyclotron frequency and the local lower hybrid frequency. The data were collected during 24 months of operation of the STAFF-SA instruments onboard the four spacecraft. We have analyzed measurements recorded during their perigee intervals at magnetic latitudes between -10° and $+10^\circ$, and at radial distances between 3.9 and 5 Earth radii. We have identified equatorial noise emissions by a combination of an automatic procedure based on an ellipticity threshold and a least-squares fit of a Gaussian model with a subsequent visual inspection.

Our results show that:

(1) Most intensity peaks of a Gaussian model of the power-spectral density of equatorial noise occur within 2° of the dipole magnetic equator. The observed small systematic shift is not significant.
(2) The full-width at half-maximum (FWHM) of the Gaussian model of the power-spectral density is below 3° in the majority of cases.
(3) The most probable frequency of emissions is between 4 and 5 local proton cyclotron frequencies. The probability density of occurrence of the emissions then slowly decreases toward higher frequencies.
(4) Variations of the ratio of amplitudes of equatorial noise increase with time delay between measurements in an interval from tenths to hundreds of minutes. These variations do not seem to increase with separations up to 0.7 Earth radii in the equatorial plane.

Acknowledgements

We sincerely thank Chris Harvey of CESR Toulouse, Michel Parrot of LPCE Orleans, Milan Maksimovic of the Meudon Observatory, and other colleagues from the STAFF team for construction, calibration and operations of the instrument and for fruitful discussions of the data. Our thanks are due to the PI of the FGM instrument (A. Balogh) for the DC magnetic field data used for reference and coordinate transformations, and to the Hungarian Cluster Data Center which provides auxiliary data. ESA and CNES are thanked for their support for the STAFF experiment. This research was supported by grants GACR 202/03/0832, MSM 113200004, and ESA PRODEX 14529.

References

Cornilleau-Wehrlin, N., Chauveau, P., Louis, S., Meyer, A., Nappa, J.M., Perraut, S., Rezeau, L., Robert, P., Roux, A., de Villedary, C., de Conchy, Y., Friel, L., Harvey, C.C., Hubert, D., Lacombe, C., Manning, R., Wouters, F., Lefeuvre, F., Parrot, M., Pinçon, J.L., Poirier, B., Kofman, W., Louarn, P., The STAFF investigator team, 1997. The Cluster spatio-temporal analysis of field fluctuations (STAFF) experiment. Space Sci. Rev. 79, 107–136.

Cornilleau-Wehrlin, N., Chanteur, G., Perraut, S., Rezeau, L., Robert, P., Roux, A., de Villedary, C., Canu, P., Maksimovic, M., de Conchy, Y., Hubert, D., Lacombe, C., Lefeuvre, F., Parrot, M., Pincon, J.L., Decrau, P.M.E., Harvey, C.C., Louarn, Ph., Santolik, O., Alleyne, H.St.C., Roth, M., STAFF team, 2003. First results obtained by the Cluster STAFF experiment. Ann. Geophys. 21, 437–456.

Gurnett, D.A., 1976. Plasma wave interactions with the energetic ions near the geomagnetic equator. J. Geophys. Res. 81, 2765–2770.

Kasahara, Y., Kenmochi, H., Kimura, I., 1994. Propagation characteristics of the ELF emissions observed by the satellite Akebono in the equatorial plane. Radio Sci. 29, 751–767.

Laakso, H., Junginger, H., Roux, A., Schmidt, R., de Villedary, C., 1990. Magnetosonic waves above f_{cH+} at geostationary orbit: GEOS 2 results. J. Geophys. Res. 95, 10,609–10,621.

Perraut, S., Roux, A., Robert, P., Gendrin, R., Sauvaud, J.-A., Bosqued, J.-M., Kremser, G., Korth, A., 1982. A systematic study of ULF waves above F_{H+} from GEOS 1 and 2 measurements and their relationship with proton ring distributions. J. Geophys. Res. 87, 6219–6236.

Russell, C.T., Holzer, R.E., Smith, E.J., 1970. OGO 3 observations of ELF noise in the magnetosphere. The nature of the equatorial noise. J. Geophys. Res. 73, 755–768.

Santolík, O., Pickett, J.S., Gurnett, D.A., Maksimovic, M., Cornilleau-Wehrlin, N., 2002. Spatio-temporal variability and propagation of equatorial noise observed by Cluster. J. Geophys. Res. 107 (A12), 1495 doi: 10.1029/2001JA009159.

Santolík, O., Parrot, M., Lefeuvre, F., 2003. Singular value decomposition methods for wave propagation analysis. Radio Sci. 38 (1), 1010 doi: 10.1029/2000RS002523.

Santolík, O., Němec, F., Gereová, K., Macúšová, E., de Conchy, Y., Cornilleau-Wehrlin, N., 2004. Systematic analysis of equatorial noise below the lower hybrid frequency. Ann. Geophys. 22, 2587–2595.

Tsyganenko, N.A., 1989. A magnetospheric magnetic field model with a warped tail current sheet. Planet. Space Sci. 37, 5–20.

Annales Geophysicae, 23, 3301–3311, 2005
SRef-ID: 1432-0576/ag/2005-23-3301

Annales Geophysicae

ELF magnetospheric lines observed by DEMETER

M. Parrot[1], **F. Němec** [2], **O. Santolík**[2], **and J. J. Berthelier**[3]

[1]LPCE/CNRS, 3A Avenue de la Recherche Scientifique, 45071 Orléans cedex 2, France
[2]Charles University, Faculty of Mathematics and Physics, Prague, Czech Republic
[3]CETP, Observatoire de Saint Maur, 4 Avenue de Neptune, 94107 Saint Maur des Fossés cedex, France

Received: 2 June 2005 – Revised: 14 September 2005 – Accepted: 16 September 2005 – Published: 30 November 2005

Abstract. The influence of man-made activity on the ionosphere may be very important. The effects induced by the Power Line Harmonic Radiation (PLHR) may change the natural wave activity and/or the ionospheric plasma components. One goal of the ionospheric satellite DEMETER launched in June 2004 is to study the ionospheric perturbations which could be related to this anthropogenic activity. As the first step, the paper presents Tram Lines (TL) which have been observed on board DEMETER with frequency intervals close to 50 Hz or 16 Hz 2/3 (the current frequency of the railways). When it is observable the frequency drift of these TL is very slow. It is shown that these events occur during periods of strong or moderate magnetic activity. A wave propagation analysis indicates that the TL observed below the low cutoff frequency of the hiss which is simultaneously present are coming from a region below the satellite. The conclusion is that these TL observed by DEMETER are produced by PLHR or radiation of railways lines.

Keywords. Ionosphere (Ionospheric disturbances; Wave propagation; Active experiments)

1 Introduction

The Power Line Harmonic Radiation (PLHR) are the ELF and VLF waves radiated by electric power systems at the harmonic frequencies of 50 or 60 Hz. Evidence of PLHR propagation in the magnetosphere was first observed on the ground (Helliwell et al., 1975; Helliwell, 1979; Park and Helliwell, 1981; Matthews and Yearby, 1981; Yearby et al., 1983). Park (1977) observed ground-based PLHR during a magnetic storm. However, direct observations by satellites are rather rare and shown in few papers (Koons et al., 1978; Bell et al., 1982; Tomizawa and Yoshino, 1985; Parrot, 1994; Rodger et al., 1995). Many observations show that the lines drift in frequencies. One must say that there is a controversy about the origin of these lines which are observed in space or on the ground because many of them are not separated by 50 or 60 Hz. They are called MLR (Magnetospheric Line Radiation) or TL, and their generation mechanism is not well determined, although it is most probably due to a nonlinear interaction between electrons and the coherent waves. In their study of ISIS2 data, Rodger et al. (1995) observed MLR and did not find a frequency correlation with 50 or 60 Hz, or multiples. It was the same for observations of MLR at Halley Bay (Rodger et al., 1999, 2000a, 2000b). In a review paper concerning observations of PLHR and MLR emissions by ground-based experiments and satellites, Bullough (1995) discussed about the possibility that MLR are due to PLHR. There are indications that PLHR influences the atmosphere-ionospheremagnetosphere coupling. This problem requires serious attention because the electrical power consumption is always increasing in the world (Parrot and Zaslavski, 1996). Theoretical works have been done to explain these effects. Nonlinear interactions between electrons and PLHR can participate in the precipitation of electrons from the slot region in the radiation belts (Bullough et al., 1976; Tatnall et al., 1983). Molchanov et al. (1991) have shown that the main part of the PLHR energy dissipates in the lower ionosphere and modifies the ionospheric currents. Simulations have also been performed by Nunn et al. (1999) to explain ground observations of PLHR and associated triggered emissions in Finland. Recently, Ando et al. (2002) analyzed the penetration of PLHR in the presence of an ionosphere with a single ion and underlined the importance of the ion gyrofrequency relative to the wave frequency of this man-made emission.

The aim of this paper is to present events recorded by the ionospheric satellite DEMETER which was launched in June 2004. Section 2 shortly describes the wave experiment on board DEMETER. Four events showing ELF magnetospheric lines are presented in Sect. 3. Analysis and discussions of these events are done in Sect. 4, whereas Sect. 5 presents conclusions.

Correspondence to: M. Parrot
(mparrot@cnrs-orleans.fr)

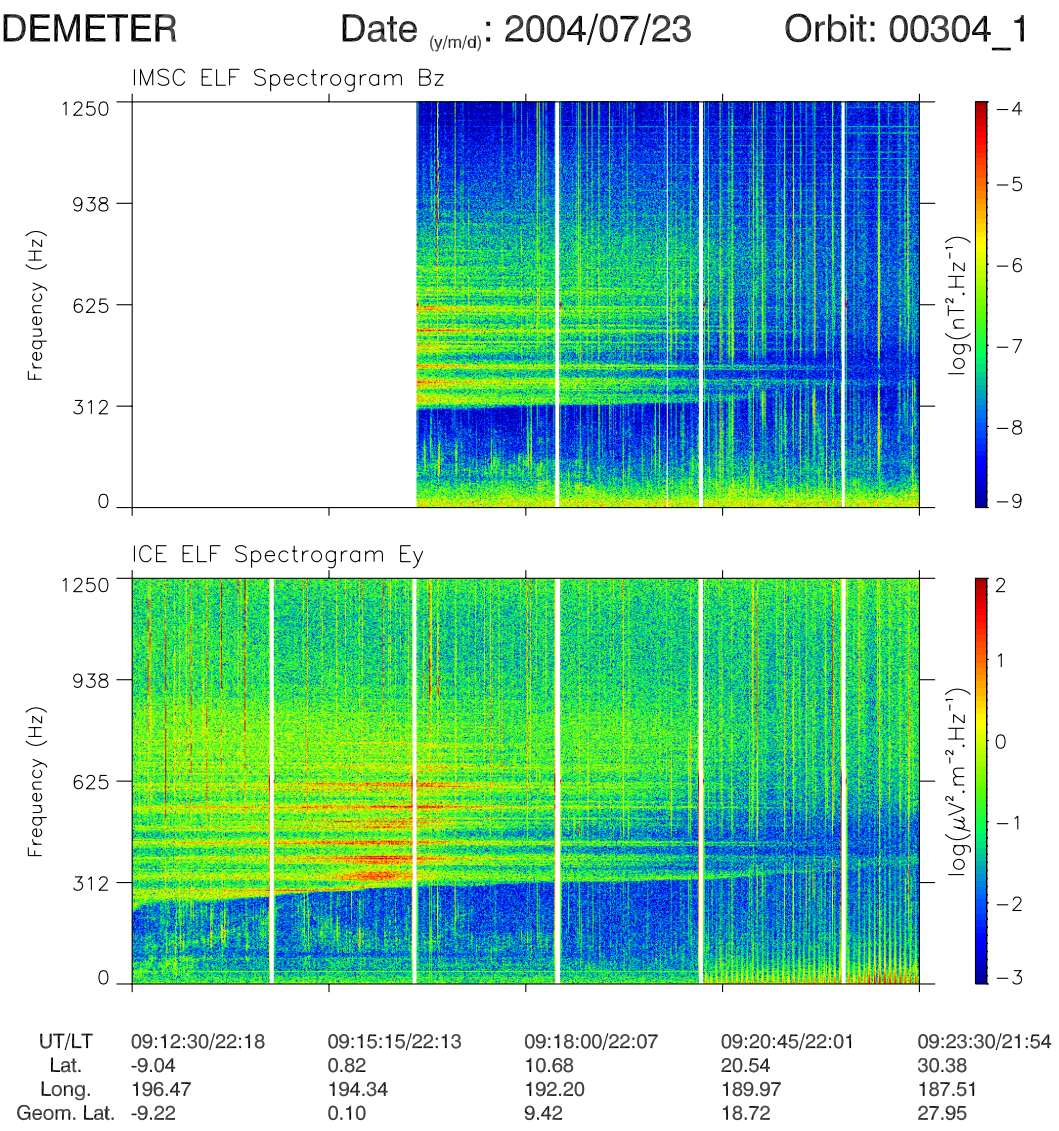

Fig. 1. Spectrograms of the magnetic component B_x (top panel) and E_y (bottom panel) recorded on 23 July 2004 (event 1). The intensity of the emissions is color-coded according to the color scale on the right. The vertical white lines indicate a change in the mode of the experiment.

2 The experiment

DEMETER is a low-altitude satellite (710 km) with a polar orbit which measures electromagnetic waves all around the Earth, except in the auroral zones. The frequency range for the electric field is from DC up to 3.5 MHz, and for the magnetic field from a few Hz up to 20 kHz. There are two scientific modes: a survey mode, where spectra of one electric and one magnetic component are computed on board up to 20 kHz, and a burst mode, where waveforms of the 6 components of the electromagnetic field are recorded up to 1.25 kHz. The burst mode allows one to perform spectral analysis with a better frequency resolution and to determine propagation characteristic of the waves. There is an onboard calibration at 625 Hz which is activated at each mode change and after every 4, 8 or 12 mn. Details of the wave experiment can be found in Parrot et al. (2005) and Berthelier et al. (2005). Data shown in this paper have been recorded during burst modes.

3 The data

3.1 Event 1 recorded on 23 July 2004

Figure 1 displays data recorded on 23 July 2004 between 09:12:30 UT and 09:23:34 UT by DEMETER during an equatorial crossing. The two panels represent spectrograms of the magnetic component B_z (top) and the electric component E_z (bottom) from 0 to 1250 Hz. Time and orbital parameters are indicated at the bottom of the figure. Data have

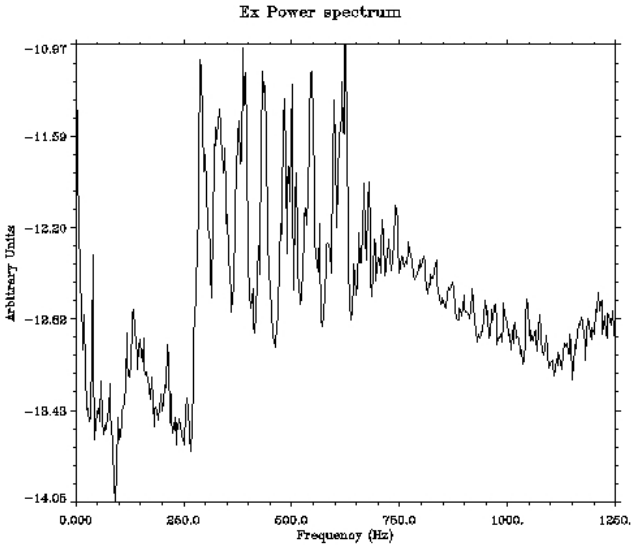

Fig. 2. Spectrum of the electric component E_x. The analysis is performed between 09:14:30 and 09:16:30 UT using a 1024 point-FFT (Δf=2.44 Hz).

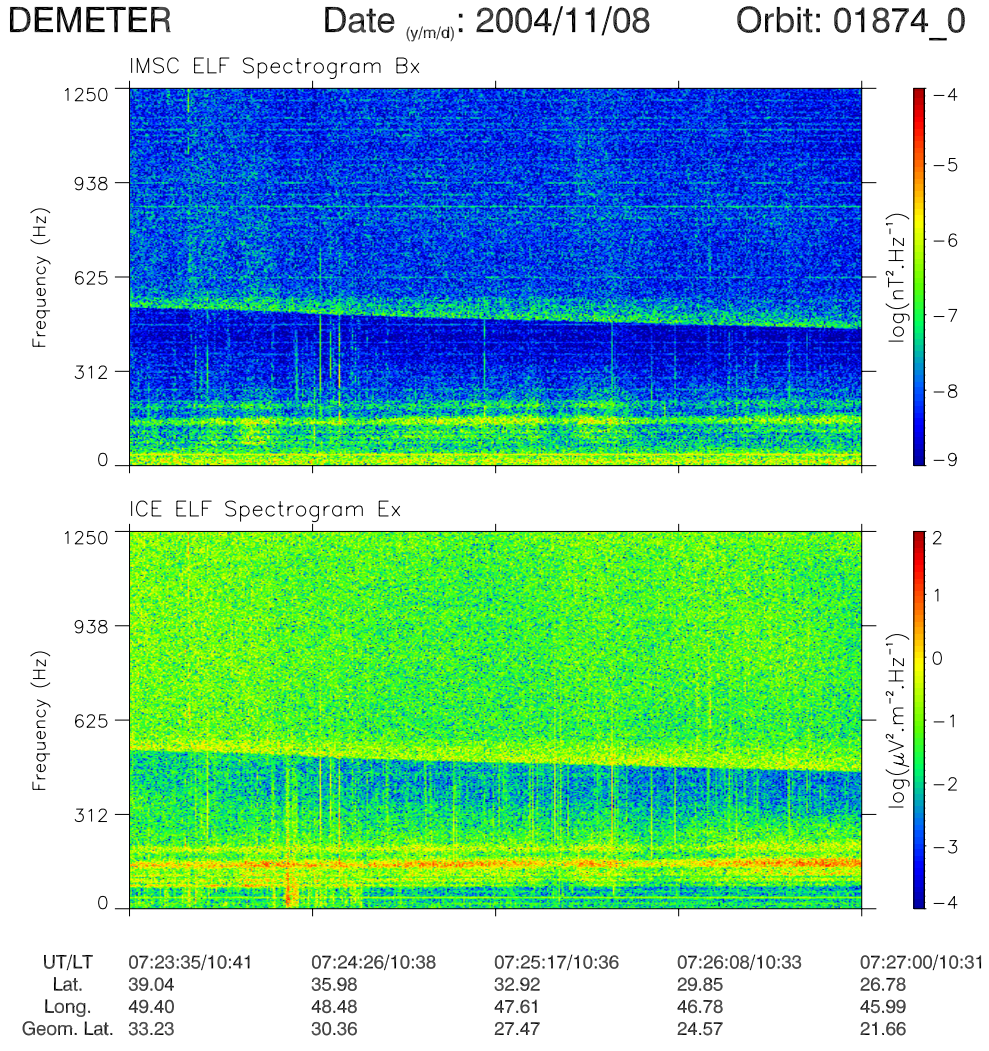

Fig. 3. Similar to Fig. 1 but recorded on 8 November 2004 (event 2).

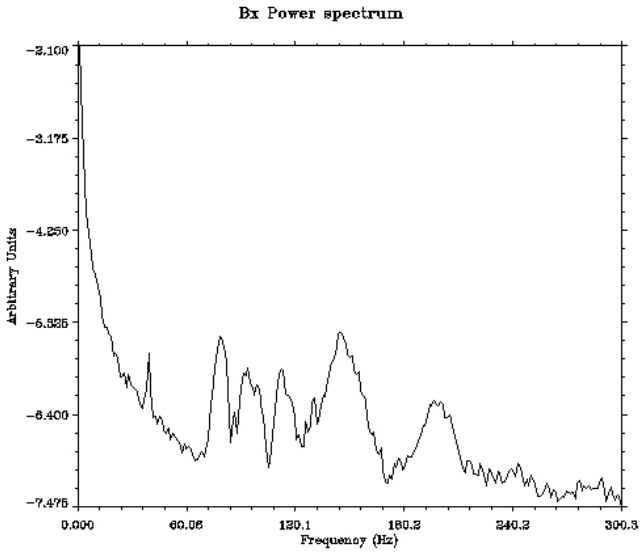

Fig. 4. Spectrum of the magnetic component calculated for the first forty seconds of Fig. 3.

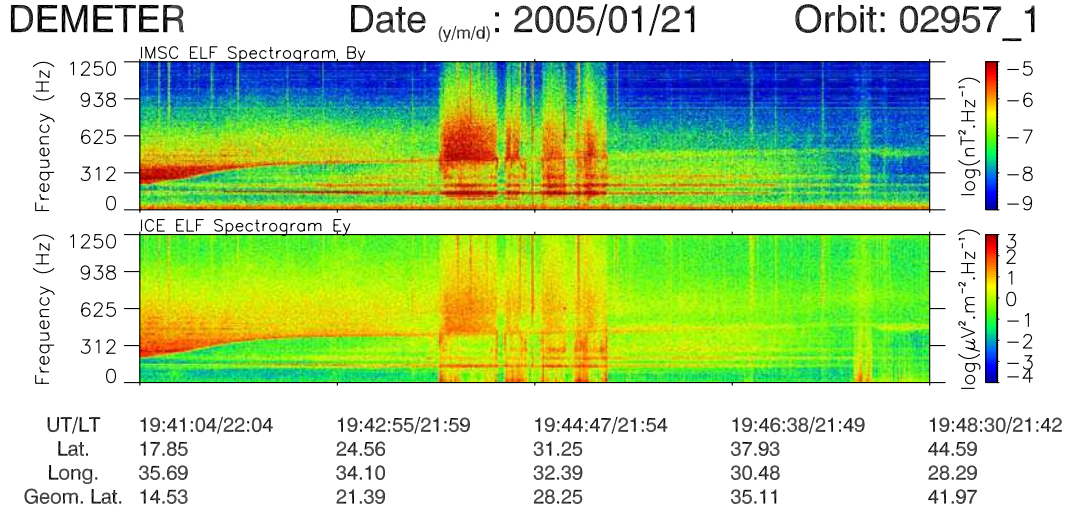

Fig. 5. Same as Fig. 1 but for the event recorded on 21 January 2005 (event 3).

been recorded in the Pacific Ocean close to the Kiribati Islands around the magnetic equator during a period of strong magnetic activity (K_p=6). At this time, the satellite was still during the commissioning phase and this is why a part of the magnetic data is missing in the top panel. The regular vertical white lines indicate changes in configuration for another experiment. Other vertical lines represent spherics. In both panels, a set of horizontal lines appears in a frequency range between 310 and 650 Hz. It is observed that these lines do not shift in frequency and that they have higher intensities when the satellite crosses the magnetic equator. Similar observations are done for the other components of the electromagnetic field. It appears that the main horizontal lines are in fact composed of many individual lines. All these lines exhibit a low cutoff frequency which is below the local proton gyrofrequency (see plots and explanation given in Sect. 4). As this low cutoff frequency increases, some low frequency horizontal lines disappear with the time. In order to check the frequencies of these lines, an averaged spectrum calculated between 09:14:30 and 09:16:30 UT is represented in Fig. 2. Seven harmonic lines are clearly observed and the first six are separated by 50 Hz, although they are not at exact multiples of 50 Hz. The center of the seventh line, which is broader in frequency, is at a little bit more than 50 Hz.

3.2 Event 2 recorded on 8 November 2004

Figure 3 is similar to Fig. 1 and corresponds to data recorded on 8 November 2004 between 07:23:35 and 07:27:00 UT when the satellite was above Iran and Iraq. It was the time of the largest magnetic storm of the year, with K_p=9. A set of horizontal lines is observed well below the cutoff frequency

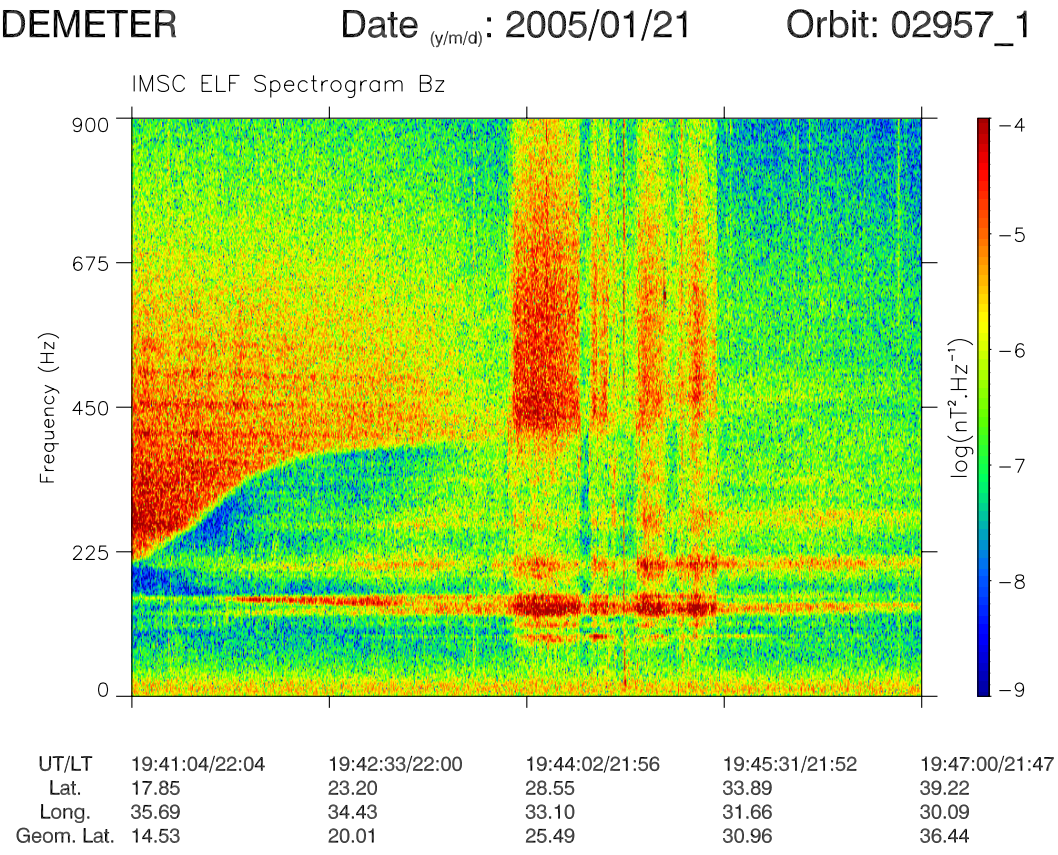

Fig. 6. Enlarged spectrogram between 0 and 900 Hz related to the event shown in Fig. 5 but with the magnetic component B_z.

of the natural hiss emission. This cutoff frequency, which is below the proton gyrofrequency, decreases with the time. All other magnetic and electric components show the same feature. A careful check of the spectra indicates that in fact there are two sets of lines: a set with thin lines and another with thick lines. The very thin line which is observed at 39 Hz has been identified as interference. The lines are very slightly drifting in frequency (∼1 Hz per 35 s). Figure 4 displays the magnetic spectrum of the B_x component which was obtained, taking into account the first forty seconds of the considered time interval and a spectral analysis with a frequency resolution of 1.2 Hz. The frequencies of the peaks were evaluated considering the half width at the half height of each peak. It gives peak frequencies at 78.0, 95.1, 114.3, 147.3, and 198.9 Hz, and, if we consider the first frequency interval as the unit bin, an average frequency interval is ∼17.2 Hz.

3.3 Event 3 recorded on 21 January 2005

Figure 5 is similar to Fig. 1 and corresponds to data recorded on 21 January 2005 between 19:41:04 and 19:48:30 UT. At this time the satellite was flying over Egypt, the Mediterranean sea, and Turkey. The magnetic activity was very high with K_p=8. As in event 2, a set of horizontal lines can be observed below the cutoff frequency. Their intensities increase between 19:43:15 and 19:45:00 UT when waves ducted by density irregularities are observed.

Another set of lines can be distinguished at the beginning of the plot above the cutoff frequency, as in event 1. Their intensity is weak relatively to the other set. A more detailed spectrogram of these lines is given in Fig. 6 for the magnetic component B_z. It is shown that the lines are separated by 50 Hz for the two sets of lines. As in event 1, the lines are not at an exact multiple of 50 Hz but slightly above (∼4 Hz). There is a broadening of the lines, which are close to 150 Hz and 200 Hz in the middle of the plot, and sidebands appear mainly at the time of the doctal waves.

3.4 Event 4 recorded on 23 January 2005

Figure 7 is similar to Fig. 1 and represents data recorded on 23 January 2005 between 02:04:10 and 02:08:30 UT during an equatorial crossing above the Indonesian Islands. The magnetic activity was moderate with K_p=4. TL mixed with natural hiss noise are detected above the cutoff frequency, as in event 1. Figure 8 displays a frequency zoom of these data for the magnetic component B_z, and it is observed that the intensity of the lines increases close to the magnetic equator crossing. As in event 1, the lines are split into several ones. On average, the frequency separation of the three main lines is ∼31.3 Hz.

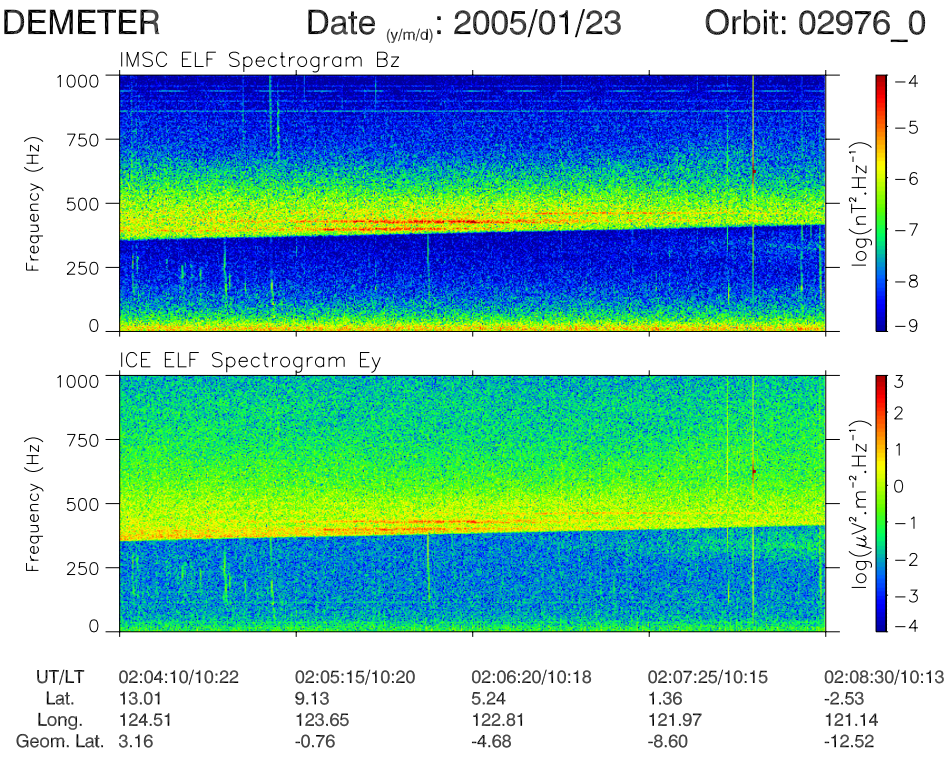

Fig. 7. Same as Fig. 1 but for the event recorded on 23 January 2005 (event 4).

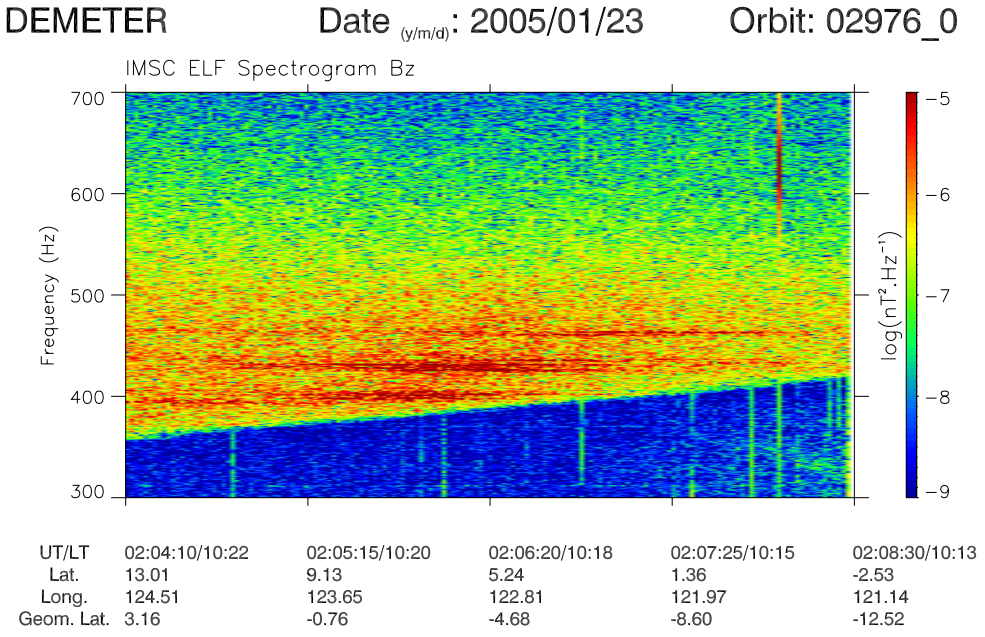

Fig. 8. Enlarged spectrogram between 0 and 700 Hz related to the data shown in the top panel of Fig. 7.

4 Analysis and discussions

It is possible to determine the propagation characteristics of the observed waves during events 2, 3, and 4, which were recorded during a burst mode. The data need to be translated in a frame of reference linked to the Earth's magnetic field B_0 and for event 1, which has been recorded during the commissioning phase, the attitude information is missing. The six components of the electromagnetic field are available, and a relevant software named PRASSADCO has been employed (Santolík, 2001). A preliminary version

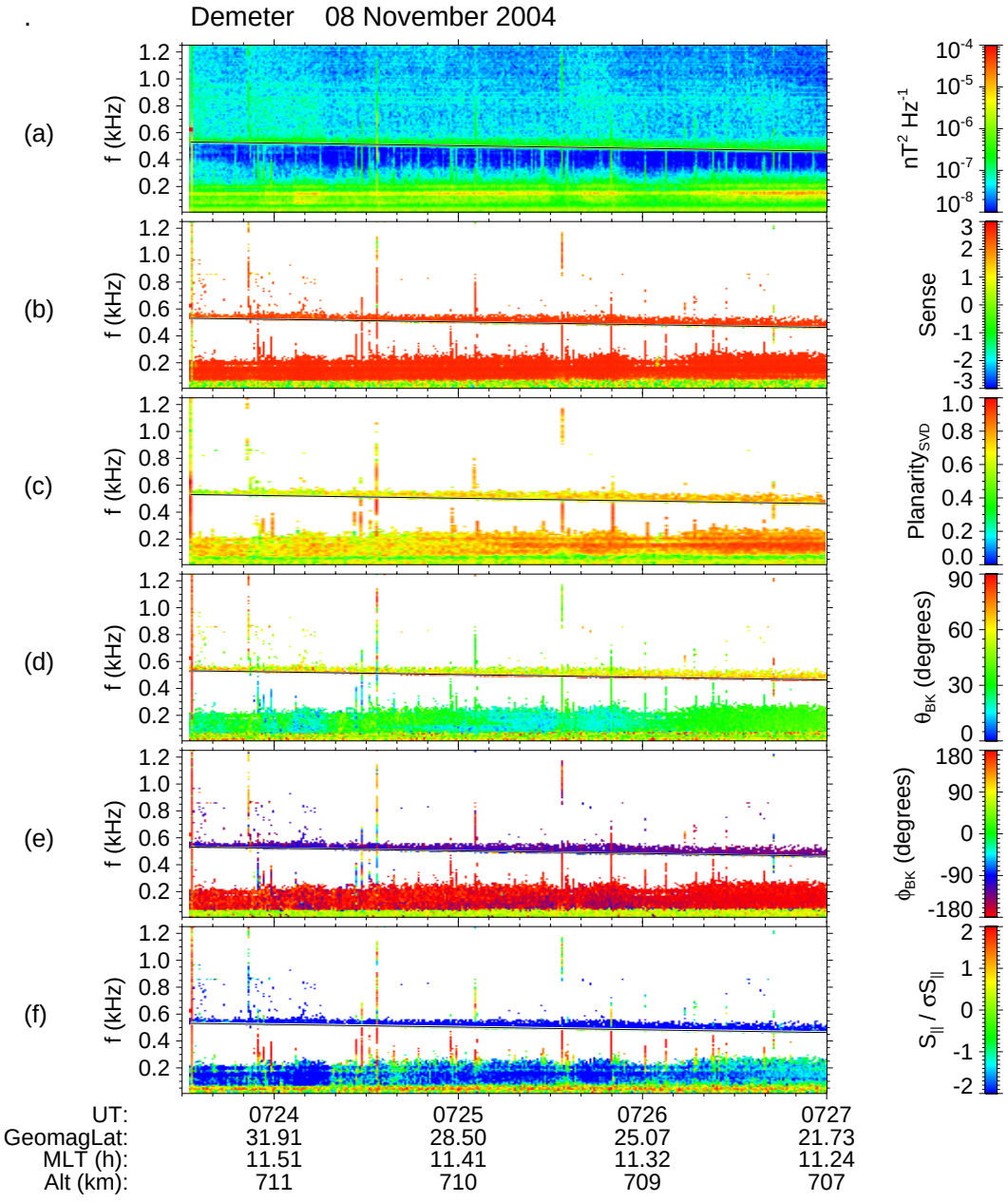

Fig. 9. Wave analysis of the event 2. **(a)** spectrogram of one magnetic component, **(b)** sense of polarization, **(c)** planarity, **(d)** and **(e)** polar and azimuthal angles of the wave vector with the Earth's magnetic field B_0, **(f)** projection of the Poynting vector onto B_0 (see text for explanation). The geophysical parameters at the bottom are the Universal Time (UT), the geomagnetic latitude, the Magnetic Local Time (MLT) and the altitude.

of this software has been used to process the data of the FREJA wave experiment (Santolík and Parrot, 1999). But it was specially developed for the data analysis of the spectral matrices computed by the STAFF experiment on board CLUSTER (see, for example, Parrot et al., 2003; Santolík et al., 2003a), and it has been adapted to process the DEMETER data (Santolík et al., 2005).

The TL observations can be divided in two parts, depending on their occurrence below or above the low frequency cutoff of the hiss, which is simultaneously observed with the TL. The TL of events 1 and 4 are observed above, TL of event 2 are observed below, and for event 3, two TL sets are observed, one is above and the other below.

Figures 9, 10, and 11 are related to the wave propagation analysis of the last 3 events. They all display the same information. The first panel shows the sum of power spectral densities of the three magnetic components. The black line (also shown in the other panels) indicates the local proton gyrofrequency given by a magnetic field model. It can be

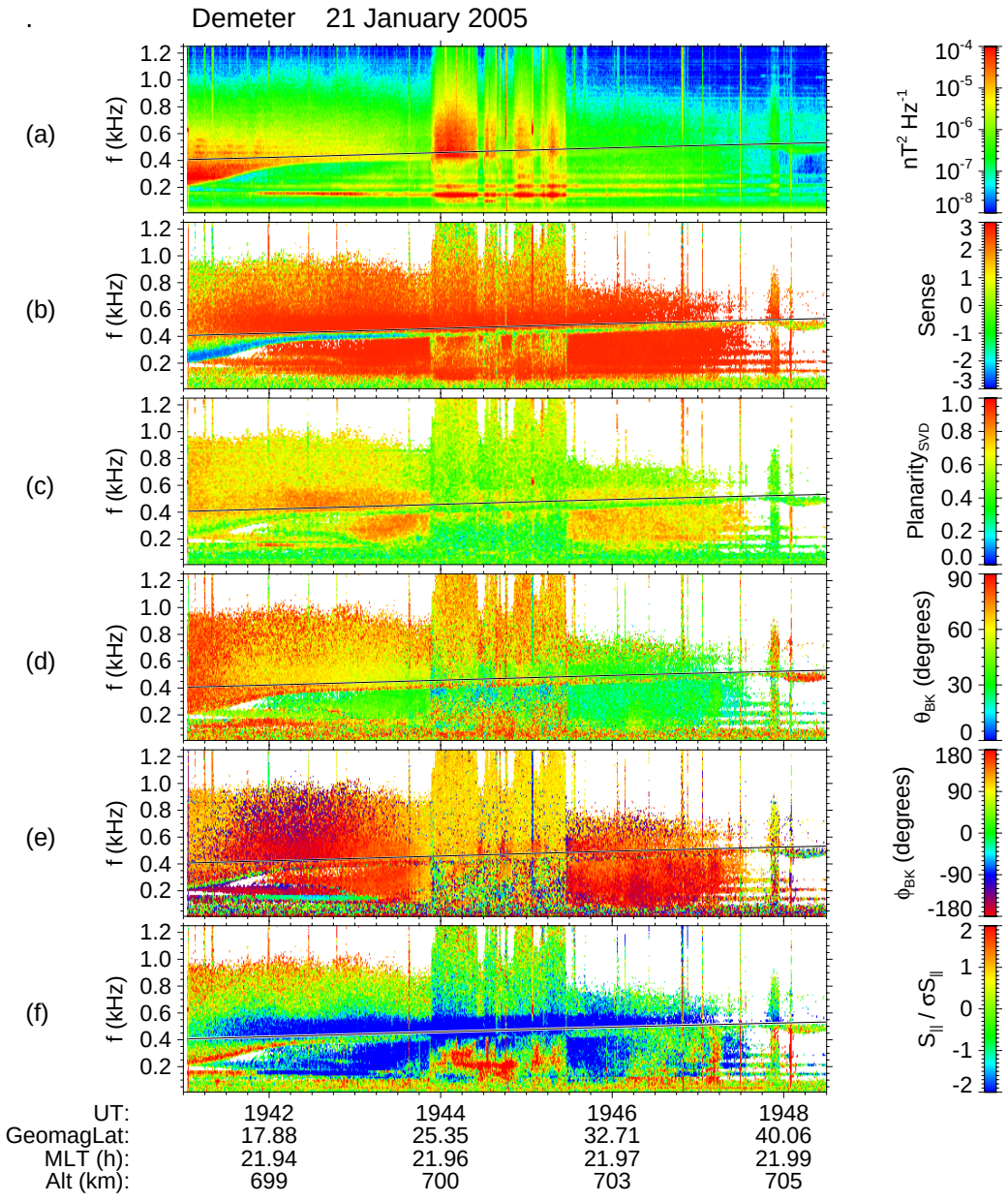

Fig. 10. Same presentation as in Fig. 9 but for the event 3.

seen (mainly for the events 3 and 4) that the local proton gyrofrequency is not the cutoff frequency of the hiss which is observed simultaneously with the TL. The cutoff is at the multi-ion cutoff frequency (see Santolík and Parrot, 1999 and references therein). The second panel displays the sense of polarization in the plane perpendicular to the field line estimated by the method of Santolík et al. (2001). A value larger than +1 (red color) corresponds to a right-hand polarization. In this panel and in the following ones, the parameters are color-coded only if the intensity of the magnetic field is larger than 10^{-7} nT^2/Hz. The third panel is related to the planarity obtained by the Singular Value Decomposition (SVD) method (Santolík et al., 2003b). A value close to 1 corresponds to the presence of a single plane wave. The two following panels are related to the direction of propagation of the waves. They give the polar and the azimuth angles between the k vector and the Earth's magnetic field B_0, respectively. Both angles are calculated using the SVD method (Santolík et al., 2003b). The last panel is related to the estimation of the component of the Poynting vector $\boldsymbol{S}_{\parallel}$, which is the projection of the Poynting vector onto $\boldsymbol{B}_0$, and $\sigma S_{\parallel}$ is a normalisation factor which corresponds to the standard deviation of $S_{\parallel}$ due to the spectral analysis. A positive value close to 2 indicates a direction of propagation which is in the direction of the magnetic field, whereas a negative value close to –2 indicates a direction which is opposite to the magnetic field. More details about this wave analysis can be found in Santolík and Parrot (1999) and references therein.

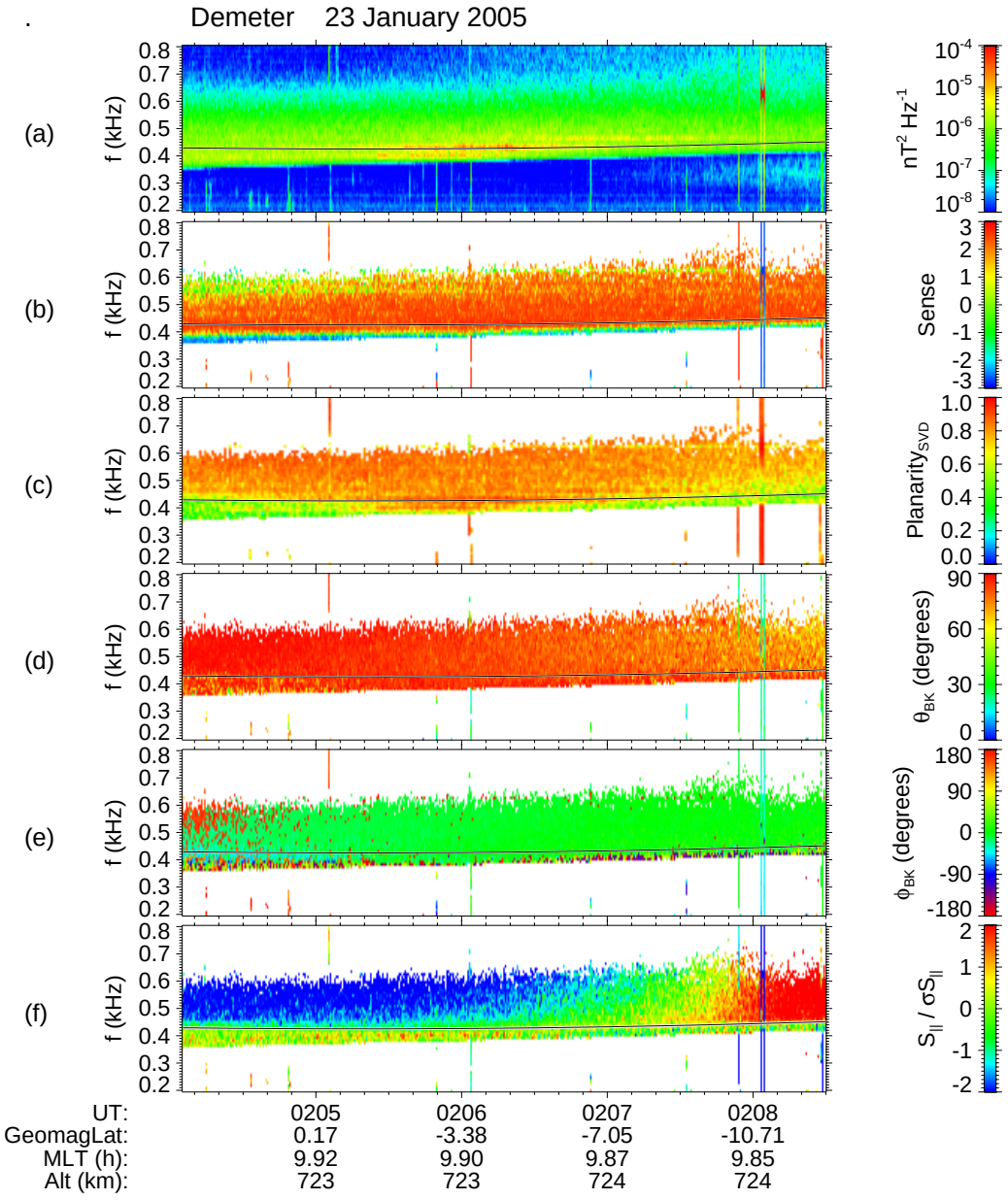

Fig. 11. Same presentation as in Fig. 9 but for the event 4.

The TL which are observed below the cutoff frequency in events 2 and 3 have similar properties concerning the propagation characteristics. The sense of polarization indicates that the waves are right-hand polarized. They propagate upwards (opposite to the magnetic field in the Northern Hemisphere) with an angle relative to the Earth's magnetic field of around 30°.

The TL which are observed above the proton gyrofrequency at the beginning of event 3 are very similar to those from event 1. The TL intensity is certainly vanishing after an increase around the magnetic equator. At this time, waves which are recorded in the survey mode (not shown) present a large intensity in this frequency range but the frequency resolution is too poor to distinguish TL.

Events 1 and 4 are similar in the sense that they exhibit an important growth close to the magnetic equator which is the favoured zone for wave-particle interactions. This is further evidence that these waves may influence the natural mechanisms in the ionosphere and could contribute to the precipitation of particles from the radiation belts. The wave analysis parameters of event 4 are displayed in Fig. 11. The sense of polarization indicates the presence of right-hand polarized waves. These waves propagate nearly perpendicular to B_0. During event 4, the color which indicates the direction of the Poynting vector changes when the satellite crosses the magnetic equator. It signifies that the direction of the hiss and of the TL, which are observed at frequencies above the cut-off frequency, is upgoing.

A question is related to the origin of the frequency intervals between the lines which are observed during these four events. The 50-Hz electric current can be found in many parts of the world, including the Pacific Islands. The other frequency interval can be related to the electrified railways. Many countries have standardized on 15 kV 16 2/3Hz (one-third the normal main frequency) system as the standard for low-frequency, high voltage electrification. All harmonics are not often observed depending on the production system which is used (Bullough, 1995). Then in event 4 the lines whose frequency interval practically equals two times the fundamental frequency may be due to the railways, as for event 2.

Why are the TL not observed at exact harmonics of 50 Hz or 16 2/3 Hz, and why are any sidebands observed? The frequency shift can be explained by a whistler mode instability during a gyroresonance interaction between the coherent waves and the particles in an inhomogeneous medium. The generation mechanism of sidebands may be due to the scattering from ionospheric irregularities which are enhanced by the magnetic activity. All these processes have been already discussed in the past (see, for example, Brinca (1972); Matthews et al. (1984); Bell (1985); Nunn (1986); Bell and Ngo (1988); Shklyar et al. (1992) and references therein).

Is there a possibility to attribute these ionospheric tram lines to natural emissions? One hypothesis is related to waves at harmonics of ion gyrofrequencies (Liu et al., 1994) which could be produced at much higher L values. These waves could propagate since the source region and could be observed at the altitude of the satellite. But in such a case the frequency drifting of the lines would be much more important than it is observed.

5 Conclusions

DEMETER is a low orbiting satellite devoted to the study of ionospheric perturbations induced by geophysical activities (earthquakes, volcanoes, thunderstorms, etc.) and man-made activities (VLF transmitters, PLHR, etc.). Therefore, it surveys the global Earth electromagnetic environment at ionospheric altitudes. When enough data is registered, geographic maps of wave emissions at various frequencies will be produced, in order to compare with regions of high industrial activity and to check if there is some anthropogenic influence in the ionosphere. At this time, this paper is related to four event studies where TL have been observed. The common features of these observations are:

1. The frequency intervals between the TL are close to 50 Hz (the usual electric current system) or to 16 2/3 Hz (the current frequency used for railways).
2. The frequency drift of the TL is very slow.
3. They are observed during periods of moderate or intense magnetic storms. This is similar to observations performed by Koons et al. (1978) with the S3-3 satellite or by Park (1977) with a ground-based experiment.
4. The wave propagation analysis indicates that the TL below the low cutoff frequency of the natural emissions simultaneously observed are coming from a region below the satellite.
5. The intensity of the TL above the low cutoff frequency of the natural emissions is enhanced close to the magnetic equator. This is an indication that they interact with particles.

Therefore, concerning these observations on DEMETER, there is evidence to suggest a link between TL and PLHR or radiation due to railways lines. A systematic search for TL with harmonics at 50 and 60 Hz has been started with an automatic software running on the DEMETER database and results will be presented soon.

Acknowledgements. Topical Editor M. Pinnock thanks two referees for their help in evaluating this paper.

References

Ando, Y., Hayakawa, M., and Molchanov, O. A.: Theoretical analysis on the penetration of power line harmonic radiation into the ionosphere, Radio Science, 37(6), 1093, doi:10.1029/2001RS002486, 2002.

Bell, T. F., Luette, J. P., and Inan, U. S.: ISEE 1 observations of VLF line radiation in the Earth's magnetosphere, J. Geophys. Res., 87, 3530–3536, 1982.

Bell, T. F.: High-amplitude VLF transmitter signals and associated sidebands observed near the magnetic equatorial plane on the ISEE 1 satellite, J. Geophys. Res., 90, 2792–2806, 1985.

Bell, T. F. and Ngo, H. D.: Electrostatic waves stimulated by coherent VLF signals propagating in and near the inner radiation belt, J. Geophys. Res., 93, 2599–2618, 1988.

Berthelier, J. J., Godefroy, M., Leblanc, F., Malingre, M., Menvielle, M., Lagoutte, D., Brochot, J. Y., Colin, F., Elie, F., Legendre, C., Zamora, P., Benoist, D., Chapuis, Y., and Artru, J.: ICE, The electric field experiment on DEMETER, Planet. Space Sci., submitted, 2005.

Brinca, A. L.: Whistler side-band growth due to nonlinear wave-particle interaction, J. Geophys. Res., 77, 3508–3523, 1972.

Bullough, K., Tatnall, A.R.L., and Denby, M.: Man-made ELF/VLF emissions and the radiation belts, Nature, 260, 401, 1976.

Bullough, K.: Power Line Harmonic Radiation: Sources and Environmental Effects in: Handbook of Atmospheric Electrodynamics, edited by: Volland, H., vol. 2, CRC Press, Boca Raton, 291–332,1995.

Helliwell, R. A.: Effects of power line radiation into the magnetosphere, 27, in: Wave Instabilities in Space Plasmas, edited by: Palmadesso, P. J. and Papadopoulos, K., D. Reidel Publishing Co., 27–36, 1979.

Helliwell, R. A., Katsufrakis, J. P., Bell, T. F., and Raghuram, R.: VLF line radiation in the Earth's magnetosphere and its association with power system radiation, J. Geophys. Res., 80, 4249–4258, 1975.

Koons, H. C., Dazey, M. H., and Edgar, B. C.: Satellite observation of discrete VLF line radiation within transmitter-induced amplification bands, J. Geophys. Res., 83, 3887–3889, 1978.

Liu, H., Kokubun, S., and Hayashi, K.: Equatorial electromagnetic emission with discrete spectra near harmonics of oxygen gyrofrequency during magnetic storm, Geophys. Res. Lett., 21(3), 225–228, 1994.

Matthews, J. P. and Yearby, K.: Magnetospheric VLF line radiation observed at Halley, Antartica, Planet. Space Sci., 29, 97–106, 1981.

Matthews, J. P., Omura, Y., and Matsumoto, H.: Some PLHR phenomena and their explanation, in: International Wroclaw Symposium on Electromagnetic compatibility, Technical University of Wroclaw, Poland, 55–59, 1984.

Molchanov, O. A., Parrot, M., Mogilevsky, M. M., and Lefeuvre, F.: A theory of PLHR emissions to explain the weekly variations of ELF data observed by a low-altitude satellite, Ann. Geophys., 9, 669–680, 1991.

Nunn, D., Manninen, J., Turunen, T., Trakhtengerts, V., and Erokhin, N.: On the nonlinear triggering of VLF emissions by power line harmonic radiation, Ann. Geophys., 17, 79–94, 1999, **SRef-ID: 1432-0576/ag/1999-17-79**.

Nunn, D.: A nonlinear theory of sideband stability in ducted whistler mode waves, Planet. Space Sci., 34, 429–451, 1986.

Park, C. G.: VLF wave activity during a magnetic storm: a case study of the role of power line radiation, J. Geophys. Res., 82 (22), 3251–3260, 1977.

Park, C. G. and Helliwell, R. A.: Power line radiation in the magnetosphere, Adv. Space Res., 1, 423–437, 1981.

Parrot, M.: Observations of PLHR by the low-altitude AUREOL-3 satellite, J. Geophys. Res., 99, 3961–3969, 1994.

Parrot, M. and Zaslavski, Y.: Physical mechanisms of man made influences on the magnetosphere, Surveys in Geophysics, 17, 67–100, 1996.

Parrot, M., Santolík, O., Cornilleau-Wehrlin, N., Maksimovic, M., and Harvey, C. C.: Source location of chorus emissions observed by Cluster, Ann. Geophys. 21, 473–480, 2003.

Parrot, M., Benoist, D., Berthelier, J. J., Błęcki, J., Chapuis, Y., Colin, F., Elie, F., Fergeau, P., Lagoutte, D., Lefeuvre, F., Legendre, C., Lévêque, M., Pinçon, J. L., Poirier, B., Seran, H. C., and Zamora, P.: The magnetic field experiment IMSC and its data processing on board DEMETER: scientific objectives, description and first results, Planet. Space Sci., in press, 2005.

Rodger, C. J., Thomson, N. R., and Dowden, R. L.: VLF line radiation observed by satellite, J. Geophys. Res., 100(A4), 5681–5689, 1995.

Rodger, C. J., Clilverd, M. A., Yearby, K. H., and Smith, A. J.: Magnetospheric line radiation observations at Halley, Antartica, J. Geophys. Res., 104 (A8), 17 441–17 447, 1999.

Rodger, C. J., Clilverd, M. A., Yearby, K. H., and Smith, A. J.: Temporal properties of magnetospheric line radiation, J. Geophys. Res., 105(A1), 329–336, 2000a.

Rodger, C. J., Clilverd, M. A., Yearby, K., and Smith, A. J.: Is magnetospheric line radiation man made?, J. Geophys. Res., 105, 15 981–15 990, 2000b.

Santolík, O. and Parrot, M.: Case studies on the wave propagation and polarization of ELF emissions observed by Freja around the local proton gyrofrequency, J. Geophys. Res., 104, 2459–2475, 1999.

Santolík, O.: Propagation Analysis of Staff-SA Data with Coherency Tests, LPCE/NTS/073.C, Lab. Phys. Chimie Environ./CNRS, Orléans, France, 2001.

Santolík, O., Lefeuvre, F., Parrot, M., and Rauch, J. L.: Complete wave-vector directions of electromagnetic emissions: Application to INTERBALL-2 measurements in the nightside auroral zone, J. Geophys. Res., 106, 13 191–13 201, 2001.

Santolík, O., Gurnett, D. A., Pickett, J. S., Parrot, M., and Cornilleau-Wehrlin, N.: Spatio-temporal structure of storm-time chorus, J. Geophys. Res., 108(A7), 1278, doi:10.1029/2002JA009791, 2003a.

Santolík, O., Parrot, M., and Lefeuvre, F.: Singular value decomposition methods for wave propagation analysis, Radio. Sci., 38(1), 1010, doi:10.1029/2000RS002523, 2003b.

Santolík, O., Němec, F., Parrot, M., Lagoutte, D., and Madrias, L.: Analysis methods for multi-component wave measurements on board the DEMETER spacecraft, Planet. Space Sci., in press, 2005.

Shklyar, D. R., Nunn, D., Smith, A. J., and Sazhin, S. S.: An investigation into the nonlinear frequency shift in magnetospherically propagated VLF pulses, J. Geophys. Res., 97(A12), 19 389–19 402, 1992.

Tatnall, A. R. L., Matthews, J. P., Bullough, K., and Kaiser, T. R.: Power-line harmonic radiation and the electron slot, Space Sci. Rev., 35, 139–173, 1983.

Tomizawa, I. and Yoshino, T.: Power line radiation observed by the satellite OHZORA, J. Geomagn. Geoelectr., 37, 309–327, 1985.

Yearby, K. H., Smith, A. J., Kaiser, T. R., and Bullough, K.: Power line harmonic radiation in Newfoundland, J. Atmos. Terr. Phys, 45, 409–419, 1983.

Available online at www.sciencedirect.com
SCIENCE DIRECT®
Advances in Space Research 37 (2006) 610–616
ADVANCES IN SPACE RESEARCH (a COSPAR publication)
www.elsevier.com/locate/asr

Equatorial noise: Statistical study of its localization and the derived number density

F. Němec [a,*], O. Santolík [a], K. Gereová [a], E. Macúšová [a], H. Laakso [b], Y. de Conchy [c], M. Maksimovic [c], N. Cornilleau-Wehrlin [d]

[a] Faculty of Mathematics and Physics, Charles University, Prague, Czech Republic
[b] ESA/ESTEC, Noordwijk, The Netherlands
[c] LESIA, Observatoire de Paris-Meudon, France
[d] CETP/IPSL, Velizy, France

Received 28 September 2004; received in revised form 17 February 2005; accepted 8 March 2005

Abstract

Results of a statistical study of equatorial noise emissions are presented. These electromagnetic emissions are observed in the inner magnetosphere in the vicinity of the geomagnetic equator at frequencies below the lower hybrid frequency. We use the data recorded by four Cluster spacecraft during years 2001–2003. The data set was processed in three steps. In the first one, we have selected the data with a nearly linear polarization (ellipticity less than 0.2), corresponding to the known properties of the equatorial noise. Secondly, we have found parameters of a Gaussian model of the frequency-averaged power-spectral density of those selected waves as a function of the geomagnetic latitude. Finally, we have analyzed the data in the latitudinal interval defined by the width of the Gaussian model. Our results show that most intensity peaks of equatorial noise occur exactly at the magnetic equator. Incidental deviations are most probably caused by problems in determination of the true magnetic equator, which is shown by using different magnetic field models. We have estimated the plasma number density at the observation points using the cold plasma theory. These estimates are, within experimental errors, close to the values obtained from the spacecraft potential data measured by the EFW instrument.

Keywords: Cluster; STAFF-SA; Equatorial noise

1. Introduction

Equatorial noise (EN) is an intense electromagnetic emission observed close to the geomagnetic equator at radial distances of a few Earth radii and at frequencies from a few Hertz to several hundreds of Hertz. It was first observed on OGO 3 by Russell et al. (1970) within 2° from the equator at frequencies between twice the local proton cyclotron frequency (f_{cH+}) and half the lower hybrid frequency (f_{lh}). These observations revealed that the magnetic field fluctuations of EN are almost linearly polarized along the local field line.

Detailed time-frequency spectrograms recorded onboard the IMP 6 and Hawkeye spacecraft were analyzed by Gurnett (1976). He found that the apparently broadband, noise-like spectrum observed in low resolution spectrograms, is in fact a system of many spectral lines with different frequency spacings from a few Hertz to a few tenths of Hertz. He suggested that these lines are created by ion cyclotron harmonic interaction in a

* Corresponding author. Tel.: +420 257 712 678.
E-mail addresses: nemec@matfyz.cz, Frantisek.Nemec@ruk.cuni.cz (F. Němec).

0273-1177/$30 © 2006 Published by Elsevier Ltd on behalf of COSPAR.
doi:10.1016/j.asr.2005.03.025

region where the local cyclotron frequency matches the observed spacing. After being generated, the waves propagate in the electromagnetic whistler mode to the observation point, which can thus be localized far away from their region of generation.

By analyzing GEOS wave and particle data, Perraut et al. (1982) proposed a model whereby these waves are generated by ions whose distribution is ring like around 90° pitch angle. Further observations (Laakso et al., 1990; Kasahara et al., 1994) revealed that equatorial noise can occur at radial distances between 2 and $7R_E$, and at latitudes within 10° from the magnetic equator. All the emissions have been detected at frequencies above the local f_{cH+}.

STAFF and WBD wave instruments onboard the four spacecraft of the Cluster project have enabled multipoint observations of EN. Santolík et al. (2002) reported results of high-resolution WBD measurements in the morning sector and demonstrated a narrow latitudinal extent of the emissions with a typical width of 2°, centered near the minimum-B equator. They showed that the wave vector had a radial component. Since the Poynting vector also has a radial component, the waves could propagate from a generation region where ion cyclotron frequencies matched the observed fine structure of spectral lines. A systematic analysis of a large number of observations of EN based on the data of the STAFF-SA instruments (Cornilleau-Wehrlin et al., 2003) on board the four Cluster spacecraft was done (Santolík, 2004; Němec et al., 2005). The occurrence rate of EN was found to be approximately 60%. Equatorial noise was identified by selecting data with nearly linearly polarized magnetic field fluctuations, and using Gaussian fits of the power spectra as a function of the geomagnetic latitude. The results showed that EN had very intense magnetic field fluctuations and thus could play a non-negligible role in the dynamics of the internal magnetosphere.

This paper is also based on the data of the Cluster mission. We present results of a survey of equatorial noise, using both an ellipticity threshold and a Gaussian model of the distribution of the power-spectral density as a function of latitude. We examine in detail the localization of the EN emissions by using the models of Tsyganenko (1989) and Tsyganenko and Stren (1996), trying to prove the hypothesis that EN emissions are centered at the minimum-B equator and observed deviations are owing to the inaccurate determination of its position. We further compare the plasma density estimated from the EN measurements with the data obtained from the analysis of the spacecraft potential measured by the EFW instruments on board Cluster (Gustafsson et al., 2001).

In Section 2 we will present the data set and describe our analysis methods. In Sections 3 and 4 we will describe results of the systematic analysis, in Section 5 we will discuss the results, and, finally, in Section 6 we will present brief conclusions.

2. Data set and processing

The data that we have used were collected during 24 months in 2001–2003 by STAFF-SA (Spatio-temporal analysis of field fluctuations) instrument on board the four Cluster spacecraft (Cornilleau-Wehrlin et al., 1997). The instrument mode we use provides us with 27 frequency channels logarithmically spaced between 8 Hz and 4 kHz. The data are pre-analyzed on board the spacecraft, forming Hermitian spectral matrices 5×5 (3 magnetic and 2 electric components are measured) for each of the frequency channels. These are then recorded with the time resolution of 1 s for power-spectral density (main diagonal elements of spectral matrix) and 4 s for the phases and coherence (off-diagonal elements of spectral matrix).

We have analyzed the available data intervals where the Cluster spacecraft were close to the equatorial plane during the perigee passages. These intervals cover all magnetic local times (MLT) and contain data measured at radial distances between 3.9 and $5.0R_E$. An example of the data is shown in Fig. 1.

The measurements have been made by Cluster 3 (Samba) on November 25, 2002. The two panels at the top of Fig. 1 represent power-spectral densities of magnetic and electric field fluctuations, respectively. The corresponding Poynting flux is in the panel at the bottom of Fig. 1. Equatorial noise is the intense electromagnetic emission observed close to the center of the time interval and to the geomagnetic equator. EN occurs at frequencies below the lower hybrid frequency (its estimate, calculated as the geometric average of the proton and electron cyclotron frequency, is plotted in the spectrogram). The middle panel represents ellipticity of polarization of magnetic field fluctuations determined by the singular value decomposition (SVD) method (Santolík et al., 2003), which varies between 0 (linear polarization) and 1 (circular polarization). It can be seen that EN can be easily distinguished by almost linear polarization (Russell et al., 1970). The fourth panel represents planarity of magnetic field fluctuations (again determined by the SVD method), which varies between 0 and 1 (a value of 1 means a strict confinement of the fluctuations to a plane). A value of ≈ 0.8 for EN suggests fluctuations very close to a single plane, with a small fraction of random 3-D fluctuations.

For our systematic survey of EN we have processed the data in several steps. First, we have selected data lying close enough to the magnetic equator (with a magnetic latitude within $\pm 10°$ of the equator) and frequency channels between 8 and 300 Hz (the upper estimate of the f_{lh} throughout the data set), which represents 16

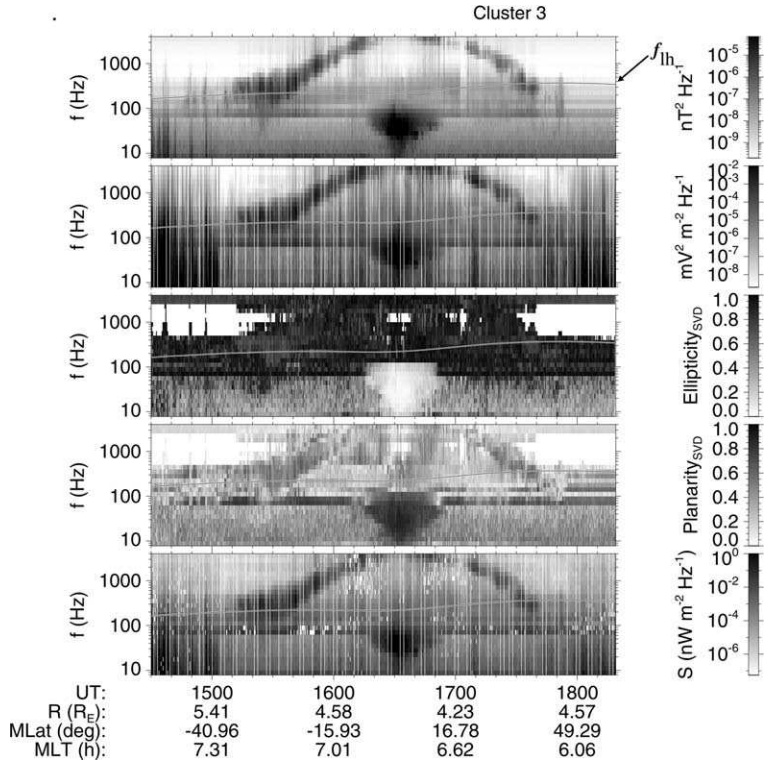

Fig. 1. Example of data collected by Cluster 3 on November 25, 2002. From the top: time-frequency power spectrograms of the magnetic and electric field fluctuations, ellipticity of polarization, planarity of polarization, and spectral density of the Poynting flux. Equatorial noise is the intense electromagnetic emission close to the center of time interval, below the local lower hybrid frequency (f_{lh}). The EN emission can be distinguished by a low ellipticity and high planarity. The ellipticity and planarity are determined using the singular value decomposition of the magnetic spectral matrix.

lowest frequency channels of the instrument. Next, we have selected the data using the ellipticity threshold (ellipticity lower than 0.2). For each event, we have then calculated the average power-spectral density and found parameters for input to our model, separately for magnetic and electric power-spectral densities, and separately for each spacecraft. The model of the power-spectral density has been chosen as a Gaussian function of geomagnetic latitude along the spacecraft orbit, with a central position, a width, and an intensity as free parameters (see Němec et al., 2005, for more details). This procedure has been done with 748 data intervals, resulting in 339 cases (45%) where the fits were successful for both electric and magnetic field fluctuations. In about 40% of the cases, EN emission did not occur at all; the remaining approximately 15% are cases with weak EN emission and unsuccessful fits. For each of the 339 successful fits, we have calculated a time-averaged spectral matrix. We have used an average over the time interval when the EN emission occurred (when the spacecraft was situated in the latitudinal interval given by a full width at half maximum of the Gaussian model), for each of the 16 lowest frequency channels separately. We have thus obtained 16 time-averaged spectral matrices (one per frequency channel) for each of these cases.

3. Localization of equatorial noise

Analysis of the EN emissions using the Gaussian fits enables us to define a localization of the emission as the position of the intensity peak in the magnetic dipole latitude. The results are quite similar for magnetic and electric field fluctuations (Němec et al., 2005). We thus define the resulting position as their arithmetic average. In a recent statistical study (Němec et al., 2005) we have shown that most intensity peaks of EN occur within 2° from the magnetic equator. However, contrary to what could be expected, the histogram is not exactly symmetric around the zero geomagnetic latitude. This could be caused by the definition of magnetic latitude we have used and the inhomogeneous coverage of magnetic local times in our data set. We have used magnetic latitude related to the ideal dipole model of the geomagnetic field. The equator in this model is defined by a plane perpendicular to the dipole axis. The true geomagnetic equator is, however, defined by a point where the magnetic field is minimum along a particular field line (min-B equator).

We have thus used more realistic modeling of the magnetic field (Tsyganenko, 1989; Tsyganenko and Stren, 1996), and calculated the dipole latitude λ_B of the min-B equator. The magnetic latitude λ_m was then corrected by subtracting λ_B. We have thus obtained a

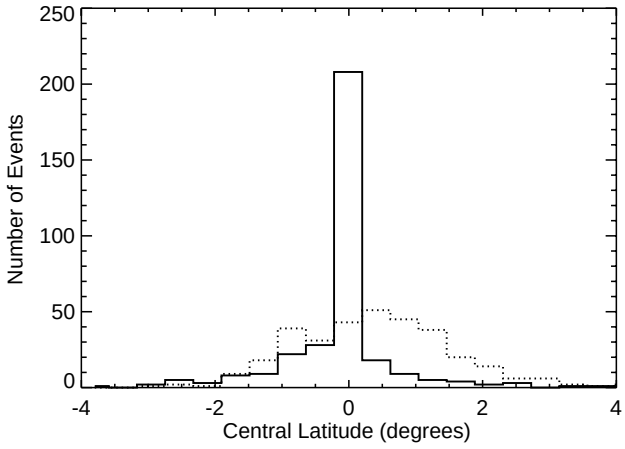

Fig. 2. Histogram of central positions of EN using the Tsyganenko 89 model for determination of the min-B equator. The same histogram using a dipole model for comparison (dotted).

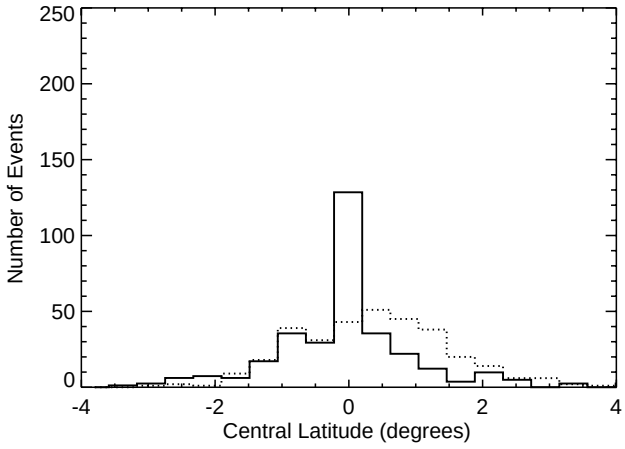

Fig. 3. Histogram of central positions of EN using the Tsyganenko 96 model for determination of the min-B equator. The same histogram using a dipole model for comparison (dotted).

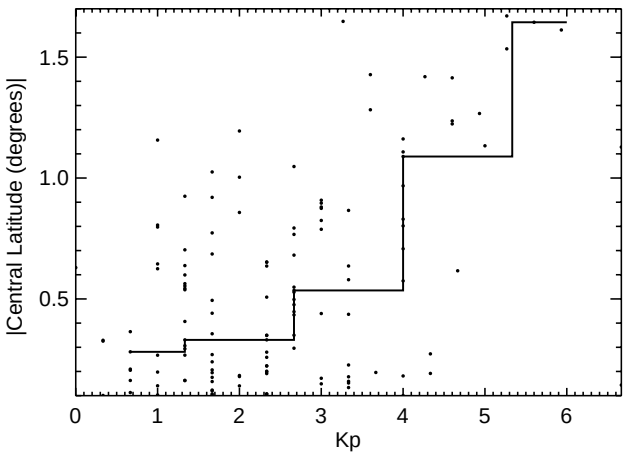

Fig. 4. Distance of EN emission from the min-B equator obtained by the Tsyganenko 89 model, as a function of the Kp index.

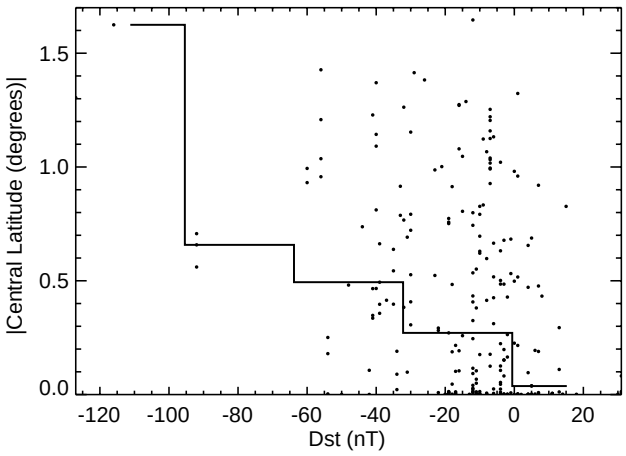

Fig. 5. Distance of EN emission from the min-B equator obtained by the Tsyganenko 96 model, as a function of the Dst index.

modified latitude $\lambda'_m = \lambda_m - \lambda_B$ which is zero at the model min-B equator. Using this modified latitude, we have re-calculated the histogram of central positions of the EN intensity peaks. The results are shown in Figs. 2 and 3 (the result for a dipole model is shown as a dotted line in both figures for comparison). It can be seen that the distribution became less spread out in latitude with most of the events located around 0° latitude (especially in the case of the Tsyganenko 89 model).

However, there are still several cases which occur quite far from the model min-B equator. We looked at these cases more in detail. Figs. 4 and 5 show the distance of the EN emission from the min-B equator as a function of a model parameter (Kp index for Tsyganenko 89 and Dst index for Tsyganenko 96, respectively). Each of the plotted points represents one EN case, the line is a median. These figures show that the high distance from the equator is systematically obtained when the model parameters have extreme values (high for Kp or highly negative for Dst).

4. Estimation of the local plasma density

The ratio of the intensities of magnetic and electric field fluctuations carries information on the plasma medium in which the waves propagate, namely the plasma density. We have used the cold plasma theory (e.g., Stix, 1992) to estimate the local plasma density. In accordance with the observed polarization of magnetic field fluctuations, we have supposed purely perpendicular propagation of whistler-mode waves. For each of the observations of EN emission we have obtained a density estimate as an arithmetic average of the estimated densities over the frequency bands where the EN emission occurred.

We have compared such estimated number densities with the values determined from the spacecraft potential data using the measurements of the EFW experiment. A slight modification of the method of Pedersen et al. (2001) was used to transform the measured voltage between the spacecraft body and the spherical probes to the plasma density estimates. The method of Pedersen et al. (2001) was improved by using more calibrated data points from the Whisper relaxation sounder and by improving the fit. The results are shown in Figs. 6 and 7. Fig. 6 shows the number densities n_{EN} estimated from the EN measurements plotted against the densities n_{EFW} obtained from the measured spacecraft potential. A logarithmic scale is used. The dotted line that is overplotted corresponds to identical values for both density estimations. It shows a rough agreement between the two methods, with a slight tendency to underestimate the density using the EN measurements.

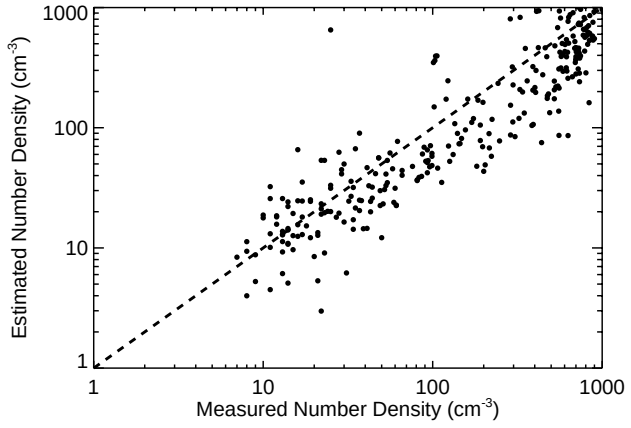

Fig. 6. Measured (from the EFW spacecraft potential data) and estimated (from B/E ratio) number densities plot one against another in a logarithmic scale.

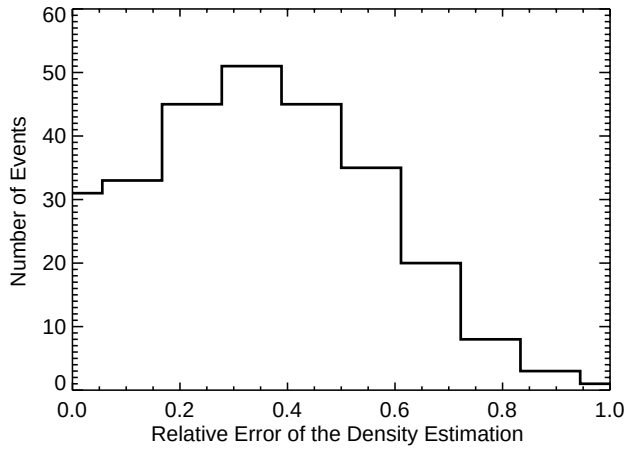

Fig. 7. Histograms of the relative errors of the estimated densities with respect to the measured ones.

Fig. 7 represents a histogram of the relative differences $|n_{EN} - n_{EFW}|/n_{EFW}$ of both density estimates. It can be seen, that the most probable relative error is around 30%.

5. Discussion

Previous investigation of the localization of equatorial noise (Němec et al., 2005) has shown that the intensity peak of the emission occurs within a few degrees of the geomagnetic equator, with a typical latitudinal extent (width of a Gaussian fit) of 2°. When using a more sophisticated model of the magnetic field than the simple dipole model, namely the Tsyganenko 89 and Tsyganenko 96 models, the position of the central peaks tend to be closer to the min-B equator (see Figs. 2 and 3). This is especially true in the case of the Tsyganenko 89 model. while this effect is not so important in the case of the Tsyganenko 96 model. This is rather unexpected because the Tsyganenko 96 model is a newer model, which uses more parameters, and could be therefore expected to give better results. However, this model is perhaps not so well optimized for the equatorial region at distances of $\approx 4R_E$. It would be necessary to carefully compare the results obtained from both models of the magnetic field and measurements in this particular region, which is beyond the scope of this paper.

Even when using better models of the magnetic field, we still obtain a fraction of cases where the central peaks are displaced from the model min-B equator by more than 1°. Looking at those cases in more detail (Figs. 4 and 5) we observe that they usually correspond to extreme values of model parameters, i.e., high values of the Kp index for the Tsyganenko 89 model and highly negative values of the Dst index for the Tsyganenko 96 model. These extreme values are not encountered very often, and, as the models are empirical, they are expected to be less accurate under such circumstances. Consequently, those displaced cases can be most probably explained by inaccuracies of the determination of the model min-B equator, supposing that in fact all the cases occur at the true min-B equator. However, we cannot completely exclude the possibility that the central positions of EN are really slightly displaced from the min-B equator under the disturbed conditions. Note also that the latitudinal extent (width of the Gaussian fit) of EN slightly increases as a function of Kp but still remains less than 3° for the majority of cases. This extent is thus usually higher than the displacement from the min-B equator.

The next part of this paper was dedicated to the study of a connection between the ratio of magnetic and electric power spectra and the number density at a given place. We have used the cold plasma theory and an assumption that the waves propagate perpendicularly to the local magnetic field, which is consistent with the

observed polarization. To prove the validity of such an approach as well as to verify if the cold plasma theory can be used in such a case, we have compared the estimated values of number density with the values obtained from the spacecraft potential (see Figs. 6 and 7). The two density estimates correlate quite well but their correspondence is not perfect. The relative errors of the density estimation show a wide distribution of values up to approximately 80%, the most probable relative error being around 30%. An important result is that there is no clear systematic difference of the two estimates and that the errors are rather random, except a slight tendency to obtain lower densities from the EN measurements. Our interpretation is that the assumptions we have made are roughly correct and that the cold plasma theory can be used in such a case. The differences are most probably connected to experimental inaccuracies of these indirect methods of density estimation. A possible reason might be that only two electric components are measured, or that the wave vector is not always exactly perpendicular to the field line. It might be also connected to the wide relative frequency intervals (~30%) where the data are integrated during the measurement. Finally, one must keep in mind that also the EFW method itself can be an important source of error, because we do not take into account the electron temperature. For temperatures between 0.1 and 1 eV the scatter of obtained densities could reach a factor of 2–3 (Laakso and Pedersen, 1998). More work is needed to explain the observed differences.

6. Conclusions

We have presented the results of a study of EN emissions observed at frequencies below the lower hybrid frequency by the Cluster spacecraft. The data were collected during three years of operation of the STAFF-SA instruments onboard the spacecraft. We have analyzed data recorded during their perigee passes at magnetic latitudes between $-10°$ and $10°$, and at radial distances between 3.9 and 5 Earth radii. We have used a procedure based on identifying the EN emissions by using an ellipticity threshold and subsequent Gaussian fits of the resulting power-spectra. Our results show that:

(1) Central latitudes of EN seem to be located exactly at the true geomagnetic equator. The observed deviations can be most probably explained by the inaccuracies in the model used for the determination of min-B equator, which are caused by extreme values of the model parameters.
(2) Using the cold plasma theory, the number density can be estimated from the ratio of magnetic and electric power spectral density. It varies from units to hundreds of particles per cubic centimeter. Our estimations of the number densities are in a rough agreement with the densities obtained from the measurements of the spacecraft potential, indicating applicability of the cold plasma theory.

Acknowledgements

We sincerely thank Chris Harvey of CESR Toulouse, Michel Parrot of LPCE Orleans, and other colleagues from the STAFF team for construction and calibration of the instrument and for fruitful discussions of the data. We are grateful to Lubomír Přech of the Charles University in Prague for his help with auxiliary data for the magnetic field models. Our thanks are due to the PI of the FGM instrument (A. Balogh) for the DC magnetic field data used for reference and coordinate transformations, and to the Hungarian Cluster Data Center which provides auxiliary data. ESA and CNES are thanked for their support for the STAFF experiment. We thank the MAG and SWEPAM instrument teams and the CDAWeb for providing the ACE data. This research was supported by Grants GACR 202/03/0832, ME 650, and MSM 113200004.

References

Cornilleau-Wehrlin, N., Chauveau, P., Louis, S., Meyer, A., Nappa, J.M., Perraut, S., Rezeau, L., Robert, P., Roux, A., Villedary, C.de., Conchy, Y.de., Friel, L., Harvey, C.C., Hubert, D., Lacombe, C., Manning, R., Wouters, F., Lefeuvre, F., Parrot, M., Pinon, J.L., Poirier, B., Kofman, W., Louarn, P.and the STAFF investigator team The Cluster spatio-temporal analysis of field fluctuations (STAFF) experiment. Space Sci. Rev. 79, 107–136, 1997.

Cornilleau-Wehrlin, N., Chanteur, G., Perraut, S., Rezeau, L., Robert, P., Roux, A., Villedary, C.de., Canu, P., Maksimovic, M., Conchy, Y.de., Hubert, D., Lacombe, C., Lefeuvre, F., Parrot, M., Pincon, J.L., Decrau, P.M.E., Harvey, C.C., Louarn, Ph., Santolik, O., Alleyne, H.St.C., Roth, M.and STAFF team First results obtained by the Cluster STAFF experiment. Ann. Geophys. 21, 437–456, 2003.

Gurnett, D.A. Plasma wave interactions with the energetic ions near the geomagnetic equator. J. Geophys. Res. 81, 2765–2770, 1976.

Gustafsson, G., André, M., Carozzi, T., Eriksson, A.I., Fälthammar, C.-G., Grard, R., Holmgren, G., Holtet, J.A., Ivchenko, N., Karlsson, T., Khotyaintsev, Y., Klimov, S., Laakso, H., Lindqvist, P.-A., Lybekk, B., Marklund, G., Mozer, F., Mursula, K., Pedersen, A., Popielawska, B., Savin, S., Stasiewicz, K., Tanskanen, P., Vaivads, A., Wahlund, J.-E. First results of electric field and density observations by Cluster EFW based on initial months of operation. Ann. Geophys. 19, 1219–1240, 2001.

Kasahara, Y., Kenmochi, H., Kimura, I. Propagation characteristics of the ELF emissions observed by the satellite Akebono in the equatorial plane. Radio Sci. 29, 751–767, 1994.

Laakso, H., Pedersen, A. Ambient electron density derived from differential potential measurements. In: Pfaff, R.F., Borovsky, J.E., Young, D.T. (Eds.), Measurement Techniques in Space Plasmas:

Particles, Geophysical Monograph, vol. 102. AGU, Washington, DC, pp. 49–54, 1996.

Laakso, H., Junginger, H., Roux, A., Schmidt, R., Villedary, C.de. Magnetosonic waves above f_{cH+} at geostationary orbit: GEOS 2 results. J. Geophys. Res. 95, 10,609–10,621, 1990.

Němec, F., Santolík, O., Gereová, K., Macúšová, E., Conchy, Y.de., Cornilleau-Wehrlin, N. Initial results of a survey of equatorial noise emissions observed by the Cluster spacecraft. Planet. Space Sci. 53, 291–298, 2005.

Pedersen, A., Décréau, P., Escoubet, C.-P., Gustafsson, G., Laakso, H., Lindqvist, P.-A., Lybekk, B., Masson, A., Mozer, F., Vaivads, A. Four-point high time resolution information on electron densities by the electric field experiments (EFW) on Cluster. Ann. Geophys. 19, 1483–1489, 2001.

Perraut, S., Roux, A., Robert, P., Gendrin, R., Sanvaud, J.-A., Bosqued, J.-M., Kremser, G., Korth, A. A systematic study of ULF waves above F_{H+} from GEOS 1 and 2 measurements and their relationship with proton ring distributions. J. Geophys. Res. 87, 6219–6236, 1982.

Russell, C.T., Holzer, R.E., Smith, E.J. OGO 3 observations of ELF noise in the magnetosphere. The nature of the equatorial noise. J. Geophys. Res. 75, 755–768, 1970.

Santolík, O., Němec, F., Gereová, K., Macúšová, E., Conchy, Y.de., Cornilleau-Wehrlin, N. Systematic analysis of equatorial noise below the lower hybrid frequency. Ann. Geophys. 22, 2587–2595, 2004.

Santolík, O., Pickett, J.S., Gurnett, D.A., Maksimovic, M., Cornilleau-Wehrlin, N. Spatio-temporal variability and propagation of equatorial noise observed by Cluster. J. Geophys. Res. 107 (A12), 1495, 2002.

Santolík, O., Parrot, M., Lefeuvre, F. Singular value decomposition methods for wave propagation analysis. Radio Sci. 38 (1), 1010, 2003.

Stix, T.H., Waves in Plasmas, Am. Inst. of Phys., New York, 1992.

Tsyganenko, N.A., Stern, D.P. Modeling the global magnetic field of the large-scale Birkeland current systems. J. Geophys. Res. 101, 27187–27198, 1996.

Tsyganenko, N.A. A magnetospheric magnetic field model with a warped tail current sheet. Planet. Space Sci. 37, 5–20, 1989.

Power line harmonic radiation (PLHR) observed by the DEMETER spacecraft

F. Němec,[1,2] O. Santolík,[3,4] M. Parrot,[1] and J. J. Berthelier[5]

Received 18 October 2005; revised 21 December 2005; accepted 4 January 2006; published 22 April 2006.

[1] Results of a systematic survey of Power Line Harmonic Radiation (PLHR) observed by a recently (June 2004) launched French spacecraft DEMETER are presented. In order to obtain a statistically significant number of events, an automatic identification procedure has been developed and all the available high-resolution data have been processed. Altogether, 58 events have been found in 865 hours of data recorded during the first year of operation. These events form three different classes: with frequency spacing of spectral lines of 50/100 Hz (10 events), with frequency spacing of 60/120 Hz (13 events), with other spacings/not clear cases (35 events). The first two classes of events are discussed in detail, showing that their origin is most probably connected with the radiation from the electric power systems which are magnetically conjugated with the place of observation. Additionally, in more than one half of the cases, the frequencies of PLHR lines well corresponded to the multiples of the power system frequency. The frequency drift of all the observed events was very slow, if observable. The events occurred without any significant preference for low or high geomagnetic activity, although more intense events were observed during disturbed times. Simultaneous observations of electric and magnetic components of PLHR suggest that the waves propagate in the electromagnetic right-hand polarized whistler mode.

Citation: Němec, F., O. Santolík, M. Parrot, and J. J. Berthelier (2006), Power line harmonic radiation (PLHR) observed by the DEMETER spacecraft, *J. Geophys. Res.*, *111*, A04308, doi:10.1029/2005JA011480.

1. Introduction

[2] Power Line Harmonic Radiation (PLHR) are electromagnetic waves radiated by electric power systems at harmonic frequencies of 50 or 60 Hz. In frequency-time spectrograms they usually look like a set of intense parallel lines with mutual distances of 50/100 or 60/120 Hz because odd/even harmonics can be strongly suppressed in some cases. There are many observations of PLHR on the ground [*Helliwell et al.*, 1975; *Park and Helliwell*, 1978; *Matthews and Yearby*, 1978; *Park and Helliwell*, 1981, 1983; *Yearby et al.*, 1983], giving evidence for its propagation through the magnetosphere. However, direct observations by satellites are still rather rare and described only in a few papers [*Bell et al.*, 1982; *Koons et al.*, 1978; *Tomizawa and Yoshino*, 1985; *Rodger et al.*, 1995; *Parrot et al.*, 2005]. Moreover, one must admit that there is quite a controversy about the origin of these events because many of the observed lines are not separated by 50/100 or by 60/120 Hz. These are usually called Magnetospheric Line Radiation (MLR) and their generation mechanism is a matter of discussion. *Rodger et al.* [1995] analyzed observations of MLR by ISIS 1 and ISIS 2 satellites and found no correlation with 50 or 60 Hz multiples. The same conclusion was obtained for ground-based observations made at the Halley station [*Rodger et al.*, 1999, 2000a, 2000b]. On the other hand, some researchers [*Park and Miller*, 1979] have reported a "Sunday effect"; they claim that the occurrence rate was significantly lower on Sundays in comparison to other days of week. *Parrot* [1991] and *Molchanov et al.* [1991] attributed this reduced occurrence not only to lower power consumption during weekends but also to different current distribution in the power systems as compared to weekdays. Finally, in a review paper concerning observations of PLHR and MLR both on the ground and satellites, *Bullough* [1995] discussed the possibility that MLR originates as PLHR.

[3] Results of a systematic survey of PLHR observed by the DEMETER spacecraft are reported in this paper. In section 2 the wave experiment on board DEMETER is briefly introduced. In section 3 an automatic identification of PLHR is described. An analysis of events is performed in section 4, whereas section 5 presents the discussion of results. Finally, section 6 contains conclusions.

2. Experiment

[4] We have used data from the French microsatellite DEMETER, which was launched in June 2004 on a low-

[1]Laboratoire de Physique et Chimie de l'Environnement, Centre National de la Recherche Scientifique, Orléans, France.
[2]Also at Faculty of Mathematics and Physics, Charles University, Prague, Czech Republic.
[3]Faculty of Mathematics and Physics, Charles University, Prague, Czech Republic.
[4]Also at Institute of Atmospheric Physics, Academy of Sciences of the Czech Republic, Prague, Czech Republic.
[5]Centre d'Etude des Environnements Terrestre et Planetaires, Centre National de la Recherche Scientifique, Saint-Maur des Fossés, France.

0148-0227/06/2005JA011480$09.00

altitude (≈710 km) nearly Sun-synchronous polar orbit. The primary purpose of the DEMETER mission is to study ionospheric effects connected with the seismic activity. The mission also aims at the analysis of anthropogenic effects in the ionosphere. The IMSC and ICE instruments on board DEMETER measure electromagnetic waves at geomagnetic latitudes less than 65 degrees. There are two principal modes of operation: the survey mode, in which spectra of one electric and one magnetic field component are calculated onboard in the VLF range (up to 20 kHz) and the burst mode, in which the waveforms of one electric and one magnetic field component are recorded in the VLF range and a full set of three electric and three magnetic components are measured in the ELF range (up to 1250 Hz). The survey mode has a limited frequency resolution (worse than 19.5 Hz), which is insufficient for a study of PLHR. Therefore we have used the burst-mode data, which are only recorded for several minutes during each half-orbit, mostly above seismic areas (the zones are marked by shading in Figures 2 and 3). Besides these zones there are about 20% of volume of the burst-mode data which are recorded above different regions of interest which can be added or modified during the operational phase of the mission. Detailed descriptions of the DEMETER wave experiments and analysis methods can be found in papers by *Berthelier et al.* [2006], *Parrot et al.* [2006], and *Santolík et al.* [2006].

3. Automatic Identification of PLHR Events

[5] The PLHR events are known to be very rarely observed on spacecraft. In order to detect a reasonably high number of such events, it is necessary to process a large amount of data. Since a visual survey of all the data would be very time-consuming (if not almost impossible), we have developed a procedure for an automatic identification of possible PLHR events. All these candidate PLHR events, found by a computer, have been visually verified and we have decided, if they correspond to real PLHR events.

[6] The automatic identification procedure, instead of searching for a group of parallel equally spaced lines on a frequency-time spectrogram (possibly drifting in frequency), has been designed to search for a single line. This simplification fails in the case of the spacecraft interferences. However, the artificial interferences always occur at the same, known, frequencies, not showing the frequency drift, and can be therefore easily distinguished.

[7] We have used electric field data obtained during the Burst mode in the VLF range. The main reason for using the electric field data was that these measurements contain significantly less interferences than the magnetic field data. In order to easily access the entire set of the DEMETER data files, the program for automatic identification of PLHR events has run in the DEMETER control center in Orléans, France as the level-3 data processing [*Lagoutte et al.*, 2006].

[8] The waveforms are recorded with a sampling frequency of 40,960 Hz. The automatic recognition procedure starts by analysis of these data sets using the fast Fourier transform (FFT) with 8192 data samples. Seven consecutive spectra are then averaged with 50 percent overlapping. This results in a frequency-time spectrogram with a frequency resolution of 5 Hz and time resolution of 0.8 s. This seems to be a good compromise between the required frequency resolution (identification of narrow lines with frequency separation of about 50 Hz), time resolution (lines are expected to drift even several Hz per second), and statistical errors of spectral estimates.

[9] The next step is to find frequencies with an intense signal at a given time. We focus on a frequency interval from 500 to 4000 Hz, because there are not many PLHR events reported outside of this interval. For a given time, we scan the power spectra, taking into account sets of N consecutive frequency points. N is one of the parameters of the method which will be discussed later. In order to suppress systematic trends across each set of N points, a least-squares polynomial fit of the nth degree is subtracted. In each corrected set, we define frequencies at which the intensity exceeds the average intensity by more than k standard deviations (k and n are additional parameters of the procedure). In the given frequency interval, all the possible sets of N consecutive frequency points are processed by the same procedure, shifting the set always by one frequency point.

[10] The final step is to search for continuation of the lines in the next time interval. Each of the frequency points found by the above procedure is initially supposed to be the beginning of a new spectral line. For each of the detected lines we store the time of its beginning, the frequency at which it was observed for the first time, and information on its estimated minimum and maximum frequency drift. In the new time interval we determine whether this line continues by comparing the presently found frequency points to the points that would correspond to the lines stored in the memory. This comparison takes into account the beginning frequency and frequency drift of each line. If the frequencies match, the line continues to the next time interval. In this case, its minimum and maximum frequency drift are recalculated.

[11] If the next time interval does not contain any frequency point corresponding to a given line, the line is terminated and its duration is compared to the predefined threshold t. If the line lasts longer than t, it is classified as a possible PLHR event: the time and frequency of its beginning are saved and a frequency-time power spectrogram containing the line is plotted. If the line does not last long enough, it is not taken into account.

[12] The above described algorithm contains several crucial parameters. Their values have been defined using test data, by requiring that 100% of the PLHR events in the test data are identified. On the other hand, we have tried to find parameters which minimize the number of ''false alarms.'' The parameters used in the present study have been defined as follows. Number of frequency points in a set, $N = 40$; degree of the fitted polynomial function, $n = 3$; minimum multiple of the standard deviation, $k = 2.5$; minimum duration of a line, $t = 5.0$ s.

4. Analysis of Events

[13] We have run the described identification procedure on the entire data set recorded by the DEMETER spacecraft during the first year of its operation, from the beginning of the mission in July 2004 till July 2005. Altogether, this represents 865 hours of the burst-mode data organized into

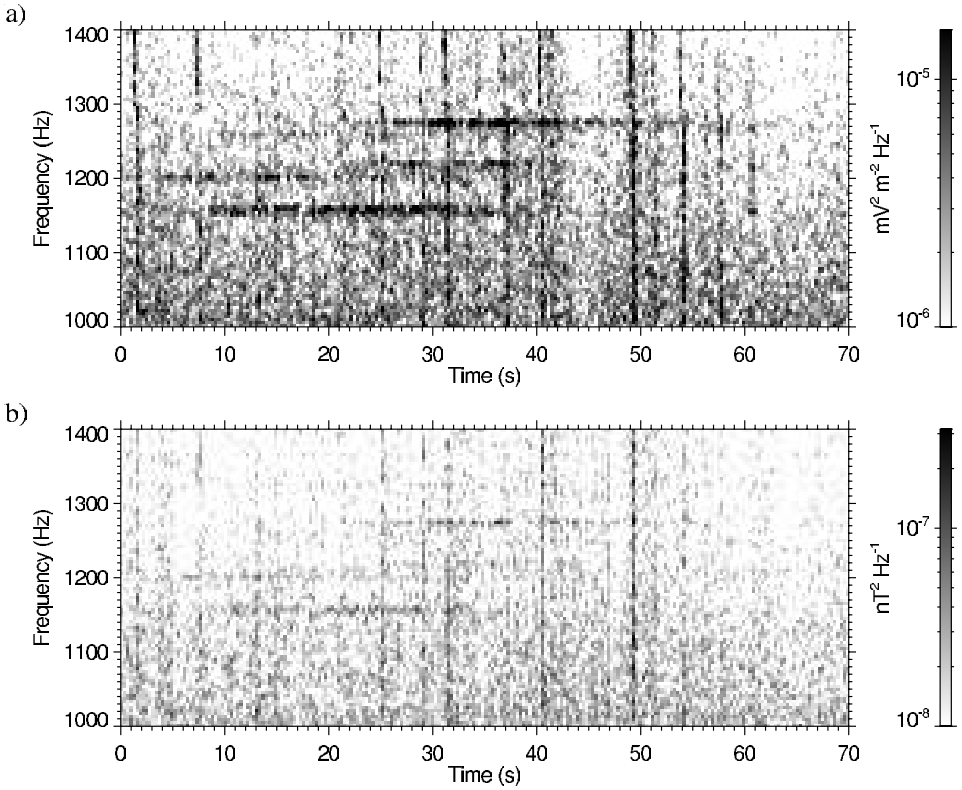

Figure 1. An example of (a) frequency-time spectrogram of the electric and (b) magnetic field fluctuations corresponding to one of the analyzed events. The data were recorded on 11 November 2004, after 1400:05 UT, when the spacecraft overflew Philippines; the frequency separation of the spectral lines is 60 Hz.

5920 half-orbits. In this data set, possible PLHR events have been identified in 317 half-orbits (about 5 percent).

[14] We have manually checked all these events for the presence of PLHR. The results revealed a large number of "false alarms." They were mostly caused by the presence of a sharp cutoff below the local proton cyclotron frequency [*Santolík and Parrot*, 1999], looking in some cases as intense spectral line on the frequency-time spectrograms. In the entire data set, we have found only 58 cases of PLHR-like events which can be divided into three classes: (1) 10 events where the frequency separation of spectral lines is equal to 50 or 100 Hz; (2) 13 events where the frequency separation of spectral lines is equal to 60 or 120 Hz; (3) 35 events which cannot be clearly classified as PLHR, where only one single spectral line was detected or, more often, where several lines were found with spacing which is neither 50/100 nor 60/120 Hz (MLR).

[15] The origin of this last class of events is not very clear. We believe that at least some of them can originate from plasma instabilities in the magnetosphere because they are mostly observed during large magnetic activities. However, a thorough discussion of these events will be the subject of another paper. In the following, we will focus on the analysis of PLHR events with 50/100 Hz and 60/120 Hz spacings.

[16] Recall that these 23 recorded events have been found by analyzing the power spectrograms of the electric field fluctuations. We have also checked the magnetic field data for these cases and found only six events (26%) where similar lines in the magnetic field spectrograms were simultaneously detectable at the same frequencies. These six events also have the largest amplitudes of the the electric field fluctuations among the 23 cases. The observed ratios of magnetic to electric power spectral densities correspond to the electron densities between 2×10^4 cm^{-3} and 3×10^5 cm^{-3}, supposing that the waves propagate in the right-hand polarized whistler mode along the magnetic field lines. This, in turn, roughly corresponds to usual values of the local electron density measured on board DEMETER. The magnetic field in the remaining 17 cases is too weak to be observable under the same hypothesis on the wave mode, given the measured intensities of the wave electric field. Consequently, all the recorded events are consistent with propagation of PLHR in the right-hand polarized electromagnetic whistler mode.

[17] Figure 1 shows an example of an event from the group of the six most intense cases. It is represented in the form of the frequency-time power spectrograms of the electric and magnetic field fluctuations. The data were recorded on 11 November 2004 between 1400:06 UT and 1401:16 UT above Philippines where a 60-Hz electrical network is used. A magnetically conjugated region is located in Taiwan where a 60-Hz network is also used. Since the magnetic field data contain spacecraft interference signals which could be confused with PLHR, we have used a tool for DEMETER data analysis allowing us to suppress a part of these interferences [*Santolík et al.*, 2006]. Three lines at frequencies of 1160, 1220, and 1280 Hz can be

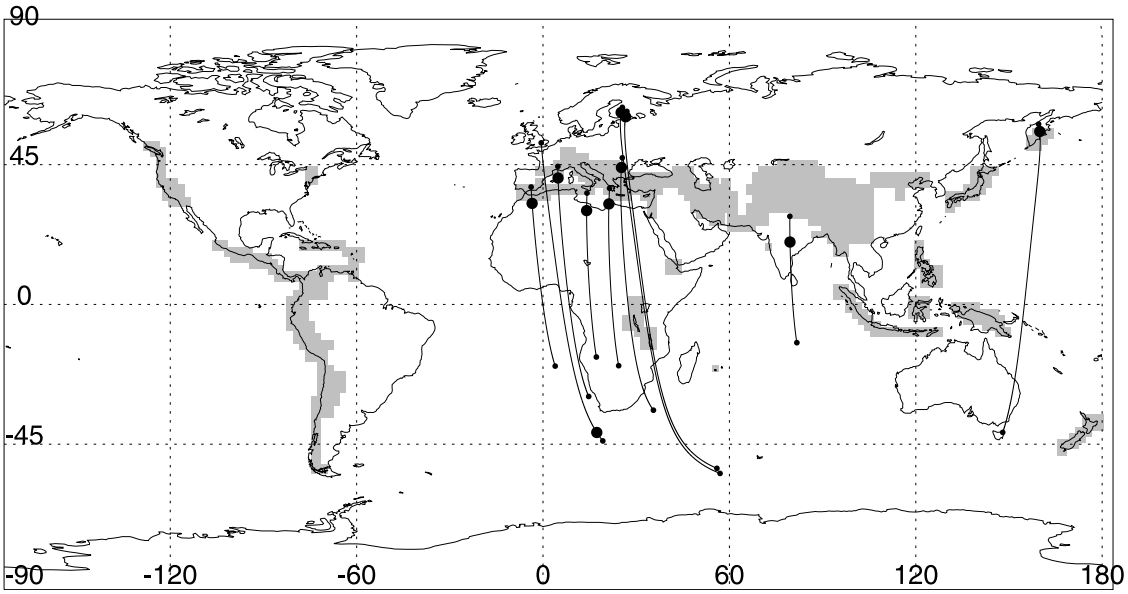

Figure 2. Geographic locations of observed PLHR with mutual distance of lines 50/100 Hz (large points). Magnetic field lines and footprints of the points of observations (thin lines and small points). Seismic zones with permanently active burst-mode coverage are shown by gray shading; the operational-phase burst-mode regions (approximately 20% of the burst-mode data volume) are not shown since their positions vary during the time interval analyzed in this study.

identified in both spectrograms, the magnetic signature being much weaker. During the first half of the time interval in which the event is detected, we can also recognize lines at 1200 and 1260 Hz which are, unlike the previous three frequencies, exact multiplies of the fundamental frequency of 60 Hz.

[18] Figures 2 and 3 show locations of PLHR events in geographic coordinates (large points on the world maps) for the frequency separations of 50/100 and 60/120 Hz, respectively. For each of these events, the following properties have been determined: spacecraft position in the time of observation, duration of the event, magnetic local time, Kp index, and the list of identified lines, which means their frequency and maximum intensity of the electric field fluctuations. We have also used the IGRF-10 model of the Earth's magnetic field implemented in the GEOPACK-2005 program (N. A. Tsyganenko, http://nssdcftp.gsfc.nasa.gov/models/magnetospheric/tsyganenko/) to calculate the magnetic footprints of the point of observation by tracing the magnetic field lines. The footprints are shown by small points on the world maps and the projections of the corresponding magnetic field lines on the Earth's surface

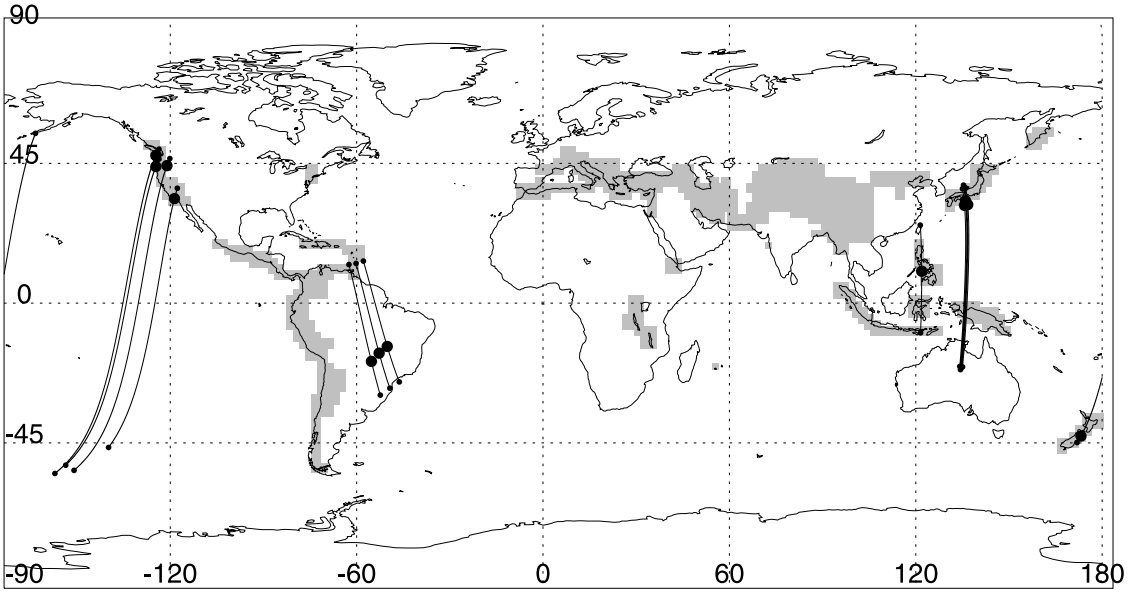

Figure 3. The same as in Figure 2 but for PLHR with mutual distance of lines 60/120 Hz.

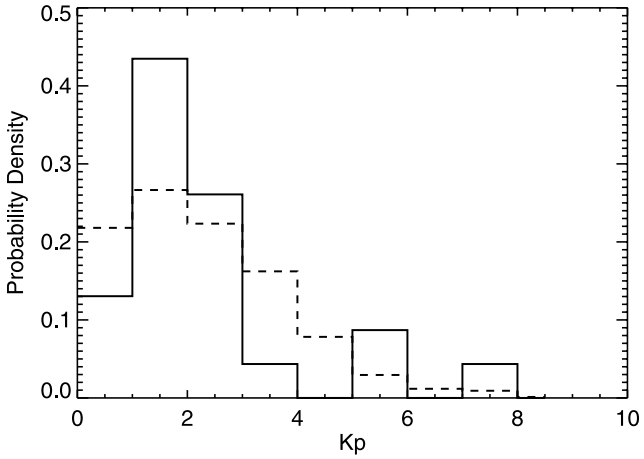

Figure 4. Histogram of Kp indices at the time of the PLHR events (solid line). Overplotted is a histogram of all Kp indices that occurred during the analyzed year (dashed line).

are shown by thin lines. This indicates possible source regions, supposing the propagation in the ducted mode.

[19] Note that the observed frequency separations of lines correspond very well to the frequencies of electric power systems in the possible geographic regions of generation. Separations of 50/100 Hz are mostly observed above Europe and Northern Africa (with a probable source region, a footprint of magnetic field line, lying in Europe for all these cases). One event is observed above India and one above northeastern Asia with a magnetic conjugate point in Australia. Separations of 60/120 Hz are observed mostly above the USA, Brazil, and Japan. One such event has been detected above Philippines and one above New Zealand. This is rather surprising because New Zealand has a power system with a frequency of 50 Hz, but we have to notice

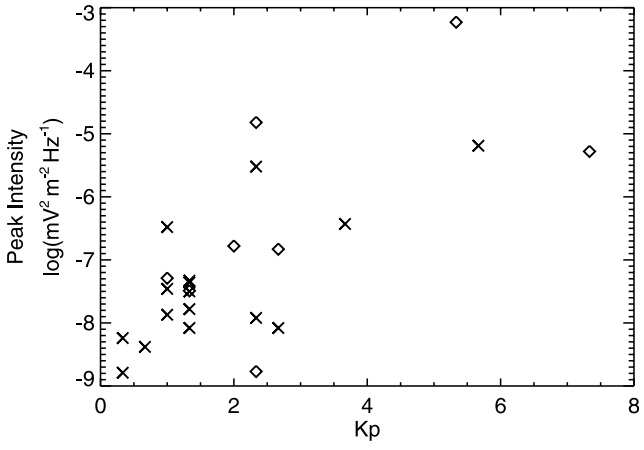

Figure 5. Peak intensity of observed PLHR events as a function of the Kp index. The events, whose frequencies correspond to the multiples of the power system frequency, are plotted as crosses. The events with frequencies not corresponding to the multiples of the power system frequency are plotted as diamonds. The time interval from Figure 1 corresponds to two events, since it successively contains both types of PLHR.

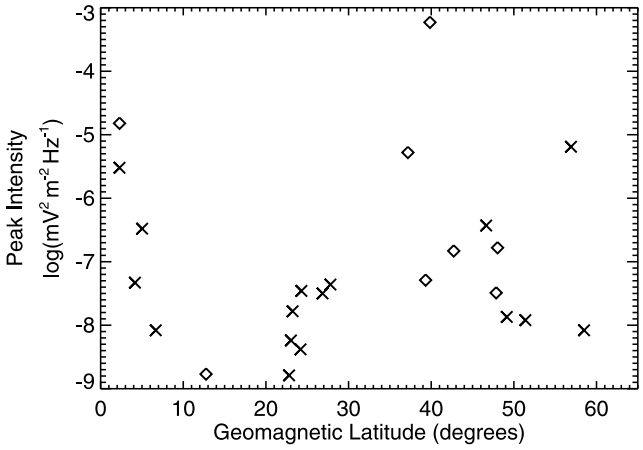

Figure 6. Peak intensity of observed PLHR events as a function of geomagnetic latitude. The symbols are the same as in Figure 5.

that the magnetic conjugate point is in Alaska where the power-system frequency is 60 Hz.

[20] Histogram of Kp indices at the time of PLHR events is shown in Figure 4 by a solid line. A histogram of all the Kp indices that occurred during the analyzed year (July 2004 to July 2005) is overplotted by a dashed line for comparison. It can be seen that the PLHR events occur during both low and high geomagnetic activity, with no significant preference for quiet or disturbed periods.

[21] All the PLHR events have occurred at frequencies higher than 1 kHz, not allowing us to analyze the wave propagation using six components of the electromagnetic field. These methods [*Santolík et al.*, 2006] can be only used in the ELF range below 1 kHz. Most of the cases have been observed at frequencies around 2 kHz, with the number of observations slowly decreasing towards higher frequencies. In 15 out of 23 cases (65%), the frequencies of observed PLHR lines have corresponded well (within the experimental error) to the exact multiples of power system frequency. The absolute position of spectral lines in the frequency spectrum of the remaining eight cases appeared to be random, with no connection to the observed line spacings. The frequency drift of all the cases was very slow, not observable within the experimental errors.

[22] Figures 5, 6, and 7 show the peak intensities of observed PLHR events as a function of the Kp index, geomagnetic latitude, and magnetic local time, respectively. For each event, the peak intensity is defined as the intensity of the most intense line. The events with frequencies corresponding to the multiples of the power system frequency are plotted as crosses, the events with frequencies not corresponding to these multiples are plotted as diamonds. Figure 5 shows that the peak intensity of PLHR increases with the Kp index. The peak intensity of PLHR seems to be independent of magnetic latitude (Figure 6). Finally, the peak intensity is higher during the night than during the day (Figure 7). Note that the bunching of observed events in two MLT intervals is connected to the nearly Sun-synchronous orbit of the DEMETER spacecraft. The MLT is thus either just before noon or just before midnight. However, approximately 1 year of data has been analyzed and therefore the distribution of sampled geo-

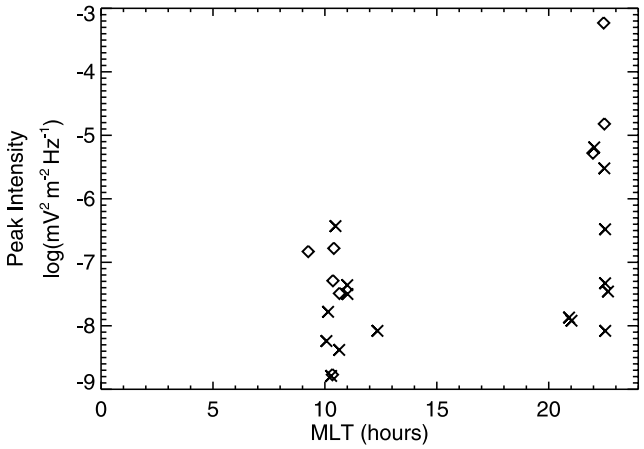

Figure 7. Peak intensity of observed PLHR events as a function of magnetic local time. The symbols are the same as in Figure 5.

graphical longitudes should be almost uniform all over the Earth for both MLT intervals. No clear dependence on whether the frequencies correspond to the multiples of power system frequency or not (crosses versus diamonds) has been observed.

5. Discussion

[23] The most problematic element in the presented study is the procedure for automatic identification of PLHR events (section 3). This procedure was needed in order to analyze a large amount of available data. However, it is very difficult to estimate the consequences of this step. There is no exact way to determine the total number of PLHR events contained in the data set. Although the parameters of the detection procedure have been set to ensure a 100% detection of the small set of the test PLHR data, there is no guarantee that we have not missed an unknown fraction of PLHR events in 865 hours of analyzed data. Another consequence could be a possible presence of a ''selection effect.'' That is, the detected events do not necessarily represent a ''randomly chosen'' subset from the total set of PLHR events contained in the data, but events with some specific signatures could be detected with a higher probability. Although we cannot exclude the presence of this effect, we have no indication that it significantly biases our results.

[24] In spite of these technical difficulties, the striking result of our study is that the occurrence frequency of PLHR events in the topside ionosphere is probably very low. Supposing the 100% detection probability of our procedure, a low orbiting spacecraft would on average detect one PLHR event per 38 hours of observations. If we miss a fraction of events the occurrence frequency would be correspondingly higher but, most probably, the results would not be significantly different.

[25] Concerning the geographical coverage of our study, recall that we have used the data obtained during the burst mode of the DEMETER spacecraft. This mode is activated regularly above the seismic zones but from time to time burst mode zones have been added in different parts of the Earth. This selection can potentially bias the analysis. The consequences for the maps of geographic locations of observed PLHR (Figures 2 and 3) are evident. Moreover, results obtained at different latitudes in Figure 6 are in fact also obtained at different longitudes. However, this probably does not strongly affect our results.

[26] Previous investigations of PLHR events have shown contradictions concerning the level of magnetic activity which is the most favorable for observations. Figure 4 shows that the PLHR events occur without any significant preference for a level of geomagnetic activity, although the number of events is not high enough to allow us to make a clear conclusion.

[27] The observed frequency spacing of all the PLHR events corresponds well to power system frequencies in possible geographical regions of generation (Figures 2 and 3). This represents a good evidence for a hypothesis that PLHR events are really caused by an electromagnetic radiation from the ground power systems. Moreover, in 15 out of the 23 cases the frequencies of the observed PLHR lines corresponded (within the experimental error) to the exact multiples of the power system frequency. This is in contradiction with previous reports [e.g., *Rodger et al.*, 1995]. However, these results were derived for MLR, while our results have been obtained for PLHR (with frequency spacing strictly 50/100 or 60/120 Hz) without any significant frequency drift. This probably shows the crucial difference between PLHR and MLR: while there is a strong evidence that PLHR events are caused by radiation from electric networks, there is no such an evidence for MLR. The question whether MLR can be created in a completely natural way or whether some PLHR-like emissions are necessary as triggers, is a matter of debate and is beyond the scope of this paper. However, it becomes clear that PLHR and MLR have to be considered separately as two different phenomena.

[28] The peak intensity of observed PLHR events does not seem to vary with the geomagnetic latitude (Figure 6), although the intensity of natural emissions is higher in subauroral areas than close to the magnetic equator [*Parrot*, 1990]. However, it increases with Kp index and it is also higher during the night (Figures 5 and 7). In this case, the peak intensity behaves in the same way as the intensity of natural emissions. There are two possible explanations of these observations. (1) The PLHR events with a low intensity compared to the natural background could be simply too weak to be observed. The average peak intensity of observed events would than necessarily be higher in places with higher intensity of natural background. (2) The electromagnetic emissions radiated by a power system could be modulated by the plasma environment in such a way that their intensity would become higher at places with more intense natural background. This second possibility seems to be more likely true. The first mechanism would, for example, just eliminate the less intense events for high geomagnetic activity when the natural background becomes stronger. In that case, however, we would observe both less intense and more intense cases at geomagnetically quiet times. This does not seem to be the case: Figure 5 indicates that only the less intense cases are observed at quiet times.

[29] The intensity of PLHR events is thus partially connected to the intensity of natural background. This

shows that although the origin of PLHR is tied to the radiation from electric power systems, some processes changing its intensity according to the level of the natural background are taking place. Moreover, these processes must have such a behavior that in many cases the frequencies of observed PLHR lines correspond to the multiples of the fundamental power system frequency.

[30] Finally, one should keep in mind that the efficiency of coupling through the ionosphere for ground transmitters depends on many parameters and could possibly explain some of the observed variations. For example, the coupling is easier on the nightside than on the dayside ([*Green et al.*, 2005]).

6. Conclusions

[31] We have presented results of an initial survey of observations of PLHR by the DEMETER spacecraft. The data were collected during the first year of its operation and an automatic procedure has been used to detect the PLHR events. Altogether, 23 PLHR events (10 with 50/100 Hz spacing and 13 with 60/120 Hz spacing) have been found in the entire set of 865 hours of available high-resolution data. Our results show the following.

[32] 1. PLHR events occur during both low and high magnetic activity. No level of activity seems to be significantly preferred.

[33] 2. The observed frequency spacings of all the PLHR events correspond well to power system frequencies in possible geographical regions of generation.

[34] 3. The frequencies of observed PLHR lines correspond to the multiples of power system frequency in 65% of cases.

[35] 4. The peak intensity of observed PLHR events increases with Kp index and it is higher during the night. The peak intensity thus seems to be partially connected to the intensity of the natural background emissions. It suggests that electromagnetic emissions radiated by a power system are modulated by the plasma environment. However, the day/night asymmetry of coupling of electromagnetic waves from the ground to the ionosphere might also play a role.

[36] 5. In 26% of most intense cases we also observe the magnetic field component of PLHR. These observations are consistent with propagation in the electromagnetic right-hand polarized whistler mode.

[37] **Acknowledgments.** We thank J.-Y. Brochot of LPCE/CNRS Orléans for his help with running the PLHR recognition algorithm as the DEMETER level-3 processing procedure. F. Němec thanks the French embassy in Prague for his support during his stay in Orléans. O. Santolík and F. Němec acknowledge additional support from the ESA PECS contract 98025 and from the GACR grant 205/06/1267.

[38] Arthur Richmond thanks Keith Yearby and another reviewer for their assistance in evaluating this paper.

References

Bell, T. F., J. P. Luette, and U. S. Inan (1982), ISEE 1 observations of VLF line radiation in the Earth's magnetosphere, *J. Geophys. Res.*, *87*(A5), 3530–3536.

Berthelier, J. J., et al. (2006), ICE, the electric field experiment on DEMETER, *Planet. Space Sci.*, in press.

Bullough, K. (1995), Power line harmonic radiation: Sources and environmental effects, in *Handbook of Atmospheric Electrodynamics*, vol. 2, pp. 291–332, CRC Press, Boca Ralton, Fla.

Green, J. L., S. Boardsen, L. Garcia, W. W. L. Taylor, S. F. Fung, and B. W. Reinish (2005), On the origin of whistler mode radiation in the plasmasphere, *J. Geophys. Res.*, *110*, A03201, doi:10.1029/2004JA010495.

Helliwell, R. A., J. P. Katsufrakis, T. F. Bell, and R. Raghuram (1975), VLF line radiation in the earth's magnetosphere and its association with power system radiation, *J. Geophys. Res.*, *80*, 4249–4258.

Koons, H. C., M. H. Dazey, and B. C. Edgar (1978), Satellite observation of discrete VLF line radiation within transmitter-induced amplification bands, *J. Geophys. Res.*, *83*(A8), 3887–3889.

Lagoutte, D., et al. (2006), The DEMETER science mission centre, *Planet. Space Sci.*, in press.

Matthews, J. P., and K. Yearby (1978), Magnetospheric VLF line radiation observed at Halley, Antarctica, *Planet. Space Sci.*, *29*, 97–106.

Molchanov, O. A., M. Parrot, M. M. Mogilevsky, and F. Lefeuvre (1991), A theory of PLHR emissions to explain the weekly variation of ELF data observed by a low-altitude satellite, *Ann. Geophys.*, *9*, 669–680.

Park, C. G., and R. A. Helliwell (1978), Magnetospheric effects of power line radiation, *Science*, *200*, 727–730.

Park, C. G., and R. A. Helliwell (1981), Power line radiation in the magnetosphere, *Adv. Space Res.*, *1*, 423–437.

Park, C. G., and R. A. Helliwell (1983), Ground observations of power line radiation coupled to the ionosphere and magnetosphere, *Space Sci. Rev.*, *35*, 131–137.

Park, C. G., and T. R. Miller (1979), Sunday decreases in magnetospheric VLF wave activity, *J. Geophys. Res.*, *84*, 943–950.

Parrot, M. (1990), World map of ELF/VLF emissions as observed by a low-orbiting satellite, *Ann. Geophys.*, *8*, 135–145.

Parrot, M. (1991), Daily variations of ELF data observed by a low-altitude satellite, *Geophys. Res. Lett.*, *18*(6), 1039–1042.

Parrot, M., F. Němec, O. Santolík, and J. J. Berthelier (2005), ELF magnetospheric lines observed by DEMETER, *Ann. Geophys.*, *23*, 3301–3311.

Parrot, M., et al. (2006), The magnetic field experiment IMSC and its data processing onboard DEMETER: Scientific objectives, description and first results, *Planet. Space Sci.*, in press.

Rodger, C. J., N. R. Thomson, and R. L. Dowden (1995), VLF line radiation observed by satellite, *J. Geophys. Res.*, *100*(A4), 5681–5689.

Rodger, C. J., M. A. Clilverd, K. H. Yearby, and A. J. Smith (1999), Magnetospheric line radiation observations at Halley, Antarctica, *J. Geophys. Res.*, *104*(A8), 17,441–17,447.

Rodger, C. J., M. A. Clilverd, K. Yearby, and A. J. Smith (2000a), Is magnetospheric line radiation man-made?, *J. Geophys. Res.*, *105*, 15,981–15,990.

Rodger, C. J., M. A. Clilverd, K. H. Yearby, and A. J. Smith (2000b), Temporal properties of magnetospheric line radiation, *J. Geophys. Res.*, *105*(A1), 329–336.

Santolík, O., and M. Parrot (1999), Case studies on wave propagation and polarization of ELF emissions observed by Freja around the local proton gyro-frequency, *J. Geophys. Res.*, *104*(A2), 2459–2475.

Santolík, O., F. Němec, M. Parrot, D. Lagoutte, L. Madrias, and J. J. Berthelier (2006), Analysis methods for multi-component wave measurements on board the DEMETER spacecraft, *Planet. Space Sci.*, in press.

Tomizawa, I., and T. Yoshino (1985), Power line radiation observed by the satellite, *J. Geomagn. Geoelectr.*, *37*, 309–327.

Yearby, K. H., A. J. Smith, and K. Bullough (1983), Power line harmonic radiation in Newfoundland, *J. Atmos. Terr. Phys*, *45*, 409–419.

J. J. Berthelier, Centre d'Etude des Environnements Terrestre et Planetaires, Centre National de la Recherche Scientifique, F-94107 Saint-Maur des Fossés Cedex, France. (jean-jacques.berthelier@cetp.ipsl.fr)

F. Němec and O. Santolík, Faculty of Mathematics and Physics, Charles University, V Holešovičkách 2, Prague 8, 180 00, Czech Republic. (nemec@matfyz.cz; os@matfyz.cz)

M. Parrot, Laboratoire de Physique et Chimie de l'Environnement, Centre National de la Recherche Scientifique, F-45071 Orléans Cedex 2, France. (mparrot@cnrs-orleans.fr)

Available online at www.sciencedirect.com
SCIENCE DIRECT
Planetary and Space Science 54 (2006) 512–527
Planetary and Space Science
www.elsevier.com/locate/pss

Analysis methods for multi-component wave measurements on board the DEMETER spacecraft

O. Santolík[a,*,1], F. Němec[a], M. Parrot[b], D. Lagoutte[b], L. Madrias[b], J.J. Berthelier[c]

[a]*Faculty of Mathematics and Physics, Charles University, Prague, Czech Republic*
[b]*Laboratoire de Physique et Chimie de l'Environnement, CNRS, Orléans, France*
[c]*CETP/CNRS, Saint-Maur des Fossés, France*

Received 7 December 2004; received in revised form 15 September 2005; accepted 14 October 2005
Available online 23 March 2006

Abstract

We describe analysis methods to estimate parameters of electromagnetic waves based on the multi-component measurements of the DEMETER spacecraft. Using the fact that the wave magnetic field is perpendicular to the wave vector, the wave normal direction can be estimated by different methods. We use these plane-wave estimates to interpret measurements of the observed wave emissions. For instance, we use the recently developed singular value decomposition (SVD) technique. The results of the plane-wave analysis have an advantage that they often allow a straightforward interpretation. These different methods have been successfully tested with the data of previous spacecraft. All these methods are also implemented in the analysis tools designed for the analysis of the DEMETER wave measurements.

We show the first results of these analysis techniques for different types of wave emissions observed on board DEMETER. Obliquely propagating right-hand polarized electromagnetic waves at a few hundreds of Hz are usually connected with a multi-ion mode structure below the local proton cyclotron frequency and with a sharp lower cutoff of left-hand polarized waves, as well as with right-hand polarized waves tunelling below the multi-ion cross-over frequency. Electron and proton whistlers are also very frequently observed on DEMETER. An unusual narrow-band emission at 140 Hz (well below the local proton cyclotron frequency) serves us as another case for a detailed analysis. We find that these waves are right-hand polarized and obliquely propagating.

Using this example case, we also present analysis methods to estimate continuous distribution of wave energy density as a function of wave vector directions. These techniques of wave distribution function (WDF) analysis need both wave and particle measurements. In the analyzed case, two different methods of WDF analysis give similar results consistent with the results of the plane-wave techniques. To identify the source region we use the backward ray-tracing method. The wave normal direction obtained by the analysis of multi-component data is used for a simulation of wave propagation from the point of measurement. By this procedure, we obtain an inverse trajectory of the wave ray. We can thus follow the ray path back to the anticipated source region which is in our case located a few degrees of latitude to the South from the spacecraft position.

Keywords: DEMETER micro-satellite; Poynting flux measurements; Wave vector measurements; Wave distribution function; Ray tracing

1. Introduction

The main purpose of the scientific experiments on board the DEMETER spacecraft is a systematic investigation of the electromagnetic wave emissions observed during earthquakes and volcanic eruptions, the ionosphere and upper atmosphere disturbances, as well as the precipitation of associated particles (Parrot et al., 1993; Parrot, 1994). Another scientific objective of the DEMETER program is to survey the electromagnetic environment of the Earth, to further investigate natural geophysical phenomena, and estimate the impact of human activity on the ionosphere (Parrot and Zaslavski, 1996).

The DEMETER spacecraft carries sophisticated scientific instrumentation to measure fluctuations of the electric

*Corresponding author. Tel.: +420 2 2191 2304; fax: +420 2 688 5095.
E-mail address: ondrej.santolik@mff.cuni.cz (O. Santolík).
[1]Also at Institute of Atmospheric Physics, ASCR, Prague, Czech Republic.

0032-0633/$ - see front matter © 2006 Elsevier Ltd. All rights reserved.
doi:10.1016/j.pss.2005.10.020

and magnetic fields by three magnetic and three electric antennas. The magnetic field experiment instrument magnetic search coil (IMSC) is described in detail by Parrot et al. (2006), and the ICE (electric field experiment) is described by Berthelier et al. (2006a). There are also up-to-date particle and plasma experiments onboard DEMETER: the ion spectrometer IAP (Berthelier et al., 2006b), the energetic particle experiment IDP (Sauvaud et al., 2006), and the Langmuir probe experiment ISL (Lebreton et al., 2006). The measurements of all scientific experiments are processed on board by the BANT device (Boitier d'Analyse Numérique et de Traitement) which also contains a neural network designed to study whistlers.

To maximize the scientific return of the DEMETER mission, these state-of-the-art data need to be processed using appropriate analysis methods. Although the use of multiple antennas on spacecraft has been proposed more than three decades ago by Grard (1968) and Shawhan (1970), some of the older analysis methods have been first developed for the ground-based geophysical measurements (e.g. McPherron et al., 1972; Means, 1972; Samson, 1973; Arthur et al., 1976; Samson and Olson, 1980). These methods, together with more newly developed techniques (e.g. Storey and Lefeuvre, 1979, 1980; Delannoy and Lefeuvre, 1986; Lefeuvre et al., 1986, 1987; LaBelle and Treumann, 1992; Lagoutte et al., 1992; Santolík and Parrot, 1996; Santolík et al., 2001a, 2003) have been tested during analysis of data of several previous spacecraft missions, as GEOS, Aureol 3, Freja, Polar, Interball 2, Cluster and Double Star. The orbits of these spacecraft are very different, but all of them have in common that they have been equipped with devices for multi-component measurements of the wave magnetic and electric fields.

Consequently, although these missions were designed to investigate different regions of the geospace, similar analysis methods can be used for the wave measurements. Numerous papers containing results of these analysis methods have been published (e.g. Lefeuvre and Helliwell, 1985; Lefeuvre et al., 1986, 1992; Parrot and Lefeuvre, 1986; Storey et al., 1991; Santolík and Parrot, 1998, 1999; Santolík et al., 2001b, 2004; Santolík and Gurnett, 2002; Cornilleau-Wehrlin et al., 2003; Parrot et al., 2003, 2004b). Analysis methods which are described in this paper, and which we intend to use for the DEMETER multi-component wave measurements rely on this heritage. The purpose of this analysis will be to investigate the sources and propagation of electromagnetic wave emissions observed during earthquakes and volcanic eruptions, and, generally, wave emissions in the electromagnetic environment of the Earth, including waves influenced by the impact of human activity on the ionosphere.

The paper is organized as follows. A short description of the analysis methods is given in Section 2. Section 3 presents analysis tools for the DEMETER wave data, and Section 4 shows several examples of a preliminary analysis of the first data received by the DEMETER spacecraft.

2. Analysis methods

The multi-component measurements of the wave magnetic and electric fields allow us to determine, for example, the average Poynting flux. Supposing the presence of a single plane wave, the direction of the wave vector can be determined. For a more complex wave field we can estimate a continuous distribution of wave energy density with respect to wave vector directions (wave distribution function). These results are useful for the localization of sources of observed emissions.

2.1. Plane-wave methods

Supposing the presence of a single plane wave at a frequency f with a wave vector $\boldsymbol{k}$, the wave magnetic field $\boldsymbol{B}$ as a function of time t and position $\boldsymbol{x}$ can be written as

$$\boldsymbol{B}(t,\boldsymbol{x}) = \Re\{\mathscr{B}(f,\boldsymbol{k})\exp[\mathrm{i}(2\pi ft - \boldsymbol{k}\cdot\boldsymbol{x})]\}, \tag{1}$$

where $\mathscr{B}$ is the "magnetic vector complex amplitude" for a given frequency f and wave vector $\boldsymbol{k}$. Under the same circumstances, similar expression can be used for the wave electric field $\boldsymbol{E}$, using the "electric vector complex amplitude" $\mathscr{E}$ instead of $\mathscr{B}$.

The second Maxwell's equation (the Faraday's law) can then be written as

$$\boldsymbol{k}\times\mathscr{E} = 2\pi f\mathscr{B}. \tag{2}$$

This implies that $\mathscr{B}$ is always perpendicular to both wave vector $\boldsymbol{k}$ and $\mathscr{E}$,

$$\boldsymbol{k}\cdot\mathscr{B} = 0, \tag{3}$$

$$\mathscr{E}\cdot\mathscr{B} = 0. \tag{4}$$

The first of these conditions implies

$$\mathsf{A}\cdot\boldsymbol{k} = \begin{pmatrix} \Re S_{xx} & \Re S_{xy} & \Re S_{xz} \\ \Re S_{xy} & \Re S_{yy} & \Re S_{yz} \\ \Re S_{xz} & \Re S_{yz} & \Re S_{zz} \\ 0 & -\Im S_{xy} & -\Im S_{xz} \\ \Im S_{xy} & 0 & -\Im S_{yx} \\ \Im S_{xz} & \Im S_{yz} & 0 \end{pmatrix} \cdot \begin{pmatrix} k_x \\ k_y \\ k_z \end{pmatrix} = 0, \tag{5}$$

where the components of the Hermitian magnetic spectral matrix S_{ij} are obtained from the three Cartesian components of the magnetic vector complex amplitude

$$\mathscr{B} = (\mathscr{B}_x, \mathscr{B}_y, \mathscr{B}_z), \tag{6}$$

using the relation

$$S_{ij} = \mathscr{B}_i\mathscr{B}_j^* . \tag{7}$$

Note that the homogeneous set of Eq. (5) can be multiplied by any real coefficient. Consequently, this set cannot be used to determine the modulus of the unknown vector $\boldsymbol{k}$. It only can determine the direction of this vector. Note also that the set of Eq. (5) naturally contains only two independent real equations corresponding to two original

real equations (3). Importance of this expansion, however, becomes evident when it is used with experimental data.

Using the experimentally measured multi-component signals of the wave magnetic field

$$\hat{\boldsymbol{B}} = (\hat{B}_x, \hat{B}_y, \hat{B}_z), \tag{8}$$

we can use spectral analysis methods (for example, fast Fourier transform or wavelet analysis) to estimate, at a given frequency, the components of the "magnetic vector complex amplitude" $\hat{\mathscr{B}}$ and, subsequently, the magnetic spectral matrix,

$$\hat{S}_{ij} = \langle \hat{\mathscr{B}}_i \hat{\mathscr{B}}_j^* \rangle, \tag{9}$$

where $\langle\,\rangle$ means average value, and the indices i and j stand for all the three orthogonal components of the wave magnetic field x, y, and z.

The homogeneous set of six Eq. (5) can then be written as

$$\hat{\mathsf{A}} \cdot \hat{\boldsymbol{\kappa}} = 0, \tag{10}$$

where the matrix $\hat{\mathsf{A}}$ is composed of the superposed imaginary and real parts of the experimental spectral matrix $\hat{S}_{ij}$ (instead of the idealized spectral matrix S_{ij}), and $\hat{\boldsymbol{\kappa}}$ is an unknown unit vector defining the estimate of the wave vector direction,

$$\hat{\boldsymbol{\kappa}} = \hat{\boldsymbol{k}}/|\boldsymbol{k}|. \tag{11}$$

Using Cartesian coordinates connected to a principal axis of the plasma medium where the waves propagate (the direction of the ambient stationary magnetic field $\boldsymbol{B}_0$), the wave vector direction can be defined by two angles θ and ϕ, where θ is the deviation from the $\boldsymbol{B}_0$ direction and ϕ is an azimuth centered, for instance, to the plane of the local magnetic meridian. The wave vector direction then reads

$$\hat{\boldsymbol{\kappa}} = (\sin\theta\cos\phi, \sin\theta\sin\phi, \cos\theta). \tag{12}$$

The unknown unit vector $\hat{\boldsymbol{\kappa}}$ thus reduces to two real unknowns θ and ϕ. As a consequence, system (10) is over-determined, containing six equations for two unknowns. Generally, these six equations are independent. This is different compared to the case of the ideal set of Eq. (5). The reason is that the matrix $\hat{\mathsf{A}}$ is composed of experimental data which can contain natural and/or experimental noise and do not necessarily exactly correspond to an ideal plane wave. Since we only have two unknowns, a subset of any two independent equations picked up from the set (5) is sufficient to obtain a unique solution for θ and ϕ. This is the basis of several analysis methods. Other methods attempt to estimate an "average" solution of the entire set (5) using different techniques.

The method of Means (1972) is based on imaginary parts of three cross-spectra and the procedure is equivalent to solving any two of the last three equations in (10). The method of Samson and Olson (1980) (their Eq. (11)) is equivalent to finding a unique solution from another subset of equations selected in (10). The method of McPherron et al. (1972) uses the first three equations and finds a unique solution using the eigenanalysis of the real part of the spectral matrix. Samson (1973), again using the eigenanalysis, presented methods of decomposition of the entire complex spectral matrix. Santolík et al. (2003) used a singular value decomposition (SVD) technique to estimate a solution of the entire set of Eq. (10) in the "least-squares" sense. This method is based on the SVD algorithm which is frequently contained in numerical libraries (e.g. Press et al., 1992). The technique is very straightforward, simply decomposing the spectral matrix into one diagonal and two orthonormal matrices. From the components of these matrices we can directly estimate the lengths and directions of the three axes of the polarization ellipsoid.

The results of the plane-wave analysis often allow a straightforward interpretation of results. The resulting angles θ and ϕ can be represented in time–frequency plots in a form similar to power spectrograms. This was found useful, for example, in the analysis of sub-auroral ELF hiss emissions from the measurements of the Aureol 3 and Freja spacecraft (Lefeuvre et al., 1992; Santolík and Parrot, 1998, 1999). These different methods often provide us also with estimates of the validity of the initial assumption of the presence of a single plane wave. Different definitions of such an estimator ("degree of polarization", "polarization percentage" or "planarity") have been introduced, based on different descriptions of the coherence of the magnetic components and their confinement to a single polarization plane (Samson, 1973; Pinçon et al., 1992; Santolík et al., 2003). Similar techniques can also allow us to estimate the sense of the magnetic polarization with respect to the ambient stationary magnetic field $\boldsymbol{B}_0$. This has been used, for example, to analyze electromagnetic emissions in the auroral region by Lefeuvre et al. (1986, 1987); Santolík et al. (2001b); Santolík and Gurnett (2002), using the data of the Aureol 3, Interball 2, and Polar spacecraft.

The above mentioned SVD technique can also be used with both the measured magnetic and electric components. In that case, an "average" solution to an over-determined set 36 equations derived from Eq. (2) is estimated. This allows us to determine also the sign of $\hat{\boldsymbol{\kappa}}$, i.e., to distinguish between the two antiparallel wave vector directions (for more details, see Santolík et al., 2003). This technique also allows us to estimate the validity of the plane-wave assumption, but this time it is defined as a measure of closeness of the observed wave fields to Eq. (2). This determination of the "electromagnetic planarity" was, for example, used by Santolík et al. (2004) to estimate the dimension of the source of chorus emissions from the data of the four Cluster spacecraft.

2.2. Wave distribution function

The wave distribution function (WDF) analysis is useful when the wave field is more complex, for example when waves from two distant sources are simultaneously detected by a spacecraft. The WDF, defined as a continuous distribution of wave energy with respect to

the wave vector direction (see a review of Storey, 1999), was introduced by Storey and Lefeuvre (1974). The theoretical relation of the WDF to the experimentally measurable spectral matrix has been called the WDF direct problem. Supposing a continuous distribution of elementary plane waves at a frequency f having no mutual coherence and a narrow bandwidth Δf, the relationship between the spectral matrix $S_{ij}(f)$ and the WDF $G_m(f,\theta,\phi)$ is given by

$$S_{ij}(f) = \sum_m \oint a_{mij}(f,\theta,\phi) G_m(f,\theta,\phi) d^2\boldsymbol{\kappa}, \tag{13}$$

where m represents the different simultaneously present wave modes. The integration is carried out over the full solid angle of wave normal directions $\boldsymbol{\kappa}$, and for a given wave mode m the integration kernels a_{mij} are calculated from

$$a_{mij}(f,\theta,\phi) = \Delta f \ \frac{\xi_{mi}(f,\theta,\phi)\xi^*_{mj}(f,\theta,\phi)}{u_m(f,\theta,\phi)}, \tag{14}$$

where ξ_{mi}, ξ_{mj} (complex amplitudes of the ith and jth elementary signals of the wave electric or magnetic fields), and u_m (energy density) correspond to an elementary plane wave propagating in a mode m with a normal direction defined by θ and ϕ. f represents the Doppler-shifted frequency in the spacecraft frame. The complex amplitudes of the wave electric or magnetic fields can be calculated by considering the physical properties of the medium. This requires the knowledge of the theoretical solutions to the wave dispersion relation. Characteristics of the particular wave experiment should be also taken into account.

The theory of the WDF direct problem for the cold-plasma approximation has been developed by Storey and Lefeuvre (1979, 1980), and revisited by Storey (1998). This basic theory has been used by Lefeuvre (1977); Lefeuvre and Delannoy (1979); Delannoy and Lefeuvre (1986) to develop practical methods for estimation of the WDF from the spacecraft measurements (the WDF inverse problem). Using a slightly different definition of the WDF and abandoning the explicit dependence of the WDF on the wave frequency, Oscarsson and Rönnmark (1989) introduced the hot plasma theory to the WDF reconstruction techniques. Santolík and Parrot (1996) used the hot plasma theory for the frequency-dependent WDF and further investigated the influence of the Doppler effect. Santolík and Parrot (2000) compared different techniques for resolution of the WDF inverse problem, mainly based on the minimization of the least-squares type merit function, in the context of the plane-wave estimates.

The WDF techniques have been used in numerous studies with both ground based and spacecraft data. For instance, Lefeuvre and Helliwell (1985); Parrot and Lefeuvre (1986); Storey et al. (1991) used the multi-component measurements of the GEOS spacecraft to characterize the WDF of the ELF chorus and hiss emissions on the equatorial region. Based on the data of the Aureol 3 and Freja spacecraft, Lefeuvre et al. (1992) and Santolík and Parrot (1998, 2000), respectively, estimated the WDF of the down-coming ELF hiss in the sub-auroral region. The up-going funnel-shaped auroral hiss has been investigated by Santolík and Gurnett (2002) using the WDF analysis of measurements of the Polar spacecraft. Simultaneous WDF estimation of the Z-mode and the whistler mode in the auroral region has been done by Santolík et al. (2001b), based on the data of the Interball 2 spacecraft.

2.3. Backward ray tracing

To obtain information on the sources of observed wave emissions we can follow the corresponding rays backward from the point of observation. The procedure can be initialized by a wave normal direction $\boldsymbol{k}$ found experimentally.

For a given dispersion relation

$$\omega = \omega(\boldsymbol{x}, \vec{k}, t), \tag{15}$$

where $\omega = 2\pi f$, we have, under the approximation of the geometric optics,

$$\frac{d\boldsymbol{x}}{dt} = \frac{\partial\omega}{\partial\boldsymbol{k}}, \tag{16}$$

$$\frac{d\boldsymbol{k}}{dt} = -\frac{\partial\omega}{\partial\boldsymbol{x}}. \tag{17}$$

These two equations can be numerically integrated to obtain evolution of the position of the ray $\boldsymbol{x}$ and the corresponding wave vector $\boldsymbol{k}$ as a function of the group time t. When the ray hits a predefined boundary, for example the approximate altitude of the ionospheric F2 layer, the procedure stops and the exit point of the ray is obtained.

Basic limitation of the method is the Wentzel-Krammers-Brillouin (WKB) approximation or limit of geometric optics. It limits the dispersive properties of the medium to slowly varying functions of space and time compared to the wavelength and wave period. This approximation fails if sharp gradients are present in the plasma and/or refractive index rapidly changes (e.g. near cutoffs and resonances).

The method also needs a realistic description of the medium in any point along the obtained ray, including the model of the magnetic field, the ion composition, and the density profile. On the practical level, we can use procedures for the magnetic field model which have been already adopted for the DEMETER project (Santolík, 2003a). The need of a realistic plasma density and composition model is a much more complicated requirement, since a possible presence of density inhomogeneities can be very important for results of the backward ray tracing. As the first approximation we can use the diffusive equilibrium model, and, subsequently, the cold plasma approximation to calculate the dispersion relation (15), as it has been implemented by Cairó and Lefeuvre (1986). This procedure was, for instance, recently used by Parrot

et al. (2004a,b) to analyze the sources of reflected chorus emissions observed by the Cluster space-fleet.

3. Tools for analysis of the DEMETER data

3.1. SWAN

Software for waveform analysis (SWAN) is fully interactive software designed for the visualization and analysis of scientific and engineering data (Lagoutte et al., 2000). The main objective is to facilitate satellite data processing providing with a package of analysis tools. The package implements a number of techniques based on waveform signals. For example, it contains the waveform viewer, spectrum analysis using the fast Fourier transform, wavelet analysis (e.g. Lagoutte et al., 1992), mutual information analysis, bi- and tri-coherence analysis, and plane wave methods of Means (1972) and McPherron et al. (1972) including estimators of ellipticity and degree of polarization.

A tool dedicated to analysis of level 1 data of the DEMETER mission (namely waveforms of the electric and magnetic fields in physical units) has been developed. Thanks to this tool, it is possible to select data by giving the period of time to analyze, the sensors (electric or/and magnetic), the bandwidths (ULF, ELF, VLF or/and HF) for each sensor and the directory where data are stored.

For each bandwidth, component(s) name(s), the data coordinate system, the presence of data attitude and the time discontinuities are described. Then, the period of time can be chosen more precisely, for instance to select waveforms with available data attitude. Depending on the characteristics of the data (component name, data coordinate system), it is possible, for instance, to improve the calibration. This operation consists in increasing the number of samples of the transfer function which converts voltage components into physical values. Moreover, for electric data, electron density and electron temperature used to compute the transfer function can be chosen by the user. It is also possible to change the coordinate system (sensor, satellite or geomagnetic) if the matrices of transformation are available.

DEMETER measurements are disturbed by onboard electronic devices. Interferences are present at two fundamental frequencies, 7.33 and 19.53 Hz, and their harmonics. In the tool for waveform data analysis of SWAN, the following method is used to suppress a part of these interferences.

We consider a signal $y(t)$. For each harmonic frequency kf_0 (where f_0 is the fundamental frequency), a comparison between the spectrum of $y(t)$ and a moving average of this spectrum is used to determine whether an interference is present or not. If a peak is detected, it is considered that there is an interference that has the form of

$$y_k(t) = A_k \cos(2\pi k f_0 t + \Phi_k). \quad (18)$$

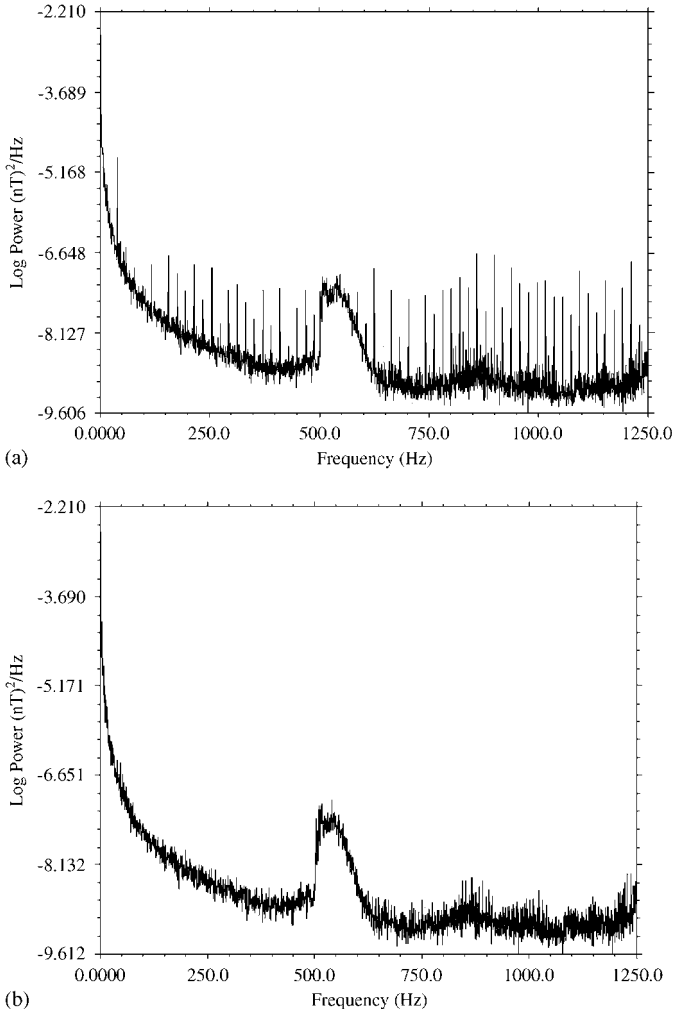

Fig. 1. Example of suppression of interferences for ELF data measured onboard DEMETER: (a) power spectrum of original signal $y(t)$; (b) power spectrum of the corrected signal $y_c(t)$.

A_k and Φ_k are estimated with an adaptive method based on spectrum calculation. The corrected signal is given by

$$y_c(t) = y(t) - \sum_k A_k \cos(2\pi k f_0 t + \Phi_k). \quad (19)$$

Fig. 1shows results of this analysis on an example data interval.

3.2. PRASSADCO

Propagation analysis of STAFF-SA data with coherency tests (PRASSADCO) is a computer program which calculates characteristics of electromagnetic waves from measurements of their electric and magnetic fields (Santolík, 2003b). The original purpose of PRASSADCO was to facilitate scientific analysis of data obtained by the STAFF-SA devices (spatio-temporal analysis of field fluctuations, spectrum analyzer) on board the four satellites of the Cluster mission (Cornilleau-Wehrlin et al., 2003). The program can however process arbitrary data containing

three-axial measurements of the magnetic field fluctuations. It also includes methods analyzing simultaneously the magnetic filed and electric field wave data.

It implements a number of methods used to estimate polarization and propagation parameters, such as the degree of polarization, planarity of polarization, sense of elliptic polarization and axes of polarization ellipse, the wave vector direction, electromagnetic planarity, the Poynting vector, and the refractive index (Means, 1972; McPherron et al., 1972; Samson, 1973; Samson and Olson, 1980; Santolík et al., 2003, 2001a). Tests have been made with simulated data as well as with the received data of the STAFF-SA instrument. The program was also used to process the data of the MEMO (Interball), HFWR (Polar), PWI (Cassini), and STAFF (Double Star) instruments. Data processing is done in the frequency domain, and a previous spectral analysis of multi-component measurements is supposed. The program is designed to produce both preview and publication-quality figures in different formats and/or to store the results in a numerical form.

For the DEMETER project, we have designed an interface to the DEMETER measurements of the high resolution waveforms of the magnetic and electric components. It is thus possible, for the data acquired during burst-mode periods, to use the entire set of analysis methods described by Santolík (2003b), including all the plane-wave methods mentioned in Section 2.1. Using the output of the PRASSADCO program, the WDF and backward ray-tracing methods described in Sections 2.2 and 2.3 can be also used.

4. Examples of analysis of multi-component wave measurements of the DEMETER spacecraft

The altitude of the DEMETER spacecraft is somewhat lower but still similar to the altitude of the Aureol 3 and Freja spacecraft. Results of the multi-component analysis of ELF electromagnetic waves measured on board those two spacecraft can be thus compared with the results obtained from the DEMETER wave measurements.

The first example in Fig. 2 shows results of analysis of data recorded in the ELF burst mode on 31 August 2004. An example of line plots corresponding to a vertical cut of Fig. 2 at 01:30 UT are shown in Fig. 3. The first two panels 2a and 2b represent the sum of the power-spectral densities of the three magnetic and three electric components, respectively. We can see that power spectra of both magnetic and electric fluctuations exhibit a sharp lower cutoff at a frequency which is by 100–150 Hz lower than the local proton cyclotron frequency (calculated from the IGRF 2000 model (Macmillan and Quinn, 2000) and shown by the nearly horizontal black lines plotted over the spectrograms).

This cutoff has been explained by Gurnett and Burns (1968) considering a mode structure connected to the presence of multiple ion species. Downward propagating right-hand polarized whistler-mode hiss encounters increasing magnetic field strength and hence increasing proton cyclotron frequency (f_{H+}). In a plasma containing a fraction of hydrogen ions, together with other ion species, the waves also encounter a multi-ion cross-over frequency (f_{co}) below f_{H+}, where the polarization changes from right-hand to left-hand (Smith and Brice, 1964). In a three-component plasma containing the electrons, hydrogen ions, and oxygen O^+ ions (we neglect here possible traces of helium ions which could be present at the DEMETER altitude), the cross-over frequency reads

$$f_{co} = f_{H^+} \frac{\sqrt{1 + P_O(R_{OH}^2 - 1)}}{R_{OH}}, \tag{20}$$

where P_O is the relative fraction of oxygen ions, and $R_{OH} \approx 16$ is the ratio of masses of oxygen to hydrogen ions.

This polarization crossover affects waves with all the possible wave vectors directions except those directed along the field lines. Subsequently, a left-hand mode cutoff frequency ($f_{L=0}$) is encountered,

$$f_{L=0} = f_{H^+} \frac{1 + P_O(R_{OH} - 1)}{R_{OH}}. \tag{21}$$

At this cutoff frequency the left-hand polarized waves are reflected. The majority of wave energy thus cannot propagate below the $f_{L=0}$ frequency, forming a sharp lower cutoff. The same cutoff has been also observed by a number of previous low-orbiting spacecraft, for instance Aureol 3 or Freja (Lefeuvre et al., 1992; Santolík and Parrot, 1999).

As follows from Eq. (21) the position of the cutoff frequency can be used for an independent estimate of the ion composition. For example, at 01:30 UT we observe the cutoff at $f_{L=0} \sim 355$–360 Hz, while the IGRF 2000 model gives us the proton cyclotron frequency of $f_{H^+} = 459$ Hz. This, using Eq. (21), corresponds to 76–77% of O^+. Simultaneous direct measurement of ion composition done by the IAP instrument (Berthelier et al., 2006b) gives the total density of 3.24×10^4 cm^{-3} with 78% of O^+, 20% of H^+, and 2% of He^+ (see Fig. 4). These results thus very well correspond to the observed cutoff.

Fig. 2c further supports this explanation showing the estimator of the polarization sense. A method defined in Eq. (4) of Santolík et al. (2001a) has been used. It consists of a statistical estimate of the imaginary part of the cross-spectrum of the two magnetic components perpendicular to $\boldsymbol{B}_0$ normalized by the standard deviation of the same cross-spectrum. Positive values mean right-hand polarization while negative values mean left-hand polarization. The absolute values of the results reflect the reliability of the estimates. The results are plotted only when the magnetic field power spectral density is higher than 10^{-7} nT^2 Hz^{-1}. The polarization is right handed in the entire time–frequency interval where the intense waves are observed, with an exception of a narrow frequency interval just above the cutoff frequency. In this interval, between the $f_{L=0}$ frequency and the cross-over frequency f_{co} we observe

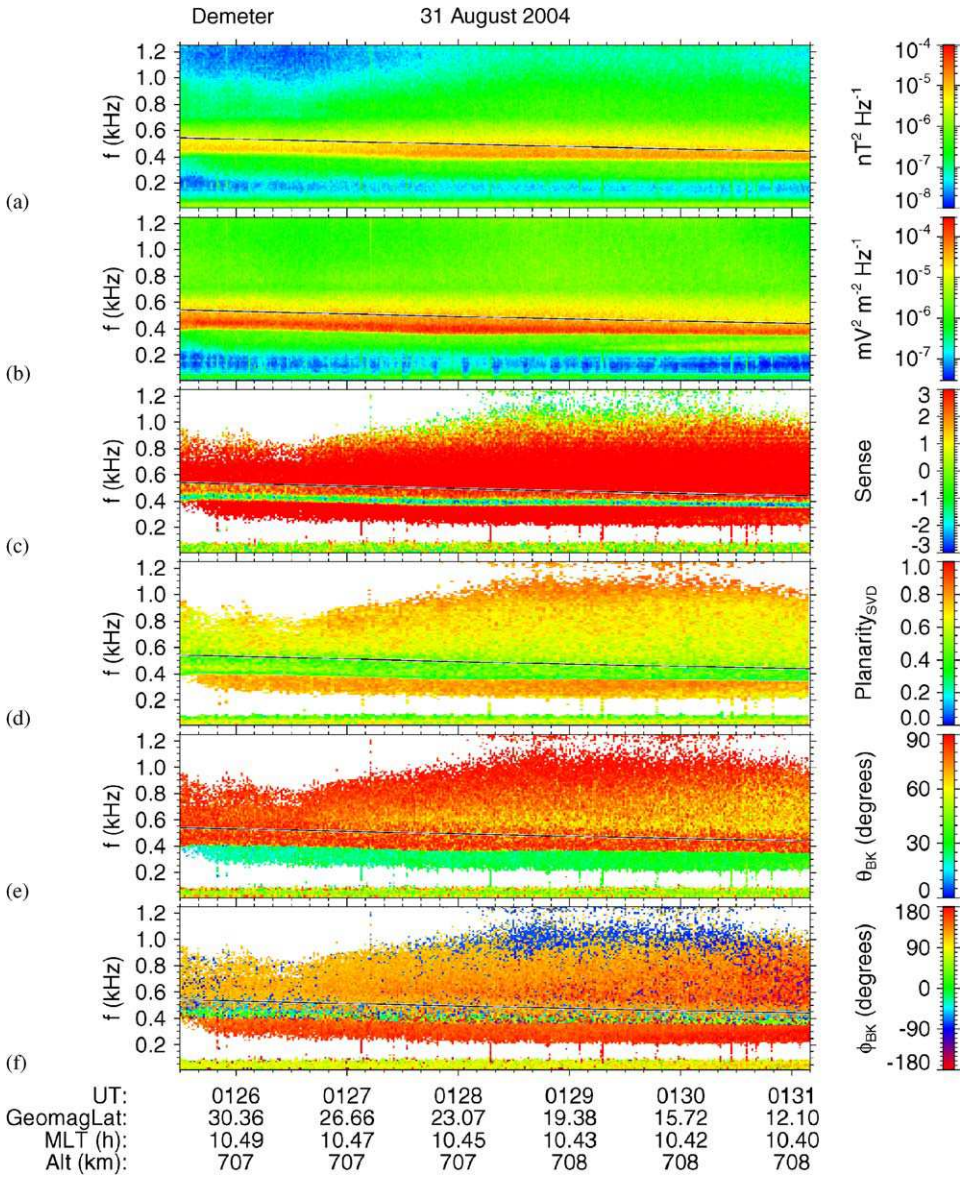

Fig. 2. Example of analysis results for multi-component ELF data measured onboard DEMETER on 31 August 2004: (a) power-spectrogram of the magnetic field fluctuations; (b) power-spectrogram of the electric field fluctuations; (c) sense of the magnetic field polarization—positive numbers mean right-hand sense; (d) planarity of the magnetic field polarization from the SVD method; (e) angle between the wave vector and the stationary magnetic field obtained by the SVD method; (f) angle azimuth of the wave vector obtained by the SVD method—0° corresponds to the local magnetic meridian plane, outward from the Earth and 90° corresponds to the direction of increasing magnetic local time. Black lines plotted over the panels (a)–(f) between 450 and 550 Hz show the local proton cyclotron frequency at the spacecraft position. Position of the spacecraft is given on the bottom. Alt—altitude in kilometers; GeomagLat—magnetic dipole latitude in degrees; MLT—magnetic local time in hours.

left-hand polarized waves, as it could be expected from the above scenario. Eq. (20) gives $f_{co} = 400$–403 Hz which well corresponds to the observations. Similar results have been obtained from the analysis of multi-component measurements of the Aureol 3 (Lefeuvre et al., 1992) and Freja spacecraft (Santolík and Parrot, 1999).

The difference compared to these measurements is that the waves are observed at lower latitudes by DEMETER. It has been shown (Lefeuvre et al., 1992; Santolík and Parrot, 1999, 2000) that waves with a similar cutoff signature exhibit a divergent propagation pattern. They were observed to propagate along the magnetic field lines downward to the Earth at magnetic latitudes between 60° and 65°, and with inclined wave normal angles at both higher and lower latitudes. Subsequently, reflected waves on both poleward side and equatorward side were observed.

The reflection process most probably still takes place at lower magnetic latitudes between 12° and 30°, as it is shown by low values of the SVD planarity estimator in Fig. 2d (see Section 2.1). The results are again plotted only when the magnetic field power spectral density is higher than $10^{-7}\,\mathrm{nT^2\,Hz^{-1}}$. Below the cutoff, the planarity is approximately 0.8 which is consistent with the polarization

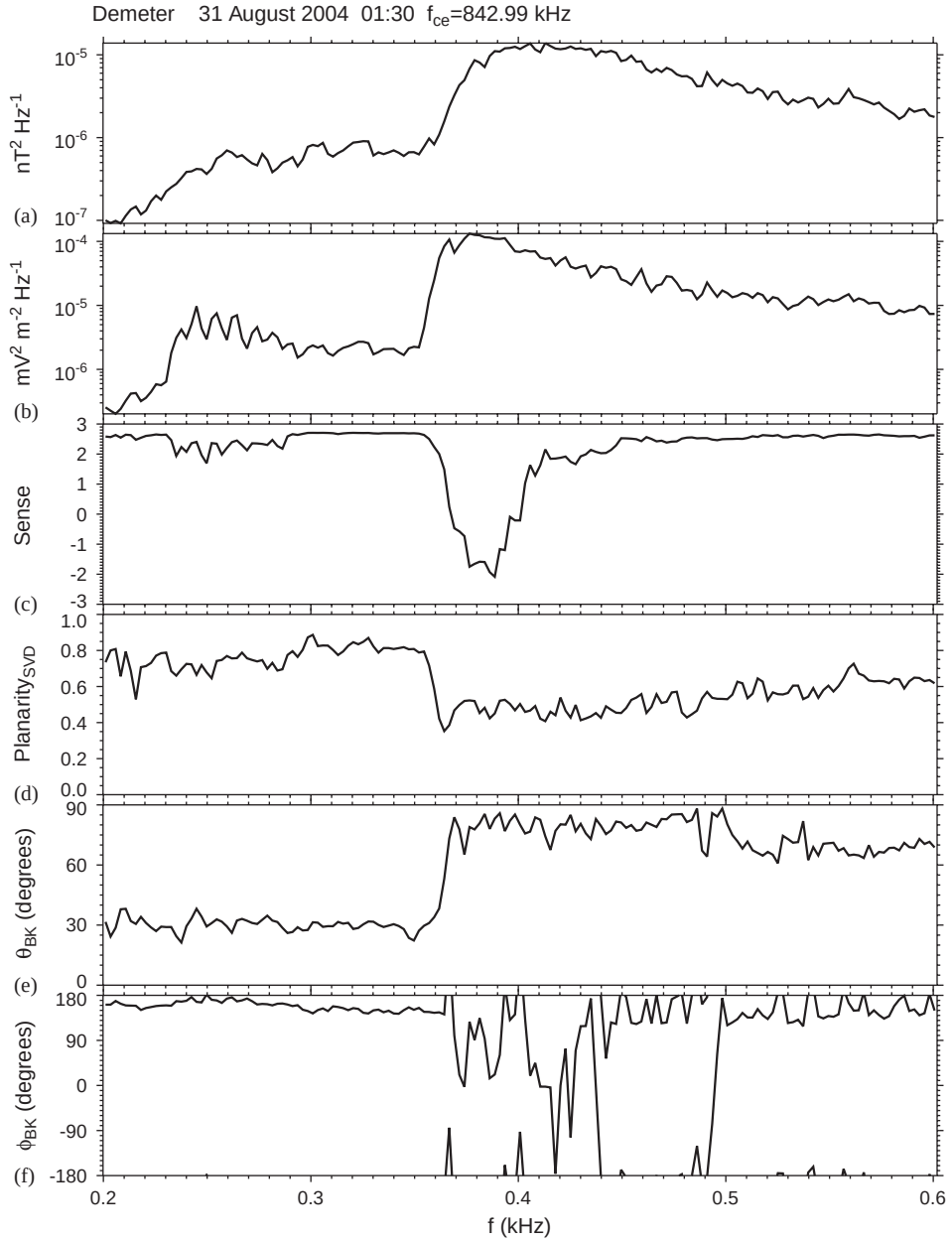

Fig. 3. Example of analysis results shown as line plots as a function of frequency from measurements recorded on 31 August 2004 at 01:30 UT. The resulting parameters plotted in panels (a)–(f) are the same as those in Fig. 2.

close to that of a single plane wave. Above the cutoff, however, the planarity abruptly decreases down to values of 0.4–0.5. These values correspond to a more complex wave field, consistent with the simultaneous presence of both the direct and reflected components.

The wave vector direction has been estimated from the three-axial measurements of the magnetic field fluctuations by the SVD method. The results are shown in Figs. 2e–f, again only for waves that are more intense than $10^{-7}\,nT^2\,Hz^{-1}$. The angle deviation of the wave vector from $\boldsymbol{B}_0$, shown in Fig. 2e, indicates very high wave normal angles above the cutoff and, abruptly, much lower wave normal angles below the cutoff. This can be explained by a scenario in which the weaker right-hand polarized waves below the cutoff originate by tunneling of the wave energy below the cross-over frequency. Staying in the right-hand polarized mode, they naturally penetrate also below the $f_{L=0}$ cutoff (Santolík and Parrot, 1998). Fig. 2f, showing the azimuth of the wave vector measured around the direction of the stationary magnetic field, indicates propagation close to the local meridian plane, both above and below the cutoff.

Fig. 5 shows another wave phenomenon which was not observed at higher latitudes by previous spacecraft equipped with multi-component devices. The data have been recorded by DEMETER on 15 September 2004, again

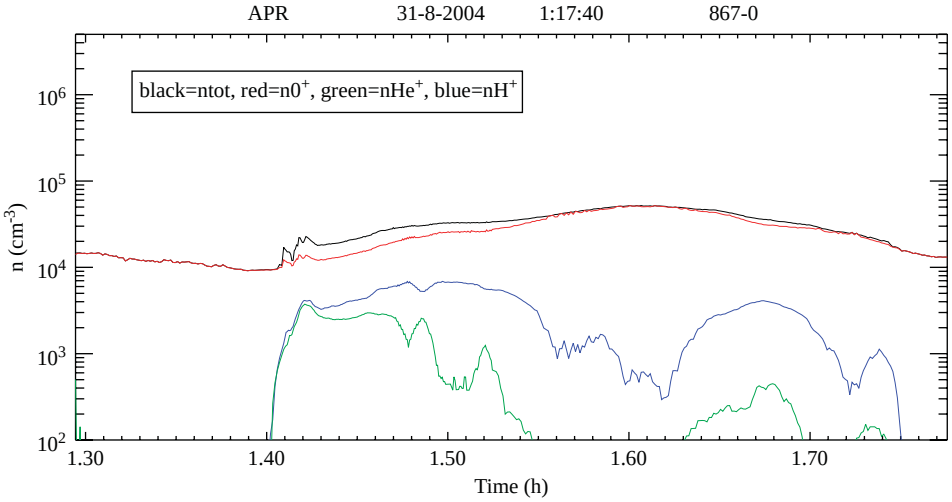

Fig. 4. Measurements of ion density onboard DEMETER on 31 August 2004 (black line) total number density, (red line) number density of O^+ ions, (blue line) number density of H^+ ions, (green line) number density of He^+ ions. Time is given on the bottom in hours from the beginning of the day.

during the ELF burst mode interval. Essentially the same types of emissions have been observed as in Fig. 2, including the right-hand polarized waves above f_{H+} propagating at high wave normal angles, the polarization crossover and the sharp lower cutoff just below f_{H+}, and, well below f_{H+}, the right-hand polarized waves at lower wave normal angles. This type of waves, however, manifests different properties than waves at similar frequencies observed at higher latitudes (see a statistical study of Santolík and Parrot, 1998). These first DEMETER observations often show rather intense waves well separated from the hiss emissions above f_{H+} by a frequency gap of decreased power. The waves propagate in the plane of the local meridian with wave normal angles increasing as the spacecraft moves toward the magnetic equator. These waves can have similar origin (tunneling below the crossover frequency) as the waves at higher latitude. Their propagation to lower latitudes will be investigated in detail and we will report the results in a future paper.

Fig. 6 shows yet another wave phenomenon which is quite often observed by DEMETER. The waves with a sharp upper cutoff at the local f_{H+} can be identified as proton whistlers, described for the first time by Gurnett et al. (1965). This interpretation also corresponds to their predominantly left-hand polarization sense (Fig. 6c). The occasional right-hand polarization sense below the local f_{H+} corresponds to the associated electron whistlers (see, e.g., Fig. 7 of Santolík and Parrot, 1999). Note that only the right-hand polarized electron whistlers are observed above f_{H+}. Both types of whistlers mainly propagate at lower wave normal angles (Fig. 6e) in the plane of the local magnetic meridian, with the azimuth apparently changing by 180° between 04:45 and 04:46 UT (at geomagnetic latitudes of ~20°). This change of azimuth may correspond to the passage through a region magnetically connected to the ionospheric region over the thunderstorms from which the waves propagate.

The last example are wave emissions observed on 21 January 2005 which are shown in Fig. 7. The format of this figure is the same as for the previous cases. An emission with a sharp lower cutoff just below the local f_{H+} and also right-hand polarized waves above 200 Hz are the same types of emissions as we have already shown in Figs. 2 and 5, except that, in this case, the wave intensity is much weaker. From the beginning of the data record until 02:17 UT we also observe a narrow-band emission at a constant frequency of ≈ 140 Hz. This type of waves is not usually observed by DEMETER. This data record precedes by nearly 3 days an earthquake of magnitude 6.2 which occurred at a geographical latitude of 1.22°S, and longitude of 119.8°E on 23 January, 2005 at 20:10:11 UT. Note that there is no proof of any direct nor indirect connection of the observed waves with this earthquake. The only objective observation is that this DEMETER data record coincides with the position of the earthquake activity. We believe that only a systematic statistical analysis of a large number of observations can give an answer to the question if such a connection is at all possible. Although we are far from believing that this case shows an earthquake precursor, this example will be used to demonstrate the some additional possibilities for a detailed analysis of the DEMETER wave measurements.

The arrows in Fig. 7 indicate an interval selected for the detailed analysis: in the time interval between 02:16:25 and 02:16:30 and in the frequency interval between 135 and 145 Hz, the spectral matrices were averaged and the result has been subjected to both the plane-wave and WDF analysis. We can see in Figs. 7a–c that the narrow-band emission is electromagnetic and right-hand polarized. Fig. 7d shows that the planarity of polarization is relatively high (≈ 0.8). We can thus expect that the wave field will be close

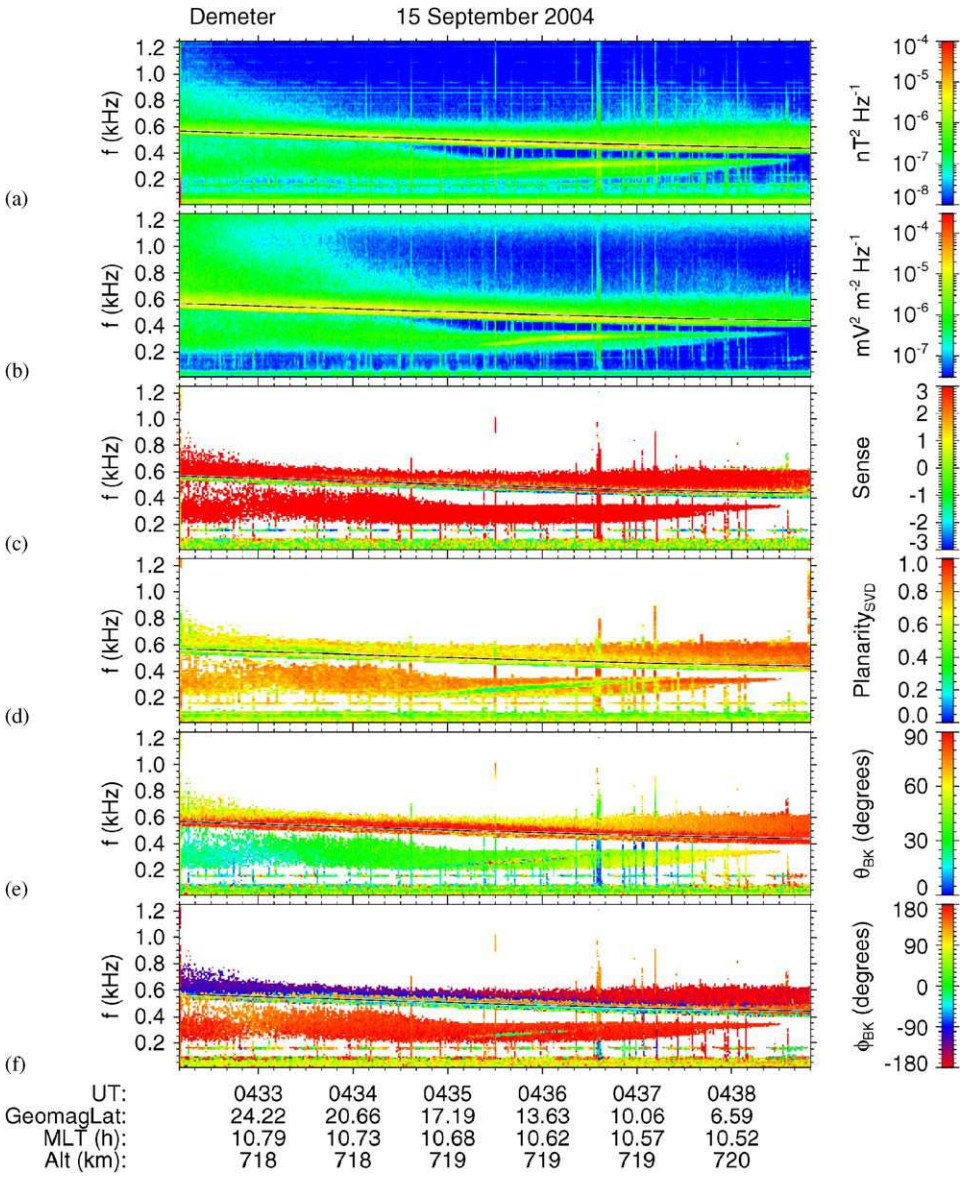

Fig. 5. Example of analysis results for multi-component ELF data measured onboard DEMETER on 15 September 2004. The panels are the same as in Fig. 2. The results in panels (c)–(f) are plotted only when the magnetic field power spectral density is higher than 10^{-7} nT^2 Hz^{-1}.

to that of a single plane wave. Figs. 7e and f indicate that the wave vector of this wave is oblique with respect to $\boldsymbol{B}_0$ and that the wave propagates close to the plane of the local magnetic meridian. The plane wave analysis of the averaged spectral matrix gives the wave vector deviated by $\theta = 54.2^\circ$ from $\boldsymbol{B}_0$ and with an azimuth $\phi = 343.8^\circ$. These values have been obtained by the SVD technique (Santolík et al., 2003). The method of Means (1972) gives very similar results ($\theta = 53.8^\circ$, $\phi = 342.9^\circ$), indicating a good validity of the plane-wave assumption. Note that these last results are based on the measured magnetic field fluctuations and that we additionally used the simultaneously measured electric field data to remove the 180° ambiguity from the determination of the wave vector direction.

We have used the same input data for the WDF analysis (see Section 2.2). This method is based on theoretical calculation of the integration kernels from the parameters of the plasma medium. We thus need to estimate the local plasma composition and density. At 02:16:30 UT, Eq. (21) gives 88–89% of O^+ for the observed $f_{L=0} = 392$–398 Hz and $f_{H+} = 443$ Hz. This is also consistent with the observed change of polarization sense at 416–418 Hz, obtained from Eq. (20). Indeed, direct measurements of the ion density by the IAP instrument are consistent with these results (Fig. 8), giving, at 02:16:30 UT, the total density of of 2.7×10^4 cm^{-3} with 90% of O^+, 10% of H^+, and less than 0.1% of He^+. These values are sufficient to perform the WDF analysis based on the cold plasma theory.

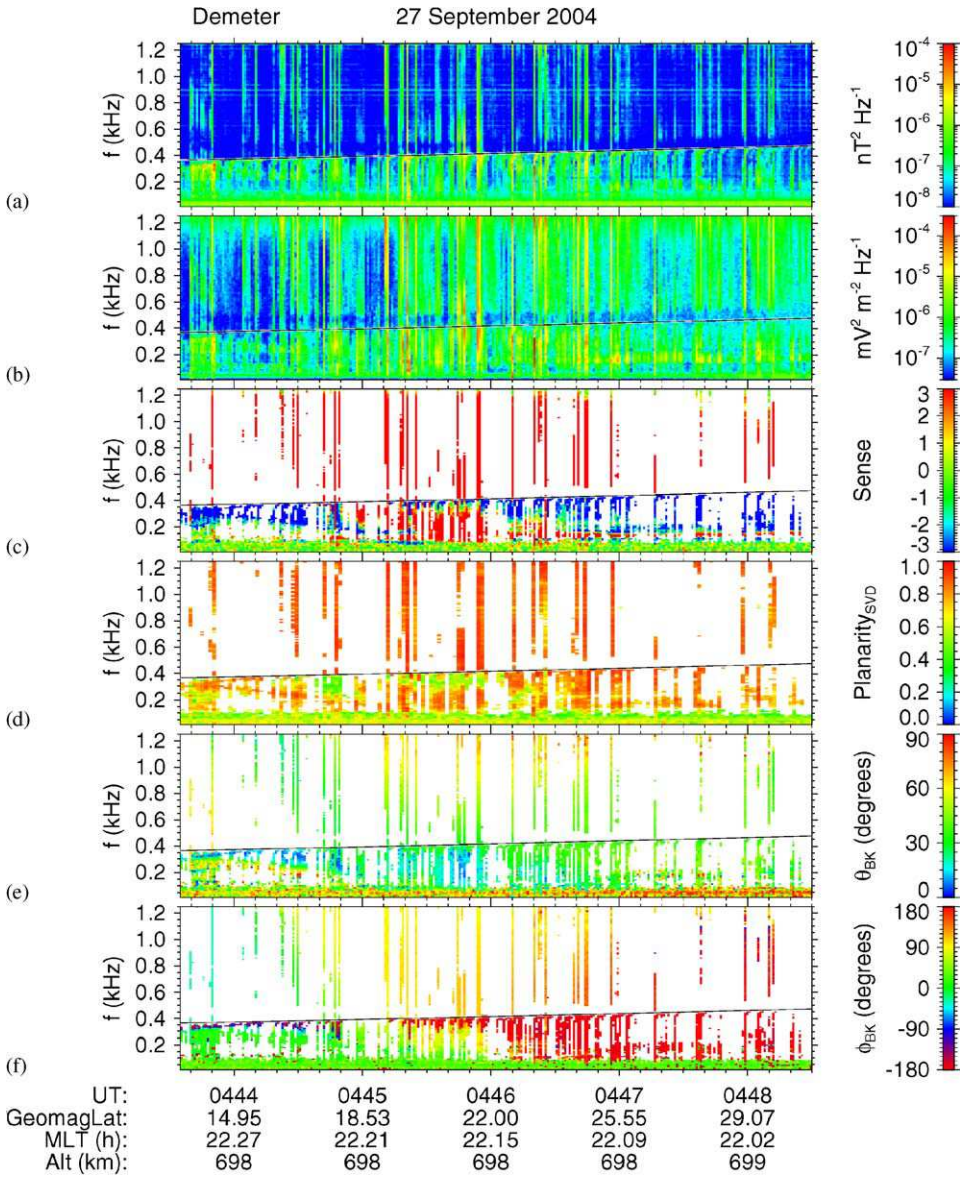

Fig. 6. Example of analysis results for multi-component ELF data measured onboard DEMETER on 27 September 2004. The panels are the same as in Fig. 2. The results in panels (c)–(f) are plotted only when the magnetic field power spectral density is higher than $10^{-7}\,\mathrm{nT^2\,Hz^{-1}}$.

Fig. 9 shows the results obtained by two different techniques to estimate the WDF. For comparison, the plane-wave SVD estimates are over-plotted as small white squares. We have used the WDF model of one Gaussian peak and an optimized model of discrete regions (see Santolík and Parrot, 2000, for more details). Both techniques give distributions of the wave energy density which are strongly concentrated at wave vector directions surrounding the plane-wave estimate. These results indeed show that the assumption of the presence of a single plane wave is very close to be valid. Note that we again used the measurements of the magnetic field fluctuations. The simultaneously measured electric field data have been used to select the hemisphere of wave vector directions for the analysis.

The WDF analysis can also give us an estimate of the energy carried by the waves. The integral spectral density of the energy density from both techniques is $u = 6 \times 10^{-20}\,\mathrm{J\,m^{-3}\,Hz^{-1}}$. Since we know that the waves propagate in the right-hand mode, we can, again using the cold plasma theory, calculate the group velocity, $v_g = 3.69 \times 10^6\,\mathrm{m\,s^{-1}}$ for $\theta = 54^\circ$. Note that the group velocity is for this wave vector direction much less deviated from $\boldsymbol{B}_0$, by an angle $\theta_g = 22^\circ$. The integral spectral density of the energy flux can then be obtained, $p = uv_g = 2.2 \times 10^{-13}\,\mathrm{W\,m^{-2}\,Hz^{-1}}$. This is consistent with the Poynting flux estimated from the measured field components. With the bandwidth of the emission of $\approx 15\,\mathrm{Hz}$, the total energy flux in these waves is $P \approx 3.3\,\mathrm{pW\,m^{-2}}$.

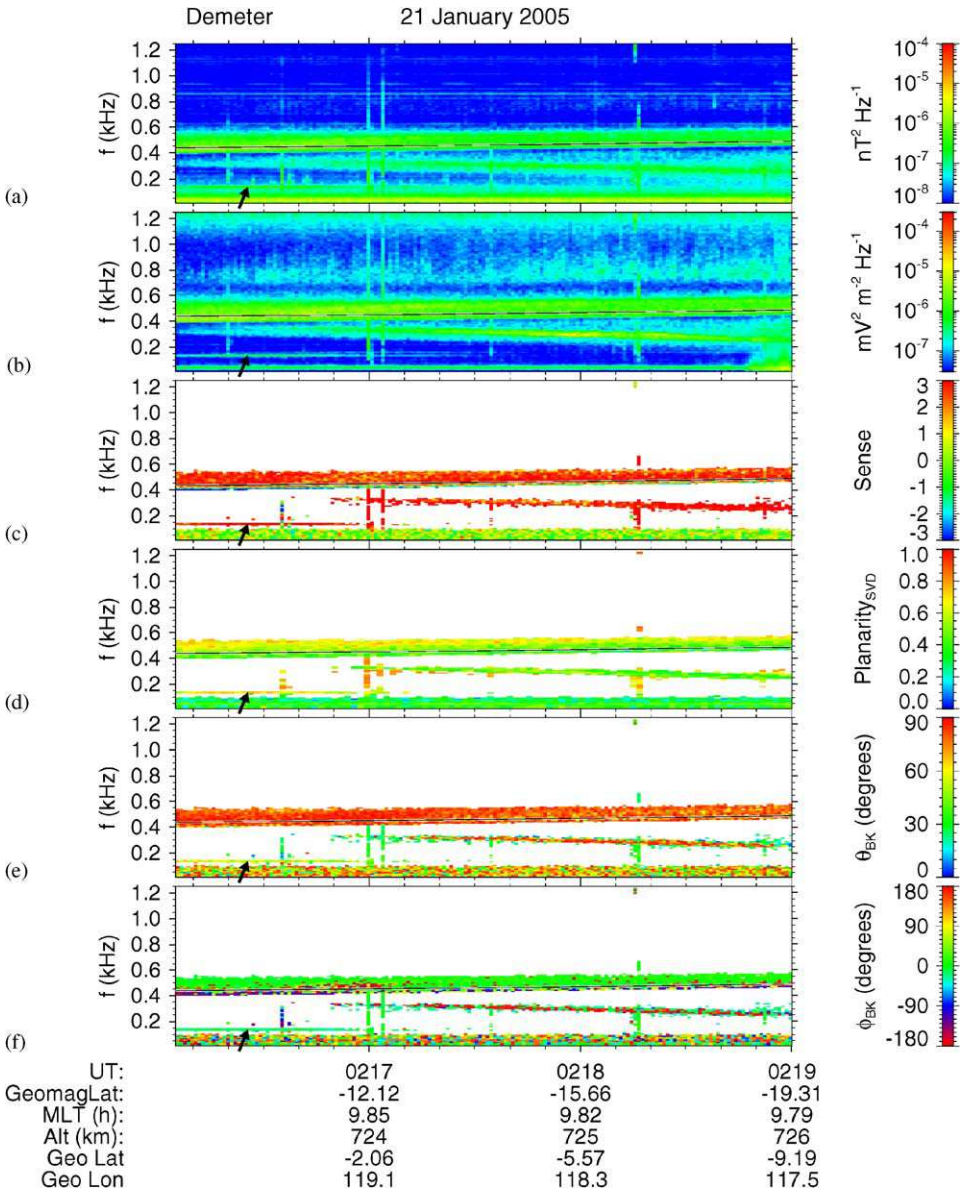

Fig. 7. Example of analysis results for multi-component ELF data measured onboard DEMETER on 21 January 2005. The panels are the same as in Fig. 2. The results in panels (c)–(f) are plotted only when the magnetic field power spectral density is higher than 10^{-7} nT^2 Hz^{-1}. Black arrow indicates wave emission selected for further analysis (see text). In addition to the geomagnetic coordinates given already on the bottom of Fig. 2, geographic latitudes and longitudes are shown on the bottom.

As these relatively weak waves are well defined by a single wave vector, we can use its direction as an input for the backward ray-tracing procedure described in Section 2.3. This will allow us to estimate the position of the source of these waves. To follow the ray back toward the source region, we need a description of the plasma parameters along its path. As the first approximation we use the diffusive equilibrium model calibrated using the ion composition and plasma density measured at the spacecraft orbit. We use the same local plasma parameters as for the WDF analysis. For the diffusive equilibrium model, we suppose a temperature of 1000 K at 1000 km of altitude.

Fig. 10 shows the results. The geomagnetic latitude and altitude of the ray path is plotted in the plane of the local magnetic meridian. We integrate the ray equations from the spacecraft position (on the top left) until the ray reaches the ionosphere defined for this purpose as the 300-km altitude level. This happens at a place located by $\approx 3.5^\circ$ of magnetic latitude to the South from the spacecraft position, and approximately on the same magnetic meridian. At this moment the wave has propagated for the total group time of 0.44 s and its wavelength changed from the initial value of 12 km at the spacecraft level down to 2.2 km in the ionosphere. The wave vector direction also changed during the propagation, as we show by arrows placed along the ray path at intervals of 0.1 s of the group time. Note that these arrows indicate the wave vectors for the original forward wave. At the 300-km level, the wave

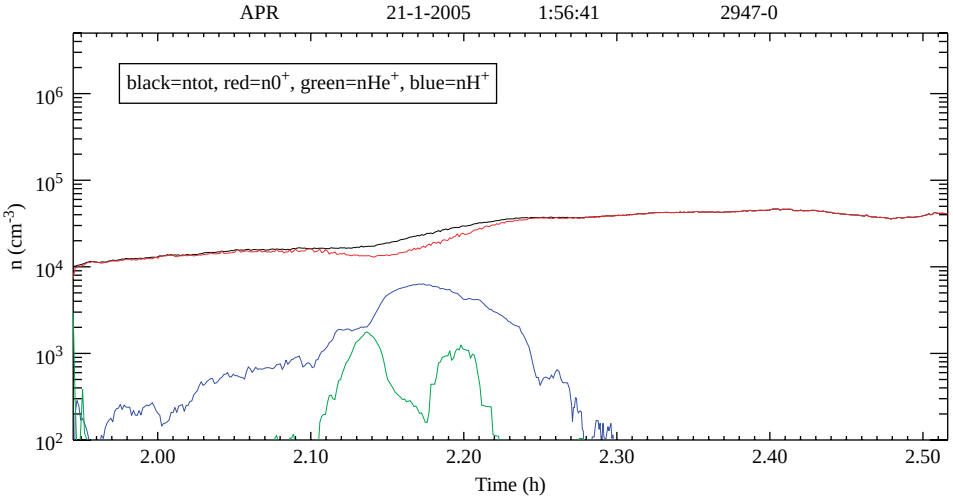

Fig. 8. Measurements of ion density onboard DEMETER on 21 January 2005: (black line) total number density, (red line) number density of O^+ ions, (blue line) number density of H^+ ions, (green line) number density of He^+ ions. Time is given on the bottom in hours from the beginning of the day.

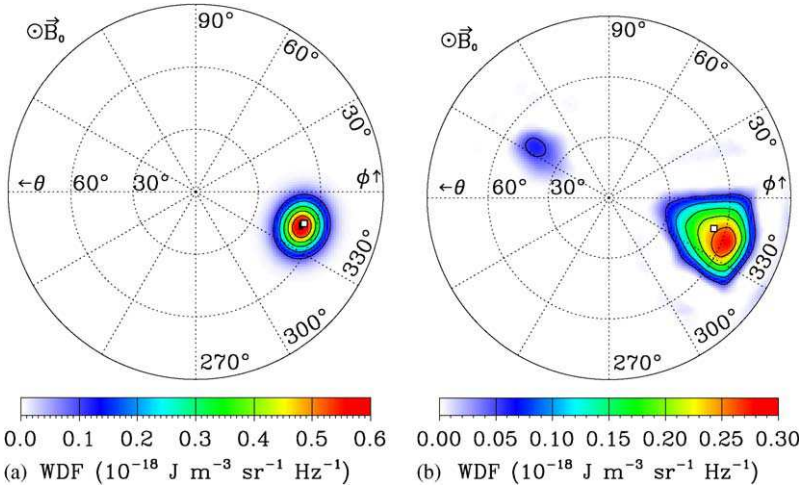

Fig. 9. Results of the wave distribution function (WDF) analysis of multi-component ELF data measured onboard DEMETER on 21 January 2005 between 02:16:25 and 02:16:30, and in the frequency interval between 135 and 145 Hz (indicated by black arrows in Fig. 7). (a) Polar plot of the WDF estimated using the model of one Gaussian peak. On this plot, the direction of the local magnetic field $\boldsymbol{B}_0$ is in the center of the circle, θ is the polar angle, and ϕ is the azimuth. (b) Similar plot of the WDF estimated using the model of discrete regions. Small white squares on both plots show the wave vector direction estimated by the SVD technique.

vector is almost vertical to the Earth's surface. This might be consistent with propagation from a low-altitude tropospheric source, where the refractive index should be close to 1. Subsequent penetration of the wave energy through the ionosphere, where the refractive index strongly increases (Helliwell, 1965), requires that the top-side wave vectors are contained in the "transmission cone" of nearly vertical wave vector directions. The short resulting wavelength might also be consistent with an additional possible role of scattering on small-scale density irregularities.

5. Conclusions

Measurements of the recently launched DEMETER spacecraft provide us with state-of-the-art measurements of the fluctuations of the magnetic field and the electric field. These measurements comprise three magnetic and three electric field components. Numerous analysis methods exist to estimate parameters of electromagnetic waves using such multi-component measurements. Methods based on the assumption of the presence of a single plane wave are useful to obtain an overview of the observed wave phenomena. For example, the recently developed techniques based on the singular value decomposition could be easily used for the analysis of the DEMETER data. More general WDF techniques and methods of backward ray-tracing can be used for the detailed interpretation of obtained results.

Basic analysis tools including these methods have been implemented for the DEMETER wave measurements. We

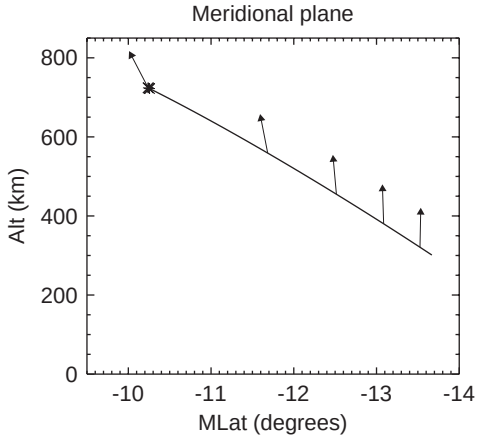

Fig. 10. Results of the backward ray-tracing analysis of the 140-Hz waves observed by DEMETER on 21 January 2005 around 02:16:30 (see Fig. 7). The ray path is shown by its geomagnetic latitude and altitude in the plane of the local magnetic meridian. Asterisk indicates the spacecraft position. Arrows show wave vector directions along the ray path at intervals of 0.1 s of the group time.

show the first results of these analysis techniques based on the DEMETER data, acquired in four different ELF burst mode intervals. The results are comparable to the published results of previous spacecraft, for instance Aureol-3 and Freja, that both were able to record multi-component measurements. Slightly different wave phenomena are observed on DEMETER most probably because the measurements take place on lower latitudes.

We demonstrate three types of ELF wave phenomena which are most frequently observed on DEMETER. The first type of emissions are obliquely-propagating right-hand polarized electromagnetic waves occurring at a few hundreds of Hz. On the power spectrograms, these waves usually show a sharp lower cutoff just below the local proton cyclotron frequency. Analysis of wave polarization then reveals that this cutoff is connected with a multi-ion mode structure below the local proton cyclotron frequency where the polarization becomes left handed at the multi-ion cross-over frequency. The sharp lower cutoff then corresponds to the multi-ion $L = 0$ cutoff of left-hand polarized waves.

The second class of wave phenomena are right-hand polarized waves below the local proton cyclotron frequency. These waves are often rather broad-band but sometimes they also manifest narrow-banded features at varying bandwidths and frequencies. At least a part of these waves most probably originates by tunelling of wave power from the above-described first type of emissions below the multi-ion cross-over frequency. This is consistent with the observed low angular deviations of the wave vectors with respect to the local magnetic field line.

The third class of waves are electron and proton whistlers which are also very frequently observed on DEMETER. We show that these measurements have a great potential for a detailed analysis of wave propagation based on polarization measurements. In the future, these results together with ground-based measurements can lead to a better characterization of the penetration of whistlers through the ionosphere.

We also show a detailed analysis of an unusual narrow-band emission at a constant frequency of 140 Hz, observed very close to a place where an earthquake occurred three days later. It is important to state that we have no reason to believe that these waves are really directly connected to this seismic activity. A systematic statistical study on a large number of cases is under way to investigate if there is any kind of connection between the ELF waves observed on DEMETER and earthquakes. We only use here these observations to demonstrate the possibilities of a detailed analysis using the DEMETER data. We show that the observed narrow-band waves propagate obliquely with respect the ambient magnetic field. They are right-hand polarized while their frequency is well below the local proton cyclotron frequency. For these waves, two different methods of WDF analysis give similar results consistent with the results of the plane-wave techniques. The obtained wave normal direction is used as an initial value for a simulation of backward wave propagation from the point of measurement. Following the ray path back toward the Earth down to the ionospheric altitudes we find that the waves come from a region located a few degrees of latitude to the South from the spacecraft position. Scattering of the wave energy by small-scale ionospheric density irregularities could be a possible mechanism for penetration of these waves from lower altitudes.

These several examples show a great potential of high resolution measurement of the full set of 6 components of the electric and magnetic field on board DEMETER. Future investigation is needed to interpret the observed wave propagation properties.

Acknowledgements

We sincerely thank our colleagues from the DEMETER team in LPCE Orleans and in CNES for construction, calibration and operations of the spacecraft and for fruitful discussions of the data. CNES is thanked for their support of the DEMETER project. F.N. thanks the French Embassy in Prague for supporting his 3-month stay in LPCE Orleans in 2004. Research at the Charles University and at the Institute of Atmospheric physics was supported by grants GAAV IAA301120601 and GACR 205/06/1267.

References

Arthur, C.W., McPherron, R.L., Means, J.D., 1976. A comparative study of three techniques for using the spectral matrix in the wave analysis. Radio Sci. 11, 833–845.

Berthelier, J., Godefroy, M., Leblanc, F., Malingre, M., Menvielle, M., Lagoutte, D., Brochot, J., Colin, F., Elie, F., Legendre, C., Zamora, P., Benoist, D., Chapuis, Y., Artru, J., 2006a. ICE, the electric field experiment on DEMETER. Planet. Space Sci. this issue, doi:10.1016/j.pss.2005.10.016.

Berthelier, J., Godefroy, M., Leblanc, F., Seran, E., Peschard, D., Gilbert, P., Artru, J., 2006b. IAP, the thermal plasma analyzer on DEMETER. Planet. Space Sci. this issue, doi:10.1016/j.pss.2005.10.018.

Cairó, L., Lefeuvre, F., 1986. Localization of sources of ELF/VLF hiss observed in the magnetosphere: three-dimensional ray tracing. J. Geophys. Res. 91, 4352–4364.

Cornilleau-Wehrlin, N., Chanteur, G., Perraut, S., Rezeau, L., Robert, P., Roux, A., Villedary, C.D., Canu, P., Maksimovic, M., Conchy, Y.D., Hubert, D., Lacombe, C., Lefeuvre, F., Parrot, M., Pincon, J.-L., Decrau, P., Harvey, C.C., Louarn, P., Santolik, O., Alleyne, H.S.C., Roth, M., STAFF team, 2003. First results obtained by the Cluster STAFF experiment. Ann. Geophys. 21, 437–456.

Delannoy, C., Lefeuvre, F., 1986. MAXENTWDF—a computer program for the maximum entropy estimation of a wave distribution function. Comput. Phys. Comm. 40, 389–419.

Grard, R., 1968. Interprétation de mesures de champ électromagnétique t.b.f. dans la magnétosphère. Ann. Geophys. 24, 955–971.

Gurnett, D.A., Burns, T.B., 1968. The low-frequency cutoff of elf emissions. J. Geophys. Res. 73, 7437–7445.

Gurnett, D.A., Shawhan, S.D., Brice, N.M., Smith, R.L., 1965. Ion cyclotron whistlers. J. Geophys. Res. 70, 1665–1688.

Helliwell, R.A., 1965. Whistlers and Related Ionospheric Phenomena. Stanford University Press, Stanford, CA.

LaBelle, J., Treumann, R., 1992. Poynting vector measurements of electromagnetic ion cyclotron waves in the plasmasphere. J. Geophys. Res. 97, 13789–13797.

Lagoutte, D., Brochot, J., Latremoliere, P., 2000. SWAN, Software for wave analysis, version 2.4, (part 1: User's guide; part 2: Analysis tools; part 3: User's project interface). Technical Report, Laboratory of Physics Chimie Environment/CNRS, Orléans, France.

Lagoutte, D., Cerisier, J., Plagnaud, J., Villain, J., Forget, B., 1992. High latitude ionospheric electrostatic disturbance studied by means of the wavelet transform. J. Atmos. Terr. Phys. 54, 1283–1294.

Lebreton, J., Stverak, S., Travnicek, P., Maksimovic, M., Klinge, D., Merikallio, S., Lagoutte, D., Poirier, B., Kozacek, Z., Salaquarda, M., 2006. The ISL langmuir probe experiment and its data processing onboard DEMETER: scientific objectives, description and first results. Planet. Space Sci. this issue, doi:10.1016/j.pss.2005.10.017.

Lefeuvre, F., 1977. Analyse de champs d'ondes électromagnétiques aléatoires observées dans la magnétosphère, à partir de la mesure simultanée de leurs six composantes. Doctoral Thesis, University of Orléans, Orléans, France.

Lefeuvre, F., Delannoy, C., 1979. Analysis of random electromagnetic wave field by a maximum entropy method. Ann. Telecommun. 34, 204–213.

Lefeuvre, F., Helliwell, R.A., 1985. Characterization of the sources of VLF hiss and chorus observed on GEOS 1. J. Geophys. Res. 90, 6419–6438.

Lefeuvre, F., Marouan, Y., Parrot, M., Rauch, J., 1986. Rapid determination of the sense of polarization and propagation for random electromagnetic wave fields. Application to GEOS1 and AUREOL3 data. Ann. Geophys. 4, 457–468.

Lefeuvre, F., Marouan, Y., Parrot, M., Rauch, J., 1987. Correction to "Rapid determination of the sense of polarization and propagation for random electromagnetic wave fields. Application to GEOS1 and AUREOL3 data". Ann. Geophys. 5, 251.

Lefeuvre, F., Rauch, J.L., Lagoutte, D., Berthelier, J.J., Cerisier, J.C., 1992. Propagation characteristics of dayside low-altitude hiss: case studies. J. Geophys. Res. 97, 10601–10620.

Macmillan, S., Quinn, J.M., 2000. The 2000 revision of the joint UK/US geomagnetic field models and the IGRF candidate model. Earth Planets Space 52, 1149–1162.

McPherron, R.L., Russel, C.T., Coleman Jr., P.J., 1972. Fluctuating magnetic fields in the magnetosphere, 2, ULF waves. Space Sci. Rev. 13, 411–454.

Means, J.D., 1972. Use of the three-dimensional covariance matrix in analyzing the polarization properties of plane waves. J. Geophys. Res. 77, 5551–5559.

Oscarsson, T., Rönnmark, K., 1989. Reconstruction of wave distribution functions in warm plasmas. J. Geophys. Res. 94, 2417–2428.

Parrot, M., 1994. Statistical study of ELF/VLF emissions recorded by a low altitude satellite during seismic events. J. Geophys. Res. 99, 23339–23347.

Parrot, M., Achache, J., Berthelier, J., Blanc, E., Deschamps, A., Lefeuvre, F., Menvielle, M., Plantet, J., Tarits, P., Villain, J., 1993. High-frequency seismo-electromagnetic effects. Phys. Earth Planet. Int. 77, 65–83.

Parrot, M., Benoist, D., Berthelier, J., Błęcki, J., Chapuis, Y., Colin, F., Elie, F., Fergeau, P., Lagoutte, D., Lefeuvre, F., Legendre, C., Lévêque, M., Pinçon, J., Poirier, B., Seran, H.-C., Zamora, P., 2006. The magnetic field experiment IMSC and its data processing onboard DEMETER: scientific objectives, description and first results. Planet. Space Sci. this issue, doi:10.1016/j.pss.2005.10.015.

Parrot, M., Lefeuvre, F., 1986. Statistical study of the propagation characteristics of ELF hiss observed on GEOS-1, outside and inside the plasmasphere. Ann. Geophys. 4, 363–384.

Parrot, M., Santolík, O., Cornilleau-Wehrlin, N., Maksimovic, M., Harvey, C., 2003. Source location of chorus emissions observed by cluster. Ann. Geophys. 21 (2), 473–480.

Parrot, M., Santolík, O., Cornilleau-Wehrlin, N., Maksimovic, M., Harvey, C., 2004a. Magnetospherically reflected chorus waves revealed by ray tracing with cluster data. Ann. Geophys. 21, 1111–1120.

Parrot, M., Santolík, O., Gurnett, D., Pickett, J., Cornilleau-Wehrlin, N., 2004b. Characteristics of magnetospherically reflected chorus waves observed by cluster. Ann. Geophys. 22, 2597–2606.

Parrot, M., Zaslavski, Y., 1996. Physical mechanisms of man made influences on the magnetosphere. Surv. Geophys. 17, 67–100.

Pinçon, J.L., Marouan, Y., Lefeuvre, F., 1992. Interpretation of measurements of the polarization percentage for plasma waves. Ann. Geophys. 10, 82–95.

Press, W.H., Flannery, B.P., Teukolsky, S.A., Vetterling, W.T., 1992. Numerical Recipes. Cambridge University Press, New York.

Samson, J.C., 1973. Descriptions of the polarization states of vector processes: applications to ulf magnetic fields. Geophys. J. R. Astron. Soc. 34, 403–419.

Samson, J.C., Olson, J.V., 1980. Some comments on the descriptions of the polarisation states of waves. Geophys. J. R. Astron. Soc. 61, 115–129.

Santolík, O., 2003a. Micro-satellite DEMETER: utilisation du modèle IGRF pour la progammation de la CU. Technical Report, Laboratory of Physics Chimie Environment/CNRS, Orléans, France (in french).

Santolík, O., 2003b. Propagation analysis of STAFF-SA data with coherency tests (a user's guide to PRASSADCO). Technical Report, Laboratory of Physics Chimie Environment/CNRS, Orléans, France.

Santolík, O., Gurnett, D.A., 2002. Propagation of auroral hiss at high altitudes. Geophys. Res. Lett. 29 (10), 1481, doi:10.1029/2001GL013666.

Santolík, O., Gurnett, D.A., Pickett, J.S., Parrot, M., Cornilleau-Wehrlin, N., 2004. A microscopic and nanoscopic view of storm-time chorus on 31 March 2001. Geophys. Res. Lett. 31 (2), L02801, doi:10.1029/2003GL018757.

Santolík, O., Lefeuvre, F., Parrot, M., Rauch, J., 2001a. Complete wave-vector directions of electromagnetic emissions: application to Interball-2 measurements in the nightside auroral zone. J. Geophys. Res. 106, 13191–13201.

Santolík, O., Lefeuvre, F., Parrot, M., Rauch, J., 2001b. Propagation of Z-mode and whistler-mode emissions observed by Interball 2 in the nightside auroral region. J. Geophys. Res. 106, 21137–21146.

Santolík, O., Parrot, M., 1996. The wave distribution function in a hot magnetospheric plasma: the direct problem. J. Geophys. Res. 101 (A5), 10639–10651.

Santolík, O., Parrot, M., 1998. Propagation analysis of electromagnetic waves between the helium and proton gyro-frequencies in the low-altitude auroral zone. J. Geophys. Res. 103 (A9), 20469–20480.

Santolík, O., Parrot, M., 1999. Case studies on wave propagation and polarization of ELF emissions observed by Freja around the local proton gyro-frequency. J. Geophys. Res. 104 (A2), 2459–2475.

Santolík, O., Parrot, M., 2000. Application of wave distribution function methods to an ELF hiss event at high latitudes. J. Geophys. Res. 105, 18885–18894.

Santolík, O., Parrot, M., Lefeuvre, F., 2003. Singular value decomposition methods for wave propagation analysis. Radio. Sci. 38 (1), 1010, doi:10.1029/2000RS002523.

Sauvaud, J., Moreau, T., Maggiolo, R., Treilhou, J., Jacquey, C., Cros, A., Coutelier, J., Rouzaud, J., Penou, E., Gangloff, M., 2006. High energy electron detection onboard DEMETER: the IDP spectrometer, description and first results on the inner belt. Planet. Space Sci. this issue, doi:10.1016/j.pss.2005.10.019.

Shawhan, S.D., 1970. The use of multiple receivers to measure the wave characteristics of very-low-frequency noise in space. Space Sci. Rev. 10, 689–736.

Smith, R.L., Brice, N.M., 1964. Propagation in multicomponent plasmas. J. Geophys. Res. 69, 5029.

Storey, L.R.O., 1998. Revision of the basic equations of wave distribution function analysis. Ann. Geophys. 16, 651–653.

Storey, L.R.O., 1999. The measurement of wave distribution functions. In: Stuchly, M.A. (Ed.), Modern Radio Science. Oxford University Press, Oxford, pp. 249–271.

Storey, L.R.O., Lefeuvre, F., 1974. Theory for the interpretation of measurements of a random electromagnetic wave field in space. In: Rycroft, M.J., Reasenberg, R.D. (Eds.), Space Research, vol. XIV. Akademie-Verlag, Berlin, pp. 381–386.

Storey, L.R.O., Lefeuvre, F., 1979. The analysis of 6-component measurement of a random electromagnetic wave field in a magneto-plasma, 1, The direct problem. Geophys. J. R. Astron. Soc. 56, 255–270.

Storey, L.R.O., Lefeuvre, F., 1980. The analysis of 6-component measurement of a random electromagnetic wave field in a magneto-plasma, 2, the integration kernels. Geophys. J. R. Astron. Soc. 62, 173–194.

Storey, L.R.O., Lefeuvre, F., Parrot, M., Cairó, L., Anderson, R., 1991. Initial survey of the wave distribution functions for plasmaspheric hiss observed by ISEE 1. J. Geophys. Res. 96, 19469–19489.

JOURNAL OF GEOPHYSICAL RESEARCH, VOL. 112, A04301, doi:10.1029/2006JA012134, 2007

Comparison of magnetospheric line radiation and power line harmonic radiation: A systematic survey using the DEMETER spacecraft

F. Němec,[1,2] O. Santolík,[1,2] M. Parrot,[3] and J. J. Berthelier[4]

Received 22 October 2006; revised 2 December 2006; accepted 26 December 2006; published 7 April 2007.

[1] Results of a systematic search for magnetospheric line radiation (MLR) observed by the DEMETER spacecraft since the beginning of the mission are presented. DEMETER is a French microsatellite (altitude of orbit about 700 km, inclination 98°) designed to study electromagnetic phenomena connected with seismic or man-made activity that has been launched in June 2004. An automatic identification procedure of possible MLR events has been used in order to analyze a large amount of measured data. It is shown that there are two principally different classes of events: (1) events with frequency spacing of 50/100 or 60/120 Hz (power line harmonic radiation, PLHR) and (2) events with a different frequency spacing. The first class of events is generated by power systems on the Earth's surface, with frequency spacing well corresponding to the fundamental frequency of the radiating power system. On the other hand, the second class is most probably generated in a completely natural way. All the detected events are thoroughly analyzed, and different properties of the two classes are statistically demonstrated. We have found that PLHR events occur both during low and high geomagnetic activity, with none of them significantly preferred. However, MLR events occur more frequently under disturbed conditions. Most of the PLHR events are observed at frequencies of 2 to 3 kHz. On the other hand, MLR events most frequently occur at frequencies below 2 kHz and seem to be more intense than PLHR. Additionally, PLHR events are more intense during the night than during the day, and there is about the same number of PLHR events observed during the day and during the night. On the contrary, no dependence of MLR peak intensities on magnetic local time was found, and more MLR events were observed during the day than during the night, although this difference is not statistically very significant. Finally, there is a group of MLR events with characteristics corresponding to the previous spacecraft observations of equatorial noise.

Citation: Němec, F., O. Santolík, M. Parrot, and J. J. Berthelier (2007), Comparison of magnetospheric line radiation and power line harmonic radiation: A systematic survey using the DEMETER spacecraft, *J. Geophys. Res.*, *112*, A04301, doi:10.1029/2006JA012134.

1. Introduction

[2] This paper deals with electromagnetic emissions propagating through the magnetosphere that exhibit a line structure. These emissions are usually called magnetospheric line radiation (MLR), and in frequency-time spectrograms, they typically look like a set of intense parallel lines whose mutual frequency separation is often the same for all consecutive lines from the set. Moreover, in some cases, the lines have a mutual distance of 50/100 or 60/120 Hz. These are believed to be caused by electromagnetic radiation from ground-based electric power systems and are called power line harmonic radiation (PLHR). Both ground [*Helliwell et al.*, 1975; *Park and Helliwell*, 1978, 1981, 1983; *Matthews and Yearby*, 1978; *Yearby*, 1982; *Yearby et al.*, 1983; *Rodger et al.*, 1999, 2000a, 2000b; *Manninen*, 2005] and satellite [*Koons et al.*, 1978; *Bell et al.*, 1982; *Tomizawa and Yoshino*, 1985; *Rodger et al.*, 1995; *Parrot et al.*, 2005, 2006a; *Němec et al.*, 2006b] observations of MLR-like phenomena were reported in the past. However, direct satellite observations of the events are rather rare, usually reporting only a few cases. Moreover, a lot of controversy still remains about the origin of these events. *Rodger et al.* [1995] analyzed observations of MLR events by satellites International Satellite for Ionosphere Studies (ISIS) 1 and ISIS 2, finding no correlation between 50/60 Hz multiples and the frequency of the observed lines. Concerning the ground-based observations, they concluded the same after

[1]Faculty of Mathematics and Physics, Charles University, Prague, Czech Republic.
[2]Also at Institute of Atmospheric Physics, ASCR, Prague, Czech Republic.
[3]Laboratoire de Physique et Chimie de l'Environnement/CNRS, Orléans, France.
[4]Centre d'Étude des Environnements Terrestre et Planétaires/CNRS, Saint-Maur des Fossés, France.

0148-0227/07/2006JA012134$09.00

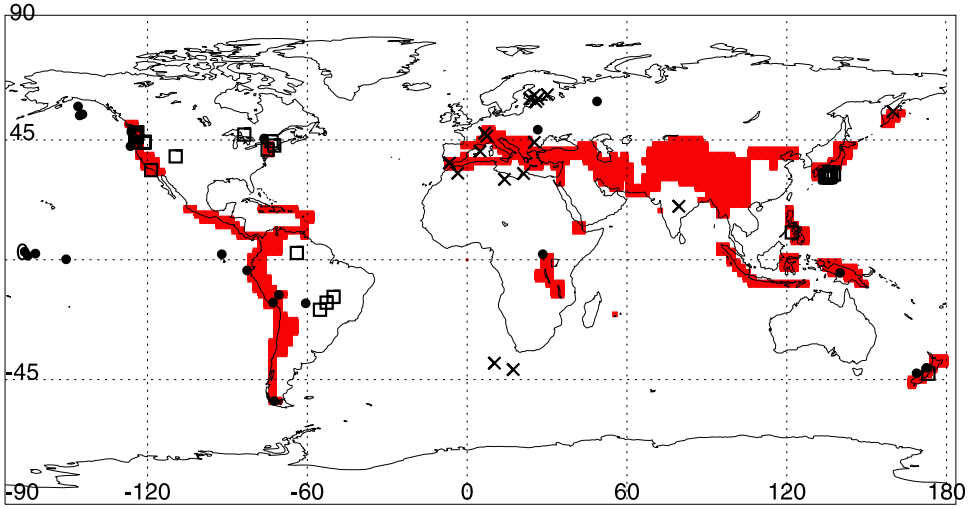

Figure 1. Map showing geographic locations of the observed events. PLHR events with 50/100 Hz spacing are plotted by crosses, PLHR events with 60/120 Hz spacing are plotted by squares, and MLR events are plotted by solid circles. Zones with the permanently active burst-mode coverage are shaded.

analyzing the data measured at Halley station [*Rodger et al.*, 1999, 2000a, 2000b]. *Němec et al.* [2006b] performed a systematic analysis of events with frequency spacing of 50/100 or 60/120 Hz (PLHR) and found that the frequency spacings of all the observed events correspond well to power system frequencies in possible regions of generation. Finally, *Parrot et al.* [2006a] described six storm-time observations of MLR-like events, performing their detail analysis and discussing a possible link to electromagnetic ion cyclotron waves at proton cyclotron harmonics emitted from the equatorial region. The role of PLHR in the ionosphere could be important because they can trigger new emissions [*Nunn et al.*, 1999].

[3] Results of a systematic survey of MLR-like events observed by the DEMETER spacecraft are reported in this paper. In section 2, the wave experiment onboard DEMETER and procedure for an automatic identification of MLR events are briefly introduced. An analysis of the detected events is described in section 3, whereas section 4 presents the discussion of results. Finally, section 5 contains conclusions.

2. Experiment and Automatic Identification of Events

[4] Wave data from the French microsatellite DEMETER (launched in June 2004, altitude of ≈710 km, nearly Sun-synchronous orbit) have been used. The primary purpose of this spacecraft is to study ionospheric effects connected with the seismic activity; the secondary goal of the mission is to study man-made effects in the ionosphere. The electromagnetic waves at geomagnetic latitudes less than 65° are measured by the Instrument Magnetometre Search Coil (magnetic field component) and the Instrument Champ Electrique (electric field component) instruments onboard DEMETER. There exist two principal modes of operation: (1) the burst mode, active mostly above the seismic areas, in which the waveforms of one electric and one magnetic component in very low frequency (VLF) range (up to 20 kHz) and a full set of three electric and three magnetic components in extremely low frequency (ELF) range (up to 1250 Hz) are recorded; and (2) the survey mode, in which power spectra of one electric and one magnetic field component are calculated onboard for VLF range. This mode has a limited frequency resolution (19.5 Hz), which is insufficient for the intended study. We are consequently forced to use the burst mode, which is active for only a few minutes during each half orbit, limiting our study only to specific areas (mostly seismic ones, but about 20% of the volume of the burst-mode data are recorded above different regions of interest and can be added/modified during the operational phase of the mission). More information concerning the DEMETER mission and onboard instruments can be found in the works of *Berthelier et al.* [2006], *Parrot et al.* [2006b], and *Santolík et al.* [2006].

[5] The spacecraft observations of MLR are rather rare. In order to detect a reasonably high number of such events, it is therefore necessary to check a large amount of data. Since a visual survey of all the measured data would be practically impossible, we have developed a procedure for an automatic identification of possible MLR. Candidate computer-found MLR events have then been visually checked, and we have decided if they correspond to the real MLR events or not. The automatic identification procedure is running in the DEMETER control center in Orléans and is described in detail by *Němec et al.* [2006b]. Altogether, 1650 hours of burst-mode data measured during the first 2 years of the DEMETER mission has been analyzed. In this data set, 764 possible MLR events have been detected. Manual verification of the events revealed that most of them are "false alarms," finally yielding only 72 MLR-like events: 17 PLHR events with frequency spacing of 50/100 Hz, 32 PLHR events with frequency spacing of 60/120 Hz, and 23 MLR events with different frequency spacing. The geographic locations of these events as well as the areas with the permanently active burst-mode coverage are shown in Figure 1. The operational phase burst-mode regions are not shown since their positions vary during the time interval analyzed in this study.

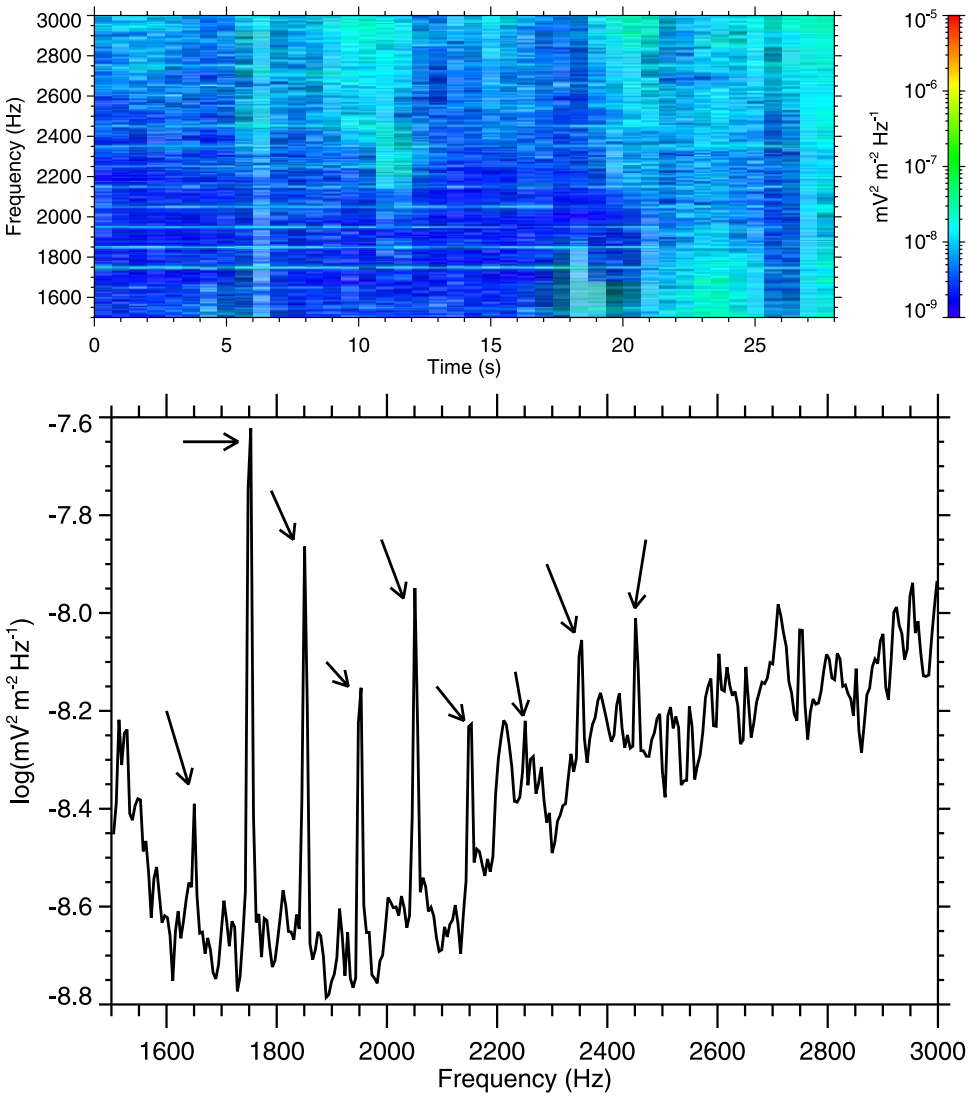

Figure 2. Top: An example of frequency-time spectrogram of electric field fluctuations corresponding to one of the analyzed PLHR events with 50/100 Hz spacing. The data were recorded on 25 March 2006 from 1913:32 UT when the spacecraft was flying over Finland. Bottom: Power spectrum of the first 18 s of data, with the most important peaks marked by arrows.

[6] The first two groups of events are most probably caused by electromagnetic radiation from power systems (PLHR) and have been quite thoroughly analyzed by *Němec et al.* [2006b]. In this paper, we compare them with the third group of events ("real MLR" events), showing that their properties are substantially different.

3. Analysis of Events

[7] An example of one of the events from the first group (frequency spacing 50/100 or 60/120 Hz) recorded on 25 March 2006 from 1913:32 UT, when the spacecraft was flying over Finland, is shown in Figure 2. It is represented in the form of a frequency-time spectrogram of electric field fluctuations (top panel) together with the power spectrum corresponding to the first 14 s of data (bottom panel). The arrows are used to mark the most important peaks of the spectrum located at frequencies 1650, 1750, 1850, 1950, 2050, 2150, 2250, and 2350 Hz. These peaks are separated by 100 Hz and located exactly at 50 Hz (odd) harmonics. Moreover, much weaker peaks can be observed at even harmonics. The observed frequencies are in a good agreement with independent ground-based measurements performed by *Manninen* [2005]. A slowly growing intensity as a function of frequency above 2000 Hz (bottom panel) is caused by naturally occurring whistlers with low dispersion, coming most probably from the lightning sources below the spacecraft.

[8] Figure 3 represents another example of one of the observed events, this time from the third group (frequency spacing other than 50/100 or 60/120 Hz), recorded on 16 May 2005 between 0816:02 and 0818:42 UT when the spacecraft was flying over the Pacific Ocean. The first two panels represent frequency-time spectrograms of electric and magnetic field fluctuations. Since this time the emissions occurred during the burst mode in the DEMETER

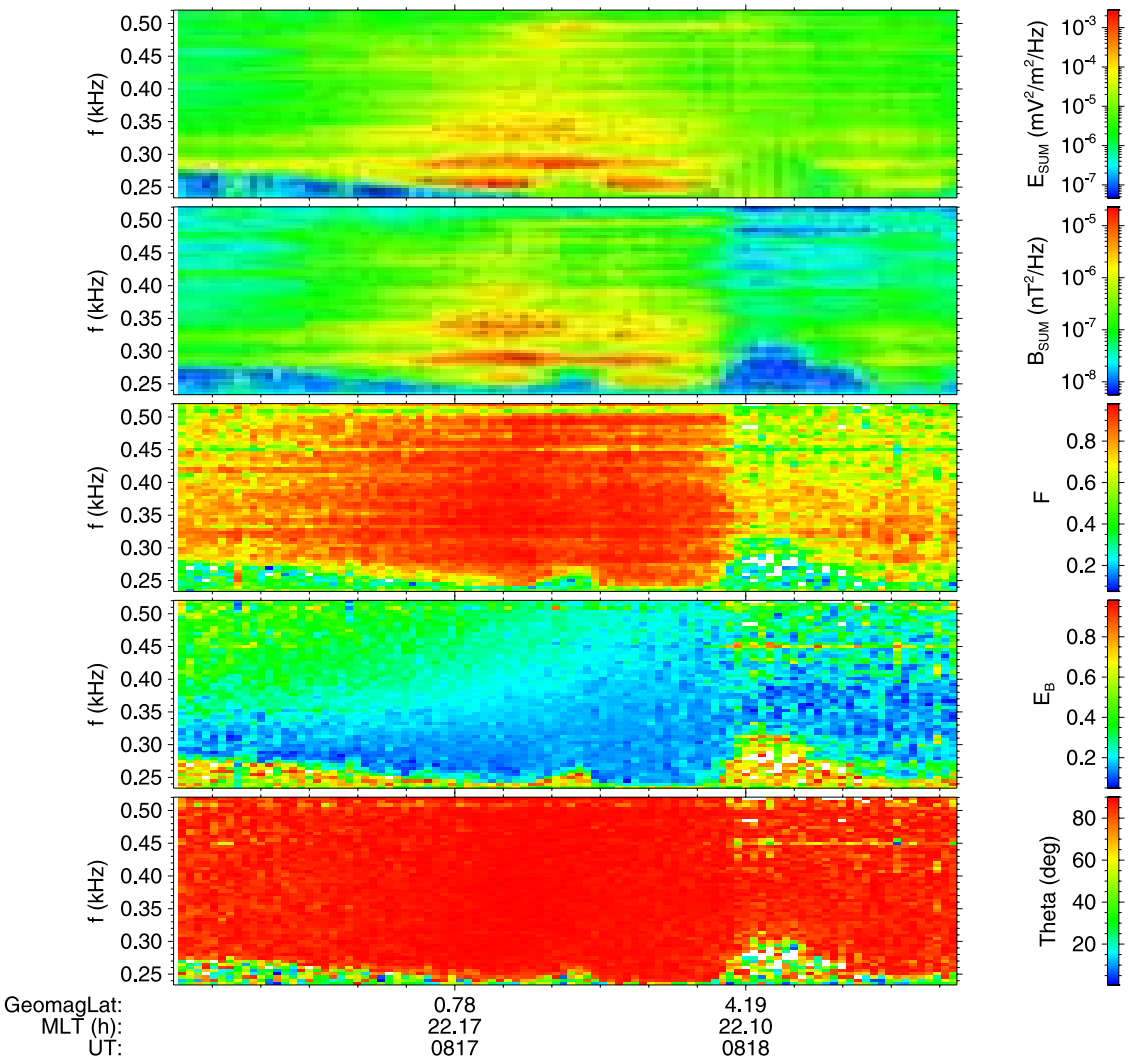

Figure 3. An example of a real MLR event (from the third group: frequency spacing other than 50/100 or 60/120 Hz). The data were obtained on 16 May 2005 between 0816:02 and 0818:42 UT, and the occurrence in ELF band allowed us to perform a detail analysis. From the top: frequency-time power spectrograms of electric and magnetic field fluctuations, of the planarity, ellipticity, and polar angle of wave vector direction with respect to the ambient magnetic field.

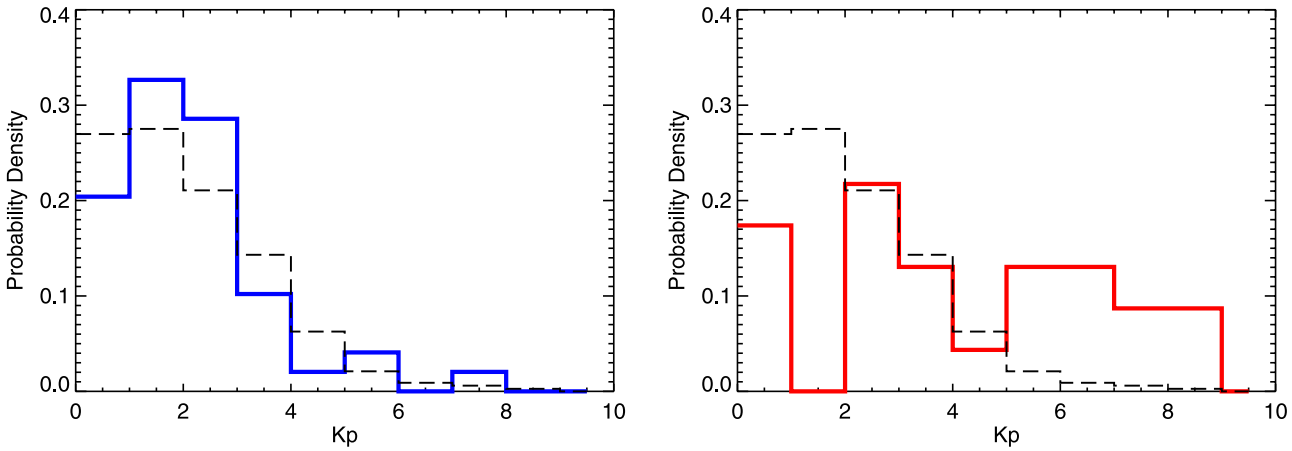

Figure 4. Histograms of Kp indices (left panel) at the time of PLHR events (solid line) and (right panel) at the time of MLR events (solid line). Histogram of all Kp indices that occurred during the analyzed year is overplotted in both panels by dashed line.

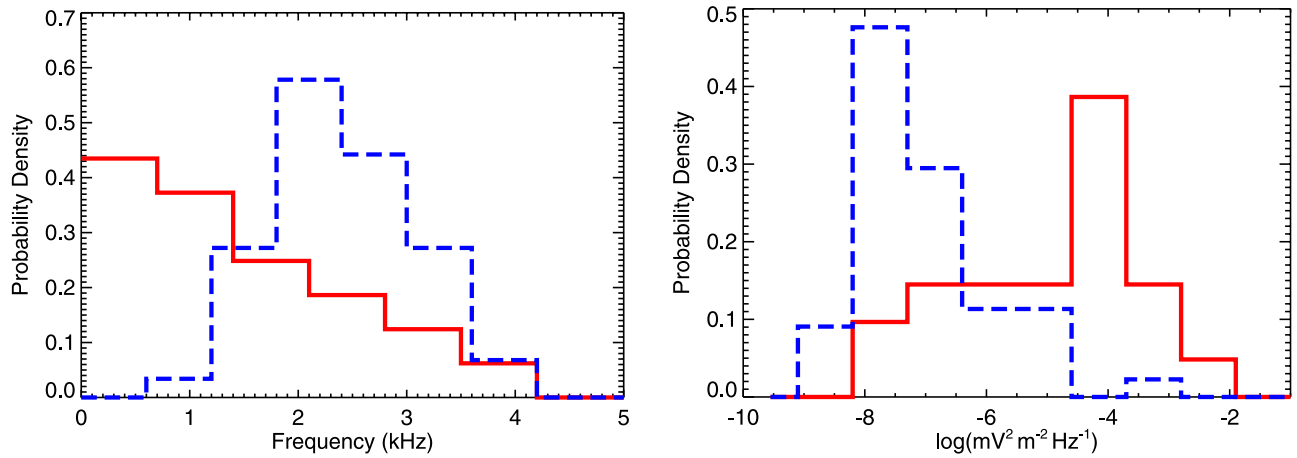

Figure 5. Left: Histograms of central frequencies of PLHR events (dashed line) and MLR events (solid line). Right: Histograms of peak intensities of PLHR events (dashed line) and MLR events (solid line).

ELF band, it was possible to perform a complex analysis. An example is presented in the last three panels of Figure 3 (see description at the end of this section for more details).

[9] Figure 4 shows histograms of Kp indices that occurred during the detected events. The left panel represents results obtained for PLHR events (frequency spacing 50/100 or 60/120 Hz), and the right panel represents results obtained for MLR events (different frequency spacing). It can be seen that while the PLHR events occur during both low and high geomagnetic activity, with no significant preference for quiet or disturbed periods, MLR events seem to occur more frequently under disturbed conditions.

[10] For each of the observed events, we evaluate a central frequency and a peak intensity. The central frequency is defined as an arithmetic average of the minimum and maximum frequencies detected in the observed set of lines. The peak intensity is defined by the most intense line. Histograms of central frequencies of the observed events are shown in the left panel of Figure 5, by a dashed line for the PLHR events, and by a solid line for the MLR events. Histograms of peak intensities of the observed events are shown in the right panel of Figure 5. It can be seen that most of the PLHR events have been observed at frequencies of 2 to 3 kHz. On the other hand, MLR events most frequently occur at frequencies below 2 kHz, with the number of observations slowly decreasing toward higher frequencies. Moreover, the MLR events are more intense than PLHR.

[11] Figure 6 represents the peak intensity of the PLHR and MLR events as a function of magnetic local time. It shows that the peak intensity of the PLHR events is higher during the night than during the day, although the peak intensity of MLR does not seem to depend on the magnetic local time. Moreover, about the same number of the PLHR events was observed during the night (24) and during the day (25). However, more MLR events were observed during the day (15) than during the night (8). The bunching of the observed events into two distinct groups is caused by the specific Sun-synchronous orbit of DEMETER. This orbit is reflected by two peaks in the MLT coverage, around 11 and 23 MLT, both of them containing the same number of orbits.

[12] Figure 7 shows how the central frequency of the observed MLR events depends on the geomagnetic latitude. It can be seen that two distinct groups of events are formed. The first of them is observed at higher frequencies and

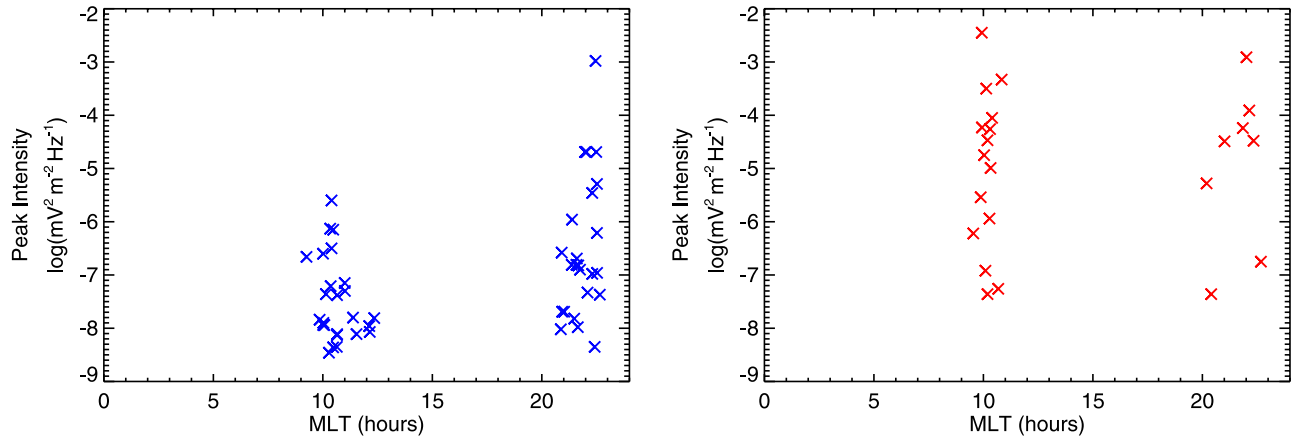

Figure 6. Left: Peak intensity of PLHR events as a function of magnetic local time. Right: Peak intensity of MLR events as a function of magnetic local time.

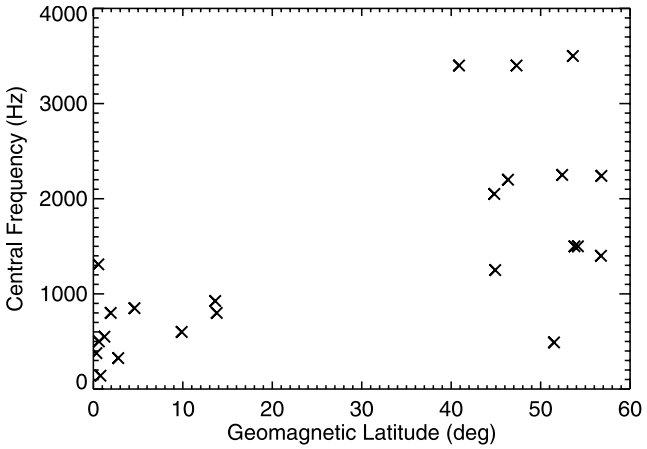

Figure 7. Central frequency of the observed MLR events as a function of geomagnetic latitude.

located at higher geomagnetic latitudes, while the second group is observed close to the geomagnetic equator at significantly lower frequencies.

[13] At frequencies below 1 kHz, we can analyze the ELF band where all the six electromagnetic components are measured. The analysis reveals that there is a group of MLR events (5 out of 23) located close to the geomagnetic equator with characteristics corresponding to recent observations of equatorial noise [*Santolik et al.*, 2002, 2004; *Němec et al.*, 2005, 2006a, and references therein].

[14] A detailed analysis of one of the events that belong to the "equatorial noise" group is shown in Figure 3. The top two panels contain spectrograms representing power-spectral densities of electric and magnetic field fluctuations, respectively. The third panel contains a spectrogram representing the planarity of magnetic field fluctuations, which is determined by the singular value decomposition (SVD) method [*Santolík et al.*, 2003]. It varies between 0 and 1 and describes a confinement of the fluctuations to a single plane: a value of 1 would represent an ideal plane wave. A value of $\approx$0.8 for the observed emissions suggests fluctuations very close to a single plane, with a small fraction of random three-dimensional fluctuations. The fourth panel contains a spectrogram representing the ellipticity of polarization of magnetic field fluctuations, which is again determined by the SVD method and varies between 0 (linear polarization) and 1 (circular polarization). It can be seen that the emissions of the equatorial noise type have polarization close to linear [*Russel et al.*, 1970]. The last panel represents a frequency-time spectrogram of polar angle of wave vector direction with respect to the ambient magnetic field (also determined by the SVD method). It shows that the wave vector is perpendicular to the ambient magnetic field.

4. Discussion

[15] A surely problematic element in the presented study is the procedure for automatic identification of MLR events. Although this procedure was necessary in order to analyze a large amount of data, it is practically impossible to determine all consequences of this step. Another basic limitation of the presented study is caused by the use of burst-mode data, which are collected only above some specific areas. Both these complications are discussed in detail by *Němec et al.* [2006b].

[16] The main purpose of this study is to demonstrate a striking difference between the two groups of events: PLHR (events with frequency spacing of 50/100 or 60/120 Hz) and "real MLR" events (with different frequency spacing). Fundamental difference in conditions needed for their generation is demonstrated in Figure 4. While PLHR events occur during both low and high geomagnetic activity, with no significant preference for any of them, MLR events occur more likely under highly disturbed conditions. This most probably suggests a completely different generation mechanism for the two classes. PLHR events seem to be electromagnetic emissions radiated by electric power systems on the ground that propagate in right-hand polarized whistler mode and are only modified by the plasma environment [*Němec et al.*, 2006b]. On the other hand, we believe that emissions that are classified as real MLR (or at least some of them) are generated in a completely natural way by instabilities of particle distribution functions. Different properties of PLHR and real MLR events are shown in Figures 5 and 6. PLHR events are less intense than real MLR and occur mostly at frequencies between 2 and 3 kHz, with a clearly distinguishable peak in probability of occurrence. On the contrary, MLR events occur mostly at frequencies below 2 kHz, with the probability of observation slowly decreasing toward the higher frequencies. This is rather different from the frequencies of MLR reported by other researchers [e.g., *Rodger et al.*, 1995, 1999]. This can be most probably explained by the fact that the events observed at low frequencies are located at low geomagnetic latitudes (see Figure 7). These low geomagnetic latitudes have not been covered by *Rodger et al.* [1995, 1999]. Furthermore, the peak intensity of PLHR events is higher during the night than during the day, but the peak intensity of MLR events does not show this effect. This could be explained by the fact that the Earth-ionosphere coupling is more efficient during the night than during the day [*Green et al.*, 2005]. This represents further support for the idea that PLHR and real MLR have to be considered as two completely different phenomena. However, this does not completely exclude the possibility that these two classes of events may be connected in some way; for example, some authors suggest that PLHR can serve as a trigger for MLR [*Bullough*, 1995; *Manninen*, 2005].

[17] More MLR events were observed during the day than during the night. This is in quite a good agreement with ground-based observations by *Rodger et al.* [2000b]. We can estimate a statistical significance of this difference. Supposing that the probability of observing MLR events is the same during the night and during the day ($p = p_1 = p_2 = 0.5$), one can calculate the mean value and standard deviation of the number of night/day observations. Having 23 MLR events altogether ($n = 23$), the two mean values are equal, $\overline{n_{\text{night}}} = \overline{n_{\text{day}}} = np = 11.5$. The standard deviations can be then obtained using binomial distribution of probability, $\sigma = \sqrt{np(1-p)} \approx 2.4$. Consequently, it can be seen that the difference between the mean value and the measured number of observations is only about 1.5 standard deviations and is therefore statistically not very significant.

[18] This simple analysis arises the question, how significant are the observed differences between PLHR and MLR? Basically, we need to determine whether two distributions (obtained experimentally and represented in the form of histograms in Figures 4 and 5) are significantly different from a statistical point of view. This can be done by the Kolmogorov–Smirnov test [*Press et al.*, 1992], which gives the probability of rejection of the null hypothesis of no difference between the two data sets. Applying this calculation to the measured data, we can conclude that the probability of the obtained distributions being the same for PLHR and MLR is less than 0.1% for all the presented histograms.

[19] There are two distinct classes regarding the geomagnetic latitude of observed MLR events: (1) events that occur close to the geomagnetic equator and (2) events located at relatively high geomagnetic latitudes ($\approx 50°$). Moreover, the events that belong to the first class usually occur at lower frequencies (up to 1 kHz). This suggests that there probably exist (at least two) different generation mechanisms of MLR events, and a lot of attention needs to be paid when classifying them and making general conclusions concerning their properties. For instance, there are 5 events (out of 23) with characteristics corresponding to the recent observations of equatorial noise. These observations are rather unique, though the altitude of the DEMETER satellite is only about 700 km and up to now the equatorial noise was believed to occur at radial distances between 2 and $7R_E$ [*Laakso et al.*, 1990; *Kasahara et al.*, 1994; *Němec et al.*, 2006b].

5. Conclusions

[20] We have presented results of a systematic survey of observations of MLR by the DEMETER spacecraft. The data were collected during the first 2 years of its operation. An automatic identification procedure has been used to detect the MLR events. Altogether, 72 events have been found in the entire set of 1650 hours of high-resolution data.

[21] There are two principally different classes of events: (1) events with frequency spacing of 50/100 or 60/120 Hz (so-called power line harmonic radiation, PLHR) and (2) events with different frequency spacing. While the first class of events originates from power systems on the Earth's surface and their frequency spacing well corresponds to the fundamental frequency of the radiating power system, the second class is most probably generated in a completely natural way.

[22] While the PLHR events occur during both low and high geomagnetic activity, with no significant preference for quiet or disturbed periods, MLR events seem to occur mostly under disturbed conditions. Most of the PLHR events have been observed at frequencies of 2 to 3 kHz. On the other hand, MLR events most frequently occur at frequencies below 2 kHz, with the number of observations slowly decreasing toward higher frequencies. Moreover, MLR events are more intense than PLHR. PLHR events are more intense during night than during the day. There is about the same number of PLHR events observed during day and night. In contrary, no dependence of MLR peak intensity on magnetic local time was found. Finally, more MLR events were observed during day than night, although this difference is not statistically very significant. There is a group of MLR events occurring close to the geomagnetic equator with characteristics corresponding to emissions of equatorial noise, known from previous spacecraft observations, but at higher radial distances.

[23] **Acknowledgments.** We thank J.-Y. Brochot of LPCE/CNRS Orléans for his help with running the PLHR recognition algorithm as the DEMETER level-3 processing procedure. F. Nemec and O. Santolik acknowledge support from the GACR grant 205/06/1267.

[24] Amitava Bhattacharjee thanks Jyrki Manninen and Vittorio Sgrigna for their assistance in evaluating manuscript 2006JA012134.

References

Bell, T. F., J. P. Luette, and U. S. Inan (1982), ISEE 1 observations of VLF line radiation in the earth's magnetosphere, *J. Geophys. Res.*, *87*(A5), 3530–3536.

Berthelier, J. J., et al. (2006), ICE, the electric field experiment on DEMETER, *Planet. Space Sci.*, *54*, 456–471.

Bullough, K. (1995), *Handbook of Atmospheric Electrodynamics*, vol. 2, chap. Power Line Harmonic Radiation: Sources and Environmental Effects, pp. 291–332, CRC Press, Boca Raton, Fla.

Green, J. L., S. Boardsen, L. Garcia, W. W. L. Taylor, S. F. Fung, and B. W. Reinish (2005), On the origin of whistler mode radiation in the plasmasphere, *J. Geophys. Res.*, *110*(A3), A03201, doi:10.1029/2004JA010495.

Helliwell, R. A., J. P. Katsufrakis, T. F. Bell, and R. Raghuram (1975), VLF line radiation in the earth's magnetosphere and its association with power system radiation, *J. Geophys. Res.*, *80*, 4249–4258.

Kasahara, Y., H. Kenmochi, and I. Kimura (1994), Propagation characteristics of the ELF emissions observed by the satellite Akebono in the equatorial plane, *Radio Sci.*, *29*, 751–767.

Koons, H. C., M. H. Dazey, and B. C. Edgar (1978), Satellite observation of discrete VLF line radiation within transmitter-induced amplification bands, *J. Geophys. Res.*, *83*(A8), 3887–3889.

Laakso, H., H. Junginger, A. Roux, R. Schmidt, and C. de Villedary (1990), Magnetosonic waves above f_{cH+} at geostationary orbit: GEOS 2 results, *J. Geophys. Res.*, *95*, 10,609–10,621.

Manninen, J. (2005), *Some Aspects of ELF-VLF Emissions in Geophysical Research*, chap. Power Line Harmonic Radiation, Magnetospheric Line Radiation, pp. 53–110, 98 Sodankylä Geophysical Observatory Publications, Sodankylä, Finland.

Matthews, J. P., and K. Yearby (1978), Magnetospheric VLF line radiation observed at Halley, Antarctica, *Planet. Space Sci.*, *29*, 97–106.

Němec, F., O. Santolík, K. Gereová, E. Macúšová, Y. de Conchy, and N. Cornilleau-Wehrlin (2005), Initial results of a survey of equatorial noise emissions observed by the cluster spacecraft, *Planet. Space Sci.*, *53*, 291–298.

Němec, F., O. Santolík, K. Gereová, E. Macúšová, H. Laakso, Y. de Conchy, M. Maksimovic, and N. Cornilleau-Wehrlin (2006a), Equatorial noise: Statistical study of its localization and the derived number density, *Adv. Space Res.*, *37*, 610–616.

Němec, F., O. Santolík, M. Parrot, and J. J. Berthelier (2006b), Power line harmonic radiation (PLHR) observed by the DEMETER spacecraft, *J. Geophys. Res.*, *111*, A04308, doi:10.1029/2005JA011480.

Nunn, D., J. Manninen, T. Turunen, V. Trakhtengerts, and N. Erokhin (1999), On the nonlinear triggering of VLF emissions by power line harmonic radiation, *Ann. Geophys.*, *17*, 79–94.

Park, C. G., and R. A. Helliwell (1978), Magnetospheric effects of power line radiation, *Science*, *200*, 727–730.

Park, C. G., and R. A. Helliwell (1981), Power line radiation in the magnetosphere, *Adv. Space Res.*, *1*, 423–437.

Park, C. G., and R. A. Helliwell (1983), Ground observations of power line radiation coupled to the ionosphere and magnetosphere, *Space Sci. Rev.*, *35*, 131–137.

Parrot, M., F. Němec, O. Santolík, and J. J. Berthelier (2005), ELF magnetospheric lines observed by DEMETER, *Ann. Geophys.*, *23*, 3301–3311.

Parrot, M., A. Buzzi, O. Santolík, J. J. Berthelier, J. A. Sauvaud, and J. P. Lebreton (2006a), New observations of electromagnetic harmonic ELF emissions in the ionosphere by the DEMETER satellite during large magnetic storms, *J. Geophys. Res.*, *111*, A08301, doi:10.1029/2005JA011583.

Parrot, M., et al. (2006b), The magnetic field experiment IMSC and its data processing onboard DEMETER: Scientific objectives, description and first results, *Planet. Space Sci.*, *54*, 441–455.

Press, W. H., S. A. Teukolsky, W. T. Vetterling, and B. P. Flannery (1992), *Numerical Recipes in C: The Art of Scientific Computing*, chap. Statis-

tical Description of Data, pp. 609–655, Cambridge Univ. Press, New York.

Rodger, C. J., N. R. Thomson, and R. L. Dowden (1995), VLF line radiation observed by satellite, *J. Geophys. Res.*, *100*(A4), 5681–5689.

Rodger, C. J., M. A. Clilverd, K. H. Yearby, and A. J. Smith (1999), Magnetospheric line radiation observations at Halley, Antarctica, *J. Geophys. Res.*, *104*(A8), 17,441–17,447.

Rodger, C. J., M. A. Clilverd, K. Yearby, and A. J. Smith (2000a), Is magnetospheric line radiation man-made?, *J. Geophys. Res.*, *105*, 15,981–15,990.

Rodger, C. J., M. A. Clilverd, K. H. Yearby, and A. J. Smith (2000b), Temporal properties of magnetospheric line radiation, *J. Geophys. Res.*, *105*(A1), 329–336.

Russel, C. T., R. E. Holzer, and E. J. Smith (1970), OGO 3 observations of ELF noise in the magnetosphere. The nature of the equatorial noise, *J. Geophys. Res.*, *73*, 755–768.

Santolík, O., J. S. Pickett, D. A. Gurnett, M. Maksimovic, and N. Cornilleau-Wehrlin (2002), Spatiotemporal variability and propagation of equatorial noise observed by Cluster, *J. Geophys. Res.*, *107*(A12), 1495, doi:10.1029/2001JA009159.

Santolík, O., M. Parrot, and F. Lefeuvre (2003), Singular value decomposition methods for wave propagation analysis, *Radio Sci.*, *38*(1), 1010, doi:10.1029/2000RS002523.

Santolík, O., F. Němec, K. Gereová, E. Macúšová, Y. de Conchy, and N. Cornilleau-Wehrlin (2004), Systematic analysis of equatorial noise below the lower hybrid frequency, *Ann. Geophys.*, *22*, 2587–2595.

Santolík, O., F. Němec, M. Parrot, D. Lagoutte, L. Madrias, and J. J. Berthelier (2006), Analysis methods for multi-component wave measurements on board the DEMETER spacecraft, *Planet. Space Sci.*, *54*, 512–527.

Tomizawa, I., and T. Yoshino (1985), Power line radiation observed by the satellite, *J. Geomagn. Geoelectr.*, *37*, 309–327.

Yearby, K. H. (1982), Magnetospheric VLF line radiation, Ph.D. Thesis, Department of Physics, The University of Sheffield, Sheffield, UK.

Yearby, K. H., A. J. Smith, and K. Bullough (1983), Power line harmonic radiation in Newfoundland, *J. Atmos. Terr. Phys.*, *45*, 409–419.

J. J. Berthelier, CETP/CNRS, 4, av. de Neptune, 94107, Saint-Maur des Fossés cedex, France. (jean-jacques.berthelier@cetp.ipsl.fr)

F. Němec and O. Santolík, Faculty of Mathematics and Physics, Charles University, V Holešovičkách 2, Prague 8, 18000, Czech Republic. (nemec@matfyz.cz)

M. Parrot, LPCE/CNRS, 3A, av. de la Recherche Scientifique, 45071, Orléans cedex 2, France. (mparrot@cnrs-orleans.fr)

Available online at www.sciencedirect.com
ScienceDirect
Advances in Space Research 40 (2007) 398–403
ADVANCES IN SPACE RESEARCH (a COSPAR publication)
www.elsevier.com/locate/asr

Power line harmonic radiation: A systematic study using DEMETER spacecraft

F. Němec [a,b,*], O. Santolík [a,b], M. Parrot [c], J.J. Berthelier [d]

[a] Faculty of Mathematics and Physics, Charles University, Prague, Czech Republic
[b] Institute of Atmospheric Physics, Czech Academy of Science, Prague, Czech Republic
[c] LPCE/CNRS, Orléans, France
[d] CETP/CNRS, Saint-Maur des Fossés, France

Received 22 October 2006; received in revised form 4 January 2007; accepted 15 January 2007

Abstract

We present results of a systematic survey of Power line harmonic radiation (PLHR) observed by the DEMETER spacecraft. DEMETER is a French micro-satellite launched in June, 2004 with an altitude of orbit of about 700 km. It is designed specifically to study electromagnetic effects connected with seismic and man-made activity. All available high-resolution burst-mode electromagnetic data measured since the beginning of the mission till July 2006 (altogether about 1650 h of data) have been analyzed using an automatic identification procedure. This procedure was specially developed to search for emissions of PLHR type. It is running in DEMETER control center in Orléans, France. 49 PLHR events with frequency spacing of 50/100 or 60/120 Hz have been found, allowing us to perform a statistical study of properties of PLHR. It is shown that for all the events, the observed frequency spacing corresponds well to the power system frequency at anticipated source locations. Moreover, the frequency of the observed lines often (80%) corresponds to the exact harmonics of the power system base frequency. Finally, the most intense events are observed at lower frequencies and no weak events are observed under geomagnetically disturbed conditions.

Keywords: Power line harmonic radiation; PLHR; Ionosphere; Man-made

1. Introduction

Power line harmonic radiation (PLHR) are electromagnetic waves radiated by power systems on the ground at harmonics of the base system frequency (typically 50 or 60 Hz, depending on the country). In frequency-time spectrograms they usually have a form of several parallel lines with frequency spacing of 50/100 or 60/120 Hz, because in some cases odd or even harmonics can be strongly suppressed. Although ground observations of such events as well as the evidence for their propagation through the magnetosphere are well documented (Helliwell et al., 1975; Park and Helliwell, 1978; Matthews and Yearby, 1978; Park and Helliwell, 1981; Park and Helliwell, 1983; Yearby et al., 1983), direct observations onboard the satellites are rather rare and usually include only a few cases (Bell et al., 1982; Koons et al., 1978; Tomizawa and Yoshino, 1985; Rodger et al., 1995; Parrot et al., 2005; Němec et al., 2006). Moreover, a controversy still exists concerning the origin of the events, because in many cases the observed frequency spacing is not 50/100, neither 60/120 Hz. These events are usually called Magnetospheric line radiation (MLR) and their generation mechanism and possible connection to PLHR is still a matter of debate (Bullough, 1995; Rodger et al., 1995; Rodger et al., 1999; Rodger et al., 2000a; Rodger et al., 2000b; Němec et al., 2006). A so-called "Sunday effect" was reported by some authors (Park and Miller, 1979). They observe a significantly lower occurrence rate of the events during Sundays, attributing

* Corresponding author.
E-mail address: frantisek.nemec@mff.cuni.cz (F. Němec).

0273-1177/$30 © 2007 Published by Elsevier Ltd on behalf of COSPAR.
doi:10.1016/j.asr.2007.01.074

this effect to a lower power consumption. Parrot (1991) and Molchanov et al. (1991) argued that the difference between the weekends and weekdays can be caused not only by lower power consumption during the weekends, but also by the different current distribution in power systems as compared to the weekdays. Other researchers (Rodger et al., 2000a; Karinen et al., 2002) who searched for a "Sunday effect" reported that it is only a statistical fluctuation. PLHR could play an important role in the ionosphere because they can trigger new emissions (Nunn et al., 1999).

First results of a survey of PLHR and its properties observed by the DEMETER spacecraft have been reported by Němec et al. (2006). They found that the PLHR events occur during both low and high geomagnetic activity, with none of them significantly preferred. The observed frequency spacing of all the PLHR events corresponded well to power system frequencies in the possible geographical regions of generation and the frequencies of the observed lines corresponded to the multiples of power system frequency in 65 percents of cases. The peak intensity of the observed PLHR events seemed to increase with Kp index and it was higher during the night than during the day. In 26 percents of cases, the magnetic field component of PLHR was observed and the observations were consistent with propagation in the right-hand polarized whistler mode.

Results of an extended study based on a twice larger data set are reported in this paper. Section 2 describes the DEMETER satellite, wave experiment onboard and an automatic procedure used to identify PLHR events. The events are systematically analyzed in Section 3 and the obtained results are discussed in Section 4. Finally, Section 5 contains conclusions.

2. Experiment and identification of events

We have used data from the French micro-satellite DEMETER, whose mass is 130 kg. It was launched in June, 2004 to a nearly Sun-synchroneous orbit with an inclination of 98 degrees. The main purpose of the DEMETER spacecraft is to investigate electromagnetic emissions (and possibly other ionospheric effects) connected with seismic-volcanic and man-made activity. Due to the limited capacity of the telemetry, there are two different modes of operation. A survey mode, measuring low-resolution data, is active during the entire orbit with an exception of the auroral zones (geomagnetic latitudes larger than 65 degrees). In the VLF band this provides us with the power spectrum of one electric and one magnetic field component. However, the limited frequency resolution (19.53 Hz of the Survey mode) is not sufficient for our purposes – the frequency resolution better than 5 Hz is needed for both identification and subsequent analysis of PLHR events. A burst-mode is activated mostly over the seismic areas. However, this may be changed using a tele-command and new burst-mode zones can be added/removed. In the VLF band this mode provides us with waveform of one electric and one magnetic field component (sampling frequency of 40 kHz). Altogether, about 1650 h of burst-mode data have been collected during 2 years of measurements between July 2004 and July 2006.

In order to identify PLHR events in such a large data set, we have developed an automatic identification procedure. It analyzes the measured data, providing us with the beginning time and frequency of each of the PLHR events and with the spectrogram of the surrounding interval in the frequency-time plane. All these positively identified events are then manually checked for the existence of PLHR to decide whether a real event was found or if a "false alarm" occurred. A detailed description of the identification procedure has been given by Němec et al. (2006).

3. Systematic analysis of events

The above described procedure has been implemented in the DEMETER control center in Orléans, France, in the frame of the level 3 data processing system. All available VLF burst-mode data have been used as the input and 49 PLHR events with frequency spacing 50/100 and 60/120 Hz have been identified. An example of one of the observed events is shown in Fig. 1. It represents the frequency-time spectrogram of electric field data measured on February 1, when the DEMETER satellite was above the North-Western part of the USA. Three lines with frequency spacing of 60 Hz, constant in frequency and located at 2100, 2160 and 2220 Hz can be clearly identified. Moreover, these frequencies correspond to the exact harmonics of base frequency of 60 Hz (35th, 36th and 37th harmonics). No similar signature is observed in the magnetic field data. However, Němec et al. (2006) have shown an evidence that the emissions are electromagnetic and propagate in the right-hand polarized whistler mode, with some of the cases being too weak to be observed in the magnetic field data. In the same way, it is reasonable to believe that there are more PLHR events occurring, but being too weak to be observed in electric field data either. This idea is further supported by the fact that the lowest observed peak intensity of PLHR events is about $3\times10^{-9}\,\mathrm{mV^2\,m^{-2}\,Hz^{-1}}$, which is quite comparable to typical intensities of background natural waves determined as the in-flight noise floor of the ICE electric field instrument in the VLF range ($2.5\times10^{-9}\,\mathrm{mV^2\,m^{-2}\,Hz^{-1}}$) by Berthelier et al. (2006).

Geographic locations of the observed PLHR events are shown by large points in Figs. 2 and 3 for events with 50/100 and 60/120 Hz frequency spacing, respectively. Magnetic field lines and the footprints of the points of observation are shown by thin lines and small points. Supposing ducted propagation, these small points indicate possible generation regions. It can be seen that the base frequency of power systems at the possible regions of generation correspond well to the observed frequency spacing. The frequency spacing of 50/100 Hz is observed mostly on

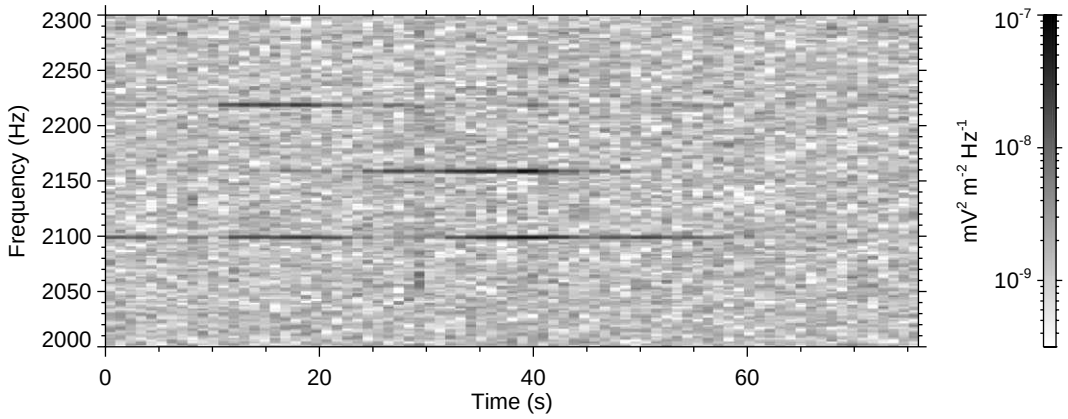

Fig. 1. Example of one of the events with 60 Hz spacing. It shows the electric field data recorded on February 1, 2006 from 19:06:32 UT, when DEMETER was flying over the North-Western part of the USA. Three lines occur at 60 Hz harmonics.

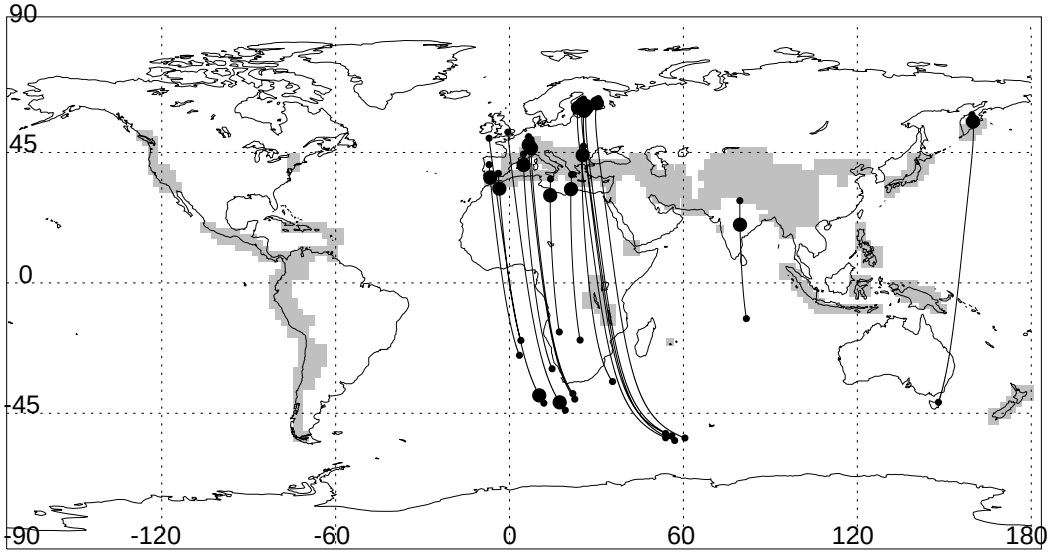

Fig. 2. Map showing geographic locations of the observed PLHR events with frequency separation of 50/100 Hz (large points). Magnetic field lines and footprints of the points of observations are plotted by thin lines and small points, respectively. Zones with permanently active burst-mode coverage are shown by gray shading; however, the operational-phase burst-mode regions, which form approximately 20% of the burst-mode data volume, are not shown since their positions vary during the time interval analyzed in this study.

field lines with one of the footprints in Europe. A few of the events are observed to the South from Africa, but with magnetic conjugate point located again in Europe. One of the events is observed over India and one over the North-East part of Asia. The frequency spacing of 60/120 Hz is observed mostly over the United States of America and Japan, a few such events are observed above Brazil, one over Philippines and one over New Zealand. This is surprising, because the power systems in New Zealand are operating at 50 Hz. Note, however that the magnetic conjugate point is in Alaska where the base system frequency is 60 Hz. It is very important to note that in 39 cases (about 80% of the total number of 49 PLHR events) not only the frequency spacing but also the frequencies of the lines themselves corresponded to the originating power systems. This means that the lines forming these PLHR events occurred at exact harmonics of base power system frequency. The typical 3 dB bandwidth of the observed PLHR lines is less than 10 Hz, which is significantly less than the bandwidth reported by e.g. Rodger et al. (1999) for ground-based observations of MLR.

For each of the observed PLHR events we define the peak intensity as an intensity of the most intense spectral line forming the event. Fig. 4 then shows the peak intensity of the events as a function of Kp index. It can be seen that while both weak and intense PLHR events are observed during geomagnetically quiet times, only PLHR events with relatively high intensity are observed during periods with a high geomagnetic activity (only events with peak intensities larger than $10^{-6}\,mV^2\,m^{-2}\,Hz^{-1}$ have been observed under Kp larger than 4).

The peak intensity of the observed events as a function of geomagnetic latitude is shown in Fig. 5. The peak intensity is almost independent on geomagnetic latitude, but no

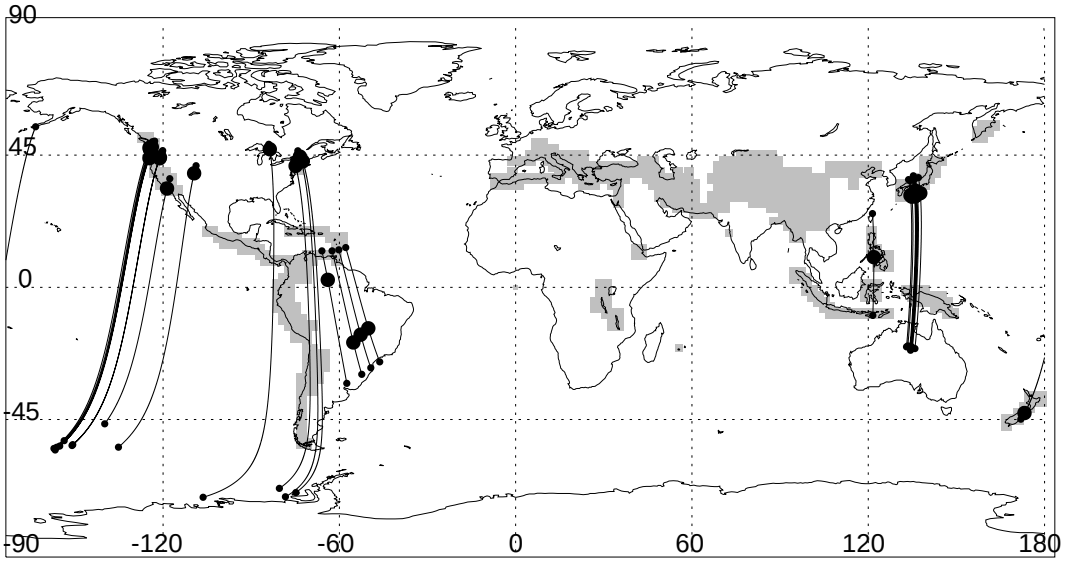

Fig. 3. Same as Fig. 2, but for PLHR events with frequency separation of lines 60/120 Hz.

intense events are observed between 15 and 35 degrees of geomagnetic latitude.

Finally, Fig. 6 represents the peak intensity of the observed events as a function of frequency. It can be seen that most of the intense PLHR events (with peak intensities larger than 10^{-6} mV^2 m^{-2} Hz^{-1}) occur at frequencies lower than 2.5 kHz.

4. Discussion

Only 49 PLHR events have been found in the data set of about 1650 h of data. This low number indicates that the occurrence rate is very low. The limitation of this study is the automatic identification procedure which may underestimate the number of events. Another limitation is the usage of burst-mode data, which are received only above specific areas. The consequences for the geographic locations of the detected events (Figs. 2 and 3) are evident. However, one must keep in mind that the results shown in Fig. 5 are also affected. This can possibly explain the lack of intense events observed at geomagnetic latitudes between 15 and 35 degrees – although quite a lot of events occurred at this interval of geomagnetic latitudes, most of them were measured above Japan and it is reasonable to expect that properties of the PLHR events can slightly change depending on the radiating region.

Geographic locations of the observed PLHR events (Figs. 2 and 3) show a good agreement between the observed frequency separation of the spectral lines and the frequency of the power systems in the anticipated regions of generation. The waves are assumed to propagate in a ducted mode along the magnetic field lines Němec et al., 2006, which is relatively well confirmed by our results. Some of the cases, but not all of them, may be also consistent with the sources located vertically below the

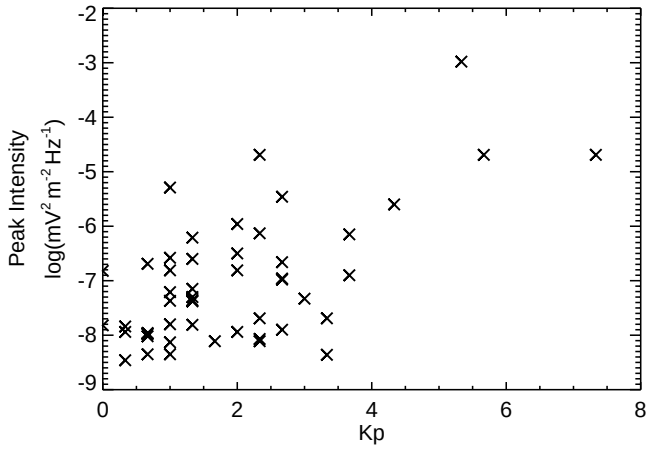

Fig. 4. Peak intensity of the observed PLHR events as a function of Kp index.

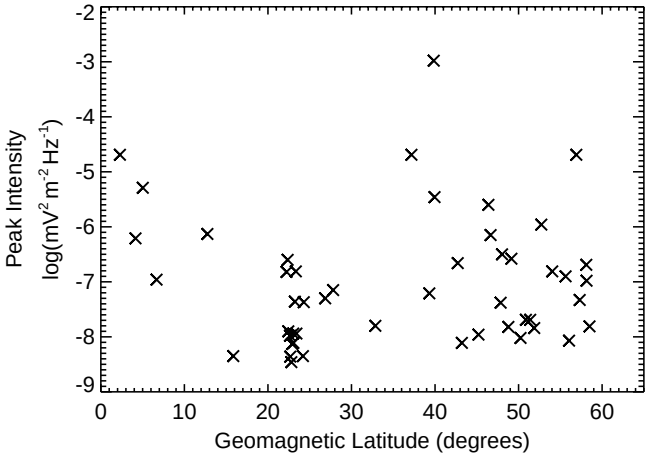

Fig. 5. Peak intensity of the observed PLHR events as a function of geomagnetic latitude.

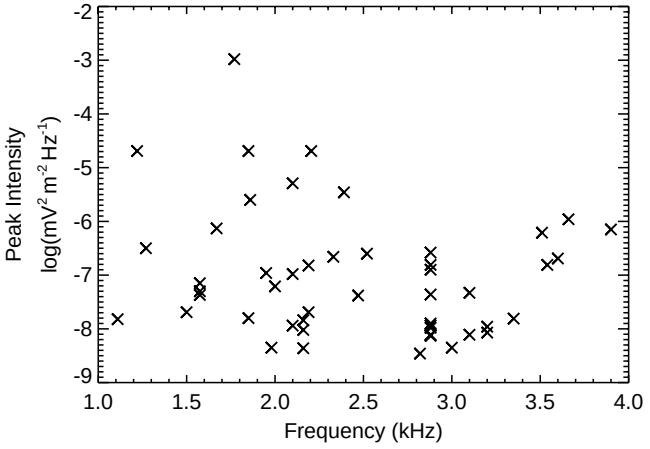

Fig. 6. Peak intensity of the observed PLHR events as a function of frequency.

spacecraft. The difference between the ducted propagation and propagation vertically from the source below the satellite is – especially at high geomagnetic latitudes – quite small. Nevertheless, the difference starts to be relatively significant at lower geomagnetic latitudes (e.g., 60 Hz cases above Brazil seem to be most likely generated on the seashore, where most of the large cities are located, consistently with the ducted propagation). Finally, the anticipated locations of generation seem to be correctly determined in this way also for the propagation from the opposite hemisphere (e.g., 60 Hz cases in the Pacific ocean are traced to the USA).

Moreover, in about 80 percents of cases, the spectral lines are observed at exact multiples of base system frequencies. This suggests that the electromagnetic waves radiated by the power systems on the ground are transported directly to the low-orbiting satellite, without any additional non-linear plasma-wave interactions, which would change their frequency. The same could be true for the remaining 20 percent of cases, supposing they are radiated by not perfectly operating power systems, i.e., with frequencies slightly off 50/60 Hz. The reason is that at higher harmonics that are typically observed even a small offset in the base frequency (too small to be seen in the frequency spacing) leads to a significant shift in the harmonic frequency.

Fig. 4 shows that only intense PLHR events are observed during geomagnetically disturbed periods. This effect has been discussed by Němec et al. (2006), who suggested that plasma-wave interactions take place and change the intensity of PLHR events in such a way that it becomes higher in more intense electromagnetic background. The alternative explanation proposed by Němec et al. (2006) was that the PLHR events observed under high Kp values are just too weak to be observed. However, the first explanation seemed to be more likely true, because there were no intense events observed under low Kp values. With more PLHR events identified in the present study, we see that quite intense events have been observed during geomagnetically quiet periods as well. Moreover, most of the intense events have been observed at frequencies below 2.5 kHz, which could correspond to higher radiated power at lower frequencies. Although a more detailed study is needed, our results indicate that PLHR events could be propagating from the generation region to the satellite without any additional plasma-wave interactions which would significantly modify the wave properties.

5. Conclusions

We have presented results of a systematic study of PLHR using the DEMETER spacecraft. Two years of burst-mode data (about 1650 h) have been analyzed using an automatic identification procedure. Altogether, 49 events had frequency spacing of 50/100 or 60/120 Hz.

The power system frequency in the anticipated regions of generation of these events (magnetic footprints of the places of observation on the Earth's surface) correspond well to the frequency separation between the observed spectral lines. Moreover, in 80 percent of the cases the lines occur at exact harmonics of the power system frequency. Only intense PLHR events are observed during geomagnetically disturbed periods and most of the intense PLHR events occur at frequencies below 2.5 kHz.

References

Bell, T.F., Luette, J.P., Inan, U.S. ISEE 1 observations of VLF line radiation in the earth's magnetosphere. J. Geophys. Res. 87 (A5), 3530–3536, 1982.

Berthelier, J.J., Godefroy, M., Leblanc, F., Malingre, M., Menvielle, M., Lagoutte, D., Brochot, J.Y., Colin, F., Elie, F., Legendre, C., Zamora, P., Benoist, D., Chapuis, Y., Artru, J., Pfaff, R. ICE, the electric field experiment on DEMETER. Planet. Space Sci. 54, 456–471, 2006.

Bullough, K., in: Handbook of Atmospheric ElectrodynamicsPower Line Harmonic Radiation: Sources and Environmental Effects, vol. 2. CRC Press, Boca Ralton, Fla., Ch., pp. 291–332, 1995.

Helliwell, R.A., Katsufrakis, J.P., Bell, T.F., Raghuram, R. VLF line radiation in the earth's magnetosphere and its association with power system radiation. J. Geophys. Res. 80, 4249–4258, 1975.

Karinen, A., Mursula, K., Ulich, T., Manninen, J. Does the magnetosphere behave differently on weekends? Ann. Geophysicae 20 (8), 1137–1142, 2002.

Koons, H.C., Dazey, M.H., Edgar, B.C. Satellite observation of discrete VLF line radiation within transmitter-induced amplification bands. J. Geophys. Res. 83 (A8), 3887–3889, 1978.

Matthews, J.P., Yearby, K. Magnetospheric VLF line radiation observed at Halley, Antarctica. Planet. Space Sci. 29, 97–106, 1978.

Molchanov, O.A., Parrot, M., Mogilevsky, M.M., Lefeuvre, F. A theory of PLHR emissions to explain the weekly variation of ELF data observed by a low-altitude satellite. Ann. Geophysicae 9, 669–680, 1991.

Němec, F., Santolík, O., Parrot, M., Berthelier, J.J. Power line harmonic radiation (PLHR) observed by the DEMETER spacecraft. J. Geophys. Res. 111, A04308, 2006.

Nunn, D., Manninen, J., Turunen, T., Trakhtengerts, V., Erokhin, N. On the nonlinear triggering of VLF emissions by power line harmonic radiation. Ann. Geophysicae 17, 79–94, 1999.

Park, C.G., Helliwell, R.A. Magnetospheric effects of power line radiation. Science 200, 727–730, 1978.

Park, C.G., Helliwell, R.A. Power line radiation in the magnetosphere. Adv. Space Res. 1, 423–437, 1981.

Park, C.G., Helliwell, R.A. Ground observations of power line radiation coupled to the ionosphere and magnetosphere. Space Sci. Rev. 35, 131–137, 1983.

Park, C.G., Miller, T.R. Sunday decreases in magnetospheric VLF wave activity. J. Geophys. Res. 84, 943–950, 1979.

Parrot, M. Daily variations of ELF data observed by a low-altitude satellite. Geophys. Res. Lett. 18 (6), 1039–1042, 1991.

Parrot, M., Němec, F., Santolík, O., Berthelier, J.J. ELF magnetospheric lines observed by DEMETER. Ann. Geophysicae 23, 3301–3311, 2005.

Rodger, C.J., Thomson, N.R., Dowden, R.L. VLF line radiation observed by satellite. J. Geophys. Res. 100 (A4), 5681–5689, 1995.

Rodger, C.J., Clilverd, M.A., Yearby, K.H., Smith, A.J. Magnetospheric line radiation observations at Halley, Antarctica. J. Geophys. Res. 104 (A8), 17441–17447, 1999.

Rodger, C.J., Clilverd, M.A., Yearby, K., Smith, A.J. Is magnetospheric line radiation man-made? J. Geophys. Res. 105, 15981–15990, 2000a.

Rodger, C.J., Clilverd, M.A., Yearby, K.H., Smith, A.J. Temporal properties of magnetospheric line radiation. J. Geophys. Res. 105 (A1), 329–336, 2000b.

Tomizawa, I., Yoshino, T. Power line radiation observed by the satellite. J. Geomag. Geoelectr. 37, 309–327, 1985.

Yearby, K.H., Smith, A.J., Bullough, K. Power line harmonic radiation in Newfoundland. J. Atm. Terr. Phys. 45, 409–419, 1983.

Simultaneous observation on board a satellite and on the ground of large-scale magnetospheric line radiation

M. Parrot,[1] J. Manninen,[2] O. Santolík,[3,4] F. Němec,[1,5] T. Turunen,[2] T. Raita,[2] and E. Macúšová[3]

Received 9 May 2007; revised 19 August 2007; accepted 4 September 2007; published 6 October 2007.

[1] Very Low Frequency (VLF) spectrograms show sometimes sets of lines called MLR (Magnetospheric Line Radiation) with frequency spacing close to 50 or 60 Hz. It is very tempting to attribute these MLR to Power Line Harmonic Radiation (PLHR). PLHR are the ELF and VLF waves radiated by electric power systems at the harmonic frequencies of 50 or 60 Hz. Here we show for the first time large scale MLR observed simultaneously on ground and on board a low altitude satellite which is flying over the same zone. This two hours event is observed over a large area in the Northern hemisphere ($\sim$7,400,000 km^2) and in the conjugate region. It is hypothesized that these MLR are due to PLHR propagating in the ionosphere and the magnetosphere. When they cross the equator, the PLHR undergo a nonlinear interaction with particles and may play a role in the dynamics of the radiation belts. **Citation:** Parrot, M., J. Manninen, O. Santolík, F. Němec, T. Turunen, T. Raita, and E. Macúšová (2007), Simultaneous observation on board a satellite and on the ground of large-scale magnetospheric line radiation, *Geophys. Res. Lett.*, *34*, L19102, doi:10.1029/2007GL030630.

1. Introduction

[2] Evidence of PLHR propagation in the magnetosphere was first observed on ground by *Helliwell et al.* [1975], who published simultaneous observations at conjugate points. Other ground observations have been done by *Matthews and Yearby* [1978], *Helliwell* [1979], *Park and Helliwell* [1981], *Yearby et al.* [1983], and *Manninen* [2005]. Direct observations by satellites are shown in a few papers [*Koons et al.*, 1978; *Bell et al.*, 1982; *Tomizawa and Yoshino*, 1985; *Parrot*, 1994; *Rodger et al.*, 1995]. More recently other observations have been done with the ionospheric satellite DEMETER [*Parrot et al.*, 2005; *Němec et al.*, 2006, 2007]. They have performed a systematic analysis of MLR events observed by the spacecraft during its first two years of operation. They found that there are principally two different classes of events: events with frequency spacing of 50/100 or 60/120 Hz (PLHR) and events with different frequency spacing. For the first class, the frequencies of all the observed events well correspond to power system frequencies in possible regions of generation. While the PLHR events occur during both low and high geomagnetic activity, with no significant preference for quiet or disturbed periods, MLR events seem to occur mostly under disturbed conditions. They also found that the MLR events are more intense than PLHR.

[3] Many observations show that the MLR lines drift in frequencies. One must say that there is a controversy about the origin of these lines which are observed in space or on ground because many of them are not separated by 50 or 60 Hz. For example there is a group of MLR events observed by DEMETER close to the geomagnetic equator with characteristics corresponding to emissions at harmonics of ion gyrofrequencies, known from previous spacecraft observations, but at higher radial distances. The generation mechanism of the MLR observed outside the equatorial plan is not well determined although it is most probably due to a nonlinear interaction between electrons and the coherent PLHR. In their study of ISIS2 data, *Rodger et al.* [1995] observed MLR and did not find a frequency correlation with 50 or 60 Hz or multiples. It was the same for observations of MLR at Halley bay [*Rodger et al.*, 1999, 2000a, 2000b]. In a review paper concerning observations of PLHR and MLR emissions by ground based experiments and satellites, *Bullough* [1995] discussed about the possibility that MLR are due to PLHR. Simulations have also been performed by *Nunn et al.* [1999] to explain ground observations of PLHR and associated triggered emissions in Finland. Recently, *Ando et al.* [2002] analyzed the penetration of PLHR through the ionosphere and underlined the importance of the ion gyrofrequency relatively to the wave frequency of this man-made emission. This paper is related to a MLR event simultaneously observed by the satellite DEMETER and a ground-based experiment during a special campaign. The satellite experiments and the ground-based experiments will be briefly described in section 2. Section 3 will present the MLR observation whereas discussion and conclusions are given in section 4.

2. Satellite and Ground-Based Experiments

[4] DEMETER is a low-altitude satellite (660 km) with a quasi sun-synchronous polar orbit which measures electromagnetic waves and plasma parameters all around the Earth except in the auroral zones. The frequency range for the electric field is from DC up to 3.5 MHz, and for the magnetic field from a few Hz up to 20 kHz. There are two scientific modes: a survey mode where spectra of one

[1] Laboratoire de Physique et Chimie de l'Environnement/Centre National de la Recherche Scientifique, Orléans, France.
[2] Sodankylä Geophysical Observatory, Sodankylä, Finland.
[3] Institute of Atmospheric Physics, Academy of Sciences of the Czech Republic, Praha, Czech Republic.
[4] Also at Faculty of Mathematics and Physics, Charles University, Praha, Czech Republic.
[5] On leave from Institute of Atmospheric Physics, Academy of Sciences of the Czech Republic, Praha, Czech Republic.

0094-8276/07/2007GL030630$05.00

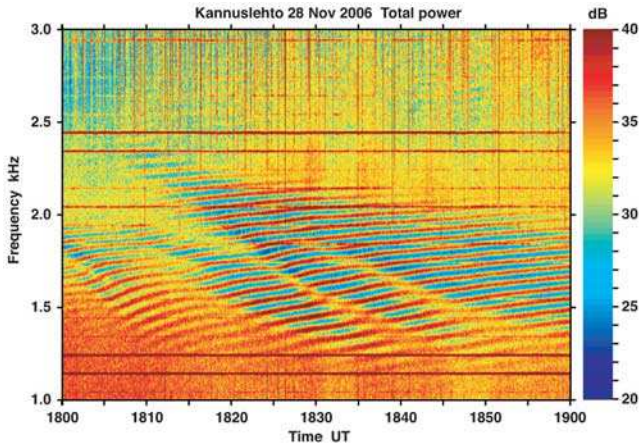

Figure 1. Spectrogram of the signal received at Kannuslehto between 18.00 and 19.00 UT. The frequency range is between 1 and 3 kHz. The signal intensity is color coded according to the scale on the right. The horizontal lines observed just above 1 kHz and between 2 and 3 kHz are the PLHR which are at exact harmonics of 50 Hz. MLR with drifting frequencies are observed between 1.2 and 2.4 kHz.

electric and one magnetic component are onboard computed up to 20 kHz and a burst mode where waveforms of two components of the electromagnetic field (one electric and one magnetic) are recorded up to 20 kHz. The burst mode allows us to perform spectral analysis with better time and frequency resolutions. Details of the wave experiment are given by *Parrot et al.* [2006b] and *Berthelier et al.* [2006].

[5] The ground-based experiment was located at Kannuslehto (67.74°N, 26.27°E, L = 5.41) in Finland. The receiver consisted of two orthogonal magnetic loop antennae with the effective area of 1000 m^2 each. The receiver has been designed for 24-bit digital recordings. The signal from both loops were sampled with frequency of 78.125 kHz and saved in the same file as 32-bit words. The lowest 8 bits were used for control information and GPS time code. Data from two orthogonal loops are handled as complex numbers in the analysis. The basic computation is the complex Fourier transform and Fourier coefficients are used for getting the estimates for signal power as a function of frequency at different polarizations. Details of the receiver and analysis method are given by *Manninen* [2005].

3. MLR Observation

[6] Figure 1 shows the data recorded at Kannuslehto during one hour on November 28, 2006. They are represented as a spectrogram between 1 and 3 kHz. We can see two different sets of lines which are rarely observed simultaneously. There is a set of horizontal lines at fixed frequencies (PLHR) with many harmonics of 100 Hz. Most intense lines are at 1150, 1250, 2050, 2350, 2450 Hz. It is typical of the PLHR observed in Finland which are radiated at frequencies f = 50 (cp ± 1) Hz with p = 12 and c = 1, 2, 3, 4, ... because the industrial plants use 12 pulse bridges to convert 220V/3 phases to DC power [*Nunn et al.*, 1999; *Manninen*, 2005]. The other set of lines is representative of MLR. Their frequency intervals are not equal to 50 or 100 Hz and the lines are drifting in frequency but the frequency drift is not equal for all lines. Its average value is ~0.11 Hz/s. The experimental device allows measuring the wave polarization and it appears that the MLR are whistler mode waves propagating along the direction of the Earth's magnetic field. It means that the MLR are coming from above towards the Earth.

[7] Ground observations are done during two hours in the local night between 17.40 and 19.40 UT. During this event DEMETER was close to Finland and it performed similar observations along its orbit from 18.15.00 UT until the end of the registration at 18.26.30 UT (see Figure 2). Figure 3 shows a spectrogram of an electric component when DEMETER is in the burst mode. There is one minute of data between 18.23.30 and 18.24.30 UT in the frequency range 1–3 kHz. MLR with lines at frequency intervals not equal to 50 or 100 Hz are observed but without PLHR as it was the case on ground. At the beginning of the burst mode a detailed spectral analysis indicates that the line frequency interval varies between 52.3 and 71.6 Hz with an average value of 59.2 Hz. The MLR are also slightly drifting in

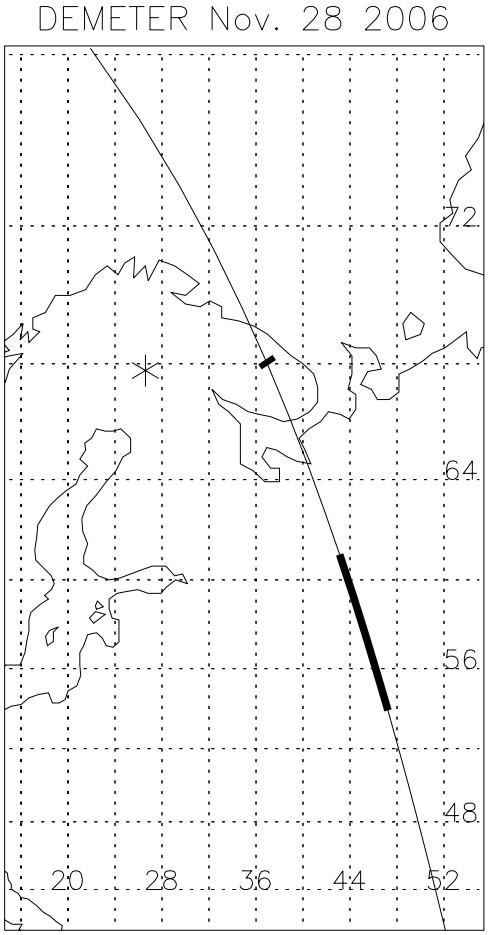

Figure 2. Map showing the area where the event has been recorded. The star indicates the position of Kannuslehto (67.74°N, 26.27°E) in Finland. The line represents the projection of the orbit of the satellite DEMETER (12842.1) on November 28, 2006. The thick part shows the location where DEMETER is in burst mode and the tick shows where DEMETER stops to record data.

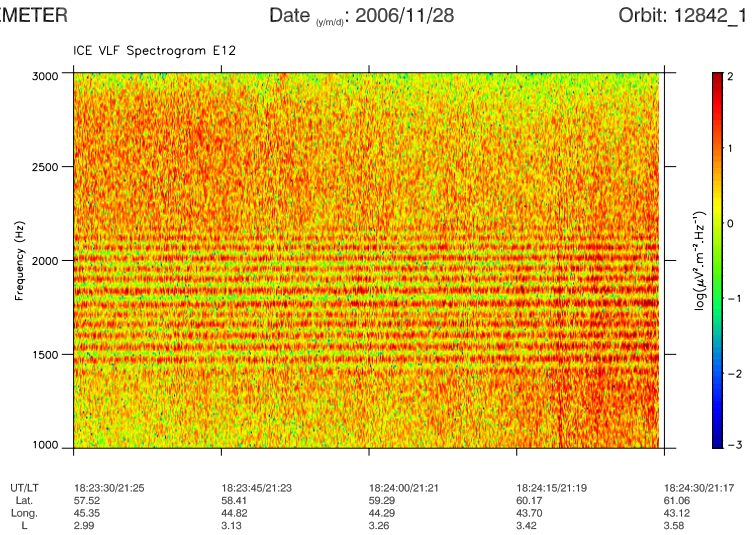

Figure 3. Spectrogram of the signal received by the satellite DEMETER between 18.23.30 and 18.24.30 UT at the end of the burst zone shown in Figure 2. The signal intensity is color coded according to the scale on the right. MLR are observed between 1.4 and 2.2 kHz. Orbital parameters are indicated at the bottom: Latitude, longitude and L value. The local time indicates that it is a night time observation.

frequency. Moreover, DEMETER also observed MLR in the conjugate hemisphere from 17.53 until 17.59 UT in the beginning of the same orbit and from 19.30 until 19.34 UT in the beginning of the next orbit which is shifted westward by 22° in longitude (not shown). But at these times DEMETER was in survey mode and no detailed analysis was possible. To estimate the space extension of this MLR emission in the north hemisphere we consider that along the orbit shown in Figure 2 DEMETER starts to record the emission at a geographic latitude of 27° and stops at 68°. Considering that the MLR are observed on two consecutive orbits it roughly gives a surface of 7,400,000 km^2.

[8] It is the first time where two independent measurements of MLR are simultaneously done on the ground and on board a spacecraft, and Figure 4 shows a comparison of the lines between the two observations. It is clear that it concerns observation of the same phenomena. Taking into account the frequency resolution of the spectral analysis, the lines are at the same frequency on ground and on the satellite. They are drifting at the same rate. On the ground and on board DEMETER the frequency drift is of the order of 0.11 Hz/second. This is in agreement with previous observations [see, e.g., *Nunn et al.*, 1999].

4. Discussion and Conclusions

[9] The fact that the drifts and the frequency spacing are identical on ground and on board the satellite indicates that this is not due to a propagation effect. It also shows that there is no Doppler shift induced by the satellite. It means that this frequency shift and the frequency interval between the lines are not induced during the propagation in a disturbed ionosphere between the satellite and the ground. The simultaneous observations of MLR on the ground, on board the satellite close to Finland at an altitude of 660 km, and in the conjugate hemisphere indicate that these waves are propagating back and forth in the magnetosphere.

[10] Our hypothesis is that the origin of these waves is due to the propagation of the PLHR observed on ground because the only other possibilities concerns:

[11] 1. The electromagnetic harmonic ELF emissions emitted in the equatorial region at the harmonics of the proton gyrofrequency. With the frequency spacing we observe (59.2 Hz) it would mean that these harmonic waves would have been generated in the magnetic equatorial plane at L = 1.95, would be propagated up to L = 5.37 (the

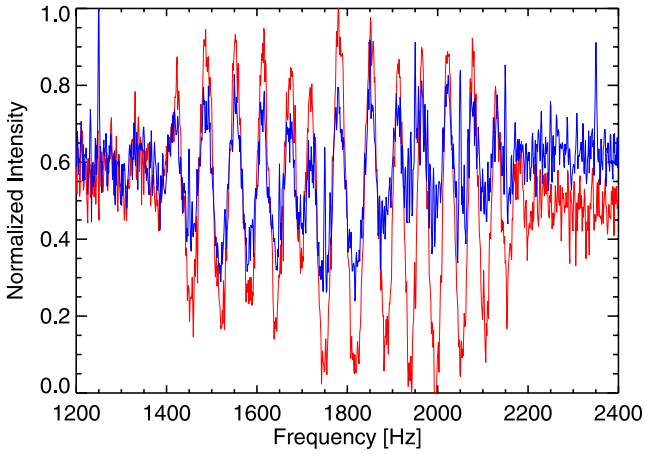

Figure 4. Comparison between the line frequencies observed at Kannuslehto (in blue) and on board the satellite (in red). The spectra are from 1200 up to 2400 Hz and their amplitudes are normalized relative to the maximum intensity of each spectrum. It corresponds to the time interval 18.24.20–18.24.30 UT. It is shown that both MLR observed at Kannuslehto and on board the satellite have similar frequencies and that even their amplitudes at the different frequencies follow the same variation. In addition to the MLR, the Kannuslehto spectrum shows clear PLHR at 1250, 1450, 1650, 1950, 2050, 2150, and 2350 Hz.

average L value of our observations) and then down to lower altitudes. These harmonic waves are effectively observed by DEMETER [*Parrot et al.*, 2006a], and even above Finland (see the quick-look of the orbit 2957.1 on the DEMETER web server http://demeter.cnrs-orleans.fr), but only during very high magnetic activity (it is not the case on Nov. 28, 2006, K_p maximum = 2^+), with a completely different duration and separation of the lines, and close to the ionospheric trough which is not the case here.

[12] 2. ELF emissions at harmonics of ion local gyrofrequencies which are also observed at low altitudes by DEMETER in the equatorial region but these waves are only enhanced at the equator and during high magnetic activity [*Němec et al.*, 2006, 2007].

[13] Then the only explanation is that on the way from the ground the PLHR undergo an interaction with particles in the magnetic equatorial region which is the most favourable region for this kind of interaction. The PLHR intensities are enhanced and their frequencies are changed. This interaction is through a cyclotron resonance mechanism. Then the frequency change of the lines can be the result of a nonlinear wave-particle interaction [*Nunn et al.*, 1999; *Shklyar et al.*, 1992]. They are observed when the waves are coming back in the ionosphere and the atmosphere.

[14] This event is a further evidence that some MLR observed in space are due to PLHR. It is important to survey these waves because the world electric power consumption is constantly increasing and there are indications that PLHR influences the atmosphere-ionosphere-magnetosphere coupling. Nonlinear interactions between electrons and PLHR can participate in the precipitation of electrons from the slot region in the radiation belts [*Bullough et al.*, 1976; *Tatnall et al.*, 1983].

[15] **Acknowledgments.** DEMETER is currently operated by CNES and the corresponding staff is deeply acknowledged. We also thank J. J. Berthelier, who is the PI of the electric field instrument. EM, FN, and OS acknowledge support of the GACR grant 205/06/1267.

References

Ando, Y., M. Hayakawa, and O. A. Molchanov (2002), Theoretical analysis on the penetration of power line harmonic radiation into the ionosphere, *Radio Sci.*, *37*(6), 1093, doi:10.1029/2001RS002486.

Bell, T. F., J. P. Luette, and U. S. Inan (1982), ISEE 1 observations of VLF line radiation in the Earth's magnetosphere, *J. Geophys. Res.*, *87*, 3530–3536.

Berthelier, J. J., et al. (2006), ICE, the electric field experiment on DEMETER, *Planet. Space Sci.*, *54*, 456–471.

Bullough, K. (1995), *Power Line Harmonic Radiation: Sources and Environmental Effects in Handbook of Atmospheric Electrodynamics*, edited by H. Volland, vol. 2, pp. 291–332, CRC Press, Boca Raton.

Bullough, K., A. R. L. Tatnall, and M. Denby (1976), Man-made ELF/VLF emissions and the radiation belts, *Nature*, *260*, 401–403.

Helliwell, R. A. (1979), Overview of power-line radiation and its coupling to the ionosphere and magnetosphere, in *Wave Instabilities in Space Plasmas*, *Astrophys. Space Sci. Libr.*, vol. 74, edited by P. J. Palmadesso and K. Papadopoulos, pp. 27–36, D. Reidel, Dordrecht, Netherlands.

Helliwell, R. A., J. P. Katsufrakis, T. F. Bell, and R. Raghuram (1975), VLF line radiation in the Earth's magnetosphere and its association with power system radiation, *J. Geophys. Res.*, *80*, 4249–4258.

Koons, H. C., M. H. Dazey, and B. C. Edgar (1978), Satellite observation of discrete VLF line radiation within transmitter induced amplification bands, *J. Geophys. Res.*, *83*, 3887–3889.

Manninen, J. (2005), Power line harmonic radiation, in *Some Aspects of ELF-VLF Emissions in Geophysical Research*, *Sodankylä Geophys. Obs. Publ.*, vol. 98, edited by J. Kultima, pp. 53–84, Oula Univ. Press, Sodankylä, Finland. (Available at http://www.sgo.fi/Publications/SGO/thesis/ManninenJyrki.pdf.)

Matthews, J. P., and K. Yearby (1978), Magnetospheric VLF line radiation observed at Halley, Antarctica, *Planet. Space Sci.*, *29*, 97–106.

Němec, F., O. Santolík, M. Parrot, and J. J. Berthelier (2006), Power line harmonic radiation (PLHR) observed by the DEMETER spacecraft, *J. Geophys. Res.*, *111*, A04308, doi:10.1029/2005JA011480.

Němec, F., O. Santolik, M. Parrot, and J. J. Berthelier (2007), Comparison of magnetospheric line radiation and power line harmonic radiation: A systematic survey using the DEMETER spacecraft, *J. Geophys. Res.*, *112*, A04301, doi:10.1029/2006JA012134.

Nunn, D., J. Manninen, T. Turunen, V. Trakhtengerts, and N. Erokhin (1999), On the nonlinear triggering of VLF emissions by power line harmonic radiation, *Ann. Geophys.*, *17*, 79–94.

Park, C. G., and R. A. Helliwell (1981), Power line radiation in the magnetosphere, *Adv. Space Res.*, *1*, 423–437.

Parrot, M. (1994), Observations of PLHR by the low-altitude AUREOL-3 satellite, *J. Geophys. Res.*, *99*, 3961–3969.

Parrot, M., F. Němec, O. Santolík, and J. J. Berthelier (2005), ELF magnetospheric lines observed by DEMETER, *Ann. Geophys.*, *23*, 3301–3311.

Parrot, M., A. Buzzi, O. Santolík, J. J. Berthelier, J. A. Sauvaud, and J. P. Lebreton (2006a), New observations of electromagnetic harmonic ELF emissions in the ionosphere by the DEMETER satellite during large magnetic storms, *J. Geophys. Res.*, *111*, A08301, doi:10.1029/2005JA011583.

Parrot, M., et al. (2006b), The magnetic field experiment IMSC and its data processing onboard DEMETER: Scientific objectives, description and first results, *Planet. Space Sci.*, *54*, 441–455.

Rodger, C. J., N. R. Thomson, and R. L. Dowden (1995), VLF line radiation observed by satellite, *J. Geophys. Res.*, *100*, 5681–5689.

Rodger, C. J., M. A. Clilverd, K. H. Yearby, and A. J. Smith (1999), Magnetospheric line radiation observations at Halley, Antarctica, *J. Geophys. Res.*, *104*, 17,441–17,447.

Rodger, C. J., M. A. Clilverd, K. Yearby, and A. J. Smith (2000a), Is magnetospheric line radiation man made?, *J. Geophys. Res.*, *105*, 15,981–15,990.

Rodger, C. J., M. A. Clilverd, K. H. Yearby, and A. J. Smith (2000b), Temporal properties of magnetospheric line radiation, *J. Geophys. Res.*, *105*, 329–336.

Shklyar, D. R., D. Nunn, A. J. Smith, and S. S. Sazhin (1992), An investigation into the nonlinear frequency shift in magnetospherically propagated VLF pulses, *J. Geophys. Res.*, *97*, 19,389–19,402.

Tatnall, A. R. L., J. P. Matthews, K. Bullough, and T. R. Kaiser (1983), Power-line harmonic radiation and the electron slot, *Space Sci. Rev.*, *35*, 139–173.

Tomizawa, I., and T. Yoshino (1985), Power line radiation observed by the satellite, *J. Geomagn. Geoelectr.*, *37*, 309–327.

Yearby, K. H., A. J. Smith, and K. Bullough (1983), Power line harmonic radiation in Newfoundland, *J. Atmos. Terr. Phys.*, *45*, 409–419.

E. Macúšová and O. Santolík, Institute of Atmospheric Physics, ASCR, Bocni II 1401, 141 31 Praha 4, Czech Republic.

J. Manninen, T. Raita, and T. Turunen, Sodankylä Geophysical Observatory, Tähteläntie 62, FIN-99600 Sodankylä, Finland.

F. Němec and M. Parrot, LPCE/CNRS, 3A Avenue de la Recherche, F-45071 Orléans cedex 2, France. (mparrot@cnrs-orleans.fr)

WDS'07 Proceedings of Contributed Papers, Part II, 64–70, 2007. ISBN 978-80-7378-024-1 © MATFYZPRESS

On the Origin of Magnetospheric Line Radiation

F. Němec
LPCE/CNRS, Orléans, France.
Charles University, Faculty of Mathematics and Physics, Prague, Czech Republic.

O. Santolík
Charles University, Faculty of Mathematics and Physics, Prague, Czech Republic.

M. Parrot
LPCE/CNRS, Orléans, France.

J. J. Berthelier
CETP/CNRS, Saint-Maur des Fossés, France.

Abstract. We present a short overview of results obtained by a systematic survey of line radiation events observed by the DEMETER spacecraft at an altitude of 700 km. We find two different classes of events that can be easily distinguished by the observed frequency separation of lines forming the event – if it is 50/100 Hz or 60/120 Hz then the event is most probably caused by electromagnetic radiation from the electric power systems on the ground (Power Line Harmonic Radiation, PLHR). Other frequency separations correspond to waves generated in a completely natural way (real-Magnetospheric Line Radiation, real-MLR). We show supporting evidence and we estimate possible source locations of both PLHR and real-MLR events. We show that the source locations of PLHR with 50/100 Hz spacing lie mostly in Europe and that the source locations of PLHR with 60/120 Hz lie mostly in the United States and Japan. The generation region of real-MLR events is most probably located in or very close to the geomagnetic equator at radial distances between 1.5 and 3 Earth radii.

Introduction

When represented in the form of frequency-time spectrogram, electromagnetic emissions are sometimes formed by several nearly horizontal, equally-spaced intense lines. These are usually called Magnetospheric Line Radiation (MLR) or Line Radiation (LR). The frequency separation of the lines may significantly vary from case to case, but in some cases it exactly (within the experimental error) corresponds to the frequency of electric power systems – it is equal to 50 or 100 Hz (second harmonic frequency) or 60 or 120 Hz. These are usually believed to be caused by electromagnetic radiation from power systems on the ground and they are called Power Line Harmonic Radiation (PLHR).

MLR-like phenomena have already been reported both in ground [Helliwell et al., 1975; Park and Helliwell, 1978; Matthews and Yearby, 1981; Park and Helliwell, 1981, 1983; Yearby et al., 1983; Rodger et al., 1999, 2000a,b] and satellite data [Koons et al., 1978; Bell et al., 1982; Tomizawa and Yoshino, 1985; Rodger et al., 1995; Parrot et al., 2005; Němec et al., 2006; Parrot et al., 2006; Němec et al., 2007a,b]. However, although the amount of observed events on the ground is relatively large, satellite observations are rather rare, usually reporting only a few cases. Moreover, some controversy still remains about the origin of the observed events. Rodger et al. [1995], who performed the first satellite survey with a significant number of events, found no evidence of a relationship between magnetospheric lines and power line harmonics. However, they briefly mentioned the existence of the second class of events ("tram lines"), which appear close to harmonics of 50/60 Hz. The same was confirmed by ground based observations performed at Halley station [Rodger et al., 1999, 2000a,b].

Němec et al. [2007a] performed a systematic survey of MLR-like events observed by the DEMETER spacecraft. They confirmed the existence of the two distinct classes of events (PLHR and "real-MLR") and demonstrated their different properties (intensity, frequency, most favorable values of Kp index, bandwidth of individual lines, observed time duration). The analysis of DEMETER observations of PLHR events [Němec et al., 2006, 2007b] has shown that the frequency spacing of the lines corresponds well to the power system frequency at possible generation regions. Theoretical analysis of PLHR penetration through the ionosphere lead Ando et al. [2002] to estimation of the dimensions of the affected region. Finally, although the role of PLHR events in the ionosphere is still questionable, it could be quite important, because numerical simulations show that they can serve as a trigger for new emissions [Nunn et al., 1999].

A short overview of MLR-like events observed by the DEMETER spacecraft and an estimation of their possible generation regions is reported in this paper. DEMETER satellite, the wave experiment on board and the resulting data set are described in the following section. Next, possible source locations of PLHR and "real-MLR" events are estimated and discussed. Finally, our results are summarized in the last section.

Data set

We have used data from the DEMETER satellite. DEMETER is a French micro-satellite (mass 130 kg) launched in June, 2004 on a nearly circular orbit with an altitude 710 km and inclination 98 degrees. The altitude of the orbit was changed to 660 km in December, 2005. The primary purpose of the satellite is to study possible ionospheric effects connected with tectonic activity, and its secondary purpose is to analyze man-made effects in the ionosphere. There are two principal modes of operation: burst mode, active only above some specific (mostly seismic) areas, during which more detail data are measured, and survey mode, which is active all around the orbit except of the auroral zones.

Data from the wave instruments have been used in the present paper. In the VLF range (up to 20 kHz), a waveform of one electric and one magnetic field component is measured during the burst mode and a spectrum of one electric and one magnetic field component is calculated on board (frequency resolution 19.53 Hz, time resolution 0.512 or 2.048 s, depending on the mode of the instrument) during the survey mode. In the ELF range (up to 1250 Hz), waveforms of all the six components of the electromagnetic field are measured during the burst mode. Since the frequency resolution during the survey mode is insufficient for our purposes, we have only used the burst mode data.

This represents about 2500 hours of burst mode data, which is too much to be manually checked for the presence of MLR/PLHR events. An automatic identification procedure for their identification has been therefore developed [Němec et al., 2006, 2007a] and run as a part of DEMETER Level-3 data processing in the DEMETER control center in Orléans, France. Altogether, 88 events have been found and confirmed by visual inspection. Further, we follow the classification introduced by Němec et al. [2006] and divide the observed events into two classes depending on the observed frequency spacing: 1) events with frequency spacing 50/100 or 60/120 Hz (PLHR, 62 events found) 2) events with other frequency spacing ("real-MLR", 26 events found).

Possible source locations of PLHR events

Figure 1 shows locations of estimated PLHR sources in geographic coordinates. The estimate was done by using an assumption that the waves propagate from their generation region up to the DEMETER altitudes along the magnetic field lines [Němec et al., 2006, 2007b]. Geographic locations corresponding to the events with frequency spacing 50/100 Hz are plotted by crosses, geographic locations corresponding to the events with frequency spacing 60/120 Hz are

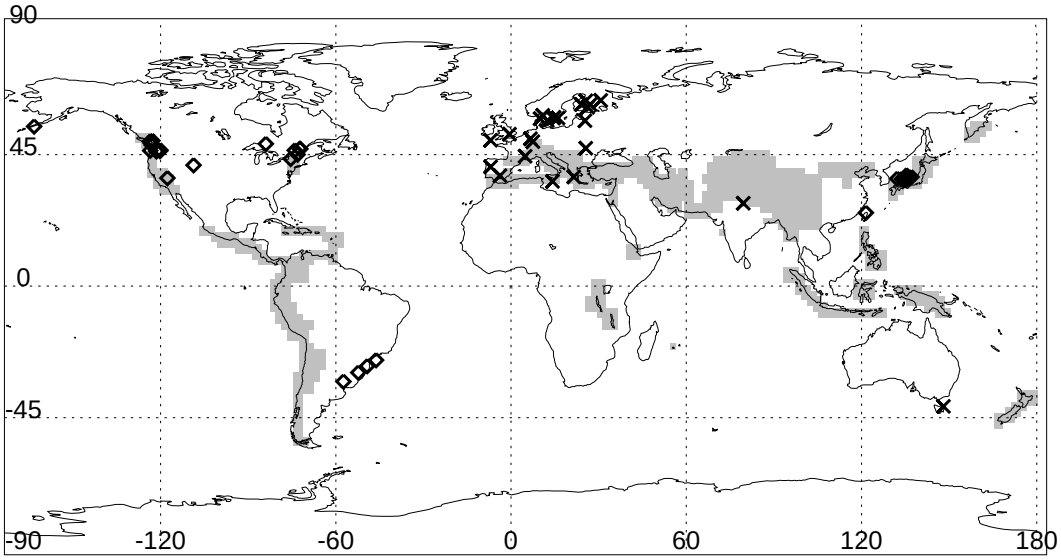

Figure 1. Locations of the estimated PLHR sources in geographic coordinates. The events with frequency spacing 50/100 Hz are plotted by crosses, the events with frequency spacing 60/120 Hz are plotted by diamonds. Seismic zones with permanently active burst mode coverage are shown by grey shading. The operational-phase burst mode regions (about 20% of the burst mode coverage) are not shown because their position may vary during the mission.

plotted by diamonds. Areas with permanently active burst-mode coverage are shown by grey shading. It can be seen that the frequency spacing of the observed events corresponds well to the base frequency of the power systems in the estimated generation region – probable source regions of events with frequency spacing 50/100 Hz are localized mostly in Europe and probable source regions with frequency spacing 60/120 Hz are localized predominantly in Japan and in the USA.

Moreover, in most of the cases not only the frequency spacing but also the frequencies of the individual lines themselves correspond to the multiples of base power system frequency in the estimated generation region. The explanation proposed by Němec et al. [2007b] can be probably used for the remaining cases – supposing the electric power system is not perfect and its base frequency is slightly off 50/60 Hz, this small offset is too small to be observed in frequency spacing, but at higher harmonics (that are typically observed) it can lead to a significant shift in frequency.

Finally, it is found that the peak intensity (that is the maximum intensity of the event) is lower during the day than during the night by about 6 dB. This difference is statistically quite significant (4.2 standard deviations). Full-wave numerical calculations [Nagano et al., 1975; Bortnik and Bleier, 2004] of the wave attenuation in the ionosphere reveal that it can be explained by the different penetration characteristics of the ionosphere during the day as compared to those during the night [Němec et al., 2007c].

This represents a strong evidence that the PLHR events observed on board DEMETER are really coming from electromagnetic radiation from electric power systems on the ground. However, it is still questionable to what extent these may undergo wave-particle interactions [Němec et al., 2007c].

Possible generation region of "real-MLR" events

Figure 2 shows an example and detail wave analysis of one of the "real-MLR" events that occurred in the ELF range. It was measured in the northern hemisphere on November 8, 2004 between 0543:59 UT and 0547:21 UT. The meaning of the individual panels is as

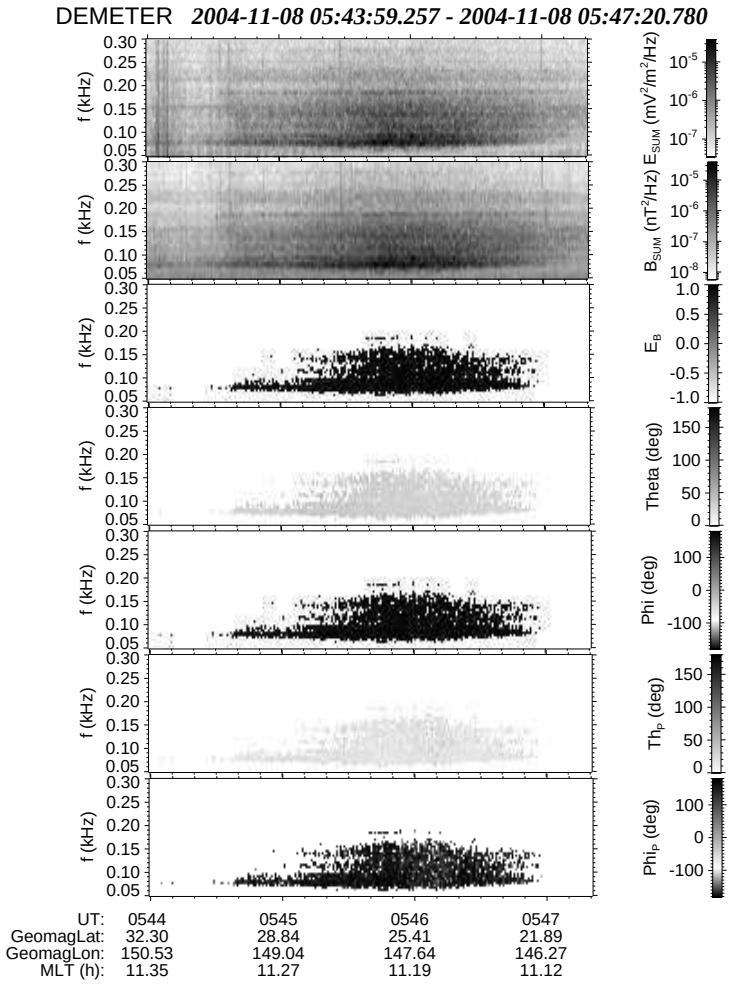

Figure 2. An example and detail wave analysis of a "real-MLR" event measured by DEMETER in the northern hemisphere on November 8, 2004 between 0543:59 UT and 0547:21 UT. The meaning of the panels is as follows: frequency-time spectrogram of electric and magnetic field fluctuations, frequency-time plot of ellipticity, polar and azimuthal angle of the wave vector direction with respect to the ambient magnetic field, polar and azimuthal angle of the Poynting vector direction with respect to the ambient magnetic field.

follows. The first two panels represent frequency-time spectrograms of power spectral density of electric and magnetic field fluctuations. The third panel represents the frequency-time plot of ellipticity obtained from the Singular Value Decomposition (SVD) method [Santolík et al., 2003, equation 13]. It ranges from -1 to 1, a sign is added to reflect the polarization sense (positive values correspond to the right-handed polarization, negative values correspond to the left-handed polarization). The fourth and fifth panel show the frequency-time plots of polar and azimuthal angle of the wave vector with respect to the ambient magnetic field (determined again by the SVD method, Santolík et al. [2003], equation 22). The polar angle is defined in such a way that a value of 0 degrees means propagation along the magnetic field line, a value of 90 degrees means propagation perpendicular to the magnetic field line and a value of 180 degrees means propagation anti-parallel to the magnetic field line. The azimuthal angle is defined in such a way that a value of 0 degrees means propagation "away from the Earth". Finally, the sixth and seventh panel represent the frequency-time plots of polar and azimuthal angle of the Poynting vector (determined directly as $\vec{E} \times \vec{B}/\mu_0$, where μ_0 is the vacuum permeability) direction. A threshold of power spectral density of magnetic field fluctuations has been used in order to select only the data corresponding to the event.

It can be seen that the waves are almost right-hand circularly polarized and that both the wave vector and Poynting vector directions are nearly parallel to the ambient magnetic field. Moreover, there is a weak perpendicular component oriented towards the Earth (ϕ angle is close to 180^o), indicating that the waves propagate from larger L shells. The similar analysis has been performed for all the cases that occurred in the ELF range [Němec et al., 2007d]. It has been found that there is a reversal of the parallel component of the Poynting vector direction localized practically in the equatorial plane (about $\pm 5^\circ$ within the geomagnetic equator). It is oriented along the magnetic field line in the northern hemisphere, while it is oriented anti-parallel to the magnetic field line in the southern hemisphere. Moreover, the waves observed close to the geomagnetic equator are almost linearly polarized, while the waves observed at larger geomagnetic latitudes are right-hand polarized.

The results strongly suggest that the generation region of the events is located in or close to the equatorial plane at larger radial distances; after being generated the waves propagate towards the Earth where they are detected by DEMETER. The polarization properties are in a good agreement with the cold plasma theory and propagation in the whistler mode.

The most probable radial distance of the source region can be estimated from the frequency spacing of the observed events, supposing that the lines are generated at multiples of local proton cyclotron frequency. The frequency separation of the lines was checked for all the events and it has been found to vary from 20 to 100 Hz [Němec et al., 2007d]. This corresponds to the radial distances of the source region from about 1.5 to 3 R_E.

This estimation of the possible generation region uses several basic assumptions. The first of them is that the waves are generated in or very close to the equatorial plane. This is well justified both by the fact that the equatorial region is the most favorable place for wave-particle interactions [e.g., Omura et al., 1991] and, even more, by the results of the wave propagation analysis that shows the reversal of the Poynting vector direction in the vicinity of the geomagnetic equator. The second assumption is the generation at the multiples of the local proton cyclotron frequency. This assumption is justified by the fact that the generation at the multiples of the local ion cyclotron frequency in the source region (local electron cyclotron frequency at the satellite position is by several orders of magnitude larger than the observed frequency spacing) is the most natural way how to obtain a line structure in frequency-time spectrum. Furthermore, the wave analysis reveals that the waves propagate towards the Earth, that is from larger L-shells, where heavier ions are rare and in addition their local cyclotron frequency is too low as compared to the observed frequency spacing. This justifies the generation at multiples of local proton cyclotron frequency at the source location instead of generation at multiples of the cyclotron frequency of heavier ions.

Conclusion

A short overview of a systematic study of observations of PLHR/MLR by the DEMETER spacecraft has been presented. An automatic identification procedure has been applied to about 2500 hours of burst mode data and 88 events (62 PLHR events and 26 MLR events) have been found.

It has been shown that for all of the events the frequency spacing corresponds well to the power system frequency in the source location. Moreover, the day-night asymmetry of the observed peak intensity can be explained by different penetration characteristics of the ionosphere during the day as compared to those during the night. This represents a strong evidence that the PLHR events are really caused by the electromagnetic radiation from power systems on the ground.

Concerning the generation region of "real-MLR" events, we have shown some evidence that it is located in or very close to the equatorial plane and that it is most probably located at radial distances between 1.5 and 3 R_E.

Acknowledgments. We thank J.-Y. Brochot of LPCE/CNRS Orléans for his help with running the PLHR recognition algorithm as the DEMETER level-3 processing procedure. We thank SPDF/Modelweb for the free access to the data from the International Reference Ionosphere model. The work was supported by the Czech Grant Agency under contract No. 202/03/H162.

References

Ando, Y., Hayakawa, M., and Molchanov, O. A., Theoretical analysis on the penetration of power line harmonic radiation into the ionosphere, *Radio Sci.*, *37*, 2002.

Bell, T. F., Luette, J. P., and Inan, U. S., ISEE 1 observations of VLF line radiation in the earth's magnetosphere, *J. Geophys. Res.*, *87*, 3530–3536, 1982.

Bortnik, J. and Bleier, T., Full wave calculation of the source characteristics of seismogenic electromagnetic singnals as observed at LEO satellite altitudes, *Eos. Trans. AGU*, *85*, Fall Meeting Suppl., Abstract T51B–0453, 2004.

Helliwell, R. A., Katsufrakis, J. P., Bell, T. F., and Raghuram, R., VLF line radiation in the earth's magnetosphere and its association with power system radiation, *J. Geophys. Res.*, *80*, 4249–4258, 1975.

Koons, H. C., Dazey, M. H., and Edgar, B. C., Satellite observation of discrete VLF line radiation within transmitter-induced amplification bands, *J. Geophys. Res.*, *83*, 3887–3889, 1978.

Matthews, J. P. and Yearby, K., Magnetospheric VLF line radiation observed at Halley, Antarctica, *Planet. Space Sci.*, *29*, 97–106, 1981.

Nagano, I., Mamabo, M., and Hutatsuishi, G., Numerical calculation of electromagnetic waves in an anisotropic multilayered medium, *Radio Sci.*, *10*, 611–617, 1975.

Nunn, D., Manninen, J., Turunen, T., Trakhtengerts, V., and Erokhin, N., On the nonlinear triggering of VLF emissions by power line harmonic radiation, *Ann. Geophys.*, *17*, 79–94, 1999.

Němec, F., Santolík, O., Parrot, M., and Berthelier, J. J., Power line harmonic radiation (PLHR) observed by the DEMETER spacecraft, *J. Geophys. Res.*, *111*, 2006.

Němec, F., Santolík, O., Parrot, M., and Berthelier, J. J., Comparison of magnetopsheric line radiation and power line harmonic radiation: a systematic survey using the DEMETER spacecraft, *J. Geophys. Res.*, *112*, 2007a.

Němec, F., Santolík, O., Parrot, M., and Berthelier, J. J., Power line harmonic radiation: A systematic study using DEMETER spacecraft, *Adv. Space Res.*, *in press*, 2007b.

Němec, F., Santolík, O., Parrot, M., and Berthelier, J. J., Power line harmonic radiation observed by satellite: Properties and propagation through the ionosphere, *J. Geophys. Res.*, *submitted*, 2007c.

Němec, F., Santolík, O., Parrot, M., and Berthelier, J. J., Magnetospheric line radiation: Wave analysis and generation region, *J. Geophys. Res.*, *submitted*, 2007d.

Omura, Y., Matsumoto, H., Nunn, D., and Rycroft, M. J., A review of observational, theoretical and numerical studies of VLF triggered emissions, *J. Atm. and Terr. Phys*, *53*, 351–368, 1991.

Park, C. G. and Helliwell, R. A., Magnetospheric effects of power line radiation, *Science*, *200*, 727–730, 1978.

Park, C. G. and Helliwell, R. A., Power line radiation in the magnetosphere, *Adv. Space Res.*, *1*, 423–437, 1981.

Park, C. G. and Helliwell, R. A., Ground observations of power line radiation coupled to the ionosphere and magnetosphere, *Space Sci. Rev.*, *35*, 131–137, 1983.

Parrot, M., Němec, F., Santolík, O., and Berthelier, J. J., ELF magnetospheric lines observed by DEMETER, *Ann. Geophys.*, *23*, 3301–3311, 2005.

Parrot, M., Buzzi, A., Santolík, O., Berthelier, J. J., Sauvaud, J. A., and Lebreton, J. P., New observations of electromagnetic harmonic ELF emissions in the ionosphere by the DEMETER satellite during large magnetic storms, *J. Geophys. Res.*, *111*, 2006.

Rodger, C. J., Thomson, N. R., and Dowden, R. L., VLF line radiation observed by satellite, *J. Geophys. Res.*, *100*, 5681–5689, 1995.

Rodger, C. J., Clilverd, M. A., Yearby, K. H., and Smith, A. J., Magnetospheric line radiation observations at Halley, Antarctica, *J. Geophys. Res.*, *104*, 17 441–17 447, 1999.

Rodger, C. J., Clilverd, M. A., Yearby, K., and Smith, A. J., Is magnetospheric line radiation man-made?, *J. Geophys. Res.*, *105*, 15 981–15 990, 2000a.

Rodger, C. J., Clilverd, M. A., Yearby, K. H., and Smith, A. J., Temporal properties of magnetospheric line radiation, *J. Geophys. Res.*, *105*, 329–336, 2000b.

Santolík, O., Parrot, M., and Lefeuvre, F., Singuar value decomposition methods for wave propagation analysis, *Radio Sci.*, *38*, 2003.

Tomizawa, I. and Yoshino, T., Power line radiation observed by the satellite, *J. Geomag. Geoelectr.*, *37*, 309–327, 1985.

Yearby, K. H., Smith, A. J., and Bullough, K., Power line harmonic radiation in Newfoundland, *J. Atm. and Terr. Phys*, *45*, 409–419, 1983.

Spacecraft observations of electromagnetic perturbations connected with seismic activity

F. Němec,[1,2,3] O. Santolík,[3,4] M. Parrot,[1] and J. J. Berthelier[5]

Received 31 October 2007; revised 29 January 2008; accepted 12 February 2008; published 15 March 2008.

[1] Results of a statistical study of intensity of VLF electromagnetic waves observed in the vicinity of earthquakes are presented. A unique set of data obtained by the micro-satellite DEMETER (altitude of about 700 km, nearly Sun-synchronous orbit) and a robust two-step data processing has been used. In the first step, all the measured data are used to construct a map of electromagnetic emissions containing a statistical description of wave intensity at a given point of the satellite orbit under given conditions. In the second step, the intensity measured close to earthquakes is analyzed using the statistical distribution of background intensity obtained in the first step. The changes of wave intensity caused by seismic activity are investigated and their statistical significance is evaluated. Altogether, more than 2.5 years of satellite data have been analyzed and about 9000 earthquakes with magnitudes larger than or equal to 4.8 that occurred all over the world during the analyzed period have been included in the study. It is shown that, during the night, there is a statistically significant decrease by 4 – 6 dB of the measured wave intensity shortly (0–4 hours) before an intense surface (depth less than or equal to 40 km) earthquake. **Citation:** Němec, F., O. Santolík, M. Parrot, and J. J. Berthelier (2008), Spacecraft observations of electromagnetic perturbations connected with seismic activity, *Geophys. Res. Lett.*, *35*, L05109, doi:10.1029/2007GL032517.

1. Introduction

[2] Electromagnetic perturbations possibly connected with seismic activity have been in the recent years reported by several authors, both from ground based measurements [*Tate and Daily*, 1989; *Asada et al.*, 2001] and from low-altitude satellite experiments [*Parrot and Mogilevsky*, 1989; *Larkina et al.*, 1989; *Molchanov et al.*, 1993; *Parrot*, 1994; *Hobara et al.*, 2005; *Molchanov et al.*, 2006]. These observations have been the subject of an intense debate in the literature [see, e.g., *Rodger et al.*, 1996] for two main reasons. The first one stems from the lack of large and reliable database: most studies in this area have been limited by a lack of enough experimental results to conduct a statistically significant analysis of the phenomena and obtain firm results. In addition, the theoretical ideas [*Molchanov et al.*, 1995; *Sorokin et al.*, 2001] and physical mechanisms [*Gershenzon et al.*, 1989; *Molchanov and Hayakawa*, 1998] that have been proposed are not convincing enough since they lack the support of reliable experimental evidence.

[3] Using a survey of electromagnetic emissions on a low-altitude satellite that includes the vast majority of orbits that occurred over 2.5 years, we have been able to perform a unique statistical study of the influence of seismic activity on the intensity of electromagnetic waves in the ionosphere.

2. Data Set

[4] Our study is based on the data from the French micro-satellite DEMETER, launched in June, 2004 on a quasi helio-synchronous circular orbit (10.30–22.30 LT) with a 98° inclination and an altitude of about 700 km [*Parrot et al.*, 2006]. It performs 14 orbits per day and the instruments are nearly continuously powered at geomagnetic latitudes between −65° to +65° thus providing a very good coverage of the Earth's seismic zones. We have used the electric and magnetic field data from the ICE [*Berthelier et al.*, 2006] and IMSC [*Parrot et al.*, 2006; *Santolík et al.*, 2006] experiments, respectively, and, more specifically, the measurements made in the VLF band (from 15 Hz to 17.4 kHz). Irrespective of the mode of operation of the satellite, power spectra of one electric and one magnetic field component are computed on-board with a frequency resolution of 19.5 Hz and a time resolution of 2 s or 0.5 s depending on the mode of operation. For the data set used in this study the selected electric component is perpendicular to the orbit plane and the magnetic field component is inclined by 45 degrees from the velocity vector direction. Data from more than 2.5 years of the satellite observations have been used, altogether representing about 11500 hours of observations organized in about 20000 half-orbits. According to the USGS catalog (http://neic.usgs.gov/neis/epic/epic_global.html), about 9000 earthquakes with magnitude larger than or equal to 4.8 occurred all over the world during the analyzed period.

3. Method of Analysis

[5] In order to search for a trend in the behavior of electromagnetic emissions above seismic regions, it is necessary to define the statistical distribution of the wave intensity in absence of seismic activity. As the first step of the data processing, we thus built a map of electromagnetic emissions, which contains a statistical description of the intensity of electromagnetic waves obtained from the entire 11500-hour data set. It can be represented by a 6-dimensional matrix. Two dimensions are the geomagnetic longitude and

[1]LPCE, CNRS, Orléans, France.
[2]Faculty of Mathematics and Physics, Charles University, Prague, Czech Republic.
[3]IAP, ASCR, Prague, Czech Republic.
[4]Also at Faculty of Mathematics and Physics, Charles University, Prague, Czech Republic.
[5]CETP, CNRS, Saint-Maur des Fossés, France.

0094-8276/08/2007GL032517$05.00

latitude of the satellite with a resolution of 10 and 2 degrees, respectively. The third dimension is the frequency. We limit our analysis to frequency range below 10 kHz in order to avoid frequencies of terrestrial VLF transmitters. We have selected 16 and 13 frequency bands (117 Hz each) for the electric and magnetic field, respectively, in such a way that these omit spacecraft interferences and cover the entire studied frequency range as uniformly as possible. The lower number of chosen frequency bands for magnetic field data is caused by a significantly larger amount of interferences, which makes the suitable choice much more difficult. The last 3 dimensions describe the magnetospheric conditions at the time of observation: Kp index for the quiet (0−1o) moderate (1+−2+) and disturbed (above 3−) geomagnetic conditions; magnetic local time (dayside and nightside), and season of the year (October−April, May−September). In each cell of this matrix we accumulate a histogram of the common logarithm of the intensity at a given place and under given conditions, using all the available data. For a given spacecraft location and magnetospheric conditions this results into an estimate of the probability density function $f(E)$ of observing a power spectral density E.

[6] The basic idea of the second step of our procedure is as follows. For a measured power spectral density of electric (magnetic) field fluctuations E_i, we determine its cumulative probability F_i as the value of the corresponding cumulative distribution function. This can be calculated as an integral of the probability density function f_i obtained for the same frequency and spacecraft location under similar magnetospheric conditions:

$$F_i = \int_{-\infty}^{E_i} f(E)\, dE \tag{1}$$

[7] In other words, this is the probability (a number between 0 and 1) of occurrence of signals with an intensity less or equal to the measured level.

[8] We calculate these cumulative probabilities for measurements of wave intensity recorded during seismic events. We select the data points for which the vertical projection of the spacecraft position to the ground was closer than 1100 km to the epicenter of an earthquake and which were measured no more than 5 days before and 3 days after the main shock. If two or more different earthquakes occur close enough, and therefore possibly influence the data, the measurement is not taken into account. This condition is equivalent to taking into account only "individually occurring" earthquakes, sufficiently separated one from another either in time or in space. Consequently, sequences of earthquakes occurring at about the same time and the same location (typically the main shock and aftershocks) are not considered and data measured in their vicinity are not used. This is done in order to not mix pre- and post- seismic effects.

[9] The obtained cumulative probabilities are organized in bins as a function of: frequency (16/13 selected bands), time to/from an earthquake (resolution of 4 hours) and distance from an earthquake (resolution of 110 km). For a bin b we define a "probabilistic intensity" as follows:

$$I_b = \frac{\sum_{i=1}^{M_b} F_i}{M_b} - 0.5 \tag{2}$$

where M_b is the number of cumulative probabilities F_i collected in a given bin. Now, if the observed intensities were significantly lower or larger than the usual ones, the attributed cumulative probabilities would be significantly different from 0.5 and the resulting probabilistic intensity would be significantly different from 0. In this way, we neutralize the influence of the distribution of intensities of natural waves on the resulting statistics. However, one problem remains: what quantitative value should we attribute to the word "significantly"? The answer can be found using basic statistical properties of the probabilistic intensity.

[10] If we calculate values of the cumulative probability from the entire original data set (not just from the selected earthquake cases), we obtain a large set of values which are uniformly distributed between 0 and 1. This is a trivial consequence of the definition of the cumulative distribution function [*Press et al.*, 1992]. Averaging them into the finite bins in position and time we sum a large number of these values. Consequently, according to the central limit theorem and supposing that M_b is sufficiently large, values of I_b follow the normal distribution with a mean value 0 and a standard deviation σ_b. If all the values F_i were independent, an estimate of σ_b would read

$$\sigma_b' = \frac{1}{\sqrt{12 M_b}} \tag{3}$$

[11] The problem when performing this calculation is that although we know the total number of cumulative probabilities in the bin M_b, we do not know how many of them can be considered as independent. We can define this number of independent cumulative probabilities as M_b'.

[12] An estimate of M_b' should be derived from the number of continuous data intervals contained in a given bin. These continuous data intervals correspond to different half-orbits of the spacecraft. Duration of a half-orbit is about 35 minutes, which is longer than a typical time scale of intensity changes of electromagnetic waves in the upper ionosphere. Moreover, data from two successive orbits cannot be contained in the same bin. The number N_b of half-orbits contributing to a given bin could be thus considered as a lower estimate of M_b',

$$M_b' = \frac{N_b}{\alpha^2}, \tag{4}$$

where $\alpha \leq 1$ is a positive number defining which relative fraction of the data from a single half-orbit can be on average considered as independent. In other words, α is the same for all the bins and represents a measure of stability of electromagnetic waves: the lower the α is, the more variable is their intensity.

[13] This provides us with an estimate of σ_b which is based on the known number N_b of half-orbits contributing to a given bin,

$$\hat{\sigma}_b = \frac{\alpha}{\sqrt{12\, N_b}}, \tag{5}$$

where α can then be estimated experimentally. The simplest approach is to select a set of bins and to suppose that the

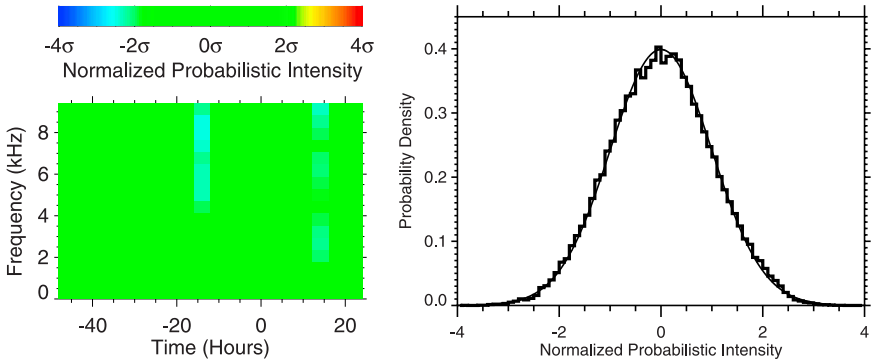

Figure 1. (left) Results from a superposed epoch method showing an example frequency-time spectrogram of normalized probabilistic intensity constructed from randomly distributed time intervals. The number and length of the time intervals corresponds to those used in the left panel of Figure 2. (right) Histogram of values of normalized probabilistic intensity obtained from randomly distributed time intervals of DEMETER data (obtained by combining 144 plots similar to the one shown in the left panel together). Over-plotted is a Gaussian distribution with mean value 0 and standard deviation 1 to demonstrate that the normalized probabilistic intensity follows this distribution.

standard deviation of the normalized probabilistic intensities I_b/σ_b should be unity within this set of bins. Since the mean value of I_b/σ_b should be zero, this leads us to an estimate of α,

$$\alpha = \sqrt{\frac{12}{Q}\sum_{b=1}^{Q} N_b I_b^2}, \tag{6}$$

where Q is the number of bins in the set.

[14] In the paper, the values of the normalized probabilistic intensity are evaluated for $Q = 48$ time bins going from 5 days before an earthquake to 3 days after it, each bin representing 4 hours of time difference. This enables us to define α (the same for all the 48 time bins), calculate $\hat{\sigma}_b$ from equation (5), and to obtain the normalized probabilistic intensities I_b/σ_b for all the bins. These are then displayed in Figures 1, 2, and 3. If systematic deviations of several standard deviations ($>3\sigma_b$) are observed, we can consider the effect to be statistically significant.

[15] The correctness of the statistical analysis is demonstrated in Figure 1, which represents the results obtained from randomly distributed time intervals of the DEMETER data. Left panel shows an example frequency-time spectrogram of normalized probabilistic intensity in order to demonstrate that the expected random fluctuations of normalized probabilistic intensity (in the absence of seismic effects) do not display any particular variation. A histogram of values of normalized probabilistic intensity is plotted in the right-hand panel. It was obtained by combining 144 plots similar to the one shown in the left-hand panel and shows a Gaussian distribution with a mean value 0 and a standard deviation 1. Additional tests have been performed by applying the data processing method to random earthquake databases constructed by: 1) keeping real locations of earthquakes, but randomly generating their times 2) keeping real times of earthquakes, but randomly

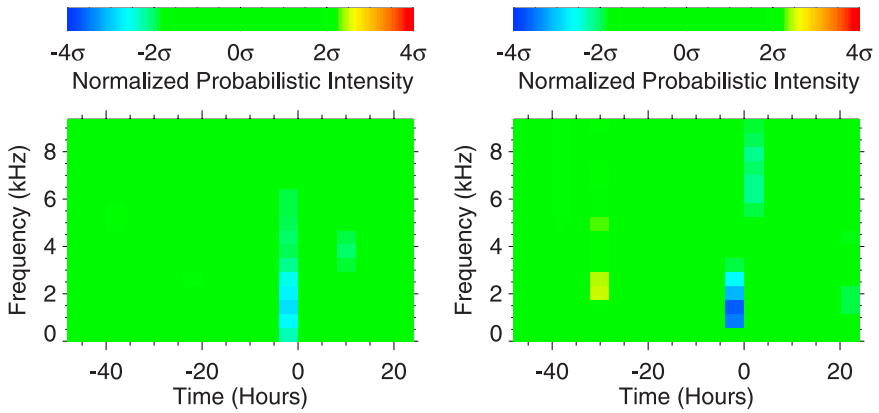

Figure 2. (left) Frequency-time spectrogram of the normalized probabilistic intensity (see text) obtained from the nighttime electric field data measured within 330 km of the earthquakes with magnitudes larger than or equal to 4.8 and depth less than or equal to 40 km. Data measured for all Kp values and seasons have been included. (right) The same but for earthquakes with magnitudes larger than or equal to 5.0.

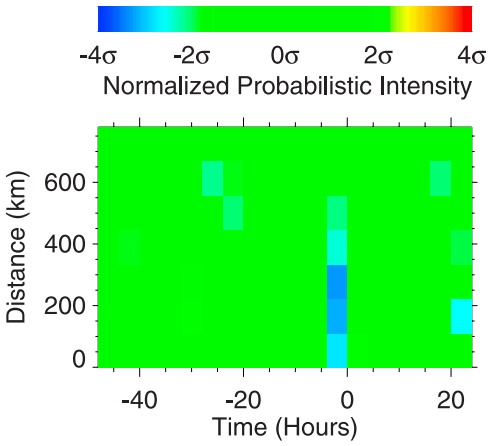

Figure 3. Normalized probabilistic intensity (see text) obtained from the night-time electric field data measured for earthquakes with magnitude larger than or equal to 5.0 and depth less than or equal to 40 km plotted as a function of the distance from the epicenters and of time from the earthquakes for a frequency band 1055–2383 Hz. Data measured for all Kp values and seasons have been included.

generating their positions. Again, no particular variation has been observed.

4. Results

[16] Since it has been reported that a depth of earthquakes can play a significant role in earthquake-related effects [e.g., *Rodger et al. 1999*], we have divided the earthquakes into two groups: surface earthquakes (depth less than or equal to 40 km) and deep earthquakes (depth larger than 40 km). Moreover, day-time and night-time data have been treated separately. Finally, all 4 different combinations of surface/deep earthquakes and day-time/night-time data have been examined for the presence of possible seismic effects.

[17] Figure 2 shows that the normalized probabilistic intensity obtained from the night-time electric field data is below the "normal" level shortly (0–4 hours) before the surface earthquakes at frequencies of about 1–2 kHz. The probabilistic intensity decreases by about 3 standard deviations for earthquakes with magnitudes larger than or equal to 4.8. This effect is based on the data collected during 50 different orbits. If we consider only surface earthquakes with magnitudes larger than or equal to 5.0, the effect becomes stronger, with the probabilistic intensity decreasing by about 4 standard deviations, and with 34 different orbits contributing to the bins where the decrease is detected. Concerning the probabilistic intensities, these correspond to values between −0.10 and −0.15. Transforming these values back to the corresponding power spectral density, we obtain a decrease between −4 and −6 dB. The decrease was observed also in the magnetic field data, but it is much weaker and its statistical significance is questionable. This can be probably explained by a lower sensitivity of magnetic field instrument and is not connected with the nature of intensity decrease. No similar effects were observed during the day (not shown). No effects were observed for deep earthquakes (not shown).

[18] Figure 3 shows that the spatial scale of the affected area is approximately 350 km (however, one should keep in mind that the spatial resolution of our bins is only about 110 km, which place rather large uncertainties on the result). This corresponds relatively well to the size of the earthquake preparation zone estimated using the *Dobrovolsky et al.* [1979] formula: 140 km for earthquakes with magnitudes 5.0 and 380 km for earthquakes with magnitudes 6.0.

5. Discussion and Summary

[19] The presented statistical study disagrees with previous systematic studies that claimed the presence of seismic effects since they mostly reported an increase in the ELF/VLF activity [*Larkina et al.*, 1989; *Parrot and Mogilevsky*, 1989; *Serebryakova et al.*, 1992; *Molchanov et al.*, 1993; *Parrot*, 1994]. These studies have been critically examined by *Henderson et al.* [1993], who underlined the importance of usage of control set of data in order to estimate statistical significance of the observed effects and who failed to indicate any significant differences between the earthquake and control orbits. More recently, a similar result was obtained by *Rodger et al.* [1996]. However, as noted by *Parrot* [1999], both these studies probably could not detect decreases in wave activity and can be therefore considered as being in agreement with our study.

[20] There are two basic possibilities for the explanation of the observed decrease: naturally occurring waves are either attenuated or diverged over earthquake epicenters (this could be caused by a decrease of the refractive index, as proposed by *Vodyanitskii et al.* [1990]). A possible explanation of why the decrease is observed only in the night-time data could be that during the day the ionospheric ionization is significantly larger. Any potential changes caused by seismic activity may be thus overwhelmed by this stronger influence. It is also important to note that the frequency band where the decrease is observed could be related to the cut-off frequency of the first TM mode in the Earth-ionosphere guide (1.7 kHz during the night-time). Finally, our analysis shows that the effect is connected only with surface earthquakes, as suggested by previous researchers [see, e.g., *Rodger et al.*, 1999, and references therein].

[21] We have statistically demonstrated that a significant intensity decrease is observed in night-time data shortly before the main shock of large surface earthquakes. Further research based on the increasing data set of DEMETER measurements will hopefully help us to understand its nature.

[22] **Acknowledgments.** FN and OS acknowledge support of the GACR grant 205/06/1267.

References

Asada, T., H. Baba, M. Kawazoe, and M. Sugiura (2001), An attempt to delineate very low frequency electromagnetic signals associated with earthquakes, *Earth Planets Space*, *53*, 55–62.

Berthelier, J. J., et al. (2006), ICE, the electric field experiment on DEMETER, *Planet. Space Sci.*, *54*, 456–471.

Dobrovolsky, I. R., S. I. Zubkov, and V. I. Myachkin (1979), Estimation of the size of earthquake preparation zones, *Pure Appl. Geophys.*, *117*, 1025–1044.

Gershenzon, N. I., M. B. Gokhberg, A. V. Karakin, N. V. Petviashvili, and A. L. Rykunov (1989), Modelling the connection between earthquake preparation processes and crustal electromagnetic emission, *Phys. Earth Planet. Inter.*, *57*, 129–138.

Henderson, T. R., V. S. Sonwalkar, R. A. Helliwell, U. S. Inan, and A. C. Fraser-Smith (1993), A search for ELF/VLF emissions induced by earthquakes as observed in the ionosphere by the DE 2 satellite, *J. Geophys. Res.*, *98*(A6), 9503–9514.

Hobara, Y., F. Lefeuvre, M. Parrot, and O. A. Molchanov (2005), Low-latitude ionospheric turbulence observed by Aureol-3 satellite, *Ann. Geophys.*, *23*, 1259–1270.

Larkina, V. I., V. V. Migulin, O. A. Molchanov, I. P. Kharkov, A. S. Inchin, and V. B. Schvetcova (1989), Some statistical results on very low frequency radiowave emissions in the upper ionosphere over earthquake zones, *Phys. Earth Planet. Inter.*, *57*, 100–109.

Molchanov, O. A., and M. Hayakawa (1998), On the generation mechanism of ULF seismogenic electromagnetic emissions, *Phys. Earth Planet. Inter.*, *105*, 201–210.

Molchanov, O. A., O. A. Mazhaeva, A. N. Goliavin, and M. Hayakawa (1993), Observation by the Intercosmos-24 satellite of ELF-VLF electromagnetic emissions associated with earthquakes, *Ann. Geophys.*, *11*, 431–440.

Molchanov, O. A., M. Hayakawa, and V. A. Rafalsky (1995), Penetration characteristics of electromagnetic emissions from an underground seismic source into the atmosphere, ionosphere, and magnetosphere, *J. Geophys. Res.*, *100*(A2), 1691–1712.

Molchanov, O., et al. (2006), Global diagnostics of the ionospheric perturbations related to the seismic activity using the VLF radio signals collected on the DEMETER satellite, *Nat. Hazards Earth Syst. Sci.*, *6*, 745–753.

Parrot, M. (1994), Statistical study of ELF/VLF emissions recorded by a low-altitude satellite during seismic events, *J. Geophys. Res.*, *99*, 23,339–23,347.

Parrot, M. (1999), Statistical studies with satellite observations of seismogenic effects, in *Atmospheric and Ionospheric Electromagnetic Phenomena Associated with Earthquakes*, edited by M. Hayakawa, pp. 685–695, Terra Sci., Tokyo.

Parrot, M., and M. M. Mogilevsky (1989), VLF emissions associated with earthquakes and observed in the ionosphere and the magnetosphere, *Phys. Earth Planet. Inter.*, *57*, 86–99.

Parrot, M., et al. (2006), The magnetic field experiment IMSC and its data processing onboard DEMETER: Scientific objectives, description and first results, *Planet. Space Sci.*, *54*, 441–455.

Press, W. H., S. A. Teukolsky, W. T. Vetterling, and B. P. Flannery (1992), Random numbers, in *Numerical Recipes in C: The Art of Scientific Computing*, pp. 274–328, Cambridge Univ. Press, New York.

Rodger, C. J., N. R. Thomson, and R. L. Dowden (1996), A search for ELF/VLF activity associated with earthquakes using ISIS satellite data, *J. Geophys. Res.*, *101*(A6), 13,369–13,378.

Rodger, C. J., R. L. Dowden, and N. R. Thomson (1999), Observations of electromagnetic activity associated with earthquakes by low-altitude satellites, in *Atmospheric and Ionospheric Electromagnetic Phenomena Associated with Earthquakes*, edited by M. Hayakawa, pp. 697–710, Terra Sci., Tokyo.

Santolík, O., F. Němec, M. Parrot, D. Lagoutte, L. Madrias, and J. J. Berthelier (2006), Analysis methods for multi-component wave measurements on board the DEMETER spacecraft, *Planet. Space Sci.*, *54*, 512–527.

Serebryakova, O. N., S. V. Bilichenko, V. M. Chmyrev, M. Parrot, L. Rauch, F. Lefeuvre, and O. A. Pokhotelov (1992), Electrodynamic ELF radiation from earthquake regions as observed by low-altitude satellites, *Geophys. Res. Lett.*, *19*, 91–94.

Sorokin, V. M., V. M. Chmyrev, and A. K. Yaschenko (2001), Electrodynamic model of the lower atmosphere and the ionosphere coupling, *J. Atmos. Sol. Terr. Phys.*, *63*, 1681–1691.

Tate, J., and W. Daily (1989), Evidence of electro-seismic phenomena, *Phys. Earth Planet. Inter.*, *57*, 1–10.

Vodyanitskii, S. Y., A. I. Daniluskin, V. V. Krasnoselskikh, V. V. Migulin, P. A. Morozov, A. M. Natanzon, and A. E. Reznikov (1990), The change of the ELF-VLF noise level at the Earth's surface in a magnetic conjugate region during the Spacelab-2 experiment, *Adv. Space Res.*, *10*(7), 789–794.

J. J. Berthelier, CETP, CNRS, Saint-Maur des Fossés F-94100, France.

F. Němec and M. Parrot, LPCE, CNRS, Orléans F-45071, France. (frantisek.nemec@cnrs-orleans.fr)

O. Santolík, Institute of Atmospheric Physics, Academy of Sciences of the Czech Republic, Prague 4, 14131, Czech Republic.

JOURNAL OF GEOPHYSICAL RESEARCH, VOL. 113, A08317, doi:10.1029/2008JA013184, 2008

Power line harmonic radiation observed by satellite: Properties and propagation through the ionosphere

F. Němec,[1,2,3] O. Santolík,[2,3] M. Parrot,[1] and J. Bortnik[4]

Received 19 March 2008; revised 25 April 2008; accepted 2 May 2008; published 27 August 2008.

[1] We present results of a systematic survey of power line harmonic radiation events observed by the low-altitude DEMETER spacecraft. Altogether, 88 events (45 with frequency spacing 50/100 Hz and 43 with frequency spacing 60/120 Hz) have been found by an automatic identification procedure and confirmed by visual inspection. Frequency-Time intervals of individual lines forming the events have been found by an automated procedure, and the corresponding frequency-time spectrograms have been fitted by a 2d-Gaussian model. It is shown that the mean time duration of the lines forming the events is 20 seconds, with median being 12 seconds (this corresponds to the spatial dimensions of 156/90 km, respectively). The full width at half maximum of the frequency range of the lines is less than 3 Hz in the majority of cases. Moreover, the lines with larger bandwidth and the lines with the largest intensities often occur off exact multiples of base power system frequency. This can be explained either by wave-particle interactions that take place and modify the radiated electromagnetic wave or by the improperly operating radiating power system. Full-wave calculation of the efficiency of coupling of electromagnetic waves through the ionosphere has been done to show that it can explain lower intensity of events observed by satellite during the day as compared with those observed during the night. Estimated radiated peak power on the ground is larger for events observed during the day than for events observed during the night, and more events are observed during the day than during the night.

Citation: Němec, F., O. Santolík, M. Parrot, and J. Bortnik (2008), Power line harmonic radiation observed by satellite: Properties and propagation through the ionosphere, *J. Geophys. Res.*, *113*, A08317, doi:10.1029/2008JA013184.

1. Introduction

[2] Power line harmonic radiation (PLHR) are electromagnetic waves radiated by electric power systems on the ground at harmonic frequencies of 50 or 60 Hz, depending on the frequency of the system. When represented in the form of frequency-time spectrograms, they usually have a form of intense parallel lines with mutual distances of 50/100 or 60/120 Hz, because odd/even harmonics can sometimes be strongly suppressed. Such emissions are often observed on the ground and evidence for their propagation through the magnetosphere has been shown [*Helliwell et al.*, 1975; *Park and Helliwell*, 1978; *Matthews and Yearby*, 1981; *Park and Helliwell*, 1981; *Park and Helliwell*, 1983; *Yearby et al.*, 1983; *Manninen*, 2005]. However, direct observations by satellites are rather rare and with a few exceptions [*Rodger et al.*, 1995; *Němec et al.*, 2006, 2007b] these studies usually reported only a low number of events [*Koons et al.*, 1978; *Bell et al.*, 1982; *Tomizawa and Yoshino*, 1985; *Parrot et al.*, 2005].

[3] *Rodger et al.* [1995] performed the first satellite survey with a significant number of included events and reported the existence of two distinct classes of events: the first of them (''Tram Lines'', TL) consisted of events that appeared to lie close to the harmonics of 50/60 Hz; the second class of events (''Magnetospheric Line Radiation'', MLR), formed by lines with larger bandwidth, did not show any evidence of a relationship with power line harmonics. *Němec et al.* [2007a] performed a systematic survey of MLR-like events using the data from DEMETER spacecraft. They confirmed the existence of the two classes of events (PLHR and ''real-MLR'') and demonstrated their different properties (intensity, frequency, most favorable values of Kp index).

[4] *Němec et al.* [2006] analyzed DEMETER observations of PLHR events and showed that the frequency spacing of the lines corresponds well to the power system frequency in possible generation regions. Moreover, they have shown that the peak intensity of PLHR is larger during the night than during the day, suggesting different penetration characteristics of the ionosphere as a possible explanation. *Ando et al.* [2002] performed a theoretical analysis of

[1]Laboratoire de Physique et Chimie de l'Environnement/CNRS, Orléans, France.
[2]Faculty of Mathematics and Physics, Charles University, Prague, Czech Republic.
[3]Institute of Atmospheric Physics, Academy of Sciences of the Czech Republic, Prague, Czech Republic.
[4]Department of Atmospheric and Oceanic Sciences, University of California Los Angeles, Los Angeles, California, USA.

0148-0227/08/2008JA013184$09.00

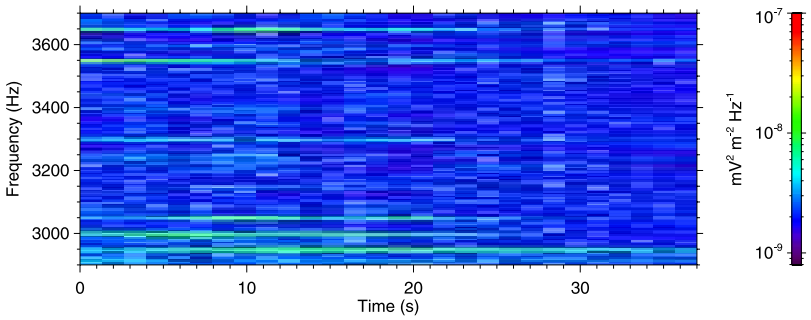

Figure 1. An example of frequency-time spectrogram of power spectral density of electric field fluctuations corresponding to one of the identified events. The data were recorded on 21 September 2006 between 10:06:02 and 10:06:39 UT. The lines occur at exact multiples of 50 Hz.

penetration of PLHR into the ionosphere and estimated the horizontal size of the region where the electromagnetic field is strong to about ±200 km from the source, not extending with higher altitude.

[5] *Park and Miller* [1979] reported the existence of "Sunday effect" – they claimed that the wave activity during Sundays was lower that the wave activity during the weekdays, attributing this difference to a lower power consumption. *Parrot et al.* [1991] and *Molchanov et al.* [1991] confirmed the existence of this effect and argued that it can be caused not only by a lower power consumption during the weekends as compared to the weekdays, but also by a different current distribution in power systems. However, other authors who searched for the existence of the effect [*Rodger et al.*, 2000; *Karinen et al.*, 2002] concluded that it is only a statistical fluctuation. The role of PLHR in the ionosphere and magnetosphere is thus still questionable, but it could be quite important, because they can serve as a trigger for naturally generated whistler-mode emissions [*Nunn et al.*, 1999; *Manninen*, 2005]. Moreover, they can be also important for electron precipitation [*Bullough*, 1995].

[6] Observations of PLHR events, some of their properties and numerical calculation of their penetration through the ionosphere up to the DEMETER altitude are reported in this paper. The wave experiment on board DEMETER is briefly introduced in section 2. An automatic procedure for identification of PLHR events and frequency-time-dependent 2d-Gaussian model of individual lines that are forming the events are described in section 3. Section 4 describes some of the properties of the observed events, whereas section 5 presents a calculation of penetration characteristics of PLHR through the ionosphere. The obtained results are discussed in section 6 and summarized in section 7.

2. Experiment

[7] We have used wave measurements from the French micro-satellite DEMETER (altitude 700 km, inclination 98 degrees, nearly Sun-synchronous orbit, mass 130 kg, launched in June 2004). [*Berthelier et al.*, 2006; *Parrot et al.*, 2006; *Santolík et al.*, 2006]. The scientific instruments placed on board DEMETER record data during the entire orbit with an exception of geomagnetic latitudes larger than 65 degrees. Because of the limited capacity of the telemetry, there are two different modes of operation. A "Survey mode" measuring low-resolution data provides us in VLF range (up to 20 kHz) with power spectra of one electric and one magnetic field component. However, the limited frequency resolution (19.53 Hz) is not sufficient for our study – both the identification of events and their subsequent analysis require frequency resolution better than 5 Hz. We have consequently used the "Burst mode", which is active only above some specific areas of interest, but provides us with waveforms of one electric and one magnetic field component (at a sampling frequency of 40 kHz).

3. Automatic Identification of Events

[8] The data set that we have used is too large to be processed manually. Instead, we have used an automatic identification procedure described by *Němec et al.* [2006]. It searches the measured data for presence of possible PLHR events and provides us with their time, frequency and spectrogram of the surrounding interval in the frequency-time plane. We have then manually checked the positively identified events and we have decided whether a real event was found or a "false alarm" occurred. Within 1499 cases identified by the automatic procedure run on the entire data set of 3378 hours of Burst mode waveform data recorded between 12 August 2004 and 3 February 2008, only 88 PLHR events have been found. Among these, 45 events have the frequency spacing of 50/100 Hz and 43 events have the frequency spacing of 60/120 Hz. This represents about twice larger data set as compared to *Němec et al.* [2007b]. Their results have been well confirmed, namely the frequency spacing of the lines corresponds well to the power system frequency in generation regions.

[9] An example of one of the identified events is shown in Figure 1. It represents the frequency-time spectrogram of power spectral density of electric field fluctuations measured on 21 September 2006 between 10:06:02 and 10:06:39 UT above the southern part of Sweden. Several lines at constant frequencies can be clearly seen. They occur at exact (within the experimental error) multiples of 50 Hz, namely at frequencies: 2950 Hz, 3000 Hz, 3050 Hz, 3300 Hz, 3550 Hz and 3650 Hz.

[10] Having the manually confirmed set of PLHR events and knowing approximately their beginning and ending times and frequency ranges, we apply another procedure to identify individual lines forming the events and to find parameters of their 2d-Gaussian model in a frequency-time plane. An input of this procedure is a frequency-time spectrogram of a PLHR event. The length of a FFT segment

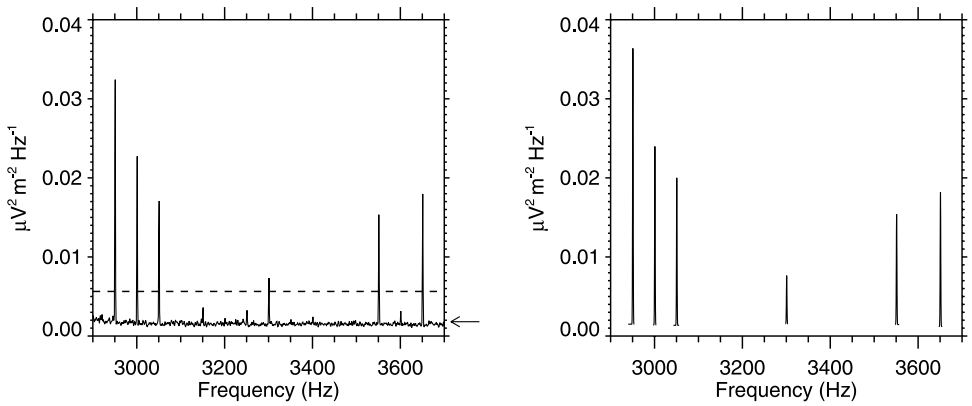

Figure 2. (left) Power spectrum corresponding to the event from Figure 1 used for the peak identification procedure. The mean value is marked by an arrow, and the minimum peak value (see text) is plotted by a dashed line. (right) Gaussian fits corresponding to the identified peaks in power spectrum.

used in the processing is 40000 points (this gives a frequency resolution of 1 Hz), overlapping is 75% and the Hanning window is used. The procedure consists of the following three steps.

[11] In the first step, peaks in the power spectrum (that is individual lines forming the events) are found and their central frequencies and widths are determined. A power spectrum that corresponds to the event presented in Figure 1 is shown in the left of Figure 2. Intense peaks located at frequencies 2950 Hz, 3000 Hz, 3050 Hz, 3300 Hz, 3550 Hz and 3650 Hz can be seen. As well as these, much weaker peaks can be observed also at frequencies 3150 Hz, 3250 Hz, 3400 Hz and 3600 Hz. The mean value of power spectral density $\bar{I}$ (marked by an arrow in the left of Figure 2) and the standard deviation σ_I of the power spectral density are calculated. Peaks are identified at frequency ranges where the power spectral density $I(f)$ is larger than a threshold value (plotted by a dashed line in the left of Figure 2)

$$I(f) > \bar{I} + \alpha\,\sigma_I \tag{1}$$

where α is a fixed constant ($\alpha = 2$). Then minimum and maximum frequencies $f^i_{\min}$ and $f^i_{\max}$ of a peak i are the closest adjacent frequencies where $I(f)$ is lower than $\bar{I}$ and reaches the local minimum. For an example case of the peak located close to 2950 Hz, these are marked by vertical lines in the Figure 3. Having found the intense peaks in power spectrum, we perform a least-squares Gaussian fit. The background intensity value ρ_i of each of the peaks is calculated as $\rho_i = (I(f^i_{\min}) + I(f^i_{\max}))/2$. This value is subtracted and the result is fitted by a Gaussian function with three free parameters: the central frequency of the peak f_i, intensity of the peak I_i and the standard deviation σ_i. The fits corresponding to the example spectrum are shown in the right of Figure 2, with frequencies f_i of the identified peaks being 2950.7 Hz, 3000.8 Hz, 3050.6 Hz, 3300.8 Hz, 3551.1 Hz and 3650.9 Hz. Figure 3 represents a detailed view of the fit performed on a peak located close to 2950 Hz. A solid line shows the measured power spectrum and the least-square Gaussian fit is over-plotted by a dashed line.

[12] The second step of the procedure consists of identification of the appropriate time intervals corresponding to individual lines which form the PLHR event. For this purpose, we calculate the time dependence of the average power spectral density in the frequency interval $(f_i - \sigma_i\sqrt{2\ln 2};\ f_i + \sigma_i\sqrt{2\ln 2})$, which is the frequency interval centered at the peak frequency of the line that has the width equal to full width of the peak at half of its maximum (FWHM). We then calculate the time-dependent "background value", which is the mean value of power spectral density in frequency intervals outside the peak, namely in intervals: $(f_i - \sigma_i\,(4 + \sqrt{2\ln 2});\ f_i - 4\,\sigma_i)$ and $(f_i + 4\,\sigma_i;\ f_i + \sigma_i\,(4 + \sqrt{2\ln 2}))$. For an example case of the peak located close to 2950 Hz, the three frequency intervals (one corresponding to the peak and two just outside of it) are marked by horizontal lines in Figure 3. This average back-

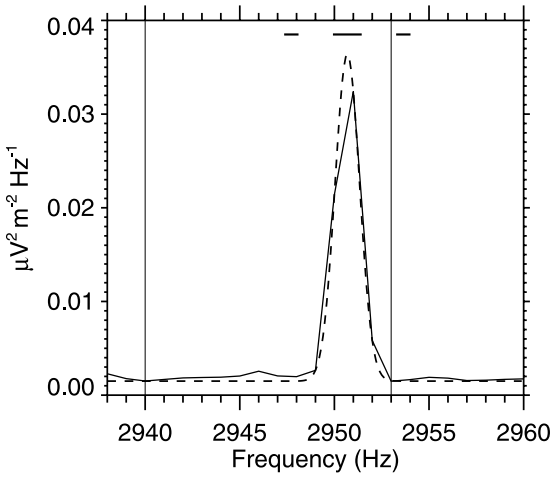

Figure 3. A detailed view of the fit performed on the peak located close to 2950 Hz. The measured power spectrum is plotted by a solid line, and the least square Gaussian fit is overplotted by a dashed line. The minimum and maximum frequencies $f^i_{\min}$ and $f^i_{\max}$ of the peak (see text) are marked by vertical lines. Horizontal lines mark the frequency intervals used in the second step of the procedure for the identification of the appropriate time interval corresponding to the line (see text).

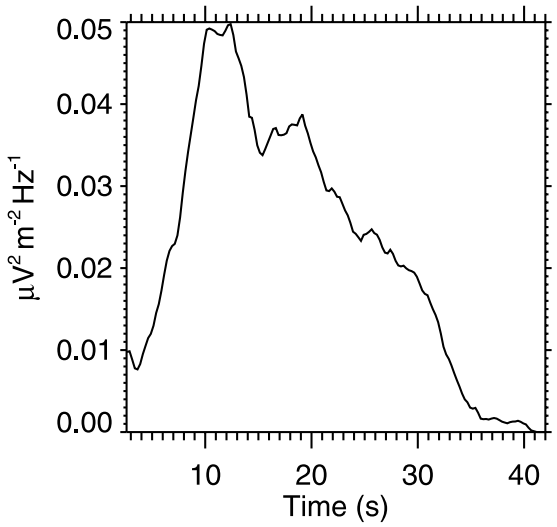

Figure 4. An example of a resulting time-dependent value of power spectral density obtained for the line located close to 2950 Hz.

ground is subtracted and a running mean over 5 seconds of data is applied. Afterwards, starting from some manually defined time when the line occurs, we span the time interval until a local minimum lower than 0 is reached on both sides. In such a way, we obtain a time interval when a given line occurs. Figure 4 shows an example of the resulting time-dependent average value of power spectral density obtained for the line located close to 2950 Hz.

[13] In the last step of the procedure a frequency-time 2d-Gaussian model is applied to the frequency-time interval corresponding to a given line:

$$I(f,t) = I_0 \exp\left(-\frac{(f-f_0)^2}{2\delta^2}\right) \exp\left(-\frac{(t-t_0)^2}{2\tau^2}\right) + I_b \quad (2)$$

The frequency interval determined in the first step, time interval determined in the second step and a moving average over 5 seconds of data are used. For each of the lines, this results in an estimate of 5 parameters: background intensity I_b, peak intensity I_0, central frequency f_0, central time t_0, characteristic time duration τ and characteristic frequency range δ. For the line considered in Figure 4, Figure 5 shows an example of its frequency-time spectrogram and its 2d-Gaussian model. All the performed fits have been visually inspected. Among 253 lines found during the first step of the procedure, 206 have been successfully fitted. In the remaining 47 cases, the fit failed, usually because of strong and varying background field intensity (typically when a whistler occurred simultaneously, being more intense than the PLHR line). Such cases have not been further used in the study.

4. Properties of the Observed PLHR Events

[14] Figure 6 represents a histogram of the FWHM of the observed time durations of individual lines forming the PLHR events (bottom scale of the x-axis) and also the same histogram but rescaled to the observed spatial dimensions (upper scale of the x-axis). The observed average FWHM of time duration is 20 seconds, with the median value of 12 seconds. This corresponds to spatial dimensions of 156 km/90 km, respectively. The difference between the mean and median values is caused by a long tail of the distribution meaning that long time durations are possible, but improbable.

[15] Figure 7 represents a histogram of FWHM of frequency ranges of individual lines forming the PLHR events. It can be seen that the frequency range of individual lines is less than 3 Hz in the majority of cases.

[16] Figure 8 represents the FWHM of the frequency range of PLHR lines as a function of peak intensity. The events with frequencies corresponding to the multiples of the power system frequency (i.e., when frequency deviation from the corresponding multiple is less than 3 Hz) are plotted by crosses, the events with frequencies not corresponding to these multiples are shown by diamonds. It can be seen that among the most intense lines, all occur off exact multiples of power system frequency. Moreover, the lines with large bandwidth occur off the exact multiples as well. This is further confirmed by Figure 9 which represents a frequency deviation from multiples of power system frequency as a function of the detected peak intensity of the events. Triangles represent lines forming the events with 50/100 Hz spacing and squares represent lines forming the events with 60/120 Hz. Similar behavior is

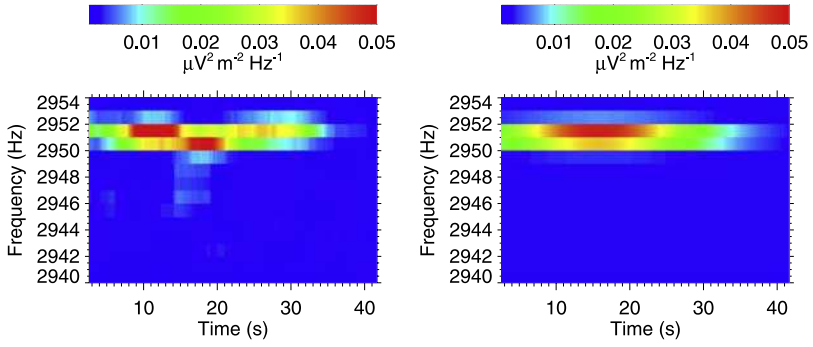

Figure 5. (left) Frequency-Time spectrogram corresponding to the line close to 2950 Hz. (right) Result of 2d-Gaussian fit.

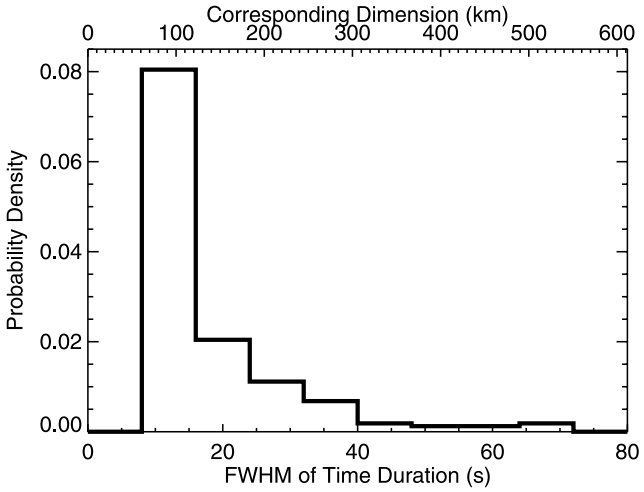

Figure 6. (Bottom scale of the x axis) Histogram of the FWHM of the time durations of the lines forming the PLHR events. (Upper scale of the x axis) Histogram of the corresponding spatial dimensions of the PLHR events.

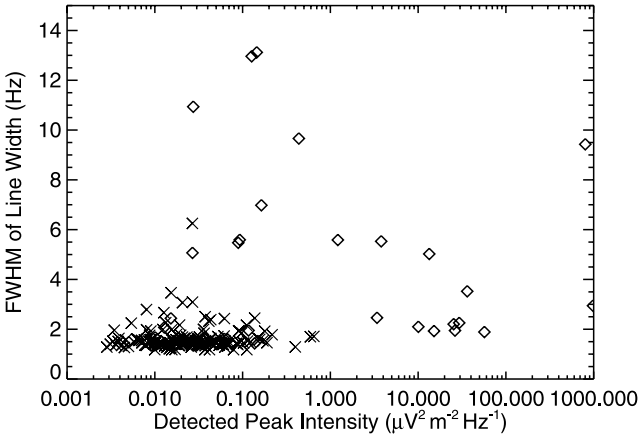

Figure 8. FWHM of frequency ranges of individual lines forming the PLHR events as a function of the peak intensity. The events with frequencies corresponding to the multiples of the power system frequency are plotted by crosses, and the events with frequencies not corresponding to these multiples are shown by diamonds.

observed for both of them. The dotted line at the frequency deviation of 3 Hz represents the chosen threshold for lines to be considered as occurring at "exact" multiple of power system frequency, as used in section 5.

5. PLHR Propagation Through the Ionosphere

[17] In the following, we consider only the lines with frequency deviation from multiples of power system frequency less than 3 Hz and generation region located just below the place of observation (not in the conjugate region) were taken into account; the events with larger deviation from multiples of power system frequency may undergo some specific interaction with the surrounding plasma environment and our calculation of the efficiency of coupling would not be consequently valid for such cases – see section 6. The left of Figure 10 represents the peak power spectral density of Poynting flux of individual lines forming the PLHR events as a function of magnetic local time. Assuming right-handed circular polarized parallel propagation [*Němec et al.*, 2006], it was calculated as

$$S = \frac{1}{2}\frac{n}{c\mu_0}E^2 \tag{3}$$

where E^2 is the peak power spectral density of electric field fluctuations of a given PLHR line, μ_0 is a permeability of vacuum, c is speed of light and n is the refractive index. The refractive index has been obtained from the cold plasma approximation, using particle concentrations from International Reference Ionosphere model [*Bilitza*, 1990] (http://modelweb.gsfc.nasa.gov/models/iri.html). Note that bunching of the observed events into two MLT intervals is

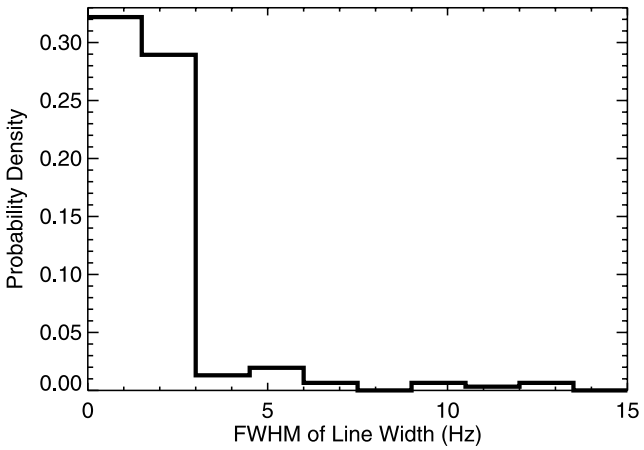

Figure 7. Histogram of the FWHM of the frequency range of the lines forming the PLHR events.

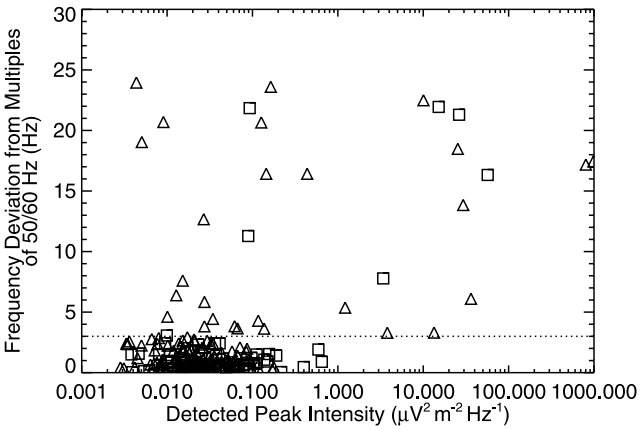

Figure 9. Frequency deviation from multiples of power system frequency as a function of the detected peak intensity. The lines forming events with frequency spacing 50/100 Hz are plotted by triangles, and the lines forming events with frequency spacing 60/120 Hz are plotted by squares.

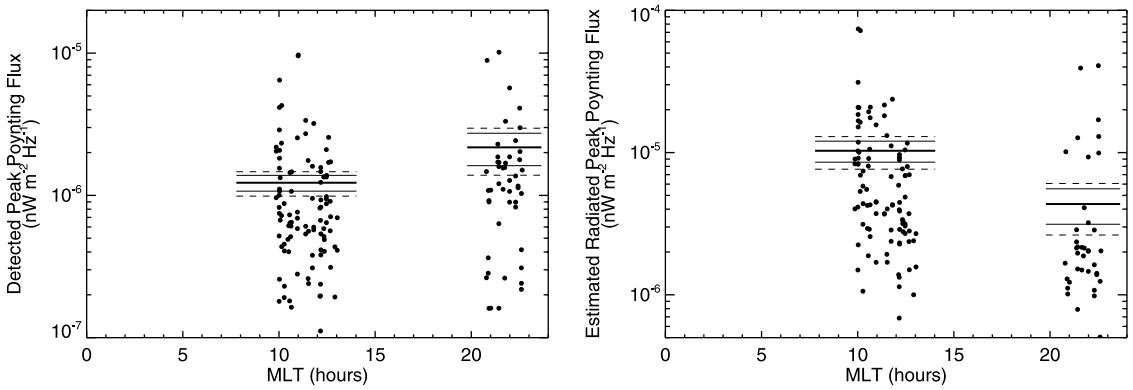

Figure 10. (left) Detected peak power spectral density of Poynting flux of individual lines forming the PLHR events as a function of the magnetic local time. The mean values for the daytime/nighttime and corresponding standard deviations (see text) are plotted by horizontal lines. (right) Estimated radiated peak power spectral density of Poynting flux of individual lines forming the PLHR events on the ground surface (calculated from the observations, taking into account the numerically calculated penetration characteristics of the ionosphere) as a function of the magnetic local time. The mean values for the daytime/nighttime and corresponding standard deviations are again marked by horizontal lines.

caused by the specific orbit of the DEMETER spacecraft. The mean peak power spectral density of Poynting flux observed during the day (43 events, 101 successfully fitted lines) is $(1.23 \pm 0.16) \cdot 10^{-6}$ nW m^{-2} Hz^{-1}. This calculation is valid if we consider individual lines as being independent, even if they form the same event (that is they are observed simultaneously, but at different frequencies). If all the lines measured within the same event were dependent, then the standard deviation would be $0.24 \cdot 10^{-6}$ nW m^{-2} Hz^{-1} instead (the standard deviation $\sigma_{\bar{x}}$ of the mean $\bar{x}$ is calculated as $\sigma_{\bar{x}} = \sigma_x/\sqrt{N_x}$ where σ_x is a standard deviation of a set x and N_x is a number of independent samples in the set x). The mean peak power spectral density of Poynting flux observed during the night (24 events, 48 successfully fitted lines altogether) is $(2.18 \pm 0.56) \cdot 10^{-6}$ nW m^{-2} Hz^{-1}, supposing the independence of the lines within the same event. For the case of completely dependent lines, the standard deviation would be $0.79 \cdot 10^{-6}$ nW m^{-2} Hz^{-1}. These values of standard deviations are marked by horizontal lines. The events observed during the night are more intense, with the difference of mean values being $(0.95 \pm 0.58) \cdot 10^{-6}$ nW m^{-2} Hz^{-1} supposing that the lines forming one event are completely independent. Supposing that the lines forming one event are completely dependent, the standard deviation increases to $0.83 \cdot 10^{-6}$ nW m^{-2} Hz^{-1}. This difference then corresponds to 1.6 and 1.1 standard deviation, respectively.

[18] *Němec et al.* [2006] suggested the efficiency of coupling through the ionosphere as a possible explanation for PLHR being more intense during the night than during the day. Here we present results of a calculation of the efficiency of coupling of electromagnetic waves through the ionosphere. The procedure of *Nagano et al.* [1975] has been followed and the full-wave code developed by *Bortnik and Bleier* [2004] has been used to obtain a full-wave solution of Maxwell's equations in the presence of electrons and several ion species. The medium is supposed to be horizontally stratified. Cold plasma approximation [*Stix*, 1992] has been used to calculate the susceptibility matrix and the effects of collisions have been included by modifying the mass of a particle m_{s0} by the collision frequency ν_s:

$$m_s = m_{s0}\left(1 - \frac{\nu_s}{\omega}\right) \tag{4}$$

To perform the calculation, the density and composition of the electron and ion populations as a function of altitude, as well as the magnetic field intensity and magnetic inclination need to be known. Moreover, it is necessary to know the collision profiles of electrons and ions since these critically control the attenuation and mode conversion.

[19] To specify electron and ion number density as a function of altitude at a given geographic location and time we have used the International Reference Ionosphere model. The collision frequency was taken from *Cummer* [2000] for the low-altitude portion of both electrons and protons (altitudes less than 300 km), where collisions with neutrals are dominant. Above this altitude, Coulomb collisions dominate and the profile from *Helliwell* [1965] has been used. Magnetic field intensity was calculated using the IGRF model at an altitude of 80 km (which is the region where most of the attenuation takes place) and was taken to be constant (though the medium is supposed to be horizontally stratified and the problem is thus effectively only 1d, we would otherwise obtain a nonphysical condition $\nabla \vec{B} \neq 0$).

[20] The efficiency of coupling of electromagnetic waves through the ionosphere is for our purposes defined as a power attenuation, that is the ratio between the final power of the wave measured on board the spacecraft and the incident power radiated from the electric power system on the ground. The calculated altitudinal dependence for two chosen geographical regions where PLHR are often observed (Finland and Japan) is plotted in Figure 11, separately for the day and the night. It can be seen that most of the attenuation takes place at altitudes of about 70–90 km (HF absorption observed by riometers is also maximum in this range of altitudes). Considering the final efficiency of

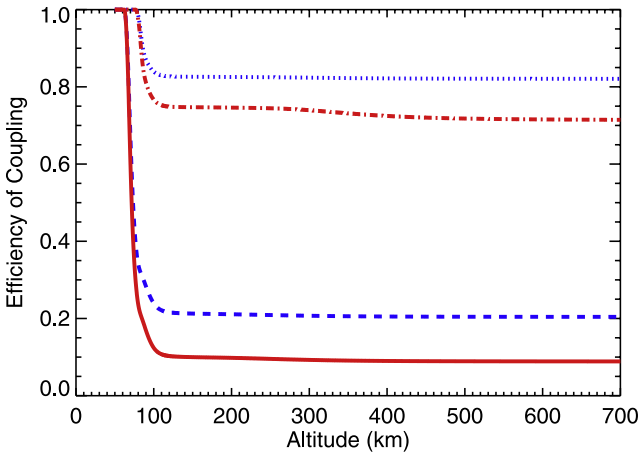

Figure 11. Efficiency of coupling for the frequency of wave 2.5 kHz as a function of the altitude for nighttime Finland region (dotted line), nighttime Japan region (dash-dotted line), daytime Finland region (dashed line), and daytime Japan region (solid line).

coupling at the altitude of DEMETER, it is about five times larger during the night (value of about 0.80, dotted and dash-dotted lines) than during the day (value of about 0.15, dashed and solid lines). Moreover, it is larger in Finland region (dotted and dashed lines) than in Japan region (dash-dotted and solid lines) – see section 6.

[21] We have calculated the efficiency of coupling of electromagnetic waves through the ionosphere for all the individual lines from the left of Figure 10. The ionospheric parameters, intensity of magnetic field and magnetic inclination were determined separately for each of them.

[22] The right of Figure 10 shows the estimated peak power spectral densities of Poynting fluxes on the ground surface that correspond to the peak power spectral densities of Poynting fluxes of individual lines measured by DEMETER, taking into account numerically calculated penetration characteristics of the ionosphere. Supposing that the individual lines are independent, the mean value of estimated peak power spectral density of Poynting flux on the ground during the day is $(1.03 \pm 0.17) \cdot 10^{-5}$ nW m^{-2} Hz^{-1}. Supposing that the lines forming one event are completely dependent, the standard deviation would be $0.27 \cdot 10^{-5}$ nW m^{-2} Hz^{-1}. The mean value of estimated peak power spectral density of Poynting flux on ground during the night is $(0.44 \pm 0.12) \cdot 10^{-5}$ nW m^{-2} Hz^{-1} and $(0.44 \pm 0.17) \cdot 10^{-5}$ nW m^{-2} Hz^{-1} for completely independent lines forming one event and completely dependent lines forming one event, respectively. The mean values and the appropriate standard deviations are again marked by horizontal lines. The estimated radiated power is therefore lower for events observed during the night, with the mean difference being $(-0.60 \pm 0.21) \cdot 10^{-5}$ nW m^{-2} Hz^{-1} and $(-0.60 \pm 0.32) \cdot 10^{-5}$ nW m^{-2} Hz^{-1} for independent/dependent lines forming one event, respectively (2.9 and 1.9 standard deviations, respectively).

6. Discussion

[23] The basic limitation of the presented study is the usage of the automatic procedure for an identification of PLHR events. This issue is discussed in detail by *Němec et al.* [2006], who used the same procedure and did not find any indication that this biases the obtained results (i.e., by the presence of a "selection effect").

[24] The recently developed procedure for an identification of individual lines forming a PLHR event described in section 3 is very simple and easy to implement. As demonstrated by Figures 2, 3, 4 and 5, it usually performs well as long as the peaks in the power spectrum are larger than the minimum peak value threshold. In about one fifth of cases (47 out of 253), the 2d-Gaussian fitting was not successful because of strong variations in the background field intensity. This principal limitation surely slightly biases the results presented in Figures 6, 7, 8, 9, 10, but the main qualitative conclusions should remain unaffected.

[25] Figure 6 shows a histogram of FWHM of the observed time durations of individual lines forming the PLHR events and corresponding spatial dimensions. Although the performed measurements (one satellite only) do not allow us to distinguish between temporal and spatial variations of the signal, it is reasonable to suppose that the electromagnetic radiation from the power systems on the ground is temporarily rather stable. Consequently, the observed time durations correspond more likely to the spatial dimensions of individual PLHR events. The average corresponding spatial dimension of 156 km (median 90 km) is in a relatively good agreement with theoretically calculated dimensions of the affected region [*Ando et al.*, 2002].

[26] Figures 8 and 9 suggest that there is a connection between the frequency deviation of individual lines forming the PLHR events from the exact harmonic multiples of power system frequency, their bandwidth and their intensity – lines with large peak intensities have also large frequency deviation from the appropriate harmonic. Moreover, the lines with large bandwidth usually occur off exact multiples of power system frequency as well. This can be caused by two different phenomena. First, while most of the PLHR events—after being radiated from an electric power system on the ground—propagate up to the satellite altitudes almost unchanged (only slightly attenuated, as shown in the numerical simulation in section 5), some of them may undergo interactions with the plasma environment, which shifts their peak frequencies (originally located close to the exact multiples of power system frequency). Such interactions can predominantly occur for events with larger observed intensity. They may be also responsible for larger bandwidth of such events. The second possible explanation is that the most intense PLHR occur due to some specific events in power systems. During these events, larger harmonics are present in the power system and its base frequency may be slightly shifted off 50/60 Hz. Afterwards, an explanation proposed by *Němec et al.* [2007b] could be used for such events: a small shift of base power system frequency off 50/60 Hz is too small to be observed in the frequency spacing between individual lines, but at higher harmonics (that are typically observed) it can lead to a significant shift in frequency. Improperly operating power systems could also explain a larger bandwidth of the observed lines. The effect of the Doppler shift does not play a significant role in the study; it causes shifts of maximally about 3 Hz, usually being much lower. Moreover, a case study performed by *Parrot et al.* [2007] has

experimentally proven that—for that particular event—the frequencies of the lines observed simultaneously by satellite and on the ground are not significantly different.

[27] The performed full-wave calculation reveals substantial variability of the efficiency of coupling of electromagnetic waves through the ionosphere. The power that penetrates up to the DEMETER altitudes is about five times less attenuated during the night than during the day. Moreover, the efficiency of coupling is larger in the Finland region as compared to the Japan region, even the difference is not so striking as the day/night asymmetry (Figure 11). This is caused by different geomagnetic latitudes of Finland (57.5°) and Japan (23°). The electromagnetic waves penetrate up to the ionosphere better at larger geomagnetic latitudes both because of magnetic inclination is closer to 90° and geomagnetic field is stronger.

[28] Comparison of the peak power spectral densities of Poynting fluxes of individual lines forming the PLHR events that were observed during the day and observed during the night reveals that the lines observed during the night are more intense than the lines observed during the day. The difference is 1.6 standard deviation, supposing that the lines forming one event are completely independent and 1.1 standard deviation, supposing that the lines forming one event can be considered as completely dependent. The real situation probably corresponds to something in between—the lines forming the same event are dependent, but only partially. The performed calculation of the efficiency of coupling of electromagnetic waves through the ionosphere seems to explain this difference completely—the estimated radiated peak power spectral density of Poynting flux corresponding to the events observed during the night is lower than during the day. The difference is statistically quite significant: 2.9 standard deviations and 1.9 standard deviation for completely independent/completely dependent lines forming one event, respectively. A possible explanation could be that during the day a power system is more loaded and the PLHR events are consequently stronger. This would also explain the larger number of PLHR events observed during the day than the night: in Figure 10 there are 43 events and 24 events, observed respectively during the day time and during the night time. Supposing a binomial distribution, this corresponds to about 2.3 standard deviations. Moreover, because of the larger efficiency of coupling even less intense events radiated during the nighttime are intense enough to be detected on board DEMETER.

[29] Finally, we can compare ground levels of estimated radiated Poynting fluxes based on DEMETER observations with the ones deduced from the ground measurements [*Bullough*, 1995, chapter 2.2]. Their estimates for Poynting fluxes at the base of the ionosphere (before the attenuation starts to take place) are in the range of $5.8 \cdot 10^{-10}$ nW m^{-2} (*Bullough* [1995], page 297, table 10.2.1, Cooks Harbour power line) up to $7.9 \cdot 10^{-4}$ nW m^{-2} (*Bullough* [1995], page 298, equation 2.9, Derbyshire Cement Works) in 1 kHz frequency band around 2.5 kHz. The estimated radiated Poynting fluxes of individual PLHR lines determined from DEMETER data are between $5.18 \cdot 10^{-7}$ nW m^{-2} and $5 \cdot 10^{-4}$ nW m^{-2} and we usually observe about three lines forming the PLHR event. One can see that the weakest lines detected on the ground are too weak to be detected on board DEMETER. However, our estimated values of Poynting flux are well within the range determined from ground-based measurements.

7. Conclusions

[30] Results of a systematic study of observations of PLHR by a low-altitude satellite have been presented. Altogether, 88 events (45 with frequency spacing 50/100 Hz and 43 with frequency spacing 60/120 Hz) have been found by an automatic identification procedure in about 3378 hours of Burst-mode data and statistically analyzed. For each of the individual lines forming the events, parameters of frequency-time-dependent 2d-Gaussian model have been found by an automatic procedure.

[31] Our results show that the mean FWHM of time duration of the observed lines is on average 20 seconds (median 12 seconds), which corresponds to average spatial dimensions of 156 km (median 90 km). The FWHM of the frequency range of individual lines is less than 3 Hz in the majority of cases. The most intense lines occur off exact multiples of base power system frequency. The lines with larger bandwidth usually occur off exact multiples of power system frequency as well. Full-wave calculation of efficiency of coupling of electromagnetic waves through the ionosphere has been done and it is shown that it can explain the lower intensity of PLHR events observed by satellite during the day as compared to those observed during the night. Estimated radiated peak power on the ground is larger for events observed during the day than for events observed during the night and more events are observed during the day than during the night.

[32] **Acknowledgments.** The authors thank J. J. Berthelier for the use of electric field data. We thank J.-Y. Brochot of LPCE/CNRS Orléans for his help with running the PLHR recognition algorithm as the DEMETER level-3 processing procedure. We thank SPDF/Modelweb for the free access to the data from the International Reference Ionosphere model. We thank M. Rycroft for useful discussion. F.N. and O.S. acknowledge support of the GACR grant 205/06/1267. F.N., O.S., and M.P. acknowledge support of the PICS grant 3725 from CNRS/DREI.

[33] Amitava Bhattacharjee thanks Mike Kosch and Michael Rycroft for their assistance in evaluating this paper.

References

Ando, Y., M. Hayakawa, and O. A. Molchanov (2002), Theoretical analysis on the penetration of power line harmonic radiation into the ionosphere, *Radio Sci.*, *37*(6), 1093, doi:10.1029/2001RS002486.

Bell, T. F., J. P. Luette, and U. S. Inan (1982), ISEE 1 observations of VLF line radiation in the earth's magnetosphere, *J. Geophys. Res.*, *87*(A5), 3530–3536.

Berthelier, J. J., et al. (2006), ICE, the electric field experiment on DEMETER, *Planet. Space Sci.*, *54*, 456–471.

Bilitza, D. (1990), *International Reference Ionosphere*, NSSDC 90-22, Greenbelt, Md.

Bortnik, J., and T. Bleier (2004), Full wave calculation of the source characteristics of seismogenic electromagnetic signals as observed at LEO satellite altitudes, *Eos Trans. AGU*, *85*(47), Fall Meet. Suppl., Abstract T51B-0453.

Bullough, K. (1995), Handbook of atmospheric electrodynamics, in *Power Line Harmonic Radiation: Sources and Environmental Effects*, vol. 2, edited by H. Volland, pp. 291–332, CRC Press, Boca Raton, Fla.

Cummer, S. A. (2000), Modeling electromagnetic propagation in the Earth-ionosphere waveguide, *IEEE Trans. Antennas Propag.*, *48*, 1420.

Helliwell, R. A. (1965), *Whistlers and Related Ionospheric Phenomena*, Stanford Univ. Press, Stanford, Calif.

Helliwell, R. A., J. P. Katsufrakis, T. F. Bell, and R. Raghuram (1975), VLF line radiation in the earth's magnetosphere and its association with power system radiation, *J. Geophys. Res.*, *80*(31), 4249–4258.

Karinen, A., K. Mursula, T. Ulich, and J. Manninen (2002), Does the magnetosphere behave differently on weekends?, *Ann. Geophys.*, *20*(8), 1137–1142.

Koons, H. C., M. H. Dazey, and B. C. Edgar (1978), Satellite observation of discrete VLF line radiation within transmitter-induced amplification bands, *J. Geophys. Res.*, *83*(A8), 3887–3889.

Manninen, J. (2005), Some aspects of ELF-VLF emissions in geophysical research, in *Power Line Harmonic Radiation*, pp. 53–84, 98, Sodankylä Geophysical Observatory Publications, Sodankylä, Finland.

Matthews, J. P., and K. Yearby (1981), Magnetospheric VLF line radiation observed at Halley, Antarctica, *Planet. Space Sci.*, *29*, 97–106.

Molchanov, O. A., M. Parrot, M. M. Mogilevsky, and F. Lefeuvre (1991), A theory of PLHR emissions to explain the weekly variation of ELF data observed by a low-altitude satellite, *Ann. Geophys.*, *9*, 669–680.

Nagano, I., M. Mambo, and G. Hutatsuishi (1975), Numerical calculation of electromagnetic waves in an anisotropic multilayered medium, *Radio Sci.*, *10*(6), 611–617.

Němec, F., O. Santolík, M. Parrot, and J. J. Berthelier (2006), Power line harmonic radiation (PLHR) observed by the DEMETER spacecraft, *J. Geophys. Res.*, *111*, A04308, doi:10.1029/2005JA011480.

Němec, F., O. Santolík, M. Parrot, and J. J. Berthelier (2007a), Comparison of magnetospheric line radiation and power line harmonic radiation: A systematic survey using the DEMETER spacecraft, *J. Geophys. Res.*, *112*, A04301, doi:10.1029/2006JA012134.

Němec, F., O. Santolík, M. Parrot, and J. J. Berthelier (2007b), Power line harmonic radiation: A systematic study using DEMETER spacecraft, *Adv. Space Res.*, *40*, 398–403.

Nunn, D., J. Manninen, T. Turunen, V. Trakhtengerts, and N. Erokhin (1999), On the nonlinear triggering of VLF emissions by power line harmonic radiation, *Ann. Geophys.*, *17*, 79–94.

Park, C. G., and R. A. Helliwell (1978), Magnetospheric effects of power line radiation, *Science*, *200*, 727–730.

Park, C. G., and R. A. Helliwell (1981), Power line radiation in the magnetosphere, *Adv. Space Res.*, *1*, 423–437.

Park, C. G., and R. A. Helliwell (1983), Ground observations of power line radiation coupled to the ionosphere and magnetosphere, *Space Sci. Rev.*, *35*, 131–137.

Park, C. G., and T. R. Miller (1979), Sunday decreases in magnetospheric VLF wave activity, *J. Geophys. Res.*, *84*(A3), 943–950.

Parrot, M., O. Molchanov, M. Mogilevski, and F. Lefeuvre (1991), Daily variations of ELF data observed by a low-altitude satellite, *Geophys. Res. Lett.*, *18*(6), 1039–1042.

Parrot, M., F. Němec, O. Santolík, and J. J. Berthelier (2005), ELF magnetospheric lines observed by DEMETER, *Ann. Geophys.*, *23*, 3301–3311.

Parrot, M., et al. (2006), The magnetic field experiment IMSC and its data processing onboard DEMETER: Scientific objectives, description and first results, *Planet. Space Sci.*, *54*, 441–455.

Parrot, M., J. Manninen, O. Santolík, F. Němec, T. Turunen, T. Raita, and E. Macúšová (2007), Simultaneous observation on board a satellite and on the ground of large-scale magnetospheric line radiation, *Geophys. Res. Lett.*, *34*, L19102, doi:10.1029/2007GL030630.

Rodger, C. J., N. R. Thomson, and R. L. Dowden (1995), VLF line radiation observed by satellite, *J. Geophys. Res.*, *100*(A4), 5681–5689.

Rodger, C. J., M. A. Clilverd, K. Yearby, and A. J. Smith (2000), Is magnetospheric line radiation man-made?, *J. Geophys. Res.*, *105*(A7), 15,981–15,990.

Santolík, O., F. Němec, M. Parrot, D. Lagoutte, L. Madrias, and J. J. Berthelier (2006), Analysis methods for multi-component wave measurements on board the DEMETER spacecraft, *Planet. Space Sci.*, *54*, 512–527.

Stix, T. H. (1992), Wave normal surfaces: Waves in a cold uniform plasma, in *Waves in Plasma*, edited by American Institute of Physics, pp. 1–46, Springer, New York.

Tomizawa, I., and T. Yoshino (1985), Power line radiation observed by the satellite, *J. Geomagn. Geoelectr.*, *37*, 309–327.

Yearby, K. H., A. J. Smith, and K. Bullough (1983), Power line harmonic radiation in Newfoundland, *J. Atmos. Terr. Phys.*, *45*, 409–419.

J. Bortnik, Department of Atmospheric and Oceanic Sciences, University of California Los Angeles, 405 Hilgard Avenue, Los Angeles, CA 90095, USA.

F. Němec and M. Parrot, Laboratorie de Physique et Chimie l'Environnement/CNRS, 3A Avenue de la Recherche Scientifique, 45071 Orléans Cedex 2, France. (frantisek.nemec@cnrs-orleans.fr)

O. Santolík, Institute of Atmospheric Physics/ASCR, Bocni II 1401, 141 31, Prague 4, Czech Republic.

WDS'08 Proceedings of Contributed Papers, Part II, 168–171, 2008. ISBN 978-80-7378-066-1 © MATFYZPRESS

Possible Seismic Influence on VLF Wave Intensity: Observations by a Low-Altitude Satellite

F. Němec,[1,2,3] O. Santolík,[2,3] and M. Parrot[1]

[1]LPCE/CNRS, Orléans, France.

[2]Faculty of Mathematics and Physics, Charles University, Prague, Czech Republic.

[3]IAP/CAS, Prague, Czech Republic.

Abstract. We present results of a statistical study of VLF (up to 10 kHz) wave intensity measured by a low-altitude spacecraft in the vicinity of earthquakes. The data from the French DEMETER spacecraft (altitude about 700 km, nearly Sun-synchronous orbit) that was specially developed for such kind of studies are used. The recently developed two-step data processing method is briefly introduced and the main obtained results are reviewed. Finally, a simple independent test of the obtained results is done in order to give an additional evidence for the existence of possible seismic-related effect. Our results indicate that there is a decrease of power spectral density of electric field fluctuations shortly (0-4 hours) before the time of the main shock. This decrease was observed close to surface earthquakes (depth less than 40 km) with magnitude larger than or equal to 4.8 and only during the night. No similar effect was observed for deep earthquakes nor during the day.

Introduction

Perturbations of the intensity of electromagnetic emissions possibly related to seismic activity have been recently reported by several authors, using both ground based measurements [Tate and Daily, 1989; Asada et al., 2001] and low-altitude satellite data [Parrot and Mogilevsky, 1989; Larkina et al., 1989; Molchanov et al., 1993; Parrot, 1994; Hobara et al., 2005; Molchanov et al., 2006; Němec et al., 2008]. Such perturbations might be very important, because they are claimed to occur even shortly before the time of the main shock and could therefore serve as short-time precursors. However, there are two main reasons for which these observations have been the subject of an intense debate in the literature (see for example Rodger et al. [1996]). The first reason is that most of the performed studies included a small number of events and the obtained results were not therefore statistically very significant. In addition, the proposed theoretical ideas [Molchanov et al., 1995; Sorokin et al., 2001] and physical mechanisms [Gershenzon et al., 1989; Molchanov and Hayakawa, 1998] are not convincing enough since they lack the support of reliable experimental evidence.

In this paper, we present a unique statistical study of the influence of seismic activity on the intensity of electromagnetic waves in the ionosphere.

Data set

We have used data from the French DEMETER spacecraft. DEMETER is a micro-satellite (weight 130 kg) launched in June, 2004 with nearly Sun-synchronous circular orbit (original altitude about 710 km, decreased to about 660 km in December, 2005). The satellite operates in two different modes, so-called "Burst" and "Survey". During the first of them, more detailed data are measured, but the mode is active only above some specific, mostly seismic, areas. The Survey mode is active all around the orbit except of the auroral zones. There are 5 different instruments placed on board: ICE (electric field instrument, operating up to 3.5 MHz), IMSC (three search-coil magnetometers, operating up to 18 kHz), ISL (Langmuir probe), IAP (particle analyzer, providing the plasma density and composition) and IDP (detector of energetic particles). Among these, only electric field data in VLF range (up to 20 kHz) obtained during

the Survey mode have been used for the present study. Altogether, data collected during about three years of satellite operation have been used and all the earthquakes with magnitude larger than or equal to 4.8 (according to the United States Geological Survey (USGS) catalog, http://neic.usgs.gov/neis/epic/epic_global.html) during the analyzed period have been included.

Results

The two-step data processing method developed by Němec et al. [2008] in order to look for possible effects connected with seismic activity is based on the intuitive idea that if we want to study some weak effect hidden in the strong and varying natural background, we need to know what are the typical values and properties of this background.

Therefore, in the first step of the data processing a map of electromagnetic emissions is constructed. In general, this can have arbitrary number of parameters; the parameters introduced by Němec et al. [2008] were geomagnetic latitude, geomagnetic longitude, frequency, Kp index, magnetic local time and season of the year. The map of electromagnetic emissions can be represented by a matrix with number of indices equal to the chosen number of parameters. Since the distribution of values of power spectral density of electric field fluctuations is far from Gaussian distribution (see Figure 1), its representation by only the first few moments (e. g. by the mean value and standard deviation) is not ideal. Consequently, a full distribution of values represented by a histogram is stored in each bin of the matrix.

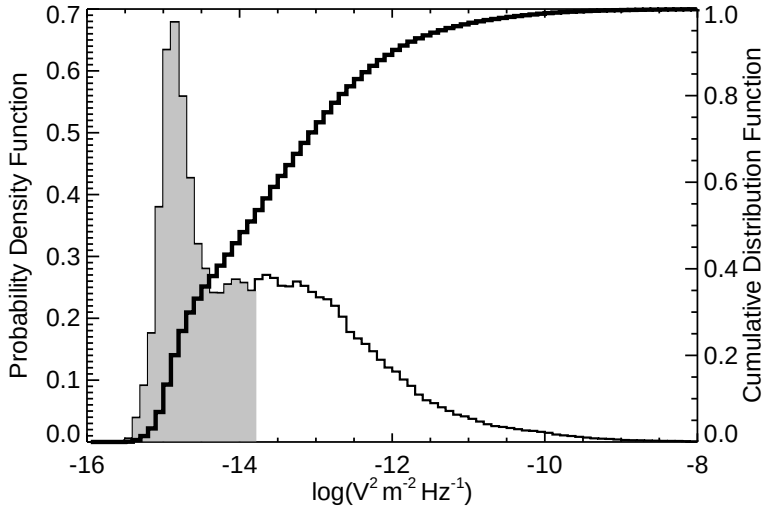

Figure 1. Probability density function of the measured power spectral density of electric field fluctuations (thin line) and corresponding cumulative distribution function (thick line). The area corresponding to the values lower than the median value (about $-13.8\log(\mathrm{V}^2\ \mathrm{m}^{-2}\ \mathrm{Hz}^{-1})$) is shaded.

The results obtained in the first step of data processing are used in the second step in order to define a "probabilistic intensity". This is in fact a value of cumulative distribution function appropriate to the measured value of power spectral density of electric field fluctuations at the given place under the given natural conditions – see Figure 1 for more details. Probabilistic intensity is therefore a uniformly (simple consequence of its definition) distributed number between 0 and 1. Larger the value is, larger is the measured power spectral density with respect to the normally measured one under the similar conditions. The values of probabilistic intensities in the vicinity of earthquakes have been then evaluated and it has been shown that during the night time the average probabilistic intensity is significantly lower than expected close to surface earthquakes (depth less than 40 km). The effect was limited to about 0–4 hours before the time of the main shock and the affected area was estimated to be approximately

300 km within the epicenter. No similar effects have been observed for deep earthquakes (depth larger than 40 km) nor during the day time.

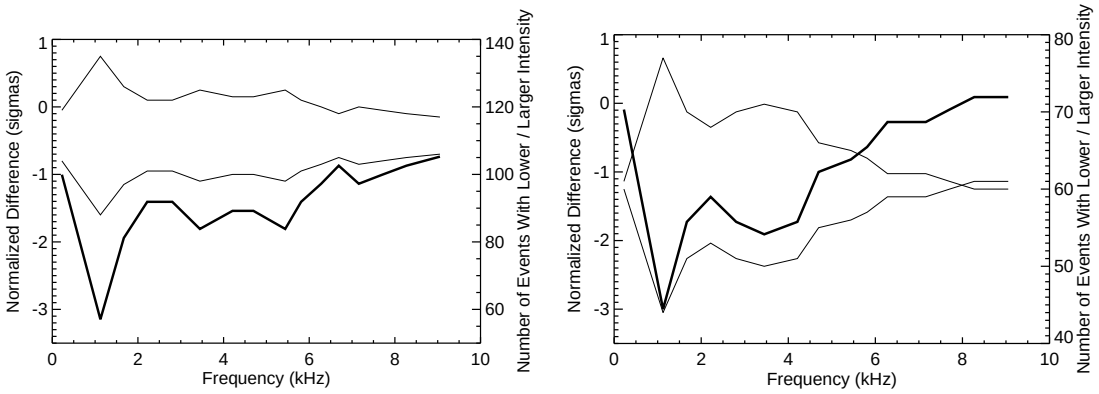

Figure 2. (left) Results for earthquakes with magnitudes larger than or equal to 4.8. (right) Results for earthquakes with magnitudes larger than or equal to 5.0. Upper thin line and the scale on the right: number of earthquakes in whose vicinity the intensity was lower than median. Bottom thin line and the scale on the right: number of earthquakes in whose vicinity the intensity was larger than median. Thick line and the scale on the left: difference expressed in number of standard deviations, supposing a binomial distribution.

Encouraged by the above mentioned results obtained by Němec et al. [2008], we tried a very simple test in order to check whether the power spectral density of electric field fluctuations is really lower than expected close to the earthquakes. This test is based simply on checking whether the measured intensity is lower than or larger than the median value obtained from all the data set. We have used all the data measured since the beginning of the mission till March, 2008 (more than 3.5 years). All strong enough surface earthquakes in USGS catalog that the satellite encountered close enough (distance less than 3 degrees to the epicenter) in the appropriate time (0-4 hours before the time of the main shock) were selected. Finally, we have checked whether the mean intensity in the vicinity of earthquake (distance between satellite and epicenter less than 3 degrees) is lower than or larger than the median value.

The results obtained close to the earthquakes with magnitudes larger than or equal to 4.8 and close to the earthquakes with magnitudes larger than or equal to 5.0 are plotted in the left and right panels of Figure 2, respectively. Thin lines and the scale on the right mark the number of events with the intensity lower than the median value (top line) and number of events with the intensity larger than the median value (bottom line). Thick lines and the scale on the left represent difference expressed in number of standard deviations. This is calculated simply as a difference between number of events with the intensity larger than the median value and the expected number of such events divided by the value of standard deviation obtained supposing the binomial distribution.

It can be seen that the number of events with the intensity lower than median is larger than the number of events with the intensity larger than median all over the studied frequency band. At frequencies around 1 kHz the difference is larger than 3 standard deviations and is therefore statistically significant. Relative number of orbits with the intensity lower than median is about 60% in the vicinity of earthquakes with magnitudes larger than or equal to 4.8. Moreover, relative number of orbits with the intensity lower than median is about 65% in the vicinity of earthquakes with magnitudes larger than or equal to 5.0.

Conclusion

Following Němec et al. [2008], we have analyzed all the night time DEMETER measurements performed in the vicinity (distance less than 3 degrees) of surface (depth less than 40

km) earthquakes with magnitudes larger than or equal to 4.8. For each of the earthquakes, we have performed a very simple test by checking whether the intensity observed nearby is larger than or lower than the median value. It has been demonstrated that the number of cases with intensity lower than the median value is larger than the number of cases with intensity larger than the median value all over the studied frequency band. The difference is most striking at frequencies around 1 kHz and is statistically significant. These results are in a complete agreement with Němec et al. [2008] and they are important for the two following reasons: 1) they were obtained by using a significantly larger data set (more than 3.5 years data as compared to about 2.5 year data in the previous study) 2) the test performed in this study is much simpler and consequently much more persuading and easier to understand.

Acknowledgments. We thank J. J. Berthelier for the use of electric field data. We thank J.-Y. Brochot of LPCE/CNRS Orléans for his help with downloading electric field data. F. N. and O. S. acknowledge support of the GACR grant no. 205/06/1267. F. N., O. S. and M. P. acknowledge support of the PICS grant no. 3725 from CNRS/DREI.

References

Asada, T., Baba, H., Kawazoe, M., and Sugiura, M., An attempt to delineate very low frequency electromagnetic signals associated with earthquakes, *Earth, Planets and Space*, *53*, 55–62, 2001.

Gershenzon, N. I., Gokhberg, M. B., Karakin, A. V., Petviashvili, N. V., and Rykunov, A. L., Modelling the connection between earthquake preparation processes and crustal electromagnetic emission, *Physics of the Earth and Planetary Interiors*, *57*, 129–138, 1989.

Hobara, Y., Lefeuvre, F., Parrot, M., and Molchanov, O. A., Low-latitude ionospheric turbulence observed by Aureol-3 satellite, *Ann. Geophysicae*, *23*, 1259–1270, 2005.

Larkina, V. I., Migulin, V. V., Molchanov, O. A., Kharkov, I. P., Inchin, A. S., and Schvetcova, V. B., Some statistical results on very low frequency radiowave emissions in the upper ionosphere over earthquake zones, *Physics of the Earth and Planetary Interiors*, *57*, 100–109, 1989.

Molchanov, O., Rozhnoi, A., Solovieva, M., Akentieva, O., Berthelier, J. J., Parrot, M., Lefeuvre, F., Biagi, P. F., Castellana, L., and Hayakawa, M., Global diagnostics of the ionospheric perturbations related to the seismic activity using the VLF radio signals collected on the DEMETER satellite, *Natural Hazards and Earth System Sciences*, *6*, 745–753, 2006.

Molchanov, O. A. and Hayakawa, M., On the generation mechanism of ULF seismogenic electromagnetic emissions, *Physics of the Earth and Planetary Interiors*, *105*, 201–210, 1998.

Molchanov, O. A., Mazhaeva, O. A., Goliavin, A. N., and Hayakawa, M., Observation by the Intercosmos-24 satellite of ELF-VLF electromagnetic emissions associated with earthquakes, *Ann. Geophysicae*, *11*, 431–440, 1993.

Molchanov, O. A., Hayakawa, M., and Rafalsky, V. A., Penetration characteristics of electromagnetic emissions from an underground seismic source into the atmosphere, ionosphere, and magnetosphere, *J. Geophys. Res.*, *100*, 1691–1712, 1995.

Němec, F., Santolík, O., Parrot, M., and Berthelier, J. J., Spacecraft observations of electromagnetic perturbations connected with seismic activity, *Geophys. Res. Lett.*, *35*, 2008.

Parrot, M., Statistical study of ELF/VLF emissions recorded by a low-altitude satellite during seismic events, *J. Geophys. Res.*, *99*, 23 339–23 347, 1994.

Parrot, M. and Mogilevsky, M. M., VLF emissions associated with earthquakes and observed in the ionosphere and the magnetosphere, *Physics of the Earth and Planetary Interiors*, *57*, 86–99, 1989.

Rodger, C. J., Thomson, N. R., and Dowden, R. L., A search for ELF/VLF activity associated with earthquakes using ISIS satellite data, *J. Geophys. Res.*, *101*, 13 369–13 378, 1996.

Sorokin, V. M., Chmyrev, V. M., and Yaschenko, A. K., Electrodynamic model of the lower atmosphere and the ionosphere coupling, *J. Atm. Solar-Terr. Phys.*, *63*, 1681–1691, 2001.

Tate, J. and Daily, W., Evidence of electro-seismic phenomena, *Physics of the Earth and Planetary Interiors*, *57*, 1–10, 1989.

JOURNAL OF GEOPHYSICAL RESEARCH, VOL. 114, A04303, doi:10.1029/2008JA013972, 2009

Decrease of intensity of ELF/VLF waves observed in the upper ionosphere close to earthquakes: A statistical study

F. Němec,[1,2,3] O. Santolík,[3,2] and M. Parrot[1]

Received 8 December 2008; revised 1 February 2009; accepted 9 February 2009; published 2 April 2009.

[1] We present results of a systematic study of intensity of VLF electromagnetic waves observed by the DEMETER spacecraft in the upper ionosphere (altitude 700 km). We focus on the detailed analysis of the previously reported decrease of wave intensity shortly before the main shock during the nighttime. Using a larger set of data (more than 3.5 years of measurements) and a newly developed data processing method, we confirm the existence of a very small but statistically significant decrease of wave intensity 0–4 hours before the time of the main shock at frequencies of about 1.7 kHz. It is shown that the decrease does not occur directly above the earthquake epicenter but is shifted about 2° in the westward direction. Moreover, it is demonstrated that the decrease occurs more often close to shallower earthquakes and close to earthquakes with larger magnitudes, as it is ''intuitively'' expected, representing an additional proof of validity of the obtained results. Finally, no dependence has been found on the occurrence of the earthquake below the ocean or below the continents.

Citation: Němec, F., O. Santolík, and M. Parrot (2009), Decrease of intensity of ELF/VLF waves observed in the upper ionosphere close to earthquakes: A statistical study, *J. Geophys. Res.*, *114*, A04303, doi:10.1029/2008JA013972.

1. Introduction

[2] The idea of additional electromagnetic phenomena accompanying earthquakes is rather old [*Milne*, 1890]. These might be of a large importance, because some of them are claimed to occur shortly (up to several days) before the time of the main shock and could therefore potentially serve as short-time precursors. Among other reported precursors (changes in temperature and concentration, resistivity changes, etc.), electromagnetic perturbations possibly connected with seismic activity have been recently discussed by several authors, both using ground-based [*Tate and Daily*, 1989; *Asada et al.*, 2001; *Bortnik et al.*, 2008] and satellite data [*Parrot and Mogilevsky*, 1989; *Larkina et al.*, 1989; *Molchanov et al.*, 1993, 2006; *Parrot*, 1994; *Hobara et al.*, 2005; *Němec et al.*, 2008]. The reported electromagnetic effects span over the large range of frequencies (from DC up to visible light), timescales (from several minutes up to a few months) and may be of various nature (enhancement of wave intensity, attenuation of wave intensity, modification of wave characteristics). On the other hand, there is a number of studies that reveal no or only a very weak correlation between the seismic activity and observed effects [*Henderson et al.*, 1993; *Rodger et al.*, 1996; *Clilverd et al.*, 1999]. These negative results might possibly be due to the fact that any potential precursors are very weak and could be therefore easily hidden in the common variations of the natural background. In addition, it is quite complicated to compare the different performed studies, because they often use very different data set and data processing methods. Finally, theoretical models that have been developed in order to explain the precursory phenomena are numerous [*Gershenzon et al.*, 1989; *Molchanov et al.*, 1995, 2001; *Molchanov and Hayakawa*, 1998; *Sorokin et al.*, 2001; *Pulinets et al.*, 2003; *Freund*, 2007], but they mostly represent only physical ideas. The mechanisms that are responsible for potential earthquake precursors are still understood very poorly.

[3] The presented paper closely follows a study by *Němec et al.* [2008], where we systematically investigated a large set of satellite data (more than 2.5 years) and showed that during the night there is a small but statistically significant decrease of wave intensity in the vicinity of large shallow earthquakes shortly (0–4 hours) before the time of the main shock. The observed effect was strongest for earthquakes with magnitudes larger than or equal to 5.0 and depths lower than 40 km. No effect was observed during the day nor for deep earthquakes.

[4] In the first part of the present paper we analyze a larger data set (more than 3.5 years) by using the same data processing method as formerly used by *Němec et al.* [2008]. Then, we apply a newly developed data processing and study the observed effect more in detail, focusing namely on its variation with different earthquake parameters: magnitude, depth, altitude of the solid surface above the hypocenter (whether the earthquake occurred below the ocean or below the continent). Data set that we have used for the

[1] Laboratoire de Physique et Chimie de l'Environnement et de l'Espace, Centre National de la Recherche Scientifique, Orléans, France.
[2] Faculty of Mathematics and Physics, Charles University, Prague, Czech Republic.
[3] Institute of Atmospheric Physics, Academy of Sciences of the Czech Republic, Prague, Czech Republic.

0148-0227/09/2008JA013972$09.00

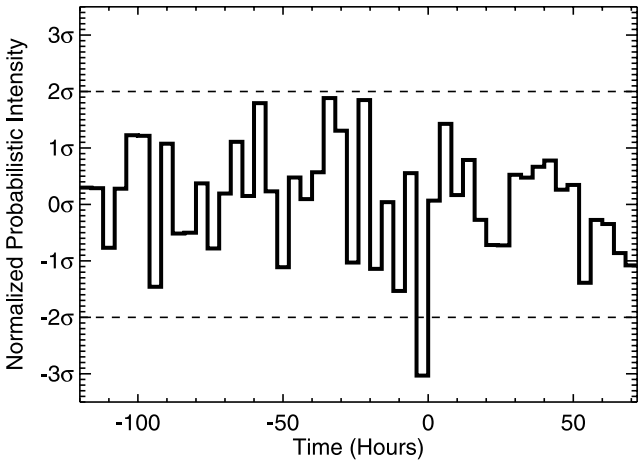

Figure 1. Normalized probabilistic intensity as a function of the time relative to the time of the main shock (see text).

study is presented in section 2. Section 3 presents results of the data processing method introduced by *Němec et al.* [2008] applied on the substantially extended data set. The newly developed data processing method is described in section 4, whereas section 5 presents the obtained results. These are discussed in section 6 and summarized in section 7.

2. Data Set

[5] For this study, data from the French spacecraft DEMETER have been used. DEMETER is a microsatellite launched in June 2004 on a circular quasi sun-synchronous orbit (10.30 and 22.30 LT) with an altitude of about 700 km [*Parrot*, 2006] and inclination 98°. The altitude was changed to about 660 km in December, 2005. The satellite performs 14 orbits per day and measures continuously between −65° and +65° of geomagnetic latitude, providing thus a very good coverage of the Earth's seismic zones. Among several instruments placed on board, we have focused on the analysis of electric field data measured by the ICE instrument [*Berthelier et al.*, 2006]. Irrespective of the mode, this provides us with on-board calculated power spectrum of one electric field component. The frequency resolution is 19.5 Hz and time resolution is 2 s or 0.5 s depending on the mode of operation. For the data set used in this study the selected electric component is perpendicular to the orbit plane. Altogether, we have used data from more than 3.5 years of the satellite measurements, representing about 9000 hours of nighttime data in about 15500 orbits. During the analyzed period about 9500 large shallow earthquakes with magnitude larger than or equal to 4.8 and depth less than 40 km occurred all over the world according to the USGS catalog (http://neic.usgs.gov/neis/epic/epic_global.html). Among these, there are more than 5500 earthquakes with magnitude larger than or equal to 5.0.

3. Verification of Results of *Němec et al.* [2008] Using a Larger Data Set

[6] We have used a larger data set (46 months as compared to 30 months of *Němec et al.* [2008]) and verified the existence of the previously reported effect [*Němec et al.*, 2008]. In order to enable a direct comparison with the formerly obtained results, we have used exactly the same data processing method (see Appendices A and B for a detailed description). We have focused on a specific frequency-time interval and a range of earthquake parameters for which the effect has been found; we have analyzed only the nighttime data and the 200 Hz wide frequency band centered at 1.7 kHz. Moreover, we have limited our study only to earthquakes with magnitudes larger than or equal to 5.0 and with depths shallower than 40 km.

[7] The results that we have obtained for distances less than 3° from the epicenters of earthquakes are represented in Figure 1. It shows the normalized probabilistic intensity as a function of the time relative to the time of the main shock, spanning from 5 days before to 3 days after. The time resolution is 4 hours. It can be seen that the normalized probabilistic intensity, normally fluctuating between $-2\ \sigma$ and $2\ \sigma$ (σ being the standard deviation), decreases shortly before the time of the main shock to less than $-3\ \sigma$. There are about 70 events included in each of the bins. The decrease occurs 0–4 hours before the time of the main shock and is formed by 2068 points coming from 64 different events. The mean value of probabilistic intensity in this bin (see Appendix B) is −0.083, corresponding to a decrease of wave intensity equal to about −2.4 dB. The median value of probabilistic intensity in this bin is −0.126, corresponding to a decrease of wave intensity equal to about −3.6 dB. Although these values represent a small but significant decrease of wave intensity as compared to the normal values, the absolute value of this decrease is somewhat smaller than the one reported by *Němec et al.* [2008] (see a detailed discussion in section 6).

[8] A distribution of all the cumulative probabilities that contribute to the bin where a decrease of wave intensity is observed is shown by a solid line in Figure 2. The mean/median value is marked by dotted/dashed line, respectively. If there were no effects connected with the seismic activity, the distribution should be approximately uniform (see Appendix A), which is not the case; lower values of cumulative probability clearly occur more often, corresponding to a decrease of wave intensity. For comparison, we show by a dash-dotted line a distribution of cumulative probabilities in all bins but the one where the effect is observed.

4. New Data Processing Method

[9] We have developed a new data processing method designed specifically to check for the presence of seismic-related effects in a given frequency and time (relative to the time of the main shock) intervals. Following the conclusions of *Němec et al.* [2008], we have focused solely on the analysis of the nighttime data, 200 Hz wide frequency band centered at 1.7 kHz and time interval 0–4 hours before the time of the main shock. These are exactly the same parameters, for which a decrease of wave intensity has been previously reported.

[10] The applied data processing can be divided into 4 steps, among which the first two are analogical to those previously introduced by *Němec et al.* [2008]; see Appendix A.

[11] The third level of data processing is different: we select a point P within ±10° in latitude and ±10° in longitude from the earthquake epicenter. For each of the orbits that enters a circle with a radius of 3° from the point P

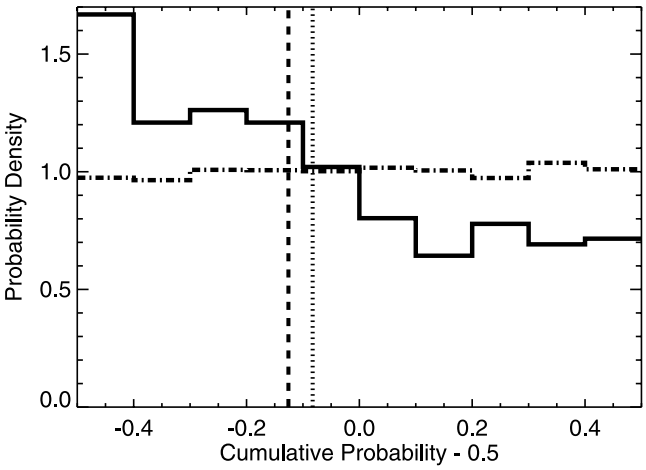

Figure 2. (solid line) Distribution of all the cumulative probabilities that contribute to the observed decrease of wave intensity. Mean/median value is plotted by a dotted/dashed line, respectively. (dash-dotted line) Distribution of cumulative probabilities in all bins, but the one wherein the effect is observed.

we check whether the values of the cumulative probability (that means the ''normalized'' intensities) are lower than or larger than normal ones close to the point. In order to do this, we take advantage of the Mann-Whitney U test [*Sheskin*, 2000]. This is a statistical test that enables, on a given level of significance, a check to see if two populations X and Y have the same mean of distribution or not. The reason for using the Mann-Whitney U test instead of the more traditional Student t test [*Sheskin*, 2000] is that we deal with non-Gaussian distributions. This does not represent a problem for the Mann-Whitney U test, which is a nonparametric test. As a population X we take the cumulative probabilities close to the point P and as a population Y we take the cumulative probabilities in the rest of the same half-orbit. The reason for this treatment is that each half-orbit lasts for only about 35 minutes, which is a relatively short time as compared to the timescale of major changes of intensity of electromagnetic waves in the upper ionosphere. The values measured all over the half-orbit are therefore dependent and it is reasonable to take as normal ''background'' values the values of cumulative probabilities in the rest of a given half-orbit.

[12] The fourth step consists of a simple statistical evaluation of the obtained results. For each of the events (that is for each of the orbits that encounters the point P sufficiently close at the given time) and a predefined level of significance there are three possibilities: (1) cumulative probabilities close to the point P are lower than in the rest of the half-orbit, (2) cumulative probabilities close to the point P are larger than in the rest of the half-orbit, and (3) cumulative probabilities are about the same close to the point P and in the rest of half-orbit; at a predefined level of significance it is not possible to decide which of them are lower.

[13] The events for which it is not possible to draw a clear conclusion using the Mann-Whitney test are not taken into account in the further data processing. We calculate the number of events for which the values of cumulative probabilities close to the point P are lower than in the rest of the half-orbit (N_d) and, in the same way, we calculate the number of events for which the values of cumulative probabilities close to the point P are larger than in the rest of the half-orbit (N_i). Directly from these two values we can calculate the probability of their random occurrence. If we suppose no effect connected with the seismic activity, the probability p_i of an increase of intensity close to the point P would be the same as the probability p_d of a decrease of intensity close to the point P and the numbers N_i and N_d would be consequently about the same. If the numbers N_i and N_d are significantly different, it means that the wave intensity is different close to the point P than in the rest of the half-orbits, indicating the existence of a seismic-related effect. The subsequent evaluation of the probability of occurrence is very trivial: since $p_i = p_d$ for an unperturbed case, all that we have to deal with is a simple binomial distribution.

5. Results

[14] A left panel of Figure 3 represents a schematic view of the geometry used for construction of latitude-longitude plot. There is an epicenter of the earthquake in the middle of Figure 3 and longitudinal/latitudinal distances from it are plotted on the horizontal and vertical axis, respectively. A dashed line represents a part of the satellite orbit and a cross in the upper right part of Figure 3 represents an arbitrary example point: we want to check whether the emissions in its vicinity have unusually large or low intensity. Consequently, we simply compare the cumulative probabilities measured close to the point (closer than 3°, following *Němec et al.* [2008], inner part of the marked circle) with the cumulative probabilities measured during the same half-orbit farther than 3° from the point using the Mann-Whitney test and use the data processing described above in section 4.

[15] The right panel of Figure 3 shows the results obtained for the latitude-longitude plot. Only sufficiently large (magnitude $\geq$ 5.0) and shallow (depth $<$ 40 km) earthquakes have been used for its construction. The longitudinal and latitudinal distances from earthquakes are plotted on the horizontal and vertical axis, respectively. The color scale represents the probability of random occurrence. It can be seen that the only exceptional effect is located close to the epicenter of earthquakes, shifted by about 2° in the Westward direction and also slightly to the North. It represents a decrease of the wave intensity. Note that this cannot be determined from the plotted color scale, because it represents only a probability that such values N_d and N_i could occur randomly, not which of them is larger. We have used the significance level for the Mann-Whitney test equal to 0.01, leading to about 50 events per each bin of the resulting plot. However, the results are independent of this threshold (see section 6 for more discussion).

[16] Having observed a decrease of the wave intensity close to the earthquakes, we have focused on its further analysis. More specifically, we were interested how it depends on various parameters. In order to do so, we have compared the data in a 3° radius around the point located 2° to the West from the epicenter (that is approximately the area where the decrease is observed) and the rests of the

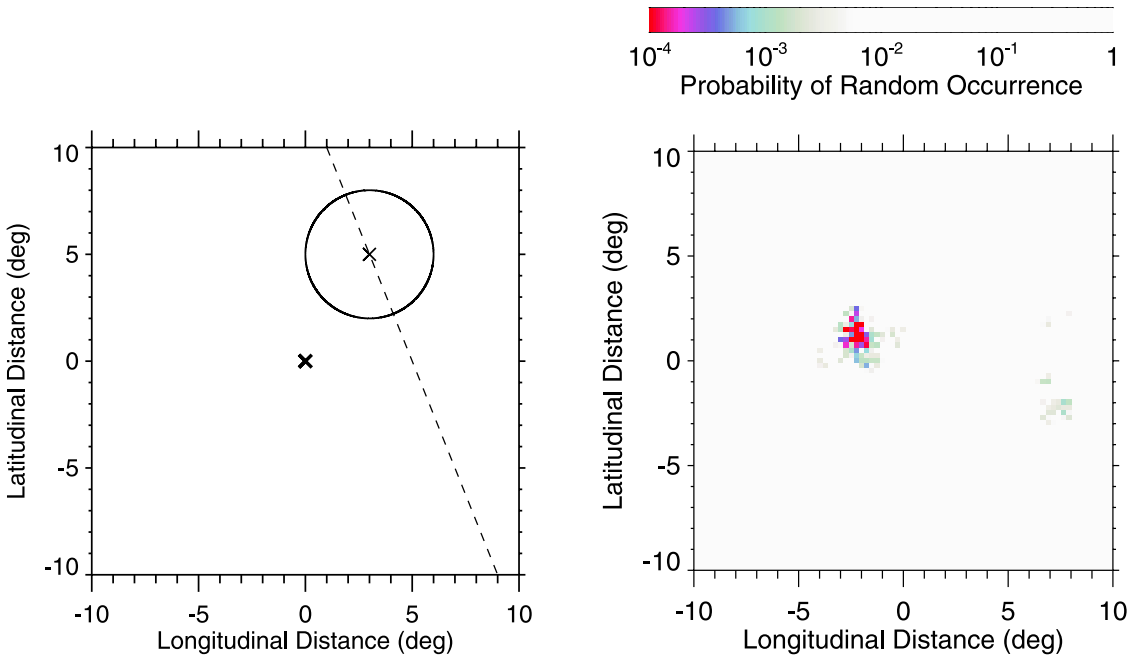

Figure 3. (left) Geometry of latitude-longitude plot: scheme of calculation. (right) Latitude-longitude plot of probability of random occurrence of such a ratio of decreases/increases for earthquakes with magnitudes of $\geq$5.0 and depths of <40 km.

half-orbits, using the data processing described in section 4. Afterward, we have checked how N_d and N_i depend on the magnitude of the earthquake, depth of the earthquake and altitude of the solid surface above the hypocenter (whether the earthquake occurred below the ocean or below the continent). The level of significance used for the Mann-Whitney test was again 0.01, as it is throughout the present paper.

[17] The results that we have obtained for the dependence on the magnitude of the earthquakes are shown in Figure 4. In Figure 4 we have slightly decreased the threshold of magnitude down to 4.8. The left panel represents N_i as a function of the magnitude of the earthquakes, while the right panel represents the same dependence of N_d. All shallow (depth < 40 km) earthquakes were taken into account when constructing the plot. As expected, weaker earthquakes occur more often and the wave intensity in their vicinity can both increase or decrease. We expect that for even lower magnitudes (<4.8) the decreases and increases would occur with about the same probability. It can be seen that for sufficiently large earthquakes (magnitude $\geq$ 5.5) there is almost always a decrease of wave intensity close to the earthquakes (15 events out of 17). Please note that the peak in the magnitude range 5.4–5.7 is most probably just a random fluctuation caused by a low number of events.

[18] Figure 5 is similar as Figure 4, but this time we have focused on the dependence of the observed effect on the depth of the earthquakes. All large (magnitude $\geq$ to 5.0) earthquakes were taken into account when constructing the plot. It can be seen that for very shallow earthquakes (depth < 20 km), decrease of wave intensity close to earthquake occurs more often. Please note that the large number of included earthquakes with depths about 10 km is already contained in the used USGS catalog, which attributes this depth to a very large number of events.

[19] After having investigated a dependence on the magnitude (Figure 4) and depth (Figure 5) of the earthquake separately, we combined them into a single plot, which is shown in Figure 6. It represents color-coded relative number of decreases (that is $N_d/(N_d + N_i)$) as a function of magnitude (horizontal axis) and depth of the earthquake (vertical axis). Relative number of decreases equal to 0.5 means that the number of decreases of the wave intensity close to earthquakes is equal to the number of increases of the wave intensity close to earthquakes, meaning thus no specific change of wave intensity connected with the earthquakes. On the other hand, relative number of decreases equal to 1 means that for all of the analyzed events the cumulative probabilities were lower in the vicinity of earthquakes than in the rest of the half-orbits (or it was not possible to decide using the Mann-Whitney test at a given level of significance, see section 6 for a detailed description). The used significance level of the Mann-Whitney test equal to 0.01 resulted in about 10 events per each bin. It can be seen that while the relative number of decreases is close to 0.5 for deep earthquakes with low magnitude (top left corner), meaning no change of wave intensity close to the earthquakes, it is equal to 1 for shallow earthquakes with large magnitudes (bottom right part).

[20] Figure 7 represents a similar plot as Figures 4 and 5, but this time the results were obtained for dependence on the altitude of the solid surface above the hypocenters of the earthquakes (magnitude $\geq$ to 5.0). It can be seen that the number of earthquakes occurring under the ocean (altitude less than 0 km) is much larger than the number of earthquakes occurring under the land (altitude larger than 0 km). However, no clear dependence of the studied effect can be

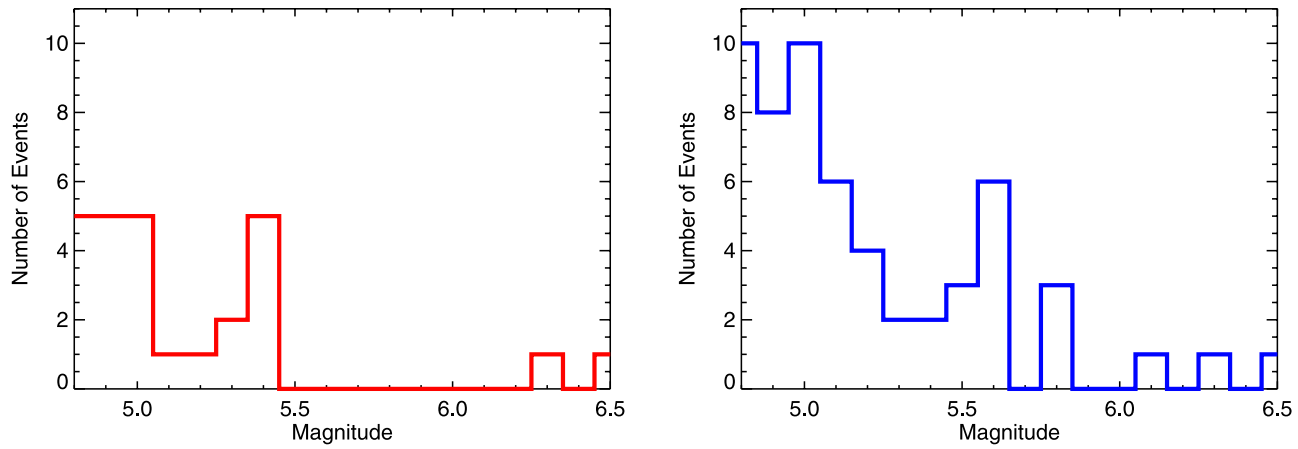

Figure 4. (left) Number of events with an increase of wave intensity close to the epicenter of earthquake (N_i) as a function of magnitude of earthquake. (right) Number of events with a decrease of wave intensity close to the epicenter of earthquake (N_d) as a function of magnitude of earthquake.

observed; the ratio of the number of wave intensity decreases to the number of wave intensity increases does not seem to depend on whether the earthquakes occur below the ocean or below the continent.

6. Discussion

[21] Data from more than 3.5 years of measurements performed by the DEMETER spacecraft and earthquakes occurring all over the world have been used. This represents a unique data set, ideal for performing large systematic studies. However, one must keep in mind a basic limitation of such kind of surveys: although a large number of earthquakes occurred during the analyzed period, there is only a small number of them which DEMETER encountered very close. This significantly complicates any statistical analysis of seismic-related effects, because it is reasonable to suppose the effects to be limited to some area around the epicenter of an earthquake. Consequently, although large volumes of data are measured, only a low number of measurements occur in the vicinity of large earthquakes and are potentially interesting. From this point of view the presented data processing that takes advantage of the map of electromagnetic emissions is optimal, because it uses these far-from-earthquakes data at least in order to estimate normal (that is seismically unperturbed) values of the wave intensity.

[22] The previously reported decrease of the wave intensity shortly before the time of the main shock [*Němec et al.*, 2008] has been confirmed when using a larger data set. However, the amplitude of the observed effect (mean/median value of −0.083/−0.126, respectively, corresponding to about −2.4 dB/−3.6 dB, respectively) is weaker than the amplitude reported by *Němec et al.* [2008] (mean/median value of −0.146/−0.176, corresponding to about −4.2 dB/−5.1 dB, respectively) using a smaller set of data. A careful check of all the 64 events forming the decrease reveals that this is due to a few recent events with large probabilistic intensities, which significantly increase the resulting mean value of the probabilistic intensity.

[23] This represents a basic constrain of the statistical method introduced by *Němec et al.* [2008]: checking the mean value of cumulative probability is a good tool for revealing any systematic changes of wave intensity connected with seismic activity using a large data set. However, the effects due to the seismic activity are very

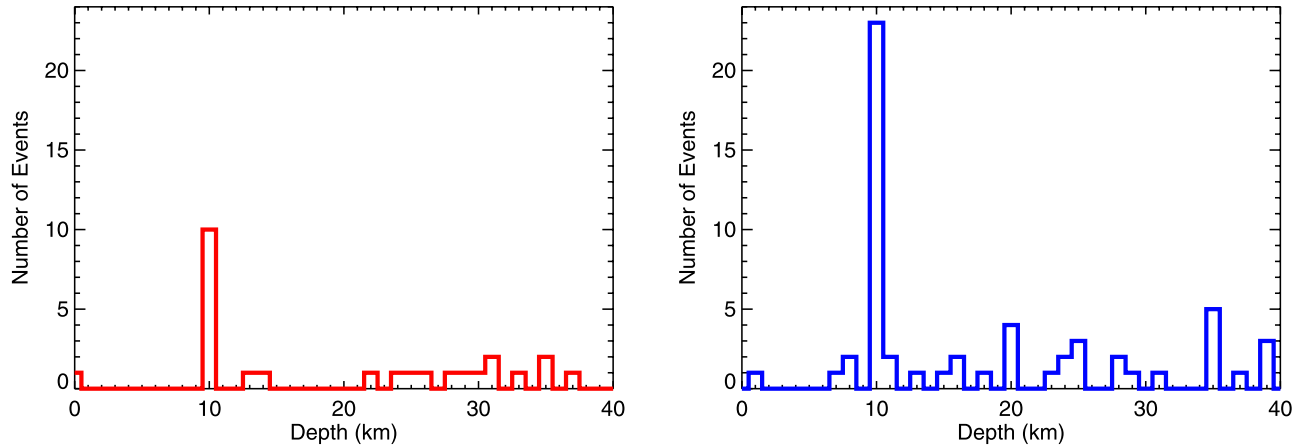

Figure 5. The same as Figure 4, but for the dependence on the depth of earthquakes.

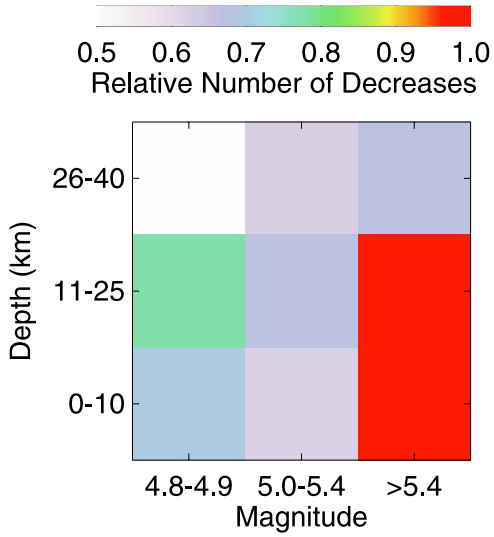

Figure 6. Relative number of decreases in the vicinity of earthquakes as a function of their depth and magnitude.

small as compared to the common natural variations of wave intensity. For an individual event (or a small number of events), the mean value of cumulative probability is therefore linked to these random natural variations rather than to seismic-related effects. A large value of the mean cumulative probability for a single event thus does not mean that there was an increase of wave intensity close to the earthquake, but more likely that the wave intensity during that time was globally larger than normal. This is a direct consequence of comparing close-quake data to the data measured at a given place under the similar conditions all over the analyzed period of several years. Surely, an inverse effect exists as well; low values of cumulative probability can be caused by the wave-quiet period and not by seismic-related effects.

[24] From this analysis, we can only conclude that although the decrease of wave intensity is statistically significant (more than 3 standard deviations), but very small (about 3 dB) as compared to the usual natural variability (about 11 dB).

[25] The newly developed data processing method takes advantage of the Mann-Whitney test at a specified level of significance. The obtained results thus necessarily depend on this choice. In order to remain consistent, we have used the value of 0.01 throughout the paper. However, it turns out (not shown) that as long as the choice of the level of significance remains "reasonable," the obtained results remain practically unchanged. If too low level of significance is required, than the test is able to provide a clear answer only for a small number of half-orbits and the resulting statistics is poor. On the other hand, if the level of significance is chosen to be too large, the test provides a result even if it is practically impossible to decide which cumulative probabilities are lower: many "unclear" events enter the statistics and the real effects are buried in a random noise.

[26] While in the former study the effect was found to occur within 3° from the epicenter of an earthquake, a newly developed data processing enables a more detailed check of the position and shape of the affected area. It turns out that instead of occurring directly above the epicenter of an earthquake, the effect is shifted by about 2° to the West and slightly to the North. The observed longitudinal shift might possibly be caused by the Earth's rotation and the resulting Coriolis force: if there are, for example, aerosols [*Pulinets and Boyarchuk*, 2004] propagating toward the larger altitudes, it would always be dragged to the west. Another possibility could be that the origin of the effect is somehow related to the ions, which drift in the westward direction because of the Earth's magnetic field. Concerning the northward drift, we do not have any explanation at this moment.

[27] A detailed analysis of the observed effect is very important for two reasons. First, a comprehension of properties of the observed phenomenon is crucial for understanding the physical mechanism which causes the effect. Second, and at the present level of research perhaps even more importantly, it can serve as an independent test of the validity of the obtained results. This is possible, because at least for some of the analyzed parameters we have a good

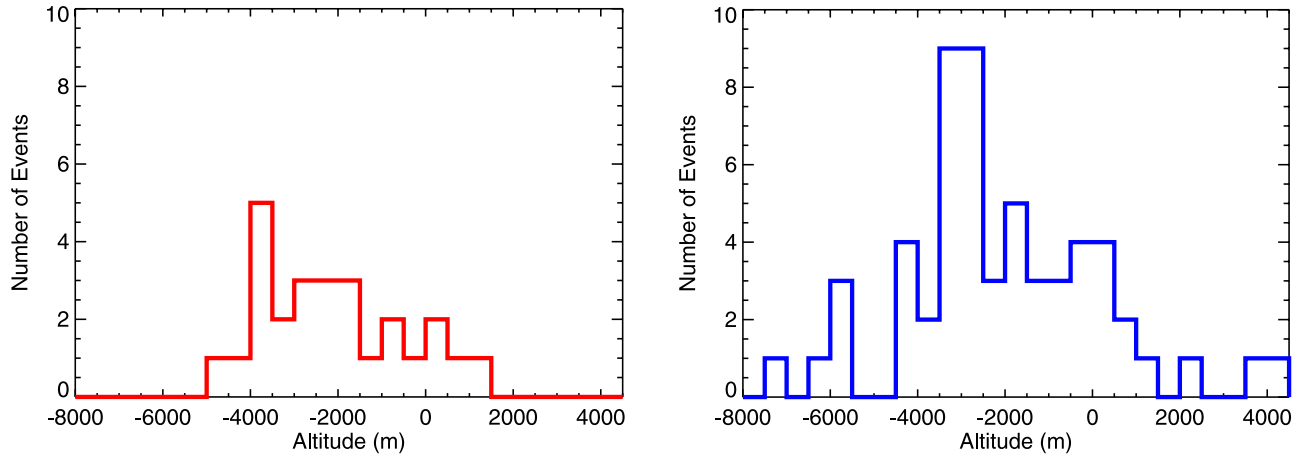

Figure 7. The same as Figure 4, but for the dependence on the altitude of solid surface above earthquake.

''intuitive'' idea of what the dependence should look like. For example, it is reasonable to expect that the observed effect would be stronger for larger earthquakes. Additionally, the effect should be stronger for shallower earthquakes: for these, any signal propagating from the region of a future earthquake does not have to pass that far through the lithospheric material before reaching the satellite altitude. Our results confirm both these ''intuitive'' expectations, which is very important.

[28] At this place we would like to shortly comment on the result shown in Figure 6. The reason is that although the relative number of wave intensity decreases is equal to 1 for large shallow earthquakes, it does not mean that the cumulative probabilities are always lower close to their epicenters than in the rest of the orbits for earthquakes with such parameters; it can also mean that in some cases there is no significant change of cumulative probabilities close to the epicenters as compared to the rests of the half-orbits. In such cases, the Mann-Whitney test cannot determine which set of values is lower and the events are not taken into account. For the used level of significance 0.01, there is usually about 50% of such events. Consequently, we can only say that if the spacecraft passes close to the large shallow earthquake, there is either no change of cumulative probability or there is a decrease of cumulative probability. Moreover, it should be noted that the statistics for this plot is rather poor, there is only about 10 events in each of the bins. Unfortunately, this cannot be improved anyhow and represents a basic limitation of all the statistical studies of this type.

[29] The last dependence that we have checked was whether the observed effect depends on the altitude of the solid surface above the hypocenter of an earthquake or not. This could help with identification of physical mechanisms which are causing the phenomenon: some of the proposed mechanisms [*Parrot*, 1995] should work for earthquakes below the sea level as well (e.g., radon emanation) while others should work only for land earthquakes. Although at the present level of knowledge we do not dare to discuss about the possible mechanism, we believe that our finding that there is no clear dependence of the effect on the altitude of the solid surface above the hypocenter of an earthquake is very important for further theoretical development.

[30] Finally, we would like to underline that although the correlation between seismic activity and intensity of electromagnetic waves is statistically significant, it is observed only due to the large number of the analyzed events. Therefore even if there is on average a decrease of wave intensity related to large surface earthquakes, individual events may exhibit rather different behavior; the natural fluctuations of intensity of electromagnetic waves are large and the observed effect is relatively weak as compared to them.

7. Conclusions

[31] We have studied the previously reported decrease of the intensity of electromagnetic waves in the vicinity of earthquakes [*Němec et al.*, 2008]. We have confirmed that during the night there is a very small but statistically significant decrease of wave intensity observed by the satellite close to large surface earthquakes shortly before the time of the main shock. Using a newly developed data processing method, we have shown that

[32] 1. the effect is stronger for larger earthquakes,

[33] 2. the effect is stronger for shallower earthquakes,

[34] 3. the effect does not seem to depend on whether the earthquake occurs below the ocean or not,

[35] 4. the effect occurs slightly ($\approx 2^\circ$) to the west from the epicenter of earthquakes.

[36] The first two points are in a good agreement with what is ''intuitively'' expected. On the other hand, the last two points might be important for understanding the physical mechanism that is responsible for the effect.

Appendix A: Detailed Description of the First Two Steps of the Data Processing, Based on *Němec et al.* [2008]

[37] The purpose of Appendix A is to provide a detailed description of the first part of the data processing method. This part is common for both the method by *Němec et al.* [2008] and the newly developed method described in section 4.

[38] In the first step of the data processing, a map of electromagnetic emissions is constructed. This is built using all the measured data and can be represented by a six-dimensional matrix with the indices of the following meaning:

[39] 1. frequency (any frequency bands that we are interested in);

[40] 2. geomagnetic longitude of the satellite (longitudinal resolution 10°);

[41] 3. geomagnetic latitude of the satellite (latitudinal resolution 2°);

[42] 4. magnetic local time (daytime and nighttime; there are no other possibilities, as described in section 2);

[43] 5. magnetospheric conditions described by the Kp index: three bins made in such a way that there is about the same amount of data accumulated in each of the bins (0−1o, 1+−2+, above 3−);

[44] 6. season of the year (October−April, May−September).

[45] In each cell of this matrix we accumulate a histogram of the common logarithm of power spectral density of electric field fluctuations. Consequently, for a given location of the spacecraft (geomagnetic longitude and magnitude), magnetospheric conditions (magnetic local time, Kp index, season of the year) and frequency we obtain an estimate of the probability density function $f(E)$ of observing a power spectral density of electric field fluctuations E.

[46] In the second step of the data processing, we attribute a cumulative probability F_i to each of the measured power spectral densities E_i. The appropriate value of the cumulative probability F_i is equal to the value of cumulative distribution function obtained for the same frequency, spacecraft location and similar geomagnetic conditions. This can be calculated directly as an integral of the appropriate probability density function obtained in the first step of the data processing:

$$F_i = \int_{-\infty}^{E_1} f(E)dE. \tag{A1}$$

Therefore the cumulative probability F_i is a number between 0 and 1 that represents the probability of

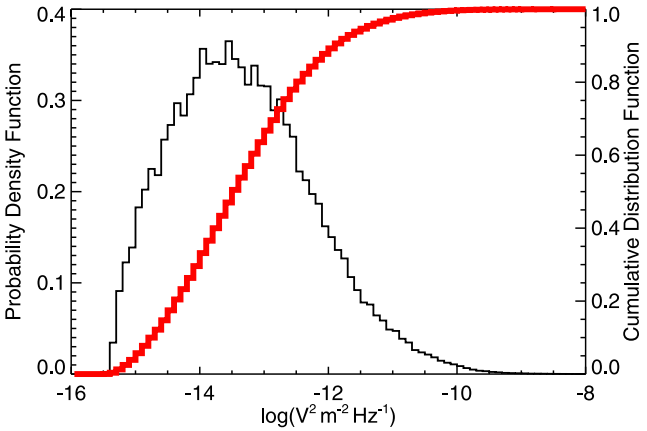

Figure A1. Probability density of observing a given power spectral density of electric field fluctuations (thin) and the corresponding cumulative distribution function (thick).

occurrence of signals with a power spectral density lower than or equal to the measured power spectral density of electric field fluctuations E_i. At this point, it is important to notice that the values of cumulative probability calculated from the entire data set (that is the same data set as has been used for construction of map of electromagnetic emissions) are uniformly distributed between 0 and 1. This is a direct consequence of the definition of cumulative probability.

[47] Figure A1 represents an example of distribution of observed power spectral densities (thin) and also the corresponding cumulative distribution function (bold). The nighttime data in a frequency band centered at 1.7 kHz measured all over the world during all the analyzed period have been used when constructing the plot. When performing the calculation, we have one such a plot for each combination of frequency band, spacecraft location, magnetic local time, geomagnetic conditions and season of the year, which enables a direct conversion between the power spectral density of electric field fluctuations and the corresponding value of the cumulative distribution function (cumulative probability).

Appendix B: Detailed Description of Data Processing Using the Normalized Probabilistic Intensity Based on *Němec et al.* [2008]

[48] The purpose of Appendix B is to provide a detailed description of the data processing method based on the normalized probabilistic intensity used by *Němec et al.* [2008].

[49] After applying the two steps described in Appendix A, data whose distance from the epicenter is lower than some threshold (a threshold of 10° has been used) and which occur in the requested time interval (a time interval from 5 days before to 3 days after the time of the main shock has been chosen) are evaluated. If two or more earthquakes occur in the required distance/time interval from the measurement (and therefore possibly influence the data), the measurement is not taken into account. This condition, which is basically similar to taking into account only "individually occurring" earthquakes, is very important, because otherwise it could happen that a single measurement is attributed to more than one earthquake and used more than once. Having selected the proper data that occur close to earthquakes (both in time and space), the corresponding cumulative probabilities are calculated. These are then organized in bins as a function of the following parameters:

[50] 1. time to/from the time of the main shock (resolution of 4 hours),

[51] 2. distance from the epicenter of earthquake (resolution of 1°),

[52] 3. frequency (the same frequency bins as for the map of electromagnetic emissions).

[53] For each of the bins we define a "probabilistic intensity." For a bin b it is calculated as follows:

$$I_b = \frac{\sum_{i=1}^{M_b} F_i}{M_b} - 0.5, \tag{B1}$$

where M_b is the number of cumulative probabilities F_i collected in a given bin. In other words, we calculate the mean value of cumulative probability in the bin and subtract one half in order to obtain a number between -0.5 and 0.5 instead of between 0 and 1. Now if the observed intensities that belong to the bin were significantly lower/larger than the usual ones, the attributed cumulative probabilities would be significantly lower/larger than 0.5 and the resulting probabilistic intensity would be significantly lower/larger than 0. The only remaining task is what quantitative value should be attributed to the word "significantly." This can be solved using statistical properties of the probabilistic intensity.

[54] The uniformly distributed values of probabilistic intensity are averaged into a bin b corresponding to a given time, position and frequency. Consequently, according to the central limit theorem and supposing that the number of averaged probabilistic intensities M_b is sufficiently large, the resulting values of probabilistic intensity I_b follow a normal distribution. The mean value of this distribution is equal to 0 and it has some standard deviation σ_b. If all the values averaged in the bin b were independent, the number of independent data points M'_b in the bin would be equal to the total number of the data points in the bin M_b and σ_b could be calculated as:

$$\sigma_b = \frac{1}{\sqrt{12 M_b}}. \tag{B2}$$

However, a problem when performing such kind of calculation is that although we know the total number of cumulative probabilities M_b included in the bin b, we do not know how many of them can be considered as independent; we do not know the value of M'_b. Now we will show how it can be estimated.

[55] As a lower estimate of M'_b it is reasonable to use the number N_b of different half-orbits of the spacecraft that contribute to the bin. This estimation is quite natural, because a duration of a half-orbit is about 35 minutes, which is longer than a typical timescale of intensity changes of electromagnetic waves in the upper ionosphere. Consequently, the data measured in the two different half orbits

must be independent. However, a problem is that there is more than one data point contributing to the bin b in each of the orbits. In order to solve this, we suppose a linear relation between M'_b and N_b:

$$M'_b = \frac{N_b}{\alpha^2}, \tag{B3}$$

where the meaning of the coefficient α is to define which relative fraction of the data coming from the same half-orbit can be considered as independent. Because at least each half-orbit can be considered as independent (see above), M'_b is larger than or equal to N_b and the coefficient α must be a positive number lower than or equal to 1. Further, we will suppose that, for a given frequency, α is a universal constant that represents a measure of stability of electromagnetic waves in the altitudes of the DEMETER spacecraft. The lower the value of α is, the more variable is the intensity of electromagnetic waves; the value $\alpha = 1$ would mean that all the data contributing to the bin from one half-orbit are dependent. Consequently, α is the same for all the bins at a given frequency and its value can be calculated directly from the experimental data.

[56] For a given frequency, we have a set of Q bins corresponding to different times (for our case we have $Q = 48$, because we take data from 5 days before to 3 days after the quake with a 4 hours resolution). For each of them we know the values of I_b (probabilistic intensity, a number between -0.5 and 0.5) and N_b (number of different half-orbits contributing to the bin). If we knew the coefficient α, we could also calculate an estimate of standard deviation σ_b using the equations (B2) and (B3):

$$\hat{\sigma}_b = \frac{\alpha}{\sqrt{12 N_b}}. \tag{B4}$$

Once knowing the standard deviation σ_b of the probabilistic intensity in the bin b, we could calculate the normalized probabilistic intensity Υ_b as:

$$\Upsilon_b = \frac{I_b}{\sigma_b}. \tag{B5}$$

The advantage of this concept is that we know exactly the expected distribution of normalized probabilistic intensities Υ: they should follow the Gaussian distribution with a mean value 0 (the same as probabilistic intensities I), but their standard deviation should be due to the normalization equal to 1. Having Q values of the normalized probabilistic intensity, we can therefore write:

$$\sqrt{\frac{1}{Q}\sum_{b=1}^{Q} \Upsilon_b^2} = 1, \tag{B6}$$

which can be rewritten using equations (B4) and (B5) in order to enable the calculation of the coefficient α:

$$\alpha = \sqrt{\frac{12}{Q}\sum_{b=1}^{Q} N_b I_b^2}. \tag{B7}$$

[57] Using the equation (B7) we can therefore calculate the value of the coefficient α directly from the experimental data. Then, equation (B4) is used to obtain the standard deviation for each of the bins. Finally, normalized probabilistic intensities $\tilde{O}_b$ are calculated according to the equation (B5). These values represent the final results: they express a change of power spectral density of electric field fluctuations as compared to the common natural background and its statistical significance.

[58] **Acknowledgments.** This work was supported by the Centre National d'Etudes Spatiales (CNES). It is based on observations with the electric field experiment ICE embarked on DEMETER. We thank J. J. Berthelier, PI of the electric field experiment, for the use of the data. We acknowledge the support of the PICS grant 3725 from CNRS/DREI. F. N. and O.S. acknowledge support of the GACR grant 205-06-1267.

[59] Amitava Bhattacharjee thanks Pier Francesco Biagi and another reviewer for their assistance in evaluating this paper.

References

Asada, T., H. Baba, M. Kawazoe, and M. Sugiura (2001), An attempt to delineate very low frequency electromagnetic signals associated with earthquakes, *Earth, Planets Space*, *53*, 55–62.

Berthelier, J. J., et al. (2006), ICE, the electric field experiment on DEMETER, *Planet. Space Sci.*, *54*, 456–471.

Bortnik, J., J. W. Cutler, C. Dunson, and T. E. Bleier (2008), The possible statistical relation of Pc1 pulsations to Earthquake occurrence at low latitudes, *Ann. Geophys.*, *26*, 2825–2836.

Clilverd, M. A., C. J. Rodger, and N. R. Thomson (1999), Investigating seismoionospheric effects on a long subionospheric path, *J. Geophys. Res.*, *104*(A12), 28,171–28,179.

Freund, F. T. (2007), Pre-earthquake signals: part 1. Deviatoric stresses turn rocks into a source of electric currents, *Nat. Hazards Earth Syst. Sci.*, *7*, 535–541.

Gershenzon, N. I., M. B. Gokhberg, A. V. Karakin, N. V. Petviashvili, and A. L. Rykunov (1989), Modelling the connection between earthquake preparation processes and crustal electromagnetic emission, *Phys. Earth Planet. Int.*, *57*, 129–138.

Henderson, T. R., V. S. Sonwalkar, R. A. Helliwell, U. S. Inan, and A. C. Fraser-Smith (1993), A search for ELF/VLF emissions induced by earthquakes as observed in the ionosphere by the DE 2 satellite, *J. Geophys. Res.*, *98*(A6), 9503–9514.

Hobara, Y., F. Lefeuvre, M. Parrot, and O. A. Molchanov (2005), Low-latitude ionospheric turbulence observed by Aureol-3 satellite, *Ann. Geophys.*, *23*, 1259–1270.

Larkina, V. I., V. V. Migulin, O. A. Molchanov, I. P. Kharkov, A. S. Inchin, and V. B. Schvetcova (1989), Some statistical results on very low frequency radiowave emissions in the upper ionosphere over earthquake zones, *Phys. Earth Planet. Int.*, *57*, 100–109.

Milne, J. (1890), Earthquakes in connection with electric and magnetic phenomena, *Trans. Seismol. Soc. Jpn.*, *5*, 135.

Molchanov, O. A., and M. Hayakawa (1998), On the generation mechanism of ULF seismogenic electromagnetic emissions, *Phys. Earth Planet. Int.*, *105*, 201–210.

Molchanov, O. A., O. A. Mazhaeva, A. N. Goliavin, and M. Hayakawa (1993), Observation by the Intercosmos-24 satellite of ELF-VLF electromagnetic emissions associated with earthquakes, *Ann. Geophys.*, *11*, 431–440.

Molchanov, O. A., M. Hayakawa, and V. A. Rafalsky (1995), Penetration characteristics of electromagnetic emissions from an underground seismic source into the atmosphere, ionosphere, and magnetosphere, *J. Geophys. Res.*, *100*(A2), 1691–1712.

Molchanov, O. A., A. Kulchitsky, and M. Hayakawa (2001), Inductive seismo-electromagnetic effect in relation to seismogenic ULF emission, *Nat. Hazards Earth Syst. Sci.*, *1*, 61–67.

Molchanov, O., et al. (2006), Global diagnostics of the ionospheric perturbations related to the seismic activity using the VLF radio signals collected on the DEMETER satellite, *Nat. Hazards Earth Syst. Sci.*, *6*, 745–753.

Němec, F., O. Santolík, M. Parrot, and J. J. Berthelier (2008), Spacecraft observations of electromagnetic perturbations connected with seismic activity, *Geophys. Res. Lett.*, *35*, L05109, doi:10.1029/2007GL032517.

Parrot, M. (1994), Statistical study of ELF/VLF emissions recorded by a low-altitude satellite during seismic events, *J. Geophys. Res.*, *99*(A12), 23,339–23,347.

Parrot, M. (1995), Electromagnetic noise due to earthquakes, in *Handbook of Atmospheric Electrodynamics*, vol. 2, chap. 4, edited by H. Volland, pp. 95–116, CRC Press, Boca Raton, Fla.

Parrot, M. (Ed.) (2006), *First Results of the DEMETER Micro-Satellite*, vol. 54, pp. 411–558, Special Issue of Planet. Space Sci., Elsevier, New York.

Parrot, M., and M. M. Mogilevsky (1989), VLF emissions associated with earthquakes and observed in the ionosphere and the magnetosphere, *Phys. Earth Planet. Int.*, *57*, 86–99.

Pulinets, S. A., and K. A. Boyarchuk (2004), *Ionospheric Precursors of Earthquakes*, 1st ed., Springer, New York.

Pulinets, S. A., A. D. Legen'ka, T. V. Gaivoronskaya, and V. K. Depuev (2003), Main phenomenological features of ionospheric precursors of strong earthquakes, *J. Atmos. Sol.-Terr. Phys.*, *65*, 1337–1347.

Rodger, C. J., N. R. Thomson, and R. L. Dowden (1996), A search for ELF/VLF activity associated with earthquakes using ISIS satellite data, *J. Geophys. Res.*, *101*(A6), 13,369–13,378.

Sheskin, D. J. (2000), *Handbook of Parametric and Nonparametric Statistical Procedures*, 2nd ed., CRC Press, Boca Raton, Fla.

Sorokin, V. M., V. M. Chmyrev, and A. K. Yaschenko (2001), Electrodynamic model of the lower atmosphere and the ionosphere coupling, *J. Atmos. Sol.-Terr. Phys.*, *63*, 1681–1691.

Tate, J., and W. Daily (1989), Evidence of electro-seismic phenomena, *Phys. Earth Planet. Int.*, *57*, 1–10.

F. Němec and M. Parrot, Laboratoire de Physique et Chimie de l'Environnement et de l'Espace, CNRS, 3A Avenue de la Recherche Scientifique, F-45071 Orléans Cedex 2, France. (frantisek.nemec@gmail.com)

O. Santolík, Institute of Atmospheric Physics, Academy of Sciences of the Czech Republic, Bocni II 1401, 141 31 Prague 4, Czech Republic.

JOURNAL OF GEOPHYSICAL RESEARCH, VOL. 114, A05203, doi:10.1029/2008JA014016, 2009

Survey of magnetospheric line radiation events observed by the DEMETER spacecraft

F. Němec,[1,2,3] M. Parrot,[1] O. Santolík,[3,2] C. J. Rodger,[4] M. J. Rycroft,[5] M. Hayosh,[3] D. Shklyar,[6] and A. Demekhov[7]

Received 23 December 2008; revised 18 February 2009; accepted 2 March 2009; published 7 May 2009.

[1] Magnetospheric line radiation (MLR) events are electromagnetic waves in the frequency range between about 1 and 8 kHz that, when presented as a frequency-time spectrogram, take the form of nearly parallel and clearly defined lines, which sometimes drift slightly in frequency. They have been observed both by satellites and ground-based instruments, but their origin is still unclear. We present a survey of these MLR waves observed by the DEMETER spacecraft (at an altitude of about 700 km). Three years of VLF Survey mode data were manually searched for MLR events, creating the largest event satellite database of about 650 events, which was then used to investigate the wave properties and geographical occurrence. Finally, the most favorable geomagnetic conditions (Kp and Dst indices) for the occurrence of MLR events have been found. It is shown that MLR events occur mostly at $L > 2$ (upper limit is given by a limitation of the spacecraft), they occur primarily inside the plasmasphere, and there is a lower number of events occurring over the Atlantic Ocean than elsewhere on the globe. The MLR events occur more often during the day and usually during, or after, periods of higher magnetic activity. Their frequencies usually lay between about 2 and 6 kHz, with the total frequency bandwidth of an observation being below 2 kHz in the majority of cases. Moreover, it is shown that the longitudinal dimensions of the MLR events can be as large as 100° and they can last for up to a few hours. Finally, we discuss a possibility that MLR events may be triggered by power line harmonic radiation (PLHR) and we report an event supporting this hypothesis.

Citation: Němec, F., M. Parrot, O. Santolík, C. J. Rodger, M. J. Rycroft, M. Hayosh, D. Shklyar, and A. Demekhov (2009), Survey of magnetospheric line radiation events observed by the DEMETER spacecraft, *J. Geophys. Res.*, *114*, A05203, doi:10.1029/2008JA014016.

1. Introduction

[2] When represented in the form of frequency-time spectrograms, electromagnetic waves observed in the magnetosphere sometimes consist of several clear lines, nearly equidistant in frequency and with a rather slow frequency drift. Such emissions are usually called Magnetospheric Line Radiation (MLR). They have been reported both in ground observations [e.g., *Rodger et al.*, 1999, 2000; *Manninen*, 2005] and low-altitude satellite data [e.g., *Bell et al.*, 1982; *Rodger et al.*, 1995; *Parrot et al.*, 2005; *Němec et al.*, 2007a]. However, their origin is still unknown.

[3] A careful analysis of satellite observations of such events with a line structure [*Němec et al.*, 2007a] showed it was possible to distinguish clearly a class of events called Power Line Harmonic Radiation (PLHR). These events are believed to be generated by electric power systems on the ground and are quite well understood [*Němec et al.*, 2006, 2007b, 2008]. They can be distinguished from MLR events by their frequency spacings corresponding exactly to 50 or 60 Hz and by very small line bandwidth (less than 3 Hz in the majority of cases, as reported by *Němec et al.* [2008]).

[4] *Parrot et al.* [2007] reported a case study of a large-scale MLR event. They used simultaneous observations on the ground and also on board a low altitude satellite to demonstrate the enormous size (area of about 7,400,000 km^2) and time duration (2 hours) of the event. Finally, they hypothesized that the MLR are due to PLHR propagating in the ionosphere and the magnetosphere and undergoing a nonlinear wave-particle interaction in the equatorial plane.

[5] Similarly, *Bullough* [1995] discussed the possibility that MLR originates as PLHR. This concept was further investigated by *Nunn et al.* [1999] using numerical simulations.

[1] Laboratoire de Physique et Chimie de l'Environnement et de l'Espace, Centre National de la Recherche Scientifique, Orléans, France.
[2] Faculty of Mathematics and Physics, Charles University, Prague, Czech Republic.
[3] Institute of Atmospheric Physics, Academy of Sciences of the Czech Republic, Prague, Czech Republic.
[4] Department of Physics, University of Otago, Dunedin, New Zealand.
[5] CAESAR Consultancy, Cambridge, UK.
[6] Space Research Institute (IKI), Russian Academy of Sciences, Moscow, Russia.
[7] Institute of Applied Physics, Russian Academy of Sciences, Nizhny Novgorod, Russia.

0148-0227/09/2008JA014016$09.00

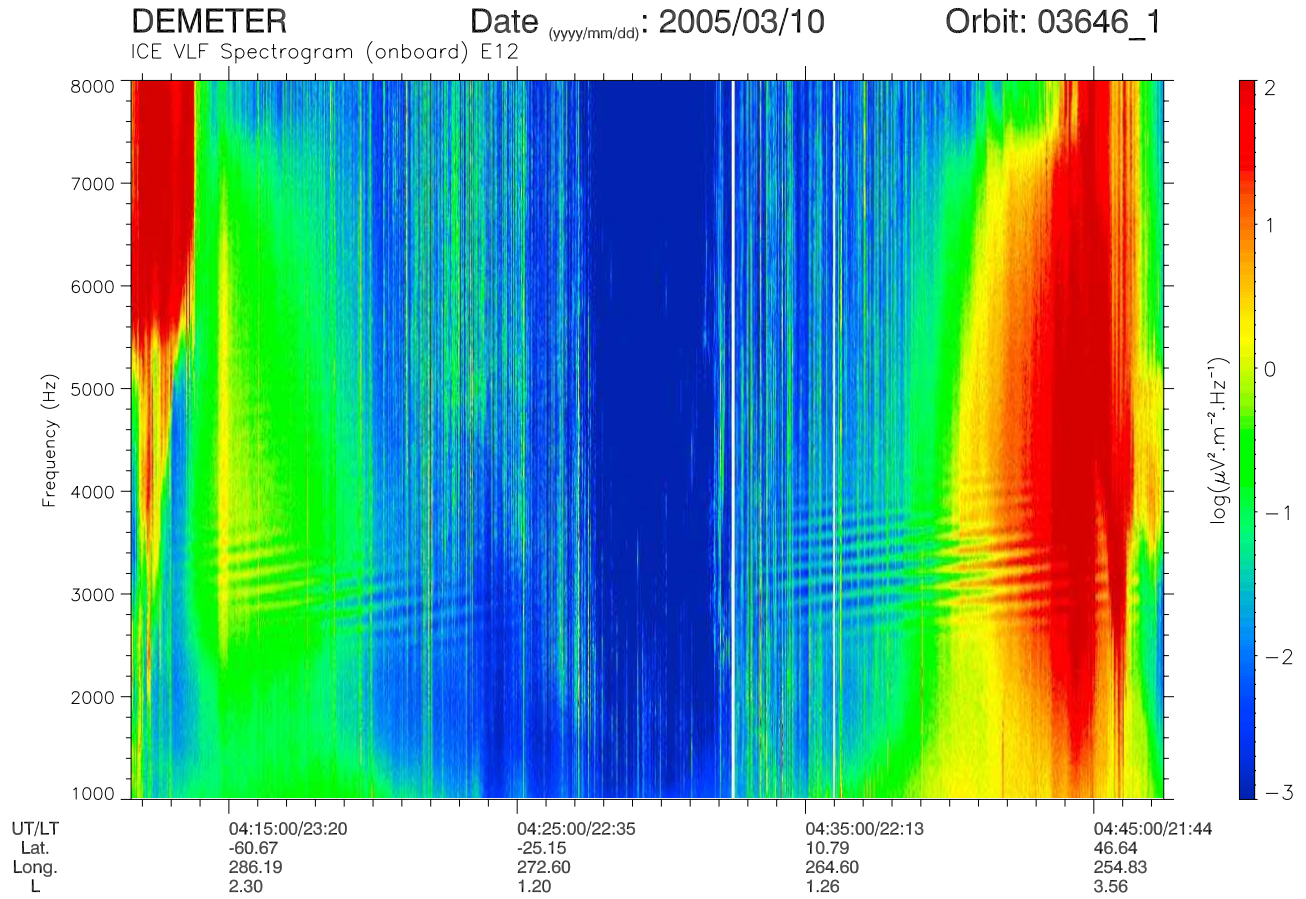

Figure 1. An example of a frequency-time spectrogram of a single half-orbit used for the identification of MLR events. Two MLR events at frequencies between about 2.5 and 4 kHz can be clearly seen, located in magnetically conjugate regions.

[6] In this paper we report upon a survey of 657 MLR events observed by the DEMETER spacecraft, their properties and occurrence. Section 2 describes the DEMETER spacecraft and the wave experiment on board as well as the method of identification of the events. The statistical results obtained are presented in section 3. Section 4 reports an observation of MLR and PLHR events during the same half-orbit. The results are discussed in section 5 and summarized in section 6.

2. Data Set and Processing

[7] Data from the DEMETER spacecraft have been used in the present study. DEMETER is a French microsatellite launched in late June 2004 into a nearly circular orbit with an altitude of 710 km [*Parrot*, 2006]. The altitude of the orbit was decreased to 660 km in December 2005. Due to the sunsynchronous orbit DEMETER always records data either around the time of the local day (10:30 LT) or local night (22:30 LT), and for all geomagnetic latitudes lower than 65 degrees. Among several instruments placed on board (electric and magnetic field measurements, plasma analyzer, energetic charged particle detector and Langmuir probe), we have focused only on the analysis of VLF (frequencies lower than 20 kHz) electric field data [*Berthelier et al.*, 2006]. The satellite's normal Survey mode, which is the most common operational state, provides us with power spectrum of one electric field component computed onboard. The frequency resolution is 19.53 Hz and time resolution is 2 s or 0.5 s, depending on the configuration of the instrument. In the Burst mode of the satellite, which is active only above some specific geographic areas, the electric field instrument provides us with a waveform of one electric field component (sampling frequency 40 kHz). The Burst mode is very useful, because it allows us to perform a detailed analysis. However, for a systematic survey of MLR events we are forced to use the Survey mode, because it is used around all the orbit (below 65 degrees geomagnetic latitude) and its occurrence is not limited to any specific areas.

[8] An example of a frequency-time spectrogram of the power spectral density of electric field fluctuations corresponding to an MLR event is shown in Figure 1. Two MLR events can be clearly seen at frequencies between about 2.5 and 4 kHz. MLR is first observed at around an L of 2.6 in the southern hemisphere, continues to be visible as the spacecraft moves equatorward to L = 1.2, and reappears in the northern conjugate hemisphere at an L of about 1.2. Given that the MLR event is seen in both hemispheres at conjugate locations which are only separated by a small amount in longitude and time, we assume that these two MLR events are due to the same source.

[9] We have analyzed the first 3 years of DEMETER data (up to the end of July, 2007), which represents 26036 half-orbits (each DEMETER orbit consists of two half-orbits:

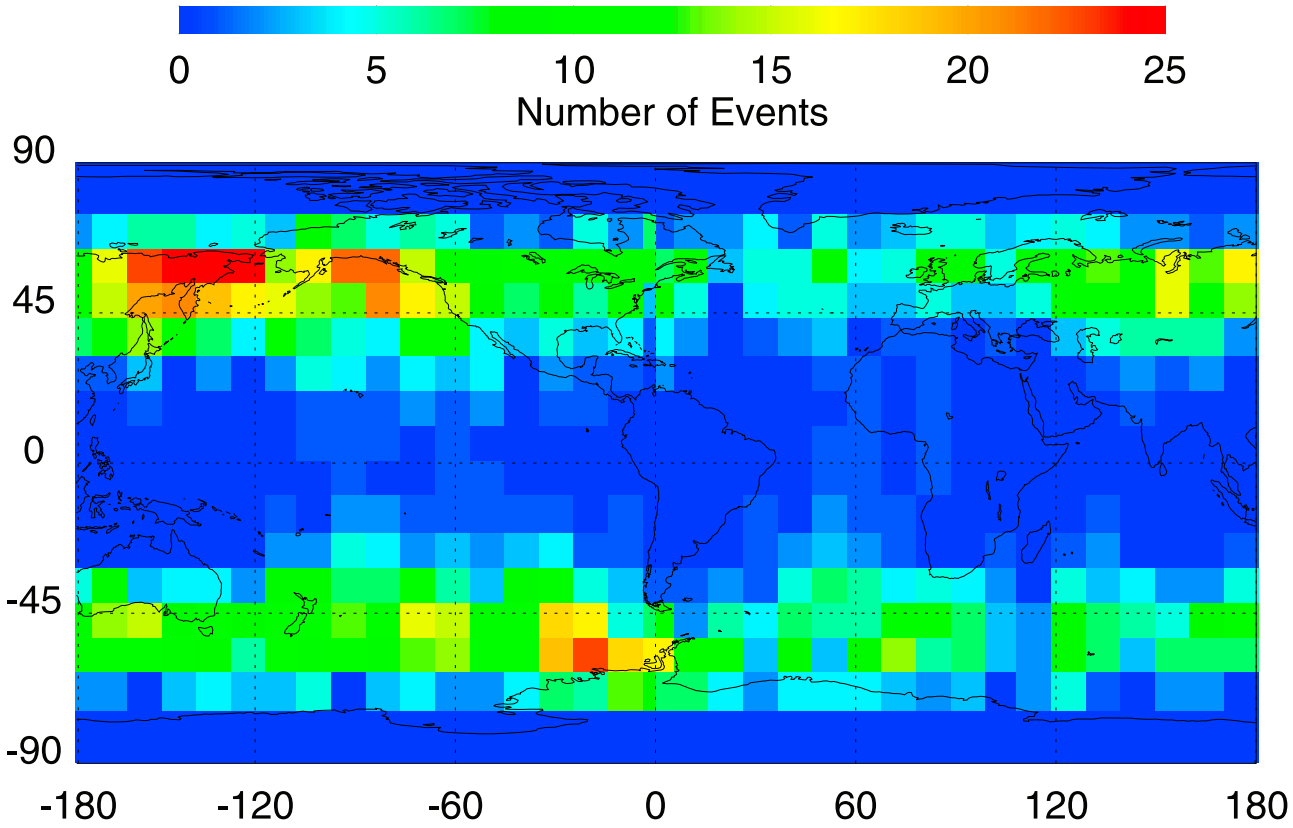

Figure 2. Map of occurrence of MLR events in geomagnetic coordinates. Shown color coded is the number of events observed in a given latitudinal-longitudinal bin.

"down" or "0" that occurs in the local day and during which the satellite moves approximately from North to South and "up" or "1" that occurs in the local night and during which the satellite moves approximately from South to North). For each of the half-orbits, we have manually checked for the presence of MLR events. In order to do so, frequency-time spectrograms similar to the one from Figure 1 were prepared and visually inspected. The plotted frequency range spans from 1 to 8 kHz and the time covers all the half-orbit (approximately 35 minutes). The color scale used ranged between -3 and 2 log (μV^2 m^{-2} Hz^{-1}) (i.e., minimum to maximum values) and was the same for all the plotted spectrograms. For each of the identified MLR events, we recorded its frequency-time interval (frequency resolution 200 Hz, time resolution 1 minute). MLR events have been found in 549 half-orbits (out of the 26036 analyzed). Altogether, we have identified 657 MLR events. The reason why the total number of identified MLR events is larger than the number of half-orbits containing these events is that there can be two MLR events per one half-orbit, located in the conjugate regions (see section 5 for a more detailed discussion). An example of this situation was shown in Figure 1.

3. Statistical Results

[10] Our large database of the MLR events enabled us to analyze in detail their occurrence and properties. Our main interest was to answer the following questions: Where do the MLR events occur? When do they occur (or, in other words, what are the most favorable conditions for them to occur)? What are their properties?

3.1. Where Do the MLR Events Occur?

[11] We have constructed an occurrence map of the MLR events (Figure 2), which represents positions of all the observed MLR events in geomagnetic dipole coordinates. The latitudinal resolution used was 10 degrees, being the same as the used longitudinal resolution. The reason for using geomagnetic coordinates is that MLR events might propagate along geomagnetic field lines into the opposite hemisphere. Geomagnetic coordinates allow a simple check to be made that the regions are conjugate: they are located at the same geomagnetic longitudes and their geomagnetic latitudes have opposite signs. The lack of events at large geomagnetic latitudes is caused by the fact that DEMETER does not operate at geomagnetic latitudes larger than 65 degrees (see section 2). It is evident that MLR events occur primarily at larger geomagnetic latitudes and that they occur at all geomagnetic longitudes. However, the number of MLR events occurring over the Atlantic Ocean seems to be lower than the number of events that occur at other geomagnetic longitudes. One can also observe some additional features in Figure 2. For example, there are the peaks in MLR occurrence over Alaska and the Eastern part of Russia. Moreover, there is a peak of MLR occurrence over the region of Antarctica which is the geomagnetic conjugate to North America, but no noticeable increase in MLR occurrence is observed above North America itself. This MLR occurrence is discussed in section 5.

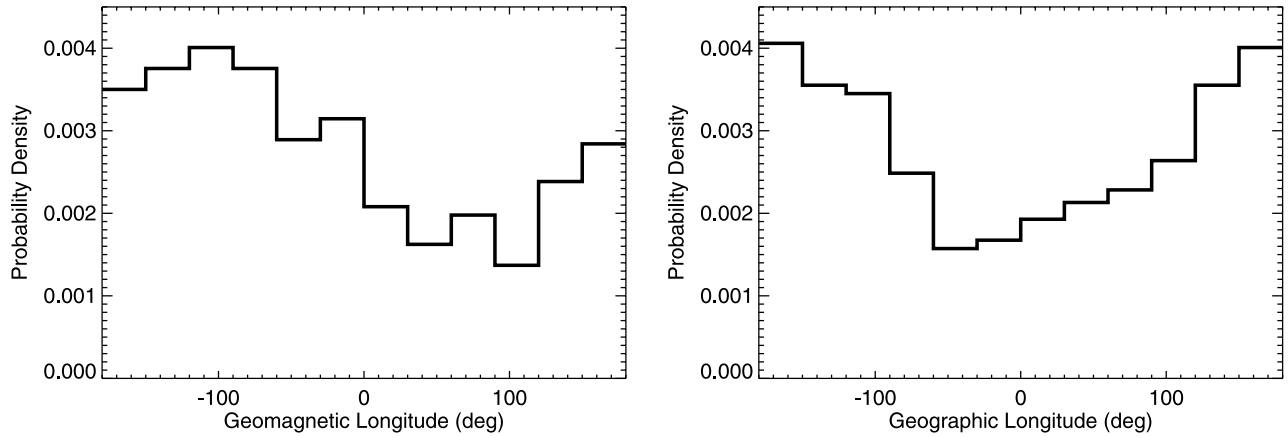

Figure 3. (left) Probability density of occurrence of MLR events as a function of geomagnetic longitude. (right) Probability density of occurrence of MLR events as a function of geographic longitude.

[12] Figure 3 enables us to study the effect of lower number of MLR events observed over the Atlantic Ocean in more detail; in the left panel it shows the probability density of occurrence of MLR events as a function of geomagnetic longitude. The probability of occurrence at geomagnetic longitudes of 0–100 degrees is almost half its value at other geomagnetic longitudes. In the right panel the probability density of occurrence of MLR events as a function of geographic longitude is depicted.

[13] Figure 4 shows the range of L shells at which the MLR events are observed. The left part of Figure 4 represents the probability density of occurrence of MLR events as a function of L shell; it shows that most of the events are observed at L values between 2 and 5. This plot was constructed in such a way that for each of the MLR events a counter was increased in all the L value bins that correspond to the range of L values of the event. The right part of the Figure 4 represents a histogram of the extent of MLR events expressed in L shells. It is clear that most of the MLR events have L extent between about 1 and 3 R_E. The L values were calculated using both the internal and external magnetic field models (N. A. Tsyganenko, http://nssdcftp.gsfc.nasa.gov/models/magnetospheric/tsyganenko).

[14] Further, we have checked whether the L shells where MLR events are observed correspond to the locations inside or outside the plasmasphere. Figure 5 shows the L shells of MLR events as a function of the model location of the plasmapause taking into account the geomagnetic activity [*Moldwin et al.*, 2002] at the time of the observation. The central L shells of the MLR events are plotted as dots and their L extents are marked by the vertical lines. Moreover, the mean values of the central L shells of the MLR events for each interval of the model location of the plasmapause are overplotted by a thick red line. Six intervals of the model L values have been chosen, spanning from L values of 2.5 up to 5.5. It can be seen that the MLR events occur inside the plasmasphere (bottom right part of Figure 5, below the thick diagonal line). Some of them seem to reach beyond, but this could be well explained by the inaccuracies of the model of the plasmapause location, as it is discussed in section 5.

3.2. When Do MLR Events Occur?

[15] Further, we have analyzed when the MLR events occur or, in other words, what are the most favored natural conditions for their occurrence. We have checked whether

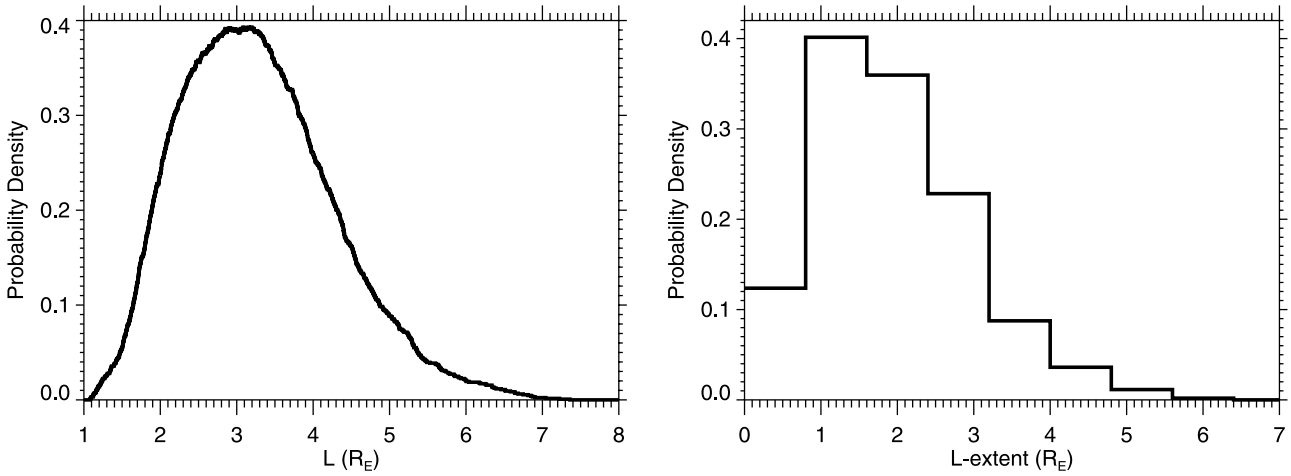

Figure 4. (left) Probability density of occurrence of MLR events as a function of L shell. (right) L extent of the observed MLR events.

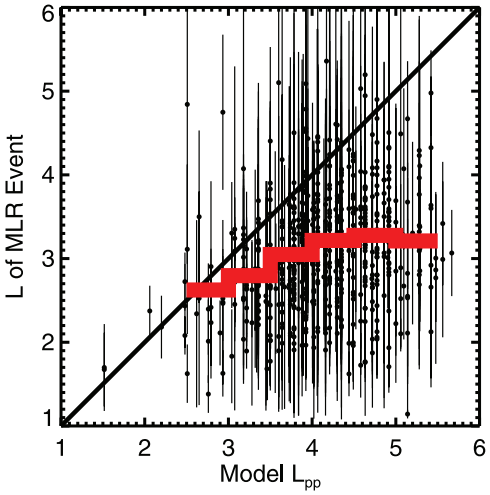

Figure 5. Central L shells of the MLR events (dots) as a function of model location of the plasmapause. Mean values of central L shells of the MLR events (thick red line) and L extents of the MLR events (vertical lines).

there is a difference in their occurrence rate between daytime and nighttime (due to the specific orbit of the DEMETER spacecraft, there are just these two possibilities, see section 2 for more details). It turns out that among the 657 observed events, 390 events occurred during the day and 267 events occurred during the night. Among the 549 half-orbits containing MLR events, 321 were daytime half-orbits and 228 were nighttime half-orbits. Therefore the MLR events seem to occur more frequently during the day than during the night. We can evaluate the statistical significance of this difference simply by using a binomial distribution. If the probability that an MLR event occurs during the day were the same as the probability that an MLR event occurs during the night, the mean number of events occurring during the day $\overline{N_d}$ would be equal to the mean number of events occurring during the night $\overline{N_n}$:

$$\overline{N_d} = \overline{N_n} = p\,N_{total} = 328.5 \tag{1}$$

where $N_{total} = 657$ is the total number of the observed MLR events and $p = 0.5$ is the probability that an MLR event occurs during the day/night supposing it is the same for the two. The appropriate standard deviation can be calculated as follows,

$$\sigma = \sqrt{p\,(1-p)\,N_{total}} \approx 12.8. \tag{2}$$

The difference between the number of events that occur during the day and the number of events that occur during the night therefore corresponds to about 4.8 standard deviations. If we perform the same calculation for the number of half-orbits containing MLR events, we find out that the difference corresponds to about 4.0 standard deviations. As such the preference for daytime MLR events appears highly statistically significant.

[16] It is of a great importance to investigate whether the geomagnetic conditions during the occurrence of MLR events differ from the normal ones or not. We have therefore used the superposed epoch analysis in order to find out what is the dependence of the value of Kp index on the time relative to the time of the MLR events. The time resolution used for the analysis was set to one hour. The results are shown in Figure 6. The left panel represents the dependence obtained for the mean value of Kp index while the right panel represents the same dependence obtained for its median value. Moreover, there is a standard deviation of the mean value σ_M marked by thin lines in the left panel. This is calculated as

$$\sigma_M = \frac{\sigma}{\sqrt{N}}, \tag{3}$$

where σ is the standard deviation of the distribution of Kp values and N is the number of averaged values. It can be seen that there is a statistically significant increase of Kp index a few days before the time of the MLR events. However, the absolute value of the increase is rather low, less than the standard deviation σ, and it becomes statistically significant only due to the large number of analyzed events (see section 5).

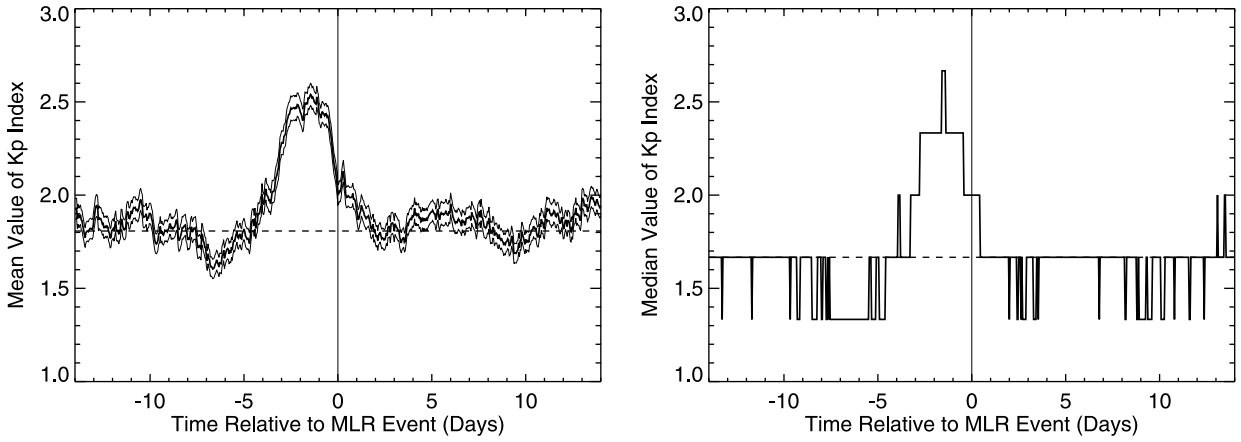

Figure 6. (left) Mean value of Kp index (bold) as a function of the time relative to the time of MLR events and standard deviation of the mean value (thin). (right) Median value of Kp index as a function of the time relative to the time of the MLR events.

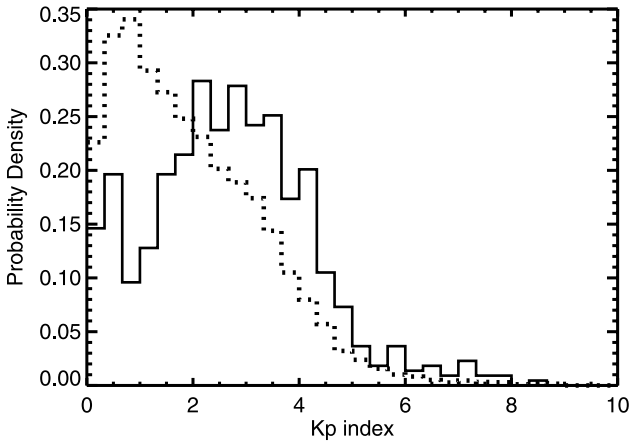

Figure 7. (solid) Histogram of Kp indices at the time of the maximum difference from the normal values obtained by the superposed epoch analysis. (dotted) Histogram of Kp indices during all the analyzed 3 years.

[17] Figure 7 shows by a bold solid line a histogram of Kp indices at the time of the maximum difference from the normal values obtained by the superposed epoch analysis (35 hours before the time of MLR events, mean value of Kp 2.5). For a comparison, a histogram of Kp indices that occurred during all the analyzed period of 3 years is plotted by a thin dotted line. It can be seen that the histogram of Kp indices shortly before the MLR occurrence is slightly shifted toward the larger values.

[18] Figures 8 and 9 represent the same dependence as Figures 6 and 7, but this time for Dst indices. From Figure 9, it can be seen that the distribution of Dst is shifted slightly toward lower values (17 hours before the time of MLR events, mean value of Dst −23.7). This is further confirmed by Figure 8 which shows that there is a decrease of the Dst index for a few days before the time of occurrence of the MLR events. Similarly to Figure 6, the decrease of the mean Dst value is statistically significant, but its absolute value is lower than the standard deviation of the distribution of Dst indices (again, see a detailed discussion in section 5).

3.3. What Are the Properties of MLR Events?

[19] The frequencies of observed MLR events are plotted in the left panel of Figure 10. Similarly to the left panel of Figure 4, this plot was constructed in such a way that for each of the MLR events we have increased a counter in all the bins in the range of frequencies corresponding to this event. Most of the events occurred at frequencies between 2 and 6 kHz. The frequency bandwidth of the events, shown in the right panel of Figure 10, is less than 2 kHz in most of the cases.

[20] Checking the number of consecutive half-orbits that contain MLR events enables us to obtain a lower estimate of their longitudinal dimensions, as well as a lower estimate of their time duration (see section 5). The results are plotted in Figure 11. Individual bins of the histogram correspond to the 1, 2, 3, 4 and 5 consecutive half-orbits of the same direction (up or down) containing MLR events, respectively. On the lower x axis, these are converted directly to the longitudinal dimension, in degrees, while on the upper x axis these are converted directly to the time duration, in hours. It can be seen that the longitudinal dimensions may be rather large, up to about 100 degrees, and that the events can last for a few hours.

4. Is an MLR Event Triggered by PLHR?

[21] In this section we report on a special kind of event, which consists of the observation of an MLR event and Power Line Harmonic Radiation (PLHR) during the same half-orbit, in conjugate hemispheres. The natural question therefore arises: does this represent a case of an MLR event triggered by PLHR? (See a more detailed discussion in section 5). Figure 12 represents a frequency-time spectrogram of all the entire half-orbit. The PLHR event occurred in the northern hemisphere and was observed approximately between 08:01:30 UT and 08:04:30 UT at frequencies between 2800 and 3600 Hz. The MLR event occurred in the conjugate region and was observed approximately between 08:31:00 UT and 08:36:00 UT at frequencies between 3200 and 4000 Hz. The MLR event was significantly more intense than PLHR event, which is in a good agreement with the statistical results reported by *Němec et al.* [2007a].

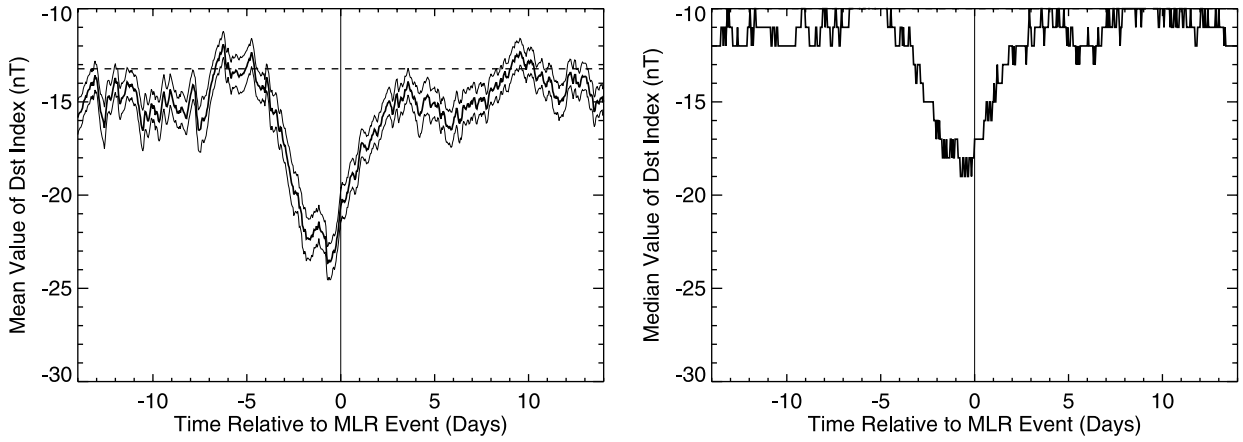

Figure 8. (left) Mean value of Dst index as a function of time relative to the time of the MLR event (bold) and standard deviation of the mean value (thin). (right) Median value of Dst index as a function of time relative to the time of the MLR event.

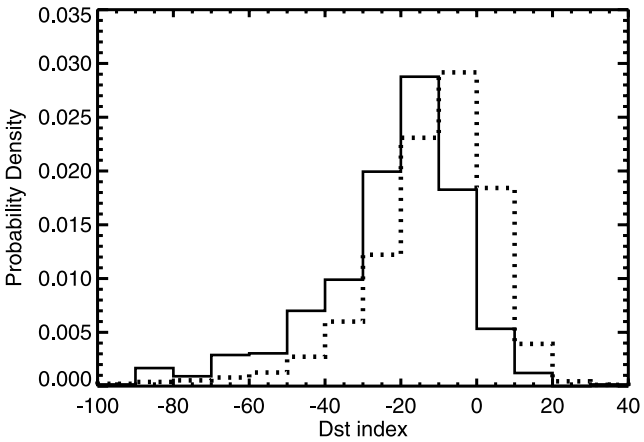

Figure 9. (solid) Histogram of Dst indices at the time of the maximum difference from the normal values obtained by the superposed epoch analysis. (dotted) Histogram of Dst indices during all the analyzed 3 years.

[22] The left panel of Figure 13 shows a detailed frequency-time spectrogram of the PLHR event from Figure 12. A set of horizontal lines can be clearly identified. Moreover, DEMETER was in the Burst mode during the observation, which allows us to construct a detailed power spectrum. This is shown in the right panel of Figure 13. Several peaks corresponding to the PLHR lines can be seen. They occur at frequencies of: 2950 Hz, 3000 Hz, 3050 Hz, 3150 Hz, 3250 Hz, 3350 Hz, 3450 Hz, 3550 Hz and 3650 Hz, which corresponds to the exact multiples of the fundamental frequency of the electrical power system of 50 Hz (within 1 Hz uncertainty). This well agrees with *Němec et al.* [2006, 2007b], because the PLHR event was observed above Russia, where the frequency of the power grid systems is 50 Hz.

[23] A detailed frequency-time spectrogram of the MLR event from Figure 12 is shown in Figure 14. A set of nearly horizontal thick lines covered by a noisy emission can be seen. The event seems to start at higher frequencies and moves toward the lower frequencies later (closer to the southern auroral zone).

[24] The idea that an MLR event can be triggered by PLHR is rather old [*Bullough*, 1995; *Nunn et al.*, 1999], but up to now it has lacked a direct experimental verification. This is why the unique measurement shown in Figures 12, 13 and 14 of an MLR event and a PLHR event that occurred during the same half-orbit is important. Located in conjugate regions, the PLHR event was detected first. Although it does not provide definite proof that MLR events are triggered by PLHR, it is rather clear that, at least for this particular event, the two phenomena are connected. Moreover, because the origin of PLHR is quite well understood [*Němec et al.*, 2006, 2007b, 2008], it is reasonable to suppose that it is the MLR event which is affected by the PLHR event, and not vice versa.

5. Discussion

[25] A crucial factor when performing a systematic surveys like that presented here is the method of constructing the database of events. There are two basic possibilities for how to identify interesting events in large data sets. The first of them is to develop an automatic procedure for their identification using some precisely given criteria. The second possibility is to perform a visual inspection and a manual identification of the events. We have chosen the second method for the two reasons: (1) MLR events are quite difficult phenomena to describe and quantify precisely, which makes the development of an automatic procedure very difficult, and (2) an automatic procedure, even if developed, is unlikely to work as well as a trained human eye and mind, and would therefore miss many of the events. The performed manual identification of the events is, in this sense, ideal; however, it is based on the "individual feeling" of the observer and cannot be precisely quantified. This problem was at least partly solved by inspecting the data twice, independently, which we believe practically excludes any false identifications. Further, a constant color scale of the power spectral density spanning from -3 to 2 log (μV^2 m^{-2} Hz^{-1}) has been used in order be consistent all over the analyzed data set. The checked frequency range was also the same for all the half-orbits, spanning from 1 to 8 kHz. Had any events that had occurred outside this frequency range, they would have remained undetected. Although we do not completely

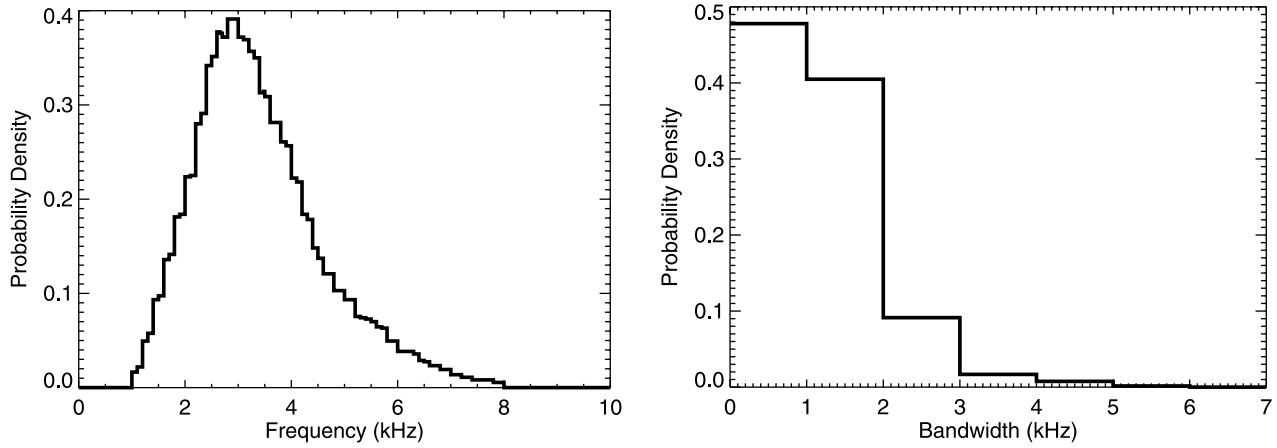

Figure 10. (left) Frequency range of the observed MLR events. (right) Frequency bandwidth of the observed MLR events.

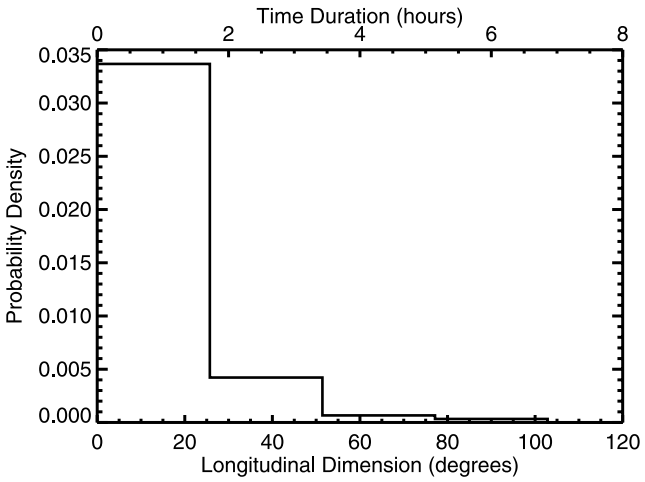

Figure 11. Lower estimate of longitudinal dimension of the observed MLR events (bottom x axis), and lower estimate of time duration of the observed MLR events (upper x axis).

exclude the possibility that some MLR events might occur at lower/larger frequencies, the left panel of Figure 10 strongly suggests that, if there are any such events, there are only few of them.

[26] MLR events have been identified in 549 half-orbits among 26036 analyzed. Their occurrence rate is therefore only a bit larger than 2%, meaning that MLR events are not a common phenomenon. There can be two MLR events occurring during a single half-orbit (located in the conjugate regions), resulting into the total number of identified MLR events being equal to 657. Although MLR events are believed to propagate along geomagnetic field lines, bouncing back and forth between the hemispheres, among the 549 half-orbits with MLR events there were only 108 half-orbits with MLR events occurring in the both hemispheres. This has two different explanations, acting simultaneously: (1) DEMETER does not encounter the conjugate points of exactly the same magnetic field line, so that it may miss one MLR event, or (2) at the time when DEMETER is in the conjugate region, the MLR event has already stopped.

[27] The three years of the data analyzed represent a sufficiently large data set required to perform a systematic survey. While there is a limitation due to the technical operation of the DEMETER spacecraft, namely that it does not make observations at geomagnetic latitudes larger than 65 degrees, we can see from Figure 2 and Figure 4 that the MLR events detected are not very much affected by this limitation, because the number of MLR events seems to be decreasing rapidly at larger geomagnetic latitudes.

[28] The results from Figures 2 and 3 show that there is a lower number of MLR events occurring at geomagnetic longitudes corresponding to the Atlantic Ocean. We propose two possible explanations for this effect. The first is that, in the drift loss cone, East of the South Atlantic geomagnetic anomaly, there are insufficient energetic electrons needed to generate the MLR events. In order to support this hypothesis, we can compare the probability density of occurrence of MLR events as a function of geographic longitude shown in the right panel of Figure 3 with electron fluxes as a function of geographic longitude obtained by *Asikainen and Mursula* [2008]. It can be seen that, going from the West, the MLR occurrence starts to decrease at about −90 degrees of geographic longitude. This corresponds well to the area of increasing precipitating electron flux. The MLR occurrence

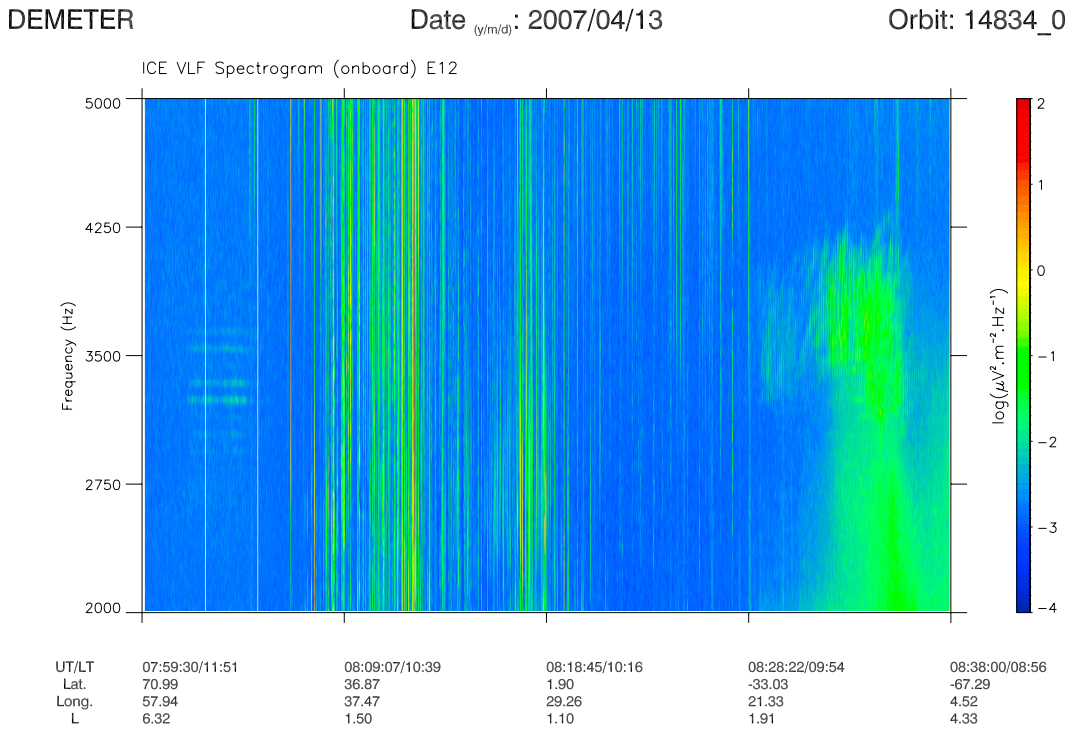

Figure 12. Frequency-time spectrogram of a half-orbit containing a PLHR event and an MLR event in geomagnetically conjugate regions.

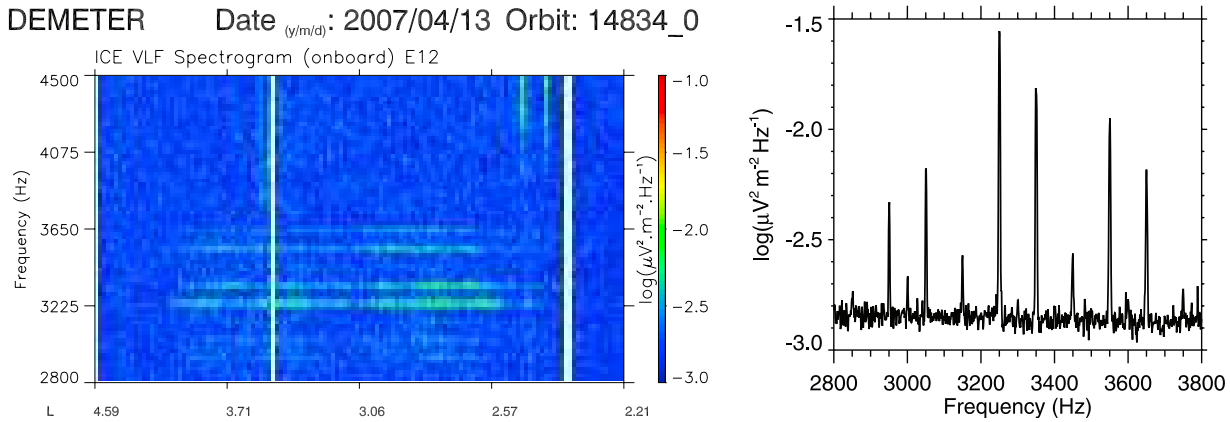

Figure 13. (left) Detailed frequency-time spectrogram of the PLHR event from Figure 12. (right) Power spectrum corresponding to the PLHR event from the left part.

reaches its minimum between −60 and 0 degrees of geographic longitude, corresponding to the peak precipitating electron flux. Afterward, it slowly increases up to about 120 degrees of geographic longitude, meaning that the occurrence of MLR events seems to be affected by the South Atlantic Anomaly much further to the East than the precipitating electron flux region. This could be caused by the fact that even after the massive precipitation of electrons stopped, it takes some time to fill-up the slot region again. The second explanation is that at the geomagnetic longitudes of the Atlantic Ocean there are no industrialized areas. Supposing that the generation of MLR events needs a trigger in the form, for instance, of PLHR, the absence of PLHR at these longitudes would explain also the absence of MLR events. It is even possible that both explanations are valid and act together. However, since the area with the lower occurrence rate of MLR events extends well into the geomagnetic longitudes of Europe, the first explanation seems to be the more probable.

[29] The main purpose of Figure 4 was to demonstrate the enormous range of L shells which can be affected by MLR emissions. Moreover, the typical range of an individual MLR event is rather large, usually about 2 L shells, but occasionally spanning up to more than 5 L shells. This clearly indicates that, during the time of their existence, MLR events could affect a huge volume of space in the inner magnetosphere.

[30] Figure 5 shows the position of MLR events with respect to the plasmapause. Because no direct measurements are available, we have used the empirical model of *Moldwin et al.* [2002], with two parameters (Kp, MLT), based on data from the CRRES spacecraft. The model is based on the linear best fit to the satellite data. Thus it expresses the average plasmapause location, but in an individual case it can significantly underestimate (or overestimate) the real location ($\sigma_{Lpp} \approx 0.5$ according to *Moldwin et al.* [2002]). Because the scatter of MLR events beyond the plasmasphere observed in Figure 5 is smaller than inaccuracies of the model L_{pp}, the

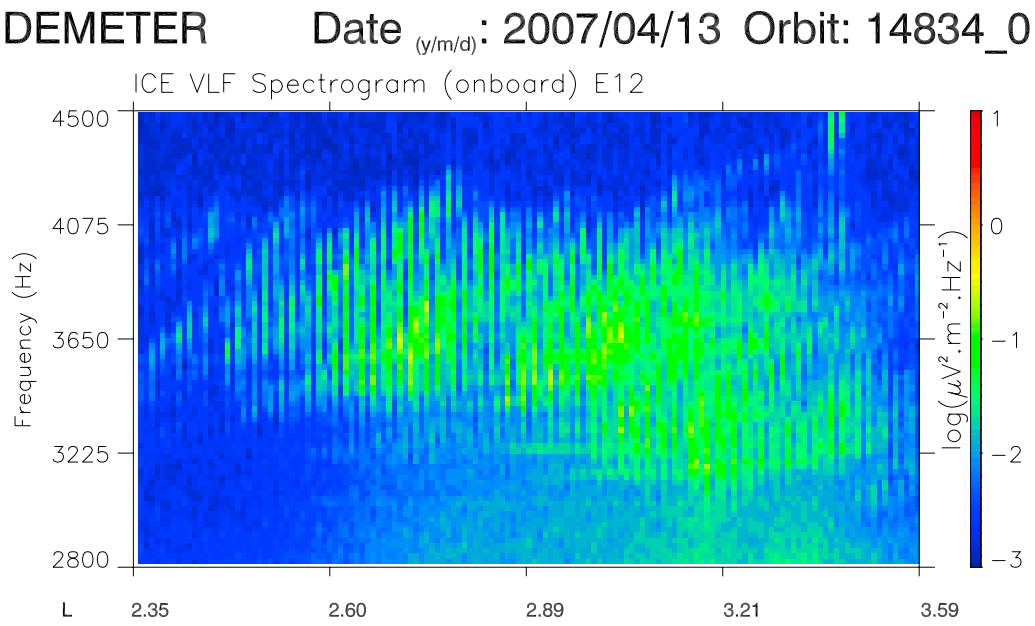

Figure 14. Detailed frequency-time spectrogram of the MLR event from Figure 12.

imperfect agreement is most probably caused solely by the inaccuracies in the used model. Moreover, a detailed examination of the events that reach beyond the model location of the plasmasphere reveals that these occurred during low values of the Kp index, but for which the Kp index was quite large about twelve hours before. Since the model of the plasmapause location takes into account the maximum value of the Kp index in the previous 12 hours, it results in a significantly compressed plasmasphere. However, because the present values of Kp are low and because the large value occurred just at the edge of the time interval taken into account by the model, it is reasonable to suppose that the plasmasphere in such cases is compressed much less than predicted. Consequently, there is no strong evidence that MLR events stretch beyond the plasmasphere; it is more likely they are strictly limited to be within the plasmapause.

[31] Figures 6, 7, 8 and 9 show that MLR events occur preferentially during or after periods of larger geomagnetic activity. Although this change in average values of geomagnetic indices (Kp, Dst) is statistically significant, its absolute value is smaller than typical fluctuations of the indices. The observed increase of Kp index is about 0.7, while the Kp index commonly varies between 0 and 5 (see dotted histogram in Figure 7). The observed decrease of Dst index is about 10 nT, while Dst commonly varies between −50 and 10 nT (see dotted histogram in Figure 9). This means that, although the occurrence of MLR events is clearly linked to the increased geomagnetic activity, this connection has been revealed only by using the superposed epoch analysis of a large number of events. It is statistically significant, but for an individual event the value of Kp/Dst can behave rather differently. The physical explanation of this observed dependence is that energetic electrons are needed in order to generate the MLR events. This result presents an evidence that the phenomenon is the result of a wave-particle interaction, probably taking place at the geomagnetic equator (which is the preferred region for such types of interaction [*Trakhtengerts and Rycroft*, 2008] and, moreover, is well consistent with MLR events often being observed in the conjugate regions).

[32] From the frequency range of MLR events depicted in the left panel of Figure 10 it can be seen that the analyzed frequency band of 1–8 kHz was well chosen: the probability density of occurrence of MLR events at frequencies close to 1 kHz and 8 kHz is close to zero. This means that, although there may be some MLR events occurring outside the frequency band analyzed, there are probably only a few of them. It is interesting to compare this frequency range with the frequency range of PLHR and MLR events reported by *Němec et al.* [2007a]. An automatic identification procedure has been used to identify PLHR events in electric field burst-mode data in the frequency range 0.5–4 kHz [*Němec et al.*, 2006]. This procedure was also able to identify some events that were classified as MLR events. Altogether, 49 PLHR events and 23 MLR-like events were identified in 1650 hours of burst-mode electric field data. It was shown [*Němec et al.*, 2007a] that PLHR events occur at frequencies between about 1 and 4 kHz, being most frequent between 2 and 3 kHz. MLR-like events were reported at all frequencies below 4 kHz, being more frequent at lower frequencies.

[33] The present study shows that the MLR events occur most frequently at frequencies between about 2 and 4 kHz, which are the frequencies well comparable with the typical frequencies of PLHR. Although MLR events seem to extend to higher frequencies than PLHR, this may be caused by the limited frequency range analyzed by *Němec et al.* [2007a].

[34] There is a significant difference between the frequency range of MLR events reported in the present study and the frequency range of MLR-like events reported by *Němec et al.* [2007a]. This can be explained by taking into account the Figure 7 of *Němec et al.* [2007a] which shows two different classes of MLR-like events: (1) events with frequencies below 1 kHz located close to the geomagnetic equator, and (2) events with frequencies well comparable with PLHR events at larger geomagnetic latitudes. Since the present study focuses solely on the frequency band 1–8 kHz, only the events from the second class are identified. The events from the first class, which we believe are naturally generated by instabilities of the ion distribution functions, will be thoroughly discussed in a separate paper.

[35] Figure 11 shows that the longitudinal dimensions of MLR events can reach up to about 100 degrees and that the events can last as long as a few hours. These estimates were determined by evaluating the number of consecutive half-orbits containing the MLR events and so represent a lower estimate of the longitudinal dimensions and time duration. This is due to the fact that there can be two reasons why an MLR event is not observed in the next half-orbit: (1) the MLR event does not extent that far, this is the reason used to find the longitudinal dimensions, or (2) the MLR event does not last long enough to survive until the next DEMETER pass, although it extended far enough during its lifetime, it is not observed, because it had already died at the time of the observation. This reason was used to determine the time duration. Because in reality both these reasons are acting simultaneously, what we obtain is a lower estimate of the longitudinal dimension and the lower estimate of the time duration. There might also occur the situation of two separate MLR events extending not very far in longitude but present at the same time. In such a situation, DEMETER would see one of them during the first pass and the other of them during the second; we would evaluate that situation as an individual MLR event extending over the two half-orbits. However, since MLR events are not so frequent and a special configuration would be required, we can estimate that this possibility is rather unlikely (about 0.04 percent). Finally, we would like to underline once more that the longitudinal and L range of MLR events, as well as their time duration, can be rather large; when present they could therefore represent an important factor in determining the dynamics of the plasmasphere.

6. Conclusions

[36] The results of a systematic study of observations of MLR events by a low-altitude satellite have been presented. Altogether, 657 events in 549 half-orbits have been identified. According to our knowledge, this represents the largest satellite database of MLR events collected to date. Their occurrence and properties have been thoroughly investigated.

[37] Our results show that MLR events occur mostly at $L > 2$ and that they do not occur outside the plasmasphere. There are fewer events at geomagnetic longitudes corresponding to the Atlantic Ocean. Moreover, the MLR events

occur slightly more often during the day than during the night. They usually occur during or after the periods of higher magnetic activity. Most often they are observed at frequencies between 2 and 6 kHz, and their frequency bandwidth is below 2 kHz in the majority of cases. Their longitudinal dimensions can extend up to about 100 degrees and they can last for as long as a few hours. Finally, we have reported the observation of MLR and PLHR events during the same half-orbit. This we have discussed in terms of the possibility that PLHR may serve as a trigger for MLR.

[38] **Acknowledgments.** The work of FN and MP is supported by the Centre National d'Etudes Spatiales. It is based on observations with the electric field experiment ICE carried on DEMETER. The authors thank CNES personnel involved in the mission development of the French DEMETER satellite, those currently in charge of the operations in Toulouse, and J. Y. Brochot of LPCE/CNRS Orléans for his help with data processing. They thank J. J. Berthelier for the use of electric field data. PICS grant 3725 from CNRS/DREI and LAPBIAT 2 program contract RITA-CT-2006-025969 from Sodankylä Geophysical Observatory, Finland.

[39] Amitava Bhattacharjee thanks the reviewers for their assistance in evaluating this paper.

References

Asikainen, T., and K. Mursula (2008), Energetic electron flux behavior at low L-shells and its relation to the south atlantic anomaly, *J. Atmos. Sol.-Terr. Phys.*, *70*, 536, doi:10.1016/j.jastp.2007.08.061.

Bell, T. F., J. P. Luette, and U. S. Inan (1982), ISEE 1 observations of VLF line radiation in the Earth's magnetosphere, *J. Geophys. Res.*, *87*(A5), 3530–3536.

Berthelier, J. J., et al. (2006), ICE, the electric field experiment on DEMETER, *Planet. Space Sci.*, *54*, 456–471.

Bullough, K. (1995), *Handbook of Atmospheric Electrodynamics*, vol. 2, chap. 10, edited by H. Volland, pp. 291–332, CRC Press, Boca Ralton, Fla.

Manninen, J. (2005), *Some Aspects of ELF-VLF Emissions in Geophysical Research*, Publ. 98, chap. 5, edited by J. Kultima, pp. 85–110, Sodankylä Geophys. Obs., Sodankylä, Finland.

Moldwin, M. O., L. Downward, H. K. Rassoul, R. Amin, and R. R. Anderson (2002), A new model of the location of the plasmapause: CRRES results, *J. Geophys. Res.*, *107*(A11), 1339, doi:10.1029/2001JA009211.

Nunn, D., J. Manninen, T. Turunen, V. Trakhtengerts, and N. Erokhin (1999), On the nonlinear triggering of VLF emissions by power line harmonic radiation, *Ann. Geophys.*, *17*, 79–94.

Němec, F., O. Santolík, M. Parrot, and J. J. Berthelier (2006), Power line harmonic radiation (PLHR) observed by the DEMETER spacecraft, *J. Geophys. Res.*, *111*, A04308, doi:10.1029/2005JA011480.

Němec, F., O. Santolík, M. Parrot, and J. J. Berthelier (2007a), Comparison of magnetospheric line radiation and power line harmonic radiation: A systematic survey using the DEMETER spacecraft, *J. Geophys. Res.*, *112*, A04301, doi:10.1029/2006JA012134.

Němec, F., O. Santolík, M. Parrot, and J. J. Berthelier (2007b), Power line harmonic radiation: A systematic study using DEMETER spacecraft, *Adv. Space Res.*, *40*, 398–403.

Němec, F., O. Santolík, M. Parrot, and J. Bortnik (2008), Power line harmonic radiation observed by satellite: Properties and propagation through the ionosphere, *J. Geophys. Res.*, *113*, A08317, doi:10.1029/2008JA013184.

Parrot, M. (Ed.) (2006), *First Results of the DEMETER Micro-Satellite*, vol. 54, pp. 411–558, Special Issue of Planet. Space Sci., Elsevier Ltd.

Parrot, M., F. Němec, O. Santolík, and J. J. Berthelier (2005), ELF magnetospheric lines observed by DEMETER, *Ann. Geophys.*, *23*, 3301–3311.

Parrot, M., J. Manninen, O. Santolik, F. Nemec, T. Turunen, T. Raita, and E. Macusova (2007), Simultaneous observation on board a satellite and on the ground of large-scale magnetospheric line radiation, *Geophys. Res. Lett.*, *34*, L19102, doi:10.1029/2007GL030630.

Rodger, C. J., N. R. Thomson, and R. L. Dowden (1995), VLF line radiation observed by satellite, *J. Geophys. Res.*, *100*(A4), 5681–5689.

Rodger, C. J., M. A. Clilverd, K. H. Yearby, and A. J. Smith (1999), Magnetospheric line radiation observations at Halley, Antarctica, *J. Geophys. Res.*, *104*(A8), 17,441–17,447.

Rodger, C. J., M. A. Clilverd, K. H. Yearby, and A. J. Smith (2000), Temporal properties of magnetospheric line radiation, *J. Geophys. Res.*, *105*(A1), 329–336.

Trakhtengerts, V. Y., and M. J. Rycroft (2008), *Whistler and Alfvén Mode Cyclotron Masers in Space*, 354 pp., Cambridge Univ. Press, Cambridge, U. K.

A. Demekhov, Institute of Applied Physics of the Russian Academy of Sciences 46, Ulyanov Street, 603950, Nizhny Novgorod, Russia.

M. Hayosh, Institute of Atmospheric Physics, ASCR, Bocni II 1401, 14131, Prague 4, Czech Republic.

F. Němec and M. Parrot, LPC2E/CNRS, 3A, Avenue de la Recherche Scientifique, F-45071 Orléans Cedex 2, France. (frantisek.nemec@gmail.com)

C. J. Rodger, Department of Physics, University of Otago, 730 Cumberland Street, Dunedin 9016, New Zealand.

M. J. Rycroft, CAESAR Consultancy, 35 Millington Road, Cambridge CB3 9HW, UK.

O. Santolík, Faculty of Mathematics and Physics, Charles University, V Holesovickach 2, 18000 Prague 8, Czech Republic.

D. Shklyar, Space Research Institute (IKI), RAS, Profsoyuznaya str. 84/32, 117997, Moscow, Russia.

Space Sci Rev
DOI 10.1007/s11214-009-9508-7

Advances in Plasmaspheric Wave Research with CLUSTER and IMAGE Observations

Arnaud Masson · Ondrej Santolík · Donald L. Carpenter · Fabien Darrouzet · Pierrette M. E. Décréau · Farida El-Lemdani Mazouz · James L. Green · Sandrine Grimald · Mark B. Moldwin · František Němec · Vikas S. Sonwalkar

Received: 13 October 2008 / Accepted: 8 April 2009

Abstract This paper highlights significant advances in plasmaspheric wave research with CLUSTER and IMAGE observations. This leap forward was made possible thanks to the new observational capabilities of these space missions. On one hand, the multipoint view of the four CLUSTER satellites, a unique capability, has enabled the estimation of wave characteristics impossible to derive from single spacecraft measurements. On the other hand, the IMAGE experiments have enabled to relate large-scale plasmaspheric density structures with

A. Masson (✉)
Science Operations Department, ESA/ESTEC, Keplerlaan 1, 2201-AZ Noordwijk, The Netherlands
e-mail: Arnaud.Masson@esa.int

O. Santolík · F. Němec
Faculty of Mathematics and Physics, Institute of Atmospheric Physics, Charles University, Praha, Czech Republic

O. Santolík
e-mail: ondrej.santolik@mff.cuni.cz

F. Němec
e-mail: frantisek.nemec@mff.cuni.cz

D.L. Carpenter
Space, Telecommunications and Radioscience Laboratory (STAR), Stanford University, Stanford, CA, USA
e-mail: dlc@nova.stanford.edu

F. Darrouzet
Belgian Institute for Space Aeronomy (BIRA-IASB), Brussels, Belgium
e-mail: Fabien.Darrouzet@oma.be

P.M.E. Décréau · F. El-Lemdani Mazouz
Laboratoire de Physique et Chimie de l'Environnement et de l'Espace (LPC2E), CNRS/Université d'Orléans, Orléans, France

P.M.E. Décréau
e-mail: Pierrette.Decreau@cnrs-orleans.fr

F. El-Lemdani Mazouz
e-mail: mazouz@cnrs-orleans.fr

Published online: 29 May 2009

wave observations and provide radio soundings of the plasmasphere with unprecedented details. After a brief introduction on CLUSTER and IMAGE wave instrumentation, a series of sections, each dedicated to a specific type of plasmaspheric wave, put into context the recent advances obtained by these two revolutionary missions.

Keywords Plasmasphere · CLUSTER · IMAGE · Waves

1 Introduction

Plasma waves play a fundamental role in our geospace environment. In particular, they are key to understand the way mass and energy are transfered from the magnetotail to the plasmasphere, the ionosphere and finally the atmosphere. Particles propagating in the magnetosphere indeed lose or gain energy via wave–particle interactions while waves are amplified or damped. Particles can also be diffused into the loss cone and precipitate to lower altitudes. But how much each type of wave contributes to this process and under which geophysical conditions? In order to answer this difficult question, a complete overview on plasma waves is needed to understand how and under which conditions waves are generated and how they propagate from their source regions.

A key region where such waves are generated is the plasmasphere, either within it or in its near vicinity. Various waves are found in this region from a few mHz to a few MHz, either electrostatic or electromagnetic. Ground-based observatories and space missions since the 1950s have collected a wealth of information about them (e.g., Lemaire and Gringauz 1998, p. 94) but many questions remained open before the launch of the European Space Agency (ESA) CLUSTER and the NASA IMAGE space missions in 2000. A review of whistler-mode type waves observed within the plasmasphere by IMAGE and DE-1 spacecraft can be found in Green and Fung (2005) and Green et al. (2005b).

This paper highlights recent advances obtained by the CLUSTER and the IMAGE missions on plasmaspheric wave phenomena in the medium frequency (MF) range (300 kHz–3 MHz) down to the very low frequency (VLF) range (3–30 kHz), the ultra low frequency (ULF) range (300 Hz–3 kHz) and the extremely low frequency (ELF) range (3–30 Hz). Both missions can be seen as a step forward in our understanding of these phenomena. On one hand, the multipoint view of the four CLUSTER satellites, a unique capability, has enabled the estimation of wave characteristics impossible to derive from single spacecraft measurements.

J.L. Green
NASA Headquarters, Washington, DC, USA
e-mail: James.L.Green@nasa.gov

S. Grimald
Mullard Space Science Laboratory (MSSL), Dorking, UK
e-mail: sg2@mssl.ucl.ac.uk

M.B. Moldwin
Institute of Geophysics and Planetary Physics (IGPP), University of California, Los Angeles, CA, USA
e-mail: mmoldwin@igpp.ucla.edu

V.S. Sonwalkar
Department of Electrical and Computer Engineering, University of Alaska Fairbanks, Fairbanks, AK, USA
e-mail: ffvss@uaf.edu

This includes the first quantitative estimation in three dimensions of the size of wave source regions (Sect. 8), their localizations and beaming properties by triangulation (Sect. 4). On the other hand, IMAGE was the first mission dedicated to remotely study the plasmasphere. The Radio Plasma Imager (RPI) onboard IMAGE was the first radio sounder launched above the plasmasphere enabling the discovery of new wave echoes, the remote derivation of density profiles and the study of field-aligned irregularities in the plasmasphere with unprecedented details (Sects. 5, 6, 7 and 11). Together with RPI, the IMAGE spacecraft carried several imagers including an Extreme UltraViolet (EUV) imager able to capture, for the first time, the entire plasmasphere—distribution of helium ions—in a single shot, every 10 minutes. Thus, EUV enabled for the first time to monitor changes in the plasma distribution of the overall plasmasphere and the size and evolution of large-scale plasmaspheric structures such as notches and plumes. As described in Sect. 3, plasmaspheric notches observed by EUV have been studied with wave measurements made by GEOTAIL to learn more about the source of kilometric continuum. Similarly, CLUSTER data have been combined with observations from the DOUBLE STAR equatorial spacecraft TC-1, which routinely detected chorus emissions, as well as the low altitude DEMETER spacecraft. Recent advances on plasmaspheric hiss have also benefited from measurements of the DE-1 and CRRES satellites (Sect. 9).

This review is the result of a collective effort, gathering the contributions of several scientists. A brief introduction to the CLUSTER and IMAGE instruments related to plasmaspheric wave phenomena is given in Sect. 2 (see also De Keyser et al. 2009, this issue). Then a series of nine sections describes the advances obtained on six waves and three types of sounding echoes. These sections are organized by decreasing frequency of the waves/echoes. Section 3 is dedicated to IMAGE and GEOTAIL observations of kilometric continuum (KC), the high-frequency range of a more general wave phenomenon called non-thermal continuum (NTC). Advances on NTC at lower frequency observed with CLUSTER are detailed in Sect. 4. The next three sections describe what has been learned so far from Z-mode (Sect. 5), whistler-mode (Sect. 6) and proton cyclotron echoes (Sect. 7) received by the RPI instrument. The following three sections are dedicated to VLF and ELF waves impacting the relativistic electron content of the radiation belts, namely: chorus (Sect. 8), plasmaspheric and mid-latitude hisses (Sect. 9), equatorial noise (Sect. 10). The last section (Sect. 11) deals with the determination of the average ion mass in the plasmasphere using ground-based ULF wave diagnostics and electron density profiles derived from RPI soundings. It is worth noting that the locations of the source regions of most of these waves are strongly linked with the position of the plasmapause, itself strongly influenced by large-scale electric fields (Matsui et al. 2009, this issue).

A set of acronyms is used throughout this paper. The Earth radius will be referred as R_E, the magnetic local time as MLT and the magnetic latitude as *MLAT*. The localisation of wave phenomena in the plasmasphere are often expressed in terms of L-shell (McIlwain 1961). For example, "$L = 4$" describes the set of the Earth's magnetic field lines, which cross the magnetic equator at 4 R_E from the center of the Earth. The plasmasphere boundary layer introduced by Carpenter and Lemaire (2004) is often abbreviated as PBL. The acronyms of the main plasma frequencies used in this paper are the following: f_{pe} for the electron plasma frequency, f_{ce} for the electron cyclotron frequency also called electron gyrofrequency, f_{uh} and f_{lh} for the upper and lower hybrid frequencies. Finally, the acronyms of the CLUSTER satellites are C1, C2, C3 and C4, conventionally color-coded as black, red, green and magenta respectively.

2 CLUSTER and IMAGE Wave Instrumentation

2.1 CLUSTER Wave Instruments

The four CLUSTER satellites carry eleven identical instruments to measure the electric field, the magnetic field and the electron and ion distribution functions (Escoubet et al. 1997). Three of them are particularly suited to study wave phenomena within or in the vicinity of the plasmasphere (see Sects. 4, 8, 9 and 10):

- The Spatio-Temporal Analysis of Field Fluctuations (STAFF) instrument measures the magnetic field between 8 Hz and 4 kHz with a three axis search coil magnetometer. Its spectrum analyzer performs auto- and cross-correlations between the three magnetic components estimated by the search coil and the two electric components measured by the Electric Field and Wave (EFW) experiment (Gustafsson et al. 2001). From auto-correlations, the energy densities of electric and magnetic components are inferred, together with the electrostatic/electromagnetic nature of the observed waves. The cross-power spectra are needed to estimate the polarization characteristics of electromagnetic waves. The time resolution varies between 0.125 s and 4 s. For a complete description of STAFF, see Cornilleau-Wehrlin et al. (2003).
- At higher frequencies (2–80 kHz), radio wave signals are continuously monitored by the active soundings and passive measurements of the Waves of HIgh frequency and Sounder for Probing of Electron density by Relaxation (WHISPER) instrument. The hardware of WHISPER mainly consists of a pulse transmitter, a wave receiver and a wave spectrum analyzer. Electric signals are acquired by the EFW electric antennas and only the onboard calculated fast fourier transform of the digital electric waveforms acquired are transmitted to the ground. A passive spectrum is recorded every 2.2 s and an active one every 52 s in normal mode for a frequency resolution of 162 Hz. Unlike a passive receiver, such a relaxation sounder enables to trigger plasma resonances when the medium does not show them naturally. For a detailed description of WHISPER, see Décréau et al. (2001).
- The Wide-Band Data (WBD) experiment consists of a wide-band passive receiver, which provides electric waveforms with high time resolution in three possible frequency bands: 100 Hz to 9.5 kHz, 100 Hz to 19 kHz and 700 Hz to 77 kHz. The first frequency band is the one mostly operated to study plasmaspheric wave phenomena. It provides continuous waveforms with a 27.4 kHz sampling rate. When no soundings are performed, WBD electric data may be seen as high resolution zooms of WHISPER spectra. For a complete description of WBD, see Gurnett et al. (2001).

2.2 IMAGE Wave Related Phenomena Instruments

IMAGE (Imager for Magnetopause to Aurora Global Exploration) was the first satellite dedicated to imaging the Earth's inner magnetosphere (Burch 2000). It was equipped with six instruments, which use neutral atom, ultraviolet and radio imaging techniques. Two of these instruments have been particularly used to study wave phenomena in the plasmasphere (see Sects. 3, 5, 6, 7 and 11):

- The Extreme UltraViolet (EUV) imager was able to picture the entire plasmasphere in a single "snapshot". It captured the helium ion (He^+) distribution outside Earth's shadow by measuring their emission line at 30.4 nm. He^+ is the second most abundant ion species in the plasmasphere accounting for roughly 20% of the plasma population while hydrogen ion (H^+), the most abundant one, has no optical emission. Because the plasmaspheric

He^+ emission is optically thin, the integrated column density of He^+ along the line-of-sight through the plasmasphere is directly proportional to the intensity of the emission. Moreover, the 30.4 nm emission line is the brightest ion emission from the plasmasphere and is spectrally isolated with a negligible background. For a full description of EUV, see Sandel et al. (2000).

– The Radio Plasma Imager (RPI) was a low-power radar with three dipole antennas. The two spin plane antennas were of lengths 370 m and 470 m tip-to-tip (Benson et al. 2003) while the one along the spin axis was 20 m long (spin rate: 0.5 rpm). The spin plane antennae are so far the longest ever deployed in space for such an instrument. RPI was able to locate regions of various plasma densities by observing radar echoes from the plasma. These echoes were reflected when the radio frequency was equal to the plasma frequency. By stepping the transmitted signal frequency through a wide frequency range (3 kHz–3 MHz), features of various plasma densities were observed. Derived densities, from those locations returning radio sounding echoes, were combined with line-of-sight images captured by EUV to infer quantitative, global distributions of plasmaspheric plasma. For a full description of RPI, see Reinisch et al. (2000).

3 Kilometric Continuum

3.1 Previous Observations

Low frequency non-thermal continuum radiation has been observed extending from ∼15 kHz to as high as ∼300 kHz although it is rarely observed above ∼90 kHz. However, Hashimoto et al. (1999) discovered a type of high frequency continuum radiation that is observed in the 100–800 kHz frequency range and as such, will escape the magnetosphere once it has been generated. These authors named this emission kilometric continuum (KC) due to the fact that the emission closely resembles the discrete emission band structure of the lower frequency non-thermal continuum in frequency–time spectrograms, has many other similar characteristics, and is probably generated by the same mechanism. It is important to note that KC is always observed without an accompanying lower frequency trapped component. The discovery of this high frequency KC emission has sparked considerable interest in further understanding various aspects of this radiation, what makes it different from its lower frequency counterpart, and the relationship with the plasmasphere and the plasmapause.

The spectrogram on Fig. 1 clearly shows the discrete emissions bands of KC extending from 17:00 to 24:00 UT. The frequency range for KC is approximately the frequency range of auroral kilometric radiation (AKR), but as shown in Fig. 1, there are significant differences that can be used to easily distinguish between these two emissions. KC has a narrow band structure over a number of discrete frequencies with time while AKR is observed to be a broader band emission with emissions extending over a large frequency range sporadically

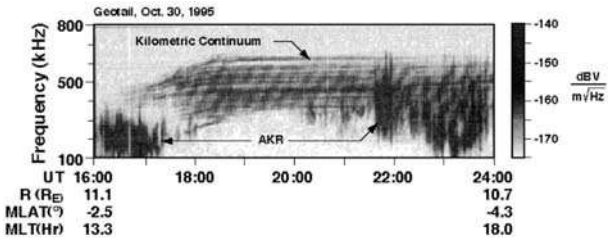

Fig. 1 A frequency–time spectrogram of KC emissions measured on 30 October 1995 by the Plasma Wave Instrument (PWI) onboard GEOTAIL. (Adapted from Hashimoto et al. 1999)

and can be seen from 16:00 to 17:00 UT and from 21:30 to 24:00 UT in that spectrogram. In order to determine the source of the KC emission Hashimoto et al. (1999) performed direction finding using spin modulation of the emission. The resulting directions (shown in Fig. 4) with time, as correlated with the spectrogram data, indicated that the emission was generated from a very broad source region of the plasmasphere. Due to the high emission frequency of KC and its lack of correlation with geomagnetic activity, the source of KC was originally believed to lie deep within the plasmasphere (Hashimoto et al. 1999). Soon after these results were published, Carpenter et al. (2000) suggested that the source region for KC was coming from plasmaspheric cavities deep within the plasmasphere. From their analysis of over 1764 near-equatorial electron density profiles from CRRES, deep density troughs or cavities were observed on ∼13% of the passes (Carpenter et al. 2000).

3.2 IMAGE Observations

It would take new observations of the plasmasphere from the EUV and RPI instruments onboard IMAGE along with simultaneous observations of KC from the Plasma Wave Instrument (PWI) onboard GEOTAIL to understand what plasmaspheric structures are the source region of KC thereby reaching a new understanding of plasmaspheric structure and dynamics. From the perspective of the CRRES observations the results of Carpenter et al. (2000) are compelling and appear to establish cavity-like structures in the plasmasphere. The IMAGE observations show them as plasmaspheric notches, which are the primary sources of KC.

Figure 2 illustrates that the location of the KC source region within a plasmaspheric notch, and the resulting emission cone pattern of the radiation, as shown from ray tracing calculations, is consistent with many of the previous observations. Figure 2a is a frequency–time spectrogram (passive mode) from PWI onboard GEOTAIL showing the banded structure of KC. The slanted vertical emissions are all Type III solar radio bursts. Figure 2b shows the magnetic longitude versus the equatorial radial distance of the plasmapause (derived from the right insert of the EUV image of the plasmasphere) and the GEOTAIL position during the KC observations of panel (**a**). As observed by EUV, plasmaspheric notch are large "bite-outs" in the plasmasphere in which plasma has largely been evacuated from a nominal plasmapause to somewhere deep within the plasmasphere (see also Darrouzet et al. 2009, this issue). This structure is significantly different than a density cavity of some size and depth within the plasmasphere. Figure 2b, left insert, presents a ray tracing analysis showing that the structure of the plasmaspheric notch has a significant effect on the shape of the resulting emission cone through refraction of the radiation generated from a small source region located at the magnetic equator deep within the plasmaspheric notch. The correspondence of KC observations with plasmaspheric notches, as shown in Fig. 2, is not an isolated instance. Green et al. (2004) found from a year's worth of observations of GEOTAIL KC measurements and EUV images of plasmaspheric notches that the vast majority (94%) of the 87 cases studied showed this correspondence. Their results also showed that a density depletion or notch structure in the plasmasphere is typically a critical condition for the generation of KC but that the notch structures do not always provide the conditions necessary for the generation of the emission.

If KC source regions were located deep within a plasmaspheric notch, they can be used to further study the properties of the KC emission cone and the depth of notches. From a statistical analysis Fig. 3a shows the number of occurrences of KC observed by PWI onboard GEOTAIL, associated with plasmaspheric notches observed by EUV onboard IMAGE, with the magnetic longitudinal extent of the emission. This analysis assumed that the plasmaspheric notches were corotating with the plasmasphere. From these events the median in the

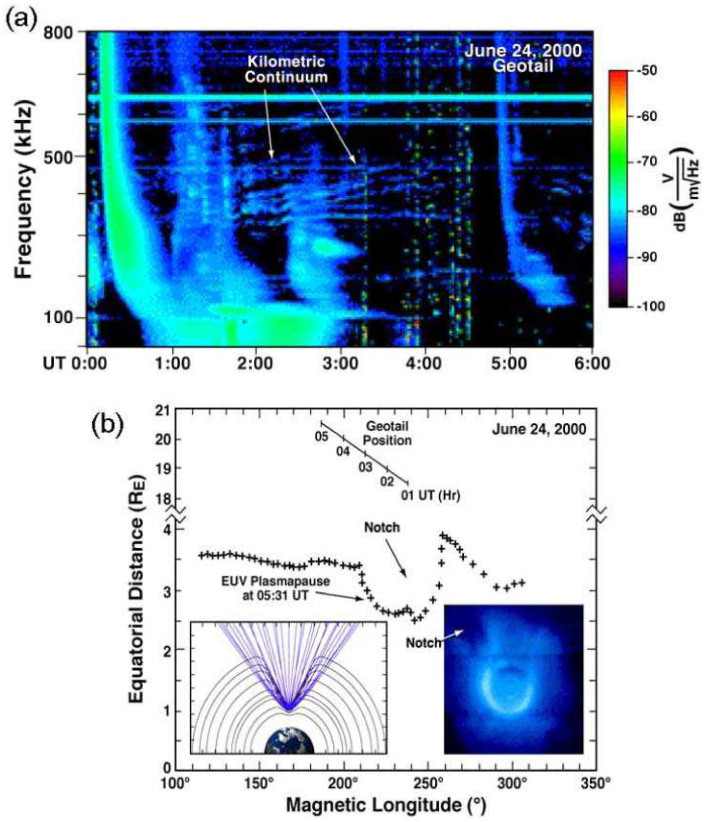

Fig. 2 (**a**) Kilometric continuum observations from PWI onboard GEOTAIL on 24 June 2000 from 00:00 to 06:00 UT. (**b**) The location of GEOTAIL during the KC observations and the extracted location of the plasmapause from IMAGE/EUV data are plotted in magnetic longitude versus equatorial distance. Inserted into panel (**b**) are model ray tracing calculations (*left*) and the EUV image data (*right*). (Adapted from Green et al. 2002, 2004)

longitudinal extent of the KC emission cone is ∼44°. Assuming an average plasmaspheric model and that KC is generated near the upper hybrid frequency an estimation of the depth of notch structures can be determined. Figure 3b shows the number of occurrences of the highest frequency source of the same KC events versus equatorial radial distance as an estimation of the deepest location of the KC source region. The distribution has a large peak with the median and the mean of the distribution at approximately the same equatorial radial distance of 2.4 R_E.

Observations of the plasmasphere and KC emissions from the IMAGE instruments provide a new perspective in which previous CRRES and GEOTAIL measurements can be interpreted self-consistently to obtain additional insights into plasmaspheric dynamics and structure. Figure 4a shows the direction finding measurements of Hashimoto et al. (1999) indicating an extensive emission region for KC. Figures 4b–f illustrate how a small source region of KC deep within in a plasmaspheric notch can generate an emission cone that is also consistent with the direction finding measurements. The proposed plasmaspheric notch and the corresponding KC emission cone all corotate with the plasmasphere and are shown over the same 12-hour period. GEOTAIL was in the proposed emission cone and ob-

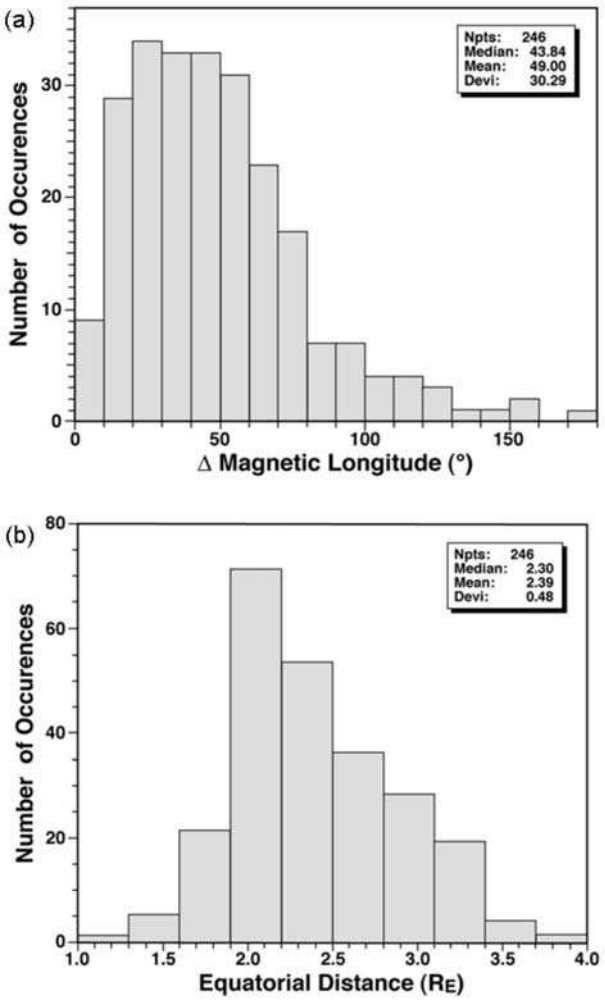

Fig. 3 (**a**) Number of occurrences of KC (observed by PWI onboard GEOTAIL) associated with plasmaspheric notches (observed by EUV onboard IMAGE) with the magnetic longitudinal extent of the emission. (**b**) Number of occurrences of the highest frequency source of the same KC events versus equatorial radial distance as an estimation of the deepest location of the KC source

served KC radiation starting at approximately 16:00 UT until 04:00 UT of the next day. During this time, the corotating plasmasphere sweeps the emission cone across and finally past the GEOTAIL spacecraft in a way completely consistent with the direction finding results.

Carpenter et al. (2000) reported significant density variations or cavities in the plasmasphere in which KC at many times were observed. The obvious confinement of KC to a cavity-like structure led those authors to propose that the radiation would be trapped in plasmaspheric cavities at frequencies below the density of the outer cavity wall. With the advent of the IMAGE mission a new interpretation has arisen to these observations as presented by Green et al. (2002). Figure 5a assumes a notch structure, like those that have been observed by EUV, would exist at the time of the CRRES observations (1990–1991). What is also shown is a typical CRRES orbit plotted in the same magnetic longitude and L coordinates. By using magnetic longitude and L coordinates the orbit of CRRES is then presented in the same reference frame as a corotating plasmasphere and notch structure. Figure 5b approxi-

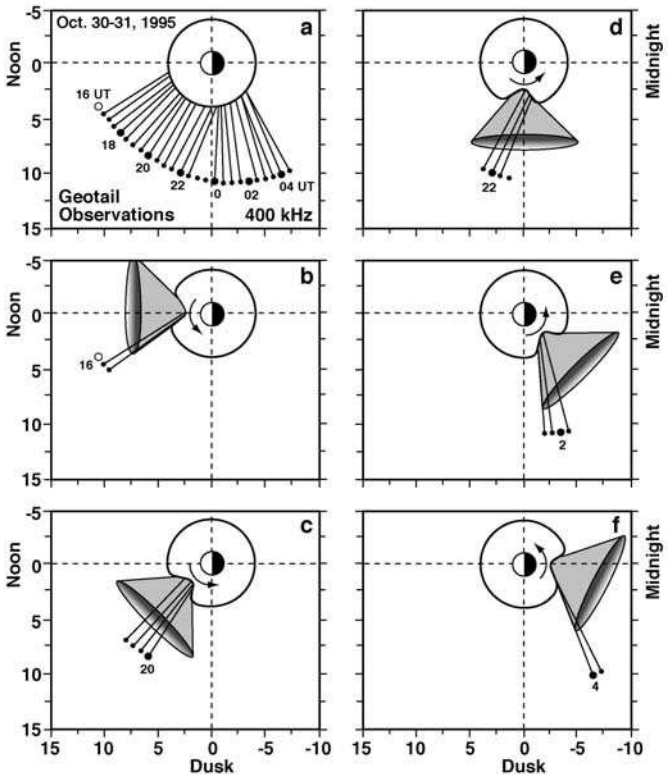

Fig. 4 Direction finding measurement (**a**) from Hashimoto et al. (1999) of KC at 400 kHz are reinterpreted as being completely consistent with respect to the source of KC emitted from a corotating plasmaspheric notch (**b**)–(**f**). (Adapted from Green et al. 2002)

mates the corresponding density structure that would be observed. The resulting qualitative density structure of the plasmaspheric notch, shown in Fig. 5b, is indistinguishable from the density cavities structures reported by Carpenter et al. (2000) and delineated as the upper hybrid resonance emissions. The CRRES observations of the confinement of KC to plasmaspheric cavities, reported by Carpenter et al. (2000) can then alternately be interpreted as KC radiation generated at the plasmapause, at the base of a plasmaspheric notch. Refraction near the source region of the steep density wall of the cavity would then confine the emission to within the notch structure as the ray tracing calculations have shown.

3.3 Conclusions

In summary, recent observations of KC from IMAGE and GEOTAIL have provided a new opportunity to understand plasmaspheric structures and dynamics. KC is always observed without an accompanying lower frequency trapped non-thermal continuum component but is almost certainly generated by the same emission mechanism. Plasmaspheric notches, reported earlier as deep plasmaspheric density cavities, are the source of KC. Much like the lower frequency non-thermal continuum emissions generated at the plasmapause, it is now well established that KC is generated at the newly established plasmapause, deep within a notch structure, near the magnetic equator. From the KC observations, plasmaspheric

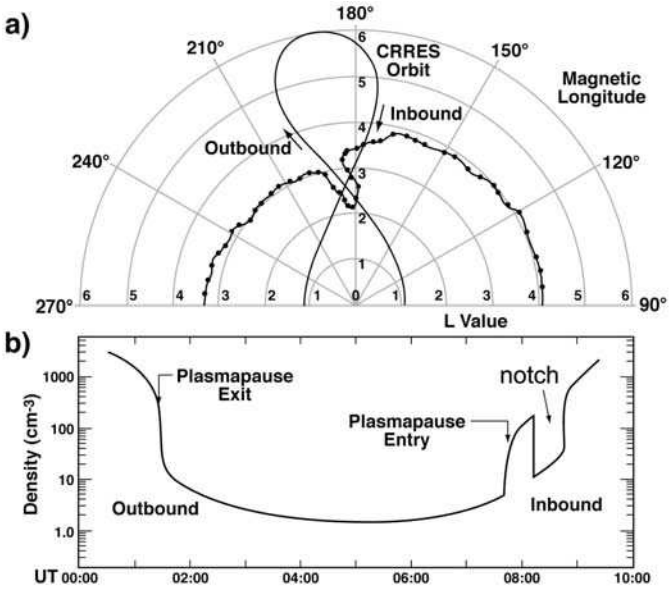

Fig. 5 (**a**) A typical orbit of the CRRES spacecraft in magnetic longitude and L value plotted over a typical plasmaspheric notch. (**b**) Approximate variation in density that would be observed assuming that a notch structure like this would exist at the time of CRRES

notches are typically as deep as $\sim 2\ R_E$ but can be deeper within the plasmasphere. The average beam width of KC has been found to be $\sim 44°$. The confinement of the KC emission cone, as shown by the ray tracing calculations, due to the steep densities of the walls of the notch structure therefore indicates that the average size of plasmaspheric notches must also be $\sim 44°$ in longitude. Due to the strong relationship between KC and plasmaspheric notches, the long term set of observations of KC by GEOTAIL, extending more than 10 years could now be use to make long-term studies that relate to plasmaspheric notch structure and dynamics.

There are a number of outstanding questions that need to be addressed concerning the generation and propagation of the KC emissions such as:

- Is the motion of the plasmapause inwards coupled with a sufficiently large density gradient necessary and sufficient for the generation of KC? Is the free energy source necessary for the creation of electrostatic waves that are precursors to KC always present, or is the free energy source dependent on the state of the magnetosphere?
- KC often exhibits a banded frequency structure consistent with $(n + \frac{1}{2}) f_{ce}$ source, but frequently the structure appears more complex. Can density ducts near the plasmapause explain the more complex structure or do other mechanisms need to be investigated like dynamic motion of the plasmasphere boundary layer?
- For highly disturbed times large changes occur in the inner magnetosphere magnetic field intensity. Can this change be detected remotely in the spectral band spacing of escaping KC? Can the analysis of the frequency structure of escaping KC indicate the state of the plasmasphere and the inner magnetosphere magnetic field?

4 Non-Thermal Continuum

4.1 CLUSTER Observations

4.1.1 Assets of the CLUSTER Mission

The WHISPER instrument measures electric field in a frequency range (2–80 kHz) well adapted to study non-thermal continuum (NTC) waves, both in the trapped frequency band (∼1–20 kHz) and in the lowest part of the escaping frequency band (∼20–200 kHz). The WBD instrument completes the view by providing high resolution snapshots and wave forms on a similar frequency range (0–77 kHz) when studying NTC waves. The major assets of the CLUSTER observatory about NTC studies are four fold.

- *Orbital characteristics.* The satellites travel from southern to northern hemisphere and cross or skim the plasmasphere around perigee at radial geocentric distances of ∼4.3 R_E. Such orbit configurations provide excellent view points on the radio beams directly emitted at close distances, from equatorial plasmapause sources, when those are placed inward from the orbit, i.e., when the plasmasphere is sufficiently contracted. The polar orbit of CLUSTER near its perigee is comparable to that of DE-1 near its apogee, of geocentric distance ∼4.5 R_E. CLUSTER platforms spin under different conditions than DE-1: Spin axis are normal to XY GSE (geocentric solar ecliptic) plane in CLUSTER case, whereas DE-1 spins in a cartwheel manner with the spin axis parallel to XY GSE plane. CLUSTER offers thus complementary views to those obtained by DE-1 in the past. As a consequence, typical DE-1 observations of NTC beaming properties can be reinterpreted in view of CLUSTER observations, in a similar manner IMAGE views help interpreting CRRES past observations of KC. Away from perigee, CLUSTER offers views at large distances from sources. The electric field measured there results often from a superposition of waves emitted from various and multiple sources. Detailed directivity estimations, made possible thanks to good frequency and time resolutions, help to distinguish each of the main source regions from the others.
- *Instrument performances.* A good time resolution (electric field spectra delivered at a rate of ∼2 s) allows directivity measurements in 2-D (direction of the wave vector in the spin plane) at successive positions on the orbit (∼300 km apart).
- *Multipoint observations.* Performances of the constellation vary according to spacecraft separation, which is varied along the mission phase. The spatio-temporal analysis of beam properties is made possible by comparing observations over small time intervals and small distances in space, i.e., during mission phases at small or medium separation (100 to 1000 km). In addition, compared wave vector directions lead to source localization. This can be done via triangulation, either from several spacecraft illuminated by the same beam at the same time (during mission phases at large separation), or from a single drifting spacecraft viewpoint, after stability of the beam has been assessed from compared observations.
- *Plasma diagnostic from a relaxation sounder.* In addition to spectral and geometric analysis of radiated beams, CLUSTER offers the possibility of analyzing intense electrostatic waves, which are potential sources of non-thermal radiations.

This section focuses on observations of NTC radiations (excluding trapped continuum signatures) when CLUSTER is either in the outer plasmasphere or in the polar cap region. The tetrahedron shape achieved at large geocentric distances turns to an elongated shape near perigee. Figure 6a displays the near Earth magnetic field configuration and the orbit

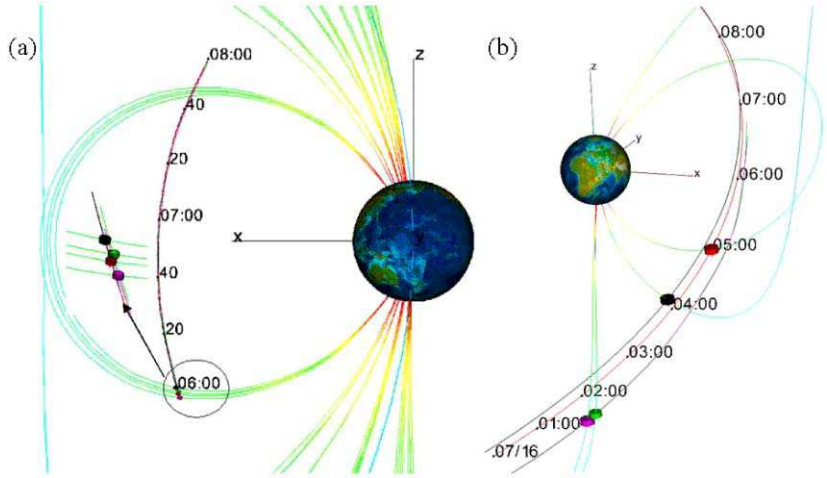

Fig. 6 Orbit tracks and constellation produced with the Orbit Visualization Tool (OVT, http://ovt.irfu.se). Magnetic field lines intercepting each satellite are shown, as well as a shell of outermost magnetospheric field lines. The model field is a combination of IGRF internal field model and Tsyganenko 87 external field model. The colour code along field line indicates magnetic field intensity. (**a**) 26 September 2003, 06:00–08:00 UT, small separation mission phase (200 km), solar magnetic (SM) coordinate system. (**b**) 16 July 2005, 01:00–08:00 UT, multi-scale mission phase (10 000 km and 1000 km), geocentric solar magnetospheric (GSM) coordinate system

of the four satellites in solar magnetic (SM) coordinates on 26 September 2003. The small spacecraft separation (200 km) does not allow distinguishing the four orbits, nor the four spacecraft, which travel from South to North. From the enlarged CLUSTER configuration shown in an insert, C1 (black) is ahead of C3 (green), C2 (red) and C4 (magenta). Figure 6b illustrates a multi-scale configuration on 16 July 2005, when the pair C3 and C4 (1000 km separation) is in the polar cap. At the same time, C1 is in the outer plasmasphere and C2 near the plasmapause.

4.1.2 Typical Spectral Signatures

Trapped continuum signatures are commonly observed in the low frequency range of WHISPER (Décréau et al. 2004). They present the smooth, large band spectral features already reported from the first observations (Gurnett 1975). It is in the "escaping continuum" frequency range ($>\sim$20 kHz) that the CLUSTER multi-view offers the best opportunities to improve our understanding of this radio emission. In this range, NTC waves can be classified according to four main types: (i) "equatorial spots", (ii) "narrow band elements", (iii) "continuum enhancements" and (iv) "wide banded emissions". Those names refer to spectral signatures, which depend on two elements: the source on one hand (position, beaming properties and main frequencies) and the observatory on the other hand (position and movement). When the observatory moves rapidly in the vicinity of a source, spectral signatures inform about position and beaming properties of the source. In contrast, a remote observatory can be illuminated by a large region, hence perceive movements of sources via the spectral signatures it records. Visions about time or space in the resulting spectrograms are thus created by one or the other of the protagonists.

The first type of NTC spectral signature, the equatorial spot, is an emission limited in time ($\sim$30 minutes) and frequency ($\sim$10–30 kHz). In the spectrogram on Fig. 7a, harmonics

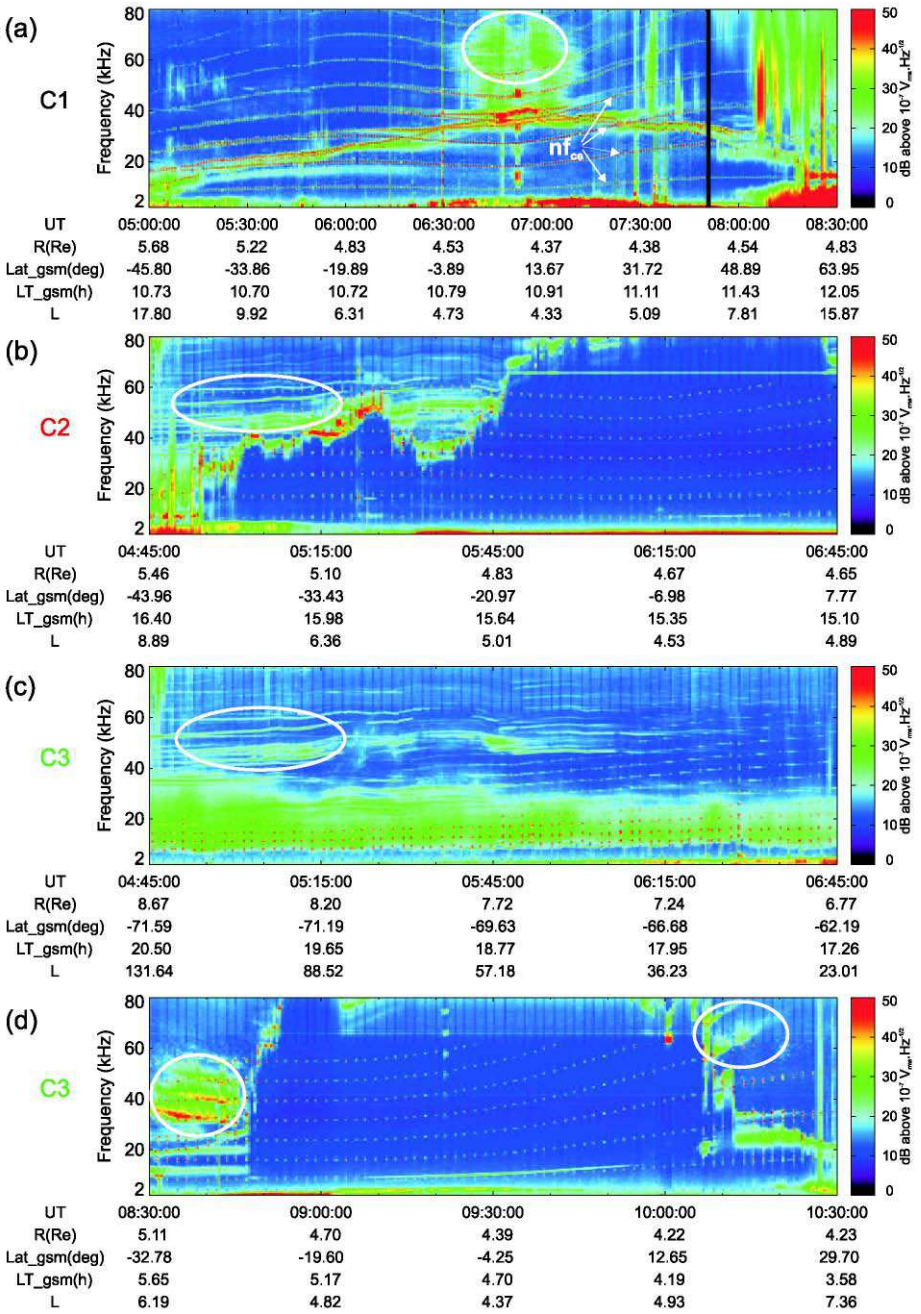

Fig. 7 Three main types of NTC spectral signatures (*white ovals*) observed with CLUSTER near perigee. (**a**) 26 September 2003, "equatorial spots"; (**b**)–(**c**) 16 July 2005, "narrow band elements"; (**d**) 30 December 2003, "wide banded emissions". CLUSTER constellation is shown in Fig. 6a for events presented in panels (**a**) and (**d**), in Fig. 6b for events presented in panels (**b**) and (**c**). *L* parameter values are calculated from the same magnetic field model than used by the OVT tool producing displays shown in Fig. 6.

of the electron gyrofrequency f_{ce}, triggered by regular sounding operations, appear as intense electrostatic emissions (small red points at ∼8–12 kHz and harmonics). Other resonant frequencies (red points between electron gyroharmonics) are the electron plasma frequency f_{pe} and the upper hybrid frequency f_{uh}. Their frequency position follows the increase of f_{pe} from 10 to 35 kHz (05:00–06:55 UT), and its decrease from 35 to 15 kHz (06:55–08:30 UT). The magnetic equator, at ∼06:55 UT, can be inferred by brief encounters of natural electrostatic emissions at $(n + \frac{1}{2}) f_{ce}$ below f_{pe}. It is worth noting that recent advances on electrostatic wave emissions at $(n + \frac{1}{2}) f_{ce}$ in the equatorial plasmasphere have been derived from CLUSTER data and detailed in El-Lemdani Mazouz et al. (2009). NTC emissions (above f_{pe}, in the frequency range 35–80 kHz) are observed on both sides of the equator between 06:35 and 07:10 UT. Time intervals when similar NTC spectral features are observed correspond most often to CLUSTER located near equator. We shall call this type of NTC emissions equatorial spot in short, standing for "near equatorial time-frequency intervals of radio emissions". This is a case when the observatory moves rapidly in the vicinity of a source region and spectral signatures inform about beaming properties.

The second type is the classical narrow band element form (Kurth et al. 1981), covering about 1 kHz or less. Such emissions appear often in series of waves at frequencies separated by a few kHz from each other, evolving together during time intervals of long duration (up to several hours). Spacing between frequencies f_n of related elements are arranged in quasi harmonic form, $f_n = (n + d) f_{ce}$ with $0 < d < 1$ and n an integer, f_{ce} being interpreted as the gyrofrequency at the source (Kurth 1982; Gough 1982). Figures 7b–c display narrow band NTC elements (40–60 kHz) observed identically and simultaneously (04:45–05:40 UT) by two different CLUSTER spacecraft located at different positions: C2 enters in the plasmasphere, while C3 is placed in the polar cap (see Fig. 6b for the configuration of the constellation).

The third type of NTC spectral form, the continuum enhancement, has been reported for the first time by Gough (1982). It develops after the start of an electron injection event, its spectral shape evolving over duration of one to several hours (Kasaba et al. 1998). Analysis of one example, observed by CLUSTER in the night sector, indicates that a region source of large dimension might be involved (Décréau et al. 2004). This form has not yet been identified by CLUSTER at perigee, either because it travels too fast in comparison to the typical time scale of the event, or because it is not placed at sufficient distance to be illuminated adequately by the various sources, which are likely at play. Indeed, the continuum enhancement scenario proposed by Gough (1982) and Kasaba et al. (1998) involves injection of electrons followed by a plasmapause inward convection. The wave sources (which are where the injection meets the plasmapause) drift likely inward and eastward. This is a case when, in order to be illuminated by the large region engulfing all successive positions of the sources, the observatory has to be remote. Numerous observations of continuum enhancements, often associated with AKR emissions, have been done by CLUSTER on the outermost part of its orbit. Some observations are also available from over the polar cap.

A fourth spectral form, the wide banded emission, has been observed for the first time with CLUSTER (Grimald et al. 2008). It consists of one or several banded emissions with a frequency separation (5–10 kHz) of the order of f_{ce} values encountered at plasmapause. When several bands are observed, they peak at harmonics of the same frequency, interpreted to be the gyrofrequency at the source. For the event presented in Fig. 7d, they appear when the observing satellite approaches the flank of a thick plasmasphere, bounded by a narrow plasmapause. Events of this type have been observed only a few times per year. They are always associated with density steps of large amplitude encountered over short distances. Some are observed on the flanks of a cusp.

4.2 Analysis

4.2.1 Beam Stability

As noted above, the limited time duration of CLUSTER observing the equatorial spots is not due to inherent time duration of the emission, but mainly to the time evolution of CLUSTER view point over the source. Indeed, a satellite observes the radiation only when it is placed inside the illumination cone formed in space by the radiated beams. From a small constellation skimming the outer plasmasphere, compared wave intensities measured at fixed frequency on the four spacecraft indicate most often that the differences observed on intensity versus time profiles are simply due to time shifts between spacecraft progressing along orbit tracks, generally close to each other. When crossing a beam illuminating a limited cone angle in space, each spacecraft observes an increase of intensity followed by a decrease (Fig. 8a). Times of maximum intensity correspond to times when the spacecraft reaches the central part of the beam. When intensities are plotted with respect to *MLAT* (Fig. 8b), their maxima are aligned with each other, indicating that the beam did not move significantly between the first and the last crossing, which are separated by 5–10 minutes. A different behaviour is obtained when time variations at the source are taking place, as illustrated in Fig. 9. For this event, narrow band elements contribute to an equatorial spot observed from ∼11:00 to 11:30 UT in the 60–80 kHz frequency band. The frequencies of elements are modulated at a time period of about 6 minutes. The bottom panel of Fig. 9, comparing intensities measured by the four spacecraft at 80 kHz, indicates three consecutive increases of intensity observed simultaneously on the four spacecraft in the southern hemisphere. Such a signature indicates a temporal evolution of the radiation properties. In contrast, intensity versus time profiles observed in the northern hemisphere (peak intensities observed as shifted in time) correspond to a beam stable in time and space.

4.2.2 Beam Geometry

The multipoint view obtained from the CLUSTER constellation yields, at least partially, an image of beam contours in space. This capacity enables to test one theory of NTC beam formation, under which the beam geometry is constrained. Indeed, in the frame of the radio window theory examined and proposed by Jones (1980), mode coupling occurs between intense upper hybrid waves produced by a warm loss-cone component of energetic electron distribution and the cold-plasma Z-mode branch of the dispersion relation. Propagation into

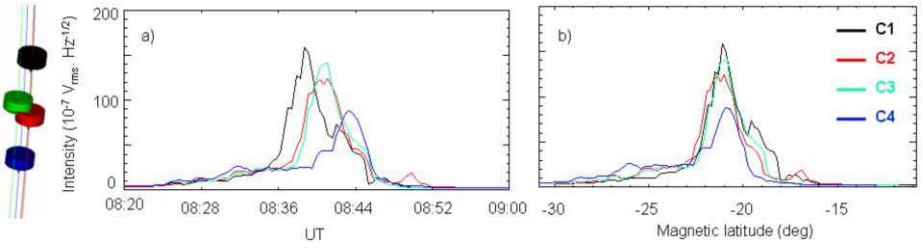

Fig. 8 Compared intensity variations at constant frequency (39.5 kHz), measured respectively by the four CLUSTER spacecraft when progressing along their orbit on 30 December 2003, (**a**) as a function of UT time, (**b**) as a function of magnetic latitude (constellation configuration shown at *left*). The corresponding beam is stable in space. (Adapted from Grimald et al. 2008)

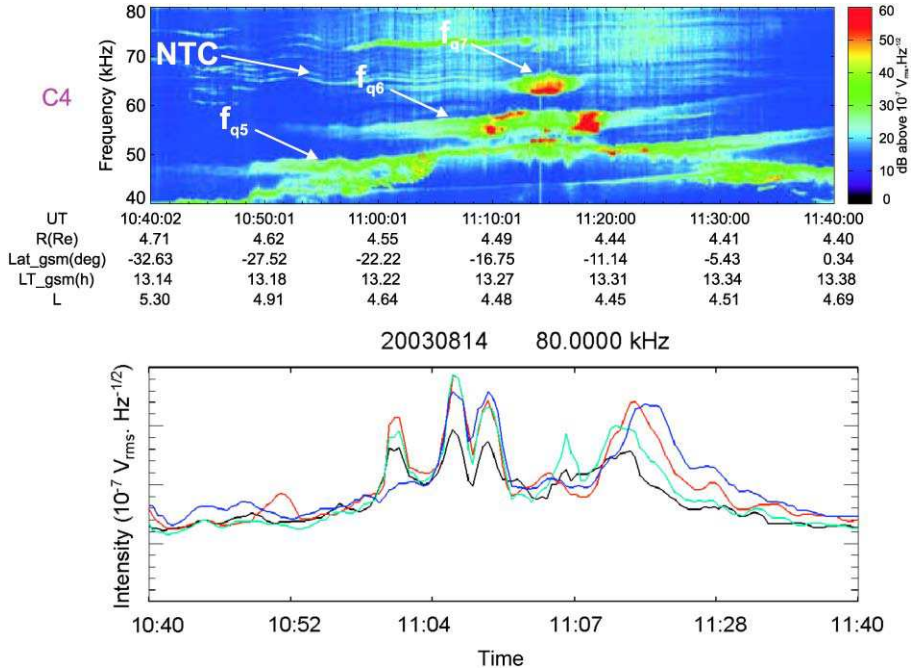

Fig. 9 (*Top*) Dynamic time electric field spectrogram of C4 for the 14 August 2003 event. Geomagnetic equator is crossed at about 11:15 UT (latitude is not expressed in SM coordinate system). NTC elements (electromagnetic waves) and a local emission (electrostatic Bernstein mode) are pointed with *arrows*. (*Bottom*) Compared intensity variations at a given frequency with *colour codes* and constellation configuration as for the event shown in Fig. 8

a slowly varying plasma density medium allows direct coupling of energy to L-O-mode waves, which propagate to lower density regions and beam away from the magnetic equator. According to this theory, the inclination angle of the beam with respect to magnetic equator is fixed by the ratio f_{ce}/f_{pe} of characteristic frequencies at the source. The source, placed at the equator (minimum in magnetic field value) radiates two beams, one in each hemisphere. The cone angle attached to each beam is typically $\sim$1–2° large (see Fig. 10a adapted from Jones 1982).

A test of validity of radio window theory (Grimald et al. 2007) has been performed in the case event presented in Fig. 7a, where the equatorial spot NTC form displays two intensity peaks, placed symmetrically to the magnetic equator, a feature, which could be attributed to the symmetrical beams displayed in Fig. 10a. This study could not draw a definitive conclusion about the validity of Jones theory. Indeed, the radio theory is compatible with quantitative observed beaming properties of a selected frequency element when an ad-hoc choice of source position in latitude is made. Although the latitude obtained thus (less than 1° off the equator) is in the expected range, the complete picture does not fit the narrowness of the beam indicated by the theory. Figure 10c displays orientations of the ray path of the 70 kHz NTC wave measured from intensity spin modulation at successive positions of the observing spacecraft on their orbit (curved arrows). Ray path orientations and orbit paths are shown projected onto the XY GSE plane, parallel to the spin plane. One insight in the third dimension is provided by the choice of two different line colours: Ray paths obtained from C4 in southern hemisphere are plotted in blue, whereas ray paths obtained from C2 in

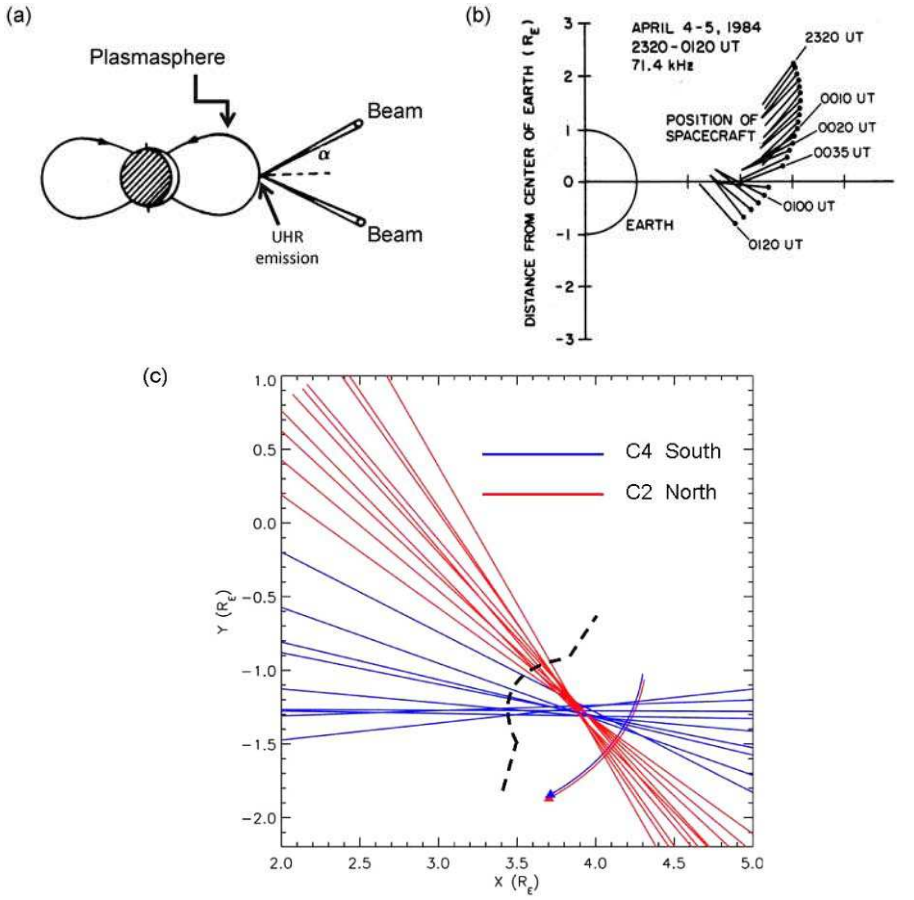

Fig. 10 Beaming properties of NTC waves: (**a**) configuration of NTC beams expected from the radio-window theory (adapted from Jones 1982); (**b**) ray path directions in a meridian plane derived from directivity measurements onboard DE-1 (adapted from Morgan and Gurnett 1991); (**c**) ray path directions of NTC element at 69 kHz derived from CLUSTER and drawn in *blue* for C4 in the southern hemisphere, in *red* for C2 in the northern hemisphere (in XY GSE plane); sketch of a possible associated plasmapause shape (*dotted line*); orbit elements of C2 and C4 shown by the *red* and *blue curves* with *arrows*. (Adapted from Grimald et al. 2007)

northern hemisphere are plotted in red. In this 2-D view, all ray paths point towards the same region, but the point of view drifts from negative ($\sim -4°$) to positive ($\sim +4°$) latitudes along the orbit element considered, which at the same time drifts of about 8° in GSE longitude (but less, below 3°, in SM longitude, corresponding to MLT). As a consequence, the sketch of Fig. 10a, which represents a meridian cut at fixed MLT, cannot be directly compared to observations. Narrow beams (of cone angle $<1°$) emitted from a single source could not be visible over such a large portion of the orbit. Furthermore, complementary observations detailed in Grimald et al. (2007) indicate that the orbit track is illuminated by several sources of small dimension and various frequencies, placed at different latitudes along roughly the same magnetic field tube, hence concentrated, after projection to the XY GSE plane, within a small area.

4.3 Interpretation

4.3.1 Main NTC Form (Quasi Equatorial Sources)

Close up View on Sources Intense electrostatic emissions at NTC frequencies are encountered in the plasmapause region (Kurth et al. 1981). They are thus considered as potential electrostatic sources radiating energy (likely by wave decay or linear conversion) in the form of continuum waves of electromagnetic nature. No simultaneous observations of such a NTC source by one CLUSTER spacecraft and of the beam emitted from that source by another spacecraft has been found. This is due to the 3-D nature of the geometry involved, the small size of sources and the limited extension of the beam near sources. Then, it has not been possible so far to directly test a generation mechanism by comparing wave characteristics at both ends of the process.

The spectrogram of Fig. 9 provides nevertheless an insight on the frequency, size and position of candidate electrostatic sources in the equatorial region. The magnetic equator is crossed at 11:15 UT when f_{pe} (narrow feature in yellow) culminates at ∼53 kHz. Above that frequency, WHISPER observes banded electrostatic emissions displaying upper frequency cut offs at the Bernstein frequencies f_q characteristic of the harmonic band considered. The intense spots (in red) showing up in the spectrogram of Fig. 9, one at ∼64 kHz at the equator, and two at ∼55 kHz on both sides of the equator, belong to the bands associated to Bernstein modes, the $[6f_{ce}-f_{q6}]$ frequency interval in the latter case and the $[7f_{ce}-f_{q7}]$ interval in the former case. These spots are candidate sources, which could participate to the generation mechanism proposed by Rönnmark (1985). Lastly, an event observed on 30 May 2003 by Canu et al. (2006), where NTC frequencies oscillate with time at similar periods than the central frequency of local Bernstein band series, completes this view. The authors interpretation is that Bernstein emissions probably play a role in the generation of NTC radiations.

A striking characteristic of NTC spectral signatures observed near the plasmapause is their splitting in fine structures. This property has been pointed out by detailed analysis of the waves forming the equatorial spots (Grimald et al. 2007). Complex spectral features of NTC observed in Fig. 9 can be interpreted as produced by a superposition of beams emitted from many sources, placed at different locations along the plasmapause and near the equator.

Ray path observations made by DE-1 while skimming the outer plasmasphere (Morgan and Gurnett 1991) can be usefully compared to CLUSTER observations (Grimald et al. 2007). Both views are complementary: DE-1 provides a view in a meridian plane and CLUSTER in the equatorial plane. The ray path directions obtained from DE-1 are more or less parallel to each other during intervals of significant duration, here from 23:20 to 00:20 UT (Fig. 10b). This could be due to sources placed in the equatorial plane at various geocentric distances. An alternative explanation is that the topology observed is due to sources placed at similar geocentric distances but at different latitudes along a single flux tube. The latter interpretation makes better sense in view of CLUSTER observations, which indicate a source region concentrated at a single geocentric distance and emitting beams inside a cone of large longitudinal extent, ∼40° (Fig. 10c). Such a large extent, similar to longitudinal cone angle of KC radiations (Fig. 4), cannot be envisaged to be produced by a plasmapause boundary smooth in azimuth. This ray path topology is not unique but representative of similar events. It could be due to a particular shape of the plasmapause, known to display density irregularities in azimuth (Darrouzet et al. 2006). In particular, ray paths being likely aligned with density gradients (Jones 1982), a small bite-out structure, sketched

in Fig. 10c, could act as a collimator concentrating radiations. This scenario would be similar to the interpretation of KC emissions proposed by Green et al. (2002) and illustrated in Fig. 2.

Propagation Effects Statistics of occurrence at CLUSTER orbit of equatorial spots and narrow band elements indicate that they are probably signatures of the same phenomena, observed from different perspectives (Grimald 2007). The underlying scenario implies wave propagation. A ray tracing study considers the fate of waves emitted from equatorial plasmapause at a given inclination angle with respect to the equatorial plane, after they have been reflected by the magnetopause density wall (Green and Boardsen 1999). Ray tracing indicates latitudinal confinement of NTC radiation emitted at small inclination angles, since those waves do not move at large distance from the equatorial plane and stay trapped between the plasmapause and magnetopause density walls. In contrast, rays emitted at higher inclination angles bounce at magnetopause, but escape a second bounce at plasmapause as they travel above the poleward plasmasphere regions. Such a scenario explains observations of narrow band elements by C3 during the event of 16 July 2005 (spectrogram in Fig. 7c): C3 is placed above the South Pole, Fig. 6b showing CLUSTER satellites positions at 05:00 UT. At that time, C3 observes a narrow band element at ∼60 kHz, observed more faintly by C2 at about 40° south latitude (Fig. 7b). Directivity analysis indicates that corresponding ray paths point both towards dayside magnetopause. The interpretation proposed in Grimald (2007) is that a common source placed near equatorial plasmapause emits a 60 kHz wave in a beam of large enough latitudinal cone angle to illuminate the four CLUSTER spacecraft after a bounce at magnetopause (spectrograms for C1 and C4, not shown, display similar narrow band spectral features). This case event demonstrates that narrow band NTC elements can illuminate large regions of the magnetosphere placed at significant distance from the equator without loosing their characteristic spectral features. The magnetopause-magnetosheath boundary, populated by complex density structures, could play a role in angle scattering. According to the above scenario, the cohesion in latitude and frequency of the equatorial spots observed in the near equatorial outer plasmasphere is lost during propagation. Only the elements emitted at highest inclination are preserved from being trapped and superposed to radiations from other sources. Among those, only the elements emitted at highest intensity would keep a sufficient level to be observable after propagation.

4.3.2 Wide Banded NTC Emissions

NTC wide banded emissions (Fig. 7d) display a spectral pattern shown in better details in Fig. 11. They present two remarkable characteristic signatures, which, combined, allow

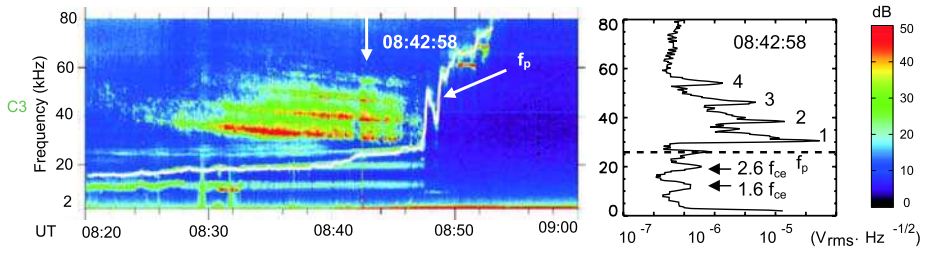

Fig. 11 WHISPER spectrogram on 30 December 2003 and individual frequency spectrum displaying four peaks above plasma frequency. (Adapted from Grimald et al. 2008)

to propose a precise location of the corresponding radio sources. The first characteristic signature is their frequency pattern, peaking at exact harmonics of a fundamental frequency, which is interpreted as the gyrofrequency at the source region. The second characteristic is the evolution of the fundamental frequency with respect to the view point of the observer, indicating that the NTC beams are narrowly collimated. During this event, C3 travels in the outer plasmasphere region, southern hemisphere, from 08:20 to 08:47 UT, at which time it crosses the plasmapause (Fig. 11). The other satellites cross the plasmapause within a few minutes time span. They form together a constellation of small size, C1 and C4 being ∼1200 km apart. The crossing area is placed at a ∼4.85 R_E geocentric distance, at $MLAT \approx 20°$ and ∼04:36 MLT. The f_{pe} measured by C3, plotted as a white solid line over the spectrogram, follows large density irregularities at plasmapause crossing, which can thus be better qualified as a structured plasmasphere boundary layer, PBL (Carpenter and Lemaire 2004). NTC emissions, present from ∼08:27 to 08:47 UT, form three clear bands (a fourth one is visible after 08:40 UT). An individual spectrum is shown on the right panel, where peaks of the four bands are labelled from 1 to 4. Compared observations of the four satellites demonstrate that the NTC beams encountered are stable in time and confirm that they are limited to a cone of small angle.

All peaks are placed at exact harmonics of a value df, which slowly decreases with increasing *MLAT* of observation. The frequency pattern observed contrasts with previous views, where frequencies emitted in a region of gyrofrequency f_{ce} are supposed to satisfy $f_n \approx (n + \frac{1}{2}) f_{ce}$ (Kurth 1982), not $f_n \approx n f_{ce}$. An additional experimental fact is the evolution of the NTC fundamental frequency encountered along the orbit element. The frequency df of the spectral pattern is higher than local gyrofrequencies and the difference progressively diminishes, until df meets local gyrofrequency at the plasmapause. This behaviour is the same in all observations of NTC features of the wide banded form. The spectrogram in Fig. 7d shows indeed another example in the northern plasmapause crossing of the same orbit. The interpretation proposed by Grimald et al. (2008) is that sources are placed at the intersection of the plasmapause magnetic shell (at $L \approx 5.5$ in this case) and of iso-gyrofrequency surfaces, leading to source positions at $MLAT \approx 20°$. This latitude is clearly higher than in the generally accepted view of equatorial sources. Together with the uncommon spectral characteristics (wide banded emissions, peaks at exact harmonics), it is possible that the generation mechanism is specific to that particular type of continuum radiation. A theory describing direct generation of electromagnetic O-mode emission at exact electron gyroharmonics, via mildly energetic electron beams in highly dense and warm plasma, has been proposed by Farrell (2001). CLUSTER observations could be related to this mechanism, and thus be a first confirmation of it.

5 Z-Mode

5.1 Active Z-Mode Experiments in Space Plasmas

Many spacecraft have generated Z-mode waves in the ionosphere and magnetosphere using radio sounders, among them the ISIS satellites and the OEDIPUS sounding rockets (e.g., Benson et al. 2006). This work has provided a powerful complement to observations of Z-mode waves of magnetospheric origin performed on rockets and satellites using plasma wave receivers (e.g., LaBelle and Treumann 2002). In this section we describe Z-mode experiments from IMAGE that provide new perspectives on the use of radio sounding at altitudes exceeding those accessible to previous missions and under comparatively more favorable conditions on transmitted frequencies and maximum observable echo delay.

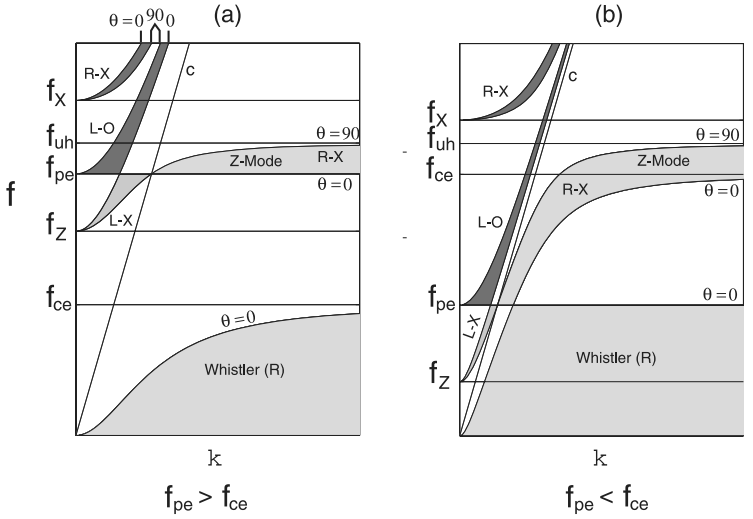

Fig. 12 Dispersion diagrams for waves in a cold plasma illustrating two conditions on the ratio of electron plasma frequency to electron gyrofrequency: (**a**) $f_{pe} > f_{ce}$ and (**b**) $f_{pe} < f_{ce}$. (Adapted from Goertz and Strangeway 1995)

By way of introduction to the IMAGE experiments, we show in Fig. 12 a schematic diagram that represents the dispersion relation for waves in a cold plasma, i.e., the scalar relation expressing the angular frequency ω in terms of the propagation vector $\boldsymbol{k}$, which is related to the refractive index $\boldsymbol{n}$ by $\boldsymbol{n} = \boldsymbol{k}c/\omega$. The diagrams represent two conditions on f_{pe}/f_{ce}, the ratio of electron plasma frequency to electron gyrofrequency. The case of $f_{pe} > f_{ce}$, represented in Fig. 12a, is typical of the plasmasphere above several 1000 km altitude, while the condition $f_{pe} < f_{ce}$, in Fig. 12b, is common at low altitudes poleward of the plasmapause and within a limited altitude range near 2000 km in the mid-latitude topside ionosphere.

5.2 Z-Mode Sounding from IMAGE

When the RPI instrument onboard IMAGE operates at altitudes above ∼20 000 km, its entire frequency range from 3 kHz to 3 MHz may fall within the domains of the free-space L-O and R-X wave modes (see Fig. 12). However, as the satellite moves to lower altitudes, some part of its operating frequency range begins to fall within the Z-mode and whistler-mode domains, and thus provides the possibility of using those wave modes to probe the plasmasphere and polar regions at altitudes less than ∼10 000 km. In response to this opportunity, new Z- and whistler-mode probing tools have been developed that complement the operation of RPI at higher frequencies as a conventional sounder. In this section we discuss three basic types of Z-mode echo activity: (i) ducted waves that are presumably constrained by field-aligned irregularities (FAI) to follow the direction of the magnetic field $\boldsymbol{B}$, (ii) non-ducted or "direct" echoes that follow ray paths extending in generally Earthward directions, (iii) scattered echoes that are believed to return to the spacecraft following interactions with FAI located in directions generally transverse to $\boldsymbol{B}$ from IMAGE. Comments on use of the echoes as plasma diagnostic tools will follow. We begin with the newly discovered phenomenon of bidirectional sounding along geomagnetic field lines using ducted Z-mode waves (Carpenter et al. 2003).

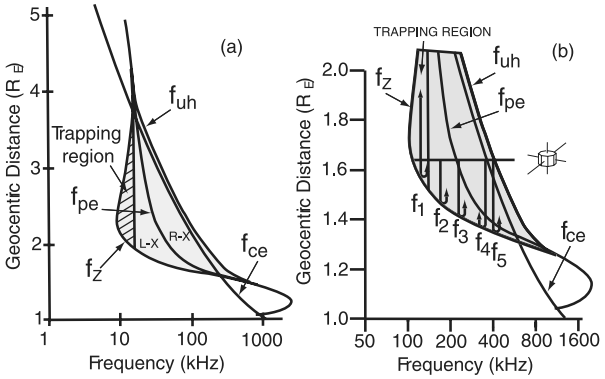

Fig. 13 (**a**) Model plot of the variation of key plasma parameters with geocentric distance along polar region field lines, showing by shading the Z-mode propagation cavity or trapping region. (Adapted from Gurnett et al. 1983.) (**b**) Number of idealized ray paths for Z-mode echoes in a particular case of sounding by RPI near $L = 3$ in the plasmasphere. (Adapted from Carpenter et al. 2003)

5.2.1 Ducted Echoes and the Z-Mode Propagation "Cavity"

Since plasma parameters such as f_{pe} and f_{ce} are known to decrease monotonically with altitude above the peak of the ionospheric F layer, and since the cutoff frequency f_Z for Z-mode propagation in a cold plasma is expressed in terms of f_{ce} and f_{pe} as:

$$f_Z = (f_{ce}/2)\left[-1 + \left(1 + 4\left(f_{pe}/f_{ce}\right)^2\right)^{\frac{1}{2}}\right], \tag{1}$$

one might expect f_Z to decrease monotonically with altitude as well. This is not true, however, as a number of authors have emphasized (Gurnett et al. 1983; LaBelle and Treumann 2002). In an altitude range extending from ~1500 km to above 5000 km, a Z-mode propagation "cavity" regularly exists over a wide range of latitudes. Waves originating at frequencies "within" the cavity can return from reflection points both above and below the wave source. This occurs in spite of the fact that the higher altitude reflection takes place in a plasma region less dense than the one at the source.

Figure 13 illustrates the cavity effect by altitude profiles of two frequencies, f_Z and f_{uh}, which (as shown in Fig. 12) locally delimit Z-mode propagation in a cold plasma. Also plotted versus geocentric distance are models of the plasma parameters f_{ce} and f_{pe}. The left-hand diagram was used in a study of natural wave activity in the auroral region, while the right-hand diagram represents conditions encountered by RPI during sounding operations at middle latitudes. It is clear that the curve for f_Z undergoes a minimum with altitude and that the minimum is reached within an altitude range in the topside ionosphere where the ratio f_{pe}/f_{ce} falls to a minimum value near or below unity. In Fig. 13a, hatching shows a range of frequencies at each altitude for which locally launched waves could be expected to return after reflection from points both above and below the source. Figure 13b shows schematically the propagation paths of a sequence of waves launched by RPI over a range of frequencies f_i from f_Z to f_{uh}. Waves at frequency f_1, just above f_Z, remain within the cavity and are reflected from both above and below RPI. In contrast, frequencies f_2, f_3, and f_4 exceed the upper frequency limit of the cavity and the corresponding waves reflect only at points below the spacecraft (assuming propagation in the general direction of $\boldsymbol{B_0}$).

Two examples of propagation within a cavity are illustrated in Figs. 14a–b on plasmagrams. On both records there is a band of no electromagnetic propagation at the lower frequencies, followed by a broad belt of noise that is attributed to a combination of scattering of RPI Z-mode pulses from irregularities located in directions generally transverse to $\boldsymbol{B_0}$

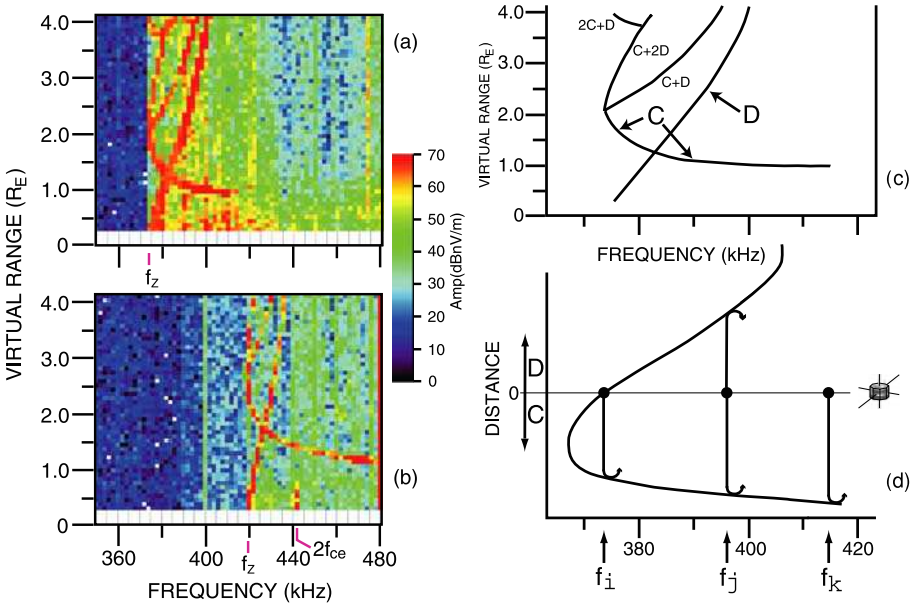

Fig. 14 (**a**)–(**b**) RPI plasmagrams from 28 July 2001 showing echo intensity in coordinates of virtual range (echo range at an assumed propagation velocity of c) versus transmitted frequency. Multicomponent Z-mode echoes are detected within the plasmasphere on successive soundings 2.5 minutes apart. (**c**)–(**d**) Interpretive model of the echoes of panel (**a**) for the case of a sounder location above the minimum in Z-mode cutoff frequency with altitude. The horizontal scale has been expanded by a factor of ∼2 to facilitate comparisons of echo delays. (Adapted from Carpenter et al. 2003)

(Muldrew 1969; Sonwalkar et al. 2004) as well as Z-mode noise from distant sources (Benson and Wong 1987; Benson 1993). The local Z-mode cutoff f_Z is found to be at or near the low-frequency edge of this band. Clearly outlined against the background noise are patterns of discrete echo traces that begin at f_Z.

An interpretation of the propagation paths of the discrete echoes shown in Fig. 14a is presented in Figs. 14c–d. Panel (**c**) is a rescaled tracing of the echo observed in Fig. 14a, while panel (**d**) shows on the same frequency scale the variation with altitude of f_Z in a postulated propagation cavity. The sounding is assumed to have taken place at an altitude above the minimum value of f_Z in the cavity. The upward and downward directions of propagation are identified as D and C, respectively. As the sounder frequency steps upward and reaches f_Z at ∼372 kHz, an echo f_i is received from a reflection altitude below IMAGE, forming the first elements of what becomes the down-sloping C echo trace. As the sounder continues above f_Z, echoes such as f_j begin to return from both higher and lower altitudes. The D echo forms near zero range and extends rapidly towards longer delays because of the small spatial gradients in f_Z encountered in the upward direction. Finally, the sounder frequency exceeds the peak value reached by f_Z above IMAGE, after which echoes such as f_k can return from below only.

The remarkable clarity of the echo traces suggests that the signals involved were guided or ducted by geomagnetic FAI, a phenomenon that has been found necessary to explain ground-observed whistler-mode signals (Smith 1961; Helliwell 1965). Ducting has recently been invoked to explain discrete O- and X-mode propagation from RPI (Reinisch et al. 2001; Fung et al. 2003) and was earlier identified from observations with ISIS satellites (Muldrew

1963; Loftus et al. 1966). The existence of a single discrete propagation path passing through the satellite position is indicated by the additional components in Fig. 14a identified as C+D, C+2D, and 2C+D in Fig. 14c. Each of the higher order components consists of some combination of the measured delays along the original C and D paths.

When RPI launches Z-mode waves from an altitude below the minimum of a Z-mode cavity, a quite different echo pattern is detected, but again there are well defined echo components from upward and downward directions as well as combinations of the two in the manner of Fig. 14c. Thus it was concluded that an explanation of events such as that of Fig. 14a requires the existence of both a propagation cavity as well as the occurrence of ducted propagation along the magnetic field (Carpenter et al. 2003).

5.2.2 Remote Sensing of Density Profiles Along the Geomagnetic Field Lines Above IMAGE

The propagation cavity is of geophysical interest for a number of reasons. In the case of the D component in Fig. 14c, representing upward propagation along the geomagnetic field from IMAGE, an inversion technique can be applied to determine the electron density profile along the path up to the altitude limit reached by the measured D component (for the conditions of Fig. 13a, that limit was predicted to be $\sim 4\ R_E$). The inversion method, described in Carpenter et al. (2003) was applied in the cases of Fig. 14a and Fig. 14b with the results shown in Fig. 15 on a plot of plasma density versus *MLAT* for $L = 2.1$ and 2.3. Density is shown from the position of IMAGE upward to a point ~5000 km above IMAGE along $\boldsymbol{B_0}$. For comparison, we show a profile for $L = 2.3$ from an empirical model obtained by Huang et al. (2004), based on X-mode sounding by RPI along multiple field-aligned paths on 8 June 2001. This profile (dashed curve) was scaled by a factor of 0.8 in order to show how well

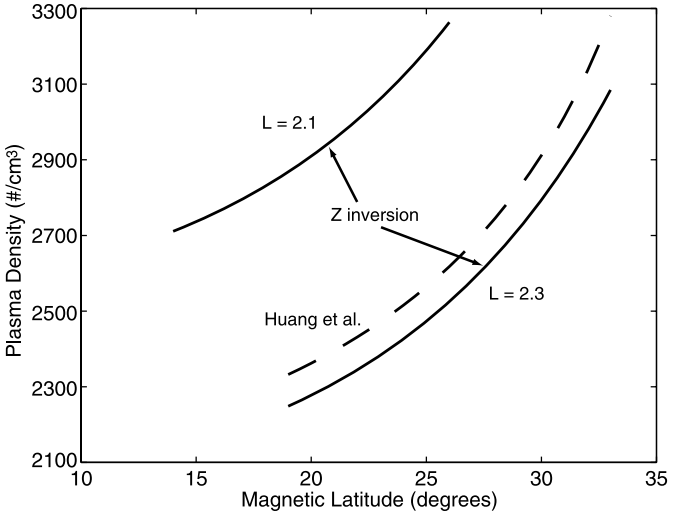

Fig. 15 Plots of electron density versus *MLAT* at $L = 2.1$ and 2.3, inferred from the upward propagating Z-mode signals illustrated in Figs. 14a–b and identified as component D in Figs. 14c–d. The *dashed curve* is for $L = 2.3$ from the Huang et al. (2004) model for a different date. That model is based upon inversion of free-space mode echoes that propagated to RPI along multiple field-aligned paths. (Adapted from Carpenter et al. 2003)

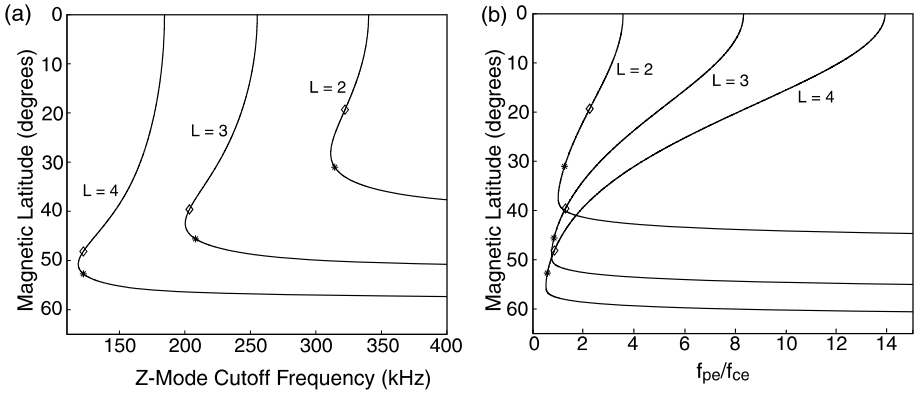

Fig. 16 (**a**) Plot of calculated Z-mode cutoff frequency f_Z versus *MLAT* along geomagnetic field lines at $L = 2$, 3, and 4, illustrating the widespread occurrence of a low-altitude minimum in f_Z within the plasmasphere. A dipole magnetic field model and a diffusive equilibrium density model were assumed. *Marks along the curves* show the locations of the 3000 km and 5000 km altitudes, respectively. (**b**) Corresponding plot for the ratio f_{pe}/f_{ce}. (Adapted from Carpenter et al. 2003)

the curves for $L = 2.3$ agree. Geomagnetic conditions relevant to the X (downward) and Z (upward) measurements ranged from calm (X profile) to quiet (Z profile) similar (near $L =$ 2.3, variations of 20–30% in the scale factor of the field-aligned electron density distribution with time, longitude, and disturbance levels are common (Carpenter and Anderson 1992)).

5.2.3 Remote Sensing of Plasma Composition Along the Geomagnetic Field Lines

The f_Z profile with altitude may be used as a diagnostic of plasma composition along $\boldsymbol{B_0}$ in the topside ionosphere region. If one assumes a three-component plasma in diffusive equilibrium above a reference altitude, a small positive electron temperature gradient along $\boldsymbol{B_0}$, and a known value of electron density at the magnetic equator, one then finds that in order to place a minimum in the f_Z profile in the 3000–5000 km altitude range where it has been observed, there are important constraints on the ion composition at the reference level.

Figure 16a is a plot of calculated f_Z profiles along $\boldsymbol{B_0}$ at three L values (2, 3, 4), with *MLAT* plotted on the vertical scale. In Fig. 16b are shown corresponding plots for the ratio f_{pe}/f_{ce}. Using the empirical model of electron density at the equator of Carpenter and Anderson (1992), an assumed ratio of He^+ to H^+ of 0.05 to 0.1 at the equator, an assumed value of 2 for the ratio of the electron temperature at the equator to the same temperature at the 1000 km reference level, it was found that a distribution of 82% O^+, 17% He^+ and 1% H^+ at the reference level would predict the profiles of Fig. 16a, which exhibit an f_Z minimum in the observed 3000–5000 km altitude range (Carpenter et al. 2003). The altitude of the minimum appeared to be sensitive to the choice of composition at the reference level, thus suggesting that further observations of this kind could be used to investigate the poorly known distribution of ions in the coupling region between the ionosphere and the plasmasphere.

Since little is known of the variations of the plasma properties along the geomagnetic field lines at altitudes below 5000 km, Z-mode probing of the kind described here can become a valuable adjunct to conventional radio sounding. The RPI data offer many as yet unexploited opportunities for application of the new method.

5.3 Additional Diagnostics Uses of Z-Mode Echoes

5.3.1 Non-Ducted or "Direct" Earthward Propagating Z-Mode Echoes

When IMAGE operated in the plasmasphere at $L < 3$ near 3000–4000 km altitude, the ratio f_{pe}/f_{ce} was frequently >1 but not $\gg 1$, and RPI was found to produce discrete, non-ducted echoes that followed ray paths extending generally Earthward from the satellite. Ducted echoes of the kind described above could also be present (as often happened in the outer plasmasphere in the case of simultaneous direct and ducted X-mode echoes). The direct Z-mode echoes represent low to medium altitude versions of phenomena familiar from topside sounding work (Carpenter et al. 2003).

Two examples of direct echoes recorded on 6 July 2001 are shown in Figs. 17a–b. They were recorded, respectively, at 3100 km altitude, $L = 2.4$ and at 4100 km altitude, $L = 2$. On both panels, a vertical spike identifies the local f_{pe}. There are two discrete Z-mode echoes, labeled Z and Z′. The Z′ trace begins at local f_{pe}, while the main Z trace rises slowly in travel time (range) from an origin at f_Z, inferred to be off scale to the left. The Z trace finally crosses over the Z′ trace and the two echoes then extend towards asymptotically long delays at a maximum frequency below f_{uh}. This maximum is associated with a limit on vertical incidence propagation (Jackson 1969).

5.3.2 Diagnostic Uses of Direct Z-Mode Echoes

The Z′ trace, as observed on topside sounders, was interpreted by Calvert (1966) as having propagated obliquely between the satellite and the O-mode reflection level at $f = f_{pe}$. The occurrence of two distinct Z-mode echo traces at $f > f_{pe}$ is a consequence of the anisotropy of the medium, such that ray paths involving two different initial wave normal angles can lead back to the satellite. The Z′ trace was explained by Calvert (1966) in terms of non-vertical propagation in a horizontally stratified ionosphere. The "reflection" does not occur at a Z-mode cutoff, but is in fact the result of refraction such that the ray path reverses direction at a level where $f = f_{pe}$. The Z′ trace can be expected to provide information that is independent of results obtained from inverting the regular Z-mode echo. Note that the trace delays are substantially longer than those of an O echo at common frequencies, accentuated by a Z-mode transition at f_{pe} from a fast mode to a slow mode. These traces are therefore more useful (given the minimum 3.2-ms RPI pulse length and receiver sampling frequency) than the O- and X-modes of the transitional altitude region. Analysis of Z and Z′ traces for particular RPI echo observations remain to be performed. However, the information on local f_{pe} provided by the Z′ trace is particularly helpful for plasma diagnostics at altitudes near 3000–5000 km in the plasmasphere, where the condition $f_{pe}/f_{ce} \approx 1$ is common and thus where estimates of f_{pe} based upon measurements of f_{uh} by passive probing may not provide desired accuracy.

5.3.3 Scattered Z-Mode Echoes

In the plasmasphere at altitudes such that the Z-mode frequency domain was broad enough to occupy a significant range of frequencies below f_{uh}, a background of diffuse Z-mode echoes was almost always present, whether or not discrete echoes were received. When discrete echoes were present, they were typically ∼20 dB above the levels of the diffuse background, as illustrated in Figs. 17a–b.

Plasmagrams from the low altitude polar regions where $f_{pe}/f_{ce} < 1$ regularly exhibited diffuse echoes with the forms illustrated in Figs. 17c–d. Distinctive features included:

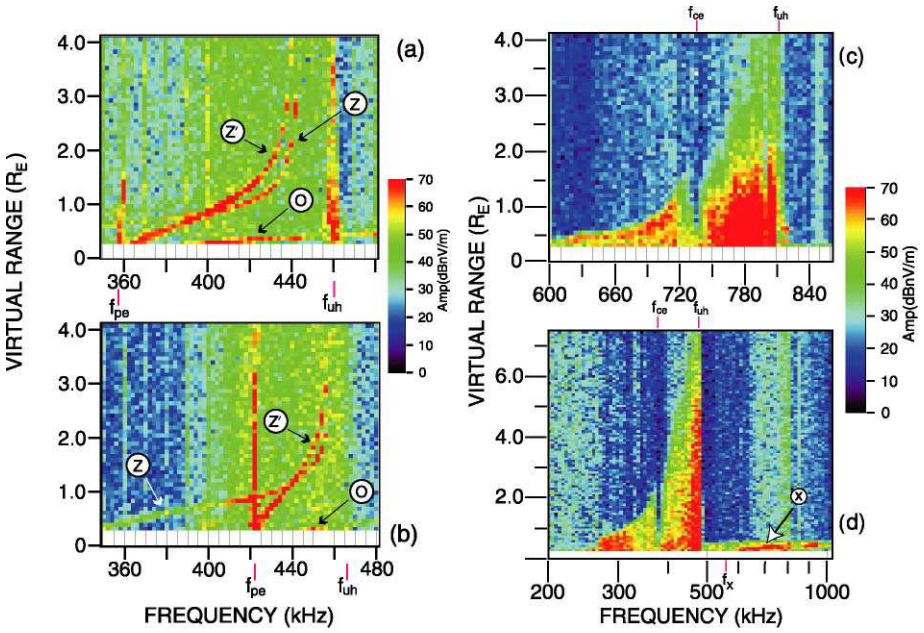

Fig. 17 (**a**)–(**b**) RPI plasmagrams illustrating Earthward propagating discrete Z and Z′ echoes seen against a background of diffuse Z-mode noise. (**c**)–(**d**) RPI plasmagrams typical of low altitude polar regions showing diffuse Z-mode echo activity useful for determining f_{ce} and f_{pe}. (Adapted from Carpenter et al. 2003)

(i) echoes with ranges substantially longer than those of order 0.5 R_E to be expected for Earthward propagating O- and X-modes, (ii) echo activity extending from the lowest detectable range to a maximum value that increased with sounding frequency, (iii) a gap or weakening of the echoes at an intermediate frequency, and (iv) a relatively abrupt upper frequency limit, inferred to be f_{uh}.

Sonwalkar et al. (2004) performed a ray tracing analysis of diffuse echo events such as those of Figs. 17c–d, finding that for Z-waves below f_{ce}, Earthward propagation to turning points in the general $\boldsymbol{B}$ direction could not be excluded, but such propagation could not explain the wide time spreading of the Z echoes and would in any case tend to be masked by them. The authors pointed out that because of the variation with altitude of the Z-mode refractive index surface, at any given frequency f below the local f_{ce}, Z-mode waves can spread out in all directions. Some of these waves, in particular those propagating in directions from IMAGE that are approximately perpendicular to $\boldsymbol{B_0}$ are scattered by FAI and can return to the satellite. Meanwhile, for frequencies between f_{ce} and f_{uh}, Z-mode propagation is allowed within a resonance cone that permits propagation in the direction roughly perpendicular to $\boldsymbol{B_0}$. These waves can also lead to echoes after scattering from FAI, as has been documented by topside sounders (e.g., Muldrew 1969; James 1979).

5.3.4 Diagnostic Uses of Scattered Z-Mode Echoes

In a case study similar to those of Figs. 17c–d, Sonwalkar et al. (2004) found that the observed echo delays could be explained by irregularities located within ∼20 to 3000 km

from IMAGE. The overall distribution of time delays was consistent with propagation theory. For frequencies above f_{pe} (true of most of the observed echoes in Figs. 17c–d) we have a slow Z-mode, with group velocity decreasing and time delay increasing with frequency for any given wave normal direction. Above f_{ce} and close to f_{uh}, the Z-mode becomes quasi-electrostatic and much longer time delays are expected, as observed. The weakening of the echoes at a frequency corresponding to local f_{ce} (Carpenter et al. 2003) is believed to be related to the change in refractive index surface from a closed to an open topology at f_{ce}, as discussed by Gurnett et al. (1983) and LaBelle and Treumann (2002).

In the polar regions at altitudes in the 1000–4000 km range, where f_{pe}/f_{ce} is typically <1, f_{uh} as observed through passive scanning may no longer be a useful source of information on f_{pe}, being dominated by the value of f_{ce}, and also because of interfering auroral noise that may be present near 1 MHz. In such cases, Z-mode echoes such as those in Figs. 17c–d can provide a useful means of measuring local f_{pe} through f_{ce}, indicated by the gap in echoes, and by the upper hybrid resonance spike, which is often marked by a an abrupt drop in intensity by $\sim$40 dB on its high frequency side.

6 Whistler-Mode Soundings at Altitudes Below ∼5000 km

New whistler-mode (WM) tools for probing at altitudes below $\sim$5000 km have been developed during work on data from the RPI sounder onboard IMAGE (Reinisch et al. 2000). These tools are based upon various physical mechanisms involved in the reflection and return propagation to IMAGE of WM waves transmitted by RPI. As described by Sonwalkar et al. (2009), these mechanisms include: (i) magnetospheric reflection (MR) at locations where the wave frequency is less than or equal to the local f_{lh}, (ii) specular reflection (SR) from the steep density gradients at the bottom side of the ionosphere, and (iii) multipath propagation and scattering due to the presence of density irregularities that are often field-aligned. In most cases, MR- and SR-WM echoes are distinguished by the distinct upper and lower limits on their frequencies, limits that depend on the value of the lower hybrid resonance at the altitude of the satellite. The two echo types also differ widely in terms of their frequency-versus-time properties, which can be separately explained through ray tracing in models of the plasma environment below $\sim$5000 km. Preliminary descriptions of echoes attributed to specular reflection, multipath propagation and scattering have been provided by Sonwalkar et al. (2009). Here we limit ourselves to a brief description of the various echoes and their apparent diagnostic potential.

6.1 Spreading of RPI Whistler-Mode Echoes in Time Delay

Sonwalkar et al. (2009) report that the spectra of all types of WM echoes detected by RPI are sensitive to the presence of FAI, and that they manifest this sensitivity on plasmagrams by various amounts of spreading in travel time, varying from 5–10 ms for the most discrete cases to 40 ms and more for the most diffuse events. The spreading can be occasioned by propagation on multiple paths through irregular regions with cross-$\boldsymbol{B_0}$ scale sizes of the order of 1–10 km or by forward and backward scattering from irregularities with scale sizes of the order of 10–100 m. Scattering may involve changes in group velocity at the time of coupling between a predominantly electromagnetic wave and a quasi-electrostatic wave at an irregularity boundary. For convenience, MR- and SR-WM echoes have been further classified by Sonwalkar et al. (2009) as either discrete, multipath or diffuse according to the amount of travel time spreading.

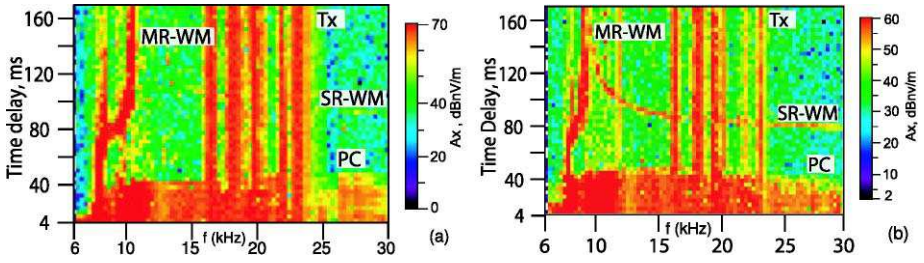

Fig. 18 (**a**) RPI plasmagram showing an MR-WM echo recorded on 23 October 2005 at 10:22:46 UT. Fixed frequency transmitter signals (Tx) are present, as well as a cluster of proton cyclotron (PC) echoes at delays <40 ms. (**b**) RPI record on 26 October 2005 at 09:32:42 UT with MR-WM echo and a well defined SR-SW echo, as well as Tx and PC echoes. (Adapted from Sonwalkar et al. 2009)

6.2 Examples of Magnetospherically Reflected and Specularly Reflected Whistler-Mode Echoes

Examples of MR- and SR-WM echoes are shown on RPI plasmagrams in Fig. 18. These records plot echo travel time in ms versus RPI transmitter frequency, which was stepped each 250 ms in 300 Hz increments from 6 to 63 kHz (only the range 6–30 kHz is displayed). In Fig. 18a, recorded at ∼2650 km and $L \approx 2.4$, a discrete MR-WM echo appears between ∼7.5 and ∼11 kHz. At ∼7.5 kHz the echo begins at the shortest delay displayed (∼4 ms) and extends with decreased amplitude to the top of the record. Beginning at a delay of ∼80 ms, the echo branches towards higher frequencies and extends to an undefined limiting delay at ∼11 kHz. Meanwhile, ground-based transmitter signals (Tx) appear between 16 and 23 kHz, extending over the full time-delay range available. Also present at frequencies above 8 kHz and at delays less than ∼40 ms is a band of proton cyclotron (PC) echoes (see Sect. 7), which are attributed to excitation of ambient protons in the antenna sheath by the leading edge of each 3.2-ms transmitter pulse (Carpenter et al. 2007).

Figure 18b, recorded at ∼2550 km and $L \approx 2.3$, also shows an MR-WM event, in this case with delimiting frequencies of ∼7 and ∼9 kHz. Transmitter signals are again present, although those near 16 and 23 kHz exhibit less spreading in frequency than those in Fig. 18a. A highlight of this record is a discrete SR-WM echo, which exhibits delays near 80 ms between ∼20 and 30 kHz but curves towards longer delays as it approaches the 9 kHz high frequency limit of the MR-WM echo.

Although examples of discrete, multipath, and diffuse SR-WM echoes were shown previously by Sonwalkar et al. (2004), RPI WM-echoes have now been observed much more extensively and categorized much more completely as a result of sounding operations at frequencies below 60 kHz in 2004 and 2005 (Sonwalkar et al. 2009).

6.3 Specularly Reflected Whistler-Mode Echoes

RPI soundings at WM frequencies regularly exhibit echoes that extend over a wide range of frequencies and are interpreted as having reflected from the steep density gradients at the bottom side of the ionosphere (Sonwalkar et al. 2004). Such SR-WM echoes often accompany MR-WM echoes, as illustrated by the example of Fig. 18b. Since an SR-WM echo provides an integral measure of the electron density between IMAGE, say at ∼3000 km, and the ionosphere at ∼100 km, it is particularly sensitive to density levels at altitudes below those reached by a simultaneous MR-WM event (∼1500 km). Thus its dispersion properties

may be used to constrain the density/plasma composition model that is found most consistent with the MR-WM event.

6.4 Magnetospherically Reflected Whistler-Mode Echoes and the Lower Hybrid Resonance

It may be seen in Fig. 12 that the Z-, O-, and X-mode dispersion diagrams each exhibit low frequency cutoffs, at which the refractive index goes to zero and the wave is reflected. That type of cutoff does not occur for WM waves. When the presence of ions is taken into account, the dispersion of WM is modified (not included in Fig. 12) such that WM waves, propagating at high wave normal angles with respect to $\boldsymbol{B_0}$ can undergo magnetospheric reflection at altitudes where $f \approx f_{lh}$. For an electron, H^+, He^+, and O^+ plasma, f_{lh} is given by the following equation:

$$\frac{1}{m_{\text{eff}}(m_p/m_e f_{lh}^2)} = \frac{1}{f_{pe}^2} + \frac{1}{f_{ce}^2}, \tag{2}$$

where m_p/m_e is the proton/electron mass ratio and the effective ion mass m_{eff} is defined as:

$$\frac{1}{m_{\text{eff}}} = \frac{\alpha}{1} + \frac{\beta}{4} + \frac{\gamma}{16}, \tag{3}$$

where α, β and γ are, respectively, the fractional abundances of H^+, He^+ and O^+.

The magnetospheric reflection is actually a refraction caused by a topological change and decrease in the size of the refractive index surface as the WM wave at large wave normal angle propagates from a region where $f_{lh} < f$ to a region where $f_{lh} > f$. When $f_{lh} < f$, the refractive index surface is "open", with a so called resonance cone (delimiting an angular region of no propagation), and when $f_{lh} > f$, it is "closed", such that the propagation is allowed at all angles with respect to $\boldsymbol{B_0}$ (Kimura 1966).

MR-WM echoes may exhibit a variety of discrete or diffuse spectral forms. MR-WM echoes with clearly identifiable forms, such as those illustrated in Fig. 18, tend to present a nose-like shape on plasmagrams because of extended time delays at the form's minimum and maximum frequencies. Those limiting frequencies, usually separated by a few kHz, are associated, respectively, with f_{lh} at the location of the satellite (the lower frequency), often near 6 kHz, and the maximum value of f_{lh} along the field line extending Earthward from IMAGE (the upper frequency), often in the range 9–12 kHz.

Key formative elements in the MR-WM echo phenomenon are believed to be: (i) propagation of RPI WM waves at high wave normal angles, near the so called resonance cone around the direction of the magnetic field; (ii) reflection of the waves near an altitude where the wave frequency is lower than but close to local f_{lh}; (iii) in the case of multipath or diffuse MR-WM echoes, refraction or scattering of the waves through encounters with FAI such that the echoes reach the satellite with varying time delays.

6.5 The Diagnostic Potential of Magnetospherically Reflected and Specularly Reflected Whistler-Mode Echoes

The time-delay-versus-frequency properties of MR-WM echoes provide a measure of f_{lh} along the field line passing through the satellite. The lower cutoff frequency of MR-WM echo, f_{lh} at the satellite, provides a measure of m_{eff} at that higher altitude where H^+ and He^+ may be dominant. The upper frequency cutoff of the MR-WM echo provides a measure

of the m_{eff} of the plasma in the important transition region (∼1000–1500 km) between the O^+ dominated lower ionosphere and the H^+ dominated region at higher altitudes. This can be seen from expressions of (2) and (3) for f_{lh} and m_{eff}, respectively. It is clear that within altitude ranges over, which the r.h.s. of (2) does not change appreciably, the value of f_{lh} will be sensitive to changes in m_{eff} (by as much as a factor of 16) associated with altitude variations in ion composition.

Ray tracing simulations of the dispersion properties of simultaneously observed MR- and SR-WM echoes may be used for remote sensing of the ion composition and total electron density along a field line between the bottom of the ionosphere and the position of IMAGE (Sonwalkar et al. 2009). As noted, the MR-WM echo provides measures of the local m_{eff} and of m_{eff} at the altitude of the maximum f_{lh} below the satellite (in the vicinity of 1000 km). Meanwhile, the SR-WM echo, because of its noted sensitivity to the ionospheric electron density profile, provides an important constraint on the overall plasma density model used in the ray tracing simulation. Assuming a diffusive equilibrium model for magnetospheric density (see also Pierrard et al. 2009, this issue), Sonwalkar et al. (2009) developed a ray tracing method that determines the diffusive equilibrium model parameters such that the MR- and SR-WM dispersion and frequency cutoffs calculated from ray tracing simulations agree with those observed within experimental uncertainties. Applying this method in two specific instances, including the case shown in Fig. 18b, Sonwalkar et al. (2009) determined within 10% the electron and ion (H^+, He^+, O^+) densities along $\boldsymbol{B_0}$ ($L \approx 2$) passing through the satellite between 3000 km and 90 km.

7 Proton Cyclotron Echoes and a New Resonance

At altitudes ranging from ∼1500 km to 20000 km in the plasmasphere, the RPI instrument onboard IMAGE can couple strongly to protons in the immediate vicinity of the satellite as it transmits 3.2-ms pulses and scans from 6 to 63 kHz or 20 to 326 kHz. Those soundings also give rise to a new resonance at a frequency ∼15% above f_{ce} (Carpenter et al. 2007). The coupling to protons is revealed in echoes that arrive at multiples of the local proton gyroperiod t_p. Lower-altitude (<4000 km) versions of several of these proton cyclotron (PC) echo forms were observed in the topside ionosphere by sounders in the ISIS satellite era, among them discrete echoes in the WM domain below f_{ce} and in the nominally non-electromagnetically propagating domain above f_{ce} (e.g., Oya 1978; Horita 1987; Muldrew 1998). Also seen on ISIS satellites were spur-like broadenings of resonances such as the one at f_{pe} (e.g., King and Preece 1967; Benson 1975; Horita 1987).

7.1 The f_{ce}^+ Echo

Figure 19a shows an example of what has been called an f_{ce}^+ echo, a phenomenon often observed in the plasmasphere by RPI at frequencies from ∼10 to 20% above f_{ce} (Carpenter et al. 2007). The plasmagram presents time delay from ∼40 to 100 ms versus frequency from 20 to 50 kHz. IMAGE was at $L \approx 3.7$, well inside an extended plasmasphere at an altitude of ∼14 000 km and in the mid-afternoon sector. The local electron density was ∼560 cm^{-3}. The local value of f_{ce} is well defined at ∼30 kHz by a resonance spike, a type of response that is regularly present on sounder records from the topside ionosphere (Benson 1977, and references cited therein). A band of WM noise extends upward in frequency to a relatively sharp cutoff at ∼26 kHz. This band is attributed to multi-path propagation and scattering of a variety of WM signals, including naturally occurring wave emissions, WM emissions

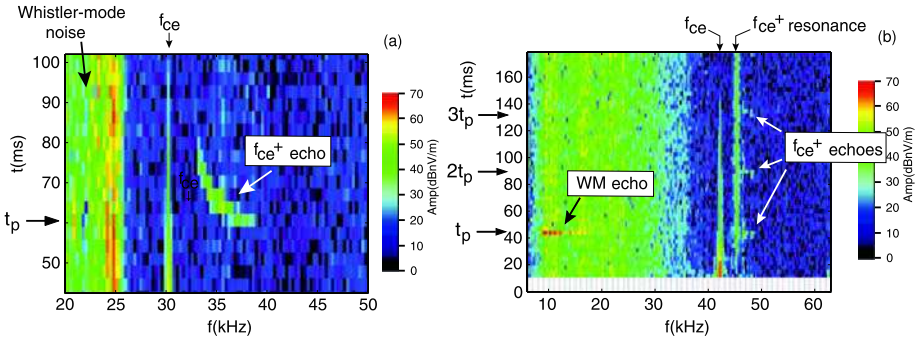

Fig. 19 (**a**) Portion of an RPI plasmagram showing a well defined proton cyclotron (PC) echo that exhibits extended delays at frequencies just above f_{ce} and then approaches a constant delay at the local value of the proton gyroperiod t_p. (**b**) RPI plasmagram illustrating three effects, a PC echo in the WM domain, a resonance at a frequency just above f_{ce}, and discrete echoes at multiples of t_p. (Adapted from Carpenter et al. 2007)

triggered by lightning, and multiple WM signals from ground-based transmitters. In the figure, the f_{ce}^{+} echo first appears at ∼33 kHz, ∼3 kHz above f_{ce}, and extends to 39 kHz. It exhibits a time-delay-versus-frequency form something like that of a hockey stick, at first falling steeply in delay with increasing frequency and then curving to reach a constant delay of ∼61 ms. That delay corresponds closely to the local $t_p = 1836/f_{ce}$. On IMAGE the occurrence rates of PC echoes above f_{ce} were highest during periods when the angle ϕ between the spacecraft velocity vector and the geomagnetic field $\boldsymbol{B_0}$ was small, near 20°, but on occasion such echoes were detected when ϕ approached 90°.

7.2 The f_{ce}^{+} Resonance

A new phenomenon, called the f_{ce}^{+} resonance, has been observed at a frequency ∼15% above f_{ce} (Carpenter et al. 2007). This resonance is apparently confined to altitudes above ∼7000 km. It is illustrated by the plasmagram of Fig. 19b, which displays time delay from 0 to 178 ms versus frequency from 6 to 63 kHz. At the time of the figure, IMAGE was at $L \approx 3.6$ and at an altitude of ∼12 000 km, well inside the plasmasphere. Three echo forms appear, a WM echo, multiple f_{ce}^{+} echoes, and an f_{ce}^{+} resonance. The WM echo, extending from ∼9 to 17 kHz at a constant delay of ∼45 ms, appears as a discrete intensity enhancement within the usual WM noise background. The value of f_{ce} is well marked by a tapered resonance spike at ∼42 kHz. Approximately 3 kHz above f_{ce} is an f_{ce}^{+} resonance. This resonance differs from the spike at f_{ce} in that it extends to the top of the record and (in this case) is not clearly defined in the first ∼30 ms after the beginning of the transmitter pulse. Along the high-frequency side of the f_{ce}^{+} resonance are f_{ce}^{+} echoes that arrived at multiples of t_p, the first at ∼44.5 ms, the second at ∼89 ms, and the third at ∼133 ms. There are differences in amplitude among the echo forms illustrated in Fig. 19b: Portions of the WM echo near 10 kHz are ∼10–15 dB stronger than the f_{ce}^{+} resonance or f_{ce}^{+} echoes.

7.3 Whistler-Mode Proton Cyclotron Echoes

Of special interest are exceptionally strong echoes in the WM domain near 10 kHz (Carpenter et al. 2007). On a given orbit, these invariably appeared at altitudes ∼5000 km and below

and could be detected at altitudes up to ∼12 000 km. In some cases, the echoes appeared on plasmagrams showing other PC echo activity (see Fig. 19b). Most of the WM echoes observed thus far were found within the plasmasphere or the PBL, at *MLAT* between −60° and +60°. They were evident on occasion at higher latitudes and over the polar regions, but tended to be obscured there by strong natural WM noise with power spectral density 10 dB or more above the noise levels in the plasmasphere. Samplings showed strong WM echo activity at several widely spaced MLT, suggesting that such echoes may occur in all local time sectors.

At each frequency during a given sounding, WM echoes tended to repeat at time delays that were multiples of t_p. Figure 20 displays such effects on plasmagrams recorded on three different orbits at altitudes ∼10 700, ∼7700, and ∼4200 km, respectively. As altitude decreased, the inter-echo time delay decreased accordingly. In the stronger magnetic fields below ∼3000 km altitude, the time interval at each frequency between successive high-order echoes fell below 6.4 ms, the minimum interval allowing separation of echoes by one 3.2-ms time delay pixel, and individual echoes could no longer be resolved. In such cases, the echoes formed a "continuous" response extending to multiple values of t_p. When

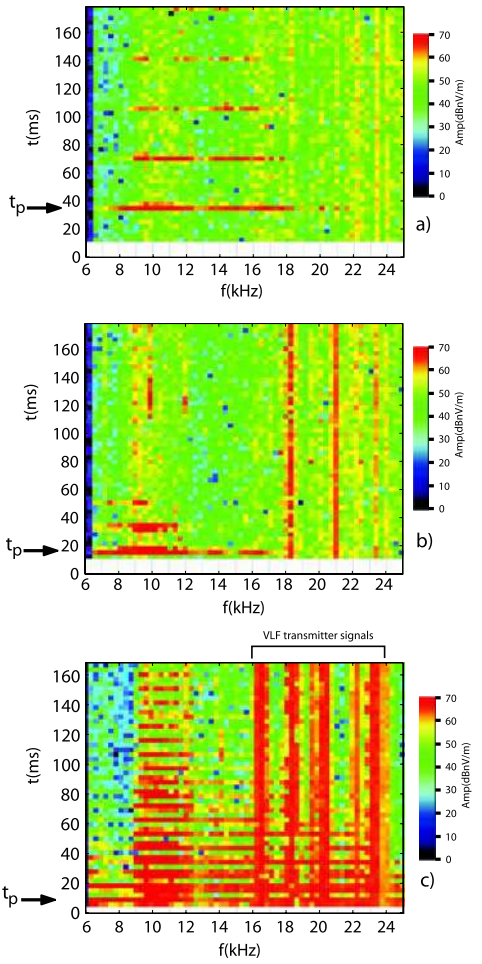

Fig. 20 RPI plasmagrams showing PC echoes in the WM domain, repeating at multiples of the local t_p. The examples were recorded on three different orbits at altitudes ∼10 700 km (**a**), ∼7700 km (**b**), and ∼4200 km (**c**). The *vertical lines* between 16 and 24 kHz in panel (**c**) represent WM transmissions from ground transmitters. (Adapted from Carpenter et al. 2007)

the angle ϕ was near a local minimum of order 10°, WM echoes were observed to repeat at multiples of t_p up to 15 or more. The data indicate that WM echo detection near 10 kHz was largely confined to a region of radius ∼300 m around the field line of excitation, and that the peak excitation of the protons occurred as a transient event at the beginning of each radio frequency (rf) pulse.

7.4 Comments on Physical Mechanisms of Proton Cyclotron Echoes

Carpenter et al. (2007) suggest that PC echoes and the new resonance are driven by a variety of mechanisms. Time delay measurements of WM echoes near 10 kHz indicated that the energization of the protons by a given 3.2-ms sounder pulse was essentially a transient process that occurred at the beginning of the pulse, and to that extent did not involve replication of the rf pulse by the echo. It was inferred that there is spatial bunching of accelerated protons during the initial formation of an electron sheath around the positive-voltage antenna element. The gyrating protons then produce a series of electrostatic pulses at multiples of t_p. Tight bunching of accelerated protons does not occur during the remainder of a 3.2-ms pulse, since ambient electrons never again appear close to the antenna during this period (due to the acceleration of protons during negative half cycles, protons near the antenna have a wide distribution of energies and thus are not subject to tight bunching during subsequent positive half cycles).

Most WM echoes were observed when IMAGE moved at low angles to $\boldsymbol{B_0}$ and was within a distance of ∼300 m transverse to the field line of original excitation of the plasma. The echoes showed no measurable WM propagation delay from a source, which is consistent with the inferred electrostatic nature of the echoes and the closeness of the antenna to the source field lines. The high intensity of the lower-order WM echoes, which regularly saturated the RPI receiver near 10 kHz, as well as the lack of detectable WM echo activity above 12 000 km altitude, were attributed in part to the fact that proton energization at the leading edge of the sounder pulse was at maximum levels when the rf of the pulse was below, but near, the local proton plasma frequency $f_{pp} = f_{pe}/43$. f_{pp} reaches a maximum of ∼13 kHz at the lower IMAGE altitudes, but falls below 6 kHz (the lowest sounder operating frequency) above 12 000 km.

In contrast to WM echoes, f_{ce}^{+} echoes occurred at frequencies well above f_{pp} and were thus outside the range where significant transient energization was expected. Also in contrast to WM echoes, f_{ce}^{+} echoes appeared to replicate the sounder pulse frequency and in so doing experienced large frequency-dependent increases in travel time as f_{ce} was approached from above. This dispersion as well as a year-to-year decrease in f_{ce}^{+} echo activity with increasing separation of the antenna from the "excited" field lines, is consistent with an explanation of f_{ce}^{+} echoes observed in the ISIS satellites in terms of thermal-mode propagation from a perturbed proton distribution (Muldrew 1998). A possible source of energy for the comparatively weak f_{ce}^{+} echoes is the quasi-static electric field that exists in the ion sheath that surrounds each antenna element in the immediate aftermath of an rf pulse, as discussed in Carpenter et al. (2007).

The new resonance above f_{ce} suggested the existence of a ringing phenomenon in the plasma that is unique to altitudes above ∼7000 km. The resonance mechanism appears to operate independently of the f_{ce}^{+} echo mechanism, although both phenomena were found within a similar range of frequencies above f_{ce}. The long enduring nature of the resonances, lasting at times for at least 300 ms, suggests that the perturbed plasma environment in which the ringing occurred was carried with the spacecraft a kilometer or more beyond the ∼300 m transverse distance within which the WM echoes were found. The collapse of the ion sheath

following an rf pulse may provide energy for the ringing process. This collapse may on occasion delay the onset of the detected resonance, in the manner proposed by Muldrew (1972), who argued that in the case of certain ionospheric resonances, the antenna sheath may temporarily exclude very short wavelength stimulated waves.

Previously suggested processes that were considered relevant to PC echoes above f_{ce} and to the new resonance include: (i) coupling between an excited Z-mode wave and longitudinal plasma waves (Benson 1975), (ii) accumulation of negative charge on an electric antenna during an rf pulse (Oya 1978), and (iii) Bernstein-mode propagation to an antenna from an excited proton population (Muldrew 1998).

8 Chorus

8.1 Observations of Whistler-Mode Chorus Emissions by CLUSTER

Whistler-mode (WM) chorus emissions are electromagnetic waves in a frequency range from a few hundreds of Hz to several kHz. Chorus was first observed on the ground (Storey 1953) but spacecraft observations in the Earth magnetosphere are also frequent. Chorus often contains many distinct short-duration wave packets, which change their frequency at time scales of a fraction of 1 s (see reviews by Sazhin and Hayakawa 1992; Omura et al. 1991). The generation mechanism of chorus is not yet well understood. It is most often accepted that chorus is generated by a nonlinear process (Nunn et al. 1997; Trakhtengerts 1999; Trakhtengerts et al. 2004), which involves the electron cyclotron resonance of WM waves with energetic electrons.

WM chorus emissions are receiving an increased attention in connection with the acceleration of energetic electrons in the radiation belts (e.g., Horne et al. 2005). Important new results on chorus has been obtained with wave and particle instruments onboard CLUSTER as well as with the DOUBLE STAR spacecraft, which routinely detects chorus emissions, and with the low altitude DEMETER spacecraft. This research provided us with tests of the existing theories of the chorus source mechanism and particle acceleration, and further motivated theoretical work. In the next two subsections we discuss results, which can have implications for plasmaspheric physics, i.e., results on position and size of the chorus source region and on propagation of chorus from its source region.

8.2 Position and Size of the Chorus Source Region

During the period of very close separation distances of the CLUSTER spacecraft (of the order of hundreds of km), very similar chorus emissions were observed in their generation region close to the magnetic equatorial plane at a radial distance of 4.4 R_E (Fig. 21). Both linear and rank correlation analysis have been used by Santolík and Gurnett (2003) and Santolík et al. (2004a) to define perpendicular dimensions of the sources of lower-band chorus elements below $\frac{1}{2} f_{ce}$. Correlation was significant in the range of separation distances of up to 260 km parallel to the field line and up to 100 km in the perpendicular plane. At these scales, the correlation coefficient was independent on parallel separations and decreased with perpendicular separation. This characteristic perpendicular scale varied between 60 and 200 km for different data intervals inside the source region. This variation was consistent with a simultaneously acting effect of random positions of locations at which the individual coherent wave packets of chorus were generated. The statistical properties of the observations were consistent with a model of the source region assuming individual sources of separate wave packets

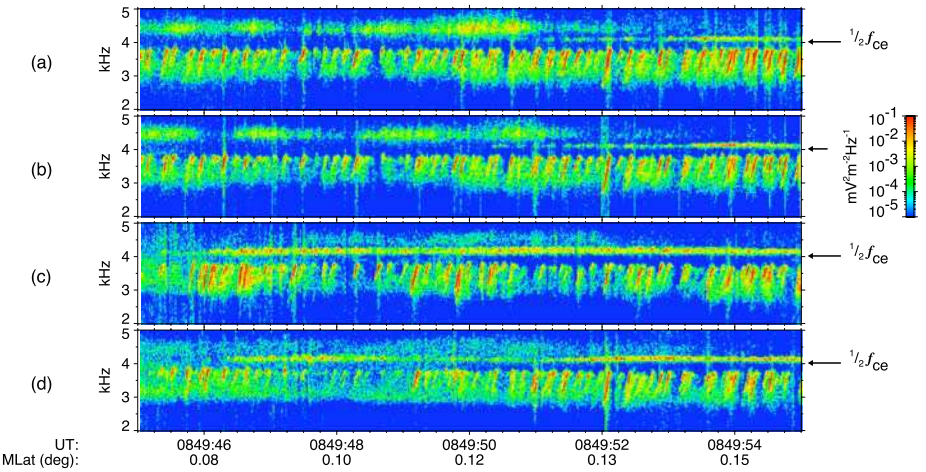

Fig. 21 Detailed time–frequency power spectrograms of electric field fluctuations in the source region recorded by the WBD instruments onboard the four CLUSTER spacecraft on 18 April 2002. Panels (**a**)–(**d**) show data from C1–C4, respectively. *Arrows* indicate local $\frac{1}{2} f_{ce}$ for each spacecraft. *MLAT* is given on the bottom for C1. Radial distance is 4.4 R_E, and MLT is 21:01 during this interval. (Adapted from Santolík and Gurnett 2003)

as Gaussian peaks of power radiated from individual active areas with a common half-width of 35 km perpendicular to the magnetic field (Santolík et al. 2004a). This characteristic scale was comparable to the wavelength of observed WM waves.

Central position of the source region from multipoint measurement of the Poynting flux is located close to the magnetic equatorial plane (Parrot et al. 2003; Santolík et al. 2003, 2004b, 2005a). Observed spatio-temporal variations of the direction of the Poynting flux consistently show that the central position of the chorus source fluctuates at time scales of minutes within a few thousands of km of the magnetic equator (Fig. 22). The typical order of magnitude of the speed of this motion is 100 km s^{-1}. Note that this is a global speed of motion of the central position of the entire source region. It has been determined from the Poynting flux measurements where we always average propagation properties of several chorus wave packets. This speed is thus different from the speed of motion of individual sources discussed by Inan et al. (2004), Platino et al. (2006), Breneman et al. (2007) and Chum et al. (2007). Estimates of the electromagnetic planarity can be used to characterize the extent of the source in the direction parallel to the field line, obtaining at a radial distance of ∼4 R_E a source extent of 3000–5000 km (Santolík et al. 2004b, 2005a). This is consistent with theoretical results (Trakhtengerts et al. 2004) and with recent numerical simulations (Omura et al. 2008).

Santolík et al. (2005b) used the first measurements of the STAFF/DWP instrument on the DOUBLE STAR TC-1 spacecraft to investigate radial variation of intensity of WM chorus for L between 4 and 12. The chorus events showed an increased intensity at $L > 6$, consistent with intensifications of chorus, which were previously observed closer to the Earth at higher latitudes.

8.3 Propagation of Chorus From its Source Region

The four CLUSTER spacecraft observed that intense chorus waves propagate away from the equator simultaneously with lower-intensity waves propagating towards the equator (Parrot

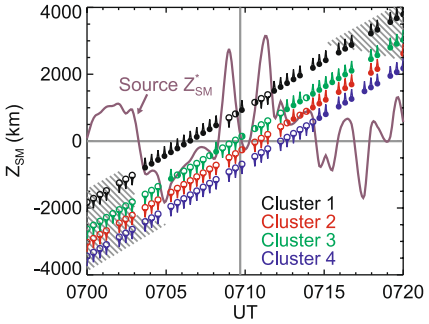

Fig. 22 Z_{SM} coordinate of the four CLUSTER spacecraft during the geomagnetic storm on 31 March 2001 as a function of time. Sign of the parallel component of the Poynting flux is shown by *downward arrows* attached to the *open symbols*, and by *upward arrows* with the *solid symbols*, for southward and northward components, respectively. The *half-filled symbols with no arrows* indicate that the sign cannot be reliably determined. *Horizontal grey line* is at the magnetic equator, *vertical grey line* shows the time when center of mass of the four spacecraft crosses the equatorial plane. *Shaded areas* bound the regions of low values of the electromagnetic planarity. *Purple line* shows the calculated position where the Poynting flux changes its sign. (Adapted from Santolík et al. 2004b)

et al. 2004a, 2004b). Using the observed wave normal directions of these waves, a backward ray tracing study predicts that the lower-intensity waves undergo the lower hybrid resonance (LHR) reflection at low altitudes (Parrot et al. 2004a). The rays of these waves then lead us back to their anticipated source region located close to the magnetic equator. This source region is, however, located at a different radial distance compared to the place of observation. The intensity ratio between magnetic component of the waves coming directly from the equator and waves returning to the equator has been observed between 0.005 and 0.01. The observations also show that waves returning to the equator after the magnetospherical reflection still have a high degree of polarization, even if they started to lose the coherent structure of the chorus elements (Parrot et al. 2004b).

Chum and Santolík (2005), Santolík et al. (2006) and Bortnik et al. (2007) showed that chorus can propagate to low altitudes towards the Earth if it is generated with Earthward inclined wave vectors. This result can be used to explain observations of low-altitude electromagnetic ELF hiss at subauroral latitudes. Santolík et al. (2006) reported observations of a divergent propagation pattern of these waves: They propagate with downward directed wave vectors, which are slightly equatorward inclined at lower *MLAT* and slightly poleward inclined at higher latitudes. Reverse ray tracing using different plasma density models indicated a possible source region near the magnetic equator at a radial distance between 5 and 7 R_E by a mechanism acting on highly oblique wave vectors. Additionally, waveforms received at altitudes of 700–1200 km by FREJA and DEMETER showed that low-altitude ELF hiss contains discrete time–frequency structures resembling wave packets of WM chorus. Detailed measurements of the CLUSTER spacecraft gave the time–frequency structure and frequencies of chorus along the reverse raypaths of ELF hiss, which are consistent with the hypothesis that the ELF hiss is a low-altitude manifestation of WM chorus. This propagation pattern applies mainly to the most frequently occurring dawn and dayside chorus. As noted in the following section these waves can also be considered as a possible additional candidate for the embryonic source of plasmaspheric hiss.

9 Hiss

The last comprehensive review on plasmaspheric and mid-latitude hiss was done by Hayakawa and Sazhin (1992). The following two sections are not an update to that work, but rather tries to put into context recent advances obtained on these natural waves thanks to the CLUSTER and IMAGE satellites.

9.1 Plasmaspheric Hiss

Plasmaspheric hiss is an electromagnetic emission confined to the plasmasphere. It occurs at all local times but is more intense on the dayside, and further intensifies with geomagnetic activity (Dunckel and Helliwell 1969; Russell et al. 1969; Thorne et al. 1973). Its spectral characteristics are similar to audible hiss: structureless and banded in frequency between ∼100 Hz and several kHz. Statistically, its intensity peaks near 500 Hz and is one order of magnitude more intense below than above 1 kHz (Fig. 23).

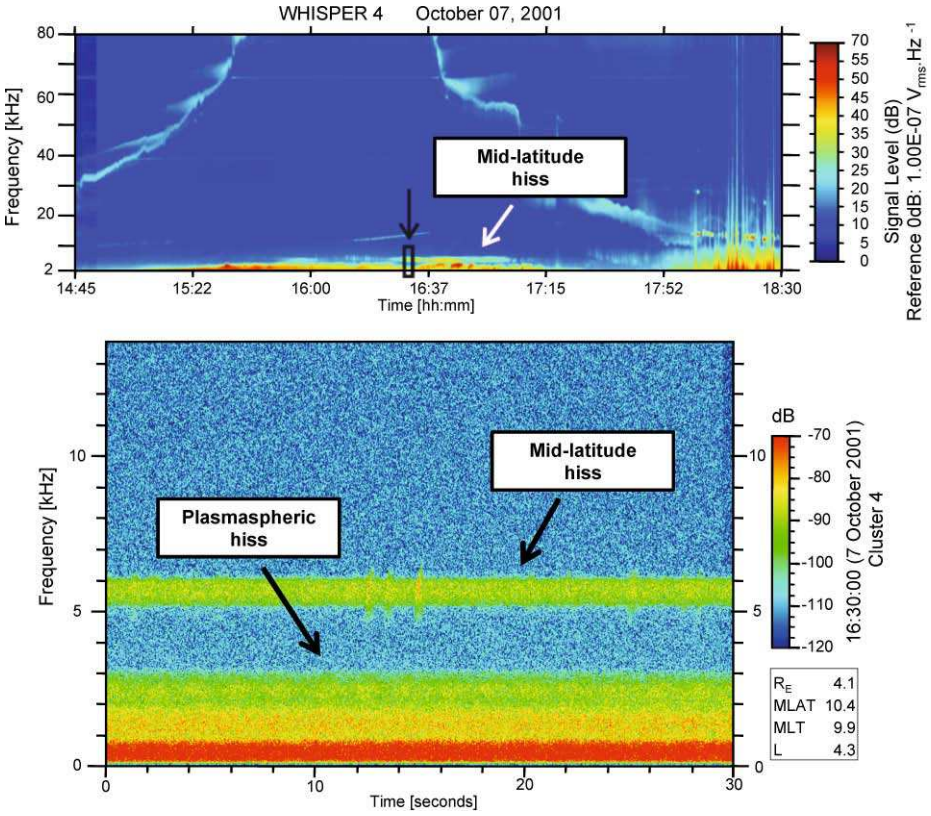

Fig. 23 (*Top*) WHISPER electric field spectrogram from C4 on 7 October 2001, from 14:45 to 18:30 UT. A banded hiss emission is observed from 16:25 to 17:04 UT (*white arrow*). The *black box* (*black arrow*) symbolizes the time period and the frequency range of the enlargement displayed in the *bottom panel*. (*Bottom*) High-time resolution WBD electric field spectrogram measured by C4 on 7 October 2001, during 30 s from 16:00:00.024 UT. The mid-latitude hiss emission is observed just above 5 kHz, while plasmaspheric hiss is observed from 100 Hz to 3 kHz with maximum spectral intensity below 700 Hz. (Adapted from Masson et al. 2004)

Plasmaspheric hiss has been studied since the late 1960s using observations from various satellites flying across the plasmasphere (Hayakawa and Sazhin 1992). It was found in particular that this emission plays a key role in the precipitation of relativistic electrons from the plasmasphere into the atmosphere (Sect. 9.1.1). However, even four decades after its discovery, its source location and generation mechanism remain controversial topics. As shown in Sect. 9.1.2, significant progresses have been made in recent years on these issues, thanks to data collected by several satellites including CLUSTER and IMAGE.

9.1.1 Impact on the Radiation Belts

The Van Allen radiation belts are two roughly concentric belts of energetic particles (>100 keV) encircling the Earth. The inner belt is characterized by a fairly stable population of high-energy protons (∼10–100 MeV), trapped between $L = 1.25$ and $L = 2$. The outer belt encircles the inner belt ($3 < L < 7$) and is characterized by a population of relativistic electrons (>1 MeV) and various ions (∼10 keV–10 MeV). However, the content of the outer belt fluctuates widely with regards to the geomagnetic activity. Between the inner and the outer belts ($2 < L < 3$), the population of relativistic electrons drops down by a factor of 10 to 100 (e.g., Brautigam et al. 2004). However, during very strong geomagnetic storms, this slot region can be filled with energetic particles. The slot region subsequently reforms on a timescale of days to weeks.

Theoretical work by Kennel and Petschek (1966) showed that natural waves propagating in the whistler mode are able to gain energy from a gyroresonance interaction with radiation belt relativistic electrons near the magnetic equator, causing them to change pitch angle and precipitate. Several types of WM waves exist in the plasmasphere (e.g., Green et al. 2005a) but plasmaspheric hiss was shown to be the dominant emission responsible for the electron scattering in the slot region (Lyons et al. 1972; Thorne et al. 1973; Abel and Thorne 1998). Plasmaspheric hiss was also found to be an important loss mechanism inside plasmaspheric plumes (Summers et al. 2008), the outer radiation belt (Meredith et al. 2007) and the upper part of the inner belt (Tsurutani et al. 1975) during magnetically disturbed periods.

Therefore understanding the origin of plasmaspheric hiss is of fundamental importance to forecast the distribution of relativistic electrons and dynamics of the radiation belts electrons.

9.1.2 Origin of Plasmaspheric Hiss

Over the years, two theories have emerged as the most likely candidates to explain the origin of plasmaspheric hiss. One of them considers the in situ growth and amplification of background electromagnetic turbulence in space, driven by unstable energetic electron populations (Thorne et al. 1973). Unfortunately, typical wave growth rates estimated in the plasmasphere are too weak to locally generate the hiss emissions with its observed power. However, once hiss is generated, its power can be maintained thanks to the presence of these anisotropic energetic electrons in the outer plasmasphere, via a physical process known as cyclotron resonant instability (Church and Thorne 1983).

The other theory considers terrestrial lightning strikes as the main energy source of plasmaspheric hiss (Dowden 1971; Sonwalkar and Inan 1989; Draganov et al. 1993; Bortnik et al. 2003). Lightning strikes trigger the emission of impulsive signals that can reach the plasmasphere. As they propagate, they undergo dispersion as lower frequencies travel slower than higher ones, sounding like a whistler when turned to audio. Several of these lightning-generated whistlers can finally merge into a broadband signal that becomes plasmaspheric hiss as originally suggested by H.C. Koons according to Storey et al. (1991).

Using a new statistical wave-mapping technique on data collected by DE-1 and IMAGE, Green et al. (2005a) showed that the distribution of hiss emissions in the plasmasphere at 3 kHz is similar to the geographic distribution of lightning strikes. In particular, the observed emissions are stronger over the continents than the oceans. The 3 kHz frequency was chosen since it is the lowest frequency of the IMAGE/RPI instrument. They claim that geographic control of a portion of the hiss spectrum exists to some extent above ∼500 Hz, although the DE/PWI data below 1.2 kHz were only examined in a qualitative manner (Green et al. 2006). They concluded that lightning is the dominant source of plasmaspheric hiss. But this conclusion has been called into question by Thorne et al. (2006) arguing in particular that the intensities of the waves above 1 kHz are much smaller than the intensities of plasmaspheric hiss below 1 kHz.

Meredith et al. (2006) subsequently analyzed the geographic distribution of hiss over a wider frequency range (0.1–5.0 kHz) using CRRES data. They found that the waves between 1.0 kHz and 5.0 kHz are most likely related to lightning-generated whistlers, confirming the results obtained by Green et al. (2005a) at 3 kHz. However, they found that the waves at lower frequencies (0.1–1.0 kHz) are independent of lightning activity. Since the emission power of plasmaspheric hiss below 1 kHz is statistically an order of magnitude higher than above 1 kHz, lightning strikes are not responsible for the bulk of the wave power of plasmaspheric hiss. As electron loss via pitch angle scattering is proportional to the wave power, this suggests that lightning strikes is not the dominant energy source, which maintains the slot region in the radiation belts during quiet to moderate geomagnetic activity. In other words, both leading models for the origin of plasmaspheric hiss are not fully backed up by observations.

An alternative explanation for the generation of plasmaspheric hiss was proposed by Chum and Santolík (2005) who discovered that chorus, a well-known intense electromagnetic emission generated outside the plasmasphere, can fill the plasmasphere and might be one of the possible sources of plasmaspheric hiss (see Sect. 8). They also found that the wave-normal angles of these waves stay far from resonance and therefore effects of Landau damping can be excluded. Additionally the wave normals are nearly field-aligned inside the plasmasphere, consistent with previous observations of plasmaspheric hiss. This makes possible further amplification of these waves by the cyclotron resonance (e.g., Santolík et al. 2001). Equatorward reflected ELF hiss at low altitudes that is also most probably related to chorus emissions might represent another simultaneously acting embryonic source (Santolík et al. 2006). The results of Chum and Santolík (2005) were reproduced and confirmed by Bortnik et al. (2008) who obtained the same effect and who verified the absence of Landau damping. According to this study, plasmaspheric hiss is driven by chorus emissions. By modeling the propagation of chorus to lower altitudes, Bortnik et al. (2008) are able to reproduce the main features of plasmaspheric hiss including its observed spectral signature, incoherent nature and day-night asymmetry in intensity.

9.2 Mid-Latitude Hiss

9.2.1 Mid-Latitude Hiss and Auroral Hiss

Mid-latitude hiss (MLH) emissions are natural radio waves that usually appear as a band-limited white noise with a central frequency contained between 2 and 10 kHz and a spectral bandwidth of 1 to 2 kHz (Fig. 23). Such hiss emissions were first discovered by ground-based observatories located at mid-latitudes (30–60°) in the 1950s and 1960s (Watts 1957; Laaspere et al. 1964; Helliwell 1965). When converted to audio range, these VLF waves (3–30 kHz) have a characteristic “hissing” sound, hence their name.

The first studies of this natural phenomenon suggested that they were just auroral hiss, sometimes called polar hiss (Ondoh 2006), propagating from auroral latitudes to mid-latitudes within the Earth-ionosphere waveguide. This was shown to be incorrect in the pioneering works by Harang (1968) and Hayakawa et al. (1975). Significant differences between auroral and MLH spectral signatures were found between simultaneous measurements from stations located at mid- (34.5°) and auroral (69°) latitudes (see Hayakawa and Sazhin 1992, for the last comprehensive review on MLH). In particular, the upper limit of MLH spectrum could extend up to 8 kHz while the auroral hiss spectrum could extend up to 500 kHz or even higher.

Since then, hiss events recorded at mid- or even low-latitude stations have been considered to be independent from auroral hiss. Mid- and low- latitude hisses are both named MLH since the maximum of their occurrence was found at middle latitudes, 55° to 65° (Helliwell 1965). This latitudinal range is magnetically connected to the plasmapause location, which explains why MLH is sometimes called narrow-band plasmapause hiss or simply plasmapause hiss (e.g., Ondoh 2006).

Thanks to satellite measurements and theoretical studies, other fundamental differences have been discovered between auroral and MLH, such as their source location and generation mechanism.

9.2.2 Source Location and Generation Mechanism

Ground-based direction finding performed by Hayakawa et al. (1986) revealed that MLH is generated mainly on the inner side of the PBL. For the first time, a survey of MLH events observed close to their source region by the CLUSTER satellites confirmed the presence of MLH around the magnetic equator, in the PBL at around 4 R_E, i.e., 25 000 km altitude (Masson et al. 2004).

MLH, like chorus, is generated near the magnetic equator and propagate via the whistler mode. Chorus often accompanies MLH and the upper cutoff of the combined band of hiss and chorus is found to be proportional to the equatorial gyrofrequency (Dunckel and Helliwell 1969). Both type of waves are believed to be generated by the electron cyclotron instability, sometimes called the whistler-mode instability. Combined ground-based and satellite measurements reveal that mid-latitude/plasmapause hiss waves are excited around the equatorial plasmapause by the cyclotron instability of electrons with energy of a few keV convected from the magnetotail (e.g., Hayakawa and Sazhin 1992; Ondoh 2006, and references therein).

Unlike MLH, auroral hiss emissions are broad, intense electromagnetic emissions, which occur over a wide frequency range from a few hundred Hz to several tens of kHz. At low frequencies, auroral hiss occurs in a narrow latitudinal band, typically only 5–10° wide, centered on the auroral zone (70–80°). At high frequencies, the emission spreads out over a broad region, both towards the polar cap, and to a lesser extent towards the equator. The anisotropic character of whistler-mode propagation causes this spreading at high frequencies.

Satellite data, such as those from POLAR, also revealed that auroral hiss is emitted in a beam around an auroral magnetic field line located between $L = 2$ and $L = 4$. Downward propagating auroral hiss emissions are closely correlated with intense, downgoing 100 eV to 40 keV electron beams precipitating from the plasmasheet boundary layer in geomagnetic quiet and disturbed periods (Gurnett and Franck 1972). Upward propagating auroral hiss is correlated with upgoing ∼50 eV electron beams.

All these facts confirm ground-based initial measurements: Auroral hiss and MLH are two distinct natural phenomena.

9.2.3 Geomagnetic Activity Impact

Several physical characteristics of MLH are affected by geomagnetic activity, starting with their duration. During quiet geomagnetic conditions, such a band-limited white noise usually lasts for an hour. However, during active periods, MLH can last for several hours showing amplitude fluctuations on a time scale of tens of minutes (see page 427 of Sonwalkar 1995).

According to Ondoh (2006), the occurrence rate of MLH is maximum under geomagnetic quiet conditions (30 nT $< AE <$ 200 nT) while the occurrence rate of auroral/polar hiss is much larger in the substorm period (200 nT $< AE <$ 924 nT). This statistical study is based on 65 MLH and 74 polar hisses observed by the ISIS-2 satellite (1400 km altitude, polar circular orbit) under various geomagnetic conditions.

Close to the source region, in the vicinity of the magnetic equator at 4 R_E, Masson et al. (2004) showed that the central frequency of MLH (f_0) is correlated with the K_p index: the higher K_p, the higher f_0. One possible explanation suggested in this paper assumes that these waves are generated in the vicinity of the plasmapause, near the magnetic equator, in a given f/f_{ce} frequency bandwidth. At the equator near the plasmapause f_{ce} is proportional to $1/L_{pp}^3$, where L_{pp} is the geocentric radial distance of the plasmapause. When geomagnetic activity is high, the plasmasphere is compressed, the plasmapause location gets closer to the Earth, and so L_{pp} decreases. In this case, f_{ce} will increase, hence f_0 increases too, according to our assumption (f_0/f_{ce} constant). This explanation is in agreement with theoretical predictions (Sazhin 1989; Hayakawa and Sazhin 1992) and with early ground-based measurements, which revealed that the central frequency of hiss usually increases with decreasing latitude (Laaspere et al. 1964). This behaviour is similar to plasmaspheric hiss, whose wave frequencies just inside the plasmapause increase with increasing K_p (Thorne et al. 1973).

10 Equatorial Noise

10.1 Introduction

Emissions called "equatorial noise" are electromagnetic waves (the term "fast magnetosonic waves" is also sometimes used, e.g., Horne et al. 2000 2007) observed close to the magnetic equator (within $\sim \pm 3°$) at frequencies between f_{ce} and f_{lh} and at radial distances $R = 2$–$7\ R_E$. They propagate in the fast magnetosonic mode coupled to the whistler mode with wave vectors nearly perpendicular to the ambient magnetic field ($\boldsymbol{B_0}$), with magnetic field fluctuations linearly polarized in the direction of $\boldsymbol{B_0}$. Electric field fluctuations are elliptically polarized with a low ellipticity (from 0.02 to 0.11, see Santolík et al. 2002), major polarization axis being oriented along the wave vector. CLUSTER observes emissions of this type during perigee passes through the equatorial region ($R \approx 4\ R_E$).

Figure 24 shows an example of equatorial noise emissions recorded by C4 on 17 February 2002 within approximately $\pm 30°$ of magnetic equator. Panels (**a**) and (**b**) represent frequency–time spectrograms of power-spectral densities of the magnetic and electric field fluctuations, respectively. Equatorial noise is the intense electromagnetic emission seen on both panels close to the center of the time interval, within a few degrees from the magnetic equator. In the frequency domain it appears as two main peaks at about 30 Hz and 70 Hz. The emission is confined below the upper estimate of f_{lh}, calculated as the geometric average of the proton gyrofrequency f_{cp} and f_{ce} (solid line at ~300 Hz). Frequency–time spectrogram of ellipticity of polarization of the magnetic field fluctuations is shown

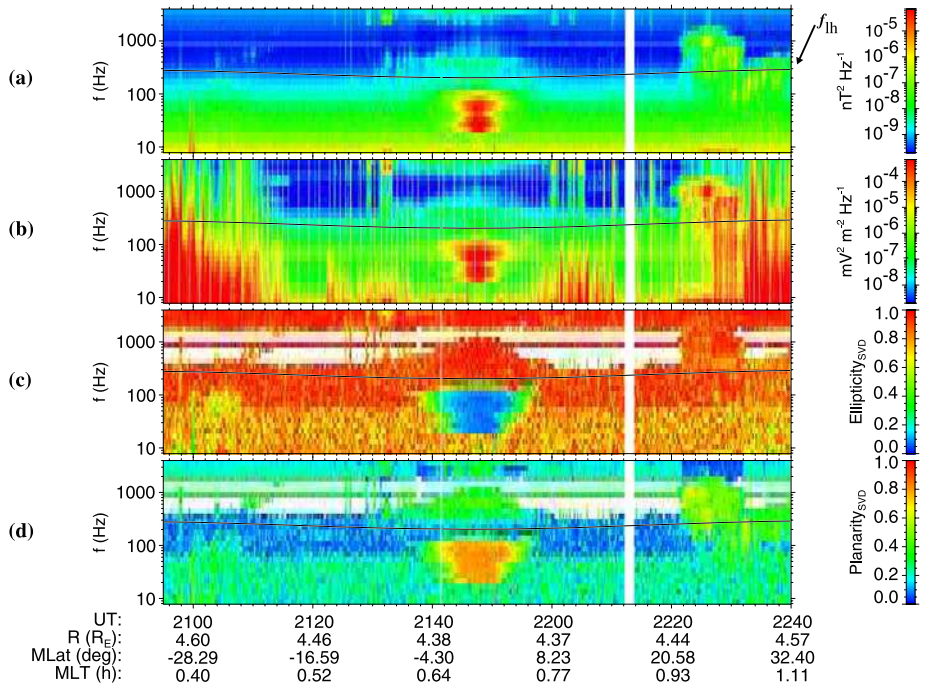

Fig. 24 STAFF data collected by C4 on 17 February 2002: (**a**) sum of the power-spectral densities of the three magnetic components, (**b**) sum of the power-spectral densities of the two electric components, (**c**) ellipticity and (**d**) planarity determined using the singular value decomposition of the magnetic spectral matrix. Maximum possible value of f_{lh} is plotted over the panels (**a**)–(**d**). The data in panels (**c**) and (**d**) are not shown for weak signals below 10^{-9} $nT^2\ Hz^{-1}$. (Adapted from Santolík et al. 2004c)

in panel (**c**). It varies between 0 (linear polarization) and 1 (circular polarization). Equatorial noise can be easily distinguished by its polarization close to linear, as it was first described by Russell et al. (1970). Panel (**d**) represents the frequency–time spectrogram of planarity of magnetic field fluctuations. A value close to 1 represents a strict confinement of the magnetic field fluctuations to a single plane, which is obviously also true for the linear polarization.

10.2 CLUSTER Observations

Santolík et al. (2002) performed a multipoint case study of equatorial noise by using both STAFF and WBD instruments onboard CLUSTER. Frequency–time spectrograms of the analyzed electric field data measured by WBD instruments are shown in Fig. 25. Dipole equator and min-B equator calculated from a Tsyganenko-IGRF model (which is about 1° northward from the dipole equator) are marked. It can be seen that what appears like a noise in a low resolution data is in fact a set of many spectral lines (Gurnett 1976) some of which follow a harmonic pattern. However, all the possible fundamental frequencies were significantly different from the local f_{cp} and they did not match the cyclotron frequencies of heavier ions either. The authors bring observational evidence that the waves propagate with a significant radial component (on average the waves propagate at ∼45° between the radial and azimuthal directions, but the wave power spreads in a large angular interval) and can thus propagate

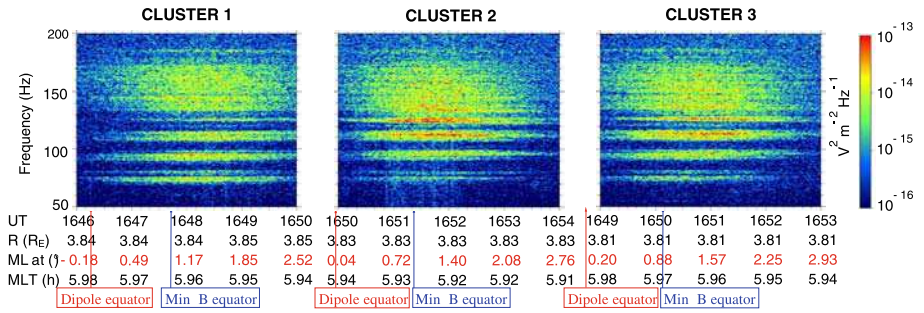

Fig. 25 Frequency–time spectrograms of electric field data recorded by the WBD instrument onboard three CLUSTER spacecraft on 4 December 2000. (Adapted from Santolík et al. 2002)

from a distant generation region located at different radial distances where ion cyclotron frequencies match the observed fine structure.

Santolík et al. (2004c) performed a systematic analysis of 2 years of STAFF data measured by CLUSTER during their perigee passes through equatorial region. A visual inspection has revealed the presence of equatorial noise in 398 of the 671 analyzed passes (each spacecraft has been treated separately), which corresponds to about 59%. They have selected 16 frequency channels between 8 Hz (the lowest frequency analyzed by the STAFF instrument) and 300 Hz (the upper estimate of the maximum f_{lh} throughout the dataset) and with the time resolution of 4 s evaluated the wave parameters within $\pm 30°$ of geomagnetic latitude (altogether, about 1.4×10^7 frequency–time intervals). They have shown that a value of 0.2 is a reasonable upper estimate of the ellipticity of magnetic field fluctuations of equatorial noise and that equatorial noise has the largest power spectral density of magnetic field fluctuations among all the natural emissions in the given interval of frequencies and latitudes.

Němec et al. (2005) have used the same dataset, but limited to only $\pm 10°$ of geomagnetic latitude. Following Santolík et al. (2004c) they selected the 16 lowest frequency bands and only the frequency–time intervals during which the ellipticity was lower than 0.2. Then they calculated average power-spectral density from the selected data in the selected frequency channels and found parameters λ_c (central latitude) and Δ (full width at half of maximum, FWHM) of a Gaussian model of the power-spectral density as a function of geomagnetic latitude. The resulting parameters were found to be about the same for magnetic and electric power spectral densities. Most of the central latitudes occur within 2° from the magnetic equator with the FWHM lower than 3°. From the original frequency-dependent data, they calculated a time-averaged spectral matrix over the time interval where the spacecraft was located inside the latitudinal interval from $\lambda_c - \Delta$ to $\lambda_c + \Delta$ and obtained the probability density of frequencies of equatorial noise emissions normalized to the local f_{cp}. It has been shown that the most probable frequency of emissions is between 4 and 5 local f_{cp}, with probability density slowly decreasing towards the higher frequencies. Finally, multipoint measurements performed by CLUSTER were used to demonstrate that variations of the ratio of amplitudes of equatorial noise increase with time delay between measurements in an interval from tenths to hundreds of minutes, but these variations do not seem to increase with separations up to 0.7 R_E in the equatorial plane.

Němec et al. (2006) performed the similar analysis, but used an improved magnetic field model to determine the min-B equator (instead of a dipole magnetic field model used in the previous study). They concluded that central latitudes of equatorial noise seem to be

located exactly at the true magnetic equator and that the observed deviations can be most probably explained by the inaccuracies in the model. They also used cold plasma theory to calculate the number density from the ratio of magnetic and electric power spectral density. The estimated values vary from units to hundreds of particles per cubic centimeter and are in a rough agreement with the densities obtained from the measurements of the spacecraft potential.

10.3 Generation Mechanism of Equatorial Noise and its Effects

A generation mechanism of equatorial noise (fast magnetosonic waves) is discussed by Horne et al. (2000). They conducted a ray-tracing analysis using a density model, which includes a plasmasphere, a plasmapause, and a radial variation in the plasma density outside the plasmasphere, as well as the proton distribution with a thermal spread of velocities taken from spacecraft observations, and a realistic plasma sheet electron distribution to represent conditions outside the plasmapause. Supposing ring distribution functions (ring velocity v_R) with a thermal spread of velocities, they showed that magnetosonic waves can be generated just outside the plasmapause and propagate well inside the plasmapause without substantial absorption. Peak growth occurs for very large angles of propagation, and thus the waves are confined in latitude to a few degrees about the magnetic equator. The instability analysis shows that a good "rule of thumb" for growth of magnetosonic waves at large angles of propagation ($\sim$89°) is $v_R > v_A$ for growth $f > 30 f_{cp}$, and $v_R > 2v_A$ for growth $f < 30 f_{cp}$ (f is the frequency of wave, v_A is the Alfvén speed).

In a recent paper Horne et al. (2007) discussed potential implications of fast magnetosonic waves for electron populations in Van Allen radiation belts and demonstrated that the fast magnetosonic waves can accelerate electrons between $\sim$10 keV and a few MeV inside the outer radiation belt. The acceleration occurs via the Landau resonance, and not Doppler shifted cyclotron resonance, due to the wave propagation almost perpendicular to the ambient magnetic field. Pitch angle and energy diffusion rates are comparable to those obtained for WM chorus. This suggests that the magnetosonic waves are very important for local electron acceleration and could play an important role in the process of energy transfer from the ring current (where ion ring distributions are formed during magnetic storms as a result of losses due to slow ion drift) to Van Allen radiation belts. Finally, since magnetosonic waves do not scatter electrons into the loss cone, the need for a continuous supply of low energy electrons is not as stringent as it is for their acceleration by chorus, and these waves, on their own, are not important for loss to the atmosphere.

11 ULF Resonances

11.1 Historical Description

The attempt to use pulsation data to remotely sense plasmaspheric mass properties has a long history (Troitskaya and Gul'Elmi 1969; Lanzerotti and Fukunishi 1975; Webb et al. 1977; Takahashi and McPherron 1982). A variety of methods have been developed to identify inner magnetospheric field line resonances, which can arise from a driving impulse. These include complex demodulation (Webb 1979), methods of evaluating the spectral matrix (Arthur 1979), such as state vector analysis techniques (Samson 1983), meridional geomagnetic gradient evaluation (Baransky et al. 1985), cross phase analysis techniques (Waters et al. 1991), and dynamic spectrum techniques (Menk 1988). It is not always easy to determine the resonant frequencies because the pulsation spectrum can be dominated by the source mechanism

(Kurchashov et al. 1987). The "gradient method" was developed by Baransky et al. (1985) to separate the mixed driving and resonant power. Field line resonant theory predicts that the wave power peaks at the resonant frequency and the spatial profile of the phase at the resonant frequency changes roughly 180 degrees across the resonant L-shell (Tamao 1964; Chen and Hasegawa 1974; Southwood 1974). Using data from two magnetometers located on the same magnetic longitude and closely separated in latitude, one can compare the wave phase or amplitude seen at both stations and obtain the eigenfrequencies of the field line midway between the two stations. The cross phase spectral technique developed by Waters et al. (1991) was used by Menk et al. (1994, 1999) to monitor the temporal evolution of plasmaspheric properties. This is done by identifying the maximum interstation phase difference between two closely spaced stations (few hundred km) to identify the eigenfrequencies of the local field line. With this diagnostic technique variations in plasmaspheric plasma parameters (such as equatorial plasma density) can be monitored and using a latitudinal array of stations, the location of the plasmapause can be determined. The techniques of Schulz (1996) and Denton and Gallagher (2000) are used to derive the equatorial mass density from the inferred eigenfrequency of the field line (Berube et al. 2003). The techniques are analogous to identifying the mass of a string by determining the sound frequency of the plucked note. By knowing the string length (field line length), string tension (strength of magnetic field line) and the frequency of oscillation, the density of the string (plasma) can be inferred. Under the usual Alfvénic travel time approximations, the eigenfrequencies can be expressed as:

$$\frac{\omega_n}{2\pi} \approx \frac{n\Delta\omega}{2\pi} \approx n\left(\int \frac{ds}{v_A}\right)^{-1}, \tag{4}$$

where v_A is the Alfvén speed, n is the harmonic number, and s is the coordinate that measures the arc length of the field line. The measure eigenfrequency is representative of the equatorial mass density because of the slow Alfvén speed there. The ability to uniquely identify the flux tubes eigenfrequency depends on having a solar wind or magnetospheric driving wave. On the dayside of the Earth, ULF waves are almost continuously present due to upstream waves impinging on the magnetopause (e.g., Yumoto 1986). These driver waves excite the field lines resonance frequency that can be separated out from the driving frequency using such methods as the cross phase technique. Therefore one limitation of using ULF waves at the present time is that inner magnetospheric mass densities can only be routinely measured during the daytime.

Figure 26 shows daily plasma mass density averages inferred from ULF resonances during 2000–2001 at $L = 1.74$. The daily averages are made from hourly estimates of the eigenfrequency. The error bars shown are representative of the variation of the mean of the hourly estimates. The December densities are 2–3 times higher than the June densities for both years. Typical uncertainties in determining the ULF resonant frequency, and hence mass density is $\pm 25\%$ (e.g., Berube et al. 2003, 2005). Annual variation of the electron density has also been observed at low latitudes using VLF measurements (e.g., Clilverd et al. 1991).

11.2 IMAGE Observations

The mass density of the inner plasmasphere is difficult to measure and the few satellites capable of making measurements did not sample the inner magnetosphere well. An exception are measurements from DE-1 (e.g., Horwitz et al. 1984). Most studies found that the relative abundances of heavy ions in the plasmasphere vary greatly. Craven et al. (1997) using data

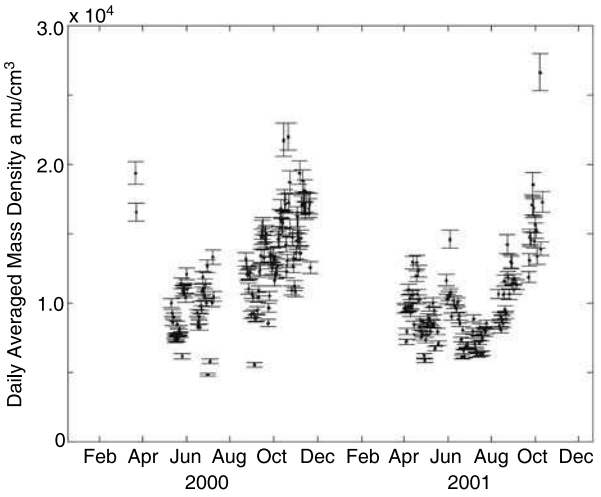

Fig. 26 The equatorial mass densities at $L = 1.74$ computed by a ULF resonance method. Note the seasonal difference in mass density. (Adapted from Berube et al. 2003)

from DE-1 found He^+ to H^+ ratios in the plasmasphere of ∼0.03–0.3, implying He^+ abundances of ∼3–23 percent by number, assuming no other heavy ions are present. Horwitz et al. (1984) found that in the aftermath of a storm, O^+ density could become comparable to H^+ density in the plasmasphere. The first empirical model of the equatorial mass density of the plasmasphere was proposed by Berube et al. (2005) using ground-based ULF wave diagnostics. Plasmaspheric mass density between $L = 1.7$ and $L = 3.2$ was determined using over 5200 hours of data from pairs of stations in the MEASURE array of ground magnetometers. The least squares fit to the data as a function of L shows that mass density falls logarithmically with L. Average ion mass as a function of L was also estimated by combining the mass density model with plasmaspheric electron density profiles determined from IMAGE/RPI instrument. Additionally, the RPI electron density database was used to examine how the average ion mass changes under different levels of geomagnetic activity. Berube et al. (2005) report that average ion mass is greatest under the most disturbed conditions. This result indicates that heavy ion concentrations (percent by number) are enhanced during large geomagnetic disturbances. The average ion mass was also found to increase with increasing L (below 3.2), indicating the presence of a heavy ion torus during disturbed times. Heavy ions must play an important role in storm-time plasmaspheric dynamics. The average ion mass was also used to constrain the concentrations of He^+ and O^+. Estimates of the He^+ concentration determined this way is useful for interpreting IMAGE/EUV images. More details on empirical models can be found elsewhere in this issue (Reinisch et al. 2009).

12 Conclusion

CLUSTER and IMAGE are pioneer space missions with regards to plasmaspheric wave phenomena thanks to their new experimental capabilities. Some of the results highlighted in this paper were considered among the science objectives of these missions such as the source location of waves (Sects. 3 and 8) or the remote sensing of density profiles along geomagnetic field lines (Sect. 5). Now, CLUSTER and IMAGE have also brought or led to a wealth of unforeseen results, just like pioneer missions do.

For instance, the database of plasmaspheric density profiles measured by IMAGE, together with ground-based ULF wave diagnostics, has helped determining the average ion

mass as a function of L under different levels of geomagnetic activity. Thanks to a better knowledge of this key physical parameter, heavy ions were found to play an important role in storm-time plasmaspheric dynamics (Sect. 11).

Similarly, the IMAGE/EUV imager uncovered the presence of density bite-outs of the plasmapause named notches. Together with local wave observations, these EUV images have enabled to identify these notches as the source of kilometric continuum (KC); recall that KC is the high-frequency range of a more general wave phenomenon known as the non-thermal continuum (NTC) radiation. As KC emission cone is constrained by the geometry of these density cavities, KC observations provide back information on this plasmaspheric structure and its dynamics (Sect. 3).

Such a link between density irregularities in azimuth and longitudinal beaming properties of radiations is likely applicable to NTC radiations at lower frequency, linking them with irregularities of smaller size (Sect. 4). CLUSTER observations in the NTC range have also revealed a new class of radio sources, emitting from the mid-latitude plasmapause boundary while new radio echoes have been discovered by IMAGE (Sects. 6 and 7).

Another striking example concerns chorus emissions. The multipoint view of CLUSTER near perigee has enabled a better understanding of the source location and size of these waves and their propagation properties from their source region (Sect. 8). This new knowledge has triggered ray-tracing studies that led to an unforeseen conclusion: Chorus is an embryonic source of plasmaspheric hiss, the dominant emission responsible for the scattering of MeV electrons in the electron slot region (Sect. 9).

As usual, scientific discoveries lead to more questions than answers. For instance, CLUSTER data strongly suggest that equatorial noise plays, like chorus, a role in the acceleration of electrons in the outskirts of the plasmasphere (Sect. 10). However, a crucial limitation of this conclusion lies in the limited range of radial distances of equatorial perigee passes (3.9–5 R_E). A full assessment of the importance of these waves requires detailed analysis of the occurrence rate of their power as a function of L, MLT and latitude.

Overall, both missions have helped to better relate plasmaspheric wave phenomena with plasmaspheric density structures, derive electron density profiles and heavy particles content of the plasmasphere, better locate the source of waves and how they propagate. They have also increased our knowledge on how electrons of magnetotail origin are accelerated up to MeV range and how these killer electrons get scattered by waves. Last but not least, these missions have linked wave phenomena together: Several waves are now considered as embryonic sources of other waves and no more studied as distinct phenomena. In other words, IMAGE and CLUSTER have helped putting the puzzle pieces together.

But the puzzle is far from being complete. Upcoming inner magnetospheric missions will all orbit the magnetic equator and carry appropriate wave instrumentation. These missions are the NASA's Radiation Belt Storm Probes (RBSP) composed of two satellites (launch planned in 2012), the ERG (Energization and Radiation in Geospace) single satellite project from Japan and the ORBITALS (Outer Radiation Belt Injection, Transport, Acceleration and Loss Satellite) project led by Canada. Up till the launch of RBSP and hopefully ERG and ORBITALS, three of the NASA's THEMIS spacecraft launched in 2007 and equipped with search coil magnetometers will survey the inner magnetosphere together with particle instrumentation. In other words, the future looks bright for plasmaspheric wave research.

Acknowledgements O. Santolík and F. Němec acknowledge grants GAAV A301120601 and ME842. F. Darrouzet acknowledges the support by the Belgian Federal Science Policy Office (BELSPO) through the ESA/PRODEX project (contract 13127/98/NL/VJ (IC)). This paper is an outcome of the workshop "The Earth's plasmasphere: A CLUSTER, IMAGE, and modeling perspective", organized by the Belgian Institute for Space Aeronomy in Brussels in September 2007. Figures 1, 2, 4, 8, 10b, 11, 13, 14, 15, 16, 17, 18, 19,

References

B. Abel, R.M. Thorne, Electron scattering loss in Earth's inner magnetosphere 1. Dominant physical processes. J. Geophys. Res. **103**(A2), 2385–2396 (1998)

C.W. Arthur, Digital techniques for ULF wave polarization analysis. Ann. Telecommun. **34**, 166–178 (1979)

L.N. Baransky, J.E. Borovkov, M.B. Gokhberg, S.M. Krylov, V.A. Troitskaya, High resolution method of direct measurement of the magnetic field lines' eigen frequencies. Planet. Space Sci. **33**(12), 1369–1374 (1985)

R.F. Benson, Ion effects on ionospheric electron resonance phenomena. Radio Sci. **10**(2), 173–185 (1975)

R.F. Benson, Stimulated plasma waves in the ionosphere. Radio Sci. **12**(6), 861–878 (1977)

R.F. Benson, Elusive upper hybrid waves in the auroral topside ionosphere, in *Auroral Plasma Dynamics*, ed. by R.L. Lysak. Geophysical Monograph Series, vol. 80 (American Geophysical Union, Washington, 1993), pp. 267–274

R.F. Benson, H.K. Wong, Low-altitude ISIS 1 observations of auroral radio emissions and their significance to the cyclotron maser instability. J. Geophys. Res. **92**(A2), 1218–1230 (1987)

R.F. Benson, V.A. Osherovich, J. Fainberg, B.W. Reinisch, Classification of IMAGE/RPI-stimulated plasma resonances for the accurate determination of magnetospheric electron density and magnetic field values. J. Geophys. Res. **108**(A5), 1207 (2003)

R.F. Benson, P.A. Webb, J.L. Green, D.L. Carpenter, V.S. Sonwalkar, H.G. James, B.W. Reinisch, Active wave experiments in space plasmas: The Z mode, in *Geospace Electromagnetic Waves and Radiation*, ed. by J.W. LaBelle, R.A. Treumann. Lecture Notes in Physics, vol. 687 (Springer, Berlin, 2006), pp. 3–36

D. Berube, M.B. Moldwin, J.M. Weygand, An automated method for the detection of field line resonance frequencies using ground magnetometer techniques. J. Geophys. Res. **108**(A9), 1348 (2003)

D. Berube, M.B. Moldwin, S.F. Fung, J.L. Green, A plasmaspheric mass density model and constraints on its heavy ion concentration. J. Geophys. Res. **110**, A04212 (2005)

J. Bortnik, U.S. Inan, T.F. Bell, Frequency-time spectra of magnetospherically reflecting whistlers in the plasmasphere. J. Geophys. Res. **108**(A1), 1030 (2003)

J. Bortnik, R.M. Thorne, N.P. Meredith, O. Santolík, Ray tracing of penetrating chorus and its implications for the radiation belts. Geophys. Res. Lett. **34**, L15109 (2007)

J. Bortnik, R.M. Thorne, N.P. Meredith, The unexpected origin of plasmaspheric hiss from discrete chorus emissions. Nature **452**(7183), 62–66 (2008)

D.H. Brautigam, K.P. Ray, G.P. Ginet, D. Madden, Specification of the radiation belt slot region: Comparison of the NASA AE8 model with TSX5/CEASE data. IEEE Trans. Nucl. Sci. **51**(6), 3375–3380 (2004)

A. Breneman, C.A. Kletzing, J. Chum, O. Santolík, D. Gurnett, J. Pickett, Multispacecraft observations of chorus dispersion and source location. J. Geophys. Res. **112**, A05221 (2007)

J.L. Burch, IMAGE mission overview. Space Sci. Rev. **91**(1–2), 1–14 (2000)

W. Calvert, Oblique z-mode echoes in the topside ionosphere. J. Geophys. Res. **71**(23), 5579–5583 (1966)

P. Canu, P.M.E. Décréau, S. Escoffier, S. Grimald, Observations of continuum radiations close to the plasmapause: Evidence for small scale sources, in *Planetary Radio Emissions VI*, ed. by H.O. Rucker, W.S. Kurth, G. Mann (Austrian Academy of Sciences Press, Vienna, 2006)

D.L. Carpenter, R.R. Anderson, An ISEE/Whistler model of equatorial electron density in the magnetosphere. J. Geophys. Res. **97**(A2), 1097–1108 (1992)

D.L. Carpenter, J. Lemaire, The plasmasphere boundary layer. Ann. Geophys. **22**(12), 4291–4298 (2004)

D.L. Carpenter, R.R. Anderson, W. Calvert, M.B. Moldwin, CRRES observations of density cavities inside the plasmasphere. J. Geophys. Res. **105**(A10), 23323–23338 (2000)

D.L. Carpenter, T.F. Bell, U.S. Inan, R.F. Benson, V.S. Sonwalkar, B.W. Reinisch, D.L. Gallagher, Z-mode sounding within propagation "cavities" and other inner magnetospheric regions by the RPI instrument on the IMAGE satellite. J. Geophys. Res. **108**(A12), 1421 (2003)

D.L. Carpenter, T.F. Bell, D. Chen, D. Ng, C. Baran, B.W. Reinisch, I. Galkin, Proton cyclotron echoes and a new resonance observed by the Radio Plasma Imager instrument on the IMAGE satellite. J. Geophys. Res. **112**, A08208 (2007)

L. Chen, A. Hasegawa, A theory of long-period magnetic pulsations, 1. Steady state excitation of field line resonance. J. Geophys. Res. **79**(7), 1024–1032 (1974)
J. Chum, O. Santolík, Propagation of whistler-mode chorus to low altitudes: divergent ray trajectories and ground accessibility. Ann. Geophys. **23**(12), 3727–3738 (2005)
J. Chum, O. Santolík, A.W. Breneman, C.A. Kletzing, D.A. Gurnett, J.S. Pickett, Chorus source properties that produce time shifts and frequency range differences observed on different Cluster spacecraft. J. Geophys. Res. **112**, A06206 (2007)
S.R. Church, R.M. Thorne, On the origin of plasmaspheric hiss: Ray path integrated amplification. J. Geophys. Res. **88**(A10), 7941–7957 (1983)
M.A. Clilverd, A.J. Smith, N.R. Thomson, The annual variation in quiet time plasmaspheric electron density, determined from whistler mode group delays. Planet. Space Sci. **39**(7), 1059–1067 (1991)
N. Cornilleau-Wehrlin, G. Chanteur, S. Perraut, L. Rezeau, P. Robert, A. Roux, C. de Villedary, P. Canu, M. Maksimovic, Y. de Conchy, D. Hubert, C. Lacombe, F. Lefeuvre, M. Parrot, J.L. Pinçon, P.M.E. Décréau, C.C. Harvey, P. Louarn, O. Santolík, H.S.C. Alleyne, M. Roth, T. Chust, O. Le Contel, STAFF team, First results obtained by the Cluster STAFF experiment. Ann. Geophys. **21**(1–2), 437–456 (2003)
P.D. Craven, D.L. Gallagher, R.H. Comfort, Relative concentration of He^+ in the inner magnetosphere as observed by the DE 1 retarding ions mass spectrometer. J. Geophys. Res. **102**(A2), 2279–2289 (1997)
F. Darrouzet, J. De Keyser, P.M.E. Décréau, J.F. Lemaire, M.W. Dunlop, Spatial gradients in the plasmasphere from Cluster. Geophys. Res. Lett. **33**, L08105 (2006)
F. Darrouzet, D.L. Gallagher, N. André, D.L. Carpenter, I. Dandouras, P.M.E. Décréau, J. De Keyser, R.E. Denton, J.C. Foster, J. Goldstein, M.B. Moldwin, B.W. Reinisch, B.R. Sandel, J. Tu, Plasmaspheric density structures and dynamics: Properties observed by the CLUSTER and IMAGE missions. Space Sci. Rev. (2009, this issue)
J. De Keyser, D.L. Carpenter, F. Darrouzet, D.L. Gallagher, J. Tu, CLUSTER and IMAGE: New ways to study the Earth's plasmasphere. Space Sci. Rev. (2009, this issue)
P.M.E. Décréau, P. Fergeau, V. Krasnosels'kikh, E. Le Guirriec, M. Lévêque, P. Martin, O. Randriamboarison, J.L. Rauch, F.X. Sené, H.C. Séran, J.G. Trotignon, P. Canu, N. Cornilleau, H. de Féraudy, H. Alleyne, K. Yearby, P.B. Mögensen, G. Gustafsson, M. André, D.A. Gurnett, F. Darrouzet, J. Lemaire, C.C. Harvey, P. Travnicek, Whisper experimenters, Early results from the Whisper instrument on Cluster: an overview. Ann. Geophys. **19**(10–12), 1241–1258 (2001)
P.M.E. Décréau, C. Ducoin, G. Le Rouzic, O. Randriamboarison, J.L. Rauch, X. Trotignon, J.G. Vallières, P. Canu, F. Darrouzet, M.P. Gough, A. Buckley, T.D. Carozzi, Observation of Continuum radiations from the CLUSTER fleet: first results from direction finding. Ann. Geophys. **22**(7), 2607–2624 (2004)
R.E. Denton, D.L. Gallagher, Determining the mass density along magnetic field lines from toroidal eigenfrequencies. J. Geophys. Res. **105**(A12), 27717–27725 (2000)
R.L. Dowden, Distinction between mid latitude VLF hiss and discrete emissions. Planet. Space Sci. **19**(3), 374–376 (1971)
A.B. Draganov, U.S. Inan, V.S. Sonwalkar, T.F. Bell, Whistlers and plasmaspheric hiss: Wave directions and three-dimensional propagation. J. Geophys. Res. **98**(A7), 11401–11410 (1993)
N. Dunckel, R.A. Helliwell, Whistler-mode emissions on the OGO 1 satellite. J. Geophys. Res. **74**(26), 6371–6385 (1969)
F. El-Lemdani Mazouz, J.L. Rauch, P.M.E. Décréau, J.G. Trotignon, X. Vallières, F. Darrouzet, P. Canu, X. Suraud, Wave emissions at half electron gyroharmonics in the equatorial plasmasphere region: CLUSTER observations and statistics. Adv. Space Res. **43**(2), 253–264 (2009)
C.P. Escoubet, C.T. Russell, R. Schmidt (eds.), *The Cluster and Phoenix Missions* (Kluwer, Dordrecht, 1997)
W.M. Farrell, Direct generation of O-mode emission in a dense, warm plasma: Applications to interplanetary type II emissions and others in its class. J. Geophys. Res. **106**(A8), 15701–15709 (2001)
S.F. Fung, R.F. Benson, D.L. Carpenter, J.L. Green, V. Jayanti, I.A. Galkin, B.W. Reinisch, Guided echoes in the magnetosphere: Observations by Radio Plasma Imager on IMAGE. Geophys. Res. Lett. **30**(11), 1589 (2003)
G.K. Goertz, R.J. Strangeway, Plasma waves, in *Introduction to Space Physics*, ed. by M.G. Kivelson, C.T. Russell (Cambridge University Press, Cambridge, 1995), pp. 356–399
M.P. Gough, Non-thermal continuum emissions associated with electron injections: Remote plasmapause sounding. Planet. Space Sci. **30**(7), 657–668 (1982)
J.L. Green, S.A. Boardsen, Confinement of nonthermal continuum radiation to low latitudes. J. Geophys. Res. **104**(A5), 10307–10316 (1999)
J.L. Green, S.F. Fung, Advances in inner magnetosphere passive and active wave research, in *The Inner Magnetosphere: Physics and Modeling*, ed. by T.I. Pulkkinen, N.A. Tsyganenko, R.H.W. Friedel. Geophysical Monograph Series, vol. 155 (American Geophysical Union, Washington, 2005), pp. 181–202

J.L. Green, B.R. Sandel, S.F. Fung, D.L. Gallagher, B.W. Reinisch, On the origin of kilometric continuum. J. Geophys. Res. **107**(A7), 1105 (2002)
J.L. Green, S. Boardsen, S.F. Fung, H. Matsumoto, K. Hashimoto, R.R. Anderson, B.R. Sandel, B.W. Reinisch, Association of kilometric continuum radiation with plasmaspheric structures. J. Geophys. Res. **109**, A03203 (2004)
J.L. Green, S. Boardsen, L. Garcia, W.W.L. Taylor, S.F. Fung, B.W. Reinisch, On the origin of whistler mode radiation in the plasmasphere. J. Geophys. Res. **110**, A03201 (2005a)
J.L. Green, S.F. Fung, S. Boardsen, H.J. Christian, Distribution and origin of plasmapsheric plasma waves, in *Inner Magnetosphere Interactions: New Perspectives from Imaging*, ed. by J. Burch, M. Schulz, H. Spence. Geophysical Monograph Series, vol. 159 (American Geophysical Union, Washington, 2005b), pp. 113–126
J.L. Green, S. Boardsen, L. Garcia, S.F. Fung, B.W. Reinisch, Reply to "Comment on "On the origin of whistler mode radiation in the plasmasphere" by Green et al." J. Geophys. Res. **111**, A09211 (2006)
S. Grimald, Etude de l'émission et de la propagation du continuum terrestre à partir des données des satellites Cluster. Ph.D. thesis, University of Orléans, France, 2007
S. Grimald, P.M.E. Décréau, P. Canu, X. Suraud, X. Vallières, F. Darrouzet, C.C. Harvey, A quantitative test of Jones NTC beaming theory using CLUSTER constellation. Ann. Geophys. **25**(3), 823–831 (2007)
S. Grimald, P.M.E. Décréau, P. Canu, A. Rochel, X. Vallières, Medium-latitude sources of plasmaspheric non-thermal continuum radiations observed close to harmonics of the electron gyrofrequency. J. Geophys. Res. **113**, A11216 (2008)
D.A. Gurnett, The Earth as a radio source: The nonthermal continuum. J. Geophys. Res. **80**(19), 2751–2763 (1975)
D.A. Gurnett, Plasma wave interactions with energetic ions near the magnetic equator. J. Geophys. Res. **81**(16), 2765–2770 (1976)
D.A. Gurnett, L.A. Franck, VLF hiss and related plasma observations in the polar magnetosphere. J. Geophys. Res. **77**(1), 172–190 (1972)
D.A. Gurnett, S.D. Shawhan, R.R. Shaw, Auroral hiss, Z mode radiation, and auroral kilometric radiation in the polar magnetosphere: DE 1 observations. J. Geophys. Res. **88**(A1), 329–340 (1983)
D.A. Gurnett, R.L. Huff, J.S. Pickett, A.M. Persoon, R.L. Mutel, I.W. Christopher, C.A. Kletzing, U.S. Inan, W.L. Martin, J.-L. Bougeret, H.S.C. Alleyne, K.H. Yearby, First results from the Cluster wideband plasma wave investigation. Ann. Geophys. **19**(10–12), 1259–1272 (2001)
G. Gustafsson, M. André, T. Carozzi, A.I. Eriksson, C.-G. Fälthammar, R. Grard, G. Holmgren, J.A. Holtet, N. Ivchenko, T. Karlsson, Y. Khotyaintsev, S. Klimov, H. Laakso, P.-A. Lindqvist, B. Lybekk, G. Marklund, F. Mozer, K. Mursula, A. Pedersen, B. Popielawska, S. Savin, K. Stasiewicz, P. Tanskanen, A. Vaivads, J.-E. Wahlund, First results of electric field and density observations by Cluster EFW based on initial months of observations. Ann. Geophys. **19**(10–12), 1219–1240 (2001)
L. Harang, VLF-emissions observed at stations close to the auroral zone at stations on lower latitudes. J. Atmos. Terr. Phys. **30**, 1143–1160 (1968)
K. Hashimoto, W. Calvert, H. Matsumoto, Kilometric continuum detected by Geotail. J. Geophys. Res. **104**(A12), 28645–28656 (1999)
M. Hayakawa, S.S. Sazhin, Mid-latitude and plasmaspheric hiss: A review. Planet. Space Sci. **40**(10), 1325–1338 (1992)
M. Hayakawa, Y. Tanaka, J. Ohtsu, The morphologies of low-latitude and auroral VLF "hiss". J. Atmos. Terr. Phys. **37**, 517–529 (1975)
M. Hayakawa, N. Ohmi, M. Parrot, F. Lefeuvre, Direction finding of ELF hiss emissions in a detached plasma region of the magnetosphere. J. Geophys. Res. **91**(A1), 135–141 (1986)
R.A. Helliwell, *Whistlers and Associated Ionospheric Phenomena* (Stanford University Press, Stanford, 1965)
R.E. Horita, Proton cyclotron echoes and spurs observed on Alouette II and ISIS II. Radio Sci. **22**(4), 671–686 (1987)
R.B. Horne, G.V. Wheeler, H.S.C.K. Alleyne, Proton and electron heating by radially propagating fast magnetosonic waves. J. Geophys. Res. **105**(A12), 27597–27610 (2000)
R.B. Horne, R.M. Thorne, Y.Y. Shprits, N.P. Meredith, S.A. Glauert, A.J. Smith, S.G. Kanekal, D.N. Baker, M.J. Engebretson, J.L. Posch, M. Spasojevic, U.S. Inan, J.S. Pickett, P.M.E. Décréau, Wave acceleration of electrons in the Van Allen radiation belts. Nature **437**(7056), 227–230 (2005)
R.B. Horne, R.M. Thorne, S.A. Glauert, N.P. Meredith, D. Pokhotelov, O. Santolík, Electron acceleration in the Van Allen radiation belts by fast magnetosonic waves. Geophys. Res. Lett. **34**, L17107 (2007)
J.L. Horwitz, R.H. Comfort, C.R. Chappell, Thermal ion composition measurements of the formation of the new outer plasmasphere and double plasmapause during storm recovery phase. Geophys. Res. Lett. **11**(8), 701–704 (1984)

X. Huang, B.W. Reinisch, P. Song, J.L. Green, D.L. Gallagher, Developing an empirical density model of the plasmasphere using IMAGE/RPI observations. Adv. Space Res. **33**(6), 829–832 (2004)
U.S. Inan, M. Platino, T.F. Bell, D.A. Gurnett, J.S. Pickett, Cluster measurements of rapidly moving sources of ELF/VLF chorus. J. Geophys. Res. **109**, A05214 (2004)
J.E. Jackson, The reduction of topside ionograms to electron-density profiles. Proc. IEEE **57**(6), 960–975 (1969)
H.G. James, Wave propagation experiments at medium frequencies between two ionospheric satellites, 3. Z mode pulses. J. Geophys. Res. **84**(A2), 499–506 (1979)
D. Jones, Latitudinal beaming of planetary radio emissions. Nature **288**, 225–229 (1980)
D. Jones, Terrestrial myriametric radiation from the Earth's plasmapause. Planet. Space Sci. **30**(4), 399–410 (1982)
Y. Kasaba, H. Matsumoto, K. Hashimoto, R.R. Anderson, J.-L. Bougeret, M.L. Kaiser, X.Y. Wu, I. Nagano, Remote sensing of the plasmapause during substorms: Geotail observation of nonthermal continuum enhancement. J. Geophys. Res. **103**(A9), 20389–20405 (1998)
C.F. Kennel, H.E. Petschek, Limit on stably trapped particle fluxes. J. Geophys. Res. **71**(1), 1–28 (1966)
I. Kimura, Effects of ions on whistler-mode ray tracing. Radio Sci. **1**(3), 269–283 (1966)
J.W. King, D.M. Preece, Observations of proton gyroeffects in the topside ionosphere. J. Atmos. Terr. Phys. **29**, 1387–1390 (1967)
I.P. Kurchashov, I.S. Nikomarov, V.A. Pilipenko, A. Best, Field line resonance effects in local meridional structure of mid-latitude geomagnetic pulsations. Ann. Geophys. **5**(6), 147–154 (1987)
W.S. Kurth, Detailed observations of the source of terrestrial narrowband electromagnetic radiation. Geophys. Res. Lett. **9**(12), 1341–1344 (1982)
W.S. Kurth, D.A. Gurnett, R.R. Anderson, Escaping nonthermal continuum radiation. J. Geophys. Res. **86**(A7), 5519–5531 (1981)
T. Laaspere, M.G. Morgan, W.C. Johnson, Chorus, hiss, and other audio-frequency emissions at stations of the whistlers-east network. Proc. IEEE **52**(11), 1331–1349 (1964)
J. LaBelle, R.A. Treumann, Auroral radio emissions, 1. Hisses, roars, and bursts. Space Sci. Rev. **101**(3), 295–440 (2002)
L.J. Lanzerotti, H. Fukunishi, Relationships of the characteristics of magnetohydrodynamic waves to plasma density gradients in the vicinity of the plasmapause. J. Geophys. Res. **80**(34), 4627–4634 (1975)
J.F. Lemaire, K.I. Gringauz, *The Earth's Plasmasphere* (Cambridge University Press, New York, 1998)
B.T. Loftus, T.E. Van Zandt, W. Calvert, Observations of conjugate ducting by the fixed-frequency topside-sounder satellite. Ann. Geophys. **22**(4), 530–537 (1966)
L.R. Lyons, R.M. Thorne, C.F. Kennel, Pitch-angle diffusion of radiation belt electrons within the plasmasphere. J. Geophys. Res. **77**(19), 3455–3474 (1972)
A. Masson, U.S. Inan, H. Laakso, O. Santolík, P. Décréau, Cluster observations of mid-latitude hiss near the plasmapause. Ann. Geophys. **22**(7), 2565–2575 (2004)
H. Matsui, J.C. Foster, D.L. Carpenter, I. Dandouras, F. Darrouzet, J. De Keyser, D.L. Gallagher, J. Goldstein, P.A. Puhl-Quinn, C. Vallat, Electric fields and magnetic fields in the plasmasphere: A perspective from CLUSTER and IMAGE. Space Sci. Rev. (2009, this issue)
C.E. McIlwain, Coordinates for mapping the distribution of magnetically trapped particles. J. Geophys. Res. **66**(11), 3681–3691 (1961)
F.W. Menk, Spectral structure of mid-latitude Pc3-4 geomagnetic pulsations. J. Geomagn. Geoelectr. **40**(1), 33–61 (1988)
F.W. Menk, B.J. Fraser, C.L. Waters, C.W.S. Ziesolleck, Q. Feng, S.H. Lee, P.W. McNabb, Ground measurements of low latitude magnetospheric field line resonances, in *Solar Wind Sources of Magnetospheric Ultra-Low-Frequency Waves*, ed. by M.J. Engebretson, K. Takahashi, M. Scholer. Geophysical Monograph Series, vol. 81 (American Geophysical Union, Washington, 1994), pp. 299–310
F.W. Menk, D. Orr, M.A. Clilverd, A.J. Smith, C.L. Waters, D.K. Milling, B.J. Fraser, Monitoring spatial and temporal variations in the dayside plasmasphere using geomagnetic field line resonances. J. Geophys. Res. **104**(A9), 19955–19969 (1999)
N.P. Meredith, R.B. Horne, M.A. Clilverd, D. Horsfall, R.M. Thorne, R.R. Anderson, Origins of plasmaspheric hiss. J. Geophys. Res. **111**, A09217 (2006)
N.P. Meredith, R.B. Horne, S.A. Glauert, R.R. Anderson, Slot region electron loss timescales due to plasmaspheric hiss and lightning-generated whistlers. J. Geophys. Res. **112**, A08214 (2007)
D.D. Morgan, D.A. Gurnett, The source location and beaming of terrestrial continuum radiation. J. Geophys. Res. **96**(A6), 9595–9613 (1991)
D.B. Muldrew, Radio propagation along magnetic field-aligned sheets of ionization observed by the Alouette topside sounder. J. Geophys. Res. **68**(19), 5355–5370 (1963)
D.B. Muldrew, Nonvertical propagation and delayed-echo generation observed by the topside sounders. Proc. IEEE **57**(6), 1097–1107 (1969)

D.B. Muldrew, Electrostatic resonances associated with the maximum frequencies of cyclotron-harmonic waves. J. Geophys. Res. **77**(10), 1794–1801 (1972)
D.B. Muldrew, Topside sounder proton-cyclotron echo generation from a plasma memory process and electron Bernstein-wave propagation. Radio Sci. **33**(5), 1395–1411 (1998)
F. Němec, O. Santolík, K. Gereová, E. Macúšová, Y. de Conchy, N. Cornilleau-Wehrlin, Initial results of a survey of equatorial noise emissions observed by the Cluster spacecraft. Planet. Space Sci. **53**(1–3), 291–298 (2005)
F. Němec, O. Santolík, K. Gereová, E. Macúšová, H. Laakso, Y. de Conchy, M. Maksimovic, N. Cornilleau-Wehrlin, Equatorial noise: Statistical study of its localization and the derived number density. Adv. Space Res. **37**(3), 610–616 (2006)
D. Nunn, Y. Omura, H. Matsumoto, I. Nagano, S. Yagitani, The numerical simulation of VLF chorus and discrete emissions observed on the Geotail satellite using a Vlasov code. J. Geophys. Res. **102**(A12), 27083–27097 (1997)
Y. Omura, H. Matsumoto, D. Nunn, M.J. Rycroft, A review of observational, theoretical and numerical studies of VLF triggered emissions. J. Atmos. Terr. Phys. **53**(5), 351–368 (1991)
Y. Omura, Y. Katoh, D. Summers, Theory and simulation of the generation of whistler-mode chorus. J. Geophys. Res. **113**, A04223 (2008)
T. Ondoh, Latitudinal changes of polar hiss and plasmapause hiss associated with magnetospheric processes. Adv. Space Res. **37**(3), 581–591 (2006)
H. Oya, Generation mechanism of proton cyclotron echoes due to pulsed radio frequency waves in space plasma. J. Geophys. Res. **83**(A5), 1991–2008 (1978)
M. Parrot, O. Santolík, N. Cornilleau-Wehrlin, M. Maksimovic, C.C. Harvey, Source location of chorus emissions observed by Cluster. Ann. Geophys. **22**(2), 473–480 (2003)
M. Parrot, O. Santolík, N. Cornilleau-Wehrlin, M. Maksimovic, C. Harvey, Magnetospherically reflected chorus waves revealed by ray tracing with CLUSTER data. Ann. Geophys. **21**(5), 1111–1120 (2004a)
M. Parrot, O. Santolík, D.A. Gurnett, J.S. Pickett, N. Cornilleau-Wehrlin, Characteristics of magnetospherically reflected chorus waves observed by CLUSTER. Ann. Geophys. **22**(7), 2597–2606 (2004b)
V. Pierrard, J. Goldstein, N. André, V.K. Jordanova, G.A. Kotova, J.F. Lemaire, M.W. Liemohn, H. Matsui, Recent progress in physics-based models of the plasmasphere. Space Sci. Rev. (2009, this issue)
M. Platino, U.S. Inan, T.F. Bell, J.S. Pickett, P. Canu, Rapidly moving sources of upper band ELF/VLF chorus near the magnetic equator. J. Geophys. Res. **111**, A09218 (2006)
B.W. Reinisch, D.M. Haines, K. Bibl, G. Cheney, I.A. Galkin, X. Huang, S.H. Myers, G.S. Sales, R.F. Benson, S.F. Fung, J.L. Green, S. Boardsen, W.W.L. Taylor, J.-L. Bougeret, R. Manning, N. Meyer-Vernet, M. Moncuquet, D.L. Carpenter, D.L. Gallagher, P. Reiff, The Radio Plasma Imager investigation on the IMAGE spacecraft. Space Sci. Rev. **91**(1–2), 319–359 (2000)
B.W. Reinisch, X. Huang, D.M. Haines, I.A. Galkin, J.L. Green, R.F. Benson, S.F. Fung, W.W.L. Taylor, P.H. Reiff, D.L. Gallagher, J.-L. Bougeret, R. Manning, D.L. Carpenter, S.A. Boardsen, First results from the Radio Plasma Imager on IMAGE. Geophys. Res. Lett. **28**(6), 1167–1170 (2001)
B.W. Reinisch, M.B. Moldwin, R.E. Denton, D.L. Gallagher, H. Matsui, V. Pierrard, J. Tu, Augmented empirical models of plasmaspheric density and electric field using IMAGE and CLUSTER data. Space Sci. Rev. (2009, this issue)
K. Rönnmark, Genereration of magnetospheric radiation by decay of Bernstein waves. Geophys. Res. Lett. **12**(10), 639–642 (1985)
C.T. Russell, R.E. Holzer, E.J. Smith, OGO 3 observations of ELF noise in the magnetosphere, 1. Spatial extent and frequency of occurrence. J. Geophys. Res. **74**(3), 755–777 (1969)
C.T. Russell, R.E. Holzer, E.J. Smith, OGO 3 observations of ELF noise in the magnetosphere, 2. The nature of the equatorial noise. J. Geophys. Res. **75**(4), 755–768 (1970)
J.C. Samson, The spectral matrix, eigenvalues, and principal components in the analysis of multichannel geophysical data. Ann. Geophys. **1**(3), 115–119 (1983)
B.R. Sandel, A.L. Broadfoot, C.C. Curtis, R.A. King, T.C. Stone, R.H. Hill, J. Chen, O.H.W. Siegmund, R. Raffanti, D.D. Allred, R.S. Turley, D.L. Gallagher, The Extreme Ultraviolet imager investigation for the IMAGE mission. Space Sci. Rev. **91**(1–2), 197–242 (2000)
O. Santolík, D.A. Gurnett, Transverse dimensions of chorus in the source region. Geophys. Res. Lett. **30**(2), 1031 (2003)
O. Santolík, M. Parrot, L.R.O. Storey, J.S. Pickett, D.A. Gurnett, Propagation analysis of plasmaspheric hiss using Polar PWI measurements. Geophys. Res. Lett. **28**(6), 1127–1130 (2001)
O. Santolík, J.S. Pickett, D.A. Gurnett, M. Maksimovic, N. Cornilleau-Wehrlin, Spatiotemporal variability and propagation of equatorial noise observed by Cluster. J. Geophys. Res. **107**(A12), 1495 (2002)
O. Santolík, D.A. Gurnett, J.S. Pickett, M. Parrot, N. Cornilleau-Wehrlin, Spatio-temporal structure of storm-time chorus. J. Geophys. Res. **108**(A7), 1278 (2003)

O. Santolík, D.A. Gurnett, J.S. Pickett, Multipoint investigation of the source region of storm-time chorus. Ann. Geophys. **22**(7), 2555–2563 (2004a)
O. Santolík, D.A. Gurnett, J.S. Pickett, M. Parrot, N. Cornilleau-Wehrlin, A microscopic and nanoscopic view of storm-time chorus on 31 March 2001. Geophys. Res. Lett. **31**, L02801 (2004b)
O. Santolík, F. Němec, K. Gereová, E. Macúšová, Y. de Conchy, N. Cornilleau-Wehrlin, Systematic analysis of equatorial noise below the lower hybrid frequency. Ann. Geophys. **22**(7), 2587–2595 (2004c)
O. Santolík, D.A. Gurnett, J.S. Pickett, M. Parrot, N. Cornilleau-Wehrlin, Central position of the source region of storm-time chorus. Planet. Space Sci. **53**(1–3), 299–305 (2005a)
O. Santolík, E. Macúšová, K.H. Yearby, N. Cornilleau-Wehrlin, H.S.C. Alleyne, Radial variation of whistler-mode chorus: first results from the STAFF/DWP instrument on board the Double Star TC-1 spacecraft. Ann. Geophys. **23**(8), 2937–2942 (2005b)
O. Santolík, J. Chum, M. Parrot, D.A. Gurnett, J.S. Pickett, N. Cornilleau-Wehrlin, Propagation of whistler mode chorus to low altitudes: Spacecraft observations of structured ELF hiss. J. Geophys. Res. **111**, A10208 (2006)
S.S. Sazhin, Improved quasilinear models of parallel whistler-mode instability. Planet. Space Sci. **37**(6), 633–647 (1989)
S.S. Sazhin, M. Hayakawa, Magnetospheric chorus emissions: A review. Planet. Space Sci. **40**(5), 681–697 (1992)
M. Schulz, Eigenfrequencies of geomagnetic field lines and implications for plasma-density modeling. J. Geophys. Res. **101**(A8), 17385–17397 (1996)
R.L. Smith, Propagation characteristics of whistlers trapped in field-aligned columns of enhanced ionization. J. Geophys. Res. **66**(11), 3699–3707 (1961)
V.S. Sonwalkar, Magnetospheric LF-, VLF-, and ELF-waves, in *Handbook of Atmospheric Electrodynamics*, ed. by H. Volland, vol. II (CRC, Boca Raton, 1995), pp. 407–462
V.S. Sonwalkar, U.S. Inan, Lightning as an embryonic source of VLF hiss. J. Geophys. Res. **94**(A6), 6986–6994 (1989)
V.S. Sonwalkar, D.L. Carpenter, T.F. Bell, M. Spasojević, U.S. Inan, J. Li, X. Chen, A. Venkatasubramanian, J. Harikumar, R.F. Benson, W.W.L. Taylor, B.W. Reinisch, Diagnostics of magnetospheric electron density and irregularities at altitudes <5000 km using whistler and Z mode echoes from radio sounding on the IMAGE satellite. J. Geophys. Res. **109**, A11212 (2004)
V.S. Sonwalkar, D.L. Carpenter, A. Reddy, B.W. Reinisch, Magnetospherically reflected (MR), specularly reflected (SR), and backscattered (BS) whistler mode (WM) echoes observed on the IMAGE satellite: Whistler-mode sounding of electron density, ion composition (H^+, He^+, O^+), and density irregularities along the geomagnetic field line. J. Geophys. Res. (2009, submitted)
D.J. Southwood, Some features of field line resonances in the magnetosphere. Planet. Space Sci. **22**(3), 483–491 (1974)
L.R.O. Storey, An investigation of whistling atmospherics. Phil. Trans. R. Soc. (Lond.) **246A**, 113–141 (1953)
L.R.O. Storey, F. Lefeuvre, M. Parrot, L. Cairó, R.R. Anderson, Initial survey of the wave distribution functions for plasmaspheric hiss observed by ISEE 1. J. Geophys. Res. **96**(A11), 19469–19489 (1991)
D. Summers, B. Ni, N.P. Meredith, R.B. Horne, R.M. Thorne, M.B. Moldwin, R.R. Anderson, Electron scattering by whistler-mode ELF hiss in plasmaspheric plumes. J. Geophys. Res. **113**, A04219 (2008)
K. Takahashi, R.L. McPherron, Harmonic structure of Pc 3-4 pulsations. J. Geophys. Res. **87**(A3), 1504–1516 (1982)
T. Tamao, The structure of three-dimensional hydromagnetic waves in a uniform cold plasma. J. Geomagn. Geoelectr. **16**(1), 89–114 (1964)
R.M. Thorne, E.J. Smith, R.K. Burton, R.E. Holzer, Plasmaspheric hiss. J. Geophys. Res. **78**(10), 1581–1596 (1973)
R.M. Thorne, R.B. Horne, N.P. Meredith, Comment on "On the origin of whistler mode radiation in the plasmasphere" by Green et al. J. Geophys. Res. **111**, A09210 (2006)
V.Y. Trakhtengerts, A generation mechanism for chorus emission. Ann. Geophys. **17**(1), 95–100 (1999)
V.Y. Trakhtengerts, A.G. Demekhov, E.E. Titova, B.V. Kozelov, O. Santolik, D. Gurnett, M. Parrot, Interpretation of Cluster data on chorus emissions using the backward wave oscillator model. Phys. Plasma **11**(4), 1345–1351 (2004)
V.A. Troitskaya, A.V. Gul'Elmi, Diagnostics of the parameters of the magnetosphere and of the interplanetary space by means of micropulsations, in *Low-Frequency Waves and Irregularities in the Ionosphere*, ed. by N. D'Angelo. Astrophysics and Space Science Library, vol. 14 (1969), pp. 120–136
B.T. Tsurutani, E.J. Smith, R.M. Thorne, Electromagnetic hiss and relativistic electron losses in the inner zone. J. Geophys. Res. **80**(4), 600–607 (1975)
C.L. Waters, F.W. Menk, B.J. Fraser, The resonance structure of low latitude Pc3 geomagnetic pulsations. Geophys. Res. Lett. **18**(12), 2293–2296 (1991)

J.M. Watts, An observation of audio-frequency electromagnetic noise during a period of solar disturbance. J. Geophys. Res. **62**(2), 199–206 (1957)
D.C. Webb, The analysis of non stationary data using complex demodulation. Ann. Telecommunic. **34**, 131–137 (1979)
D.C. Webb, L.J. Lanzerotti, C.G. Park, A comparison of ULF and VLF measurements of magnetospheric cold plasma densities. J. Geophys. Res. **82**(32), 5063–5072 (1977)
K. Yumoto, Generation and propagation mechanisms of low-latitude magnetic pulsations–A review. J. Geophys. **60**, 79–105 (1986)

Available online at www.sciencedirect.com
ScienceDirect
Advances in Space Research 44 (2009) 979–986
ADVANCES IN SPACE RESEARCH (a COSPAR publication)
www.elsevier.com/locate/asr

MLR events and associated triggered emissions observed by DEMETER

M. Parrot [a,*], F. Němec [a,b,c]

[a] LPC2E/CNRS, Laboratoire de Physique et Chimie de l'Environment et de l'Espace, 3A Avenue de la Recherche Scientifique, 45071 Orléans cedex 2, France
[b] Institute of Atmospheric Physics, Academy of Sciences of the Czech Republic, Prague, Czech Republic
[c] Faculty of Mathematics and Physics, Charles University, Prague, Czech Republic

Received 17 April 2009; received in revised form 19 June 2009; accepted 4 July 2009

Abstract

This paper gives an overview of different sets of new Magnetospheric Line Radiation (MLR) observed by the satellite DEMETER. Different types of emissions have been observed: emissions called Power Line Harmonic Radiation (PLHR) with frequency lines exactly separated by 50/100 or 60/120 Hz, emissions with frequency lines not exactly separated by 50/100 or 60/120 Hz and drifting in frequency (MLR). By comparison with past observations one can say that some MLR events are due to man-made PLHR which may suffer a non-linear gyro-resonant interaction at the magnetic equator. It is also shown that periodic emissions are very often associated with the MLR. In this case the origin of these waves is natural. The lines are produced by the periodicity and the frequency band limits of the individual elements which causes the appearance of lines on the spectrograms. Finally the paper shows that MLR can trigger emissions.

Keyword: Magnetospheric Line Radiation, Ionosphere

1. Introduction

Electromagnetic waves observed by a low-orbiting satellite represented in the form of the frequency–time spectrogram sometimes consist of several nearly horizontal and almost equidistant intense lines (Bell et al., 1982; Rodger et al., 1995; Parrot et al., 2005, 2006a, 2007; Němec et al., 2006b, 2007a,b, 2008, 2009). These are called Magnetospheric Line Radiation (MLR). They have been reported also in the ground-based data and the evidence for their propagation through the magnetosphere has been given (Helliwell et al., 1975; Park and Helliwell, 1978; Matthews and Yearby, 1981; Park and Helliwell, 1981, 1983; Yearby et al., 1983; Rodger et al., 1999, 2000; Manninen, 2005). In some cases, mutual frequency separation of the lines is 50/100 or 60/120 Hz. These are usually called Power Line Harmonic Radiation (PLHR) and are believed to be caused by an electromagnetic radiation from electric power systems on the ground (e.g. Němec et al., 2006b, 2007a,b, 2008). It must be noticed that an individual PLHR line may not be at an exact harmonic frequency of 50 or 60 Hz because the power system may not operate at precisely the nominal frequency. A small frequency shift cannot be recognized when looking at frequency spacing between two lines, but at ~50th harmonic, it can easily shift the lines by several Hz (Němec et al., 2007b). The PLHR role in the ionosphere is still questionable, because they can serve as a trigger for new emissions (Nunn et al., 1999; Manninen, 2005). Rodger et al. (1995) performed a satellite survey using data from ISIS 1 and ISIS 2 satellites and reported the existence of two distinct classes of MLR-like events: the first of them ("Tram Lines", TL) consisted of events that appeared to lie close to the harmonics of 50/60 Hz; the second class of events ("Magnetospheric Line Radiation", MLR), formed by lines with larger bandwidth, did not show any evidence of a relationship with power line harmonics. This was further investigated by Němec et al. (2007a),

* Corresponding author. Tel.: +33 238 255291; fax: +33 238 631234.
E-mail address: mparrot@cnrs-orleans.fr (M. Parrot).

0273-1177/$36.00 © 2009 COSPAR. Published by Elsevier Ltd. All rights reserved.
doi:10.1016/j.asr.2009.07.001

who performed a systematic survey of MLR-like events using the data from the DEMETER spacecraft. They confirmed the existence of the two classes of events (PLHR and "real-MLR") and demonstrated their different properties (intensity, frequency, most favourable values of Kp index).

A systematic study of satellite observations of PLHR was performed by Němec et al. (2006b, 2007b, 2008). They showed that the frequency spacing of the lines corresponds well to the base power system frequency at possible generation regions. Moreover, they presented a numerical calculation of penetration characteristics of the ionosphere and suggested that it could explain larger peak intensities of PLHR observed during the night. Ando et al. (2002) performed a theoretical analysis of penetration of PLHR into the ionosphere and estimated the area of the affected region. Parrot et al. (2007) showed for the first time large scale MLR observed simultaneously on ground and on board a low-altitude satellite which was flying over the same zone. Parrot et al. (2006a) described six storm-time observations of real-MLR events measured by DEMETER. They performed a detailed analysis of the events and discussed their possible link to electromagnetic ion cyclotron waves at proton cyclotron harmonics emitted from the equatorial region. Němec et al. (2009) analyzed several tens of real-MLR observations, performed a detailed analysis of wave properties and estimated the source region to be located in the equatorial plane at radial distances of 1.5–3.5 R_E. Finally, it has been shown (Němec et al., 2007a, 2009) that the events observed close to the geomagnetic equator have similar properties as equatorial noise emissions routinely observed at radial distances 2–7 Earth radii and within 10° from the magnetic equator (Russel et al., 1970; Gurnett, 1976; Laakso et al., 1990; Kasahara et al., 1994; Santolík et al., 2002, 2004; Němec et al., 2005, 2006a).

The purpose of this paper is to present specific new MLR events observed by DEMETER. Some events show associated periodic emissions and others triggered emissions. Section 2 will briefly describe the wave experiment onboard the satellite. The events will be described in Section 3 whereas conclusions will be given in Section 4.

2. The wave experiment

DEMETER is low-altitude satellite (700 km) with a polar circular orbit which measures electromagnetic waves all around the Earth except in the auroral zones. The frequency range for the electric field is from DC up to 3.5 MHz, and for the magnetic field from a few Hz up to 20 kHz. There are two scientific modes: a survey mode where spectra of one electric and one magnetic component are onboard computed up to 20 kHz and a burst mode where waveforms of one electric field component and one magnetic field component are recorded with a sampling frequency of 40 kHz. The burst mode allows performing spectral analysis with better time and frequency resolution. All events shown in this paper have been recorded during the burst mode of the experiment. The geographical locations of the burst mode are mainly linked to the seismic regions due to the main scientific objectives of the project. They have also been put in other regions but irregularly. Details of the wave experiment can be found in Parrot et al. (2006b) and Berthelier et al. (2006).

3. Selection of events

Fig. 1 shows a VLF spectrogram of an electric field component recorded on 13 August 2006 during one minute between 21:42:30 and 21:43:30 UT. The frequency range is between 2 and 5 kHz. A set of three lines can be observed just above 3.5 kHz. The frequencies of lines are close to 3603, 3711, and 3808 Hz, which means that the frequency interval is approximately equal to 100 Hz. There is no apparent frequency shift of the lines during the observation. The event was measured close to the New Zealand and from 21:41:30 to 21:46:00 UT when the satellite stops the registration at high latitudes. Relatively thin lines forming the event and frequency spacing close to the multiple of base power system frequency (50 Hz at New Zealand) represent a good indication that the event is caused by PLHR.

Fig. 2 shows an event recorded on 15 September 2005 during a long time interval. It is located between the west coast of US and Hawaii. It starts at 07:17:00 UT close to the equator and it is not seen after 07:33:58 UT when the satellite stops recording data above Alaska. The spectrograms were computed onboard with data from an electric component (top) and a magnetic component (bottom) between 0 and 2 kHz. A set of lines drifting in frequency can be observed all the time both with electric and magnetic component showing the nature of the electromagnetic whistler mode wave. This event is very similar to the one described in Parrot et al. (2007). The vertical white lines delimit the occurrence of a burst mode between 07:30:30 and 07:31:30 UT. A detailed spectral analysis indicates that the frequency interval between the lines is ~68 Hz at this time. This event belongs to the "real-MLR" class according to the classification introduced by Němec et al. (2007a).

Fig. 3 displays an event recorded on 18 October 2006 when the satellite was above the west coast of US. Fig. 3a shows the spectrogram of an electric field component from 0 up to 20 kHz, the totality of the VLF range observed by DEMETER. From the bottom to the top we observed the cutoff frequency of the hiss which is between 1 and 3 kHz, the set of MLR lines which are around 5 kHz, the lower hybrid frequency around 8 kHz which is increasing in frequency with the time, a VLF wave by a ground-based transmitter just above 15 kHz. The lines are embedded with periodic emission. A zoom of these lines is shown in Fig. 3b. The spectrogram is between 4 and 6 kHz. It is seen that the periodic elements start at frequencies which are on a given line. These elements are not synchronized for different starting frequency lines. The frequency length of these rising elements is several hundreds of Hz. It is also seen, particularly with the top

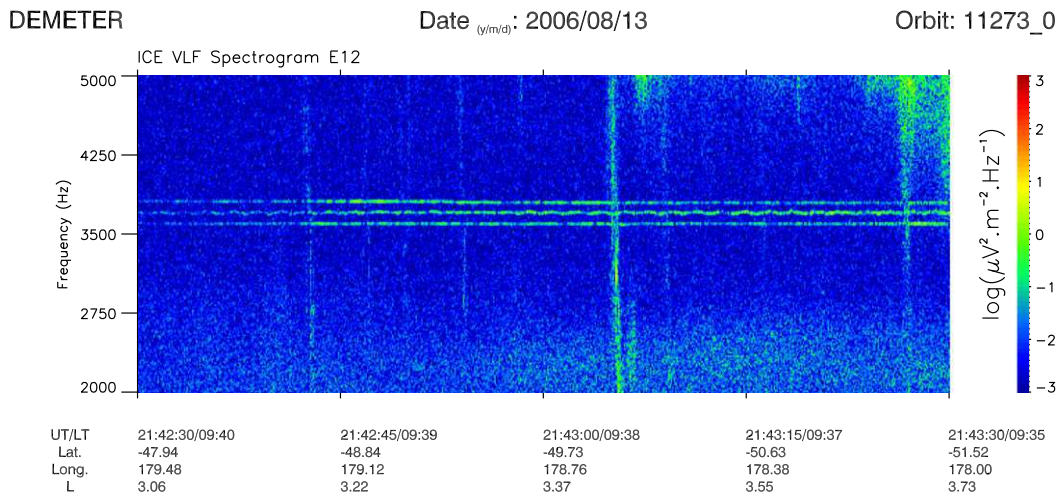

Fig. 1. Spectrogram of an electric field component recorded on 13 August 2006 between 2 and 5 kHz. The time interval (21:42:30–21:43:30 UT), the local time (LT) the geographic position (Lat. and Long.), and the *L*-value are indicated below. The intensity is color-coded according to the scale on the right. (For interpretation of the references to color in this figure legend, the reader is referred to the web version of this paper.)

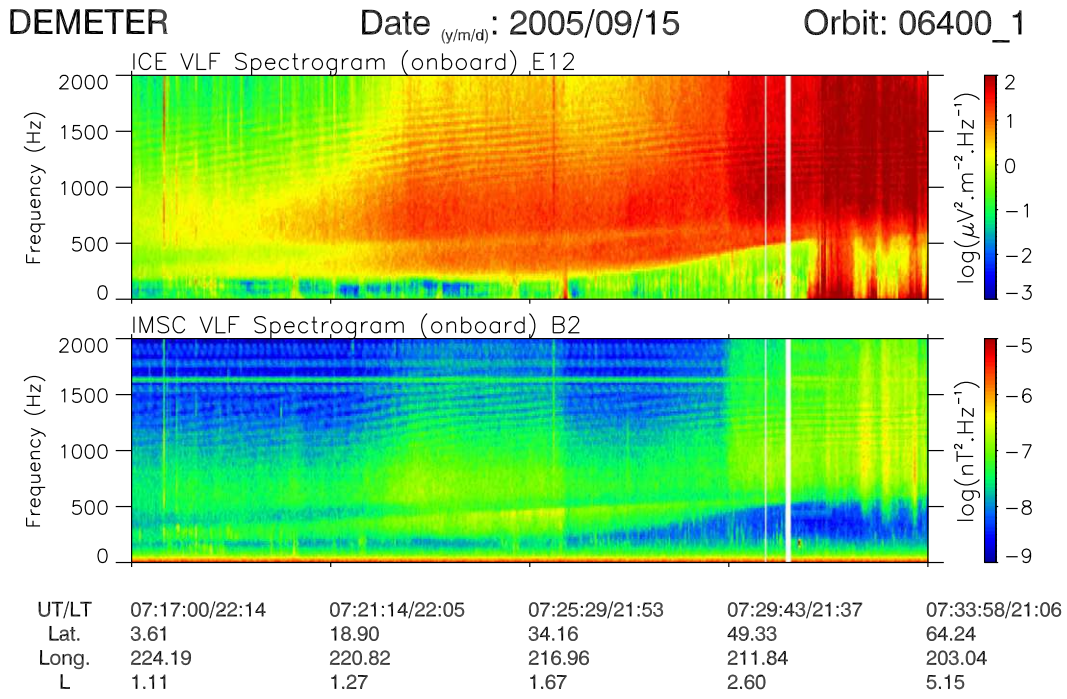

Fig. 2. Spectrograms of an electric field component (top) and a magnetic field component (bottom) recorded on 15 September 2005 between 07:17:00 and 07:33:58 UT. The frequency range is 0–2 kHz. The universal time (UT), the local time (LT), the geographic position (Lat. and Long.), and the *L*-value are indicated below. The intensities are color-coded according to the scales on the right. (For interpretation of the references to color in this figure legend, the reader is referred to the web version of this paper.)

set of periodic elements that the time interval between them is of the order of 4 s which is the 2 hop bounce wave period due to propagation in the magnetosphere and reflection in the opposite hemisphere. Due to the fact that the timing of the periodic emissions depends on the frequency of the corresponding line, their patterns are much more complicated. Other MLR events similar to Fig. 3 have been observed close to the west coast of US. A very different pattern is observed in Fig. 4. Fig. 4 is similar to Fig. 3 but the data are recorded on 4 April 2007. The MLR event is recorded during an orbit which is not very far from the east coast of Japan and ends over Kamchatka. It is observed in a frequency band between 2.6 and 3.7 kHz and consists of periodic falling elements with a time period of ~3.4 s. Different sets of elements with a negative slope appear because they are not synchronized. It depends on the frequency as it is with the periodic elements in Fig. 3. In fact in Figs. 3 and 4 MLR only appears due to the pattern displayed on

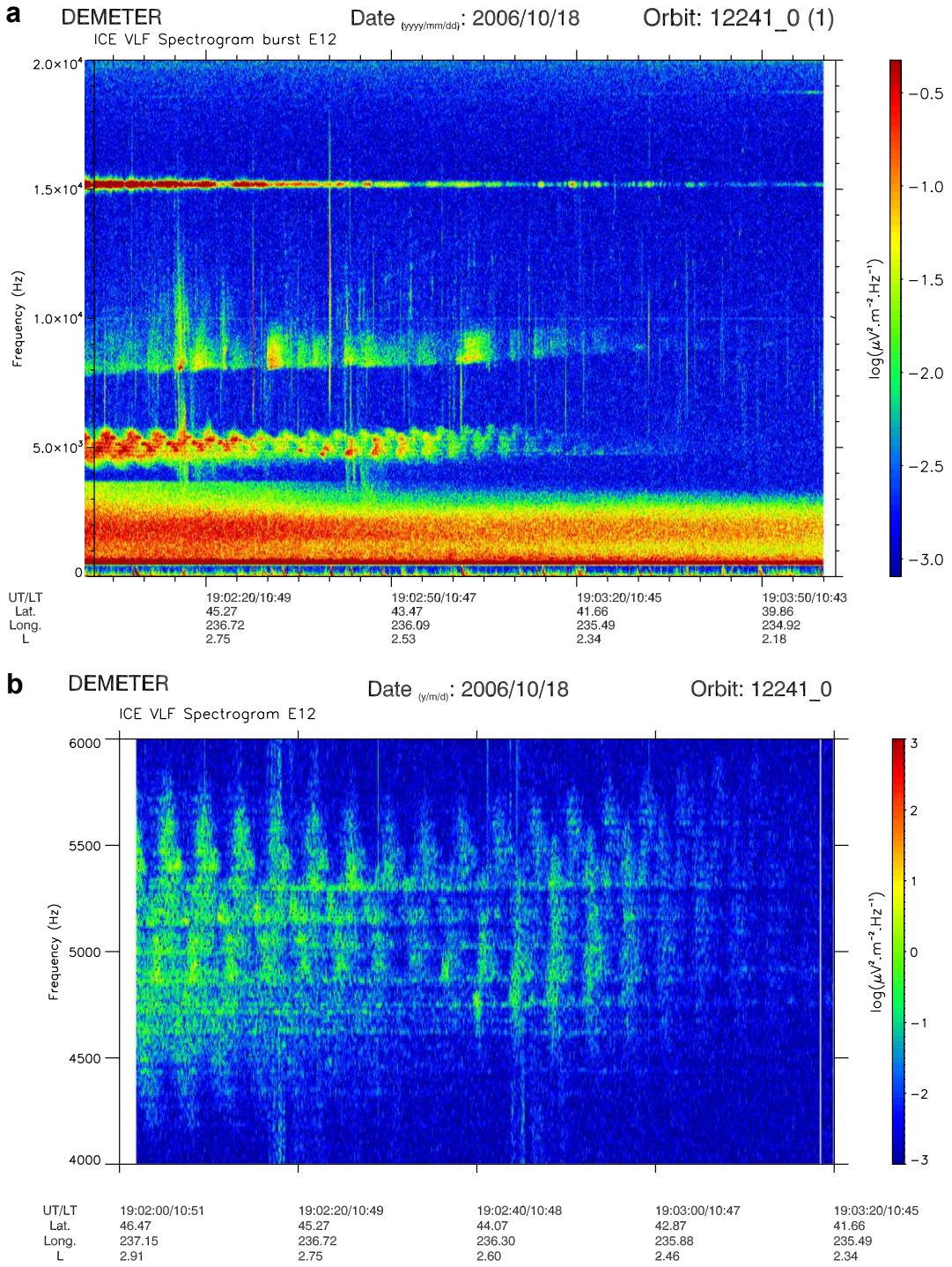

Fig. 3. (a) Two minute spectrogram of an electric field component recorded on 18 October 2006 between 2 and 5 kHz. The universal time (UT), the local time (LT), the geographic position (Lat. and Long.), and the *L*-value are indicated below. The intensities are color-coded according to the scales on the right. (b) Zoom of the spectrogram shown in (a). The frequency band is now between 4 and 6 kHz and the time interval between 19:02:00 and 19:03:20 UT. (For interpretation of the references to color in this figure legend, the reader is referred to the web version of this paper.)

the spectrogram by the periodic elements. These periodic emissions are very similar to the emissions previously observed by Helliwell (1965) on ground. In this case the MLR have a natural origin.

Fig. 5 displays triggered emissions related to MLR. Two rising elements can be observed in Fig. 5a. The first one is clearly supported by a parent line at a frequency of ~2314 Hz whereas the second appears even when the intensity of the line is too low to be detected. Finally, Fig. 5b shows rising hooks with at high frequencies several branches of triggered emissions. They also show a nearly 4 s periodicity corresponding to bouncing waves in the

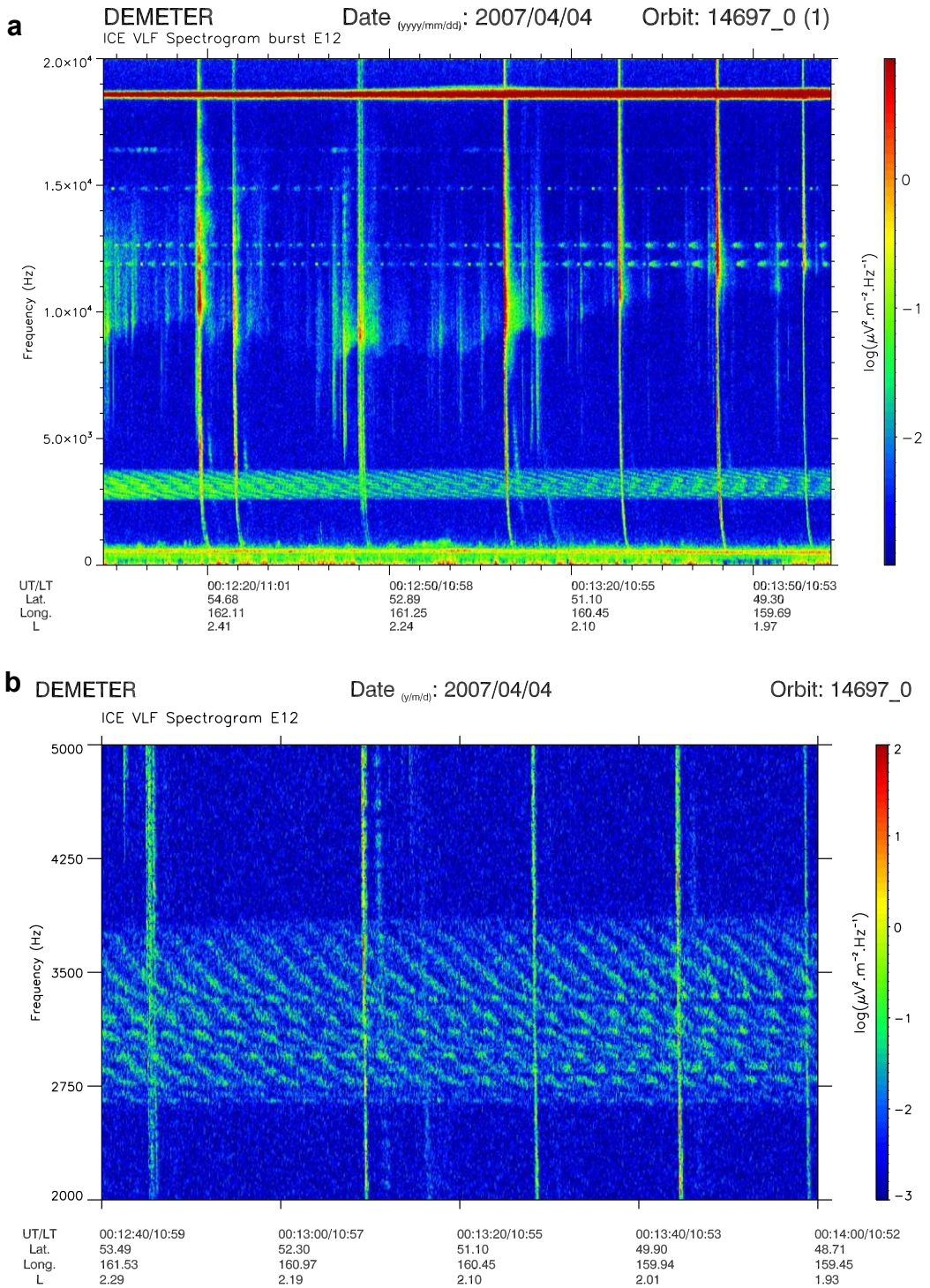

Fig. 4. Similar to Fig. 3 but for an event recorded on 4 April 2007.

magnetosphere. They were recorded on 19 May 2005 above Finland. No supporting lines can be detected but these elements are very similar to those detected on ground in the same region some years ago (Fig. 1 of Nunn et al., 1999). On ground the PLHR were observed but not at the altitude of the satellite because they are too weak. It was also the case during the event above Finland reported by Parrot et al. (2007).

4. Conclusions

The low-orbiting satellite DEMETER is an ideal platform to survey man-made waves due to the sensibility of the wave sensors, the time and frequency resolution of the experiment, and the data registration all around the Earth. However, statistical survey of geographical occurrence of the events cannot be performed because the

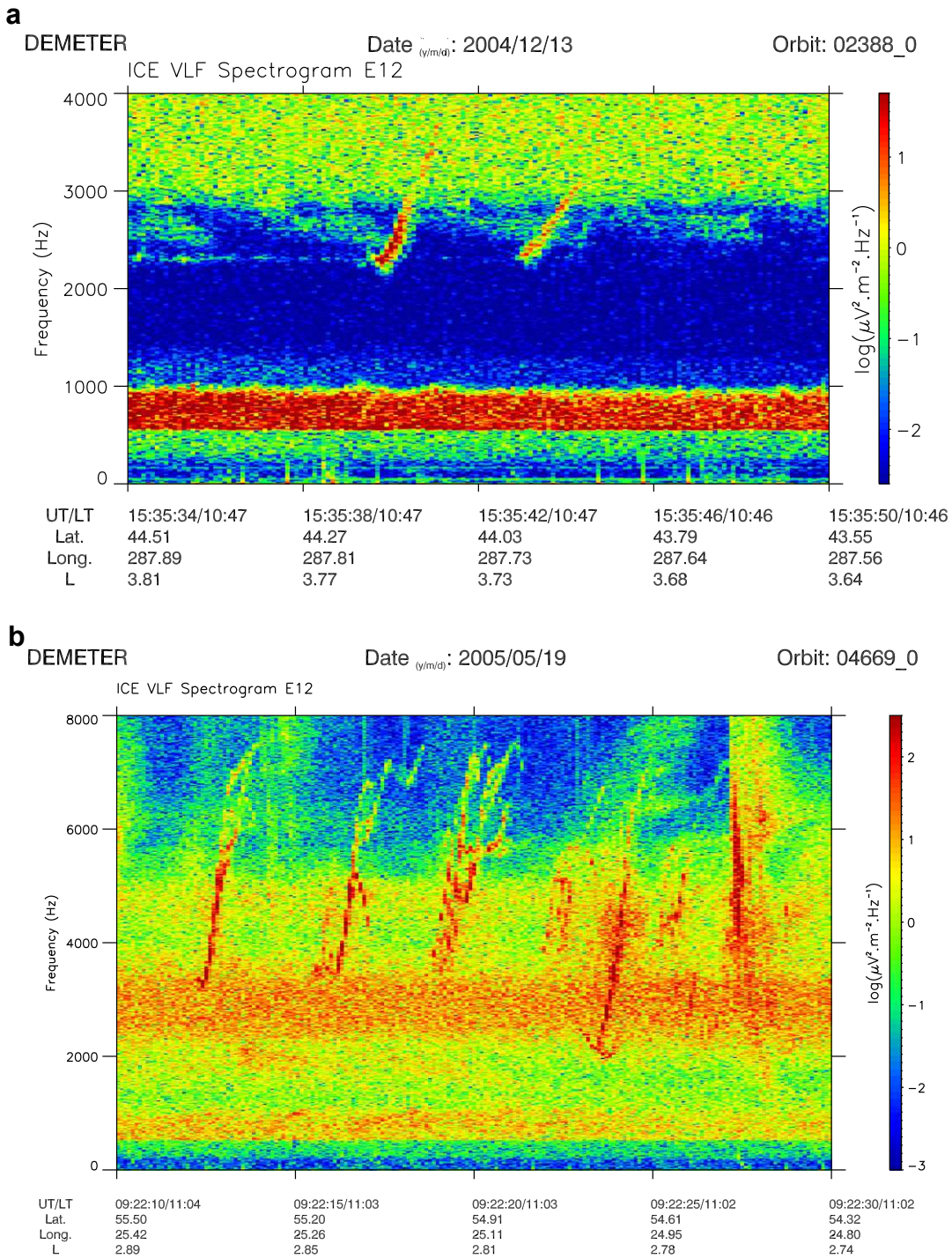

Fig. 5. Spectrograms of an electric field component recorded on 13 December 2004 (a) and on 19 May 2005 (b). The universal time (UT), the local time (LT), the geographic position (Lat. and Long.), and the L-value are indicated below. The intensities are color-coded according to the scales on the right. (For interpretation of the references to color in this figure legend, the reader is referred to the web version of this paper.)

observations are limited by the geographical positions of the burst mode. A variety of new MLR events recorded by DEMETER have been presented in this paper. The common feature is that they are observed in a frequency band from 2 kHz up to 5 kHz. Concerning these MLR events DEMETER observes four different kinds of waves:

1. Emissions directly related to PLHR (Fig. 1) where the frequency interval between the lines is a multiple of 50 or 60 Hz. The lines are observed at high frequencies because, for example in Finland, the industrial plants use 12 pulse bridges to convert 220 V/3 phases to DC power, and harmonics are radiated at frequencies $f = 50\ (cp \pm 1)$ Hz with $p = 12$ and $c = 1,\ 2,\ 3,\ 4,\ldots$

(Nunn et al., 1999). Generally these emissions are only observed on ground and rarely observed onboard satellites because they are too weak.

2. Emissions with a line structure (Fig. 2) whose frequency spacing is not a multiple of base power system frequency (''real-MLR'' events according to the classification introduced by Němec et al. (2007a)). By comparison with the event reported by Parrot et al. (2007) where this kind of emissions was observed both in the North and in the South hemisphere, it is hypothesized that this event is due to PLHR. The PLHR propagates in the ionosphere and the magnetosphere, where they may suffer a non-linear gyro-resonant interaction with energetic particles at the magnetic equator (the most favourable region for this interaction). They can be enhanced, their spectral peaks can be broadened and their frequencies can be shifted.
3. Natural periodic emissions (Figs. 3 and 4) of which the spectrogram presents lines because the periodic elements are frequency limited. The periodicity of the elements corresponds to a 2 hop bouncing wave which propagates in the magnetosphere. These events have been classified as ''real-MLR'' by Němec et al. (2007a), since they distinguished only two classes of events.
4. Triggered emissions (Fig. 5). These triggered emissions are associated with MLR. It is shown that the periodicity of the triggered elements also corresponds to a 2 hop bouncing wave. It means that these waves influence the particles in the radiation belts.

Acknowledgements

This work is supported by the Centre National d'Etudes Spatiales (CNES). It is based on observations with the magnetic field experiment IMSC and the electric field experiment ICE embarked on DEMETER. The authors thank CNES personnel involved in the mission development of the DEMETER satellite and those currently in charge of the operations in Toulouse. They thank J.J. Berthelier for the use of the electric field data. They acknowledge support of the PICS Grant No. 3725 from CNRS/DREI.

References

Ando, Y., Hayakawa, M., Molchanov, O.A. Theoretical analysis on the penetration of power line harmonic radiation into the ionosphere. Radio Sci. 37 (6), doi:10.1029/2001RS002486, 2002.

Bell, T.F., Luette, J.P., Inan, U.S. ISEE 1 observations of VLF line radiation in the earth's magnetosphere. J. Geophys. Res. 87 (A5), 3530–3536, 1982.

Berthelier, J.J., Godefroy, M., Leblanc, F., Malingre, M., Menvielle, M., Lagoutte, D., Brochot, J.Y., Colin, F., Elie, F., Legendre, C., Zamora, P., Benoist, D., Chapuis, Y., Artru, J. ICE, the electric field experiment on DEMETER. Planet. Space Sci. 54 (5), 456–471, 2006.

Gurnett, D.A. Plasma wave interactions with energetic ions near the magnetic equator. J. Geophys. Res. 81, 2765–2770, 1976.

Helliwell, R.A. Whistlers and Related Ionospheric Phenomena. Stanford University Press, Stanford, California, USA, 1965.

Helliwell, R.A., Katsufrakis, J.P., Bell, T.F., Raghuram, R. VLF line radiation in the Earth's magnetosphere and its association with power system radiation. J. Geophys. Res. 80, 4249–4258, 1975.

Kasahara, Y., Kenmochi, H., Kimura, I. Propagation characteristics of the ELF emissions observed by the satellite Akebono in the equatorial plane. Radio Sci. 29, 751–767, 1994.

Laakso, H., Junginger, H., Roux, A., Schmidt, R., de Villedary, C. Magnetosonic waves above fcH+ at geostationary orbit: GEOS 2 results. J. Geophys. Res. 95, 10,609–10,621, 1990.

Manninen, J.. Some aspects of ELF–VLF emissions in geophysical research, chap. Power Line Harmonic Radiation. Sodankylä Geophysical Observatory Publications, Sodankylä, Finland, pp. 53–84, 98, 2005.

Matthews, J.P., Yearby, K. Magnetospheric VLF line radiation observed at Halley, Antarctica. Planet. Space Sci. 29, 97–106, 1981.

Němec, F., Santolík, O., Gereová, K., Macúšová, E., de Conchy, Y., Cornilleau-Wehrlin, N. Initial results of a survey of equatorial noise emissions observed by the cluster spacecraft. Planet. Space Sci. 53, 291–298, 2005.

Němec, F., Santolík, O., Gereová, K., Macúšová, E., Laakso, H., de Conchy, Y., Maksimovic, M., Cornilleau-Wehrlin, N. Equatorial noise: statistical study of its localization and the derived number density. Adv. Space Res. 37, 610–616, 2006a.

Němec, F., Santolík, O., Parrot, M., Berthelier, J.J. Power line harmonic radiation (PLHR) observed by the DEMETER spacecraft. J. Geophys. Res. 111, doi:10.1029/2005JA011480, 2006b.

Němec, F., Santolík, O., Parrot, M., Berthelier, J.J. Comparison of magnetospheric line radiation and power line harmonic radiation: a systematic survey using the DEMETER spacecraft. J. Geophys. Res. 112, doi:10.1029/2006JA012134, 2007a.

Němec, F., Santolík, O., Parrot, M., Berthelier, J.J. Power line harmonic radiation: a systematic study using DEMETER spacecraft. Adv. Space Res. 40, 398–403, 2007b.

Němec, F., Santolík, O., Parrot, M., Bortnik, J. Power line harmonic radiation observed by satellite: properties and propagation through the ionosphere. J. Geophys. Res. 113, A08317, doi:10.1029/2008JA013184, 2008.

Němec, F., Parrot, M., Santolík, O., Rodger, C.J., Rycroft, M.J., Hayosh, M., Shklyar, D., Demekhov, A. Survey of magnetospheric line radiation events observed by the DEMETER spacecraft. J. Geophys. Res. 114, A05203, doi:10.1029/2008JA014016, 2009.

Nunn, D., Manninen, J., Turunen, T., Trakhtengerts, V., Erokhin, N. On the nonlinear triggering of VLF emissions by power line harmonic radiation. Ann. Geophys. 17, 79–94, 1999.

Park, C.G., Helliwell, R.A. Magnetospheric effects of power line radiation. Science 200, 727–730, 1978.

Park, C.G., Helliwell, R.A. Power line radiation in the magnetosphere. Adv. Space Res. 1, 423–437, 1981.

Park, C.G., Helliwell, R.A. Ground observations of power line radiation coupled to the ionosphere and magnetosphere. Space Sci. Rev. 35, 131–137, 1983.

Parrot, M., Němec, F., Santolík, O., Berthelier, J.J. ELF magnetospheric lines observed by DEMETER. Ann. Geophys. 23, 3301–3311, 2005.

Parrot, M., Buzzi, A., Santolík, O., Berthelier, J.J., Sauvaud, J.A., Lebreton, J.P. New observations of electromagnetic harmonic ELF emissions in the ionosphere by the DEMETER satellite during large magnetic storms. J. Geophys. Res. 111, doi:10.1029/2005JA011583, 2006a.

Parrot, M., Benoist, D., Berthelier, J.J., Blecki, J., Chapuis, Y., Colin, F., Elie, F., Fergeau, P., Lagoutte, D., Lefeuvre, F., Legendre, C., Lévêque, M., Pinçon, J.L., Poirier, B., Seran, H.C., Zamora, P. The magnetic field experiment IMSC and its data processing onboard DEMETER: scientific objectives, description and first results. Planet. Space Sci. 54 (5), 441–455, 2006b.

Parrot, M., Manninen, J., Santolík, O., Němec, F., Turunen, T., Raita, T., Macúšová, E. Simultaneous observation on board a satellite and on

the ground of large-scale magnetospheric line radiation. Geophys. Res. Lett. 34, L19102, doi:10.1029/2007GL030630, 2007.

Rodger, C.J., Thomson, N.R., Dowden, R.L. VLF line radiation observed by satellite. J. Geophys. Res. 100 (A4), 5681–5689, 1995.

Rodger, C.J., Clilverd, M.A., Yearby, K.H., Smith, A.J. Magnetospheric line radiation observations at Halley, Antarctica. J. Geophys. Res. 104 (A8), 17,441–17,447, 1999.

Rodger, C.J., Clilverd, M.A., Yearby, K.H., Smith, A.J. Temporal properties of magnetospheric line radiation. J. Geophys. Res. 105 (A1), 329–336, 2000.

Russel, C.T., Holzer, R.E., Smith, E.J. OGO 3 observations of ELF noise in the magnetosphere. The nature of the equatorial noise. J. Geophys. Res. 73, 755–768, 1970.

Santolík, O., Pickett, J.S., Gurnett, D.A., Maksimovic, M., Cornilleau-Wehrlin, N. Spatio-temporal variability and propagation of equatorial noise observed by cluster. J. Geophys. Res. 107 (A12), doi:10.1029/2001JA009159, 2002.

Santolík, O., Němec, F., Gereová, K., Macúšová, E., de Conchy, Y., Cornilleau-Wehrlin, N. Systematic analysis of equatorial noise below the lower hybrid frequency. Ann. Geophys. 22, 2587–2595, 2004.

Yearby, K.H., Smith, A.J., Bullough, K. Power line harmonic radiation in Newfoundland. J. Atmos. Terr. Phys. 45, 409–419, 1983.

František NĚMEC

Ondes électromagnétiques TBF observées par DEMETER

Résumé

Les résultats basés sur les mesures d'ondes électromagnétiques effectuées par le satellite DEMETER sont présentés. Nous nous concentrons sur deux phénomènes différents : 1) les effets liés à l'activité sismique 2) les émissions avec des structures fréquentielles linéaires.

1) Nous présentons une étude statistique de l'intensité des ondes électromagnétiques observées à proximité des tremblements de terre. Nous montrons que pendant la nuit il y a une diminution statistiquement significative de l'intensité des ondes peu avant le choc principal.

2) Nous présentons une étude systématique des événements ayant des structures fréquentielles linéaires. Un ensemble d'événements statistiquement significatif a été obtenu en utilisant une procédure automatique ainsi qu'une inspection visuelle des données. Tous les événements sont entièrement analysés et classifiés. Dans la gamme EBF (ou toutes les six composantes électromagnétiques sont mesurées pendant le mode Burst), une analyse détaillée des ondes a été faite.

Mots clés : plasma spatial, ondes électromagnétiques, effets séismo-électromagnétiques, PLHR, MLR

VLF electromagnetic waves observed by DEMETER

Abstract

Results based on wave measurements performed by the DEMETER spacecraft are presented. We focus on two different phenomena : 1) effects possibly connected with seismic activity 2) emissions with a line structure.

1) We present a statistical study of intensity of electromagnetic waves observed in the vicinity of earthquakes. It is shown that during the night there is a statistically significant decrease of wave intensity shortly before the time of the main shock.

2) We present a survey of the events with a line structure. A statistically significant set of events has been obtained both by using an automatic identification procedure and visual inspection of the data. All the events are thoroughly analyzed and classified. Moreover, in the ELF range (where all the six electromagnetic field components are measured during the Burst mode), a detailed wave analysis has been performed.

Keywords : space plasma, electromagnetic waves, seismo-electromagnetic efects, PLHR, MLR

LPC2E/CNRS, 3A Avenue de la Recherche Scientifique, 45071 Orléans Cedex 2